

**Strength, textures, microfabrics and
acoustic properties of active plate margin
sediments on- and offshore SW Japan**

DISSERTATION

zur Erlangung des Doktorgrades

an der Mathematisch-Naturwissenschaftlichen Fakultät

der Christian-Albrechts-Universität zu Kiel

vorgelegt von

Kai Schumann

Kiel, 2013

Referent:Professor Jan H. Behrmann

Koreferent: Professor Volker Feeser

Tag der mündlichen Prüfung:06. Februar 2014

Zum Druck genehmigt:10. Februar 2014

.....

Der Dekan

Hiermit erkläre ich, dass ich die vorliegende Doktorarbeit selbständig und ohne Zuhilfenahme unerlaubter Hilfsmittel erstellt habe. Weder diese noch eine ähnliche Arbeit wurde an einer anderen Abteilung oder Hochschule im Rahmen eines Prüfungsverfahrens vorgelegt, veröffentlicht oder zur Veröffentlichung vorgelegt. Ferner versichere ich, dass die Arbeit unter Einhaltung der Regeln guter wissenschaftlicher Praxis der Deutschen Forschungsgemeinschaft entstanden ist.

Kiel, den

Kai Schumann

To my wife

Preface

This thesis comprises three independent articles, submitted for publication to international journals. Hence, the articles may be revised during the process of publication. Each article is a stand-alone article with its own abstract, introduction, method chapter, results and discussion chapter, conclusion and reference list. The articles are:

1. P and S wave velocity measurements of water-rich sediments from the Nankai Trough, Japan
by Kai Schumann, Michael Stipp, Jan H. Behrmann, Dirk Klaeschen and Detlef Schulte-Kortnack;
Journal of Geophysical Research, 119 doi: 10.1002/2013JB010290
2. Texture development in naturally compacted and experimentally deformed silty clay sediments from the Nankai Trench, Japan (NanTroSEIZE, IODP Expeditions 315, 316, 333)
by Kai Schumann, Michael Stipp, Bernd Leiss and Jan H. Behrmann;
submitted to Tectonophysics
3. Geotechnical behavior of mudstones from the Shimanto and Boso accretionary complexes, and implications for the recently active Nankai Accretionary Prism
by Kai Schumann, Jan H. Behrmann, Michael Stipp, Yuzuru Yamamoto, Yujin Kitamura and Christof Lempp;
submitted to Earth, Planets and Space

During preparation of the articles I applied seismic time series analysis to sonic velocity measurements conducted during triaxial deformation of marine sediments, carried out sample preparation and point counting, used x-rays to conduct Rietveld-based synchrotron texture analysis, measured shape preferred orientation of micropores and mineral grains using Scanning Electron micrographs and, furthermore, conducted element dispersive x-ray measurements. In addition, I sampled outcrops of the Shimanto belt during a comprehensive field work campaign on Shikoku Island (Japan). The main technical objectives of my

work were the data acquisition, data processing as well as data presentation on conferences and, moreover, the preparation of the three manuscripts.

In addition to the three major manuscripts that form the main body of this thesis (chapters 2, 3 and 4), I contributed data, observations and interpretations as co-author to one more scientific article containing information pertaining to my thesis project. It is entitled:

“Strong sediments at the deformation front, and weak sediments at the rear of the Nankai accretionary prism, revealed by triaxial deformation experiments”

by Michael Stipp, Malte Rolf, Yujin Kitamura, Jan H. Behrmann, Kai Schumann, Detlef Schulte-Kortnack and Volker Feeser, published in *Geochemistry, Geophysics, Geosystems*. This work is presented as chapter 5 of the thesis, of which the major results are summarized in chapter 6. Additional material belonging to chapter 2, 3, 4 and 5 is enclosed in the appendix.

During the completion of my thesis-related work, I further cooperated with members of other project and working groups at GEOMAR, and contributed to the following articles which are not part of the thesis:

1. Acoustic mapping of the Ilulissat Ice Fjord mouth, West Greenland;
by Kai Schumann, David Völker, Wilhelm R. Weinrebe
published in *Quaternary Science Reviews*, 40, 78-88, 2012
2. Insights from trace element geochemistry as to the roles of subduction zone geometry and subduction input on the chemistry of arc magmas;
by Heidi Wehrmann, Kaj Hoernle, Dieter Garbe-Schönberg, Guillaume Jacques, Julia Mahlke, Kai Schumann
submitted to *International Journal of Earth Sciences*.
3. Sulphur and chlorine geochemistry of mafic to intermediate tephras from the Chilean Southern Volcanic Zone (33-43°S) compared with those from the Central American Volcanic Arc;
by Heidi Wehrmann, Kaj Hoernle, Guillaume Jacques, Dieter Garbe-Schönberg, Kai Schumann, Julia Mahlke, Luis Lara
submitted to *International Journal of Earth Sciences*.

Abstract

Earthquakes are the violent expression of plate motion caused by a sudden release of elastic energy along fault planes known from a variety of tectonic settings. The seismically most active regions on Earth are the subduction zones, where lithospheric plates descend. Especially the Nankai subduction zone southeast of the Japanese islands of Honshu and Shikoku is known for the repeated occurrence of strong earthquakes and devastating tsunamis. The large-scale processes of stick-slip instabilities responsible for earthquake generation are vastly studied, but at least in parts not well understood. This thesis aims to investigate the fundamental processes of faulting and earthquake generation in a setting of converging lithospheric plates. Deformation processes in front of the seismogenic zone and in the accretionary wedge are in the main focus of this work. The question whether the rocks of the Nankai accretionary prisms are capable to produce surface breaks and related tsunamis by brittle faulting, or whether these rocks are capable of distributing deformation within large volumes (slow, stable slip) will be answered. For this purpose, deformation experiments of drill cores from the Nankai accretionary prism were conducted to provide information on the geotechnical properties of the near-surface sediments. Analogue cases exposed along the coast line of Shikoku Island and Boso Peninsula cover those parts in the accretionary prism not accessible by deep sea drilling, so far. Microstructural studies will connect the laboratory data to the natural case.

The first study provides a unique dataset of sonic velocities measured during triaxial deformation under laboratory conditions. The silty clay and clayey silt samples were obtained from IODP Expeditions 315, 316 and 333. Seismic time series analysis helped to increase the data quality and to identify erroneous first arrival picks identified by trace-by-trace picking. During axial deformation, the compressional and shear wave velocities (V_p and V_s) range between 1300 – 2200 m/s and 150 -800 m/s, respectively. Different velocities were measured for the tectonic settings. Samples from the frontal thrust (accretionary prism toe) show higher V_p compared to the samples from the megasplay fault settings, whereas lowest V_p were measured for the incoming plate sediments, being characterized by higher clay contents compared to the accretionary prism sediments. Generally,

V_p increases slightly with increasing effective confining pressure and effective principal stress. Similar observations were made for V_s , irrespective of tectonic setting and composition. Shear, bulk and elastic moduli were calculated from the velocities to differentiate between tectonic settings. The shear moduli ranges between 0.2 – 1.3 GPa and the bulk modulus between 3.8 – 8.4 GPa, while the elastic moduli, ranges between 0.5 – 3.8 GPa pointing to over-consolidation of the accretionary prism toe samples and normal consolidation of the footwall of the megasplay fault and incoming plate.

The results of Rietveld refinement-based synchrotron texture analysis and microfabric studies of the slity clay and clayey silt samples are reported in the second part of the thesis. Crystallographic preferred orientation (CPO) of illite, kaolinite and smectite basal planes is bedding-parallel and increases with depth. Bedding parallel orientation of the basal planes of the phyllosilicates is preserved in samples tilted by tectonic deformation, indicating progressive burial and compaction as texture forming processes. Shape preferred orientation (SPO) of micropores and detrital illites investigated by Scanning Electron micrographs indicate natural compaction as well. Samples deformed in triaxial experiments differ from these observations as basal planes of phyllosilicates and calcite are oriented almost always perpendicular to the experimental shortening direction. SPO analyses indicate reorientation or flattening of the micropores due to experimental deformation. From these data we show that even in water-rich fine-grained and phyllosilicate rich sediments synchrotron x-ray radiation allows to quantify textures.

In the third part, the results of triaxial deformation tests of mudstone samples derived from the tectonically exhumed accretionary prisms belonging to the Boso and Shimanto Belts, representing pre-exhumation burial depths up to 9000 m are presented. To investigate the geomechanical properties of these rocks, pressure stepping tests, constant confining pressure tests and a cyclic loading tests were conducted. To determine the effective shear parameters angle of internal friction and cohesion experimental results were used. Friction angles between 30 and 50° are rather high. The sample cohesion for Boso and Shimanto ranges between 2 and 6 MPa and 13 and >30 MPa, respectively. Due to structural and compositional similarities to the Nankai accretionary prism, the results can be

used to estimate the geomechanical properties of the deeper parts of the Nankai accretionary prism, which are not accessible by deep sea drilling. The data shows that the forearc rocks are relatively strong. Diagenesis and/ or low-grade metamorphism increase the cohesion. From the data we conclude that stresses up to 18 MPa can be transmitted to the updip limit of the seismogenic zone and between 5 to 13 MPa to the actively deforming frontal prism.

In the article of Stipp et al. (2013), to which I contributed as co-author, whole-round core samples drilled during IODP Expedition 315, 316 and 333 were experimentally deformed in a triaxial cell having been drilled in depths between 28 – 128 m below sea floor (mbsf). During undrained experimental deformation, at 400 to 1000 kPa confining pressure, between 0.001 – 9.0 mm/min displacement rate, up to ~64% axial compressive strain was reached. Although composition and grain size distribution of the silty clay and clayey silt samples is rather similar, geomechanical data lead to the distinction of two ‘rheological groups’. (1) Structurally weak samples, showing peak deviatoric stress conditions after few percent of compressional strain, continuous stress decrease after peak conditions and contractant behavior (increasing pore pressure) and (2) structurally strong samples, showing continuous strength increase or weaken only moderately at much higher strength levels and higher strains. Strong samples from the accretionary prism toe are overconsolidated, while the weak samples from further upslope are normally consolidated, similar to the samples from the incoming plate.

The mechanical state of the décollement can be inferred from the results of the triaxial tests. Up to 18 MPa can be transmitted to the updip limit of the seismogenic zone and up to 13 MPa to the backstop of the active deforming prism. Overconsolidated frontal thrust sediments are able to stable slip and strain partitioning resulting in folding. The middle part of the accretionary prism tends to creep under cyclic loading. Normal consolidated sediments of the megasplay setting are capable to unstable slip and brittle faulting and thus can produce surface breaks. Crystallographic preferred orientation and shape preferred orientation may act as runaway structures transmitting strains to the (near) sea floor.

Kurzfassung

Erdbeben sind Erschütterungen des Erdkörpers, welche durch das plötzliche Freisetzen von Bewegungsenergie entlang von Bruchfugen entstehen, ein Prozess der besonders an Plattengrenzen auftritt. Zu den seismisch aktivsten Zonen der Erde gehören die Kollisionszonen an denen Lithosphärenplatten abtauchen. Die Nankai Subduktionszone, südöstlich der japanischen Inseln Honshu und Shikoku, ist bekannt für das wiederholte Auftreten von Erdbeben mit Stärken über $8 M_w$, die zerstörerische Tsunamis zur Folge hatten. Die großmaßstäblichen Prozesse der Erdbebenentstehung wurden umfangreich untersucht, sind aber nur teilweise verstanden. Die vorliegende Arbeit untersucht die grundlegenden Prozesse der Erdbebenentstehung an konvergenten Plattengrenzen. Dazu werden Deformationsprozesse die auf der Plattengrenze (Décollement) oberhalb der seismogenen Zone sowie im Akkretionskeil stattfinden untersucht. Dabei soll geklärt werden, ob die Sedimente und Sedimentgesteine des Nankai Akkretionskeils spröde versagen und Oberflächenbrüche erzeugen und somit zerstörerische Tsunamis zur Folge haben können, oder ob die Gesteine eher zum langsamen Kriechen neigen und Deformationsbewegungen in großen Gesteinsvolumina verteilt werden. Diese Fragestellung wird mittels Deformationsexperimenten an Bohrkernen des Nankai Akkretionskeils und zwei an Land aufgeschlossenen Analogfällen untersucht. Zusätzlich werden experimentell erzeugte Mikrostrukturen mit den natürlich auftretenden Mikrostrukturen in Bohrkernen verglichen. Diese Ergebnisse ermöglichen die Projektion der im Labor gewonnenen Daten auf die in der Natur auftretenden Prozesse.

Im ersten Teil der Arbeit werden die Ausbreitungscharakteristika von Schallwellengeschwindigkeiten untersucht. Dazu wurden triaxiale Scherversuche an siltigen Ton und tonigen Silt durchgeführt. Die verwendeten Bohrkern wurden während der IODP Bohrfahrten 315, 316 und 333 im Nankai Akkretionskeil erbohrt. Unter Verwendung der seismischen Zeitreihenanalyse konnte die Qualität der Messdaten deutlich verbessert werden und die zuvor im Labor bestimmten Ersteinsätze kontrolliert und korrigiert werden. Während der Deformationsexperimente wurden Kompressionswellengeschwindigkeiten (V_p) zwischen 1300 und 2200 m/s gemessen. Die Scherwellengeschwindigkeiten (V_s)

lagen zwischen 150 und 800 m/s. Die verschiedenen tektonischen Bereiche im Akkretionskeil konnten durch charakteristische Schallwellengeschwindigkeiten differenziert werden. Sedimente vom Fuß des Akkretionskeils zeigten höhere V_p im Vergleich zu Sedimenten des oberen Hanges im Bereich einer Zweigstörung. Die geringsten P-Wellen Geschwindigkeiten wurden in den unverformten Sedimente der abtauchenden Platte gemessen. Im Verlauf der Experimente zeigte sich, dass V_p mit steigendem Umschließungsdruck und steigendem axialen Druck nur leicht ansteigt. Ähnliche Beobachtungen wurden auch für V_s gemacht, wobei hier ein stärkerer Anstieg während der Deformation festgestellt werden konnte. Aus den gewonnenen Geschwindigkeitsdaten konnten die Scher-, Kompressions- und Elastizitätsmoduln der Proben bestimmt werden. Die Scher- und Kompressionsmoduln liegen dabei zwischen 0,2 und 1,3 GPa bzw. zwischen 3,8 und 8,4 GPa. Die Elastizitätsmoduln liegen zwischen 0,5 und 3,8 GPa. Die Auswertung der Messdaten deutet auf eine Überkonsolidierung der Sedimente vom Fuß des Akkretionskeils hin, während die Sedimente im Bereich der Zweigstörung und der abtauchenden Platte normal konsolidiert sind.

Die Untersuchung der Mikrostrukturen und Texturen der Proben wird im zweiten Teil der Arbeit vorgestellt. Zur Untersuchung der Texturen wurde Synchrotron Röntgenstrahlung angewendet und die Datenauswertung mittels Rietveldverfeinerung ermöglichte die Bestimmung der kristallographischen Vorzugsorientierung (CPO). Die CPO der Basisflächen von Illit, Kaolinit und Montmorillonit sind parallel zur sedimentären Schichtung ausgerichtet und nehmen mit zunehmender Bohrlochtiefe zu. Diese Vorzugsorientierung bleibt in tektonisch verkippten Sedimenten erhalten und deutet somit auf Versenkung und Kompaktion als texturformende Prozesse hin. Die Vorzugsorientierung nach der Kornform (SPO) von Mikroporen und detrischen Illiten wurde mittels rasterelektronenmikroskopischen Gefügebildungen bestimmt. Diese Untersuchungen zeigen ebenfalls die natürliche Kompaktion als texturformenden Prozess an. In experimentell verformten Proben wurden andere Vorzugsorientierungen gefunden. Die Basisflächen der Phyllosilikate sowie von Kalzit sind fast ausschließlich rechtwinklig zur Experimentellen Deformation ausgerichtet. SPO Untersuchungen der experimentell verformten Proben zeigen ebenfalls eine Rotation bzw. Reorientierung der Mikroporen durch die

experimentelle Deformation an. Anhand dieser Ergebnisse konnte gezeigt werden, dass bereits wasserhaltige Sedimente mit geringer Versenkungstiefe Vorzugsorientierungen ausbilden und diese durch die lokalen tektonischen Prozesse geprägt werden.

Im dritten Teil der Arbeit werden Tonsteine des an Land exhumierten Shimanto Gürtels und des Boso Akkretionskeiles untersucht. Beide Akkretionskeile stellen Analogfälle des rezenten Nankai Akkretionskeils dar und repräsentieren unterschiedliche Versenkungstiefen. Proben des Boso Akkretionskeiles repräsentieren Versenkungstiefen von ca. 1000 m. Die Versenkungstiefen des Shimanto Gürtels liegen bei 7800 m bzw. 9000 m. Zur Untersuchung der geotechnischen Eigenschaften wurden Versuche mit variablem Umschließungsdruck und konstantem Porendruck, mit konstantem Umschließungsdruck und variablem Porendruck sowie ein Versuch unter zyklischer Belastung durchgeführt. Die experimentellen Ergebnisse wurden genutzt, um die effektiven Scherparameter der getesteten Gesteine zu bestimmen. Die Werte des inneren Reibungswinkels sind teilweise relativ hoch und liegen zwischen 30 und 50°. Die Kohäsion der Boso Proben liegt zwischen 2 und 6 MPa und zwischen 13 und >30 MPa für die Tonsteine von Shimanto. Beide Akkretionskeile sind strukturell sowie in ihrer Zusammensetzung dem Nankai Akkretionskeil sehr ähnlich und können aus diesem Grund zur Abschätzung der geomechanischen Parameter des Nankai Akkretionskeils genutzt werden. Somit lassen sich geomechanische Parameter in Bereichen abschätzen, die bisher nicht durch Bohrungen erreicht werden konnten. Dabei zeigt sich, dass die Gesteine des Forearcs relativ fest sind. Aus den Ergebnissen lässt sich schließen, dass Drucke bis 18 MPa zur oberen Grenze der seismogenen Zone geleitet werden können und zwischen 5 bis 13 MPa bis zum sich aktiv verformenden Teil des Akkretionskeils.

Im letzten Teil der Arbeit, einem wissenschaftlichen Artikel von Stipp et al. (2013) zu dem ich als Ko-Autor beigetragen habe, werden die Ergebnisse der triaxialen Scherversuche des Nankai Akkretionskeils vorgestellt. Bei den Proben handelt es sich um die Sedimente die bereits im ersten und zweiten Teil der Arbeit vorgestellt wurden. Die Proben wurden in tiefen zwischen 28 und 128 m unter dem Meeresboden erbohrt. Während der undrainierten Deformation bei Umschließungsdrücken zwischen 400 bis 1000 kPa und Versatzraten zwischen

0,001 und 9,0 mm/min wurden Verformungen bis 64% erreicht. Obwohl die Proben in ihrer Zusammensetzung und Korngrößenverteilung sehr ähnlich sind, führten die Experimente zur Differenzierung zweier rheologischer Gruppen. Es wurden strukturell schwache Proben, welche die maximale deviatorische Spannung bereits nach wenigen Prozent Verformung erreichten und einen kontinuierlichen Spannungsabbau zeigten, von strukturell starken Proben mit stetig steigenden deviatorischen Spannungen bzw. nur geringem Spannungsabbau unterschieden. Die strukturell starken Proben treten am Fuß des Akkretionskeils auf und sind überkonsolidiert, während die strukturell schwachen Proben im Bereich einer Zweigstörung auftreten und normal konsolidiert sind. Die Proben der abtauchenden Platte zeigen ebenfalls normale Konsolidierung.

Aus den Ergebnissen der Arbeit kann auf die mechanischen Eigenschaften des Décollements geschlossen werden. Bis zu 18 MPa können demnach auf der Plattengrenze bis zum oberen Ende der seismogenen Zonen transportiert werden. Zwischen 5 und 13 MPa bis zum aktiv verformenden Teils des Akkretionskeils. Die überkonsolidierten Sedimente vom Fuß des Akkretionskeils sind in der Lage stabil zu gleiten, während die Gesteine des mittleren Teils des Akkretionskeils unter zyklischer Belastung kriechen. Die normal konsolidierten Gesteine im Bereich der Zweigstörung neigen zu sprödem Bruchverhalten und können Oberflächenbrüche ausbilden. Diese Eigenschaft wird vermutlich durch Schwächezonen begünstigt, die mit der Ausbildung von Vorzugsorientierungen im Sediment im Zusammenhang stehen. Schwächezonen wirken dabei als Strukturen durch die Versätze bis zum Meeresboden geleitet werden können, wodurch es zur Ausbildung von Tsunamis kommen kann.

Contents

1	Introduction	1
1.1	Background and rationale	1
1.2	Aims of this study	3
1.3	Deduction of working packages	4
1.3.1	Triaxial testing and velocity measurements (WP1)	4
1.3.2	Microstructural analysis (WP2)	5
1.3.3	Triaxial tests of natural analogue cases (WP3)	5
1.4	Subduction zones	6
1.4.1	Structural elements of subduction zones	9
1.4.2	Accretionary and erosive subduction zones	11
1.5	Geological setting	12
1.5.1	Tectonic evolution of the Japanese Islands	13
1.5.2	The Shimanto Belt on Shikoku Island	16
1.5.3	The Boso-Miura accretionary prism	17
1.5.4	Nankai trough	18
1.6	References from introduction	20
2	Manuscript #1	31
3	Manuscript #2	81
4	Manuscript #3	137
5	Manuscript #4	183
6	Synopsis – conclusion – outlook	229
6.1	Synopsis	229
6.2	Conclusion	234
6.3	Outlook	236
6.4	References	239
7	Appendix	246

List of Tables

Manuscript #1

Table 2. 1: List of investigated samples	38
Table 2. 2 Phases of pressure increase during the experiments.	44
Table 2. 3: Overview of the experiments	49
Table 2. 4: Shear, bulk and elastic moduli of the samples.	62

Manuscript #2

Table 3. 1: Composition of the samples.	89
Table 3. 2: Point counting results.....	103
Table 3. 3: Comparison of the sample compositions	109
Table 3. 4: Results of strain analyses of the incoming plate sediments.	122

Manuscript #3

Table 4. 1: Overview of the experimental samples.....	151
Table 4. 2: Experimental conditions	152
Table 4. 3: Mineralogical composition of Shimanto samples.....	155
Table 4. 4: Mineralogical Boso accretionary prism samples	156
Table 4. 5: Effective shear parameters determined from the triaxial tests.....	163

Manuscript #4

Table 5. 1: List of drill core.	192
Table 5. 2: Shear parameters	205

List of Figures

Introduction

Figure 1. 1: Worldwide distribution of earthquake.	7
Figure 1. 2: Sketch of a subduction zone	9
Figure 1. 3: The position of the study areas.	12
Figure 1. 4: Paleogeographic evolution of the Japanese Islands.....	14
Figure 1. 5: Detailed paleogeographic maps of Japan.	15
Figure 1. 6: Evolution of the Nankai accretionary prism.....	18

Manuscript #1

Figure 2. 1: Setting and of the Nankai Trough.....	36
Figure 2. 2: Picking and processing procedures.....	47
Figure 2. 3: V_p (A) and V_s (B) versus the effective confining pressure.	53
Figure 2. 4: V_p (A) and V_s (B) versus the effective confining pressure	56
Figure 2. 5: V_p (A) and V_s (B) versus the effective principal stress.	57
Figure 2. 6: V_p (A) and V_s (B) versus the effective principal stress.	59
Figure 2. 7: V_p -porosity relationships	60
Figure 2. 8: P-wave velocity measurements of Site C0001D	63
Figure 2. 9: V_p/V_s versus the effective principal stress.....	68
Figure 2. 10: Plot of Poisson's ratio versus effective largest principal stress...	69

Manuscript #2

Figure 3. 1: Setting of the Nankai Trough	88
Figure 3. 2: Microstructural analysis	94
Figure 3. 3: Plate detector images	97
Figure 3. 4: Refined spectrum and 2D-Multiplot.....	100
Figure 3. 5: Point counting results	102
Figure 3. 6: Rose diagrams.....	106
Figure 3. 7: Pole figure of experimental undeformed samples	112
Figure 3. 8: Pole figures of experimentally deformed samples	116
Figure 3. 9: CPO intensities of illite, kaolinite and calcite	119
Figure 3. 10: CPO intensity of illite, kaolinite and calcite.....	121

Figure 3. 11: SEM micrograph	124
------------------------------------	-----

Manuscript #3

Figure 4. 1: Seismic section through the Nankai accretionary prism	142
Figure 4. 2: Map of central Japan	144
Figure 4. 3: Shimanto Belt stratigraphy	146
Figure 4. 4: Stress-strain plots.....	157
Figure 4. 5: Drill cores after triaxial testing.....	159
Figure 4. 6: Stress-strain plots.....	160
Figure 4. 7: Stress-strain plots.....	161
Figure 4. 8: Stress-strain plot	161
Figure 4. 9: Cyclic deformation experiment.	162
Figure 4. 10: Mohr Circle constructions.	165
Figure 4. 11: p'-q'- plot.....	166
Figure 4. 12: Determination of effective shear parameters.....	167
Figure 4. 13: Plot of cohesion versus depth of burial.	172

Manuscript #4

Figure 5. 1: Map of Nankai Trough area	190
Figure 5. 2: Seismic cross section.	191
Figure 5. 3: Undeformed and deformed samples	194
Figure 5. 4: Mineral composition.....	197
Figure 5. 5: Smear slide analysis	198
Figure 5. 6: Grain size distribution	199
Figure 5. 7: Compression test	201
Figure 5. 8: Results of pressure stepping experiments.....	201
Figure 5. 9: Results of rate stepping experiments	202
Figure 5. 10: Mohr-Coloumb diagrams.	206
Figure 5. 11: Stress path diagrams	207
Figure 5. 12: Distribution of structurally weak and strong samples.	216

1 Introduction

1.1 Background and rationale

Convergent plate margins are the seismically most active regions on Earth. Porous sediments are brought to the subduction zone by the plate motion and are added to the accretionary prism. During accretion and incorporation into the accretionary prism, sediments undergo considerable bulk strain (Davis et al., 1983; Morgan et al., 2007; Underwood 2007). At the frontal thrust zone, sediments deform until a critical wedge taper is reached, at which they are amenable to stable sliding (e.g. Davis et al., 1983). Most of the strain in accretionary wedges is accommodated by frontal accretion and tectonic shortening (e.g. Brown et al., 1990). As burial depth increases, enhanced pressure conditions and lithification change the physical properties of the accreted sediments, turning them into rocks (e.g. Carson et al., 1982; Moore and Vrolijk 1992; Erickson and Jarrard 1998; Bilek and Lay 1999; Morgan et al., 2007; Moore and Saffer 2001). The transition of porous sediments to brittle rocks is matter of debate and is not well understood. Considering the transition from aseismic to seismic behavior, the so-called updip limit of the seismogenic zone, several processes such as changes in the physical properties due to increased pressure conditions, increasing pore pressure due to mineral transitions, evolution of mineral fabric, changes in the frictional behavior due to increased thermal conditions are discussed in the literature (e.g. Logan and Rauenzahn 1987; Byerlee 1990; Scholz 1990; Hyndman and Wang 1993; Tichelaar and Ruff 1993; Hyndman et al., 1995, 1997; Marone et al., 1998; Oleskevich et al., 1999; Moore and Saffer 2001; Saffer and Marone 2003; Morgan et al., 2007; Underwood 2007). For a better understanding of the faulting process and earthquake generation, the NanTroSEIZE drilling in the Japan forearc was initiated to core, sample and instrument the seismogenic portion of a plate-boundary fault (Tobin and Kinoshita 2006). Seismic studies provide an insight into the structural framework of the accretionary prism (e.g. Moore et al., 2009). Data of Moore et al. (2009) indicate a highly complex frontal thrust zone at the seaward edge of the accretionary prisms (accretionary prism toe), characterized by active thrusts and a steep slope of $\sim 10^\circ$. Landward of this structure, a presently inactive imbricate thrust zone follows, characterized by

thrust packages of accreted sediments. This section is overlain by undeformed slope sediments. Further landward, the slope of the accretionary prism increases again, and a regional out-of-sequence thrust crosscuts the accretionary prism. The so-called megasplay fault (Park et al., 2002) branches in approximately 10 km depth from the décollement (Park et al., 2002; Moore et al., 2009), crosscuts the whole forearc and reaches the seafloor in the vicinity of the drill sites C0001 and C0004. Landward of the megasplay fault the Kumano forearc basin follows, filled by more than 2 km of sediment (Moore et al., 2009). The plate boundary fault (décollement) separates offscraped accreted sediments and underthrust strata (Moore 1989). Since the mechanical properties of the accreted sediments and also of the décollement are influenced by factors such as sediment composition, sediment texture, grain fabric and many other factors (Lupini et al., 1981; Mitchell 1993; Underwood 2007), it is important to drill, sample and characterize the accretionary prism materials. The scientific results of the IODP Expeditions 315, 316 and 333, were reported by the Expedition 315 Scientists (2009), Expedition 316 Scientists (2009a-d) and the Expedition 333 Scientists (2012a, b). To approximate the geotechnical parameters of deeper parts of the accretionary prism not accessible by drilling, the exhumed Shimanto belt and the Boso accretionary prism are studied. Because of their similar composition, age and state of diagenesis, both ancient accretionary prisms are geotechnical reference cases to the active Nankai accretionary prism. The Cretaceous to Tertiary Shimanto belt (e.g. Kumon 1983; Aitchison 1986; DiTullio and Hada 1993; Underwood et al., 1993) extends parallel to the Nankai Trough (Kawabata et al., 2007) over 1500 km along the coast of south-east Japan (Kumon 1983; Aitchison 1986; DiTullio and Byrne 1990), represents pre-exhumation depths of 7800 m and 9000 m (Underwood et al., 1992) and are thought to represent seismogenic fault zone rocks (Ikesawa et al., 2003; Kitamura et al., 2005). The Miocene Boso-Miura accretionary prism (Yamamoto 2006) is exposed in the Tokyo bay region on the Boso- and Miura peninsulas (Honshu Island). High preserved porosities ranging between 30 and 50% indicate burial depths of less than 1000 m (Yamamoto et al., 2005).

1.2 Aims of this study

To advance the question whether rocks of the Nankai accretionary prism are prone to brittle faulting and, thus, to produce surface breaks resulting in devastating tsunamis in the consequence of large seismic events, or if the rocks are amenable to slow, stable slip and strain distribution within large volumes, triaxial deformation experiments, sonic velocity measurements were conducted, and the microstructure and texture of the samples was investigated.

By triaxial testing, principal geotechnical properties can be determined (Byerlee 1978). Rheology and strength characteristics of the silty clay and clayey silt samples can be determined and since experimental conditions are very similar to nature, the experimental results can be used to characterize the Nankai accretionary prism sediments. Compaction, dewatering and tectonic deformation in nature and during experimental shear change the sediments physical properties (e.g. Carson et al., 1982; Moore and Vrolijk 1992; Erickson and Jarrard 1998; Bilek and Lay 1999; Moore and Saffer 2001). Sonic velocities are dependent on the physical properties such as porosity, pore water content, effective confining pressure, and effective principal stress (e.g. Bourbie et al., 1987). For this reason, sonic velocities can be used to estimate the lithological and mechanical properties and to characterize the sediments of the Nankai through. In addition to triaxial results (Stipp et al., 2013; chapter 5), the sonic velocities, especially the V_p/V_s ratio is used to characterize the sediments (e.g. Pickett 1963; Tsuji et al., 2011) and to determine the shear, bulk and elastic modulus. Compacted and deformed sediments evolve anisotropies regarding shear strength, acoustic velocity and permeability (e.g. Bennett et al., 1981; Fawad et al., 2010; Jones 1994; Rai and Hanson 1988; Voltolini et al., 2009) controlled by the sediments' fabrics (e.g. Donath 1961; Rai and Hanson 1988; Shea and Kronenberg 1993; Johansen et al., 2004; Beeler 2007; Voltolini et al., 2009). The microstructure of the natural and experimental deformed samples was investigated by scanning electron micrographs and synchrotron x-ray texture analysis. The microstructure analysis can be used to characterize the response of the constituent minerals to experimental deformation. Comparing natural and experimental microstructures allows to identify the deformation mechanics and to assess whether natural and experimental deformation are similar. The knowledge of the deformation

processes is then used to correlate the experimental results to the natural case and possible, to extrapolate the experimental results to greater depth. To guide the extrapolation, geotechnical reference cases of Shimanto and Boso, both representing exhumed ancient accretionary prisms, are investigated by triaxial deformation experiments. Due to the structural and compositional similarity, rock samples from both accretionary prisms can be used to deduce the geotechnical properties of deep buried sediments in the Nankai accretionary prism not accessible by drilling. In combination with the data presented by Stipp et al. (2013), the data allow to evaluate the evolution of the geotechnical parameters with burial depth in the Nankai accretionary prism. Additionally, Nankai drilling, seismic cross sections and geotechnical and microstructural analysis can be linked and basic parameters of the rocks forming the décollement zone and the accretionary prism above the décollement can be deduced.

1.3 Deduction of working packages

1.3.1 Triaxial testing and velocity measurements (WP1)

Triaxial testing of cylindrical samples (50 mm diameter) from Nankai accretionary prism was conducted in a triaxial apparatus with a maximal axial load of 10 kN and confining pressure of 1000 kPa. In the consolidated undrained tests, the principal stresses were set to be $\sigma_1 > \sigma_2 = \sigma_3$. The apparatus is equipped with a controlling system for axial load, cell pressure, displacement, pore pressure, backpressure and a controlling computer. These data allow deriving strength properties of the tested materials. Prior to triaxial testing, a phase of saturation and consolidation was carried out. Multiple deformation cycles were conducted to determine the friction coefficient at different confining pressures. Additionally, the triaxial apparatus is equipped with Global Digital Systems Ltd bender elements to measure travel times during triaxial testing. The piezoelectric bender elements produce a sine wave with 5 and 10 kHz frequency to generate the sonic signal.

1.3.2 Microstructural analysis (WP2)

X-ray texture analysis of the natural and experimental deformed samples was conducted at the beam line W2 of the HASYLAB x-ray wiggler hall at the German Electron Synchrotron source (DESY) in Hamburg. High energy low wavelength x-ray radiation (hard x-rays) is characterized by relatively low absorption coefficients and allow sample penetration of several centimeters. In advantage to neutron radiation and common x-rays, synchrotron x-rays are not influenced by the pore water content. The plate detector images display Debye-Scherrer cones as rings, in which each ring represents a (hkl) plane. Data analysis was conducted using the MAUD program, which combines the crystal structure refinement by the Rietveld method (Rietveld 1969) with quantitative texture analysis. In addition to x-ray investigation, scanning electron microscopy and electron microprobe analysis were carried out using a JEOL JXA 8200 electron microprobe. Natural and experimental deformed sample material was used to investigate the shape preferred orientation of micropores and mineral grains.

On the base x-ray investigation and microstructural data sets we were able to infer deformation mechanisms for the natural and the experimental samples.

1.3.3 Triaxial tests of natural analogue cases (WP3)

For triaxial testing of the samples representing the deeper part of the Nankai accretionary prisms, a 70 MPa pressure vessel capable to control the pore pressure and a hydraulic 5 MN pressure device was used for triaxial testing. For the triaxial tests, drill cores of 70 mm diameter and between 100 to 140 mm length were used. Deformation experiments were carried out at 25 and 65 MPa confining pressures (σ_3) and pore pressure conditions ranging between 25% and 90% of σ_3 . Samples were axially loaded with displacement rates of 5.7×10^{-6} /s (length normalized strain rate) until maximum differential stress of the pre-failure phase was reached.

1.4 Subduction zones

This thesis focuses on processes observed along convergent plate margins, for this reason convergent margins are described in further detail. Oceanic lithosphere is formed by active sea-floor spreading at mid ocean ridges. Over geological time, the lithosphere moves away from the active spreading center, cools down and becomes denser by thermal contraction (Turcotte and Schubert 2002). The descent of the oceanic lithosphere into the mantle is controlled by density contrasts (e.g. Richter 1977). On the one hand, cooling of the oceanic lithosphere itself can increase the density until it sinks into the mantle, whereas on the other hand, the density contrast of continental and oceanic lithosphere (compositional differences) results in the subduction of the oceanic lithosphere underneath the continental lithosphere. The subducted plate is pulled to the trench by gravitational forces. This effect is called slab pull and is one of the major driving forces of the continental drift (e.g. Forsyth and Uyeda 1975; Chapelle and Tullis 1977; Hager and O'Connell 1981; Turcotte and Schubert 2002; Collins 2003; Conrad et al., 2004; Wu et al., 2008). Another driving mechanism for continental drift is the gravitational collapse at the mid ocean ridges, pushing the oceanic plates to both sides. This process is called ridge push (e.g. Orowan 1964, 1965; Forsyth and Uyeda 1975; Bott 1991). The subduction process approximately balances the formation of oceanic lithosphere at the mid ocean ridges.

Due to the descending subduction slab, the oceanic lithosphere bends (e.g. Kohlstedt et al., 1995; Turcotte and Schubert 2002; Wu et al., 2008) and tensional forces cause faulting in the upper oceanic lithosphere. Sediments may enter the faults and grabens and become incorporated into the subduction process.

Most of the sediments, brought to subduction zones by the motion of the plates, are off-scraped at the deep-sea trench and are added to the accretionary prism, forming the landward side of the trench. The continuous process of plate convergence and ongoing accretion cause intense and complex deformation of the accreted sediments. Due to plate convergence, off-scraping, accretion and deformation, subduction zones are tectonically the most active regions on earth (e.g. Moores and Twiss 1995; Ruff 1996; Pacheco and Sykes 1992; Stern 2002) expressed by the occurrence of earthquakes.

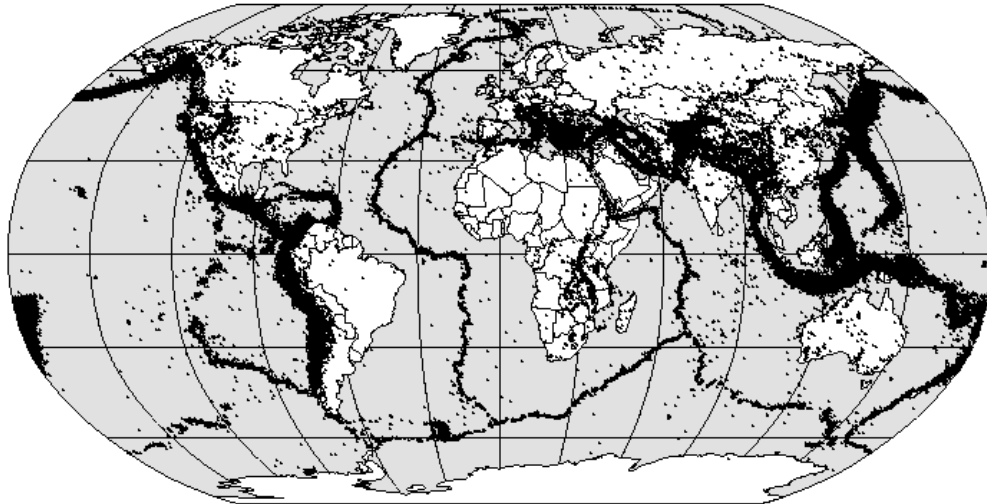


Figure 1. 1: Worldwide distribution of earthquake epicenters between the years 1963 and 1998 (358,214 events are shown). The position of earthquake occurrence highlights the plate boundaries. The divergent plate boundaries are characterized by thin lines of earthquake occurrence in the middle of the oceans, while the subduction zones are characterized by broad-banded occurrence of earthquakes. Map is taken from Lowman and Montgomery (1998).

Earthquakes occur on all types of plate boundaries (Figure 1. 1), but especially subduction zones are known for their devastating large earthquakes and generate most of the global seismicity (Ruff 1996). Two types of earthquakes can be found in subduction zones, intraplate and interplate earthquakes. Intraplate earthquakes may occur at the outer rise, in the Wadati-Benioff zone and in the overlying plate. Outer-rise earthquakes are caused by tensional forces and bending of the oceanic lithosphere due to subduction. These earthquakes are linked to normal faulting of the upper oceanic lithosphere (Ruff 1996). The deeper Wadati-Benioff seismicity is caused by down-dip tension within the subducted oceanic plate (Isacks et al., 1968; Vassiliou and Hager 1988) in depths between 300 km and ~700 km (Ruff 1996). Earthquakes in the overlying plate are associated to the occurrence of volcanoes along the arc (ascending magmas) and tectonic activity in the back-arc region (Ruff 1996). Interplate earthquakes are associated with frictional forces at the plate interface. These plate interface earthquakes occur along the seismogenic zone down to 50 km depth (Ruff 1996), caused by the process of underthrusting. The magnitude of these events is more dependent on the down-dip rupture length than on the rupture along strike width (Ruff 1989).

The world's greatest earthquakes and also the greatest subduction zone earthquakes occur at the plate interface between the subducted plate and

overriding plate (e.g. Ruff 1996; Ruff and Tichelaar 1996). The down-dip occurrence of these strong subduction zone earthquakes is limited to a rather narrow zone, the so called seismogenic zone (e.g. Ruff and Tichelaar 1996). The updip limit of the seismogenic zone is important for the understanding of tsunami generation (Park et al., 2002). The downdip limit and thus the extent of the seismogenic zone, is important to understand the magnitude of earthquakes (Park et al., 2002; Hyndman 2004). According to Hyndman (2004), the temperature is the factor which controls the extension of seismogenic zones, while pressure and depth have only an indirect influence. Several studies have addressed the processes controlling the updip and downdip limit of seismogenic zones (e.g. Logan and Rauenzahn 1987; Byrne et al., 1988; Byerlee 1990; Scholz 1990; Vrolijk 1990; Hyndman and Wang 1993; Tichelaar and Ruff 1993; Hyndman et al., 1995, 1997; Ruff and Tichelaar 1996; Marone et al., 1998; Oleskevich et al., 1999; Moore and Saffer 2001; Saffer and Marone 2003; Morgan et al., 2007; Underwood 2007). The position of aseismic to seismic transition is thought to be controlled by changes of physical properties of accreted sediments. Most probably, the breakdown of clay minerals is crucial for initiation of seismic behavior. At temperatures of 100-150°C smectite dehydrates and illite and chlorite are the products of this reaction. Especially illite is thought to constrain seismogenic behaviour (Moore and Moore 1998; Hyndman 2004). Another important change is the transition from shale to slate at approximately 200-250°C, resulting in an increase of the rock strength. Dehydration results in the discharge of fluids and increased pore pressures in deeper portions of the accretionary prism, which may approach lithostatic pressure, thus exerting control on the effective stress (Moore and Moore 1998). According to Tichelaar and Ruff (1993), Seno (2005) and Hyndman (2004), the downdip edge of the seismogenic zone is in depths of ~50 km, with some variation. The downdip limit of the seismogenic zone is controlled by stable sliding of crustal rocks above 350°C (temperature controlled changes in the rock rheology, Moore and Moore 1998), dewatering reactions and pore space collapse at greater depths, which produce large amounts of water, causing extensive serpentinization of the fore-arc mantle rocks. Serpentinites exhibit stable sliding below 500-600°C. Thus only a narrow zone of the total plate interface is seismogenic (2-5%, Stern 2002).

1.4.1 Structural elements of subduction zones

The principal structural elements of subduction zones are: (a) the outer rise, (b) the trench, (c) the fore-arc, (d) the magmatic arc and (e) the back-arc (Figure 1. 2).

(a) The descent of the subducting slab causes upward bending of the oceanic lithosphere (e.g. von Huene and Scholl 1991; Kohlstedt et al., 1995; Moores and Twiss 1995; Stern 2002; Turcotte and Schubert 2002; Wu et al., 2008) forming the outer rise, a distinctive topographic high (e.g. Moores and Twiss 1995; Stern 2002; Ranero et al., 2003). Bending generates tensional forces in the upper part of the oceanic lithosphere, coupled to the seismic activity and the generation of trench-parallel normal faults cutting deep into the rigid oceanic lithosphere (von Huene and Scholl 1991; Moores and Twiss 1995).

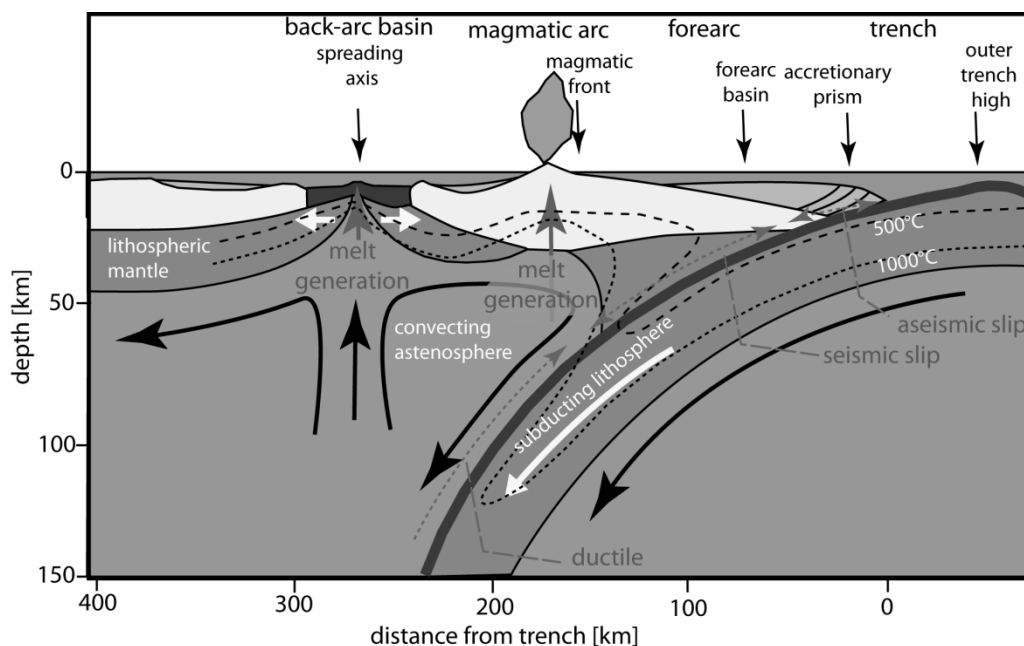


Figure 1. 2: Sketch of a subduction zone showing the main structural elements of subduction zones. Sketch is redrawn and modified according to Byrne et al. (1988) and Stern (2002).

(b) Bending of subducting plates and the beginning descent of the lithospheric slab cause the formation of a distinctive topographic depression, the deep-sea trench (e.g. von Huene and Scholl 1991; Moores and Twiss 1995; Stern 2002). Deep-sea trenches can reach depths of several kilometers. The Mariana Trench, located in the western Pacific Ocean to the east of the Mariana Islands is the deepest

depression on earth (~11000 m; Kyo et al., 1995). Deep-sea trenches can be filled by fine grained turbiditic sediments derived from the continental slope (Figure 1. 2, von Huene and Scholl 1991).

- (c) The fore-arc is a sediment filled depression between the edge of the overriding plate (deep-sea trench) and the volcanic arc. Accreted sediments from the oceanic lithosphere and sediments originating from the adjacent continent or island arc making up the sedimentary infill. At the deformation front, sediments are offscraped and transferred to the accretionary complex (von Huene and Scholl 1991; Moores and Twiss 1995; Stern 2002). Due to the evolving tectonic stress, complex deformation structures are formed in the accretionary complex. Thrust faults frequently occur within the accreted sediments (Figure 1. 2, e.g. Stern 2002). If oriented far landward and “out of sequence” referred to as a “splay faults”. This type of reverse fault is also observed in the Nankai accretionary complex (Park et al., 2000, 2002; Baba et al., 2006; Moore et al., 2007; Strasser et al., 2009). The fore-arc basin overlies the accretionary prism and is filled by sediments of the adjacent arc system (Figure 1. 2, Condie 2005).
- (d) The volcanic arc (also magmatic arc) is a narrow region of active volcanisms, formed approximately 100-200 km behind the trench. Two different varieties of arcs exist: island arcs (ocean-ocean collision) and continental arcs (ocean-continent collision, Press and Siever 2003). The occurrence of active volcanism in the volcanic arc results from dehydration reactions of crustal rocks and subducted sediments of the descending plate (e.g. Pawley and Holloway 1993; Moores and Twiss 1995; Stern 2002) causing partial melting of the mantle wedge due to the reduction of the melting temperature (e.g. Pawley and Holloway 1993; Moores and Twiss 1995; Stern 2002).
- (e) The back-arc is the most landward structural element found in subduction zones. It is located directly behind the magmatic arc. Most back-arcs are characterized by extensional tectonics and subsidence (e.g. Moores and Twiss 1995; Stern 2002). Extension in the back-arc region can lead to active spreading and to the formation of oceanic

lithosphere, such as in the case of the Japanese Islands which were separated by back-arc spreading from the Asian mainland.

1.4.2 Accretionary and erosive subduction zones

Sediments lying on top of the oceanic plate are transported towards the subduction zone by the motion of the oceanic plate. Frontal and basal accretion transfers the off-scraped sediments to the accretionary prism. However, in some subduction zones, material from the overriding plate is removed by tectonic erosion (erosion at the base of the overriding plate). Thus, it is possible to distinguish between accretionary and erosive subduction zones (e.g. von Huene and Scholl 1991; Clift and Vannucchi 2004; Bilek 2010). The process of sediment accretion by scraping off sediments from the downgoing oceanic plate is well-understood, whereas several models for subduction erosion exist. In particular, one model assumes that the friction of the plate interface is high and thus, the overriding plate is eroded at its base (e.g. von Huene et al., 2004; Bilek 2010). Another model suggests a weak plate interface and hydrofracturing at the base of the overriding plate. The fractured material is removed and involved into the subduction process (Bilek 2010). A third model suggests that erosive subduction zones evolve when the convergence rate is higher than 6 ± 0.1 cm/yr, and where the trench fill sediments do not exceed 1 km thickness while accretionary margins are thought to be formed when the convergence rate is below 7.6 cm/yr and the trench fill sediments exceed 1 km thickness (Clift and Vannucchi 2004). The theory of Clift and Vannucchi (2004) implies long-term (> 10 Ma) stable conditions. Especially the Nankai margin, which is in the focus of this thesis, experienced local erosional conditions due to the subduction of seamounts, although it is a long-term accretionary margin (Clift and Vannucchi 2004).

1.5 Geological setting

This thesis focuses on the Nankai accretionary prism located southeast (SE) of the coast of southern Japan and the geotechnical analogue cases of the Boso and Shimanto accretionary prisms. For a better understanding, the regional geology and the tectonic setting of Japan is described in the following section (Figure 1. 3).

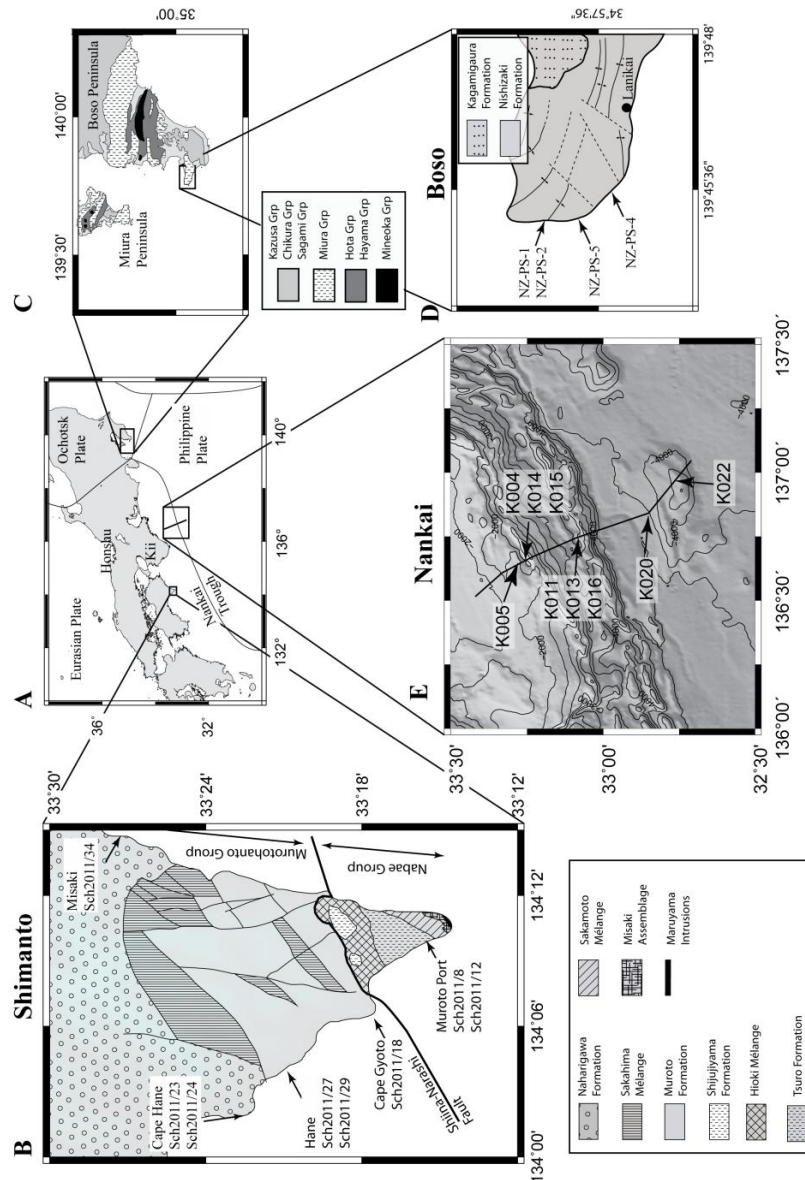


Figure 1. 3: (A) Map of central Japan. The position of the study areas are indicated by rectangular frames and shown in detail in B, C and E. (B) Geological map of Muroto Peninsula, southern Shikoku Island, after Katto et al. (1991). (C) Map of the Tokyo Bay area showing the location of the Miura and Boso Peninsulas, modified after Saito 1992 and Fujiwara et al. (1999). (D) Zoom-in of the western Boso Peninsula headlands, showing the sample positions in the Nishizaki Formation, geological units according to Yamamoto et al. (2005). (E) Bathymetric map of the Nankai Trough area with indicated sample locations at IODP drillsites. Black line marks the Kumano transect taken for the IODP drilling campaign in the Nankai Trough.

1.5.1 Tectonic evolution of the Japanese Islands

A detailed overview of the evolution of the Japanese Islands is provided by Uyeda and Miyashiro (1974), Kimura et al. (1991), Taira et al. (1992), Maruyama et al. (1997) and Taira (2001). The information given in the following section is closely related to Maruyama et al. (1997).

The geological evolution of the Japanese islands can be tracked back into the Silurian (~750-700 Ma). At that time, the Earth's landmass was amalgamated to form a supercontinent named Rodinia. At ~750 Ma, the Yangtze Craton (South China) began to separate from Rodinia, initiated by the upwelling of a mantle-plume. Between ~700-600 Ma, oceanic lithosphere was formed causing the segregation of the Yangtze Craton (Figure 1. 4). The active spreading continued until the previously existing super ocean was completely consumed and the supercontinent Gondwana was formed (~530 Ma). At that time, the Yangtze Craton was located close to the Australian part of Gondwana (~500 Ma) and developed as an active continental margin (~480 Ma, Figure 1. 4) to form proto-Japan (~450 Ma). In the Carboniferous (~300 Ma), proto-Japan was still located in the southern hemisphere facing the Panthalassic Ocean. In the late Carboniferous, the Paleo-Tethyan Seaway was successively closed and the Yangtze Craton moved northward across the equator to merge with Siberia (Figure 1. 4 and Figure 1. 5). In the time between ~280 and 60 Ma, proto-Japan, located east of the Yangtze Craton, moved further north until it came into full contact with the Asian mainland (Figure 1. 5). Between the Paleocene (~60 Ma) and the Eocene (~40 Ma), continuous subduction of the Pacific Ocean caused domal uplift in eastern Asia and induced an extensional regime (Figure 1. 5).

At the ocean side, the Philippine Sea Plate began to form at the Izu-Bonin arc. Beginning from approximately 25 Ma (Miocene), upwelling of a plume in eastern Asia culminated and resulted in extensional tectonics and the rifting of several basins, such as the Baikal Rift and the (proto)-Japan Sea (Figure 1. 5). The newly formed back-arc basins reaching their maximum extend in the late Miocene (~15 Ma), opened and began to form the Japan Sea (Figure 1. 5). The continuous subduction of the newly formed Philippine Sea plate and the Pacific Plate beneath Japan caused the collision and subduction of the Izu-Bonin arc with Japan.

This tectonically highly active history resulted in the fact that Japan recently is located on four distinct plates, the Eurasian Plate, the Okhotsk Plate (North America), the Philippine Sea Plate and the Pacific Plate.

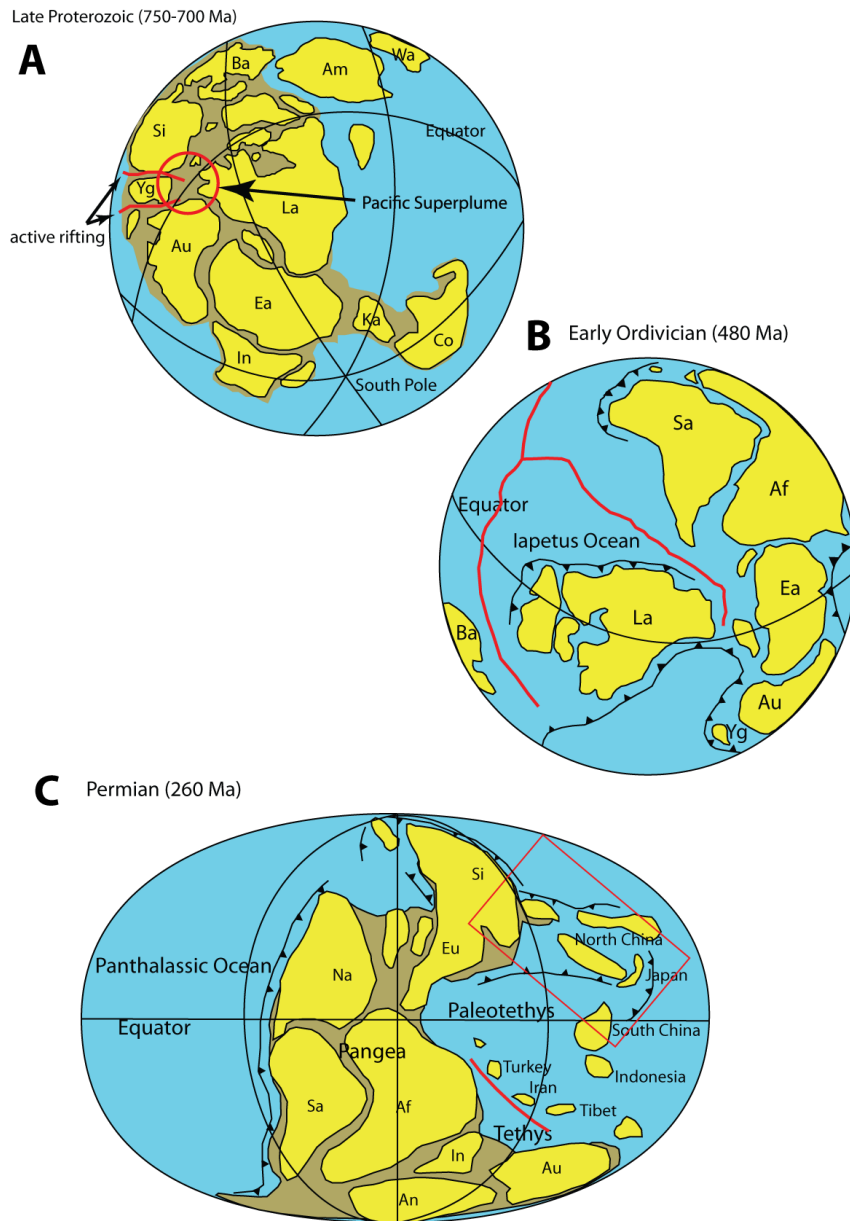


Figure 1. 4: Paleogeographic reconstructions of the evolution of the Japanese Islands. (A) In the Late Proterozoic, the Yangtze Craton was located in the west of the supercontinent Rodinia. Upwelling of a plume induced an extensional regime and caused the breakout of Rodinia. (B) In the early Ordovician, the Yangtze Craton was still located southwest of Australia and turned into a subduction regime. (C) The Yangtze Craton rotated around Australia and moved northward to merge with China and Siberia.

La: Laurentia, Ea: East Antarctica, Au: Australia, Yg: Yangtze, Si: Siberia, Ba: Baltica, Am: Amazonia, Wa: West Africa, Ka: Kalahari, Co: Congo, In: India, Sa: South America, Af: Africa, An: Antarctica, Na: North America, Eu: Europe, In: India

Redrawn and modified according to Maruyama et al. (1997), Scotese (2008), Kani et al. (2013) and the International Commission on Stratigraphy (2012).

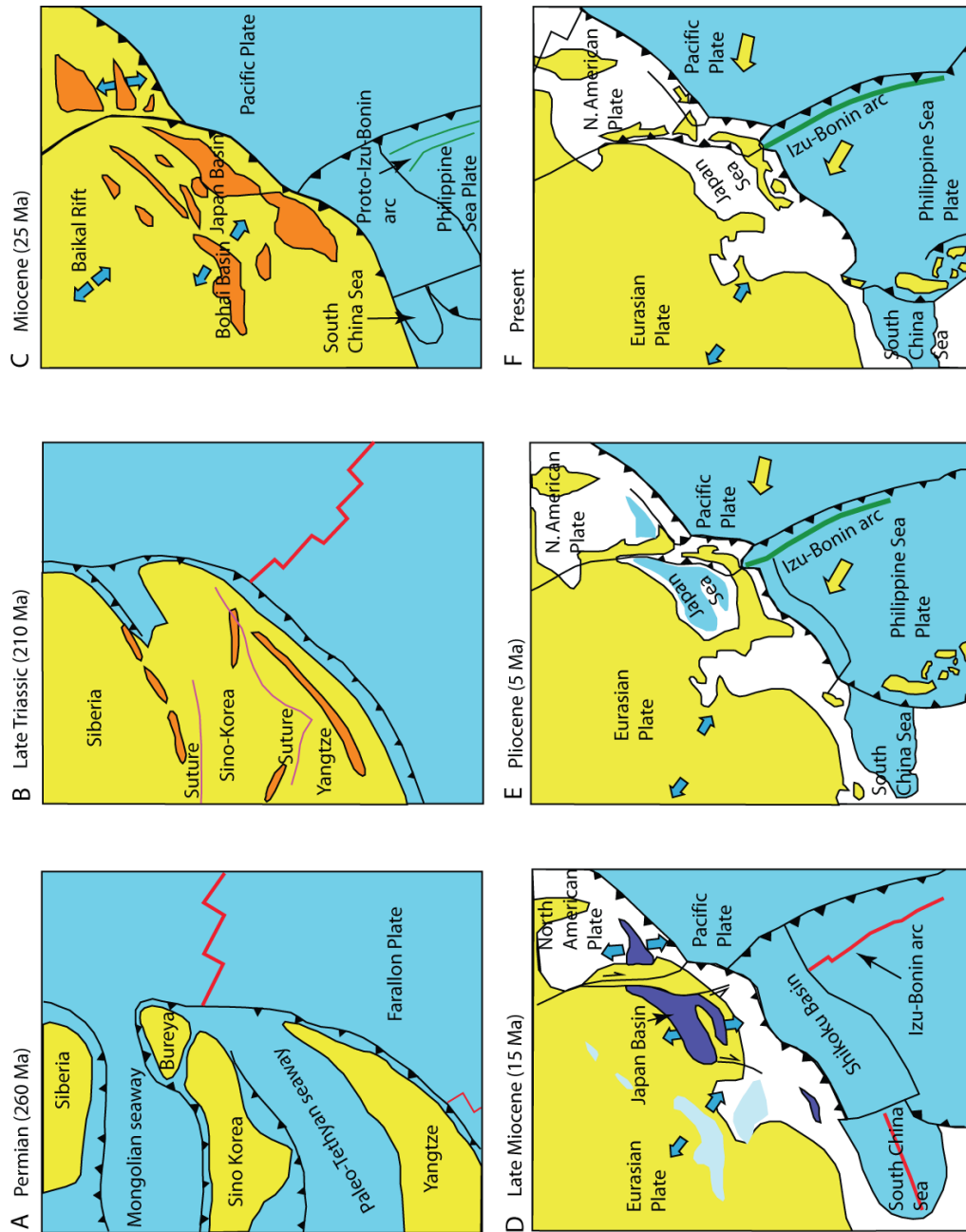


Figure 1. 5: Detailed paleogeographic maps showing the evolution of Japan. (A) In the Permian, the Yangtze Craton moved north to get in full contact with the Asian mainland. Proto-Japan is located at the southeastern margin of Yangtze. (B) In the Triassic, the Mongolian seaway was mostly closed. Granit batholiths were formed (orange). (C) Upwelling of a superplume accelerated the rifting of several basins. (D and E) Back-arc spreading caused the formation of the Japan Sea and the Japanese Islands became an island arc. (E) The subduction of the Philippine Sea Plate caused the collision of the Izu-Bonin arc against Japan. (F) Map of the modern Japanese Islands. Redrawn according to Maruyama et al. (1997).

1.5.2 The Shimanto Belt on Shikoku Island

The Shimanto Belt is located at the southeastern zone of southwest (SW) Japan and extends over 1500 km along the Japanese coastline (Kumon 1983; Aitchison 1986; DiTullio and Byrne 1990). Complexly folded turbiditic rocks, bounded by high-angle reverse faults, form the Shimanto Belt. Mélange zones include allochthonous blocks of chert, basalt and shale, overlain by successions of deep water sediments and turbidites (Aitchison 1986). Petrographic analyses indicate that the Shimanto Belt rocks were formed by the erosion of an ancient volcanic arc (Aitchison 1986; Taira et al., 1982, 1991).

A structurally nearly complete Shimanto Belt profile is exposed on Shikoku Island. Especially on Muroto Peninsula, the strata are well accessible along the coastline, allowing convenient sampling. Many early studies investigated the geological history of the Shimanto Belt (e.g. Suzuki and Hada 1979, 1983; Taira et al., 1982; Kumon 1983; Aitchison 1986; Underwood et al., 1993; DiTullio and Hada 1993). More recent studies on the Shimanto Belt are available from e.g. Hasebe and Tagami (2001) and Kimura et al. (2012).

Underthrusting causes northward decreasing ages within the formations, while the overall trend shows decreasing ages to the south. The single formations are separated by steeply northward dipping thrust faults.

The following section is closely related to Aitchison (1986). Generally, the Shimanto Belt can be subdivided into a Cretaceous part (northern Shimanto Belt) and a Tertiary part (southern Shimanto Belt), divided by the Aki-Tectonic-Line. The Cretaceous and Tertiary belts are further divided into four subbelts, the Shinjogawa and Taisho Groups of Cretaceous age and the Murotohanto and Nabae Groups of Tertiary age. The zeolite facies metamorphosed Shinjogawa Group and Taisho Group stratum is formed by sandstone and shale beds. The Tertiary Murotohanto Group contains shallow marine sand- and siltstones, resedimented conglomerate, turbidites and boulders of crystalline schist. The whole stratum is additionally extensively slumped. The Nabae Group consists of basaltic blocks in a muddy matrix, shallow marine sandstones, shales and olistostromal rocks. All Groups are further subdivided by the different

investigators and detailed information on the stratigraphy is given especially in Aitchison (1986).

According to Underwood et al. (1992), the paleotemperatures determined by vitrinite reflectance in the Cretaceous Murotohanto Group increases from 215 °C in the north to approximately 290 °C in the south. The same trend was observed in the Tertiary Nabae Group but due to a vertical offset of approximately 1200 m (Underwood et al., 1992), the paleotemperatures are ~90 °C below the temperatures of the Murotohanto Group. Paleotemperatures in the Nabae Group increase from 135°C in the north to 285°C in the south. At the southern tip of Muroto Peninsula, gabbroic rocks intruded the Nabae Group and increased the temperatures regionally. The maximal pressure experienced by the Shimanto Belt rocks was not greater than 2.5 kbar (Underwood et al., 1992), equivalent to 9000 m burial in the Murotohanto Group, and ~7800 m in the Nabae Group.

1.5.3 The Boso-Miura accretionary prism

The upper Miocene Boso-Miura accretionary prism (Yamamoto 2006) is exposed in the Tokyo bay region on the Boso- and Miura peninsulas (Honshu Island). The Miura Group was accreted to the Honshu arc from the Izu-Ogasawa arc. The depositional ages range from late Miocene (9.9 to 6.8 Ma; Yamamoto and Kawakami 2005). Since samples from the Boso peninsula were used in this thesis, only the Boso geology is described in further detail. The upper Miocene Nishizaki Formation is the oldest formation of this accretionary prism, without a known base (Soh et al., 1989) and is unconformably overlain by the Kagamigaura Formation (4.19-3.75 Ma, Kameda et al., 2010). The Kagamigaura Formation represents trench-slope cover sediments and is overlain by younger cover sediments of the Chikura Group (Kameda et al., 2010). The Nishizaki Formation consists of siltstones, scoriaceous siltstone and glassy tuff, while the Kagamigaura Formation is composed of volcanoclastic conglomerates and siltstones (Kameda et al., 2010). The Chikura Group is interpreted as trench-fill sediments and contains red recrystallized chert from the Honshu island arc (Yamamoto 2006). The paleowater depth of the Nishizaki Formation is estimated to be 2000 – 3500 m and 1000 – 2000 m for the Chikura Group (Saito 1992). The Nishizaki Formation

is highly deformed by the process of accretion (Soh et al., 1989; Yamamoto et al., 2005; Yamamoto and Kawakami 2005). The sediments of the Boso-Miura accretionary prisms represent burial depths of less than 1000 m indicated by high preserved porosities between 30% and 50% (Yamamoto et al., 2005). Vitrinite reflectance analyses indicate paleotemperatures below 50°C (Yamamoto et al., 2005). Thus, the sediments are not overprinted by any metamorphism, and only show weak sign of diagenesis.

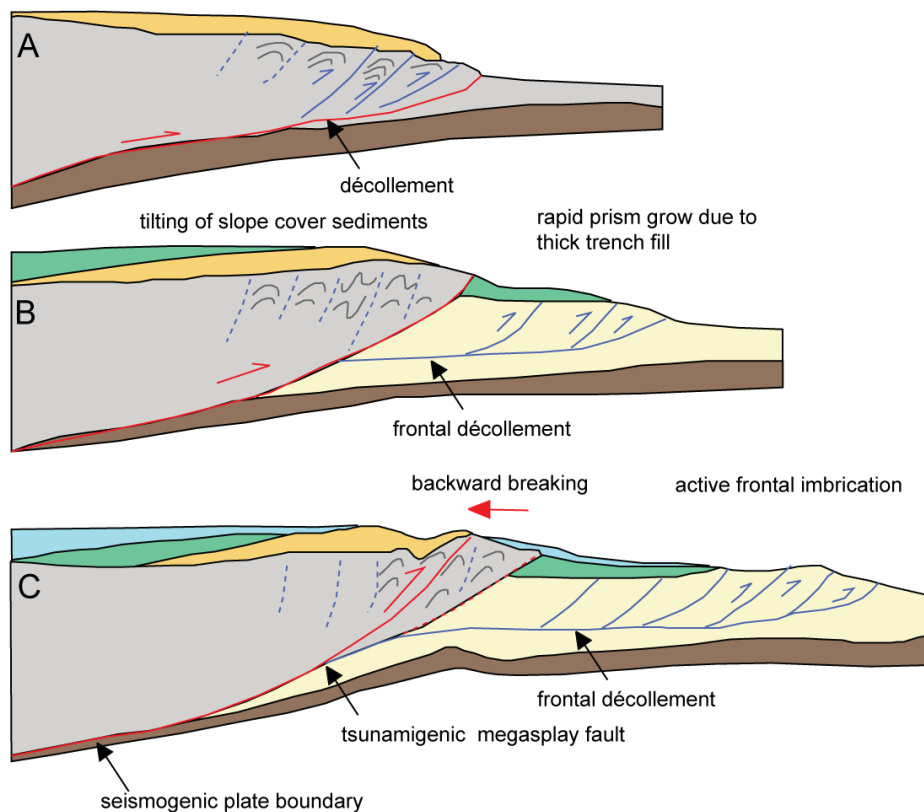


Figure 1. 6: Schematic cross sections showing the evolution of the Nankai accretionary prism. Normal thrusting (A) is followed by rapid prism grow (B) and backward breaking of an out-of-sequence fault (megaspay fault), responsible for tsunami generation. Redrawn and modified according to Moore et al. (2007).

1.5.4 Nankai trough

The Nankai trough is formed by the subduction of the Phillipine Sea Plate beneath SW of Japan (e.g. Taira et al., 1991; Seno et al., 1993; Taira 2001; Moore et al., 2009) and spans about 1500 km from the Izu-Bonin arc in the northeast (NE) to the Kyushu Ridge in the SW (Ike et al., 2008). According to Seno et al.

(1993) and Zang et al. (2002), the Philippine Sea Plate moves to the NW azimuth of $\sim 300^\circ$ to 315°) at a convergence rate of ~ 4 - 6.5 cm/y. The subduction of the Philippine Sea Plate has been active since the Miocene (Nakamura et al., 1984). The northern edge of the Philippine Sea Plate, the Shikoku Basin, is formed by back-arc spreading at the Izu-Bonin arc (Moore et al., 2009) and is filled by turbidites and hemipelagic sediments (Ike et al., 2008; Moore et al., 2009). A major feature of the Nankai subduction zone is an out-of-sequence thrust fault (splay fault, Figure 1. 6) branching from the plate boundary (~ 10 km depth) upward to the sea floor (e.g. Park et al., 2002; Moore et al., 2007). This approximately 30 km long thrust fault lies within the rupture area of the 1944 Tonankai earthquake ($M= 8.1$) and is thought to be responsible for tsunami generation (Park et al., 2002; Moore et al., 2007).

1.6 References from introduction

- Aitchison, J. (1986): Stratigraphy, sedimentology and tectonic evolution of the Shimanto Terrane, Southwest Japan. *Earth Science; Journal of the association for the geological collaboration in Japan* 40, 337-363
- Baba, T.; Cummins, P.R.; Hori, T.; Kaneda, Y. (2006): High precision slip distribution of the 1944 Tonankai earthquake from tsunami waveforms: Possible slip on a splay fault. *Tectonics*, 426, 119-134
- Beeler, N.M. (2007): Laboratory-observed faulting in intrinsically and apparently weak materials. In: Dixon, T.H.; Moore J.C. (eds.): *The seismogenic zone of subduction thrust faults*. Columbia University Press, New York, pp. 370-449.
- Bennett, R.; Bryant, W.; Keller, G. (1981): Clay fabric of selected submarine sediments: Fundamental properties and models. *Journal of Sedimentary Petrology* 51, 217-232
- Bilek, S.L. (2010): The role of subduction erosion on seismicity. *Geology*, 38, 479-480, doi: 10.1130/focus052010.1
- Bilek, S.L.; Lay, T. (1999): Rigidity variations with depth along interplate megathrust faults in subduction zones. *Letters to Nature*, 400, 443-446.
- Bott, M.H.P. (1991): Ridge push and associated plate interior stress in normal and hot spot regions. *Tectonophysics*, 200, 17-32
- Bourbié, T., O. Coussy, and B. Zinszner (1987), *Acoustics of porous media*. Editions Technip, Paris
- Brown, K.M.; Mascle, A.; Behrmann, J.H. (1990): Mechanisms of accretion and subsequent thickening in the Barbados Ridge accretionary complex: balanced cross sections across the toe of the wedge. *Proceedings of the Ocean Drilling Program, Scientific Results*, 110, 209-227.
- Byerlee, J. (1978): Friction of rocks. *Pure and Applied Geophysics*, 116, 615-626
- Byerlee, J. (1990): Friction, overpressure and fault normal compression. *Geophysical research letters*, 17, 2109-2112
- Byrne, D.E.; Davis, D.M.; Sykes, L.R. (1988): Loci and maximum size of thrust earthquakes and the mechanics of the shallow region of subduction zones. *Tectonics* 7, 833-857
- Carson, B.; von Huene, R.; Arthur, M. (1982): Small-scale deformation structures and physical properties related to convergence in Japan Trench slope sediments, *Tectonics*, 1, 277-302.
- Chapelle, W.M.; Tullis, T.E. (1977): Evaluation of the forces that drive plates. *Journal of the Geophysical Research*, 82, 1967-1984
- Clift, P.; Vannucchi, P. (2004): Controls on tectonic accretion versus erosion in subduction zones: Implications for the origin and recycling of the continental crust: *Reviews of Geophysics*, 42, RG2001, doi: 10.1029/2003RG000127

-
- Collins, W.J. (2003): Slab pull, mantle convection, and Pangaeian assembly and dispersal. *Earth and Planetary Science Letters*, 205, 225-237
- Condie, K.C. (2005): *Earth as an evolving system*. Elsevier.
- Conrad, C.P.; Bilek, S.; Lithgow-Bertelloni, C. (2004): Great earthquakes and slab pull: interaction between seismic coupling and plate-slab coupling. *Earth and Planetary Science Letters*, 218, 109-122, doi: 10.1016/S0012-821X(03)00643-5
- Davis, D.; Suppe, J.; Dahlen, F.A. (1983): Mechanics of fold-and-thrust belts and accretionary wedges. *Journal of Geophysical Research*, 88, 1153-1172
- DiTullio, L.; Byrne, T. (1990): Deformation paths in the shallow levels of an accretionary prism: The Eocene Shimanto belt of southwest Japan. *Geological Society of America Bulletin*, 102, 1420-1438, doi: 10.1130/0016-7606(1990)102<1420:DPITSL>2.3.CO;2
- DiTullio, L.; Hada, S. (1993): Regional and local variations in the thermal history of the Shimanto Belt, southwest Japan. In: Underwood, M.B. (eds.): *Thermal Evolution of the tertiary Shimanto Belt, Southwest Japan: An example of Ridge-Trench Interaction*. Geological Society of America, Special Paper 273.
- Donath, F.A. (1961): Experimental study of shear failure in anisotropic rocks. *Bulletin of the Geological Society of America*, 72, 155-163
- Erickson, S.; Jarrard, R. (1998): Velocity-porosity relationship for water-saturated siliciclastic sediments. *Journal of Geophysical Research*, 103(B12), 30385-30406.
- Expedition 315 Scientists (2009): Expedition 315 Site C0001. In: Kinoshita, M.; Tobin, H.; Ashi, J.; Kimura, G.; Lallemand, S.; Screaton, E.J.; Curewitz, D.; Masago, H.; Moe, K.T.; and Expedition 314/315/316 Scientists (2009), *Proceedings of the International Ocean Drilling Program, Volume 314/315/316*. Washington DC, doi: 10.2204/iodp.proc.314315316.123.2009
- Expedition 316 Scientists (2009a): Expedition 316 Site C0004. In: Kinoshita, M.; Tobin, H.; Ashi, J.; Kimura, G.; Lallemand, S.; Screaton, E.J.; Curewitz, D.; Masago, H.; Moe, K.T.; and Expedition 314/315/316 Scientists (2009), *Proceedings of the International Ocean Drilling Program, Volume 314/315/316*. Washington DC, doi: 10.2204/iodp.proc.314315316.133.2009
- Expedition 316 Scientists (2009c): Expedition 316 Site C0007. In: Kinoshita, M.; Tobin, H.; Ashi, J.; Kimura, G.; Lallemand, S.; Screaton, E.J.; Curewitz, D.; Masago, H.; Moe, K.T.; and Expedition 314/315/316 Scientists (2009), *Proceedings of the International Ocean Drilling Program, Volume 314/315/316*. Washington DC, doi: 10.2204/iodp.proc.314315316.135.2009
- Expedition 316 Scientists (2009d): Expedition 316 Site C0008. In: Kinoshita, M.; Tobin, H.; Ashi, J.; Kimura, G.; Lallemand, S.; Screaton, E.J.; Curewitz, D.; Masago, H.; Moe, K.T.; and Expedition 314/315/316 Scientists (2009), *Proceedings of the International Ocean Drilling Program, Volume 314/315/316*. Washington DC, doi: 10.2204/iodp.proc.314315316.136.2009

- Expedition 316 Scientists, (2009b): Expedition 316 Site C0006. In: Kinoshita, M.; Tobin, H.; Ashi, J.; Kimura, G.; Lallemand, S.; Screaton, E.J.; Curewitz, D.; Masago, H.; Moe, K.T.; and Expedition 314/315/316 Scientists (2009), Proceedings of the International Ocean Drilling Program, Volume 314/315/316. Washington DC, doi: 10.2204/iodp.proc.314315316.134.2009
- Expedition 333 Scientists (2012a): Expedition 333 Site C0011. In: Henry, P.; Kanamatsu, T.; Moe, K.T.; and Expedition 333 (2012), Proceedings of the International Ocean Drilling Program, 333, doi: 10.2204/iodp.proc.333.104.2012
- Expedition 333 Scientists (2012b): Expedition 333 Site C0012. In: Henry, P.; Kanamatsu, T.; Moe, K.T.; and Expedition 333 (2012), Proceedings of the International Ocean Drilling Program, 333, doi: 10.2204/iodp.proc.333.105.2012
- Fawad, M.; Mondol, N.H.; Jahren, J.; Bjørlykke, K. (2010): Microfabric and rock properties of experimentally compresses silty-clay mixtures. *Marine and Petroleum Geology* 27, 1698-1712
- Forsyth, D.; Uyeda, S. (1975): On the relative importance of the driving forces of plate motion. *Geophysical Journal of the Royal Astronomical Society*, 43, 163-200
- Fujiwara, T.; Kinoshita, H.; Morijiri, R. (1999): Magnetic structure of the southern Boso Peninsula, Honshu, Japan, and its implications for the formation of the Mineoka Ophiolite Belt. *Jamstec*
- Hager, B.H.; O'Connell, R.J. (1981): A simple global model of plate dynamics and mantle convection. *Journal of Geophysical Research*, 86, 4843-4867
- Hasebe, N.; Tagami, T. (2001): Exhumation of an accretionary prism – results from fission track thermochronology of the Shimanto Belt, southwest Japan. *Tectonophysics*, 331 (3), 247-267
- Hyndman, R.D. (2004): Controls on Subduction Thrust Earthquakes: Downtip Changes in Composition and State. In: Karner, G.D.; Taylor, B.; Driscoll, N.W.; Kohlstedt, D.L. (Eds.), Columbia University Press, New York, New York, 166-178
- Hyndman, R.D.; Wang, K. (1993): Thermal constraints on the zone of major thrust earthquake failure: The Cascadia subduction zone. *Journal of Geophysical Research*, 98, 2039-2060
- Hyndman, R.D.; Wang, K.; Yamano, M. (1995): Thermal constraints on the seismogenic portion of the southwestern Japan subduction thrust. *Journal of geophysical Research* 100, 15373-15392
- Hyndman, R.D.; Yamano, M.; Oleskevich, D.A. (1997): The seismogenic zone of subduction thrust faults. *The Island Arc*, 6, 244-260
- Ike, T.; Moore, G.F.; Kuramoto, S.; Par, J.-O.; Kaneda, Y; Taira, A. (2008): Variation in sediment thickness and type along the northern Philippine Sea

-
- Plate at the Nankai Trough. *Island Arc*, 17, 343-357, doi: 10.1111/j.1440-1738.3008.00624.x
- Ikesawa, E., Sakaguchi, A., and Kimura, G., 2003, Pseudotachylite from an ancient accretionary complex: Evidence for melt generation during seismic slip along a master decollement? *Geology*, 31, 637-640.
- International Commission on Stratigraphy (2012): Permian World, Subcommittee on Permian Stratigraphy. <http://permian.stratigraphy.org/ann/end.asp?ID=113> (last accessed 17.06.2013)
- Isacks, B.; Oliver, J.; Sykes, L. (1968): Seismology and the new global tectonics. *Journal of Geophysical Research*, 73, 5855-5899
- Johansen, T.A.; Bent, O.R.; Jakobsen, M. (2004): Effect of grain scale alignment on seismic anisotropy and reflectivity of shales. *Geophysical Prospecting* 52, 133-149
- Jones, M. (1994): Mechanical principles of sediment deformation. In: Maltman, A. (ed.): *The Geological Deformation of sediments*. Chapman and Hall, London, 37-71
- Kameda, J.; Yamamoto, Y.; Kimura, G. (2010): Smectite swelling in the Miura-Boso accretionary prism: Possible cause for incipient décollement zone formation. *Tectonophysics*, 494, 75-84, doi: 10.1016/j.tecto.2010.08.008
- Kani, T.; Hisanabe, C.; Isozaki, Y. (2013): The Capitanian (Permian) minimum of $^{87}\text{Sr}/^{86}\text{Sr}$ ratio in the mid-Panthalassan paleo-atoll carbonates and its demise by the deglaciation and continental doming. *Gondwana Research*, 24, 212-221
- Katto, J.; Hada, M.; Tashiro, M.; Taira, A.; Terado, T. (1991): Geological and Mineral Spring Resources Map of Kochi Prefecture. Kochi Prefecture Government
- Kawabata, K.; Tanaka, H.; Kimura, G.; (2007): Mass transfer and pressure solution in deformed shale of accretionary complex: Examples from the Shimanto Belt, southwestern Japan. *Journal of Structural Geology*, 29, 697-711
- Kimura, G.; Yamaguchi, A.; Hojo, M.; Kitamura, Y.; Kameda, J.; Ujiie, K.; Hamada, Y.; Hamahashi, M.; Hina, S. (2012): Tectonic mélange as fault rock of subduction plate boundary. *Tectonophysics*, 568, 25-38
- Kimura, T.; Hayami, I.; Yoshida, S. (1991): *Geology of Japan*. University of Tokyo Press, 277p.
- Kitamura, Y., Sato, K., Ikesawa, E., Ikehara-Ohmori, K., Kimura, G., Kondo, H., Ujiie, K., Onishi, C.T., Kawabata, K., Hashimoto, Y., Mukoyoshi, H., and Masago, H. (2005): Mélange and its seismogenic roof decollement: A plate boundary fault rock in the subduction zone - An example from the Shimanto Belt, Japan: *Tectonics*, 24, TC5012, doi: 10.1029/2004TC001635.
- Kohlstedt, D.L.; Evans, B.; Mackwell, S.J. (1995): Strength of the lithosphere: Constraints imposed by laboratory experiments. *Journal of the Geophysical Research*, 100, 17587-17602

- Kumon, F. (1983): Coarse clastic rocks of the Shimanto Supergroup in eastern Shikoku and Kii Peninsula, southwest Japan. *Memories of the faculty of science, Kyoto University, Series of Geology and Mineralogy* 49, 63-109
- Kyo, M.; Miyazaki, E.; Tsukioka, S.; Ochi, H.; Amitani, Y.; Tsuchiya, T.; Aoki, T.; Takagawa, S. (1995). The sea trial of “KAIKO”, the full ocean depth research ROV. *Oceans '95. 1991-1996*, doi: 10.1109/OCEANS.1995.528882
- Logan, J.M.; Rauenzahn, K.A. (1987): Frictional dependence of gouge mixtures of quartz and montmorillonite on velocity, composition and fabric. *Tectonophysics*, 144, 87-108.
- Lowman, P.D.; Montgomery, B.C. (1998). Data source: Seismicity catalogs, Volume 2, global and regional. The National Geophysical Data Center and The National Earthquake Information Center. (<http://denali.gsfc.nasa.gov/dtam/images/global.gif>, last access 16.06.2013)
- Lupini, J.F.; Skinner, E.; Vaughan, P.R. (1981): The drained residual strength of cohesive soils. *Geotechnique*, 31, 181-213
- Marone, C. (1998): Laboratory-derived friction laws and their application to seismic faulting. *Annual Review of Earth and Planetary Sciences*, 26, 643-696
- Maruyama, S.; Isozaki, Y.; Kimura, G.; Terabayashi, M. (1997): Paleogeographic maps of the Japanese islands: Plate tectonic synthesis from 750 Ma to the present. *The Island Arc*, 6, 121-142
- Mitchell, J.K. (1993): *Fundamentals of soil behavior*, 2nd ed., Wiley, Hoboken
- Moore, G.; Moore, C. (1998): The Seismogenic Zone Experiment (SEIZE) Workshop – Final Report. <http://www.soest.hawaii.edu/moore/seize/> (last accessed 16.06.2013)
- Moore, G.F.; Bangs, N.L.; Taira, A.; Kuramoto, S.; Pangborn, E.; Tobin, H.J. (2007): Three-Dimensional splay fault geometry and implications for tsunami generation. *Science*, 318, 1128-1131
- Moore, G.F.; Park, J.-O.; Bangs, N.L.; Gulick, S.P.; Tobin, H.J.; Nakamura, Y.; Sata, S.; Tsuji, T.; Yoro, T.; Tanaka, H.; Uraki, S.; Kido, Y.; Sanada, Y.; Kuramoto, S.; Taira, A. (2009): Structural and seismic stratigraphic framework of the NanTroSEIZE stage 1 transect. In: Kinoshita, M.; Tobin, H.J.; Ashi, J.; Kimura, G.; Lallemant, S.; Screaton, E.J.; Curewitz, D.; Masago, H.; Moe, K.T.; Expedition 314/315/316 Scientists, *Proceedings of the Integrated Ocean Drilling Program 314/315/316*. doi: 10.2204/iodp.proc.314315316.102.2009
- Moore, J.C. (1989): Tectonics and hydrogeology of accretionary prisms: Role of the décollement zone. *Journal of Structural Geology*, 11, 95-106
- Moore, J.C.; Saffer, D. (2001): Updip limit of the seismogenic zone beneath the accretionary prism of southwest Japan: An effect of diagenetic to low-grade metamorphic processes and increasing effective stress. *Geology* 29, 183-186, doi: 10.1130/0091-7613(2001)029<0183:ULOTSZ>2.0.CO;2.

-
- Moore, J.C.; Vrolijk, P. (1992): Fluids in Accretionary Prisms, *Reviews of Geophysics*, 30, 113-135.
- Moore, E.M.; Twiss, R.J. (1995): *Tectonics*: New York, W. H. Freeman, 415p.
- Morgan, J.K.; Ramsey, E.B.; Ask, M.V.S. (2007): Deformation and mechanical strength of sediments at the Nankai subduction zone. In: Dixon, T.H.; Moore J.C. (eds.): *The seismogenic zone of subduction thrust faults*. Columbia University Press, New York, pp. 210-256.
- Nakamura, K.; Shimazaki, K.; Yonekura, N. (1984): Subduction bending and extension. Present and Quaternary tectonics of the northern border of the Philippine Sea Plate, *Bulletin de la Societe Geologique de France*, 26, 221-243
- Oleskevich, D.A.; Hyndman, R.D.; Wang, R. (1999): The updip and downdip limits to great subduction earthquakes: Thermal and structural models of Cascadia, south Alaska, SW Japan, and Chile. *Journal of Geophysical research* 104, 14965-14991
- Orowan, E. (1964): Continental drift and the origin of mountains. *Science*, 146, 1003-1010
- Orowan, E. (1965): Convection in a non-Newtonian mantle, continental drift, and mountain building. *Philosophical Transactions of the Royal Society A*, 258, 284-313
- Pacheco, J.F.; Sykes, L.R. (1992): Seismic moment catalog of large shallow earthquakes, 1900 to 1989. *Bulletin of the Seismological Society of America*, 82, 1306-1349
- Park, J.; Tsuru, T.; Kodaira, S.; Cummins, P.R.; Kaneda, Y. (2002): Splay fault branching along the Nankai subduction zone. *Science*, 297, 1157-1160
- Park, J.; Tsuru, T.; Kodaira, S.; Nakanishi, A.; Miura, S.; Kaneda, Y.; Kono, Y. (2000): Out-of-sequence thrust faults developed in the coseismic slip zone of the 1946 Nankai earthquake (Mw=8.2) off Shikoku, southwest Japan. *Geophysical Research Letters*, 27, 1033-1036
- Pawley, A.R.; Holloway, J.R. (1993): Water sources for subduction zone volcanism: New experimental constraints. *Science*, 260, 664-667
- Pickett, G. R. (1963): Acoustic character logs and their application in formation evaluation, *Journal of the Canadian Petroleum Technology*, 15, 659-667.
- Press, F.; Siever, R. (2003): *Allgemeine Geologie, Einführung in das System Erde*: München, Elsevier GmbH
- Rai, C.S.; Hanson, K.E. (1988): Shear-wave velocity anisotropy in sedimentary rocks: A laboratory study. *Geophysics* 53, 800-806
- Ranero, C.R.; Morgan, J.P.; McIntosh, K.; Reichert, C. (2003): Bending-related faulting and mantle serpentinization at the Middle America trench. *Nature*, 425, 367-373, doi: 10.1038/nature01961

- Richter, F.M. (1977): On the driving mechanisms of plate tectonics. *Tectonophysics*, 38, 61-88
- Rietveld, H.M. (1969): A Profile Refinement Method for Nuclear and Magnetic Structures. *Journal of Applied Crystallography* 2, 65-71
- Ruff, L.J. (1989): Do trench sediments affect great earthquake occurrence in subduction zones? In: Ruff, L.J.; Kanamori, H. (1989): *Subduction Zones Part II, Pure and Applied Geophysics*, 129, 263-282
- Ruff, L.J. (1996): Large Earthquakes in subduction zones: Segment interaction and recurrence times. In: Bedout, G.E.; Scholl, D.W.; Kirby, S.H.; Platt, J.P. (1996): *Subduction from top to bottom*. American Geophysical Union, Florida
- Ruff, L.J.; Tichelaar, B.W. (1996): What controls the seismogenic plate interface in subduction zones? In: Bedout, G.E.; Scholl, D.W.; Kirby, S.H.; Platt, J.P. (1996): *Subduction from top to bottom*. American Geophysical Union, Florida
- Saffer DM, Marone C (2003) Comparison of smectite- and illite-rich gouge frictional properties: application to the updip limit of the seismogenic zone along subduction megathrusts. *Earth and Planetary Science Letters* 215:219-235. doi:10.1016/S0012-821X(03)00424-2
- Saito, S. (1992): Stratigraphy of Cenozoic strata in the southern terminus area of Boso Peninsula, central Japan. *Contributions of the Institute of Geology and Paleontology Tohoku University*, 93, 1-37
- Scholz, C.H. (1990): *The mechanics of earthquakes and faulting*. 2nd edition, Cambridge University Press
- Scotese, C.R. (2008): PALEOMAP Project. <http://www.scotese.com> (last accessed 17.06.2013)
- Seno, T. (2005): Variation of downdip limit of the seismogenic zone near the Japanese islands: Implications for the serpentization mechanism of the forearc mantle wedge. *Earth and Planetary Science Letters*, 231, 249-262
- Seno, T.; Stein, S.; Gripp, A.E. (1993): A model for the motion of the Philippine Sea Plate consistent with NUVEL-1 and geological data. *Journal of Geophysical Research*, 98, 17941-17948
- Shea, W.T., Kronenberg, A.K. (1993): Strength and anisotropy of foliated rocks with varied mica content. *Journal of Structural Geology*, 15, 1097-1121
- Soh, W.; Taira, A.; Ogawa, A.; Taniguchi, H.; Pickering, K.T.; Stow, D. (1989): Submarine depositional processes for volcanoclastic sediments in the Mio-Pliocene Misaki Formation, Miura Group, Central Japan. 619-630, In: Taira A. & Masuda F. 1989. *Sedimentary Facies in the Active Plate Margin*. Terra Scientific Publishing Company
- Stern, R. (2002): Subduction zones. *Reviews of Geophysics*, 40, 38p., doi: 10.1029/2001RG000108

- Stipp, M.; Rolfs, M.; Kitamura, Y.; Behrmann, J.H.; Schumann, K.; Schulte-Kortnack, D.; Feeser, V. (2013): Strong sediments at the deformation front, and weak sediments at the rear of the Nankai accretionary prism, revealed by triaxial deformation experiments. *Geochemistry Geophysics Geosystems*, Vol. 14, 4791-4810, doi: 10.1002/ggge.20290
- Strasser, M.; Moore, G.F.; Kimura, G.; Kitamura, Y.; Kopf, A.; Lallemand, S.; Park, J-O.; Sreaton, E.J.; Su, X.; Underwood, M.B.; Zhao, X. (2009): Origin and evolution of a splay fault in the Nankai accretionary wedge. *Nature Geoscience*, Vol. 2, 648-652, doi: 10.1038/NGEO609
- Suzuki, T.; Hada, S. (1979): Cretaceous tectonic mélange of the Shimanto Belt in Shikoku, Japan. *Journal of the Geological Society of Japan*, 85, 467-479
- Suzuki, T.; Hada, S. (1983): Accretionary mélange of Cretaceous age in the Shimanto Belt in Japan. In: Hashimoto, M.; Uyeda, S. (eds.): *Accretion tectonics in the circum-pacific regions*. Terra Science Publications Corporation, Tokyo.
- Taira, A. (2001): Tectonic evolution of the Japanese island arc system. *Annual Review of Earth and Planetary Science*, 29, 109-134
- Taira, A.; Byrne, T.; Ashi, J. (1992): *Photographic Atlas of an Accretionary Prism, Geologic Structures of the Shimanto Belt, Japan*. Springer. 124 p.
- Taira, A.; Hill, I.; Firth, J. and the shipboard scientific party (1991): Geological Background and objectives. *Proceedings of the Ocean Drilling Program, Initial Reports*, 131
- Taira, A.; Okada, H.; Withaker, J.H.; Smith, A.J. (1982): The Shimanto Belt of Japan: Cretaceous-lower Miocene active margin sedimentation. In: Leggett, J.K. (eds.): *Trench-Forearc Geology*. Geological Society of London, Special Publications, 10, 2-26
- Tichelaar, B.; Ruff, L.J. (1993): Depth of seismic coupling along subduction zones. *Journal of Geophysical Research*, 98, 2017-2037
- Tobin, H.J.; Kinoshita, M. (2006): NanTroSEIZE: The IODP Nankai trough seismogenic zone experiment. *Scientific Drilling*, 2, 23-27
- Tsuji, T.; Dvorkin, J.; Mavko, G.; Nakata, N.; Matsuoka, T.; Nakanishi, A.; Kodaira, S.; Nishizawa, O. (2011): Vp/Vs ratio and shear-wave splitting in the Nankai Trough seismogenic zone: Insights into effective stress, pore pressure, and sediment consolidation, *Geophysics*, 76(3), 71-82, doi:10.1190/1.3560018.
- Turcotte, D.L.; Schubert, G. (2002): *Geodynamics*. Second edition, Cambridge University Press
- Underwood, M.B. (2007): Sediment inputs to subduction zones: why lithostratigraphy and clay mineralogy matter. In: Dixon, T.H.; Moore J.C. (eds.): *The seismogenic zone of subduction thrust faults*. Columbia University Press, New York, pp. 42-85.

- Underwood, M.B.; Byrne, T.; Hibbard, J.P.; DiTullio, L.; Laughland, M.M. (1993): The effect of ridge subduction on thermal structure of accretionary prisms: A Tertiary example from the Shimanto Belt of Japan. *Geological Society of America* 273
- Underwood, M.B.; Laughland, M.M.; Byrne, T.; Hibbard, J.P.; DiTullio, T. (1992): Thermal evolution of the Tertiary Shimanto Belt, Muroto Peninsula, Shikoku, Japan. *The Island Arc*, 1, 116-132
- Uyeda, S.; Miyashiro, A. (1974): Plate tectonics and the Japanese Islands: A synthesis. *Geological Society of America Bulletin*, 85, 1159-1170, doi: 10.1130/0016/7606(1974)85<1159:PTATJI>2.0.CO;2
- Vassiliou, M.; Hager, B.H. (1988): Subduction zone earthquakes and stress in slabs. *Pure and Applied Geophysics*, 128, 547-624
- Voltolini, M.; Wenk, H.-R.; Mondol, N.H.; Bjørlykke, K.; Jahren, J. (2009): Anisotropy of experimentally compressed kaolinite-illite-quartz mixtures. *Geophysics* 74 (1), 13-23
- von Huene, R.; Ranero, C.R.; Vannucchi, P. (2004): Generic model of subduction erosion. *Geology*, 32, 913-916, doi: 10.1130/G20563.1
- von Huene, R.; Scholl, D.W.;(1991): Observations at convergent margins concerning sediment subduction, subduction erosion, and the growth of continental crust. *Reviews of Geophysics*, 29, 279-316, doi: 10.1029/91RG00969.
- Vrolijk, P. (1990): On the mechanical role of smectite in subduction zones. *Geology*, 18, 703-707, doi: 10.1130/0091-7613(1990)018<0703:OTMROS>2.3.CO;2
- Wu, B.; Conrad, C.P.; Heuret, A.; Lithgow-Bertelloni, C.; Lallemand, S. (2008): Reconciling strong slab pull and weak plate bending: The plate motion constraint on the strength of mantle slabs. *Earth and Planetary Science Letters*, 272, 412-421, doi: 10.1016/j.epsl.2008.05.009
- Yamamoto, Y. (2006): Systematic variation of shear-induced physical properties and fabrics in the Miura-Boso accretionary prism: The earliest processes during off-scraping. *Earth and Planetary Science Letters*, 244, 270-284, doi: 10.1016/j.epsl.2006.01.049
- Yamamoto, Y.; Kawakami, S. (2005): Rapid tectonics of the late Miocene Boso accretionary prism related to the Izu-Bonin arc collision. *The Island Arc*, 14, 178-198
- Yamamoto, Y.; Mukoyoshi, H.; Ogawa, Y. (2005): Structural characteristics of shallowly buried accretionary prism: Rapidly uplifted Neogene accreted sediments on the Miura-Boso Peninsula, central Japan. *Tectonics*, 24, doi: 10.1029/2005TC001823

Zang, S.X.; Chen, Q.Y.; Ning, J.Y.; Shen, Z.K.; Liu, Y.G. (2002): Motion of the Philippine Sea Plate consistent with the NUVEL-1A model. *Geophysical Journal International*, 150, 809-819, doi: 10.1046/j.1365-246X.2002.01744.x

2 Manuscript #1

P and S wave velocity measurements of water-rich
sediments from the Nankai Trough, Japan

Kai Schumann ¹, Michael Stipp ¹, Jan H. Behrmann ¹, Dirk Klaeschen ¹ and
Detlef Schulte-Kortnack ²

¹ *Marine Geodynamics, GEOMAR Helmholtz Centre for Ocean Research Kiel*

² *Institute of Geosciences, Kiel University*

Journal of Geophysical Research Solid Earth

119, doi: 10.1002/2013JB010290

P and S wave velocity measurements of water-rich sediments from the Nankai Trough, Japan

Kai Schumann¹, Michael Stipp¹, Jan H. Behrmann¹, Dirk Klaeschen¹ and Detlef Schulte-Kortnack²

¹ *Marine Geodynamics, GEOMAR Helmholtz Centre for Ocean Research Kiel*

² *Institute of Geosciences, Kiel University*

Corresponding author: K. Schumann, Marine Geodynamics, GEOMAR Helmholtz Centre for Ocean Research Kiel, Wischhofstr. 1-3, D-24148 Kiel, Germany. (kaschumann@geomar.de)

Key Points:

- Sonic velocity measurements conducted during triaxial deformation tests
- Improved data processing of sonic velocity measurements
- Differentiation of variably consolidated sediments using acoustic properties

Index Terms:

- Acoustic properties
- Subduction zones
- Physical properties of rocks

Abstract

Acoustic velocities were measured during triaxial deformation tests of silty clay and clayey silt core samples from the Nankai subduction zone (Integrated Ocean Drilling Program Expeditions 315, 316, and 333). We provide a new data set, continuously measured during pressure increase and subsequent axial deformation. A new data processing method was developed using seismic time series analysis. Compressional wave velocities (V_p) range between about 1450 and 2200 m/s, and shear wave velocities (V_s) range between about 150 and 800 m/s. V_p slightly increases with rising effective confining pressure and effective axial stress. Samples from the accretionary prism toe show the highest V_p , while fore-arc slope sediments show lower V_p . Samples from the incoming plate, slightly richer in clay minerals, have the lowest values for V_p . V_s increases with higher effective confining pressures and effective axial stress, irrespective of composition and tectonic setting. Shear and bulk moduli are between 0.2 and 1.3 GPa, and 3.85 and 8.41 GPa, respectively. Elastic moduli of samples from the accretionary prism toe and the footwall of the megasplay fault (1.50 and 3.98 GPa) are higher than those from the hanging wall and incoming plate (0.59 and 0.88 GPa). This allows differentiation between normal and overconsolidated

sediments. The data show that in a tectonosedimentary environment of only subtle compositional differences, acoustic properties can be used to differentiate between stronger (accretionary prism toe) and weaker (fore-arc slope, incoming plate) sediments. Especially V_p/V_s ratios may be instrumental in detecting zones of low effective stress and thus high pore fluid pressure.

1. Introduction

The Nankai accretionary complex, located at the Pacific side of SW Japan (Figure 2.1), belongs to one of the most intensively studied subduction zones on Earth. In this region, the Philippine Sea plate is subducted beneath the Eurasian plate with a convergence azimuth of $\sim 80^\circ$ [e.g., Taira et al., 1991] and a dip angle of 10° to 22° [e.g., Xu and Kono, 2002]. Over the historical record, earthquakes of magnitude >8 repeatedly occurred in this region with intervals of 100 to 200 years [e.g., Ando, 1975; Park et al., 2002a]. This has led to the planning and implementation of the Nankai Trough Seismogenic Zone Experiment (NanTroSEIZE), forming part of the Integrated Ocean Drilling Program (IODP). NanTroSEIZE is designed to drill, to sample, and to monitor the plate boundary thrust and elucidate earthquake-generating processes around the updip end of the seismogenic zone. Drilling into the seismogenic portion of the plate boundary yields the possibility to sample deformed rocks from a recently seismically active fault zone, which ruptured during the 1944 Tonankai earthquake [Tobin and Kinoshita, 2006]. The mechanical characteristics of these rocks directly control the strength and frictional behavior of faults in accretionary prisms and thus play a key role in earthquake rupture dynamics [e.g., Scholz, 2002]. To determine the mechanical characteristics in laboratory tests, drilling and sampling of fault zones at depth is essential.

In the case of the Nankai trench, the initially unlithified sediments of the Philippine Sea Plate are scraped off and added to the accretionary prism at the leading edge of the overriding Eurasian plate. A slope of clastic sediments derived from the Japanese Islands lies on top of the accreted sediments. Compaction and dewatering within the accretionary prism caused by progressive burial and tectonic deformation results in changing physical properties [e.g., Carson et al., 1982; Moore and Vrolijk, 1992; Erickson and Jarrard, 1998; Bilek and Lay, 1999;

Moore and Saffer, 2010], such as porosity, density, shear strength, and compressibility. Mechanical compaction at shallow depth and low temperatures is mainly a function of effective confining pressure, before becoming dominantly controlled by diagenetic mineralogical and fabric changes toward greater depth [e.g., Mondol et al., 2007]. Lithological and mechanical properties were determined in order to relate these to elastic wave velocities and their changes during experimental deformation. Seismic time series analysis was applied to sonic velocity measurements, enabling fast processing and good detection of first arrivals. We chose samples from different tectonosedimentary environments at the Nankai trench and forearc to investigate the question whether incoming sediment on the oceanic plate, sediment cover of the frontal thrust zone, and the megasplay setting possess distinct acoustic characteristics. Measurements during the experimental deformation stages were conducted in order to quantify the effects of fabric changes on the acoustic properties that would be associated with tectonic shearing of the sediments.

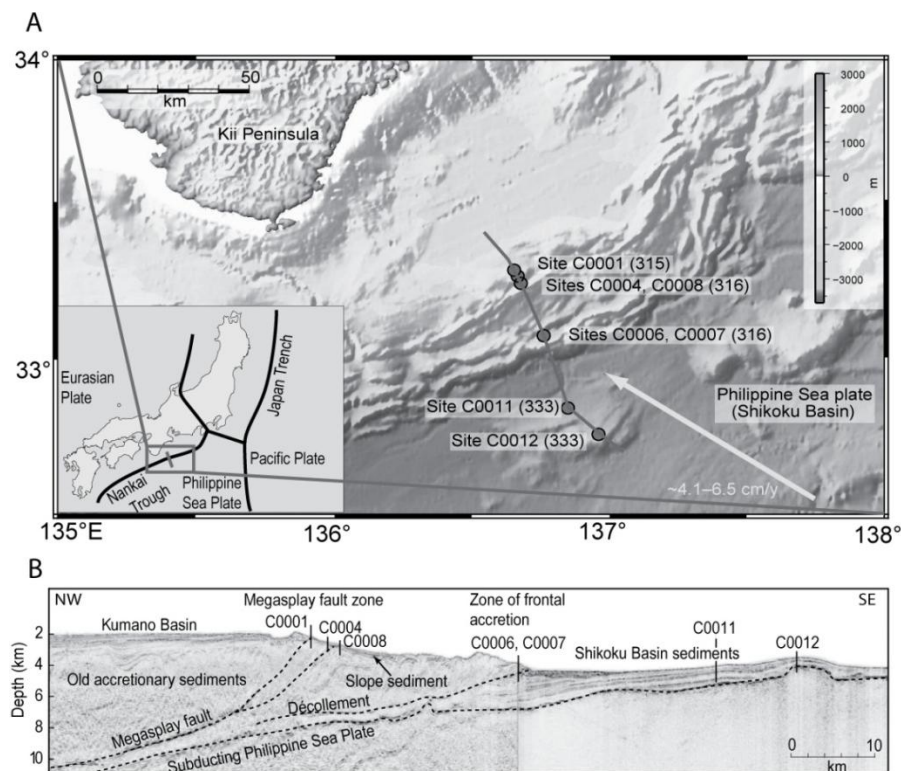


Figure 2. 1: (A) Tectonic setting and the location of the Nankai Trough (inset) and detailed bathymetric map [Becker et al., 2009] of the Kumano Basin showing the locations of the IODP drill sites (dots, expedition numbers are given in brackets) along the seismic profile. The arrow indicates the plate convergence direction. (B) Seismic profile across the Nankai accretionary complex [after Kinoshita et al., 2012]. IODP drill sites are projected onto the profile. IODP Sites C0011 and C0012 are located on the incoming plate.

2. Geological setting and sample description

The growth of the Japanese Island arc system was initiated in the Permian by the subduction of ancient Pacific Ocean floor [Taira, 2001]. Since the Miocene [Nakamura et al., 1984], the Philippine Sea Plate is subducted beneath the Eurasian Plate at the Nankai subduction zone off the coast of SE Japan. Presently, the Philippine Sea Plate moves to the northwest with a convergence rate of ~ 4 cm a⁻¹ [Seno et al., 1993]. Sediments of the Shikoku Basin, forming the northwestern edge of the Philippine Sea Plate, are partially accreted to the front of the 100 km wide Nankai accretionary wedge in a series of fault-fold packets [Park et al., 2002b] southeast of Shikoku Island (Figure 2. 1A). Further upslope and landward of the zone of frontal accretion there is an important out-of-sequence megasplay fault branching off the plate boundary thrust at depth (Figure 2. 1B) [e.g., Park et al., 2002a; Baba et al., 2006; Wang and Hu, 2006; Tobin and Kinoshita, 2006; Moore et al., 2007]. Horizontal and vertical offset is at least 1250 m and 750 m, respectively [Moore et al., 2009]. The fault zone is thought to be weak [Park et al., 2002b], prone to seismic reactivation, and transferring displacement near to the seafloor [Moore et al., 2007]. The megasplay fault lies in the coseismic rupture area of the 1944 Tonankai earthquake (M 8.0) and the 1946 Nankaido earthquake (M 8.1) [Park et al., 2002a; Baba and Cummins, 2005; Baba et al., 2006] and, thus, may have initiated historic tsunamis [Park et al., 2002a; Wang and Hu, 2006; Kimura et al., 2011]. During IODP Expeditions 314, 315, 316, 319, 322, 326, 332, 333, and 334, a transect of 12 sites (and multiple holes) were drilled on the Kumano transect perpendicular to the trench axis and across the accretionary prism and incoming plate (Figure 2. 1A) [Park et al., 2000; Baba and Cummins, 2005]. The water depths are between ~ 2500 and ~ 4100 m at the drill sites. In this study we focus on seven drill sites, from which we investigated a suite of nine whole round samples from a depth range between 28.9 and 127.97 mbsf (meters below seafloor; Table 2. 1). Samples of the accretionary prism were collected during IODP Expedition 315 (Site C0001), Expedition 316 (Sites C0004, C0006, C0007, and C0008), and from the incoming Philippine Sea Plate during Expedition 333 (Sites C0011 and C0012, Figure 2. 1A).

Table 2. 1: List of investigated samples

core number	333-C0012C-4H-5	333-C0011D-2H-2	316-C0007C-7X-1			316-C0006E-8H-1		316-C0006E-20X-2		316-C0008C-7H-8		316-C0008A-9H-3			316-C0004C-8H-2		315-C0001E-11H-1	
experimental subsample	K022	K020	K011	K012	K016	K007	K009	K013	K019	K015	K018	K002	K006	K014	K004	K010	K003	K005
depth [mbsf]	28.9	33.1	6.2	6.8	6.8	4.8	4.8	1.9	1.9	6.9	6.9	7.6	7.6	7.6	6.2	6.5	9.6	9.6
lithology	hemipelagic pyroclastic clay, silty clay and clayey silt	hemipelagic/ pyroclastic sediments, ash	olive gray fine-grained sand			black fine-grained sand		fine grained sand. silty sand and silty clay		silty clay		silty clay			silty clay		silty clay. clayey silt and volcanic ash	
characterization	hemipelagic/ pyroclastic facies	hemipelagic/ pyroclastic facies	trench wedge			sand-dominated trench wedge		mixed sand-mud trench wedge		slope basin sediments		slope basin sediments			slope-apron facies		slope-apron facies	
quartz (%)	20	8	27			25.8		26.5		24.8		30.2			20.7		19.4	
plagioclase (%)	17	30	36			29.4		23.3		29.6		21.7			15.9		18.1	
calcite (%)	0	0	0			0.2		0		0.4		4.4			17.3		16.9	
total clay (%)	63	62	37			44.6		50.2		45.2		43.7			46.1		45.7	

Core numbers and experimental subsample numbers are given. The data are taken from Expedition Scientists [2009] and Expedition Scientists [2009a-d]. Data in bold type are taken from Expedition 333 Scientists [2012a, 2012b]

The following characterizations of IODP Sites C0011 and C0012 follow Expedition 333 Scientists [2012a, 2012b], and those of the accretionary prism sites (IODP Sites C0001, C0004, C0006, C0007, and C0008) follow Expedition 315 Scientists [2009] and Expedition 316 Scientists [2009a, 2009b, 2009c, 2009d].

The most seaward drill Site (C0012) is located on the incoming Philippine Sea Plate. Hemipelagic/pyroclastic clay, silty clay, and clayey silt of Unit I (Holocene to Miocene) are deposited above sandy volcanic turbidites of Unit II (upper Miocene). The sample investigated in this study (C0012C-4H-5, 28.9 mbsf, experimental subsample K022) belongs to Subunit IA.

Five lithological units were identified during IODP Expedition 322 at Site C0011. Later, the uppermost two units were the drilling target of IODP Expedition 333 at Site C0011. Unit I consists of hemipelagic/pyroclastic sediments (Holocene to upper Miocene), and Unit II is characterized as volcanic turbidite facies, dominated by tuffaceous sandstone, gravel, and sand beds (late Miocene). The sample investigated in this study (C0011D-2H-2, 33.1mbsf, experimental subsample K020) belongs to Subunit IA.

IODP Sites C0007 and C0006 are located at the frontal thrust zone (accretionary prism toe). Four units were identified at Site C0007. Unit I is formed by Pleistocene fining-upward cycles of silty clay, sand, and silty sand. Based on a coarsening-upward trend of silt, sand, and gravel, Unit II is subdivided into four Subunits. Unit III is formed by Pliocene clay and silty clay with ash content. The boundary of Unit III and Unit IV is defined by a thrust fault and the occurrence of sand (possibly of Pleistocene age). The sample investigated in this study belongs to Subunit IIA (C0007C-7X-1, 62.89 mbsf, experimental subsamples K011, K012, and K016). Bedding planes were observed in subsample K012 (10 to 15° dip). Particle size analyses of this core section indicate 75% clay, 20% fine silt, and 5% medium silt [Stipp et al., 2013].

Site C0006 is located landward of Site C0007 but still in the frontal thrust zone. Three lithological units were defined. Unit I is characterized as trench to slope transition facies formed by structureless Pleistocene clay. Unit II sediments are trench deposits of Pleistocene age. Generally, the sand and silt content

increases upward in Unit II. Unit III consists of Pleistocene to late Miocene silty clay with intercalated tuff layers. The sequence is interpreted as hemipelagic deep marine basin sediments. Two core samples from Site C0006 were investigated, both representing trench deposits: sample C0006E-8H-1 (48.23 mbsf, Subunit IIA, experimental subsamples K007 and K009) and sample C0006E-20X-2 (127.97 mbsf, Subunit IIB, experimental subsamples K013 and K019). Particle size analyses of core section C0006E-8H-1 indicate 85% clay, 10% fine silt, and 5% medium silt, and for core section C0006E-20X-2 60% clay, 30% fine silt, and 10% medium silt [Stipp et al., 2013].

Drilling at IODP Site C0008 recovered slope basin sediments seaward of the megasplay fault, i.e., in its footwall. Two lithological units were defined. Unit I is of Pleistocene to Pliocene age, with two subunits of silty clay, separated by the occurrence of mudclasts. The sand-rich turbidites of Unit II (Pliocene) are formed of pebbly sandstone with silty clay interbeds. Two samples from Site C0008 were investigated: sample C0008A-9H-3 (76.06 mbsf, experimental subsamples K002, K006, and K014) and C0008C-7H-8 (60.96 mbsf, experimental subsamples K015 and K018), both belonging to Unit I. Two aggregates of oxidized pyrite and some millimeter-sized white spots (possibly calcareous aggregates or shell fragments) at the surface and the sidewalls of the sample cylinder were observed during preparation. Sample C0008C-7H-8 contained a coarsegrained sand layer dipping with $\sim 15^\circ$ representing bedding (subsample K018). This sample showed several horizontal and vertical cracks. Both samples are similar in their particle size distribution of 75% clay, 20% fine silt, and 5% medium silt [Stipp et al., 2013].

Site C0004 is located ~ 1 km landward of Site C0008 in the immediate hanging wall of the megasplay fault. Four lithological units were identified. Unit I (Pleistocene) is a slope-apron facies, formed by silty clay with up to 25% nannofossils. Unit II (Pliocene) is subdivided in two subunits, a mass transport deposit (Subunit IIA) and silty clays (Subunit IIB). The upper and lower boundaries of the volcanic ashbearing Unit III are marked by age reversals. The silty clays of Unit IV are characterized as underthrust slope facies. The analyzed sample (C0004C-8H-2, 65.26 mbsf, experimental subsamples K004 and K010) belongs to Unit I. Particle size analyses indicate 60% clay, 30% fine silt, and 10% of medium silt [Stipp et al., 2013].

Site C0001 is the most landward one investigated in this study. Two lithologic units were defined at this site. Unit I with three subunits is made up of silty clay, clayey silt, and volcanic ash layers in slope-apron facies of Quaternary to late Pliocene age. The boundary to Unit II is formed by an unconformity. The upper accretionary prism sediments of Unit II (late Pliocene to late Miocene age) are dominated by bioturbated silty clay to clayey silt. The sample investigated in this study (C0001E-11H-2, 90.6 mbsf, experimental subsample K003 and K005) belongs to Subunit IA. Particle size analyses indicate 60% clay, 30% fine silt, and 10% medium silt [Stipp et al., 2013].

3. Methods

Sonic travel times were measured during pressurization and triaxial deformation tests on the sample material. Only sections of whole round cores that were classified as undisturbed in computer tomography (CT) inspection aboard D/V CHIKYU were used to minimize errors caused by cracks and sample disruption. For the triaxial tests, we used a modified Moser Systemtechnik deformation apparatus at Kiel University with a maximal axial load of 10 kN and a maximal confining pressure (σ_3) of 1000 kPa (Figure 2. 2). The apparatus is equipped with axial load, cell pressure, and displacement transducers, a pore pressure (σ_{pore}) and back pressure (σ_{back}) controlling system, a computer for operation and data acquisition, and Global Digital Systems Ltd bender elements mounted to the upper and lower pistons. The piezoelectric bender elements induce the sonic signal (a sine wave with a frequency of 5 kHz, and 10 kHz in experiment K022), and vice versa, they produce the electrical signal as a receiver. Displacement is generated in our experiments by the stepper motor (Figure 2. 2) slowly moving the lower piston upward. The displacement transducers are capable to measure with 0.5 μm accuracy and thus with a negligibly small error.

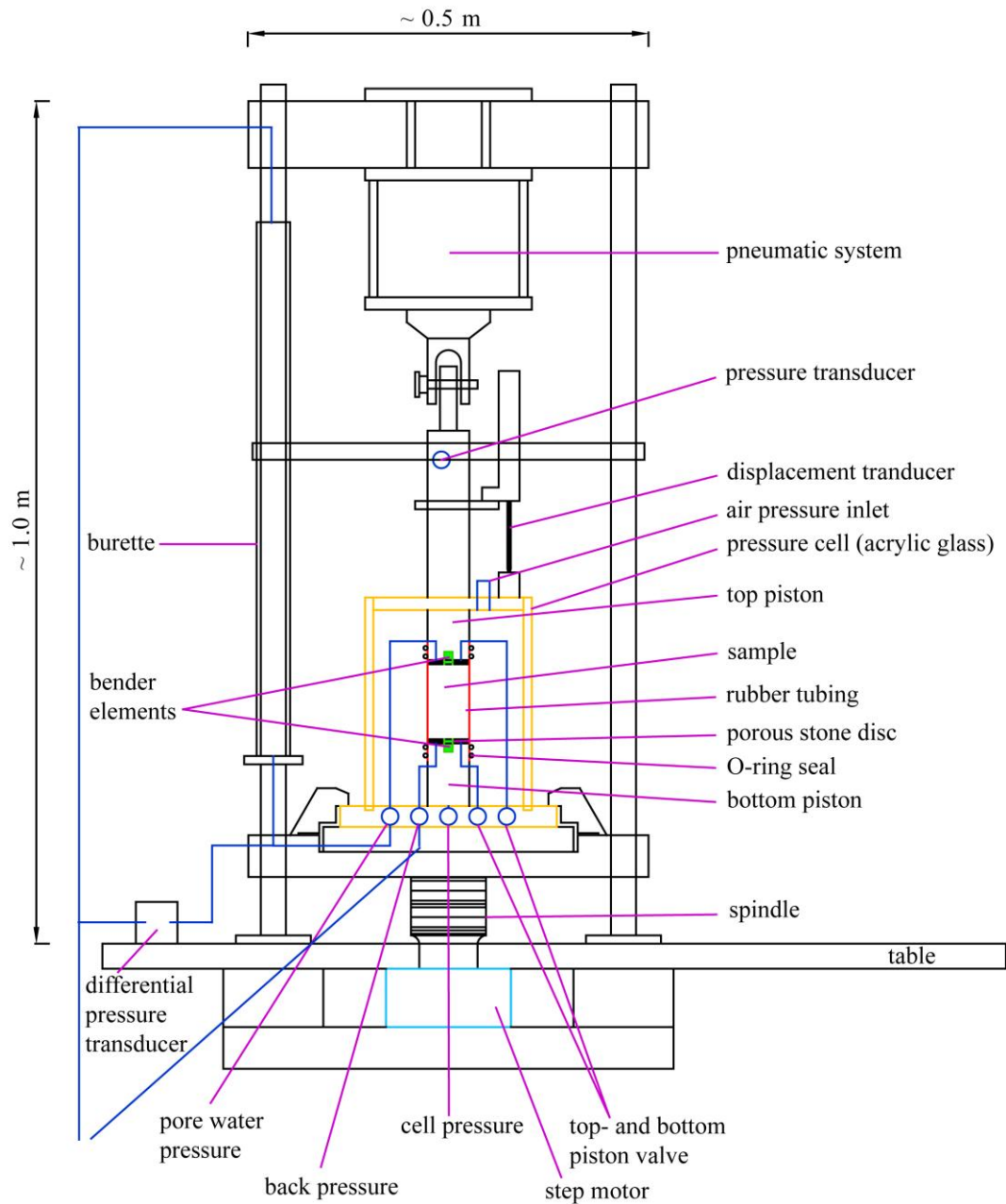


Figure 2. 2: Schematic chart of the deformation apparatus from Moser Systemtechnik used for the triaxial deformation experiments (modified after M. Rolfs, unpublished manuscript, 2010).

Cylindrical samples of 50mm in diameter and 48–102mm in length prepared from the IODP drill cores were resaturated and pressurized in the triaxial deformation apparatus. Sonic measurements from the pressure increase stage after saturation as well as from the deformation stage of the experiments will be presented in this study. Deformation was carried out in three different types of geotechnical tests: (1) single step compression tests at constant confining pressure of 1000 kPa and constant displacement rates of 0.01 or 0.1mm/min, (2) pressure

stepping tests at constant displacement rates of 0.01 or 0.1mm/min and stepwise increasing confining pressure (400 kPa, 640 kPa, and 1000 kPa) in three different deformation steps, and (3) rate stepping tests at constant confining pressure of 1000 kPa and stepwise increasing displacement rate in the range between 0.01 mm/min and 9mm/min. Further information on the deformation apparatus, the experimental procedures, stress/strain and pore pressure/strain-diagrams, and plots of V_p , V_s , and displacement versus time are given in the Appendix A 1.1, Figures A 1.1; A 1.2 and A 1.3 in the supporting information.

Porosities of the drilled cores were initially determined by onboard pycnometer measurements (Table 2) [Expedition 316 Scientists, 2009e]. Changes in the sample porosities during experimental testing were calculated for the stages of pressure increase based on the expelled pore water (Table 2). This expelled pore water in the burette (Figure 2. 2) could be measured with an accuracy of 0.075ml for 50ml pore water. During experimental deformation, the pore space is assumed to be constant since the deformation stages were conducted under undrained conditions. The density of the samples was determined after the triaxial deformation tests using a helium pycnometer with an error of $\sim 0.2\%$ (Quantachrome Corporation, 2011–2013). The error might be slightly increased due to effects caused by small pore radii in the fine-grained samples. To keep this error as low as possible, we purged the samples inside the sample chambers using helium with a pressure of 1.8 bars for up to 5min. To control the density measurements, a sample with known density was measured during each analytical run in varying sample chambers. The sample mass was determined using a high-precision balance.

Sonic velocity measurements were performed using bender elements capable of generating both, compression waves (P waves) and shear waves (S waves). The resulting wavelength is 30 cm (for V_p of 1500 m/s) and 6 cm (for V_s of 300 m/s) in case of 5 kHz and 15 cm and 3 cm in case of 10 kHz. For the P waves, this results in a wavelength of up to 5 times the sample length. For the S waves the wavelength is much shorter due to lower V_s . As a result, we were not able to interpret the wavelet after the first arrival, since it is influenced by interference and extinction of the transmitted signal, reflected and converted signals from

Table 2. 2 Expelled pore water and porosity changes during the phases of pressure increase during the experiments.

sample	location	depth mbsf	density beg. [g/cm ³]	density end [g/cm ³]	porosity beg. [%]	expelled pore water [ml]	porosity end [%]	Δ porosity
K020	IP	33.1	1.72	1.84	64.00	18.70	58.92	5.08
K022	IP	28.9	1.46	~2.1	72.00	33.00	49.13	14.87
K007	T	48.2	1.84	2.31	48.90	10.50	42.69	5.51
K009	T	48.2	1.84	2.11	48.90	16.50	39.60	8.60
K011	T	62.8	1.62	2.23	51.64	13.20	44.96	6.68
K012	T	62.8	1.62	2.15	51.64	10.00	46.90	4.74
K016	T	62.8	1.62	2.20	51.64	3.80	49.70	1.94
K013	T	127.9	1.89	2.0	47.70	10.40	41.57	6.13
K019	T	127.9	1.89	1.99	47.40	9.80	42.10	5.30
K015	FW	60.9	1.73	2.08	56.79	12.90	50.31	6.48
K018	FW	60.9	1.73	2.01	56.79	8.00	52.78	4.01
K002	FW	76.0	1.87	nv	52.19	9.60	47.21	4.98
K006	FW	76.0	1.87	2.01	52.19	4.00	50.02	2.17
K014	FW	76.0	1.87	1.9	52.19	14.30	44.13	8.06
K003	HW	90.6	1.6	1.85	61.73	14.80	55.83	5.90
K010	HW	65.2	1.7	1.8	63.82	24.30	54.50	9.32

No pore water measurements are available for experiments K004 and K005. Porosity and density data of the beginning (beg.) are taken from Expedition 315 Scientists (2009), Expedition 316 Scientists (2009 a-d), and Expedition 333 Scientists (2012a, b). IP = incoming plate, T = accretionary prism toe, FW = footwall of the megasplay fault, HW = hanging wall of the megasplay fault

the sidewalls, multiples, and noise. For this reason, frequency and amplitude of the signal cannot be analyzed. However, the first arrivals were useable, and after data processing, we were able to reliably identify first arrivals. A vertical wave path parallel to the core axis was chosen. Compressional (V_p) and shear (V_s) wave velocities were calculated from the travel times and the sample lengths. The most important uncertainties in velocity measurements are caused by the quality of the receiver signal [e.g., Leong et al., 2005], which depends on the specimen-transducer coupling and the noise produced by the shear apparatus. To optimize coupling, Dyvik and Madshus [1985] introduced plate-like bender elements. The prismatic end faces of the bender elements extend into the specimen, ensuring an optimal soil transducer coupling [Lee and Santamarina, 2005].

During the initial pressure increase, V_p and V_s measurements were conducted in ~100 kPa steps, except for experiments K020 and K022, for which the

velocities were measured in time steps of ~ 60 s. During the deformation stages, V_p and V_s were determined in axial strain intervals of ~ 2 to 3%, except for the fast rate stepping tests. In experiments K020 and K022, we performed six velocity measurements in time steps of ~ 300 s. The number of sonic velocity measurements are in the range between three and ten measurements per deformation stage (dependent on strain), resulting in 15 to 39 sonic velocity measurements for each experiment including the pressurization stage, except for experiments K020 (~ 1220 P and S wave measurements) and K022 (~ 600 P and S wave measurements).

The travel time measurements are a source of error, since reflection and refraction at the side walls can cause interference of the waves [Leong et al., 2005]. Several methods for travel time determination have been proposed; nevertheless, the derived velocities are similar [e.g., Viggiani and Atkinson, 1995; Santamarina and Fam, 1997; Leong et al., 2005]. We used first arrival picking [Viggiani and Atkinson, 1995; Arulnathan et al., 1998]. Leong et al. [2005] report on different methods for the identification of the first arrivals: (a) first deflection of the receiver signal and (b) first reversal point of the receiver signal. We used the first negative deflection as first arrival in our study. The high sampling rate (1 MHz) ensured good data resolution, and we were able to identify this point with high accuracy by color coding of the wavelet (Figure 2. 3). The picking error is estimated to be 0.0015 ms and 0.003 ms for the P and the S waves, respectively. This results in velocity errors between 3 and 10%, depending on the travel time. We conducted two reference studies (K020 and K022) with high data redundancy to eliminate potential errors in the velocity measurements.

No temperature correction was applied, since absolute velocity changes are minor for a temperature rise from 10 to 100°C [Bourbié et al., 1987]. A V_p decrease of 1.7% and a V_s decrease of 0.9% was determined for a temperature rise of 100°C [Timur, 1977]. The temperature in the laboratory was held at 20–22°C, while downhole temperatures in the drill holes range between 3.2°C (316-C0006E-8H-1) and 5.5°C (316-C0006E-20X-2) [Expedition 316 Scientists, 2009b]. Thus, the temperature difference would cause an estimated error of $\sim 0.25\%$ (V_p) and $\sim 0.13\%$ (V_s), respectively.

For data analysis, we allocated P and S wave pairs into common shear test gathers to identify misfits of manual first arrival time picks. For first data analysis in the laboratory, we picked the maximum amplitude of the first recorded signal and subtracted half the length of the transmitted signal to determine the first arrivals. This method has several potential sources of errors. First, the length of the transmitted and the received signal is not identical, caused by attenuation and distortion [Arulnathan et al., 1998; Leong et al., 2005]. The length of the received signal decreases with increasing principal stress (σ_1) due to increased grain-grain contacts and decreased damping and, thus, leads to systematic misinterpretation of the first arrivals (Figures 2. 3a and 3b). Second, picking of the maximal amplitude occasionally leads to detection of multiple and converted signals as well as to detection of S waves produced by the side lobes of the bender elements or by poor soil-transducer coupling (especially in case of P wave measurements). Multiple, converted, and reflected signals such as reflection and refraction from the sample boundary [Leong et al., 2005] occasionally cause misinterpretation of the first arrivals. According to Lee and Santamarina [2005] and Leong et al. [2005], especially reflected P waves may interfere with direct S waves resulting in an overestimation of V_s . Therefore, filters were used to eliminate noise, produced by the side lobes of the bender elements and by the deformation apparatus.

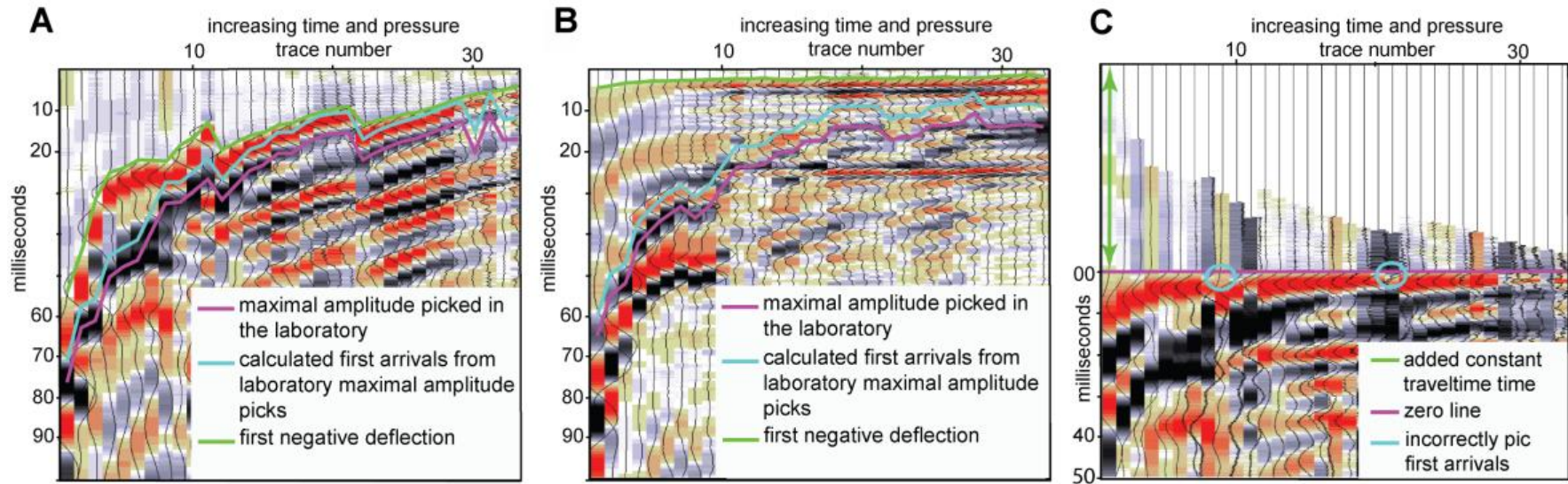


Figure 2. 3: Data example to illustrate the picking and processing procedures. The wave records were color-coded for better first arrival detection. Negative deflections are shown in red, positive deflections in black. (A) Shear test gather of the s-wave recorded from sample K016. Single trace measurements conducted during the triaxial deformation experiments are aligned (x-axis) to clarify variations in the travel time of the acoustic waves (y-axis). For first data evaluation, maximum amplitudes were picked in the laboratory (purple line). Half the length of the transmitted signal was subtracted from the maximum amplitude to identify the first arrivals (blue line). Sorting the data into common shear test gathers and color-coding helped to identify correct first arrivals. First arrivals are hand-picked during reprocessing (green line). (B) Shear test gather of the p-waves of sample K016. Maximum amplitudes picked in the laboratory (purple line) can be identified as multiples by sorting into the shear test gather. Hand-picked first arrivals are indicated by a green line. (C) Application of a static correction to the identified first arrivals, to minimize picking errors. A theoretical constant travel time (green line) was added to the data and the previously picked first arrival travel time was subtracted. This ideally projects the first arrivals into a straight line (zero line, purple). A mismatch of the first negative deflection and the purple line is indicative for erroneous first arrival picking (blue circles). After correction of erroneous picks, the travel time manipulations were reversed and sonic velocities were recalculated.

Reprocessing of the data was carried out using the Omega 2 software (WesternGeco–Schlumberger). Seismic time series analysis helped to identify primary, multiple, and reflected signals, especially P waves generated at the side lobes of the bender element [Santamarina and Fam, 1997]. The data are presented as color-coded wiggle plots (Figures 2. 3a and 3b) enabling an easy identification and control of the first arrivals. The static correction (Figure 2. 3c) comprises a second quality check. For this, we add a constant travel time value to the measured travel time and then subtract the initial first arrival times. This projects the first arrivals ideally into a straight line and enables easy checking of the picked arrivals (first arrivals should then lie in a zero line in Figure 2. 3c). After checking of the arrivals, we reverse the travel time manipulations and recalculate the wave velocities. This procedure guaranteed good quality first arrival detection.

Mechanical and petrophysical properties can be determined by measuring compression wave and shear wave velocities (V_p and V_s). From the following equations we calculated the shear and bulk modulus:

$$V_p = \sqrt{(\kappa + 3/4\mu)/\rho} \quad (1)$$

and:

$$V_s = \sqrt{\mu/\rho} \quad (2)$$

where μ is the shear modulus, κ is the bulk modulus and ρ is the density. From the shear and bulk moduli we calculated the elastic modulus according to the following equation:

$$E = 9\kappa\mu/3\kappa + \mu \quad (3)$$

The equations assume isotropy of the sample material. The effect of anisotropy on sonic velocity [e.g., *Johnston and Christensen, 1993*], however, cannot be neglected for our study, because we used naturally compacted samples as starting material and these samples were deformed up to a maximum axial shortening strain of ~64%. We therefore come back to this topic in the discussion.

Table 2. 3: Overview of the experiments

sample	core section	type		experimental conditions	axial strain
K002	316-C0008A-9H-3	constant rate	strain	confining pressure: 1000 kPa displacement rate: 0.01 mm/min	12 %
K003	315-C0001E-11H-1	constant rate	strain	confining pressure: 1000 kPa displacement rate: 0.01 mm/min	36 %
K004	316-C0004C-8H-2	pressure stepping		confining pressure: 400 kPa,, 640 kPa, and 1000 kPa displacement rate: 0.01 mm/min	first step: 10 % second step: 14 % third step: 37 %
K005	315-C0001E-11H-1	pressure stepping		confining pressure: 400 kPa, 640 kPa, and 1000 kPa displacement rate: 0.01 mm/min	first step: 13 % second step: 17 % third step: 40 %
K006	316-C0008A-9H-3	constant rate	strain	confining pressure: 1000 kPa displacement rate: 0.1 mm/min	31 %
K007	316-C0006E-8H-1	constant rate	strain	confining pressure: 1000 kPa displacement rate: 0.01 mm/min	22 %
K009	316-C0006E-8H-1	pressure stepping		confining pressure: 400 kPa, 640 kPa, and 1000 kPa displacement rate: 0.01 mm/min	first step: 41 % second step: 46 % third step: 61 %
K010	316-C0004C-8H-2	velocity stepping		confining pressure: 1000 kPa displacement rate: 0.5 mm/min, 1.0 mm/min, 5.0 mm/min, and 9.0 mm/min	first step: 16 % second step: 19 % third step: 23 % fourth step: 44 %
K011	316-C0007C-7X-1	pressure stepping		confining pressure: 400 kPa, 640 kPa, and 1000 kPa displacement rate: 0.01 mm/min	first step: 19 % second step: 22 % third step: 42 %
K012	316-C0007C-7X-1	velocity stepping		confining pressure: 1000 kPa displacement rate: 0.5 mm/min, 1.0 mm/min, 5.0 mm/min, and 9.0 mm/min	first step: 14 % second step: 21 % third step: 25 % fourth step: 36 %
K013	316-C0006E-20X-2	pressure stepping		confining pressure: 400 kPa, 640 kPa, and 1000 kPa displacement rate: 0.01 mm/min	first step: 17 % second step: 24 % third step: 42 %
K014	316-C0008A9H-3	pressure		confining pressure: 400 kPa, 640	first step: 20 %

		stepping	kPa, and 1000 kPa displacement rate: 0.01 mm/min	second step: 27 % third step: 43 %
K015	316-C0008C-7H-8	pressure stepping	confining pressure: 400 kPa, 640 kPa, and 1000 kPa displacement rate: 0.01 mm/min	first step: 9 % second step: 12 % third step: 19 %
K016	316-C0007C-7X-1	pressure stepping	confining pressure: 400 kPa, 640 kPa, and 1000 kPa displacement rate: 0.01 mm/min	first step: 15 % second step: 20 % third step: 38 %
K018	316-C0008C-7H-8	velocity stepping	confining pressure: 1000 kPa displacement rate: 0.01 mm/min, 0.05 mm/min, and 0.1 mm/min	first step: 19 % second step: 24 % third step: 28 %
K019	316-C0006E-20X-2	velocity stepping	confining pressure: 1000 kPa displacement rate: 0.01 mm/min, 0.05 mm/min, 0.1 mm/min, 0.5 mm/min, 0.5 mm/min, and 1.0 mm/min	first step: 16 % second step: 20 % third step: 23 % fourth step: 26 % fifth step: 29 % sixth step: 46 %
K020	333-C0011D-2H-2	pressure stepping	confining pressure: 400 kPa, 640 kPa, and 1000 kPa displacement rate: 0.01 mm/min	first step: 6 % second step: 13 % third step: 19 %
K022	333-C0012C-4H-5	pressure stepping	confining pressure: 400 kPa, 640 kPa, and 1000 kPa displacement rate: 0.01 mm/min	first step: 8 % second step: 13 % third step: 37 %

The type of triaxial shear test and the strain rates of the single deformation phases are given in the table.

4. Results

4.1. Porosity and density

Shipboard measurements [*Expedition 315 Scientists, 2009, Expedition 316 Scientists, 2009a-d,*] indicate that porosities decrease with sediment depth (Table 2. 2) ranging between 72% (333-C0011D-2H-2) and 64% (333-C0012C4H-5) for the incoming plate, between 48.9% (316-C0007C-7X-1) and 47.7% (316-C0006E-20X-2) for the prism toe, between 56.8% (316-C0008C-7H-8) and 52.2% (316-C0008A-9H-3) for the footwall of the megasplay fault and between 63.8% (316-C0004C-8H-2) and 61.7% (315-C0001E-11H-1) for the hanging wall of the megasplay fault. The only exception to this trend is observed for the samples from core segment 316-C0007C-7X-1 (K011, K012 and K016) which show higher porosities of 62.8% compared to shallower sediments of core segment 316-C0006E-8H-1 (1.84 g/cm³); both come from the prism toe area. The same is observed for the densities of the hanging wall sediments, where the density decreases with depth from 1.7 g/cm³ in 65.2 mbsf (316-C0004C-8H-2) to 1.6 g/cm³ in 90.6 mbsf (316-C0001E-11H-1). During pressurization, bulk density of the samples is increased and ranges between 1.8 and 2.3 g/cm³ after completion of the experiments (Table 2). The estimated porosity losses during the experiments are in the range between 1.94% (K016) and 14.87% (K022). The porosity loss depends on the initial porosity, the pressurization, the fabric, and other factors. No trend for the different drill sites and tectonic settings could be determined. A detailed overview of the amounts of expelled pore water and the resulting porosity changes is given in Table 2.

4.2 Velocity data

In the following section, we describe the results of the p- and s-wave velocity measurements arranged in diagrams for the different types of test. Data points are marked for the different tectonic settings and are described along the IODP cross section (Figure 2. 1) in direction towards the coast.

4.2.1 Stage of pressure increase

This stage comprises the phases of pressure increase ($\sigma_1 = \sigma_3$) subsequent to the sample saturation and also between the deformation steps of the pressure stepping tests. For single-step compression tests and rate stepping tests, we increased $\sigma_1 = \sigma_3$ from 300 to 1000 kPa. For the pressure stepping tests, we increased $\sigma_1 = \sigma_3$ in three steps from 300 to 400 kPa, from 400 to 640 kPa, and from 640 to 1000 kPa (Table 3). These stages of confining pressure increase were carried out under consolidated drained conditions.

In the single-step compression tests and the rate stepping tests, P wave velocities are more or less constant or display only a slight increase for some of the samples with increasing effective confining pressure (Figure 2. 4a). Samples from the accretionary prism toe (K012 and K019; Figure 2. 4a) have the highest values of V_p ranging between ~ 1550 m/s and ~ 1800 m/s except for sample K007 and the first data point of sample K019. This sample displays unrealistically low V_p values below V_p in water (between ~ 600 and ~ 1040 m/s, and 1250 m/s, respectively) which was probably caused by incomplete coupling between bender elements and sample surface. Therefore, we have not interpreted the results of K007 and the first data point of K019 any further.

Samples K002 and K006 from the megasplay footwall show V_p values ranging between ~ 1100 m/s and ~ 1560 m/s except for one unrealistically low data point of ~ 800 m/s (Figure 2. 4a), may be caused by incomplete coupling at the given low effective confining pressure. Low starting values of V_p could generally be caused by this effect. A third sample from the same setting (K018) was the only sample in which the pore water content has been proven to be not fully saturated (see Figure S1). That is why we exclude this sample from any further interpretation. Also, sample K002 displays very low V_p values, but we have no evidence for undersaturated pore water conditions or missing coupling between sample and bender elements. Samples from the megasplay hanging wall (K003 and K010) are characterized by intermediate V_p values in the range between ~ 1350 m/s and ~ 1600 m/s (Figure 2. 4a).

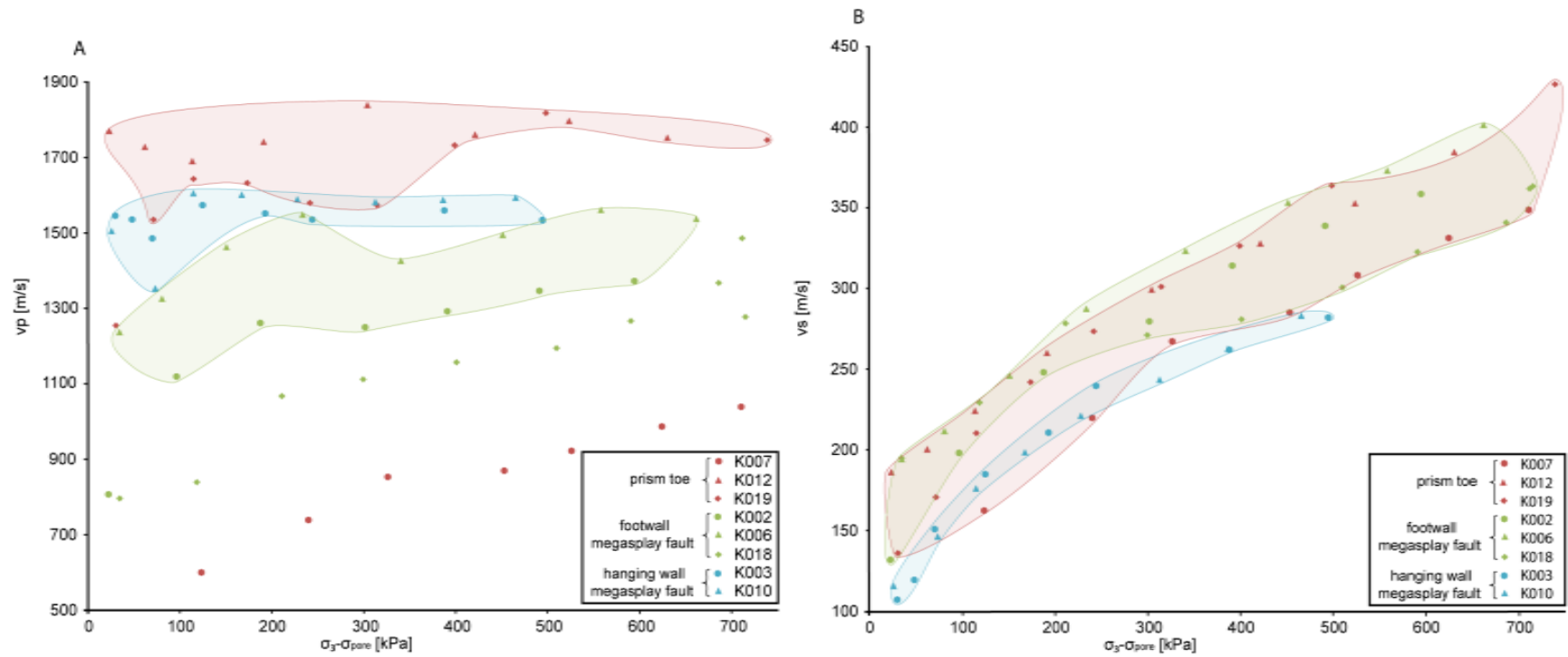


Figure 2. 4: Plots of the values for V_p (A) and V_s (B) versus the effective confining pressure (σ_3 -pore water pressure) measured during the stage of confining pressure increase (from 300 to 1000 kPa) in the single step compression tests and the rate stepping tests. The low velocities recorded for sample K007 and the first data points of K002 and K019 are related to poor sample-transducer coupling. Low velocities in sample K018 are related to incomplete sample saturation.

S wave velocities of the single step compression tests and the rate stepping tests show a significant and consistent increase with increasing effective confining pressure for all of the samples (Figure 2. 4b). The highest velocity increase from $\sim 136\text{m/s}$ to $\sim 430\text{m/s}$ is observed for sample K019 from the accretionary prism toe. There is also no widespread for the different tectonic settings, but the V_s values of the different samples are rather similar at the same effective confining pressure ranging within 100m/s and mostly around 50 m/s (Figure 2. 4b).

In the pressure stepping tests, we also observed a rather constant V_p for the three stages of pressure increase (Figure 2. 5a). The samples from the incoming plate show the lowest V_p values ranging between $\sim 1540\text{m/s}$ and $\sim 1640\text{m/s}$ for sample K020 and between $\sim 1455\text{m/s}$ and $\sim 1510\text{m/s}$ for sample K022. A rather wide range of V_p is observed for the accretionary prism toe samples (K009, K011, K013, and K016). The lowest velocity was found in samples K011 ($\sim 1540\text{m/s}$), which overlaps with the data of the incoming plate sediments, while the majority of the V_p values of the prism toe are higher than the data from the other tectonic settings (Figure 2. 5a). Samples from the megasplay footwall (K014 and K015) show relatively uniform velocities of $\sim 1600\text{m/s}$ except for two very low data points of 1250 m/s and 1440 m/s from sample K014 which might be caused by incomplete coupling between bender elements and sample surface at the given low effective confining pressures. These two data points are not further considered. The samples from the megasplay hanging wall (K004 and K005) display slightly lower V_p values of $\sim 1550\text{m/s}$, and their spread is even smaller than for the footwall samples (Figure 2. 5a).

V_s data of the pressure stepping tests are characterized by a clear increase with increasing effective confining pressure for the different tectonic settings (Figure 2. 5b). The incoming plate samples (K020 and K022) generally show the lowest velocities ranging between $\sim 130\text{ m/s}$ and $\sim 380\text{m/s}$. The abnormal trend in K020 (first stage of pressure increase, marked by an arrow in Figure 2. 5b) is caused by decreasing effective confining pressure due to strongly increasing pore water pressure. The samples from the accretionary prism toe (K009, K011, K013, and K016) display the highest velocities (Figure 2. 5b). In sample K009, the velocity increases from $\sim 115\text{m/s}$ to $\sim 520\text{ m/s}$ at the end of the third pressure increase. Intermediate velocities (between $\sim 150\text{ m/s}$ and $\sim 380\text{ m/s}$) but significantly

overlapping with the prism toe data set were observed for the samples from the megasplay footwall (K014 and K015) and from the megasplay hanging wall (K004 and K005). These velocity data spread only slightly for a specific effective confining pressure (Figure 2. 5b).

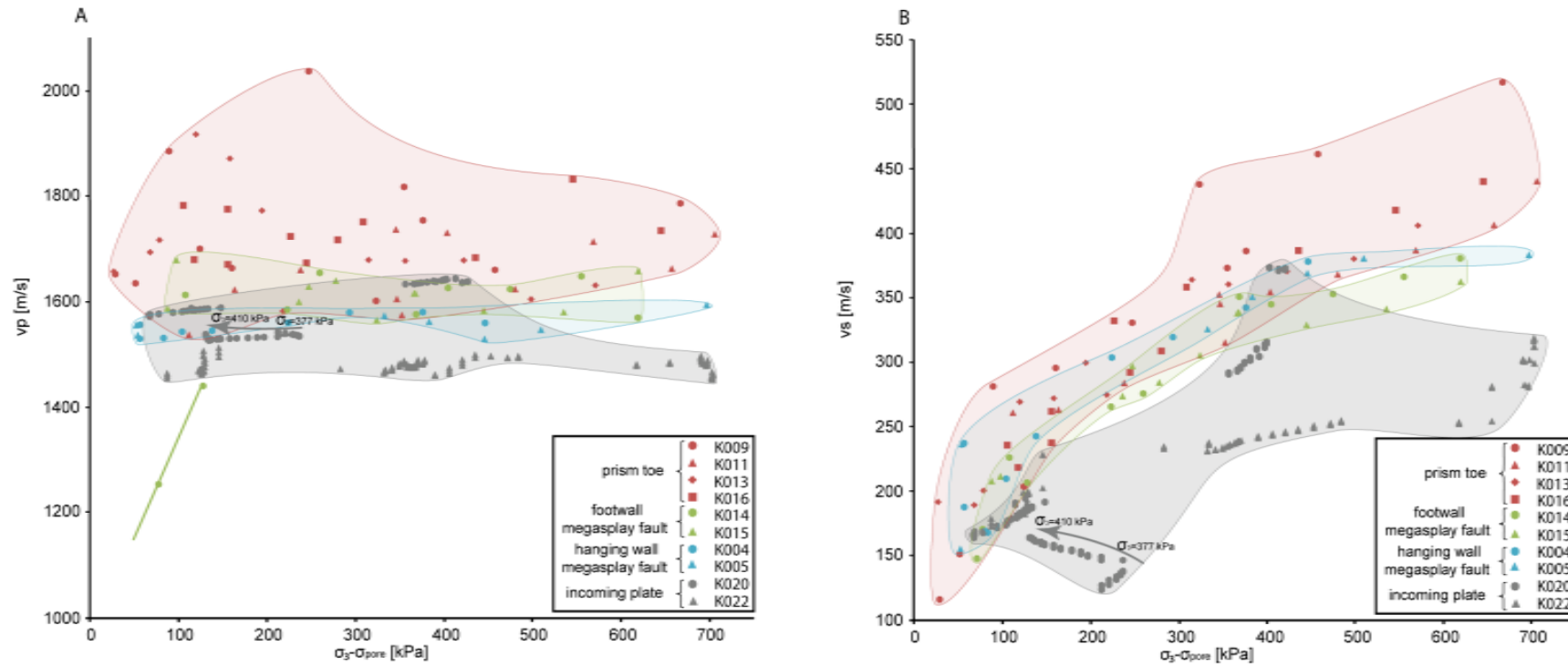


Figure 2. 5: Plots of the values for V_p (A) and V_s (B) versus the effective confining pressure (σ_3 -porewater pressure), recorded during the stages of confining pressure increase in the pressure stepping tests. Confining pressures were increased in three steps (300 to 400 kPa, 400 to 640 kPa, 640 to 1000 kPa). During deformation intervals, the confining pressure was held constant. The strong increase in V_p recorded in sample K014 is attributed to poor sample-transducer coupling at low confining pressure. The grey arrow shows the evolution of V_p in experiment K020. In response to a strong deformation-related increase in pore water pressure, the effective σ_3 decreases.

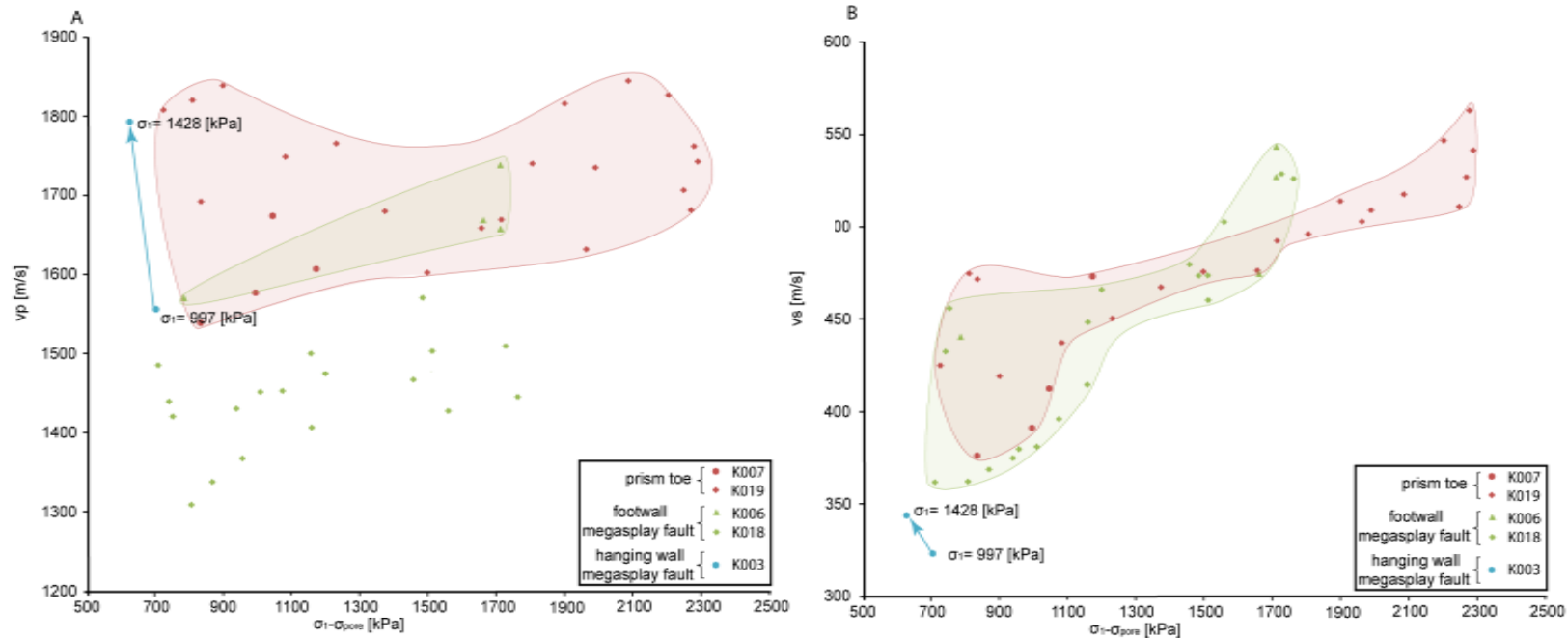


Figure 2. 6: Plots of the values for V_p (A) and V_s (B) versus the effective principal stress (σ_1 -porewater pressure) measured during the deformation stages of the single step compression tests and the rate stepping tests. Both, single step compression tests and rate stepping tests were conducted at 1000 kPa confining pressure. The effective principal stress decrease observed in experiment K003 is due to a strong deformation-related increase in pore water pressure. Values for the increasing effective principal stress are indicated.

4.2.2 Deformation stage

In the single-step compression tests and the rate stepping tests, V_p data are characterized by a widespread and a weak increase with increasing effective stress (Figure 2. 6a). Samples from the accretionary prism toe (K007 and K019) show the highest velocities (~ 1540 m/s to ~ 1800 m/s), with velocities at high largest principal stress being slightly faster than those at low principal stress. V_p values from the megasplay footwall (K006) are lower (~ 1570 m/s and ~ 1700 m/s) overlapping with the prism toe velocities, and they increase also slightly toward largest principal stress (Figure 2. 6a). The V_p data of sample K018 are not considered further in this data set due to uncertain sample saturation conditions. The data set from the megasplay hanging wall (K003) is too small for meaningful interpretation.

The available S wave velocities from the accretionary prism toe and the megasplay footwall largely overlap with a relatively small spread (Figure 2. 6b). They become clearly higher with increasing effective stress ranging between ~ 360 m/s and ~ 560 m/s. The lowest V_s values between ~ 320 and ~ 340 m/s were measured for the hanging wall sample K003, which was only tested at low effective axial stress (Figure 2. 6b).

Sonic velocity measurements conducted during the pressure stepping experiments indicate that there are rather constant or slightly increasing P wave velocities with increasing effective stress and a partial overlap of the four tectonic settings (Figure 2. 7a). The data set displays a large spread for specific effective stresses. The incoming plate sample K022 shows the lowest values for V_p of up to ~ 1500 m/s. The data of sample K020 overlap with those from the megasplay footwall and hanging wall samples. The highest velocities were measured in the

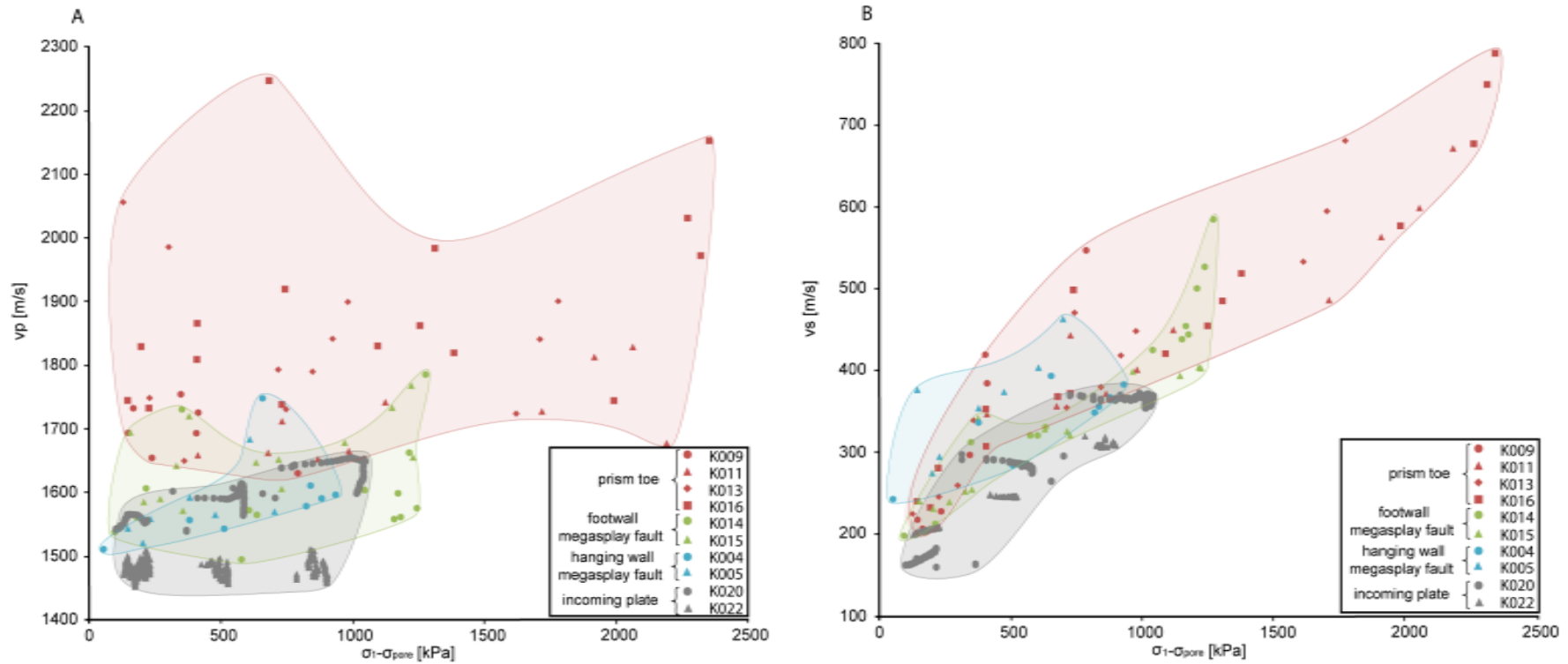


Figure 2. 7: Plots of the values for V_p (A) and V_s (B) versus the effective principal stress (σ_1 -porewater pressure) measured during the deformation stages of the pressure stepping tests. Between the deformation stages of the pressure stepping tests, confining pressure was increased stepwise from 300 to 400 kPa, from 400 to 640 kPa and then from 640 to 1000 kPa.

sediments from the accretionary prism toe (K009, K011, K013, and K016), ranging between ~ 1660 m/s (K009) and ~ 2250 m/s (K016). Samples from the megasplay footwall (K014 and K015) and hanging wall (K004 and K005) are comparable and range between ~ 1540 m/s and ~ 1730 m/s (K015) at the end of the deformation (Figure 2. 7a).

S wave velocities show a clear increase with increasing effective axial stress (Figure 2. 7b). The trend of the entire data set is very clear with only a small spread. Data largely overlap and there is no clear difference in the V_s values between the four tectonic settings, with the exception of the two samples from the incoming plate (K020, K022), which show slightly lower velocities (V_s between ~ 160 m/s and ~ 360 m/s). Samples from the accretionary prism toe extend toward higher V_s and stress values. The highest V_s of ~ 790 m/s was measured at the highest effective stress (sample K016).

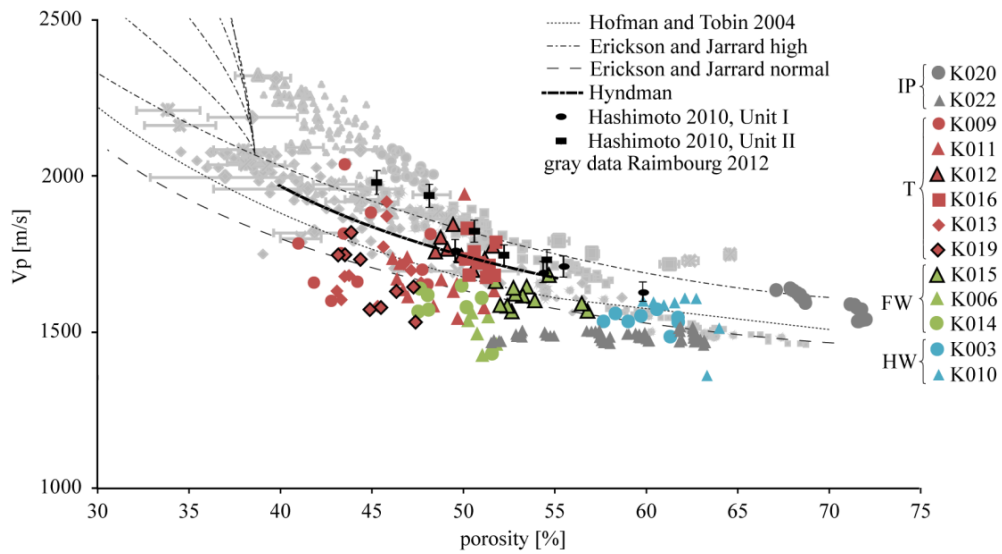


Figure 2. 8: Compilation of V_p -porosity relationships in comparison to different published studies. A few data sets are not included, because they are unreliable due to poor sample-transducer coupling and incomplete pore water saturation (see text for further explanation). Porosity data were calculated from the initial porosity and the amount of expelled pore water. IP = incoming plate; T = accretionary prism toe; FW = footwall of the megasplay fault; HW = hanging wall of the megasplay fault. Compiled published data sets: Raimbourg et al. [2011] from IODP Sites C0001, C0002, C0006 and C0007 as well as from ODP Site 1173 from the Nankai accretionary prism (in grey); Hashimoto et al. [2010] from Site C0001 (in black); Hoffman and Tobin [2004] from the Shikoku Basin (ODP Site 1173) (dotted line); Hyndman et al. [1993] from ODP Site 808 at the outermost toe of the Nankai accretionary prism (thick dashed line); global velocity-porosity trend of Erickson and Jarrard [1998] for highly and normally consolidated sediments (thin dashed lines).

The reliable Vp data from the pressure increase stages are plotted against the porosity evolving under the drained conditions (Figure 2. 8; porosities were calculated from the initial porosity and the amount of expelled pore water). Our data are compared to velocity-porosity data from other studies and different tectonic settings. A global Vp porosity relationship for highly and normally consolidated sediments based on Ocean Drilling Program data from Amazon Fan is proposed by Erickson and Jarrard [1998]. The empirical relationship of Hoffman and Tobin [2004] is derived from sediments of the Shikoku Basin (Ocean Drilling Program Site 1173). Data from Hyndman et al. [1993] were determined on sediments from the toe of the Nankai accretionary prism (Ocean Drilling Program Site 808). Hashimoto et al. [2010] measured also on samples from the hanging wall of the megasplay fault (IODP Site C0001). Further samples from the hanging wall of the megasplay fault (IODP Sites C0001 and C0002) and from the accretionary prism toe (IODP Sites C0006 and C0007) as well as from the Shikoku Basin (Ocean Drilling Program Site 1173) were analyzed by Raimbourg et al. [2011].

4.3 Shear parameters

From the velocity data at σ_{1max} the shear modulus (μ) and the bulk modulus (κ) were calculated using equations (1) and (2). Moduli calculation was done for all samples yielding reliable velocity measurements, and results are given in Table 4. The two samples from the incoming plate have the lowest shear moduli of 0.20 GPa and 0.24 GPa. Shear moduli from the accretionary prism toe are the highest ranging between 0.52 GPa and 1.37 GPa. The sediments from the megasplay footwall display shear moduli between 0.32 GPa and 0.65 GPa and those for the megasplay hanging wall between 0.22 GPa and 0.30 GPa. Bulk moduli for the samples from the incoming plate range between 4.40 GPa and 4.42 GPa, from the accretionary prism toe between 4.94 GPa and 8.41 GPa, from the megasplay footwall between 3.85 GPa and 5.85 GPa, and from the megasplay hanging wall between 4.53 GPa and 5.67 GPa, (Table 4). The elastic modulus (E) is a direct measure of the stiffness of a material and can be determined from the shear and the bulk modulus using equation (3). The elastic moduli for the incoming plate samples range

between 0.59 GPa and 0.69GPa, from the accretionary prism toe between 1.5GPa and 3.89 GPa, from the megasplay footwall between 0.95GPa and 1.87GPa, and from the megasplay hanging wall between 0.64GPa and 0.88GPa (Table 4).

Table 2. 4: Shear, bulk and elastic moduli of the samples.

sample	location	V_p [m/s]	V_s [m/s]	density [g/cm ³]	shear modulus [GPa]	bulk modulus [GPa]	elastic modulus [GPa]
K020	IP	1598.60	357.07	1.84	0.24	4.40	0.69
K022	IP	1493.82	308.44	2.10	0.20	4.42	0.59
K007	T	1607.42	473.35	2.31	0.52	5.28	1.50
K011	T	1677.94	671.23	2.23	1.01	4.94	2.82
K016	T	2153.27	787.41	2.21	1.37	8.41	3.89
K013	T	1901.02	680.38	2.01	0.93	6.02	2.65
K019	T	1743.08	541.60	2.00	0.59	5.29	1.69
K015	FW	1733.92	393.26	2.09	0.32	5.85	0.95
K006	FW	1658.17	543.61	2.02	0.60	4.75	1.71
K014	FW	1785.73	584.35	1.90	0.65	5.20	1.87
K004	HW	1579.01	348.26	1.94	0.24	4.53	0.69
K003	HW	1793.25	343.97	1.85	0.22	5.67	0.64
K005	HW	1684.13	403.24	1.85	0.30	4.85	0.88

Shear and bulk moduli are calculated using the wet bulk density and the velocity measured at σ_{1max} in the deformation experiments. The density of K022 is calculated from the sample volume and the sample mass subsequent to the triaxial testing. For samples K002, K009, K010, K012 and K018, no reliable velocity data were available. From the shear and bulk moduli, the elastic modulus was calculated. IP = incoming plate, T = accretionary prism toe, FW = footwall of the megasplay fault, HW = hanging wall of the megasplay fault

5. Discussion

5.1. P-wave velocities of Nankai Trough sediments

Logging while drilling (LWD) data of Hole C0001D from the hanging wall of the megasplay fault [Kinoshita et al., 2009] are in good agreement to the V_p data of our samples from the same location and Hole C0004 measured during the pressure increase stage (see Figure 2. 9). The V_p values from footwall and incoming plate samples are close to the LWD data of Hole C0001D, while

samples from the accretionary prism toe deviate significantly and show consistently higher V_p values.

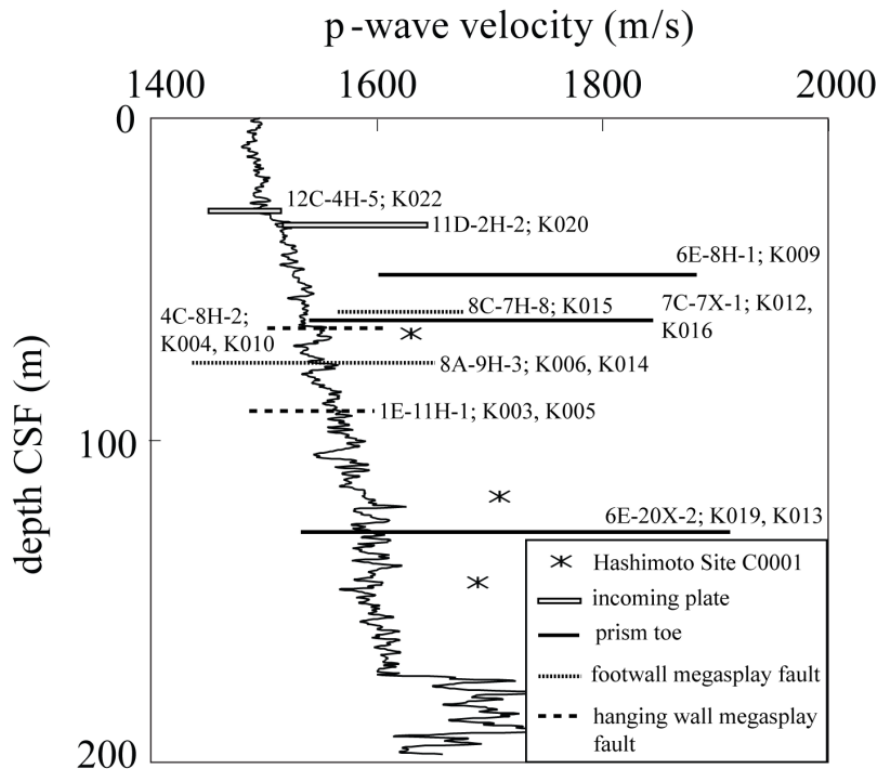


Figure 2. 9: Logging while drilling p -wave velocity measurements of Expedition 315 Site C0001D from Expedition 315 Scientists [2009] in comparison to V_p -data from this study and from Hashimoto et al. [2010]. The megasplay hanging wall data coincide with the LWD data. Data from the other tectonic settings deviate partly to a greater extent.

The V_p data of Hashimoto et al. [2010] on cores of Site C0001 from similar depth (1630–1710 m/s at 390–712 kPa effective confining pressure) are slightly higher than those determined in our study for the hanging wall (about 1530–1650 m/s; see Figures 2. 5, 2. 8, and 2. 9), which is probably due to the slightly higher effective confining pressures in the study of Hashimoto et al. [2010]. The testing methods are also slightly different in the two studies, but differences in the velocities are small and within the range of experimental errors discussed above in section 3. Shikoku Basin sediment data of Hoffman and Tobin [2004] corrected for in situ conditions, data from ODP Site 808 under in situ pressure conditions [Hyndman et al., 1993], from Sites C0001, C0002, C0006, and C0007 as well as from ODP Site 1173 from isotropic loading tests extrapolated to in situ conditions [Raimbourg et al., 2011], show similar or slightly increased V_p values, if compared to our data (Figure 2. 8). Lower values of our study result from variable

confining pressure levels, lower than the in situ pressure conditions. A few very low velocity data points could also be caused by insufficient coupling between the bender elements and the samples. As has been pointed out before, this coupling problem does not occur during deformation at elevated principal stresses and hence elevated contact pressures indicating that it is likely induced by low effective confining pressure during the stage of pressure increase.

What becomes evident from the work cited above and from our data is that compressional wave velocities of fine-grained sediments from the hanging wall of the megasplay fault are similar or slightly higher than the values reported by Shumway [1960] for unconsolidated marine sediments ranging from shallow water sands to deep-sea clays and values from Hamilton [1970] and Hamilton and Bachman [1982] for near-mudline, water-saturated sediments from the Northern Pacific. Since diagenetic effects like cementation can be excluded in our samples, we infer that most if not all of the changes in the acoustic velocities are caused by fabric changes in response to consolidation and/or natural or experimental deformation and by compositional differences. Shape and crystallographic preferred orientation analysis indicates that samples from the topmost sedimentary sequence down to 128 mbsf show already a preferred alignment of the clay minerals [Milliken and Reed, 2010; Saffer et al., 2011; Raimbourg et al., 2011; K. Schumann, Texture development in naturally compacted and experimentally deformed silty clay sediments from the Nankai Trench, Japan (NanTroSEIZE, IODP Expeditions 315, 316, 333), submitted to *Tectonophysics*, 2013].

5.2. P- and s-wave velocities with increasing confining pressure

During the stage of pressure increase in the experiments, two characteristic features of V_p can be observed for all the samples. First, there is a constant to slightly increasing V_p with increasing effective confining pressure, and second, the velocities are significantly different for the four tectonic settings (see Figures 2. 4a and 2. 5a). Experimental pressurization was carried out under drained conditions, with pore water being squeezed out of the samples. Reduction of the pore water volume is indicative of the pore space reduction, which is the dominant control on velocity [Wyllie et al., 1956; Erickson and Jarrard, 1998; Mavko et al., 1998]. From synchrotron texture analysis of the experimental deformed sample

material it is evident that the degree of crystallographic preferred orientation increases during the experimental deformation (K. Schumann et al., submitted manuscript, 2013). V_p in clay minerals is highest parallel to the basal plane and lowest parallel to the c axis [Hamilton, 1970; Franklin and Mattson, 1972]. Reorientation of the clay minerals with the basal planes perpendicular to the principal stress direction, and thus the direction of the lowest V_p parallel to the wave path, counteracts the velocity increase resulting from the increased pressure conditions [Mondol et al., 2007]. For this reason, V_p is rather constant or only slightly increases during the stage of pressure increase.

The varying V_p data for the different tectonic settings are probably due to structural (microfabric) and/or mineralogical differences and different initial porosities. Prism toe sediments are affected by overconsolidation because of erosion of the original overburden as well as tectonic deformation [e.g., Kinoshita et al., 2009; Sreaton et al., 2009; Tsuji et al., 2011], while samples from the footwall and the hanging wall of the megasplay fault represent a normally sedimented slope cover without significant tectonic overprinting [Expedition 316 Scientists, 2009a; Kinoshita et al., 2009]. Lateral tectonic loading as well as overconsolidation at the accretionary prism toe decrease the porosity in comparison to samples of the megasplay fault area or the incoming plate from similar depth (Table 2) and enhance the grain-grain contacts of the sediments [Stoll, 1989; Erickson and Jarrard, 1998; Gettemy and Tobin, 2003; Hashimoto et al., 2011; Raimbourg et al., 2011]. Resulting V_p data of the prism toe are higher than those from the other three settings (Figures 2. 5 and 2. 6). Samples from the incoming plate are richer in clay minerals and are not affected by deformation and overconsolidation [cf. Expedition 333 Scientists, 2012a, 2012b; Stipp et al., 2013]. They show the highest porosities and the lowest velocities in our data (Figure 2. 6).

The S wave velocity is defined as the ratio of the shear modulus and the density (see equation (2)). Since water does not transfer shear impulses, S waves cannot propagate through liquids. For this reason, decreasing pore water content due to increasing confining pressure increases V_s [Toksöz et al., 1976; Mondol et al., 2007]. As a consequence, lower pore water content leads to an increase of the interparticle coupling and friction which additionally enhances the S wave

propagation [Wyllie et al., 1956; Bourbié et al., 1987; Mondol et al., 2007]. Both effects are reflected by the consistently increasing V_s values of the samples with increasing effective confining pressure (Figures 2. 4b and 2. 5b). Unlike the case of the P wave velocities (Figures 2. 4a and 2. 5a), the S wave velocities show no clear differentiation with respect to the accretionary prism toe and megasplay fault tectonic settings, but the two samples from the incoming plate have lower S wave velocities (see Figure 2. 5b). This is probably caused by the higher porosities and the higher clay contents of the incoming plate sediments in comparison to all other samples.

The lithology control on P and S wave velocities is known to be weak [Erickson and Jarrard, 1998; Raimbourg et al., 2011], but the clay content directly changes the porosity, which exerts a primary control on the velocities [Han and Nur, 1986; Marion et al., 1992; Hoffman and Tobin, 2004; Tsuji et al., 2011]. Increasing clay content causes increasing porosities and thus decreasing P and S wave velocities [Erickson and Jarrard, 1998]. Additionally, this effect of increasing porosities is amplified by decreased interparticle coupling due to electrostatic repulsion of the clay minerals [Chiou et al., 1991; Mitchell, 1993].

5.3. P- and s-wave velocities during triaxial deformation

As triaxial deformation in the experiments was conducted under consolidated and undrained conditions, porosity and density of the samples should be constant at this stage. Water is incompressible at the given very low confining pressures. Hence, there should be little influence on P wave velocities by changes in pore water pressure. Indeed, V_p is rather constant during deformation with only a slight increase in a few of the data sets (Figures 2. 6a and 2. 6a). This small increase can reflect fabric changes with increasing strain and/or grain-to-grain contact with increasing effective axial stress. What remains different during deformation are the V_p values from the different tectonic settings. Samples from the toe of the accretionary wedge show higher V_p data than the samples from the megasplay fault area and the hemipelagic soft sediments from the incoming plate (Figures 2. 6a and 2. 7a). This difference is likely preserved from the pressurization stage

(Figures 4a and 5a), during which the prism toe samples displayed the highest V_p data, while the measured velocities of the other tectonic settings largely overlap. Such a continuation in V_p data from drained pressure increase to undrained deformation stage can be seen when comparing velocities of the related diagrams, i.e., Figures 2. 4a and 2. 6a and Figures 2. 5a and 2. 7a, respectively.

In contrast to V_p , V_s values clearly increase with increasing effective axial stress during the deformation stage of the experiments (Figures 2. 6b and 2. 7b). Without measurable porosity and pore water effects during deformation (as explained above) and at the given constant composition, solely the microstructural rearrangement (shapepreferred orientation and crystallographic preferred orientation development) due to increasing strain and increasing grain to grain contacts with increasing principal stress can cause the strongly increasing V_s values in these experiments. Similar to V_p , V_s is the highest parallel to the basal plane. The increasing V_s could be due to an increasing crystallographic preferred orientation of the clayminerals (mainly illite and kaolinite) with increasing strain (cf. K. Schumann et al., submitted manuscript). Since V_s increases during the stage of experimental deformation while the clay minerals align perpendicular to the shortening axis, it becomes obvious that higher interparticle coupling due to clay mineral reorientation and increased principal effective stress causes the V_s increase and not the crystallographic preferred orientation itself. Samples from all tectonic settings largely overlap in their V_s $\sigma_{1\text{eff}}$ trend. Only the hemipelagic soft sediments from the incoming plate show somewhat lower V_s data for a given effective axial stress (Figure 2. 7b), which we attribute to the higher initial porosities and the higher clay content of these samples. This is in agreement to the slightly lower V_s values of the incoming plate samples during the stage of pressure increase just before starting the triaxial deformation (Figure 2. 5b).

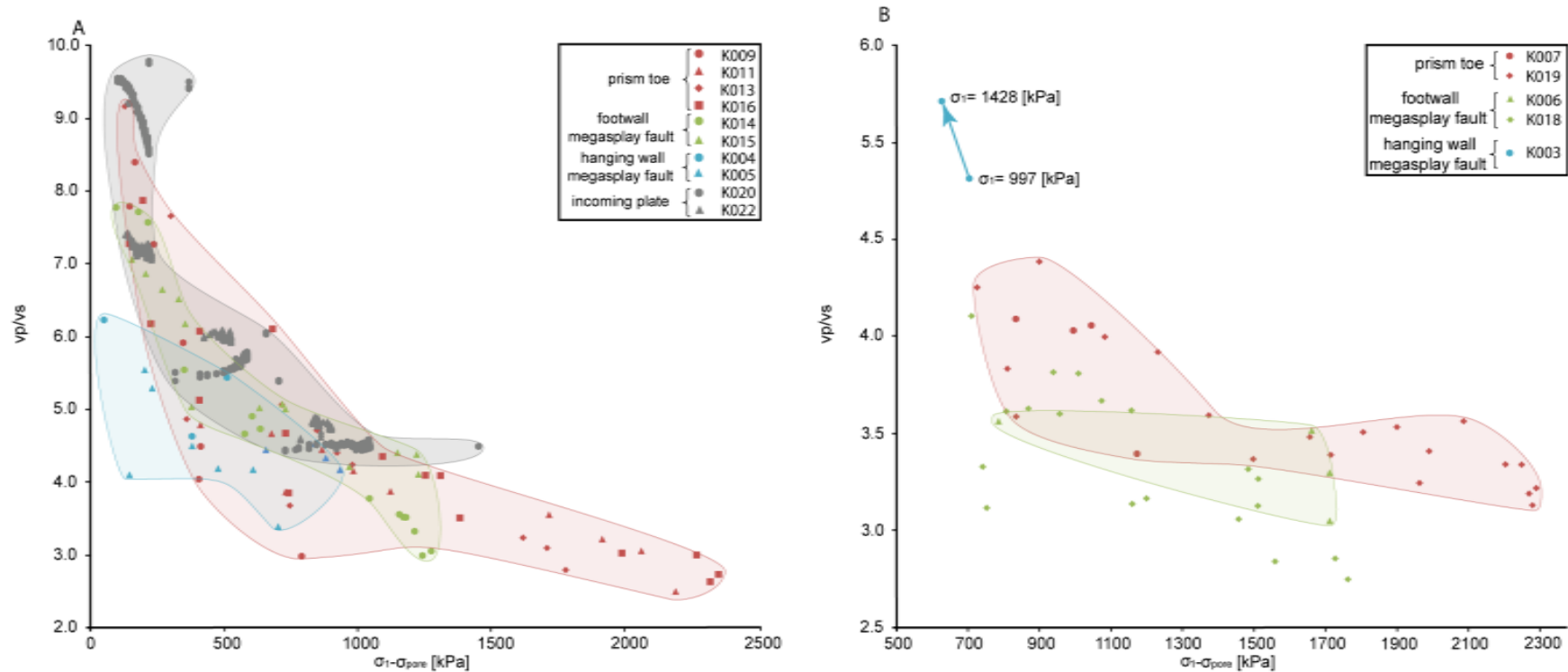


Figure 2. 10: (A) Plot of V_p/V_s -ratio versus the effective principal stress (σ_1 -porewater pressure) measured during triaxial deformation of the pressure stepping tests. Between the deformation stages, confining pressure was increased in three steps (from 300 to 400 kPa, from 400 to 640 kPa and from 640 to 1000 kPa). (B) Plot of V_p/V_s -ratio versus the effective principal stress (σ_1 -porewater pressure) of the single step compression and the rate stepping tests. Blue arrow indicates decrease in effective largest principal stress in experiment K003 due to a strongly increasing pore water pressure. Values for the increasing principal stress are indicated.

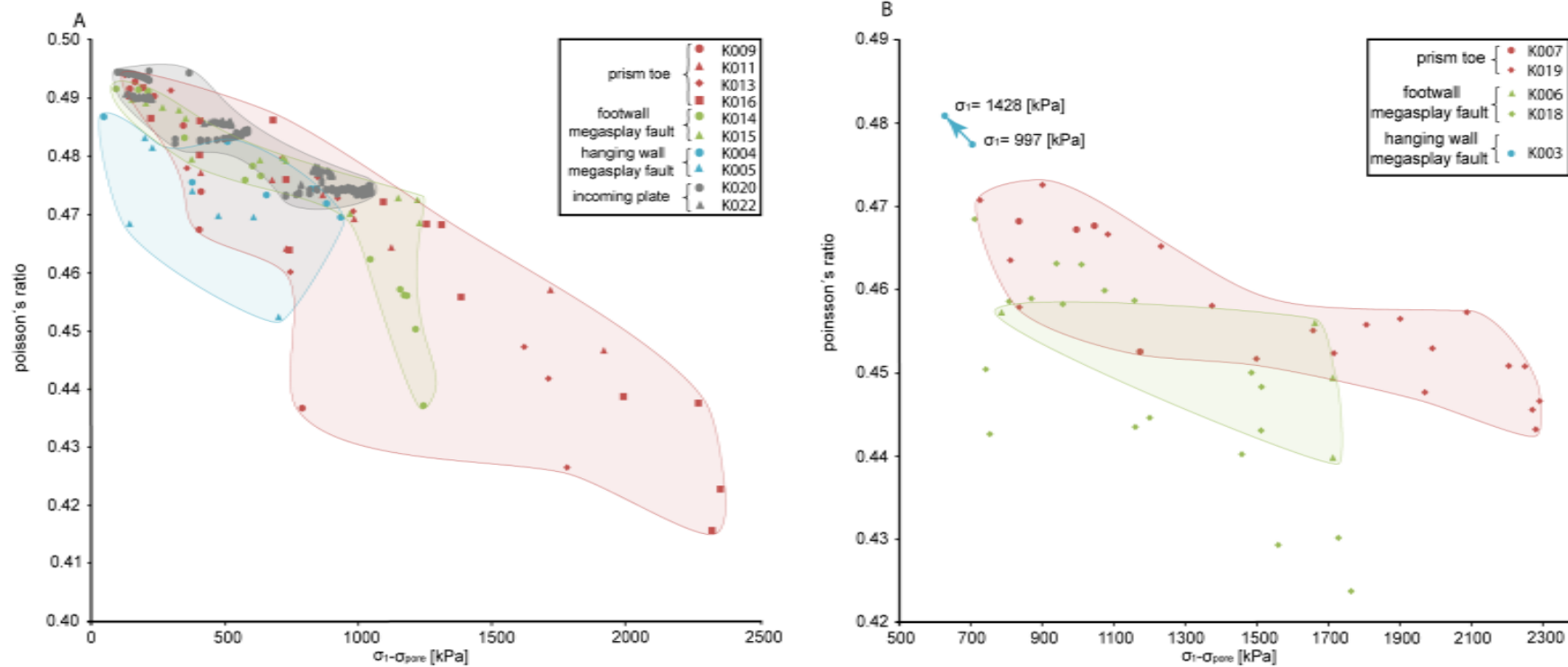


Figure 2. 11: (A) Plot of Poisson's ratio versus the effective largest principal stress (σ_1 -porewater pressure) measured during triaxial deformation of the pressure stepping tests. Confining pressure steps are from 300 to 400 kPa, from 400 to 640 kPa and from 640 to 1000 kPa. (B) Plot of Poisson's ratio versus the effective largest principal stress (σ_1 -porewater pressure) measured during triaxial deformation of the single step compression and the rate stepping tests. Blue arrow indicates decrease in effective largest principal stress in experiment K003 due to a strongly increasing pore water pressure. Values for the increasing largest principal stress are indicated.

5.4. Shear parameters

As unconsolidated sediments have high water contents, and interparticle coupling is weak, the initial V_p/V_s ratio is expected to be high. It will decrease during the course of compaction and deformation in the experiments [Tsuji et al., 2011; Zimmer et al., 2002], a fact that is evident from our data (Figures 2. 10 and 11). The deformation stages were conducted under undrained conditions. For this reason, pore water content and pore space are constant. At increasing effective axial stresses, more grain-grain contacts result in higher V_s and lower V_p/V_s ratios. Anomalous trends, i.e., increasing V_p/V_s ratios and increasing Poisson's ratios with increasing effective axial stress, as observed for sample K003 (Figures 2. 10b and 2. 11b) reflect increasing pore pressure and related pore space collapse induced by deformation.

Previous studies [e.g., Pickett, 1963; Tsuji et al., 2011] have used the V_p/V_s ratio as an indicator for the state of consolidation. This is reflected in the pressure stepping test results (Figure 2. 10a), where the normally consolidated samples from the incoming plate have somewhat higher V_p/V_s ratios than those from the other tectonic settings. On the other hand, this may simply be related to the higher clay content in the incoming plate sediments [cf. Eastwood and Castagna, 1986]. In the geoaoustic results of our study, overconsolidation due to material removal from IODP Sites C0006 and C0007 (accretionary prism toe) [Screaton et al., 2009] and from IODP Site C0008 (footwall of the megasplay fault) [Kimura et al., 2011; Conin et al., 2011; Strasser et al 2011] is not obvious, when the V_p/V_s ratios (Figure 2. 10) and Poisson's ratios (Figure 2. 11) are compared between overconsolidated (prism toe, megasplay footwall) and normally consolidated (incoming plate, megasplay hanging wall) settings.

The shear moduli determined in this study range between 0.2 and 1.37 GPa, and the bulk moduli range between 3.85 and 8.41 GPa (Table 4). Hashimoto et al. [2011] presented shear and bulk moduli data from Site C0002 of IODP Expedition 315 and Site C0004 of IODP Expedition 316. In this study, only one sample from similar depth is described (97 mbsf). The shear modulus of this sample is 0.79

GPa, and the bulk modulus is 4.18 GPa [Hashimoto et al., 2011], thus being in the range of the values in our study.

The low shear, bulk, and elastic moduli determined for samples from the incoming plate and the hanging wall of the megasplay fault are indicative of a lower degree of consolidation. The highest values were measured for the accretionary prism toe sediments, indicating overconsolidation due to erosional material removal [Screaton et al., 2009] and tectonic overprint at the accretionary prism toe. At the footwall of the megasplay fault, the shear, bulk, and elastic moduli are higher than those from the incoming plate and the megasplay hanging wall. Again, this is attributed to erosional material removed at Site C0008 [Kimura, 2011; Conin et al., 2011; Strasser et al., 2011], resulting in slight overconsolidation in these near-surface sediments.

6. Summary and Conclusions

Although frequencies used were not optimal for the sample lengths (especially for P waves), the new method of data processing yields reliable information on P and S wave velocities. This is shown by reference measurements with high data redundancy (samples K020 and K022). Optical single trace first arrival detection performed in the laboratory during the triaxial deformation tests resulted in picking strong reflections not belonging to first arrivals. Instead, multiple and reflected signals were picked. In case of the S waves, however, first raw picking yielded good results. Time series analysis and manually picked first arrivals in common shear test gathers helped to identify erroneous signals. In combination with filters and static corrections, first arrival detection was refined and data quality could be checked by visualization as color-coded wiggle plots.

The measured P wave velocities differ slightly depending on the tectonic setting, with highest velocities measured for the accretionary prism toe sediments ranging from ~1650 to ~2200 m/s and lowest velocities measured for the incoming plate sediments ranging from ~1450 to ~1650 m/s. In contrast, S wave velocities are similar in all tectonic settings ranging from ~150 to ~780 m/s. As a result, parameters like V_p/V_s ratios, shear, bulk, and the elastic moduli can be used to characterize tectonic settings in an environment of only subtle

compositional differences of the sediments. Most probably, these differences result from different compaction paths and deformation histories. Sediments from the accretionary prism toe are influenced by tectonic compaction, which decreases porosity and increases stiffness, resulting in higher velocities. The elastic moduli point to less consolidated sediments on the incoming plate and the hanging wall of the megasplay fault, unaffected by deformation and tectonic overprinting. Overconsolidation due to erosional material removal and tectonic overprint is reflected in highest elastic moduli found in sediments from the accretionary prism toe. Elastic moduli from the footwall of the megasplay fault are intermediate, reflecting a lesser degree of overconsolidation.

In general, the analysis confirms previous observations regarding the dependence of V_p and V_s on parameters such as porosity, pore water content, effective confining pressure, and effective axial stress of deep marine sediments. The data show that V_p is correlated to porosity and mineralogy of the samples and, to a minor extent, to the confining pressure and stress conditions prevailing during the experiments. In the case of V_s , the increasing grain-grain contacts positively influence wave propagation, as shown by the velocity increases with increasing effective stress

Acknowledgements

This study used samples and data provided by the Integrated Ocean Drilling Program (IODP). The authors would like to thank the Scientific Parties of IODP Expeditions 315, 316 and 333 aboard D/V CHIKYU for sample collection and data acquisition. Furthermore, we would like to thank Y. Kitamura, V. Feeser, M. Rolfs, and R. Hinkes for samples supply, technical support and discussions of the triaxial test data. This work was funded by the Deutsche Forschungsgemeinschaft (DFG) through Grant BE1041/28 to J.H.B and M.S. We also thank editor A. Revil, and reviewers Y. Hashimoto and B. Carpenter for very thorough and helpful reviews.

References

- Ando, M. (1975), Source mechanisms and tectonic significance of historical earthquakes along the Nankai Trough, Japan, *Tectonophysics*, 27, 119-140.
- Arulnathan, R., R. W. Boulanger, and M. F. Riemer (1998), Analysis of Bender Element Tests, *Geotechnical Testing Journal*, 21(2), 120-131.
- Baba, T., and P. R. Cummins (2005), Contiguous rupture areas of two Nankai Trough earthquakes revealed by high-resolution tsunami waveform inversion, *Geophysical Research Letters*, 32(8), L08305, doi:10.1029/2004GL022320.
- Baba, T., P.R. Cummins, T. Hori, and Y. Kaneda (2006), High precision slip distribution of the 1944 Tonankai earthquake inferred from tsunami waveforms: Possible slip on a splay fault, *Tectonophysics*, 426, 119-134.
- Becker, J. J., D.T. Sandwell, W.H.F. Smith, J. Braud, B. Binder, J. Depner, D. Fabre, J. Factor, S. Ingalls, S-H. Kim, R. Ladner, K. Marks, S. Nelson, A. Pharaoh, R. Trimmer, J. Von Rosenberg, G. Wallace, and P. Weatherall., (2009) Global Bathymetry and Elevation Data at 30 Arc Seconds Resolution: SRTM30_PLUS, *Marine Geodesy*, 32(4), 355-371.
- Bilek, S. L., and T. Lay (1999), Rigidity variations with depth along interplate megathrust faults in subduction zones, *Letters to Nature*, 400, 443-446.
- Bourbié, T., O. Coussy, and B. Zinszner (1987), Acoustics of porous media. Editions Technip, Paris.
- Carson, B., R. von Huene, and M. Arthur (1982), Small-scale deformation structures and physical properties related to convergence in Japan Trench slope sediments, *Tectonics*, 1(3), 277-302.
- Chiou, W. A., W. R. Bryant, and R. H. Bennet (1991), Clay fabric of gassy submarine sediments, in Bennet, R.H.; Bryant, W.R.; Hulbert, M.H., Microstructure of fine grained sediments, pp. 5-32 Springer-Verlag, New York.
- Conin, M., P. Henry, S. Bourlange, H. Raimbourg, and T. Reuschlé (2011), Interpretation of porosity and LWD resistivity from the Nankai accretionary wedge in light of clay physicochemical properties: Evidence for erosion and local overpressuring, *Geochemistry, Geophysics, Geosystems*, 12, doi:10.1029/2010GC003381.
- DIN 18137 (2011) Soil, investigation and testing – Determination of shear strength – Part2: Triaxial test (German industry standards). Berlin, Deutsches Institut für Normung,
- Dyvik, R., and C. Madshus (1985), Lab measurements of G_{max} using bender elements, in Khosla, V. (1985), Advances in the Art of Testing soils under cyclic conditions, *American Society of Civil Engineers*, 186-196.
- Eastwood, R. L., and J.P. Castagna (1986), Interpretation of Vp/Vs ratio from sonic logs, in Domenico, S.N. Ed. (1986), Shear-wave exploration. *Society of exploration geophysics*, 139-153

- Erickson, S., and R. Jarrard (1998), Velocity-porosity relationship for water-saturated siliciclastic sediments, *Journal of Geophysical Research*, 103(B12), 30385-30406.
- Expedition 315 Scientists (2009), Expedition 315 Site C0001. In: Kinoshita, M., H. Tobin, J. Ashi, G. Kimura, S. Lallemand, E. J. Screaton, D. Curewitz, H. Masago, K. T. Moe, and Expedition 314/315/316 Scientists (2009), *Proceedings of the International Ocean Drilling Program, Volume 314/315/316*. Washington DC, doi: 10.2204/iodp.proc.314315316.123.2009
- Expedition 316 Scientists (2009a), Expedition 316 Site C0004. In: Kinoshita, M., H. Tobin, J. Ashi, G. Kimura, S. Lallemand, E. J. Screaton, D. Curewitz, H. Masago, K. T. Moe, and Expedition 314/315/316 Scientists (2009), *Proceedings of the International Ocean Drilling Program, Volume 314/315/316*. Washington DC, doi: 10.2204/iodp.proc.314315316.133.2009
- Expedition 316 Scientists, (2009b), Expedition 316 Site C0006. In: Kinoshita, M., H. Tobin, J. Ashi, G. Kimura, S. Lallemand, E. J. Screaton, D. Curewitz, H. Masago, K. T. Moe, and Expedition 314/315/316 Scientists (2009), *Proceedings of the International Ocean Drilling Program, Volume 314/315/316*. Washington DC, doi: 10.2204/iodp.proc.314315316.134.2009
- Expedition 316 Scientists (2009c), Expedition 316 Site C0007. In: Kinoshita, M., H. Tobin, J. Ashi, G. Kimura, S. Lallemand, E. J. Screaton, D. Curewitz, H. Masago, K. T. Moe, and Expedition 314/315/316 Scientists (2009), *Proceedings of the International Ocean Drilling Program, Volume 314/315/316*. Washington DC, doi: 10.2204/iodp.proc.314315316.135.2009
- Expedition 316 Scientists (2009d), Expedition 316 Site C0008. In: Kinoshita, M., H. Tobin, J. Ashi, G. Kimura, S. Lallemand, E. J. Screaton, D. Curewitz, H. Masago, K. T. Moe, and Expedition 314/315/316 Scientists (2009), *Proceedings of the International Ocean Drilling Program, Volume 314/315/316*. Washington DC, doi: 10.2204/iodp.proc.314315316.136.2009
- Expedition 316 Scientists (2009e), Expedition 316 methods. In: Kinoshita, M., H. Tobin, J. Ashi, G. Kimura, S. Lallemand, E. J. Screaton, D. Curewitz, H. Masago, K. T. Moe, and Expedition 314/315/316 Scientists (2009), *Proceedings of the International Ocean Drilling Program, Volume 314/315/316*. Washington DC, doi: 10.2204/iodp.proc.314315316.132.2009
- Expedition 333 Scientists (2012a), Expedition 333 Site C0011. In: Henry, P., T. Kanamatsu, K. T. Moe, and Expedition 333 (2012), *Proceedings of the International Ocean Drilling Program, 333*, doi: 10.2204/iodp.proc.333.104.2012
- Expedition 333 Scientists (2012b), Expedition 333 Site C0012. In: Henry, P., T. Kanamatsu, K. T. Moe, and Expedition 333 (2012), *Proceedings of the International Ocean Drilling Program, 333*, doi: 10.2204/iodp.proc.333.105.2012
- Franklin, A. G., and P. A. Mattson (1972), Directional variation of elastic wave velocities in oriented clay, *Clays and Clay Minerals*, 20, 285-293.

-
- Gettemy, G. L., and H. J. Tobin (2003), Tectonic signatures in centimeter-scale velocity-porosity relationships of Costa Rica convergent margin sediments, *Journal of Geophysical Research*, 180 (B10), 2494, doi:10.1029/2001JB000738
- Han, D., and A. Nur (1986), Effects of porosity and clay content on wave velocities in sandstones, *Geophysics*, 51, 2093-2107, doi:10.1190/1.1442062.
- Hashimoto, Y., H. J. Tobin, M. Knuth, and A. Harada (2011), Data report: compressional and shear wave velocity measurements on sediment in the hanging wall and the footwall of megasplay fault, NanTroSEIZE Stage 1, in Kinoshita, M., H. Tobin, J. Ashi, G. Kimura, S. Lallemand, E. J. Screaton, D. Curewitz, H. Masago, K. T. Moe, and the Expedition 314/315/316 Scientists. Proceedings of the Integrated Ocean Drilling Program, Volume 314/315/316, doi:10.2204/iodp.proc.314315316.217.2011.
- Hashimoto, Y., H. Tobin, and M. Knuth (2010), Velocity-porosity relationship for slope apron and accreted sediments in the Nankai Trough Seismogenic Zone Experiment, Integrated Ocean Drilling Program Expedition 315 Site C0001, *Geochemistry, Geophysics, Geosystems*, 11, Q0AD05, doi:10.1029/2010GC003217.
- Hamilton, E. L. (1970), Sound velocity and related properties of marine sediments, North Pacific, *Journal of Geophysical Research*, 75(23), 4423-4446.
- Hamilton, E. L., and R. T. Bachman (1982), Sound velocity and related properties of marine sediments, *Journal of the acoustic society of America*, 72(6), 1891-1904.
- Hoffman, N. W., and H. J. Tobin (2004), An empirical relationship between velocity and porosity for underthrust sediments in the Nankai Trough accretionary prism, *Proceedings of the Integrated Ocean Drilling Program Scientific Results*, 190-196, 1-23
- Hyndman, R. D., G. F. Moore, and K. Moran (1993), Velocity, porosity, and pore-fluid loss from the Nankai subduction zone accretionary prism, *Proceedings of the Integrated Ocean Drilling Program Scientific Results*, 131, 211-220
- Johnston, J. E., and N. I. Christensen (1993), Compressional to shear velocity ratios in sedimentary rocks, *International Journal of Rock Mechanics and Mining Sciences & Geomechanics Abstracts*, 30(7), 751-754.
- Kimura, G., G. F. Moore, E. Screaton, D. Curewitz, C. Streiff, and H. Tobin (2011), Spatial and temporal evolution of the megasplay fault in the Nankai Trough, *Geochemistry, Geophysics, Geosystems*, 12(3), 23, doi:10.1029/2010GC003335.
- Kinoshita, M., H. Tobin, J. Ashi, G. Kimura, S. Lallemand, E. J. Screaton, D. Curewitz, H. Masago, K. T. Moe, and the Expedition 314/315/316 Scientists (2009), Proc. IODP, 314/315/316: Washington, DC (Integrated Ocean Drilling Program Management International, Inc.). doi:10.2204/iodp.proc.314315316.123.2009.

- Kinoshita, M., H. Tobin, N. Eguchi, and N. Simon (2012), IODP Expedition 326 Operations: First Stage of Nankai Trough Plate Boundary Riser Drilling, *Scientific Drilling*, 4, 30-33, doi:10.2204/iodp.sd.14.03.2012
- Kitajima, H., F. M. Chester, and G. Biscontin (2012), Mechanical and hydraulic properties of Nankai accretionary prism sediments: effect of stress path. *Geochemistry, Geophysics, Geosystems*, 13, Q0AD27, doi:10.1029/2012GC004124
- Lee, J., and C. Santamarina (2005), Bender Elements: Performance and Signal interpretation, *Journal of Geotechnical and Geoenvironmental engineering*, 131(9), 1063-1070, doi:10.1061/(ASCE)1090-0241(2005)131:9(1063).
- Leong, E. C., S. H. Yeo, and H. Rahardjo (2005), Measuring shear wave velocity using bender elements, *Geotechnical Testing Journal*, 28(5), 488-498.
- Marion, D., A. Nur, H. Yin, and D. Han (1992), Compressional velocity and porosity in sand-clay mixtures, *Geophysics*, 57(4), 554-563.
- Mavko, G., T. Mukerji, and J. Dvorkin (1998), *The Rock Physical Handbook, Tool for Seismic Analysis in Porous Media*, 329 pp., Cambridge University Press, Cambridge, U. K.
- Milliken, K. L., and R. M. Reed (2010), Multiple causes of diagenetic fabric anisotropy in weakly consolidated mud, Nankai accretionary prism, IODP Expedition 316, *Journal of Structural Geology*, 32, 1887-1898.
- Mitchell, J. K. (1993): *Fundamentals of soil behavior*. Second edition, Wiley New York.
- Mondol, N. H., K. Bjørlykke, J. Jahren, and K. Høeg (2007), Experimental mechanical compaction of clay mineral aggregates – Changes in physical properties of mudstones during burial, *Marine and Petroleum Geology*, 24, 289-311.
- Moore, G. F., N. L. Bangs, A. Taira, S. Kuramoto, E. Pangborn, and H. J. Tobin (2007), Three-dimensional splay fault geometry and implications for tsunami generation, *Science*, 318, 1128-1131, doi:10.1126/science.1147195.
- Moore, G. F., J. Park, N. L. Bangs, S. P. Gulick, H. J. Tobin, Y. Nakamura, S. Sato, T. Tsuji, T. Yoro, H. Tanaka, S. Uraki, Y. Kido, Y. Sanada, S. Kuramoto, and A. Taira (2009), Structural and seismic stratigraphic framework of the NanTroSEIZE Stage 1 transect, in Kinoshita, M., H. Tobin, J. Ashi, G. Kimura, S. Lallemand, E. J. Screaton, D. Curewitz, H. Masago, K. T. Moe, and the Expedition 314/315/316 Scientists, *Proceedings of the IODP*, 314/315/316 doi:10.2204/iodp.proc.314315316.102.2009.
- Moore, J. C., and D. Saffer (2010), Updip limit of the seismogenic zone beneath the accretionary prism of southwest Japan: An effect of diagenetic to low-grade metamorphic processes and increasing effective stress, *Geology*, 29(2), 183-186, doi: 10.1130/0091-7613(2010)029<0183:ULOTSZ>2.0.CO;2.

-
- Moore, J. C., and P. Vrolijk (1992), Fluids in Accretionary Prisms, *Reviews of Geophysics*, 30(2), 113-135.
- Nakamura, K., K. Shimazaki, and N. Yonekura (1984), Subduction bending and education. Present and Quaternary tectonics of the northern border of the Philippine Sea Plate, *Bulletin de la Societe Geologique de France*, 26(2), 221-243.
- Park, J., T. Tsuru, S. Kodaira, A. Nakanishi, S. Miura, Y. Kaneda, and Y. Kono (2000), Out-of-sequence thrust faults developed in the coseismic slip zone of the 1946 Nankai earthquake (Mw=8.2) off Shikoku, southwest Japan, *Geophysical Research Letters*, 27(7), 1033-1036.
- Park, J., T. Tsuru, S. Kodaira, R. Cummins, Y. Kaneda (2002a), Splay fault branching along the Nankai subduction zone, *Science*, 297, 1157-1160, doi:10.1126/science.1074111.
- Park, J., T. Tsuru, N. Takahashi, T. Hori, S. Kodaira, A. Nakanishi, S. Miura, and Y. Kaneda (2002b), A deep strong reflector in the Nankai accretionary wedge from multichannel seismic data: Implications for underplating and interseismic stress release, *Journal of Geophysical Research*, 107(B4), ESE 3-1 – ESE 3-16, doi:10.1029/2001JB000262.
- Pickett, G. R. (1963), Acoustic character logs and their application in formation evaluation, *Journal of the Canadian Petroleum Technology*, 15, 659-667.
- Quantachrome Corporation, Penta-Pycnometer manual, <http://www.quantachrome.com/instruments.html>
- Raimbourg, H., Y. Hamano, S. Saito, M. Kinoshita, and A. Kopf (2011), Acoustic and mechanical properties of Nankai accretionary prism core samples, *Geochemistry, Geophysics; Geosystems*, 12, Q0AD10, doi:10.1029/2010GC003169
- Rolfs, M. (2010), Geotechnische Untersuchung an Sedimenten des Nankai-Akkretionskeils östlich vor Shikoku (Japan), (unpublished student research project).
- Saffer, D., J. Guo, M. B. Underwood, W. Likos, R. M. Skarbek, I. Song, and M. Gildow (2011), Date report: consolidation, permeability, and fabric of sediments from the Nankai continental slope, IODP Sites C0001, C0008, and C0004, In: Kinoshita, M., H. Tobin, J. Ashi, G. Gimura, S. Lallemand, E. J. Screaton, D. Curewitz, H. Masago, K. T. Moe, and the Expedition 314/315/316 Scientists, *Proceedings of the Integrated Ocean Drilling Program*, Washington, DC
- Santamarina, J. C., and M. A. Fam (1997), Interpretation of bender element tests – discussion, *Géotechnique*, 47(4), 873-877.
- Scholz, C. H. (2002), The mechanics of earthquakes and faulting. Second edition. Cambridge.

- Schumann, K., M. Stipp, B. Leiss, and J. H. Behrmann (in preparation), Texture development in naturally compacted and experimentally deformed silty clay sediments from the Nankai Trench, Japan (NanTroSEIZE, IODP Expeditions 315, 316, 333)
- Screaton, E., G. Kimura, D. Curewitz, G. Moore, F. Chester, O. Fabbri, C. Fergusson, F. Girault, D. Goldsby, R. Harris, F. Inagaki, T. Jiang, Y. Kitamura, M. Knuth, C. F. Li, L. Claesson Liljedahl, L. Louis, K. Milliken, U. Nicholson, N. Riedinger, A. Sakaguchi, E. Solomon, M. Strasser, X. Su, A. Tsutsumi, A. Yamaguchi, K. Ujje, and X. Zhao (2009), Interactions between deformation and fluids in the frontal thrust region of the NanTroSEIZE transect offshore the Kii Peninsula, Japan: Results from IODP Expedition 316 Sites C0006 and C0007, *Geochemistry, Geophysics, Geosystems*, 10, doi:10.1029/2009GC002713.
- Stoll, R. D. (1989), *Sediment Acoustics*, Springer-Verlag, New York
- Seno, T., S. Stein, and A. E. Gripp (1993), A model for the motion of the Philippine Sea plate consistent with NUVEL-1 and geological data, *Journal of Geophysical Research*, 98(B10), 17941-17948.
- Shumway, G. (1960), Sound speed and absorption studies of marine sediments by a resonance method. Part I, *Geophysics*, 25(2), 451-467.
- Stipp, M., M. Rolf, Y. Kitamura, J. H. Behrmann, K. Schumann, D. Schulte-Kortnack, V. Feeser (subm.), Strong sediments at the deformation front, and weak sediments at the rear of the Nankai accretionary prism, revealed by triaxial deformation experiments, *Geochemistry, Geophysics, Geosystems*
- Stoll, R. D. (1989), *Sediment Acoustics*: New York (Springer Verlag), Lecture Notes in Earth Sciences, 26
- Strasser, M., G. F. Moore, G. Kimura, A. Kopf, M. B. Underwood, J. Guo, and E. Screaton (2011), Slumping and mass transport deposition in the Nankai fore arc: Evidence from IODP drilling and 3-D reflection seismic data, *Geochemistry, Geophysics, Geosystems*, 12(5), doi:10.1029/2010GC003431.
- Taira, A. (2001), Tectonic Evolution of the Japanese Island Arc System, *Annual Review of Earth and Planetary Science*, 29, 109-134.
- Taira, A., I. Hill, J. Firth, and shipboard scientific party (1991), Geological background and objectives, *Proceedings of the Ocean Drilling Program, Initial Reports*, 131.
- Timur, A. (1977) Temperature dependence of compressional and shear wave velocities in rocks, *Geophysics*, 42(5), 950-956.
- Tobin, H., and M. Kinoshita (2006), 1 NanTroSEIZE: The IODP Nankai Trough Seismogenic Zone Experiment, *Scientific Drilling*, 2, 23-27, doi:10.2204/iodp.sd.2.06.2006.
- Toksöz, M. N., C. H. Cheng, and A. Timur (1976), Velocities of seismic waves in porous rocks, *Geophysics*, 41(4), 621-645.

-
- Tsuji, T., J. Dvorkin, G. Mavko, N. Nakata, T. Matsuoka, A. Nakanishi, S. Kodaira, and O. Nishizawa (2011), Vp/Vs ratio and shear-wave splitting in the Nankai Trough seismogenic zone: Insights into effective stress, pore pressure, and sediment consolidation, *Geophysics*, 76(3), 71-82, doi:10.1190/1.3560018.
- Viggiani, G., and J. H. Atkinson (1995), Interpretation of bender element tests, technical note, *Géotechnique*, 45(1), 149-154.
- Wang, K., and Y. Hu (2006), Accretionary prisms in subduction earthquake cycles: the theory of dynamic Coulomb wedge, *Journal of Geophysical Research*, 111, B06410, doi:10.1029/2005JB004094.
- Wood, A. B. (1941), *A Textbook of Sound*, G. Bell, London
- Wyllie, M. R. J., A. R. Gregory, L. W. Gardner (1956), Elastic wave velocity in heterogeneous and porous media, *Geophysics*, 21(1), 41-70.
- Xu, J., and Y. Kono (2002), Geometry of slab, intraslab stress field and its tectonic implication in the Nankai trough, Japan, *Earth Planets Space*, 54, 733-742.
- Zimmer, M., M. Prasad, and G. Mavko (2002), Pressure and porosity influences on Vp-Vs ratio in unconsolidated sands, *The Leading Edge*, 21, 178-183, doi:10.1190/1.1452611.

3 Manuscript #2

Texture development in naturally compacted and
experimentally deformed silty clay sediments from the
Nankai Trench, Japan (NanTroSEIZE, IODP
Expeditions 315, 316, 333)

Kai Schumann¹, Michael Stipp¹, Bernd Leiss² and Jan H. Behrmann¹

¹*Marine Geodynamics, GEOMAR Helmholtz Centre for Ocean Research Kiel*

²*Geoscience Centre, University of Göttingen, Goldschmidtstr. 3, D-37077
Göttingen, Germany*

submitted to
Tectonophysics

Texture development in naturally compacted and
experimentally deformed silty clay sediments from the
Nankai Trench, Japan (NanTroSEIZE, IODP
Expeditions 315, 316, 333)

Kai Schumann^{a*}, Michael Stipp^a, Bernd Leiss^b, Jan H. Behrmann^a

^a*GEOMAR Helmholtz Centre for Ocean Research Kiel, Wischhofstr. 1-3, D-24148 Kiel, Germany, kaschumann@geomar.de, mstipp@geomar.de, jbehrmann@geomar.de*

^b*Geoscience Centre, University of Göttingen, Goldschmidtstr. 3, D-37077 Göttingen, Germany, bleiss1@gwdg.de*

**corresponding author: kaschumann@geomar.de, +49 431 6002418*

Abstract

The results of Rietveld-based synchrotron texture analysis and microfabric studies are reported on compositionally homogeneous silty clay drillcore samples from the Nankai Accretionary Prism slope and the incoming Philippine Sea plate. Basal planes of illite, kaolinite and smectite show bedding-parallel crystallographic preferred orientations (CPO), increasing with drillhole depth, thus reflecting progressive burial and compaction. In a few samples calcite and albite display a CPO due to crystallographically controlled non-isometric grain shapes, or nanofossil tests. When bed tilting is observed in response to tectonic deformation, bedding-normal maxima are preserved. Scanning Electron Micrographs indicate preferred orientations of micropores and detrital illite flakes, reflecting natural compaction as well. Consolidated-undrained experimental deformation of a suite of thirteen samples from the prism slope shows that phyllosilicate and calcite basal plane CPOs develop normal to the experimental shortening axis. There is at least a qualitative relation between CPO intensity and strain magnitude, validating the March model. Reorientation and flattening of micropores is normal to axial shortening, indicating that they are sensitive strain gauges. We show that synchrotron texture analysis is a new and valuable tool to quantify textures of water-saturated fine-grained phyllosilicate-rich sediments, and assess the effects of compaction and tectonic deformation. (199 words)

Keywords: Crystallographic preferred orientation; synchrotron texture analysis; compaction, deformation; Nankai Accretionary Prism; subduction

1. Introduction

Sediment packages in accretionary prisms that are offscraped from the downgoing plate in subduction zones undergo considerable bulk strain while remaining at a low degree of lithification (e.g. Morgan et al., 2007, or Underwood, 2007 for a review of the topic). Deformation is in response to the need of an accretionary wedge to retain a critical taper (e.g. Davis et al., 1983), in a regime of changing mechanical properties of the rocks themselves and changing

plate tectonic boundary conditions. Much, if not most of the strain in accretionary wedges is accommodated during frontal accretion (e.g. Brown et al., 1990). In the SW Japan forearc the case is illustrated by the NanTroSEIZE drilling transect (Figure 3. 1) of the Integrated Ocean Drilling Program (IODP), which is the stage of the first-ever attempt to core and instrument the updip end of the seismogenic part of a subduction zone (see review in Dixon and Moore 2007, or Tobin et al., 2009). Processes of compaction and tectonic deformation greatly impact the fabrics of the accreted and underthrust sediments. Therefore, it is important to study sediment fabrics to identify the deformation processes that act on a microscale and change petrophysical properties. Compacted and deformed sediments are highly anisotropic regarding acoustic velocity, permeability, and shear strength (e.g. Bennett et al., 1981, Fawad et al., 2010, Jones, 1994, Rai and Hanson 1988, and Voltolini et al., 2009). Fabrics control this anisotropy, which in turn has implications for seismic modeling and other seismic studies (e.g. Johansen et al., 2004, Rai and Hanson 1988, and Voltolini et al., 2009). Fabric genesis also changes the frictional behavior of clay-bearing sediments (e.g. Jones, 1994 and Scholz, 2002). The most important factor controlling anisotropy in sediments is grain alignment (e.g. Johansen et al., 2004, Sondergeld and Rai, 2011 and Voltolini et al., 2009). Crystallographic preferred orientation (termed CPO or texture in the following text) of clay minerals is a result of burial and compaction of sediments (e.g. Bowles et al., 1969, Fawad et al., 2010, Mitchell, 1956 and O'Brien and Slatt, 1990) or tectonic shearing (Buatier et al., 2012, Janssen et al., 2012, Schleicher et al., 2009 and Wenk et al., 2010,). Phyllosilicates become aligned perpendicular to the maximum shortening direction during compaction and diagenesis (Kawamura and Ogawa, 2004). Due to surface charge (negatively charged surfaces and positively charged edges) uncompacted clays form cardhouse or honeycomb structures (e.g. Bennett et al., 1991 and Mitchell, 1956) dominated by edge-to-face grain contacts, and thus explaining the high porosity of clays, muds and mudstones. Due to burial, compaction or tectonic shearing the edge-to-face contacts increasingly become replaced by face-to-face contacts during the evolution of CPO and porosity reduction (Bennett et al., 1981, Carson et al., 1982 and Kawamura and Ogawa, 2004). Since similarly charged crystal faces repel each other, parallel alignment in clays is thought to play an important

role in reducing sediment stiffness (Bennett et al., 1991). Furthermore, pore space collapse has the effect of increasing pore pressure under natural conditions (e.g. Bennett et al., 1981, Brace, 1978, Carson et al., 1982 and Kawamura and Ogawa, 2004). High pore pressures is thought to decrease friction and thus to decrease shear strength of sediments (e.g. Rice, 1992) by the reduction of effective stresses (Bangs et al., 2009, Brace, 1972, Moore et al., 1995 and Tobin and Saffer, 2009).

Previous studies (e.g. Agar et al., 1989, Fawad et al., 2010, Janssen et al., 2012, Krinsley et al., 1983 and Prior and Behrmann, 1990a, 1990b;) used backscattered electron microscopy to investigate microfabric. Other investigators (e.g. Aplin et al., 2006, Behrmann and Kopf, 1993, Curtis et al., 1980, Ho et al., 1999, Kopf and Behrmann, 1997, Oertel, 1983, Oertel and Curtis, 1972, Schleicher et al., 2009 and van der Pluijm et al., 1994) used x-ray texture goniometry (XTG) to quantify preferred orientations of clay-bearing sediments. The routine approach using XTG is to measure the CPO of basal [001] planes of phyllosilicates (e.g. Baker et al., 1969, Oertel and Curtis, 1972 and van der Pluijm et al., 1994). Pole figures usually show maxima of poles to [001] in the direction of maximum shortening, be it by compaction (e.g. Bennett et al., 1981, Bowles et al., 1969 and Vasseur et al., 1995) or tectonic shearing (e.g. Janssen et al., 2012, Schleicher et al., 2009 and Wenk et al., 2010). In soft and unconsolidated, water-rich and polymineralic sediments, SEM and XTG, are difficult to apply due to small grain size, poor crystallinity, low scattering, high stacking disorder, broadening of diffraction peaks, and complex composition. Also, the investigation of highly porous sediments is challenging because of difficult sample preparation (e.g. Behrmann and Kopf, 1993). During the last years, synchrotron techniques for texture analysis have become available to researchers (e.g. Lonardelli et al., 2005 and Wenk et al., 2010, 2008). Due to high brilliance and high energy, low-scattering materials can be investigated. The high energy enables sample penetration of several cm, and allows investigations of entire sample volumes instead of the thin surface layers investigated by XTG. Image plate detectors enable the determination of complex texture information within short time. The presence of water slightly increases the background scattering, but synchrotron radiation is not significantly affected by water, allowing the measurement of sediment samples with pore water under “as-is conditions” without additional sample preparation

and drying. Only high energy monochromatic x-rays allow to penetrate the soft, water-containing material and short measurement times keep the material in shape and avoid dehydration. This helps to minimize changes in the material properties, which are restricted to the immediate contact zone of the sample material with the container wall. Exploiting these advantages of synchrotron radiation, we investigated CPOs of a sample set of variably compacted silty clay sediments and also of experimentally deformed samples from the Nankai accretionary prism and the incoming Philippine Sea plate offshore Japan. We are interested in the effects of compaction and deformation on the CPO and compare this also to shape fabric data from the sample set.

2. Geological setting and sample description

At the Nankai convergent margin offshore SW Japan, the Philippine Sea Plate is subducted beneath the Eurasian Plate with a rate of ~ 4 cm/a (Seno et al., 1993). At the plate boundary, a thick sequence of pelagic sediments belonging to the Shikoku Basin on the incoming Philippine Sea Plate (Ike et al., 2008a), is overlain by sand-rich trench sediments (Moore et al., 2009 and Tsuji et al., 2011). The upper part of the trench fill is tectonically accreted to the overriding Eurasian Plate (Figure 3. 1). Within this accretionary complex, several out-of-sequence thrust faults accommodate horizontal compressive deformation (Song et al., 2011). NanTroSEIZE drilling focuses on the Kumano transect, south of Kii peninsula (Honshu island), located in the 1944 Tonankai earthquake rupture area (Baba and Cummins, 2005 and Park et al., 2000). Perpendicular to the trench, a geological transect of 13 drillsites with multiple holes was drilled during several IODP expeditions. This study focuses on sites drilled during IODP Expeditions 315 (Holes C0001E, C0001F and C0001H, see Expedition 315 Scientists, 2009), 316 (Holes C0004C, C0006E, C0007C and C0008A; see Expedition 316 Scientists, 2009a, 2009b, 2009c, 2009d and Tobin et al., 2009), and 333 (Holes C0011D, C0012C and C0012E; see Expedition 333 Scientists, 2012a, 2012b) (Figure 3. 1). IODP Expeditions 315 and 316 investigated the accretionary prism, while IODP Expedition 333 was dedicated to the incoming plate sediments. In the following, we briefly summarize the information relevant to our study given by

Expedition 315 Scientists (2009), Expedition 316 Scientists, 2009a, 2009b, 2009c, 2009d, Expedition 333 Scientists, 2012a, 2012b and Tobin et al. (2009). Sample material used in this study is listed in Table 3. 1.

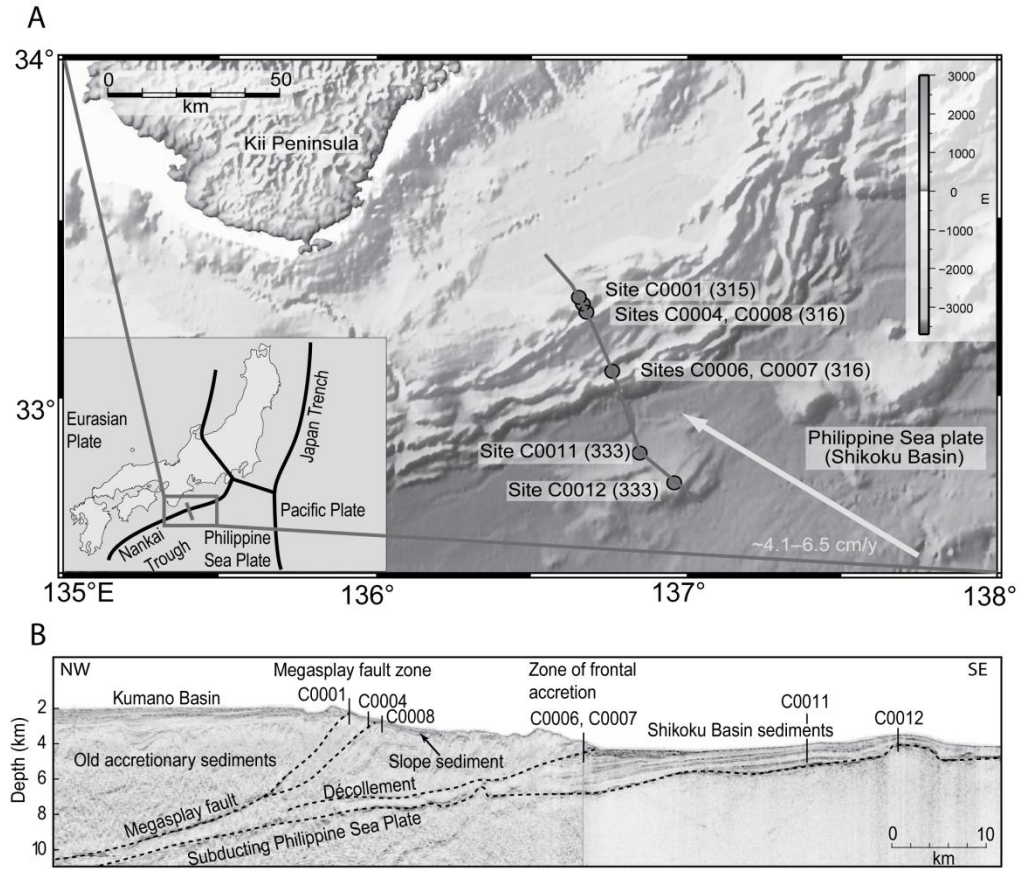


Figure 3. 1: (A) Geographical position and tectonic setting of the Nankai Trough (inset) and detailed bathymetric map (Becker et al., 2009) with the IODP drill sites in the Kumano Basin SE of Honshu Island. The arrow indicates the plate convergence direction. (B) Seismic cross section through the drill sites with tectonic interpretation after Kinoshita et al., (2012). IODP Sites C0001, C0004 and C0008 are above and below the Megaspaly fault, C0006 and C0007 are at the accretionary prism toe and IODP Sites C0011 and C0012 are located on the incoming plate.

Table 3. 1: Composition of the samples.

sample name (IODP)	subsample	depth	normalized (wt%)					Gou and Underwood, 2012				
			clay	quartz	plagioclase	albite	calcite	total clay	smectite	illite	kaolinite	chlorite
316-C0006E-30X-1		221.3	48.2	23.4	28.4		0	48	15	17	1	16
	G001	221.3	42.4	32.1			20.4	4.7				
316-C0008A-9H-3		76.1	43.7	30.2	21.7		4.4	44	11	16	7	9
	K006	76.1	24	42.3			29.2	4.2				
	K014	76.1	36.3	31.2			25.6	6.6				
	original	76.1	26.5	35			32	6				
315-C0001E-11H-1		90.6	45.7	19.4	18.1		16.9	46	15	18	2	11
	K003	90.6	34	27.4			20.6	17.7				
315-C0001E-11H-1		90.6	45.7	19.4	18.1		16.9	46	15	18	2	11
	K005	90.6	49.4	20.6			12.9	16.8				
	original	90.6	30	26.3			26.5	16.9				
316-C0004C-8H-2		65.3	46.1	20.7	15.9		17.3	46	17	19	3	8
	K004	65.3	39.2	26.3			20.1	14.1				
	K010	65.3	25.9	28.9			25	20				
316-C0006E-8H-1		48.2	44.6	25.8	29.4		0.2	53	13	22	6	12
	K007	48.2	25.9	35.6			32.7	6.2				
	K009	48.2	39.9	27.6			25.8	6.4				

316-C0007C-7X-1	62.9	37	27	36	0	37	9	16	1	11
K012	62.9	31.7	35.8		32.2	0	15.4	2.8	13	0.5
K016	62.9	29.7	38.1		31.8	0.1	1.4	18.5	9.8	0
316-C0006E-20X-2	128	50.2	26.5	23.3	0	49	9	24	0	16
K019	128	44	23.4		23.1	9.2	6.2	7.5	30.3	0
316-C0008C-7H-8	61	45.2	24.8	29.6	53	16	22	5	10	
K015	61	34.4	34.7		25.6	5.1	3.2	11.7	19	0.5
K018	61	26.4	39.4		29.3	4.7	3.1	7.9	15.4	0
315-C0001F-14H-3	210.9	58.4	23.2	18.2	0.1		21	21	3	12
	210.9	30.8	30.5		33.8	4.6	2.3	12.2	16.3	0
315-C0001H-19R-2	398.2	62.4	18.6	16.8	2.2		28	22	4	9
	398.2	48.5	22.4		24.2	4.8	8.9	28.3	11.3	0
333-C0011D-26X-1	206.2	69	19	11	0					
	206.2	34.6	32.2		27.7	5.1	3.9	17.1	13.3	0.3
333-C0011D-41X-4	316	63	16	10	11					
	316	33.9	30.6		15	20.5	3.6	7.3	23	0
333-C0012C-4H-5	28.9	63	20	17	0					
	28.9	35.1	28.3		29.8	6.6	4.7	13.8	16.6	0
333-C0012C-9H-6	75.9	68	20	12	0					
	75.9	45.9	28.1		19.5	6.2	4.7	34	7.2	0

333-C0012C-15H-5	<i>121.6</i>	<i>70</i>	<i>17</i>	<i>11</i>	<i>3</i>				
	121.6	41.6	30.4		23.4	4.3	5.9	11.7	24
333-C0012E-3X-4	<i>522.9</i>	<i>69</i>	<i>11</i>	<i>5</i>	<i>15</i>				
	522.9	31.2	23.9		21	23.7	6.5	12.4	12.3

The composition of the samples investigated in this study is given in the table. Values for quartz, plagioclase, albite and calcite printed in italic of IODP Expedition 315 and 316 are taken from the Expedition 315 Scientists, 2009 and Expedition 316 Scientists 2009a-d, from Expedition 333 Scientists 2012a-b for IODP Expedition 333 and from Gou and Underwood, 2012 for the clay minerals. Values printed in bold represent this study. Note that the samples are from the same core segment and from a similar depth, but are not completely identic. Internal inhomogeneity may occur although the overall composition is rather similar.

Samples from two sites located on the incoming plate were analyzed in this study. Site C0012, the most seaward one, was drilled at the crest of a basement knoll, whereas Site C0011 is located closer to the trench on the northwestern flank of a prominent bathymetric high (Ike et al., 2008b, Figure 3. 1). At both sites, Shikoku Basin sediments were drilled. Samples from Site C0012 represent two lithological units. Sediments composed of clay, silty clay and clayey silt, were recovered at Hole **C0012C**, while Hole **C0012E** cored the transition between Shikoku Basin sediments and the igneous oceanic crust. The sediments are silty clays, clayey silts and clays intercalated with volcanic ash layers.

Sites C0006, C0007 and C0008 cored during IODP Expedition 316 are located seaward of a major fault system within the accretionary complex, the so-called megasplay fault (Moore et al., 2009, Figure 3. 1b). Sites C0006 and C0007 are located at the prism toe. Samples from Site **C0007C** belong to Unit II of this drill hole, characterized by a coarsening upward trend with increasing silt, sand and gravel contents. Coring at Site **C0006, Hole E** recovered trench deposit sediments, mainly fine-grained sand, silty sand and silty clay. Within Unit II of Site C0006E, three subunits could be identified: Subunit IIA is a sand-dominated trench wedge facies (Sample 316-C0006E-8H-1, experimental subsamples K007 and K009), Subunit IIB is a mixed sand-mud trench wedge facies (Sample 316-C0006E-20X-2, experimental subsample K019), and Subunit IIC is a mud-dominated trench wedge facies (Sample 316-C0006E-30X-1).

Site C0008 is located in the footwall of the megasplay fault. Both holes, **C0008A** and **C0008C**, penetrated Lithological Unit I composed of slope sediments. The dominant lithology of this unit is silty clay and minor volcanic ash.

Site C0004, cored during IODP Expedition 316, and Site C0001, cored during IODP Expedition 315, were drilled into the hanging wall of the megasplay fault. Samples from Hole **C0004C** belong to Lithological Unit I of this hole, which is dominated by silty clay and characterized as slope-apron facies. Multiple holes were drilled at Site **C0001**. Hole **C0001E** was drilled through Lithological Unit I, the slope-apron facies, made up of silty clay to clayey silt, and Lithological Unit II, the upper accretionary prism facies, formed by bioturbated silty clay to clayey silt. Lithological Units I and II of Hole **C0001E** are separated by an unconformity.

Samples from holes **C0001F** and **C0001H** belong to Unit II (upper accretionary prism facies), which is mainly formed by bioturbated silty clay to clayey silt.

Samples were cored from drillhole depths between 28.9 and 522.9 meters below sea floor (mbsf). Natural (experimentally undeformed) core samples as well as experimentally deformed samples were used for texture investigation in this study. Experimental samples were deformed under consolidated-undrained conditions in a triaxial apparatus (Stipp et al., in press). Triaxial tests were conducted at a maximum of 1000 kPa confining pressure. The axial shortening strains attained during the experiments range from 12% (experimental subsample K002, core segment 316-C0008A-9H-3) to 60% (experimental subsamples K009, core segment 316-C0006E-8H-1).

3. Methods

3.1. Smear slide point counting

For a first composition analysis and especially the determination of the ash and biogenic material contents, smear slide point counting on 18 samples was conducted. After drying of the dispersed samples on microscopic slides using a heating plate (~60°C), Cargille Meltmount was added, and the sample was then covered by a cover slip. For the point counting, an automatic precision stepping stage device (Conwy Valley Systems Limited) mounted onto a ZEISS Axioskop microscope was used to provide a statistical distribution of ~400 counting points across each smear slide. Five component groups are distinguished. Agglomerates of minerals are named “lithics” and volcanic glass chards are named “ash”. Minerals, mainly quartz, feldspar and mica are summarized as “minerals”, foraminifera, diatoms, sponge needles and radiolarians are summarized as “biogenic material”. Material, which could not be resolved due to its small grain size, is termed “submicroscopics”. To provide a rough estimate, submicroscopics are taken to be more or less equal to the clay content of the samples.

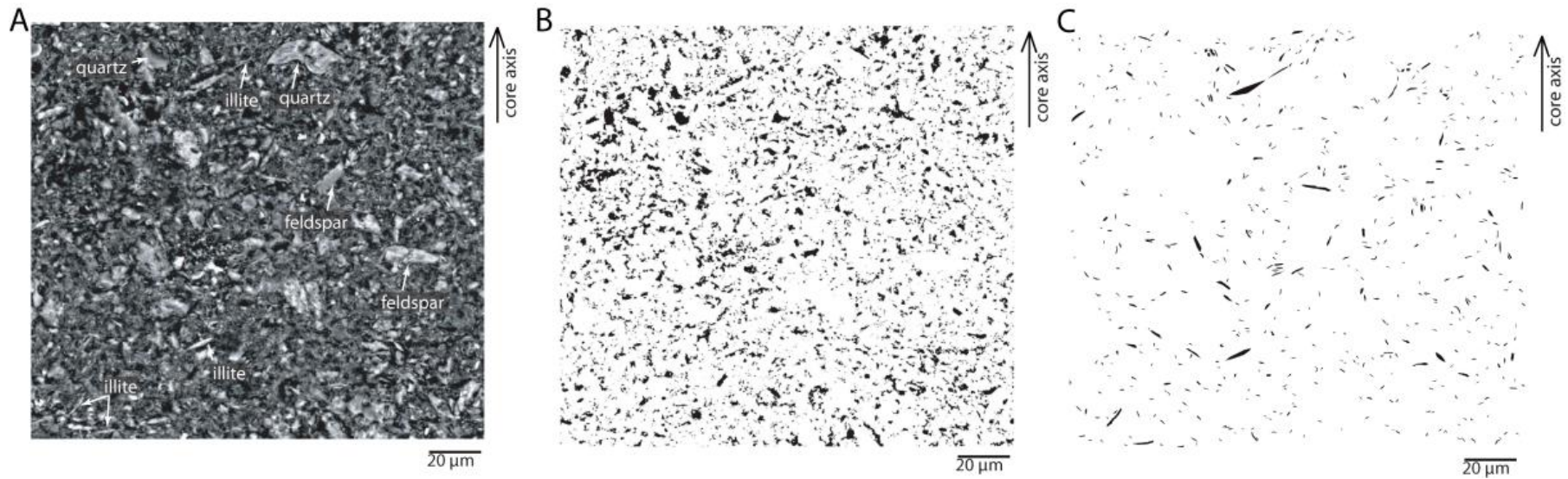


Figure 3. 2: Microstructural analysis of the experimentally deformed subsample K010 from drill core 316-C0004C8H-2. Drill core axis is vertically oriented for all three images with arrow pointing upwards. A) Merged image of 16 detailed BSE images. Mineral grains analyzed by element dispersive x-rays (EDX) are indicated. (B) Binary image from the same section as in (A) showing the threshold result for pores in black and rock material in white. (C) Binary image from the same section as in (A) showing manually outlined illite grains. Images of (B) and (C) are the original data images for the shape preferred orientation analysis of pores and detrital illite grains.

3.2. Shape preferred orientation (SPO) analysis

Preferred long axes orientations of minerals and pores were determined on backscattered and secondary electron (BSE and SE) images using a JEOL JXA 8200 electron microprobe. As we used the microprobe for our study preferentially in high resolution imaging mode in analogy to a scanning electron microscope (SEM), we term these investigations SEM analysis in the following. Samples were dry cut, freeze-dried, and the water-free pore space was stabilized by Araldite 2020 epoxy resin under vacuum (using a water-jet vacuum pump, max. ~15 torr). This preparation method minimizes microstructural modifications by swelling or drying. To further prevent swelling of the freeze-dried clay minerals, ethylene alcohol was used as lubricant and for cooling during grinding and polishing (see Prior and Behrmann, 1990a).

For SEM analysis, an acceleration voltage of 20 kV was used to achieve a high resolution down to a grain size of 0.5 - 1 μm . Mosaics of detailed BSE images (2000 times magnification) were merged together to obtain detailed overview images. 3 mosaics (~200 μm x ~180 μm in size) were analyzed in each of the 8 investigated samples, each mosaic merged from 16 detailed images. The long and short axes of the investigated mineral grains (mainly detrital illite) and pores were determined using the image analysis software “Scion Image” (Scion Corporation 2000-2001). Illite grains and pore spaces were separated from other phases and the fine-grained matrix based on gray-scale value thresholding and manual selection. The semiautomatic thresholding procedure was controlled by energy dispersive x-ray microanalysis (EDX). EDX also enabled to identify mineral phases during imaging and shape analysis. Single mineral grains down to a grain size of 2 μm could be analyzed allowing for the differentiation of smectite and illite from feldspar, quartz and calcite (Figure 3. 2, Appendix A 2.1). Fine grained “matrix” minerals (less than 1 μm) could not be analyzed by EDX.

For the BSE images we used a constant threshold value of 220 within a 256 gray-value range to separate the pore space (Figure 3. 2, Appendix A 2.1). Further image processing largely followed the steps described by Worden et al., (2005). Long axes orientations of pores and mineral grains were plotted in rose diagrams

using the “StereoNett” software package (<http://www.ruhr-uni-bochum.de/hardrock/downloads.html>).

3.3. Synchrotron texture measurements

Hard synchrotron x-ray diffraction was applied at the beam line W2 of the HASYLAB x-ray wiggler hall operated by the Helmholtz-Zentrum Geesthacht, Centre for Materials and Coastal Research (GKSS, DORIS W2) at the German Electron Synchrotron source (DESY) in Hamburg. Relatively low absorption coefficients of hard synchrotron radiation in condensed matter allow to penetrate samples with a thickness of several centimeters. In contrast to neutron radiation, pore water content ranging between 30% (Sample 316-C0006E-30X-1) and 65% (Sample 315-C0001E-11H-1) does not affect the measurements with synchrotron radiation. Additionally, synchrotron diffraction results in a relatively high resolution of 2Θ angles. This is a significant advantage for the analysis of mineralogically complex mud and mudstone samples.

To keep mechanical manipulations of the sample material as low as possible, we developed a cutter to punch cylindrical samples of 17 mm diameter and ~18 mm length from the drill core and to transfer them into acrylic glass sample holders. The sample holders were then sealed to avoid desiccation. Thus, the only fabric change of the clay material takes place at the cylinder wall of the cutter. This, however, makes up only a very small fraction of the total irradiated sample volume. Thus the methodical error induced by sample preparation is reduced to a minimum. The cylindrical sample shape ensures a constantly irradiated volume while rotating the samples in the beam, and a sample shape correction is not necessary. The DORIS electron acceleration ring provides a monochromatic high-energy x-ray beam with a wavelength of $\sim 0.12 \text{ \AA}$ and 100 keV energy. The synchrotron beam with a size of 1x1 mm was directed perpendicular to the axis of the drill cores, i.e. perpendicular to the sample cylinder axis. Transmission diffraction patterns were recorded using a 30x30 cm mar345 image plate detector with a resolution of 2000x2000 pixels, mounted ~1.3 m behind the samples. Samples were rotated in 5° steps from -90° to $+90^\circ$ around the core axis, with 4 s

counting time per image. The resulting 37 images allow for 100% pole figure coverage (Lonardelli et al., 2005).

To assess mineralogical compositions of the samples, the 37 different measurements on each sample were summarized for calculations of averaged diffraction spectra. Such spectra also facilitate an easy and fast preliminary refinement of the crystal structure parameters. Such starting parameters reduce the following computation time of the final phase and texture refinement.

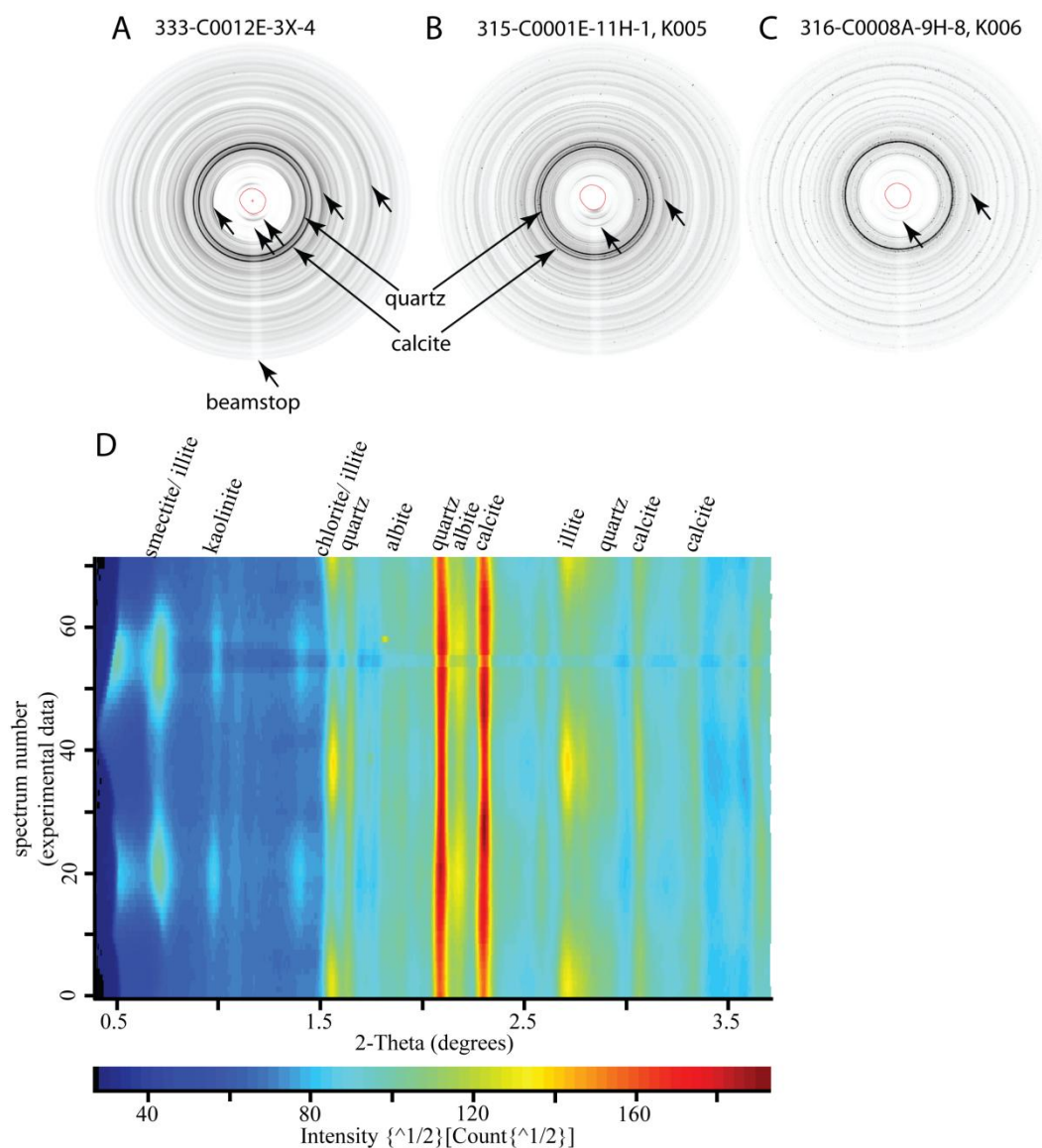


Figure 3. 3: Plate detector images of three different samples. Variable Debye-Scherrer ring intensity immediately shows texturation (short arrows). Smooth rings in (A) are indicative for fine-grained sample material, while spotty plate detector images point to coarse-grained samples and single crystal reflections (increased number of strong point reflexes in B and C). The position of the beam stop (a massive lead block) is indicated by red circles. The straight lighter line in the lower part of the plate detector images is caused by the acrylic glass beam stop holder. (D) An unrolled plate detector image of the sample 333-C0012E-3X-4 (also shown in A) shows variable reflex intensity pointing to texturation of the sample material.

Textured sample material does not influence the synchrotron data, since summed spectra of each sample were refined before the final refinement step. Sample rotation and plate detector image integration over 72 single spectra results in the refinement of 37 x 72 single spectra by using parameters previously determined from an average spectrum. Thus, texture effects on the composition are minimized. Although sample volumes can be measured, layering, internal sample inhomogeneity and variable grain size may increase the error.

The plate detector images display Debye-Scherrer cones as rings, in which each one represents a (hkl) plane. The darker the ring, the higher is the corresponding diffraction index. Discontinuous rings indicate CPO, so that these can be directly derived from the ring patterns on the plate images, and in unrolled 2D-plots of the data (Figure 3. 3). For quantitative texture analyses and adequate graphical representation of the textures in correlation with the sample coordinate system, further data processing has to be carried out (Appendix A 2.2). The data processing strategy can be sketched as follows:

- (1) Image format conversion from the detector format into a 16bit tiff-format needed for further interpretation steps (program Marcvt by Marresearch GmbH).
- (2) Wavelength determination of the synchrotron radiation by means of an Al₂O₃ (corundum) standard sample, beam center determination and spectra summation of the data (program FIT2D, Hammersley, 1998).
- (3) Final crystal parameter refinement and texture calculations were carried out by means of MAUD (**m**aterial **a**nalysis **u**sing **d**iffraction, Lutterotti et al., 1997), a Rietveld-based code.

Diffraction peak intensities are not only functions of the crystal structure (atomic parameters), but also of the CPO (Matthies et al., 1997). The MAUD program combines the crystal structure refinement by the Rietveld method (Rietveld, 1969) with quantitative texture analysis.

Full 360° plane detector images were integrated over 5° steps into 72 slices, i.e. 2 Θ profiles. This procedure results in 37x72=2664 spectra with an overall number of 3 to 3.5 million data points per sample used for phase and texture refinement. We used a 2 Θ range between 0.45 and 3.5° for our analysis, which corresponds to a range in d-spacings between 1.9 Å to 20 Å. Due to the lead beam stop mounted

in the center of the detector, 2Θ angles smaller than 0.45° are not displayed in the plate detector images (Figure 3. 3). Increasing the 2Θ range did not lead to better data bases due to superposed peaks. The refinement steps generally followed Lonardelli et al. (2005) and Wenk et al. (2010, 2008), see also Appendix A 2.2:

- (1) Background and scale parameter setting and analysis (“wizard tool” of MAUD).
- (2) Refinement of the beam center, sample-detector distance and the wavelength (starting values are previously graphically determined using the “beam center” function of FIT2D). The sample detector distance (directly measured in the lab) was refined in case of an inclined sample axis, which results in elliptic sample rotations causing variable sample detector distances and variably radiated sample volumes.
- (3) Refinement of the crystal parameters with the Rietveld method until a good visual fit of the theoretical and the observed spectrum was achieved (Figure 3. 4). Each of the refinement steps was done in at least five iterations.

Mineral phases for the Rietveld refinement were chosen according to the composition analyses of Expedition 315 Scientists (2009), Expedition 316 Scientists 2009a, 2009b, 2009c, 2009d, Guo and Underwood (2012) and our own EDX analyses. Crystal structure data of the existing mineral phases are required for Rietveld refinement with the MAUD software. These data were taken from the American Mineralogist Crystal Structure Date Base (Downs and Hall-Wallace, 2003). In this study, we used the smectite structure of Gournis et al. (2008), the illite structure of Gualtieri et al. (2008), the kaolinite structure of Bish and Von Dreele (1989), chlorite of Zanazzi et al. (2009), albite of Harlow and Brown (1980), calcite of Maslen et al. (1995), and quartz of Dušek et al. (2001).

For texture refinement, an E-WIMV algorithm (a modified WIMV algorithm; see Matthies and Vinel, 1982) was applied. The modification of the WIMV algorithm improves the integration between the Rietveld method and the texture calculation, and provides the ability to enter data in arbitrary positions (Wenk et al., 2003).

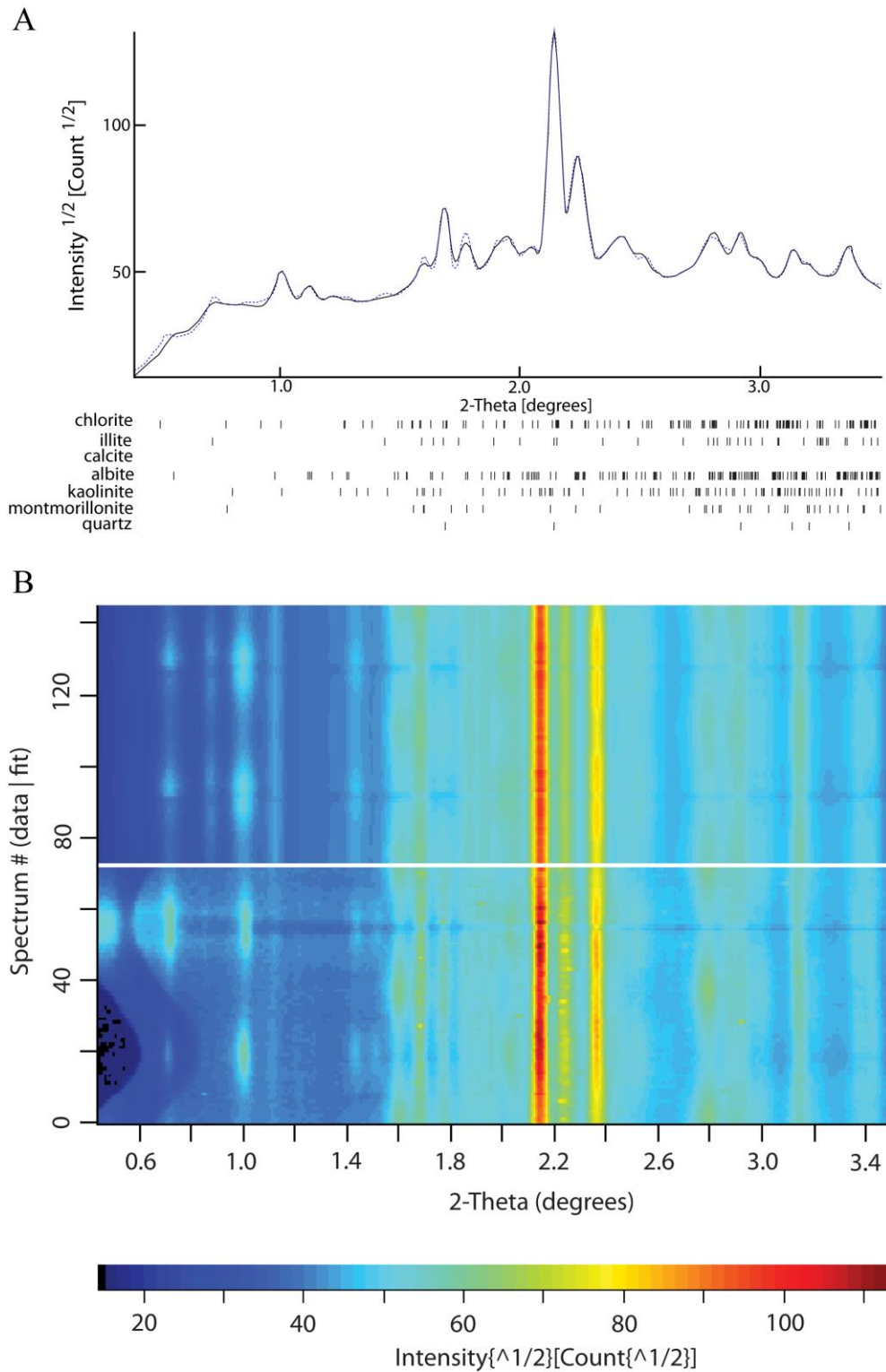


Figure 3. 4: (A) Refined spectrum showing the experimental data (dotted line) and the fitted curve (solid line). The peak positions of the refined mineral phases are indicated. Note that the fitted solid line indicates the best fit for the whole dataset (37 ω -rotations), while the experimental data represent only a single measurement at one ω -position. Variations between the two lines can be caused by preferred orientation of the mineral phases and are not necessary indications of a bad fit result. (B) 2D-Multiplot of the measured data (lower part) and the fitted data (upper part). Different intensities along vertical lines directly indicate texturation of the sample material.

Possible error sources were assessed by adding crystallographic information files. This is essential for the Rietveld refinement. Especially chemical compositions of complex low-symmetry minerals, such as clays, can only be approximated in the crystallographic information files. Furthermore, crystal disorder is a common phenomenon in clay minerals (e.g. Ufer et al., 2004 and references therein). Stacking disorder causes asymmetric peaks, and enlarges the width of basal peaks (e.g. Wenk et al., 2008). We applied a turbostratic disorder model (Ufer et al., 2004) to take into account disorder of smectite, which does not enhance the experimental fit. Since this study focuses on CPO and not on structural parameters, we did not concentrate on further structural refinement. The overall weighted residual index R_w (for more information see Wenk et al., 2008) is automatically calculated by the MAUD program after each refinement step, and can be used as an index for the quality of the refinement. Low R_w values are indicative for a good data fit. The calculated R_w values lie in the range between 7.0 and 15.2 apart from two exceptional values of 19.1 and 19.5%. For comparison, Wenk et al. (2008) achieved R_w values between 6.2 and 9.8% for the analyzed shales. An example for a refined spectrum is given in Figure 3. 4a. However, the R_w value indicates only the bulk error of the entire refinement, the quality of the individual fits cannot be derived and needs to be checked by optical comparison (Toby, 2006). Such an optical comparison of the modeled spectra and the observed spectra indicates a good refinement fit (Figure 3. 4b).

4. Sample composition

The point counting data of the smear slides (cf. Stipp et al., in press) show variable sample compositions (see Figure 3. 5 and Table 3. 2). The content of lithics is highly variable across the sample set and ranges between 1.8 and 46.8%. The content of biogenic material is similarly variable and ranges between 0.3 and 46%. Samples from the accretionary prism toe (T in Figure 3. 5) have the highest contents of submicroscopic material (between 43.4 and 78%), while samples from the hanging wall of the megasplay fault (HW in Figure 3. 5) and from the footwall of the megasplay fault (FW in Figure 3. 5) have lower contents ranging between 39.7 and 50.9% and between 32.6 and 56%, respectively. Assuming that the clay

minerals are below the resolution of the optical microscope used for point counting, the abundance of submicroscopics probably more or less resembles to the total clay contents in the synchrotron data (see below). The hanging wall samples of the megasplay fault have the lowest contents of “minerals” (between 6.5 and 10.4%). Samples from the footwall of the megasplay fault and the accretionary prism toe have slightly higher contents of “minerals” ranging between 12.8 and 16% and between 11.8 and 17.3%, respectively. Ash contents are small throughout and only slightly variable between the different settings ranging between 1% and 8.6%. No smear slides analyses of the incoming plate sediments have been carried out, but the shipboard data of Expedition 333 Scientists (2012a, 2012b) indicate that clay minerals and nannofossils as most abundant constituents.

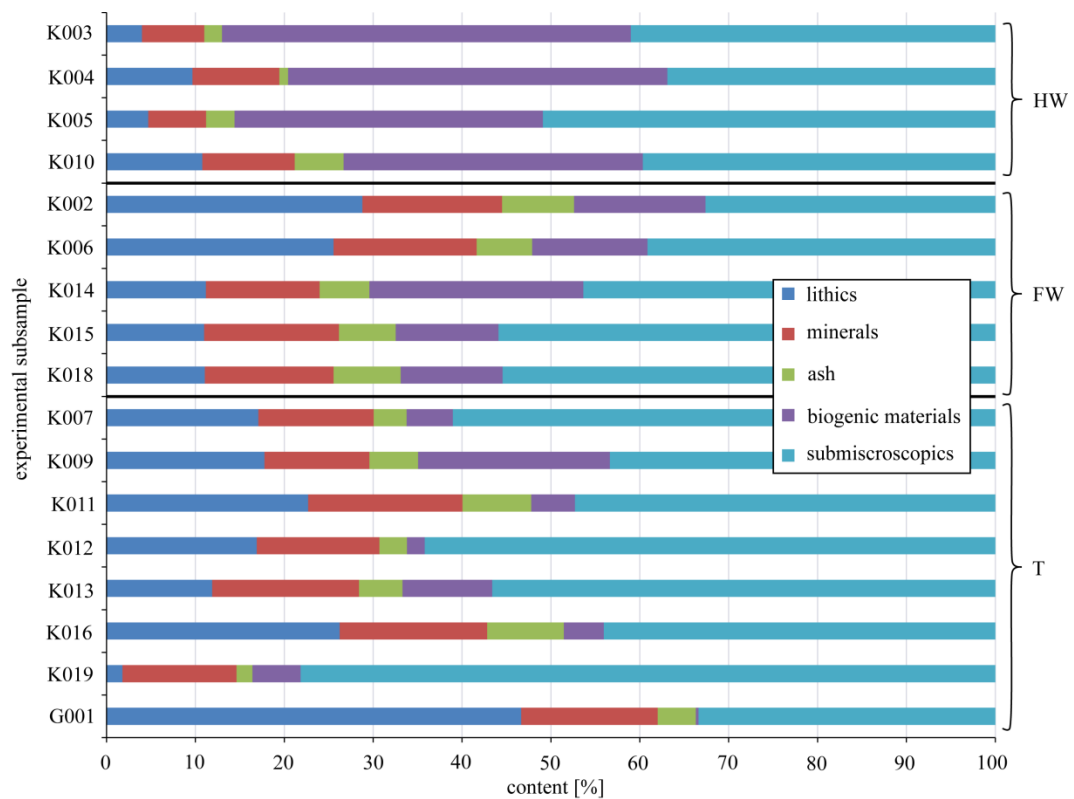


Figure 3. 5: Point counting results displaying the sample compositions (volume percentage) with respect to lithics = mineral agglomerates; minerals = mainly quartz, feldspar, mica and calcite; ash = volcanic glass chards; biogenic materials = foraminifera, diatoms, sponge needles and radiolarian; submicroscopics = material below the resolution of the optical microscope. Experimental subsample names can be related to the IODP drill core sections using Table 3. 2. Positions across the accretionary prism (HW = hanging wall of the megasplay fault, FW = footwall of the megasplay fault, T = frontal thrust zone at the accretionary prism toe) are indicated.

Rietveld refinement of the synchrotron data indicate between 21% and 43% quartz, between 13% and 33% feldspar, between 24% and 50% total clay and up to 24% calcite (Table 3. 1). The compositions of the investigated core samples of the Nankai accretionary prism are characteristic for recent marine sediments (Biscaye, 1965 and Petschick et al., 1996) and the results are in good agreement with the compositions reported by Expedition 315 Scientists (2009), Expedition 316 Scientists (2009a, 2009b, 2009c, 2009d) and Expedition 333 Scientists (2012a, 2012b).

Table 3. 2: Point counting results

sample	location	lithics	minerals	ash	biogenic	submicroscopic
K003	HW	4	7	2	46	41
K004	HW	9.7	9.8	1	42.8	37
K005	HW	4.7	6.5	3.2	34.7	50.9
K010	HW	10.8	10.4	5.5	33.7	39.7
K002	FW	28.8	15.7	8.1	14.8	32.6
K006	FW	25.4	16	6.2	12.9	38.9
K014	FW	11.2	12.8	5.6	24.1	46.4
K015	FW	11	15.2	6.4	11.6	56
K018	FW	11	14.4	7.5	11.4	55.1
K007	T	17.1	13	3.7	5.2	61.1
K009	T	17.8	11.8	5.5	21.6	43.4
K011	T	22.6	17.3	7.7	4.9	47.1
K012	T	16.9	13.8	3.1	2	64.2
K013	T	11.9	16.5	4.9	10.1	56.6
K016	T	26.2	16.6	8.6	4.5	44
K019	T	1.8	12.8	1.8	5.4	78
G001	T	46.8	15.4	4.3	0.3	33.5

Contents of the different components in vol.-%; lithics = mineral agglomerates; minerals = mainly quartz, feldspar, mica and calcite; ash = volcanic glass chards; biogenic material = foraminifera, diatoms, sponge needles and radiolarians; submicroscopic material = matrix below the resolution of the optical microscope, most probably clay minerals; HW = hanging wall of the megasplay fault; FW = footwall of the megasplay fault; T = accretionary prism toe.

Clay contents determined by synchrotron-based Rietveld refinement of the incoming plate hemipelagics are somewhat higher compared to the samples from the accretionary prism (also evident in the data of Expedition 315 Scientists, 2009, Expedition 316 Scientists, 2009a, 2009b, 2009c, 2009d and Expedition 333 Scientists 2012a, 2012b). Compositional differences are also evident in the

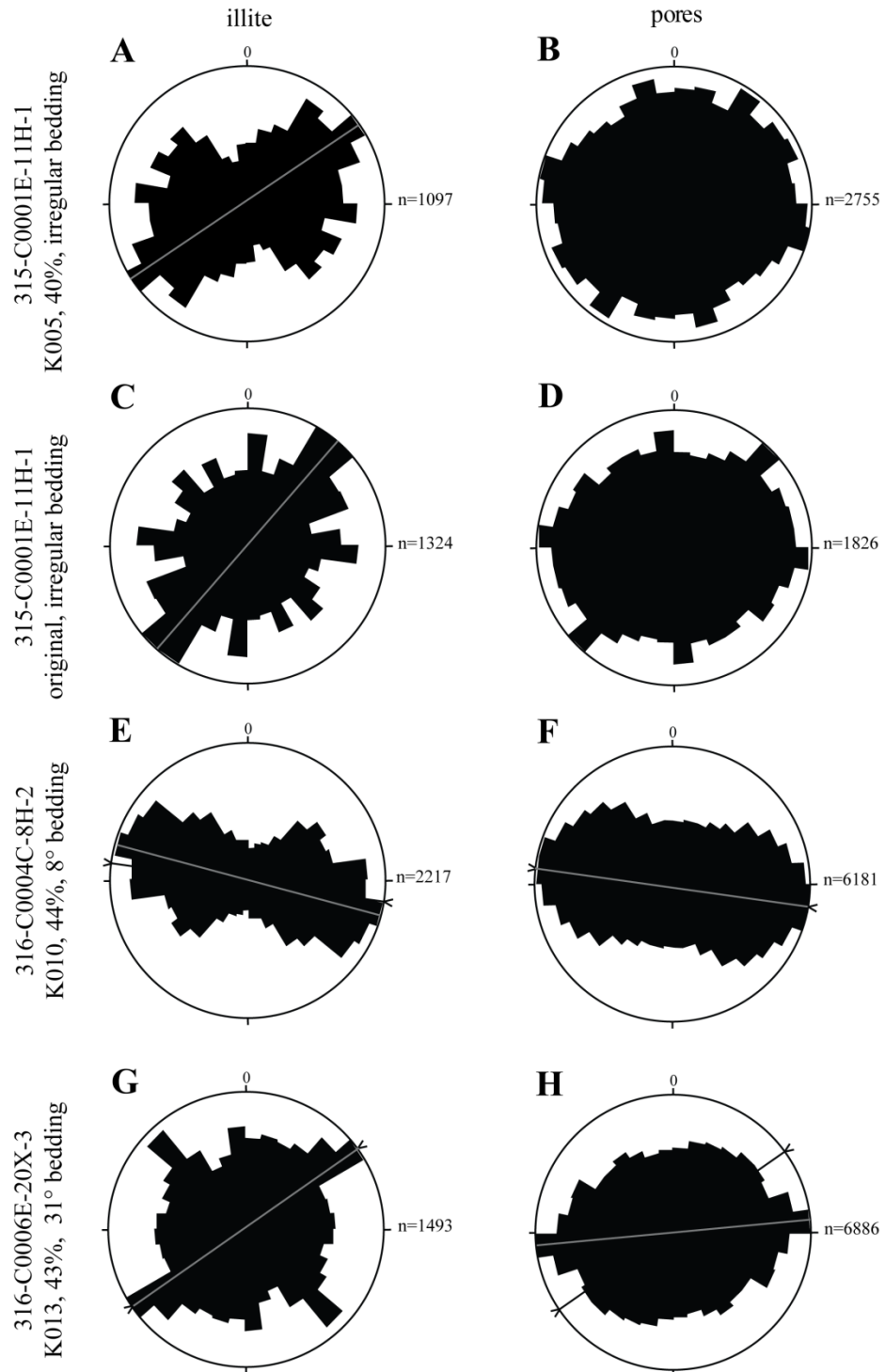
accretionary prism samples (Table 3. 1). Samples from the hanging wall of the megasplay fault (315-C0001E-11H-1 and 316-C0004C-8H-2) represent slope apron facies and show similar clay contents, while Samples 315-C0001F-14H-3 and 315-C0001H-19R-2 (sampled at greater depth) show somewhat higher clay contents and represent upper accretionary prism facies (Expedition 315 Scientists, 2009).

The slope sediments (Expedition 316 Scientists, 2009d) from the footwall of the megasplay fault (316-C0008C-7H-8 and 316-C0008A-9H-3) display slightly lower clay contents in comparison to the slope apron sediments from the hanging wall of the megasplay fault. At the accretionary prism toe, Sample 316-C0007C-7X-1 (not further characterized by Expedition Scientists, 2009c) shows similar clay contents compared to the slope sediments (footwall samples) and thus is interpreted to represent deformed and overthrust slope sediments or slope apron sediments. The samples drilled at IODP Site C0006 have been characterized as trench wedge sediments. According to Expedition Scientists (2009b) Sample 316-C0006E-8H-1 consists of sand-dominated trench wedge sediments, while Sample 316-C0006E-20X-2 represents sand-mud trench wedge sediments and Sample 316-C0006E-30X-1 represents mud-dominated trench wedge sediments.

5. Results

5.1 Shape preferred orientations of minerals and pores

Shape preferred orientation (SPO) analyses were carried out on detrital illites and pores. In the SEM images, illite grains of up to 40 μm in length were identified. Preferred orientations can qualitatively be recognized in binary images processed from BSE data (Figure 3. 2) and are clearly evident in the rose diagrams (Figure 3. 6) for both detrital illite grains and pores.



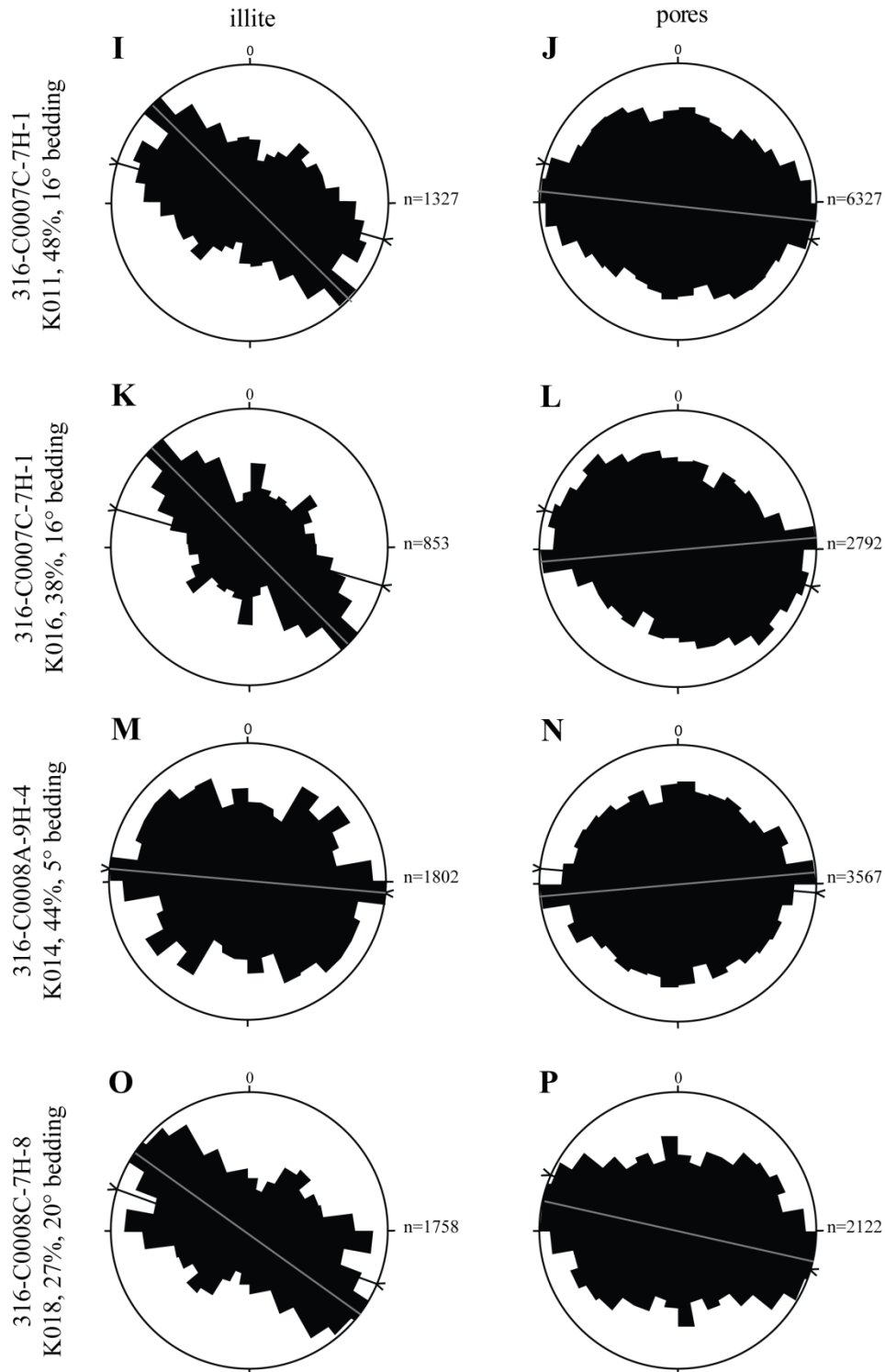


Figure 3. 6: Rose diagrams of the shape preferred long axis orientations of detrital illite grains and pores from one original (experimentally undeformed) and seven experimentally deformed IODP core samples. The drill core axes are vertically oriented. Bedding planes observed by the shipboard scientific party (Expedition 315 Scientists, 2009; Expedition 316 Scientists, 2009a-d; Expedition 333 Scientists, 2012a, 2012b) are indicated by black lines with arrowheads, while the observed preferred orientation of illite grains and pores is indicated by gray lines. Dip directions are grouped in 10°-bins. Experimental subsample names, axial shortening strain in percent, and bedding dip is indicated.

Microstructural analyses were conducted on Sample 315-C0001E-11H-1 and on an experimentally deformed aliquot from the same core (subsample K005; 40% axial shortening). The bedding of this core segment is not clearly defined and has been described as being irregular (Expedition 315 Scientists, 2009). Long axes orientations of the illites in the experimentally deformed sample is tilted $\sim 40^\circ$ to the horizontal, while in the original core segment, the illite long axes are tilted 46° to the horizontal. The long axes of the pores are nearly randomly oriented in both cases (Figure 3. 6).

In experimental subsample K010 (316-C0004C-8H-2), the long axes of the detrital illites and pores are approximately parallel to the bedding plane, which is tilted 8° (Expedition 316 Scientists, 2009a), and thus, more or less perpendicular to the axis of maximum shortening in the deformation experiment.

The illite long axes of experimental subsample K013 (316-C0006E-20X-2) are parallel to the inclined bedding plane, with a second maximum approximately perpendicular to the bedding (Figure 3. 6). In contrast, the long axes of the pores have a nearly horizontal orientation maximum, which is perpendicular to the axis of maximum experimental shortening. In the experimental subsamples K011 and K016 (316-C0007C-7H-1), the illite long axes are rotated $\sim 20\text{-}25^\circ$ from the previously assumed bedding trend (Expedition 316 Scientists, 2009c) towards the core axis. The long axes of the pores in these two samples are almost parallel to the horizontal, i.e. normal to the axis of maximum experimental shortening.

In the experimental subsample K014 (316-C0008A-9H-3) both, the illite long axes and the pore long axes are oriented parallel to the bedding plane, which is almost horizontal. All fabrics, thus, show maxima normal to the experimental shortening axis. In sample K018 (316-C0008C-7H-8), the illite long axes are tilted 20° to the bedding plane, and more than 30° to the flattening plane. In contrast, the pore long axes are approximately horizontally aligned, and perpendicular to the axis of maximum experimental shortening.

5.2 Texture analysis

Textures were calculated for all mineral phases of the different samples and are represented by a selection of recalculated pole figures (equal area projection, lower hemisphere). The units of the contour line distribution densities are multiples of random distribution (mrd); the lowest contour line is equal to 1.0 mrd (random distribution). Rietveld refinement indicates sample compositions containing quartz between 16% and 42%, albite between 12% and 33%, illite between 3% and 34%, kaolinite between 7% and 30%, calcite between 2% and 23%, smectite between 2% and 16%, and minor chlorite (up to 3%) (Table 3. 1). To verify our results, x-ray powder diffraction (XRD) analysis of three samples (316-C0008A-9H-3, 316-C0007C-7X-1 and 316-C0006E-20X-1) was conducted (Table 3. 3). These results are roughly similar to the standard shipboard XRD data acquired by Expedition 315 Scientists (2009), Expedition 316 Scientists (2009a, 2009b, 2009c, 2009d), see Table 3. 1.

With respect to the shallow depths from which the samples originate, one may generally expect weak textures. Below, we describe only textures of the major mineral constituents of the samples. There is a focus on the [001] pole figures of the sheet silicates, [010] pole figures of albite, and the first order prism [100] pole figures for quartz.

5.2.1 Natural core samples (experimentally undeformed)

Bedding plane attitudes of the original samples vary from almost horizontal to very steep, with dip angles up to 60° (Expedition 315 Scientists, 2009, Expedition 316 Scientists, 2009a, 2009b, 2009c, 2009d and Expedition 333 Scientists, 2012a, 2012b, Figure 3. 7). In one sample (315-C0001H-19R-2) the bedding plane could not be observed and is also not documented in the IODP Expedition 315 report (Expedition 315 Scientists, 2009). Samples are described below from the most seaward drillsite at the incoming plate (Site C0012) to the most landward site on the accretionary prism (Site C0001), and are sorted by depth within the drillsites.

Table 3. 3: Comparison of the sample compositions determined by different methods in different studie

sample	316-C0008A-9H-3			316-C0007C-7X-1				316-C0006E-20X-2				
	this study	BGR	Expedition 316 Scientists	Guo	this study	BGR	Expedition 316 Scientists	Guo	this study	BGR	Expedition 316 Scientists	Guo
Smectite	1.5-4.4	7.0		11.0	1.4-15.4	15.9		9.0	6.2	23.1		9.0
Muscovite		13.5				10.3				12.4		
Chlorite	0-0.3	2.9		16.0	0-0.5	4.2		11.0	0.0	5.5		16.0
Kaolinite	10-21.3	6.7		1.0	9.8-13	1.2		1.0	30.3	1.4		0.0
Illite	4.4-15			16.0	2.8-18.5			16.0	7.5			24.0
total clay	24-36.3	30.1	47.3	48.0	25.9-39.9	31.6	37.0	37.0	44.0	42.4	50.2	49.0
Plagioclase (16 An)		15.2				16.0				13.7		
Plagioclase (50 An)		7.3				13.4				9.3		
Orthoclase		4.6				4.5				4.2		
Feldspar	25.6-32		21.7		31.8-32.2		36.0		23.1		23.3	
Hornblende		1.5				1.5				1.5		
Augite						0.8						
Quartz	31.2-42	36.2			35.8-38.1	30.1	27.0		23.4	26.0	26.5	
Calcite	4.2-6	3.4	4.4		0-0.1	1.1	0.0		9.2	1.8	0.0	

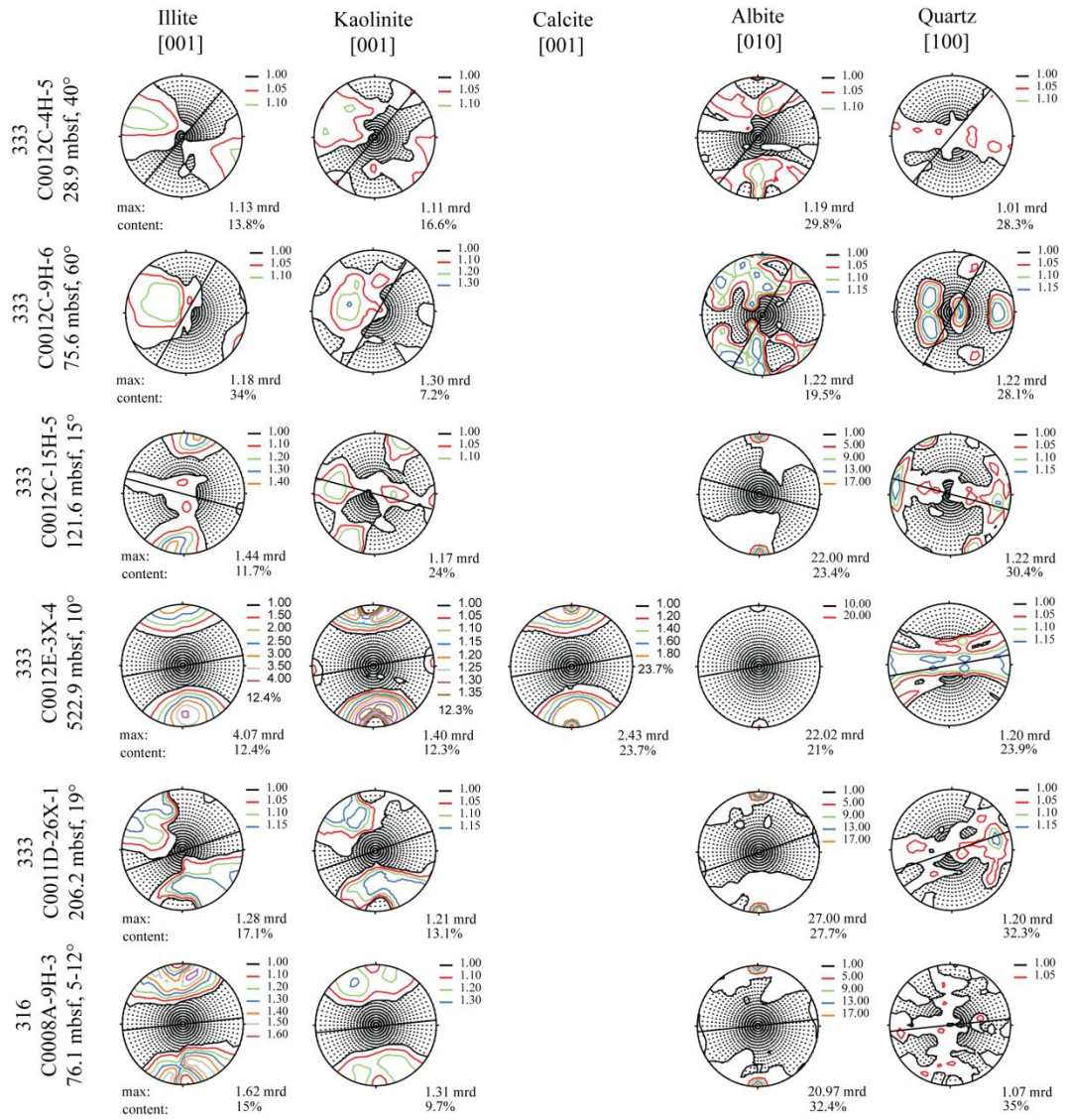
Sample composition of this study is derived from Rietveld refinement of synchrotron data of the complete samples. Data from the BGR (Bundesanstalt für Geowissenschaften und Rohstoffe) are determined by x-ray powder diffraction (XRD) of the complete samples. Data from Expedition 316 Scientists, 2009b-d are determined using XRD analysis to measure total clay, quartz, plagioclase and calcite aboard D/V CHIKYU. Guo and Underwood, 2012 only used the clay sized fraction (<2 μm) for their XRD analysis and only investigated the clay minerals.

Quantitative synchrotron texture analyses generally reveal weak intensity maxima well below 2 multiples of random distribution (mrd), and topologies that are axially symmetric around the pole to the bedding planes (see Figure 3. 7, Appendix A 2.3). Only in the deepest sample (333-C0012E-3X-4) the intensity maximum for poles to illite [001] is as high as 4.07 mrd (Figure 3. 7). Four samples from the most seaward site (C0012) were investigated. Sample 333-C0012C-4H-5 (28.9 mbsf) shows weak [001]-maxima of illite and kaolinite (1.13 mrd and 1.11 mrd, respectively) approximately normal to the sedimentary bedding plane. Poles to albite [010] and quartz [100] are almost randomly oriented. Similar types of CPO are observed for sample 333-C0012C-9H-6 (75.5 mbsf), but the [001] illite and kaolinite textures are slightly stronger (1.18 mrd and 1.30 mrd, respectively). In sample 333-C0012C-15H-5, the illite [001]-maximum is normal to the sedimentary bedding plane, while the [001] kaolinite shows a point maximum normal to the bedding plane, which is combined with a weak girdle distribution in the bedding plane (Figure 3. 7). The albite [010]-maximum is very strong (22.00 mrd) in this sample, and is oriented parallel to the core axis. In sample 333-C0012E-3X-4 (522.9 mbsf), the illite [001]-maximum is normal to the bedding plane, while the [001] kaolinite and the [006]-maxima of calcite form small circle distributions (opening angle approximately 25°) around the pole to bedding (Figure 3. 7). The albite [010]-maximum again forms a very strong (22.02 mrd) point maximum parallel to the core axis. A very weak (1.20 mrd) girdle distribution of poles to [100] of quartz is observed in this sample lying in the sedimentary bedding plane.

Sample 333-C0011D-26X-1 (206.2 mbsf), derived from the incoming plate at IODP Site C0011 shows poles to [001]-maxima illite and kaolinite of 1.28 mrd and 1.21 mrd, respectively, slightly tilted away from the bedding plane normal (Figure 3. 7). The [001] albite point maximum is very strong (27.69 mrd), again parallel to the core axis. Poles to [001] of quartz again show a very weak girdle distribution parallel to the bedding.

Sample 316-C0008A-9H-3 (76.1 mbsf) from the footwall of the megasplay fault shows small circle distributions (opening angles approximately 20°) of poles to [001] of illite and kaolinite around the normal to the sedimentary bedding plane (Figure 3. 7). The poles to [010] albite point maximum is very strong (20.97 mrd),

and is oriented parallel to the core axis. Poles to [100] of quartz are randomly distributed.



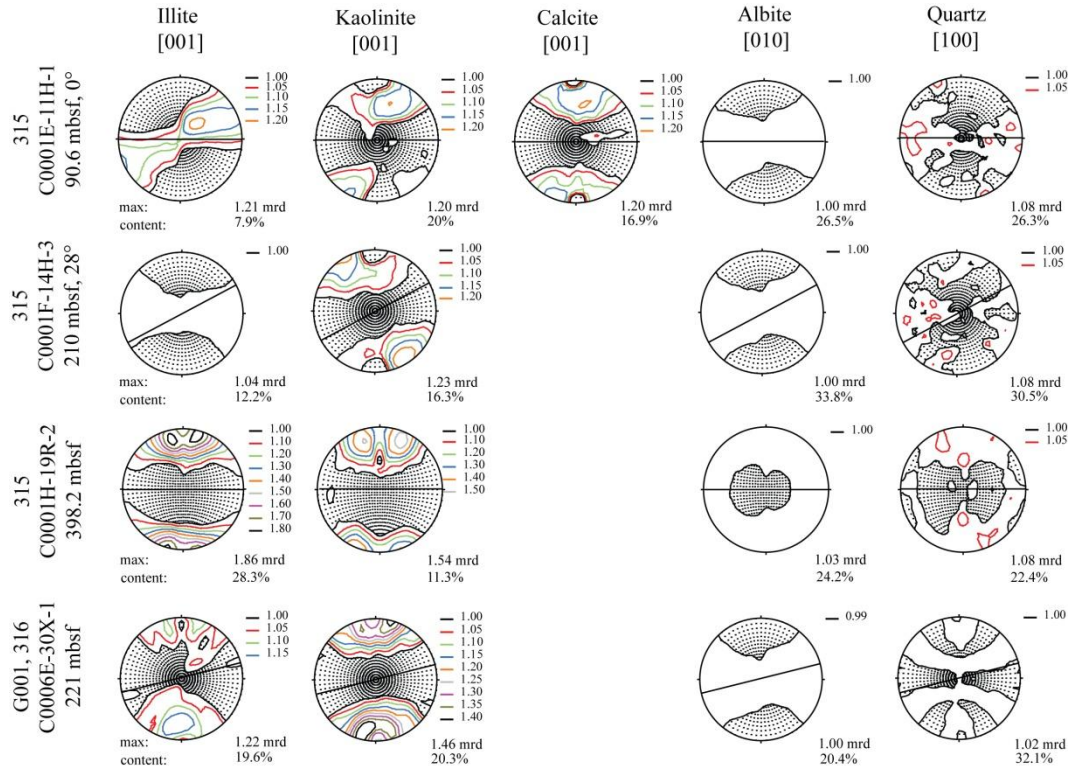


Figure 3. 7: Pole figure plots of the main phases of the natural (experimentally undeformed) samples. The axes of the drill cores and sample cylinders are vertically oriented. The bedding dip is indicated by a solid black line, except for sample 315-C0001H-19R-2 where no information on the bedding could be found. Sampling depth in meter below sea floor (mbsf) and bedding dip in degree are indicated for each sample. Pole figure densities are given in multiples of random distribution (mrd), contour lines below 1 are not shown. Contour levels of the pole figure plots are variable depending on maxima strength and complexity. Pole figure maximum and volume percentage for each phase are indicated below each pole figure.

Samples from the hanging wall of the megasplay fault (Site C0001) and of the accretionary prism toe (Site C0006) show texture maxima up to 1.86 mrd. Topologies of the phyllosilicate CPO are mostly similar to those of the samples from the incoming plate, but differ from them in one important aspect. Where bedding is horizontal, point maxima or small circle maxima of poles to [001] are axially symmetric around the bedding plane normal, and thus around the core axis (Figure 3. 7). However, where bedding is tilted (Samples 315-C0001F-14H-3 and 316-C0006E-30X-1), the CPO remains axially symmetric around the core axis, and thus the vertical. Illite [001] CPO in sample 315-C0001F-14H-3 is almost random, an observation that contrasts with the corresponding CPO of kaolinite (Figure 3. 7). This, however, may be a sampling effect due to the low concentration of illite (12.2%). The calcite [006]-maximum calcite forms a small circle distribution around the core axis, just like in Sample 333-C0012E-3X-4, but CPO intensity is much weaker (Figure 3. 7). This may be due to the much lower

depth (compare 90.6 mbsf to 522.9 mbsf). Poles to [010] of albite and to [100] of quartz are randomly distributed in all five samples coming from the megasplay and accretionary prism toe. The deepest sample from this IODP Site C0001, sample 315-C0001H-19R-2 (398.2 mbsf) shows the most pronounced [001]-maxima of illite (1.86 mrd) and kaolinite (1.54 mrd) in this series of samples from the megasplay hanging wall (Figure 3. 7).

5.2.2 Experimentally deformed samples

Since several experimental subsamples were obtained from some of the IODP drill core whole round samples, we use the labels of the experiments for the texture description instead of the IODP core and sample numbers. Relations between experiment labels and core/sample numbers, however, are given in Table 3. 1. Only samples from the accretionary prism were experimentally deformed and are described below from the most seaward site (C0007) to the most landward site (C0001) of the accretionary prism. Samples from the same site are sorted in Figure 3. 8 by depth and the achieved finite experimental strain (see also Appendix A 2.4).

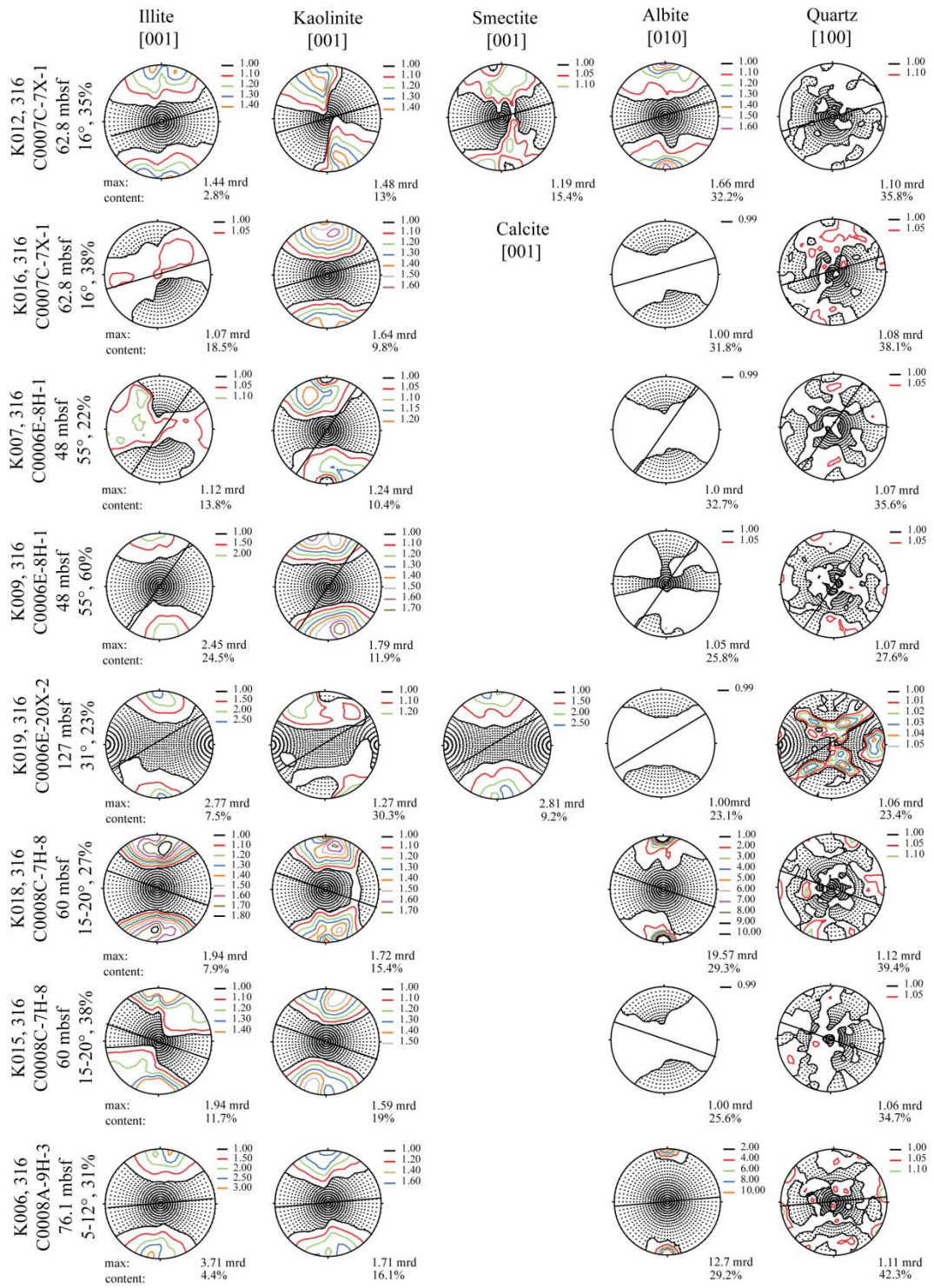
In summary, most of the phyllosilicate CPOs of the experimentally deformed samples are slightly stronger than those of the original core samples. But the texture maxima exceed values of around 2.0 mrd only in a few cases (Figure 3. 8). CPO intensification is a consequence of the experimental strains being superimposed on the natural compaction history. Strengthening of the CPO is expected in case of an original shallow dip of bedding, which is true except for one sample (K007, Figure 3. 8).

At the accretionary prism toe (IODP Sites C0007 and C0006), the phyllosilicate [001] texture maxima reach up to 2.81 mrd (Figure 3. 8). These are point maxima of poles to [001] at or close to the axis of maximum loading and maximum shortening (N-S in the examples shown in Figure 3. 8). In sample K012 (35% axial shortening), the [001] illite, kaolinite and smectite point maxima and the [010] albite point maximum are approximately parallel to the core axis, while poles to [100] of quartz are randomly distributed. The same is the case for the CPO of kaolinite [001] of the other samples coming from the hanging wall of the

prism toe (IODP Sites C0006 and C0007; Samples K016, K007, K009, K019, Figure 3. 8). These are either point maxima or small circle girdles with a narrow (20° - 30°) opening angle about the shortening axis. The strongest CPO occur for sample K009, which has the highest axial shortening (60%). In two of the samples (K009, K019) illite [001] mimics the kaolinite CPO, in two other samples (K016, K007) illite CPO is almost random (Figure 3. 8). Poles to [010] of albite and [100] of quartz are randomly distributed in all four samples. Calcite [006] poles have a point maximum around the shortening axis in sample K019, which is similar to those in the naturally compacted samples presented in Figure 3. 7.

Samples from the footwall of the megasplay fault (IODP Site C0008; samples K018, K015, K006 and K014), show the same kind of [001]-maxima of kaolinite and illite as the samples from the prism toe, with the exception of kaolinite [001] in sample K014, which has a random distribution (Figure 3. 8). Maxima are up to 3.71 mrd. Strong [010]-maxima of albite parallel to the shortening axis are present in Samples K018 and K006 (19.57 mrd and 12.70 mrd, Figure 3. 8). Again, this is similar to some of the samples which only experienced natural compaction (Figure 3. 7). Poles to [100] of quartz are randomly distributed in the whole subset of samples.

In the hanging wall of the megasplay fault (IODP Sites C0004 and C0001; Samples K004, K003, K005), the phyllosilicate [001]-maxima reach up to 1.87 mrd. In sample K004 (37% axial strain), the illite [001]-maximum is weak (1.13 mrd) and is oblique to the bedding plane normal, while the kaolinite [001]-maximum is stronger (1.58 mrd) and is oriented normal to the bedding plane and parallel to the axis of maximum experimental shortening. In all three samples the poles to [006] of calcite show point maxima parallel to the axis of maximum experimental shortening. Poles to [010] of albite and [100] of quartz are randomly oriented.



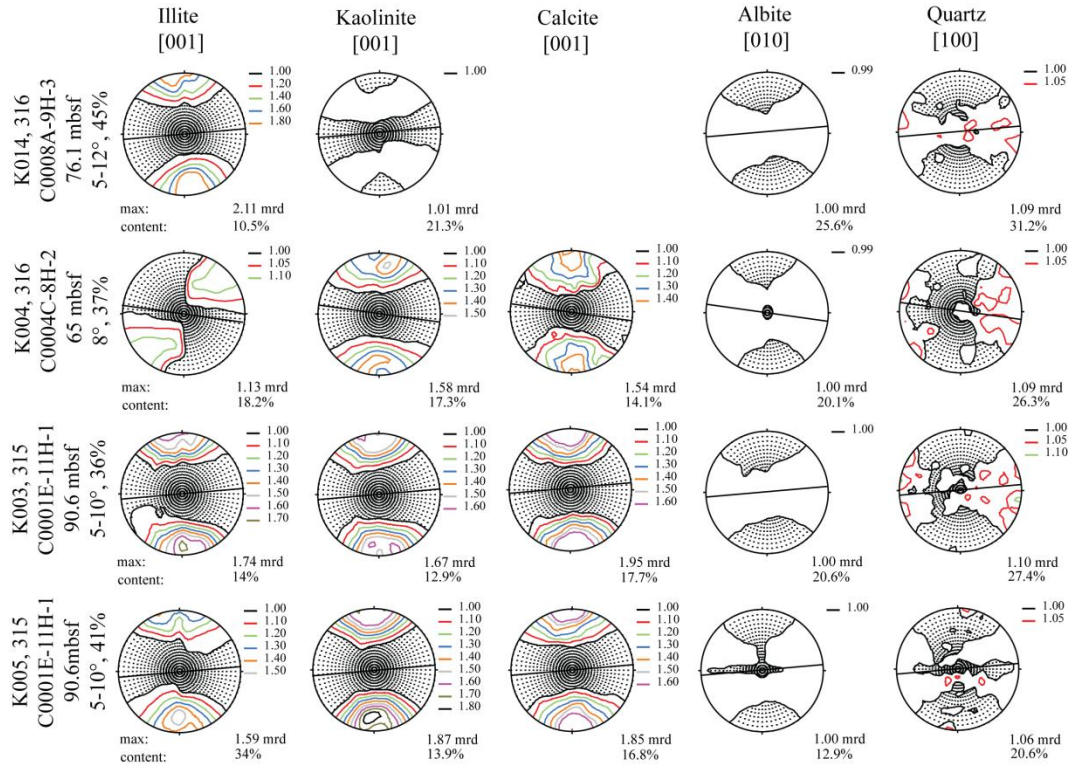


Figure 3. 8: Pole figures of the main phases of the experimentally deformed samples. The axes of the drill cores and sample cylinders as well as the experimental shortening axes are vertically oriented. The bedding dip is indicated by a solid black line. Sampling depth in meter below sea floor (mbsf), bedding dip in degree and experimental shortening strain in percent are indicated for each sample. Pole figure densities are given in multiples of random distribution (mrd), contour lines below 1 are not shown. Contour levels of the pole figure plots are variable depending on maxima strength and complexity. Pole figure maximum and volume percentage for each phase are indicated below each pole figure. In sample K012 (316-C0007C7X-1), smectite accounts for more than 10 vol.-% and is additionally depicted.

6. Discussion and interpretation

In this section we discuss the mechanisms that create textures in deep marine sediments involved in compaction and accompanying tectonic deformation in a typical convergent margin setting. The sediments are all naturally compacted, and a reasonable range of burial depths is available. The “tectonic” shearing aspect, however, is treated through the results of triaxial deformation experiments on a suite of sediments from the different tectonic settings of the Nankai trench and forearc. While diagenesis and cementation is not considered as a major player at least in the shallow parts of accretionary wedges, maybe with the exception of settings where young and hot oceanic crust is subducted (e.g. Behrmann et al., 1994), loss of porosity is of overriding importance for the acquisition of SPO and

CPO in marine sediments. We finish the discussion by reconsidering some of the advantages synchrotron texture analysis has over conventional methods.

6.1 Natural compaction in Nankai sediments: drivers, mechanisms, and fabric response

Perhaps the most obvious parameter to study in relation of CPO intensity is depth of burial of the sediments. As there is a good range of burial depths for the naturally compacted sediments, we take the approach to plot CPO intensity in mrd against the sampling depth below seafloor for the incoming plate samples and those from the accretionary prism (Figure 3. 9a). Obviously there is a wide range of CPO intensity even within individual samples, if we take kaolinite and illite [001] and calcite [006] pole figures into account. In Figure 3. 9a only pole figures are used that are derived from mineral phases with abundances of more than 10%, because it cannot be excluded that CPO can be due to incomplete sampling of phases with low abundances. Samples with shallow burial depths have less intense CPO than the more deeply buried ones. This relationship is only roughly defined, however, and it is probably because only the very fine-grained clay mineral phases were sedimented in a flocculated form to produce isotropic basal plane distributions in freshly sedimented marine muds. One indication to support this is that illite CPO is somewhat more strongly developed than kaolinite CPO. This can be explained by the effect the detrital illites (see Figure 3. 6) have on the overall CPO intensity. Detrital illites were probably transported and sedimented in non-flocculated form as individual large grains, and a primary SPO will then result from sedimentary transport and deposition processes. The results generally confirm the observation of Vasin et al. (2013), who found a less pronounced CPO of kaolinite and smectite in comparison with illite in Kimmeridge clays. Our data indicate that this effect also occurs in young sediments that lack any significant diagenetic overprint.

One interesting aspect of the CPO is that maxima of poles to clay basal planes, but also of calcite [006] directions are almost always sub-perpendicular to the bedding orientations in the core (Figure 3. 7). Where bedding is strongly tilted relative to the core axis (the vertical), these maxima are tilted in the same way. Bedding tilt

in the Nankai accretionary prism is primarily a result of tectonic deformation, faulting, and folding. This observation proves that the CPO are indeed compactional fabrics, formed by progressive dewatering and porosity reduction as sediments were overlain by younger sedimentary layers. This tilting of phyllosilicate CPO maxima was also observed in some samples analyzed by Behrmann and Kopf (1993) from ODP Site 808, drilled in the toe of the Nankai accretionary prism, but was then interpreted as resulting from tectonic deformation due to lateral contraction in the accretionary prism toe. Our data show that tilting of compactional fabrics may be the more likely explanation, making CPO development an early part of the fabric evolution. The tilting effect is also observed in samples from IODP Sites C0011 and C0012 (Figure 3. 7), which are located far seaward of the Nankai deformation front (Figure 3. 1). Tilting in these samples is caused by hemipelagic deposition on a basement knoll (Expedition 333 Scientists, 2012b) and slumping (especially Subunit IB, samples 333-C0012C-9H-6 and 333-C0012C-15H-5; Expedition 333 Scientists, 2012b).

Another parameter that varies systematically with depth is porosity. We have taken the approach to use the porosity-depth functions of the drillholes cored and sampled in IODP Expeditions 315, 316 and 333 to associate a value for porosity loss (from ratios of initial porosity and measured porosity) to each specimen. A measure of initial porosity is provided by the average of shipboard measurements on samples from the uppermost ten meters of the drillhole a specific sample was taken from, akin to the procedure described by Behrmann and Meissl (2012). Plotting CPO intensity of illite and kaolinite [001] and calcite [006] against sample porosity, the CPO intensity increases with decreasing porosity for the incoming plate sediments (Figure 3. 10a), while such a relationship is less obvious for the samples from the accretionary wedge (Figure 3. 10b). CPO intensity only slightly increases as porosity decreases. It becomes obvious, that vertical loading of the incoming plate sediments results in progressive flattening of the sediments accompanied by the reduction of the pore space and expulsion of the pore fluid (Behrmann and Kopf, 1993), while the CPO intensity of the accretionary prism sediments is less obviously dependent on burial and porosity loss.

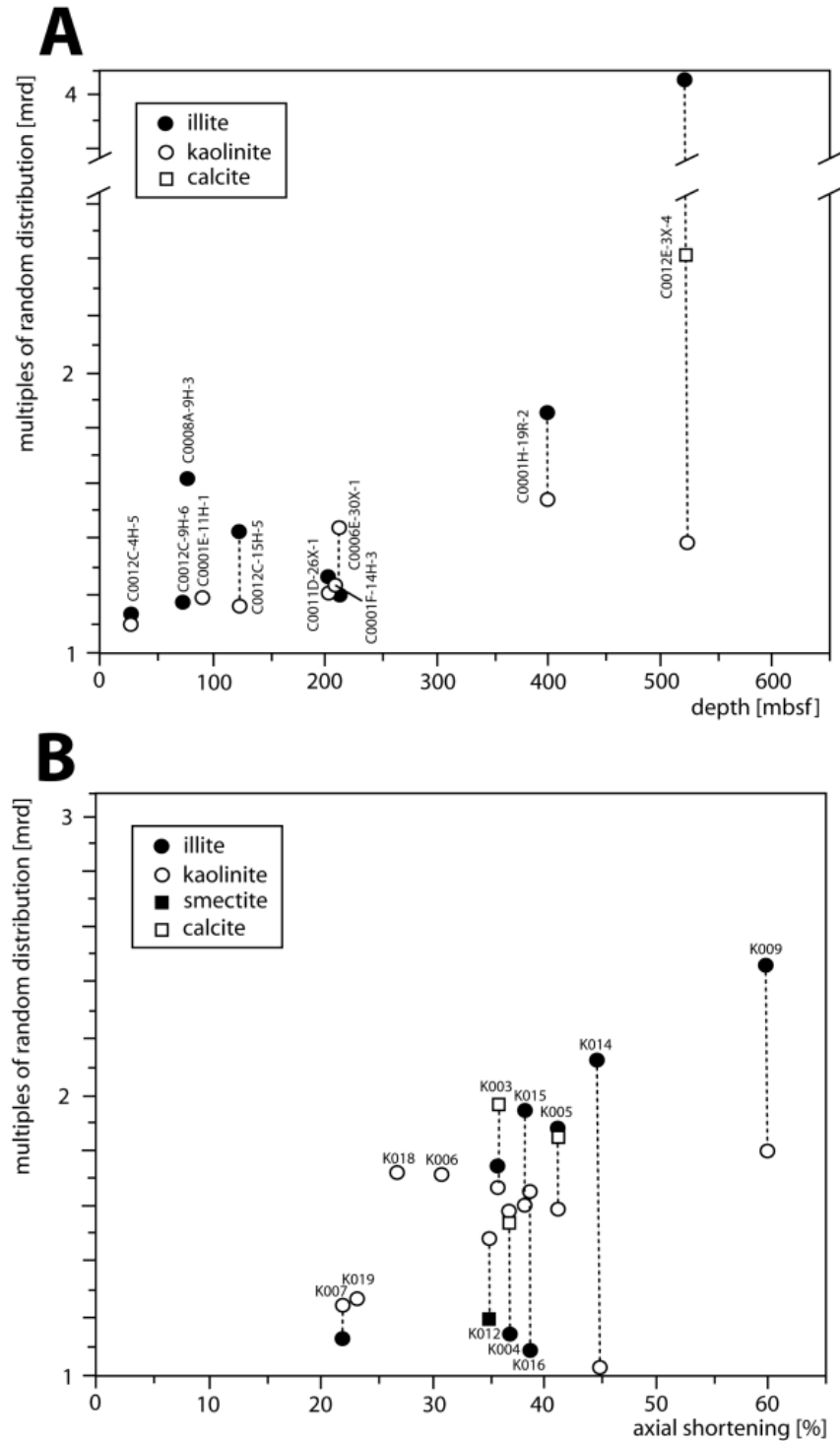


Figure 3. 9: (A) CPO intensities of illite, kaolinite and calcite versus depth of the incoming plate sediments and the accretionary prism samples. (B) CPO intensities of illite, kaolinite, smectite and calcite versus the experimental shortening strain.

Strain can be calculated using the sample porosities (equation 1, Kopf and Behrmann, 1997) and using the CPO intensities of the phyllosilicates (equation 2) on the basis of the March theory (Behrmann and Kopf, 1993, Kopf and Behrmann

1997, Lipshie, 1984 and Oertel, 1985). Using porosities, the compactional strain (e_{pore}) is defined by

$$e_{\text{pore}} = (P_0 - P_d) / (P_d - 100) \quad (1)$$

where P_0 is the initial porosity at, or close to the mudline, and P_d is the porosity at depth. Using the March model (March, 1932) CPO intensities of the phyllosilicates, the compactional strain (e_v) from CPO intensity of phyllosilicate basal planes and calcite c-axes is given by

$$e_v = I_v^{-1/2} - 1 \quad (2)$$

where I_v is the multiple of random distribution on the basal plane. The results obtained from the two methods of strain calculation are given in Table 3. 4. A diagram of the strain plotted against the sampling depth of the incoming plate samples (Figure 3. 10c) indicates that the strain data determined from porosity loss and from the illite CPO correlate well, while the March strains from the kaolinite CPO give somewhat lower values. However, from these data it is obvious that the porosity variations with depth reflect the compactional strain and thus support vertical loading and pore space reduction as the texture forming process for the incoming plate samples. The strains determined for the accretionary prism samples do not correlate well (Figure 3. 10d), indicating that vertical compaction is not the only texture forming process. Other processes such as tectonic overprint, akin to the inferences made by Behrmann and Kopf (1993) may influence texture formation in these samples.

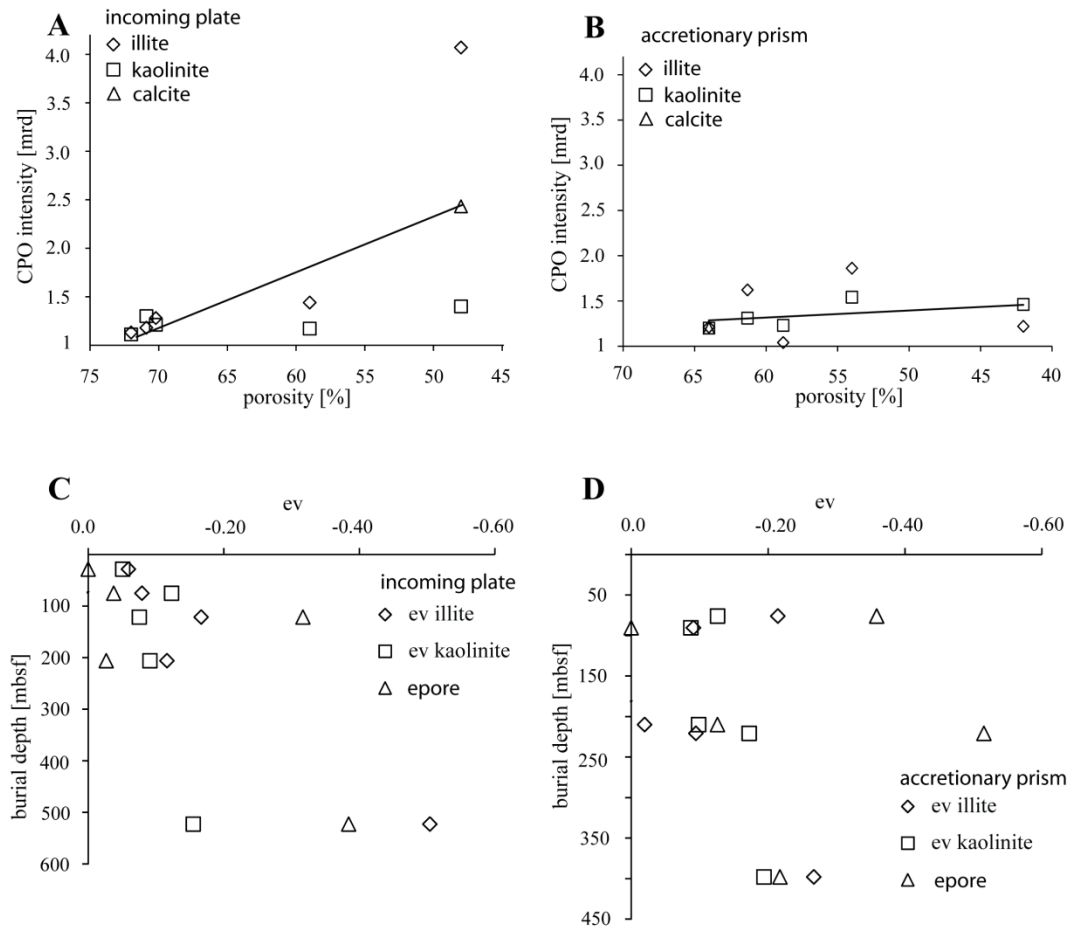


Figure 3. 10: CPO intensity of illite, kaolinite and calcite versus the porosity of the incoming plate sediments (A) and the accretionary prism sediments (B). Strains calculated from the CPO of illite grains (diamonds), kaolinite (squares) and pores (triangles) versus the burial depth of the incoming plate samples (C) and the accretionary prism samples (D).

Table 3. 4: Results of strain analyses of the incoming plate sediments.

sample	depth [mbsf]	CPO illite [mrd]	CPO kaolinite [mrd]	e_v illite	e_v kaolinite	P_d [%]	P_0 [%]	e_{pore}
333-C0012C-4H-5	28.9	1.13	1.11	-0.06	-0.05	72	72	0
333-C0012C-9H-6	75.6	1.18	1.30	-0.08	-0.12	70.9	72	-0.03
333-C0012C-15H-5	121.6	1.44	1.17	-0.17	-0.08	59	72	-0.31
333-C0012E-3X-4	522.9	4.07	1.40	-0.50	-0.15	48	68	-0.38
333-C0011D-26X-1	206.2	1.28	1.21	-0.12	-0.09	70.2	71	-0.02
316-C0008A-9H-3	76.1	1.62	1.31	-0.21	-0.13	61.3	75.19	-0.35
315-C0001E-11H-1	90.6	1.21	1.20	-0.09	-0.09	64	64	0
315-C0001F-14H-3	210.0	1.04	1.23	-0.02	-0.10	58.8	64	-0.12
315-C0001H-19R-2	398.2	1.86	1.54	-0.27	-0.19	54	64	-0.21
316-C0006E-30X-1	221.0	1.22	1.46	-0.09	-0.17	42	71.9	-0.51

The results of the strain analyses using the CPO of illite (e_v illite) and kaolinite (e_v kaolinite) and the strain analyses using the porosity data (e_{pore}). The porosity at depth (P_d) and the initial porosity (P_0) are from the Expedition 315 Scientists (2009), Expedition 316 Scientists (2009a-d) and the Expedition 333 Scientists (2012a, 2012b). See text for further explanation.

While phyllosilicate CPO as response to compaction can be easily understood, the interpretation of calcite CPO, shown by the [006] pole figures (Figure 3. 7) is less straightforward. Carlson and Christensen (1979) pointed out that the observed strong acoustic anisotropy of calcite-rich deep sea sediments may be related to the preferential alignment of bio-detrital microfossil platelets parallel to bedding. Indeed, there are high-abundance taxa of calcareous micro- and nannofossils, like coccolithophoridae and discoasters, that show a highly ordered arrangement of calcite c-axes normal to the plate-like shapes (e.g. Black, 1972, 1963). These likely constitute a major part of the biogenic detritus documented in the sediment compositions (Figure 3. 5 and Figure 3. 11a), and their preferential alignment will be just like that of phyllosilicates, and explain the CPO of calcite observed.

Extremely strong albite [010]-maxima of up to 27.69 mrd are evident in some of the samples. These are exclusively from IODP Sites C0008, C0011 and C0012, and maxima are always oriented subnormal to bedding and parallel to the drill core axis (see Figure 3. 7 and Figure 3. 8). All the samples are from sediment sequences free of tectonic overprint from the incoming plate (IODP Sites C0011 and C0012) or the slope cover on the footwall of the megasplay fault (IODP Site C0008). Since the core axis parallel orientation is observed in some experimental samples as well as in the natural samples, and is absent in others (see Figure 3. 7 and Figure 3. 8) the preferred orientation of albite cannot be simply attributed to compaction. Several reasons for the existence or non-existence of strong [010] albite pole figure maxima are conceivable, such as coarse mineral grains derived from ash (Figure 3. 11b), localized reworking or drilling disturbance. No drilling disturbance and reworking is evident from the expedition reports (Expedition 315 Scientists, 2009, Expedition 316 Scientists 2009a, 2009b, 2009c, 2009d and Expedition 333 Scientists 2012a, 2012b). Furthermore, the [001] pole figure plots of the clay minerals in the samples from the incoming plate do not indicate drilling disturbance or re-deposition. Thus, we rule out these processes. Coarse albite grains, possibly derived from ash, are evident in backscattered and secondary electron images (Figure 3. 2). Glass chards were identified during point counting in all samples (Figure 3. 5), and volcanic ash is also reported by Expedition 315 Scientists (2009), Expedition 316 Scientists (2009a, 2009b, 2009c, 2009d) and Expedition 333 Scientists (2012a, 2012b), from which

idiomorphic albite grains can originate (Figure 3. 11c). Moreover, large mineral grains can produce strong single crystal maxima, also providing a possible explanation for this type of CPO.

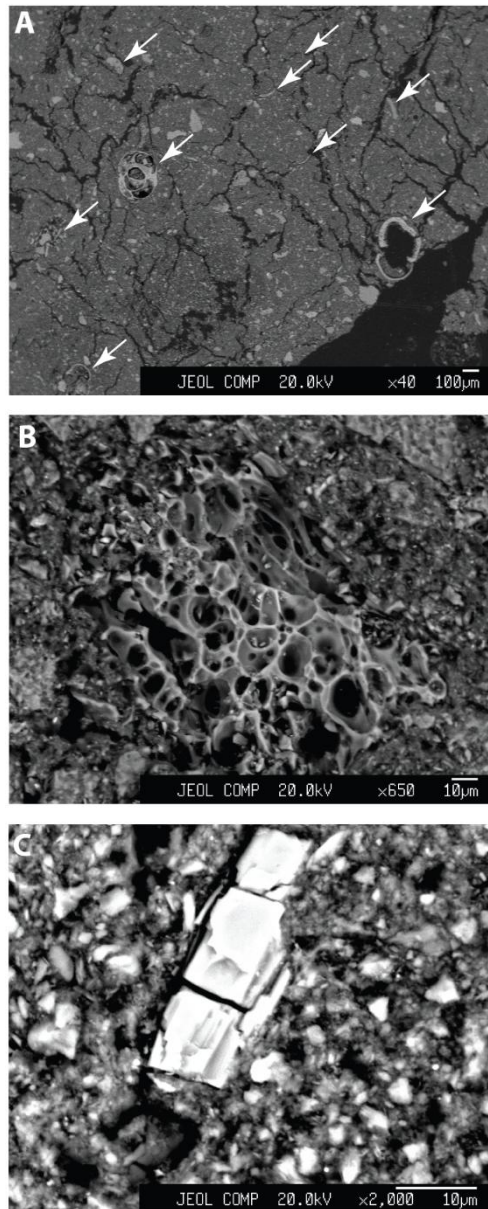


Figure 3. 11: SEM micrograph of (a) microfossil shell fragments in core sample 315-C0001E-11H-1, (b) volcanic glass (experimental subsample K018) and (c) a relatively large idiomorphic feldspar crystal (experimental subsample K018).

6.2 Texture genesis in constant-volume shearing

Experimental deformation was conducted under consolidated and undrained conditions, which means that shearing proceeded at constant volume, and shape and texture anisotropy, therefore, reflects an axial symmetric (biaxial) state of strain. For this reason, increasing axial strain during the experiments should result in increasing CPO (March, 1932). In a plot of experimental strain versus CPO intensity (Figure 3. 9b), it can be seen that the results generally confirm the predictions of the March model.

The pore space anisotropy in response to the experimental deformation is expressed by the ratio of the maximum frequency per petal divided by the uniform frequency per petal ($f_{\max}/f_{\text{uniform}}$) in the rose diagram (Figure 3. 6). The pore long axes are preferentially oriented perpendicular to the axis of shortening (Figure 3. 6) and thus, mimic the maximum finite stretching in the flattening plane. Thus, pores are sensitive strain gauges. Differences in the calculated strains from fabrics and the strain achieved during the triaxial deformation experiments are attributed to the reorientation or rotation of mineral grains and the deformation of pores as experimental deformation proceeded. Primary CPO and SPO of the natural samples were formed during compaction (Fawad et al. 2010 and Mitchell 1956), and later at least in part tilted by tectonic deformation (see Figure 3. 7), and then overprinted by the experimental deformation (Bowles et al., 1969). Such effects are also evident in tilted bedding orientations and pole figure maxima oblique to the shortening axes in Figure 3. 8.

The absence of quartz CPO in all samples, even after the experimental deformation, is an effect caused by the shape of the detrital quartz. In the SEM images, well-rounded clastic quartz grains occur. Clast shape of quartz has usually no relation to crystal axis orientation. Thus, even an SPO, if present, will not result in a CPO. A different effect is observed in the case of albite CPO, as discussed above. Three of the experimentally deformed sediment samples show strong CPO, while all the others do not (Figure 3. 8). Apart from the possibility of single crystal effects, as discussed above, volcanic plagioclase derived from ash (evident in the smear slides) usually forms albite-twinned crystal laths. Feldspar laths should therefore respond to experimental strain in a similar way as the phyllosilicates, attenuating the CPO of [010]. We cannot distinguish in the

dataset, however, if the albite CPO in the experimentally deformed samples is inherited from the original fabric and hence induced by burial and compaction.

6.3 Sample composition

Differences in the sample composition (especially for sample 316-C0008A-9H-3) are probably due to sample heterogeneities, because the data refer to different subsamples. In addition, there are also some methodical differences. IODP expedition shipboard scientists (Expedition 316 Scientists, 2009e) used x-ray diffraction analysis to investigate the sample composition. Due to the number of poorly crystalline mineral phases and superposed peaks (especially for the clay minerals) methodical errors can be considerable. Guo and Underwood (2012) used the grain size fraction $<2\ \mu\text{m}$ to determine the clay mineral assemblages. In the BSE studies, we found clay mineral grains exceeding $2\ \mu\text{m}$ and detrital illite flakes of up to $40\ \mu\text{m}$ in size. In addition, the filter-peel method (Moore and Reynolds, 1989) used by Guo and Underwood (2012) produces textured samples (clay mineral basal planes parallel to the filter paper; cf. Moore and Reynolds, 1989). Preferred orientations increase peak intensity and peak area, thus causing a misinterpretation of the clay content.

6.4 Aspects of Synchrotron Texture Analysis

Sample preparation using standard techniques is erroneous and complex (see Behrmann and Kopf, 1993), while punching cylindrical samples and the absence of any further preparation step decreases errors linked to the sample preparation to a minimum. It can be assumed that disturbance of the sample material only occurs very close to the sidewalls of the sample cylinder. Thus, measurement artifacts are negligible, considering that synchrotron texture analysis is on the whole sample volume (Wenk et al., 2008), instead of analyzing a very thin surface layer (standard XTG, Behrmann and Kopf, 1993). Additional advantages arise from using the Rietveld method, because the background radiation is much better approximated by a Rietveld fit in synchrotron texture analysis, than in simple

scans across the diffraction peaks in x-ray texture goniometry (Wenk et al., 2010). Also, synchrotron analysis offers clear advantages in distinguishing clay minerals with superposed and overlapping peak spectra by using the whole diffraction spectrum (Wenk et al., 2010, 2008).

Synchrotron texture analysis is a new method, which means that synchrotron radiation for the application of this method is not yet easily accessible to a wide community. However, there is potential for a large increase in research efficiency in using this method. For example, the dataset presented in this study required only two days at the DESY beamline.

7. Conclusions

From the synchrotron texture and microstructural analysis of silty clay sediments from the Nankai Trench obtained during IODP Expedition 315, 316 and 333, we conclude that Rietveld-based synchrotron texture goniometry is a new and valuable analytical tool to quantify textures of fine-grained phyllosilicate-rich sediments. The method allows to analyze comparatively large volumes of water-saturated sediment, and profits from good diffraction peak definition and background-peak ratios.

In the naturally compacted samples from the Nankai accretionary wedge and from the incoming Philippine Sea Plate [010]-planes of illite, kaolinite and smectite show bedding-parallel CPOs, increasing with drillhole depth, thus reflecting progressive burial and compaction. The strongest CPOs were recorded in the samples with the deepest burial. In a few samples calcite and albite display a CPO due to crystallographically controlled non-isometric grain shapes, or nannofossil tests. When bed tilting is observed in response to tectonic deformation, the CPO reflects compaction normal to bedding, and bedding-normal maxima are preserved. Scanning Electron Micrographs indicate preferred orientations of micropores and detrital illite flakes, reflecting the same natural vertical compaction.

Thirteen slope sediment samples were experimentally deformed in triaxial compression. Experimental deformation results in reorientation and/or flattening of micropores normal to the applied axial stress, showing that these are sensitive

strain gauges. Phyllosilicate and calcite CPOs develop normal to the experimental shortening axes, and there is at least a qualitative relation between CPO intensity and strain magnitude, validating the March model for texture formation for low degrees of deformation and absence of diagenetic effects.

Acknowledgements

This study used samples and data provided by the Integrated Ocean Drilling Program (IODP). The authors would like to thank the Scientific Parties of IODP Expedition 315, 316 and 333 aboard D/V CHIKYU for sample collection and data acquisition. We would like to thank Y. Kitamura for sample supply, and G. Tondock for the construction of a clay sampling device and the acrylic sample holders. Furthermore, we are grateful to L. Raue, J. Walter and K. Ullemeyer for assistance during the measurements, support during data analysis, and discussion. We acknowledge K. Ufer from BGR, Hannover, and R. Kaden from University of Halle for conducting comparative phase analysis. This work was funded by Deutsche Forschungsgemeinschaft (DFG) through Grant BE1041/28 to JHB and MS.

References

- Agar, S.M., Prior, D.J., Behrmann, J.H., 1989. Back-scattered electron imagery of the tectonic fabrics of some fine-grained sediments: Implications for fabric nomenclature and deformation processes. *Geology* 17, 901-904
- Aplin, C.A., Matenaar, I.F., McCarty, D.K., van der Pluijm, B.A., 2006. Influence of mechanical compaction and clay mineral diagenesis on the microfabric and pore-scale properties of deep-water Gulf of Mexico mudstones. *Clays and Clay Minerals* 54 (4), 500-514, doi: 10.1346/CCMN.2006.0540411
- Baba, T., Cummins, P.R., 2005. Contiguous rupture areas of two Nankai Trough earthquakes revealed by high-resolution tsunami waveform inversion. *Geophysical Research Letters* 32 (8), doi:10.1029/2004GL022320
- Baker, D.W., Wenk, H.R., Christie, J.M., 1969. X-ray analysis of preferred orientation in fine-grained quartz aggregates. *Journal of Geology* 77, 144-172
- Bangs, N.L., Moore, G.F., Gulick, S.P., Pangborn, E.M., Tobin, H.J., Kuramoto, S., Taira, A., 2009. Broad weak regions of the Nankai megathrust and implications for shallow coseismic slip. *Earth and Planetary Science Letters* 284, 44-49, doi:10.1016/j.epsl.2009.04.026
- Becker, J.J., Sandwell, D.T., Smith, W.H.F., Braud, J., Binder, B., Depner, J., Fabre, D., Factor, J., Ingalls, S., Kim, S-H., Ladner, R., Marks, K., Nelson, S., Pharaoh, A., Trimmer, R., Von Rosenberg, J., Wallace, G., Weatherall, P., 2009. Global Bathymetry and Elevation Data at 30 Arc Seconds Resolution: SRTM30_PLUS, *Marine Geodesy*, 32 (4), 355-371
- Behrmann, J.H., Kopf, A., 1993. Textures and microfabrics in fine-grained muds and mudstones from Site 808, Nankai accretionary prism. In: Hill, I.A., Taira, A., Firth, J.V., et al., 1993. *Proceedings of the Ocean Drilling Program, Scientific results* 131
- Behrmann, J.H., Lewis, S.D., Cande, S.C., 1994. Tectonics and geology of spreading ridge subduction at the Chile Triple Junction: a synthesis of results from Leg 141 of the Ocean Drilling Program. *Geologische Rundschau* 83, 832-852
- Behrmann, J.H., Meissl, S. 2012. Submarine Landslides, Gulf of Mexico Continental Slope: Insights into Transport Processes from Fabrics and Geotechnical Data. In: Yamada, Y. et al., (eds.). *Submarine Mass Movements and Their Consequences. Advances in Natural Technological Hazards Research* 31
- Bennett, R., Bryant, W., Keller, G., 1981. Clay fabric of selected submarine sediments: Fundamental properties and models. *Journal of Sedimentary Petrology* 51, 217-232
- Bennett, R.H., O'Brien, N.R., Hulbert, M.H., 1991. Determination of clay and shale microfabric signatures: processes and mechanisms. In: Bennett, R.H.,

- Bryant, W.R., Hulbert, M.H. (ed.): Microstructure of fine-grained sediments. Springer-Verlag. New York, 5-32
- Biscaye, P.E., 1965. Mineralogy and sedimentation of Recent Deep-Sea Clay in the Atlantic Ocean and Adjacent Seas and Oceans. Geological Society of America Bulletin 76, 803-832
- Bish, D.L., Von Dreele, R.B., 1989. Rietveld refinement of non-hydrogen atomic positions in kaolinite. Clays and Clay Minerals 37 (4), 289-296
- Black, M., 1963. The fine structure of the mineral parts of coccolithophorids. Proceedings of the Royal Society of London 174, 41-46
- Black, M., 1972. Crystal development in Discoasteraceae and Braarudshaeraceae (planktonic algae). Paleontology 15 (3), 476-489
- Bowles, F.A., Bryant, W.R., Wallin, C., 1969. Microstructure of unconsolidated and consolidated marine sediments. Journal of Sedimentary Research 39, 1546-1551
- Brace, W.F., 1972. Laboratory studies of stick-slip and their application to earthquakes. Tectonophysics, 189-200
- Brace, W.F., 1978. A note on permeability changes in geological material due to stress. Pure Applied Geophysics 116, 627-633
- Brown, K.M., Mascle, A., Behrmann, J.H., 1990. Mechanisms of accretion and subsequent thickening in the Barbados Ridge accretionary complex: balanced cross sections across the toe of the wedge. Proceedings of the Ocean Drilling Program, Scientific Results 110, 209-227
- Buatier, M.D., Chauvet, A., Kanitpanyacharoen, W., Wenk, H.R., Ritz, J.F., Jolivet, M., 2012. Origin and behavior of clay minerals in the Bogd fault gouge, Mongolia. Journal of Structural Geology, 34, 77-90
- Carlson, R.L. and Christensen, N.I., 1979. Velocity anisotropy in semi-indurated calcareous deep-sea sediments. Journal Geophysical Research 84. 205-211
- Carson, B., von Huene, R., Arthur, M., 1982. Small-scale deformation structures and physical properties related to convergence in Japan Trench slope sediments. Tectonics 1 (3), 277-302
- Curtis, C.D., Lipshie, S.R., Oertel, G., Pearson, M.J., 1980. Clay orientation in some Upper Carboniferous mudrocks, its relation to quartz content and some inferences about fissility, porosity and compactional history. Sedimentology 27, 333-339
- Davis, D., Suppe, J., Dahlen, F.A., 1983. Mechanics of fold-and-thrust belts and accretionary wedges. Journal of Geophysical Research 88, 1153-1172
- Dixon, T.H., Moore J.C., 2007. The seismogenic zone of subduction thrust faults. Columbia University Press, New York (665 pp.).

-
- Downs, R.T., Hall-Wallace, M., 2003. The American Mineralogist Crystal Structure Database. *American Mineralogist* 88, 247-250
- Dušek, M., Petříček, V., Wuschel, M., Dinnebier, R.E., van Smaalen, S., 2001. Refinement of modulated structures against X-ray powder diffraction data with JANA2000. *Journal of Applied Crystallography* 34, 398-404
- Expedition 315 Scientists, 2009. Expedition 315 Site C0001. In: Kinoshita, M., Tobin, H., Ashi, J., Kimura, G., Lallemand, S., Screaton, E.J., Curewitz, D., Masago, H., Moe, K.T., Expedition 314/315/316 Scientists, 2009. Proceedings of the International Ocean Drilling Program, Volume 314/315/316. Washington DC, doi: 10.2204/iodp.proc.314315316.123.2009
- Expedition 316 Scientists, 2009a. Expedition 316 Site C0004. In: Kinoshita, M., Tobin, H., Ashi, J., Kimura, G., Lallemand, S., Screaton, E.J., Curewitz, D., Masago, H., Moe, K.T., Expedition 314/315/316 Scientists, 2009. Proceedings of the International Ocean Drilling Program, Volume 314/315/316. Washington DC, doi: 10.2204/iodp.proc.314315316.133.2009
- Expedition 316 Scientists, 2009b. Expedition 316 Site C0006. In: Kinoshita, M., Tobin, H., Ashi, J., Kimura, G., Lallemand, S., Screaton, E.J., Curewitz, D., Masago, H., Moe, K.T., Expedition 314/315/316 Scientists, 2009, Proceedings of the International Ocean Drilling Program, Volume 314/315/316. Washington DC, doi: 10.2204/iodp.proc.314315316.134.2009
- Expedition 316 Scientists, 2009c. Expedition 316 Site C0007. In: Kinoshita, M., Tobin, H., Ashi, J., Kimura, G., Lallemand, S., Screaton, E.J., Curewitz, D., Masago, H., Moe, K.T., Expedition 314/315/316 Scientists, 2009. Proceedings of the International Ocean Drilling Program, Volume 314/315/316. Washington DC, doi: 10.2204/iodp.proc.314315316.135.2009
- Expedition 316 Scientists, 2009d. Expedition 316 Site C0008. In: Kinoshita, M., Tobin, H., Ashi, J., Kimura, G., Lallemand, S., Screaton, E.J., Curewitz, D., Masago, H., Moe, K.T., Expedition 314/315/316 Scientists, 2009. Proceedings of the International Ocean Drilling Program, Volume 314/315/316. Washington DC, doi: 10.2204/iodp.proc.314315316.136.2009
- Expedition 316 Scientists, 2009e. Expedition 316 methods. In: Kinoshita, M., Tobin, H., Ashi, J., Kimura, G., Lallemand, S., Screaton, E.J., Curewitz, D., Masago, H., Moe, K.T., and the Expedition 314/315/316 Scientists, *Proc. IODP, 314/315/316*: Washington, DC (Integrated Ocean Drilling Program Management International, Inc.). doi:10.2204/iodp.proc.314315316.132.2009
- Expedition 333 Scientists, 2012a. Expedition 333 Site C0011. In: Henry, P., Kanamatsu, T., Moe, K., Expedition 333, 2012. Proceedings of the International Ocean Drilling Program, 333, doi: 10.2204/iodp.proc.333.104.2012
- Expedition 333 Scientists, 2012b. Expedition 333 Site C0012. In: Henry, P., Kanamatsu, T., Moe, K., Expedition 333, 2012. Proceedings of the International Ocean Drilling Program, 333, doi: 10.2204/iodp.proc.333.105.2012

- Fawad, M., Mondol, N.H., Jahren, J., Bjørlykke, K., 2010. Microfabric and rock properties of experimentally compressed silty-clay mixtures. *Marine and Petroleum Geology* 27, 1698-1712
- Gournis, D., Lappas, A., Karakassides, M.A., Többens, D., Moukarika, A., 2008. A neutron diffraction study of alkali cation migration in montmorillonites. *Physics and Chemistry of Minerals* 35, 49-58, doi:10.1007/s00269-007-0197-z
- Gualtieri, A.F., Ferrari, S., Leoni, M., Grathoff, G., Hugo, R., Shatnawi, M., Paglia, G., Billinge, S., 2008. Structural characterization of the clay mineral illite-1M. *Journal of Applied Crystallography* 41, 402-415, doi:10.1107/S0021889808004202
- Guo, J., Underwood, M., 2012. Data Report: Clay Mineral Assemblages from the Nankai Trough and Kumano Basin, IODP Expedition 315 and 316, NanTroSEIZE Stage 1. In: Kinoshita, M., Tobin, H., Ashi, J., Kimura, G., Lallemand, S., Screaton, E.J., Curewitz, D., Masago, H., Moe, K.T., and the Expedition 314/315/316 Scientists, *Proceedings of the Integrated Ocean Drilling Program 314/315/316*, doi:10.2204/iodp.proc.314315316.202.2012
- Hammersley, A.P., 1998. FIT2D V10.3 Reference Manual V4.0 ESRF98HA01T.
- Harlow, G.E., Brown, G.E., 1980. Low albite: An X-Ray and neutron diffraction study. *American Mineralogist* 65, 986-995
- Ho, N-C., Peacor, D.R., van der Pluijm, B.A., 1999. Preferred orientation of phyllosilicates in Gulf Coast mudstones and relation to the smectite-illite transition. *Clays and Clay Minerals* 47 (4), 495-504
- Ike, T., Moore, G.F., Kuramoto, S., Park, J., Kaneda, Y., Taira, A., 2008a. Variations in sediment thickness and type along the northern Philippine Sea Plate at the Nankai Trough. *Island Arc* 17, 342-357, doi:10.1111/j.1440-1738.2008.00624.x
- Ike, T., Moore, G.F., Kuramoto, S., Park, J.O., Kaneda, Y., Taira, A., 2008b. Tectonics and sedimentation around Kashinosaki Knoll: a subducting basement high in the eastern Nankai Trough. *Island Arc* 17 (3), 358-375, doi:10.1111/j.1440-1738.2008.00625.x
- Janssen, C.M., Kanitpanyacharoen, W., Wenk, H.R., Morales, L., Rybacki, E., Kienast, M., Dresen, G., 2012. Clay fabrics in SAFOD core samples. *Journal of Structural Geology* 43, 118-127
- Johansen, T.A., Bent, O.R., Jakobsen, M., 2004. Effect of grain scale alignment on seismic anisotropy and reflectivity of shales. *Geophysical Prospecting* 52, 133-149
- Jones, M., 1994. Mechanical principles of sediment deformation. In: Maltman, A. (Ed.): *The Geological Deformation of sediments*. Chapman and Hall, London, 37-71

-
- Kawamura, K., Ogawa, Y., 2004. Progressive change of pelagic clay microstructure during burial process: examples from piston cores and ODP cores. *Marine Geology* 207, 131-144
- Kopf, A., Behrmann, J.H., 1997. Fabric evolution and mechanisms of diagenesis in fine grained sediments from the Kita-Yamato trough, Japan Sea, *Journal of Sedimentary Research* 67, 604-614
- Krinsley, D.H., Pye, K., Kearsly, A.T., 1983. Application of backscattered electron microscopy in shale petrology. *Geological Magazine* 120, 109-114
- Lipshie, S.R., 1984. Development of phyllosilicate preferred orientation in naturally and experimentally metamorphosed and deformed rocks [unpublished Ph.D. thesis]: University of California, Los Angeles.
- Lonardelli, I., Wenk, H.R., Lutterotti, L., Goodwin, M., 2005. Texture analysis from synchrotron diffraction images with the Rietveld method: dinosaur tendon and salmon scale. *Journal of Synchrotron radiation*, 12, 354-360, doi:10.1107/S090904950500138X
- Lutterotti, L., Mathies, S., Wenk, H.R., Schultz, A.J., Richardson, J., 1997. Texture and structure analysis of deformed limestone from neutron diffraction spectra. *Journal of Applied Physics* 81 (2), 594-600
- March, A., 1932. Mathematische Theorie der Regelung nach der Korngestalt bei affiner Deformation. *Zeitschrift für Kristallographie* 81, 285-297
- Maslen, E.N., Streltov, V.A., Streltsova, N.R., Ishizawa, N., 1995. Electron Density and Optical Anisotropy in Rhombohedral Carbonates. III. Synchrotron X-ray Studies of CaCO₃, MgCO₃ and MnCO₃. *Acta Crystallographica B* 51, 929-939
- Mathies, S., Lutterotti, L., Wenk, H.R., 1997. Advances in the texture analysis from diffraction spectra. *Journal of applied Crystallography* 30, 31-42
- Mathies, S., Vinel, G.W., 1982. On the Reproduction of the Orientation Distribution Function of Texturized Samples from Reduced Pole Figures Using Conception of a Conditional Ghost Correction. *Physica Status Solidi (b)* 112, K111
- Mitchell, J.K., 1956. The fabric of natural clays and its relation to engineering properties. Highway Research Board, NAS-NRC 35, 693-713
- Moore, D.M., Reynolds, R.C., 1989. X-ray diffraction and the identification and analysis of clay minerals. Oxford University Press. Oxford 332 pp.
- Moore, G.F., Park, J.-O., Bangs, N.L., Gulick, S.P., Tobin, H.J., Nakamura, Y., Sato, S., Tsuji, T., Yoro, T., Tanaka, H., Uraki, S., Kido, Y., Sanada, Y., Kuramoto, S., and Taira, A., 2009. Structural and seismic stratigraphic framework of the NanTroSEIZE Stage 1 transect. In: Kinoshita, M., Tobin, H., Ashi, J., Kimura, G., Lallemand, S., Sreaton, E.J., Curewitz, D., Masago, H., Moe, K.T., Expedition 314/315/316 Scientists, *Proceedings of the IODP, 314/315/316*, doi:10.2204/iodp.proc.314315316.102.2009

- Moore, J.C., Shipley, T., Goldberg, D., Ogawa, Y., Filice, F., 1995. Abnormal fluid pressure and fault-zone dilation in the Barbados accretionary prism: Evidence from logging while drilling. *Geology* 23, 605-608, doi:10.1130/0091-7613(1995)023<0605:AFPAFZ>2.3.CO;2
- Morgan, J.K., Ramsey, E.B., Ask, M.V.S., 2007. Deformation and mechanical strength of sediments at the Nankai subduction zone. In: Dixon, T.H., Moore J.C., (eds.). *The seismogenic zone of subduction thrust faults*. Columbia University Press, New York, 210-256
- O'Brien, N.R., Slatt, R.M., 1990. *Argillaceous Rock Atlas*. Springer, New York (141 pp.).
- Oertel, G., 1983. The relationship of strain and preferred orientation of phyllosilicate grains in rocks – A Review. In: Friedman, M., Toksöz, M.N., (ed). *Continental Tectonics: Structure, Kinematics and Dynamics*. *Tectonophysics* 100, 413-447
- Oertel, G., 1985. Reorientation due to grain shape. In: Wenk, H.R., (ed.). *Preferred orientation in deformed metals and rocks: An introduction to modern texture analysis*. Orlando, Florida, Academic Press, 259-265
- Oertel, G., Curtis, C.D., 1972. Clay-Ironstone concretion preserving fabrics due to progressive compaction. *Geological Society of America Bulletin* 83, 2597-2606
- Park, J-O., Tsuru, T., Kodaira, S., Nakanishi, A., Miura, S., Kaneda, Y., Kono, Y., 2000. Out-of-sequence thrust faults developed in the coseismic slip zone of the 1946 Nankai earthquake (Mw=8.2) off Shikoku, southwest Japan. *Geophysical research letters* 27 (7), 1033-1036
- Petschick, R., Kuhn, G., Gingele, F. 1996. Clay mineral distribution in surface sediments of the South Atlantic: source, transport, and relation to oceanography. *Marine Geology* 130, 203-229
- Prior, D.J., Behrmann, J.H., 1990a. Backscatter SEM imagery of fine-grained sediments from Site 671, Leg 110-preliminary results. In: Moore, J.C., Mascle, A., et al. *Proceedings of the ODP, Scientific Results. 110* College Station, TX (Ocean Drilling Program) 245-255
- Prior, D.J., Behrmann, J.H., 1990b. Thrust-related mudstone fabrics from the Barbados forearc: a backscattered Scanning Electron Microscope study. *Journal of Geophysical Research* 95, 9055-9067
- Rai, C.S., Hanson, K.E., 1988. Shear-wave velocity anisotropy in sedimentary rocks: A laboratory study. *Geophysics* 53, 800-806
- Rice, J.R., 1992. Fault stress states, pore pressure distribution, and weakness of the San Andreas Fault. In: Evans, B., Wong, T-F., (ed). *Fault mechanics and transport properties of rocks*. Academic Press limited (524 pp.).
- Rietveld, H.M., 1969. A Profile Refinement Method for Nuclear and Magnetic Structures. *Journal of Applied Crystallography* 2, 65-71

-
- Schleicher, A.M., Warr, L.N., van der Pluijm, B.A., 2009. On the origin of mixed-layered clay minerals from the San Andreas Fault at 2.4-3 km vertical depth (SAFOD drillhole at Parkfield, California). *Contributions to Mineralogy and Petrology* 157, 173-187
- Scholz, C.H., 2002. *The mechanics of earthquakes and faulting*. Second edition. Cambridge (466 pp.).
- Seno, T., Stein, S., Gripp, A.E., 1993. A model for the motion of the Philippine Sea plate consistent with NUVEL-1 and geological data. *Journal of Geophysical Research* 98, 17941-17948
- Sondergeld, C.H., Rai, C., 2011. Elastic anisotropy of shales. *The Leading Edge* 30, 324
- Song, I., Saffer, D.M., Flemings, P.B., 2011. Mechanical characterization of slope sediments: Constraints on in situ stress and pore pressure near the tip of the megasplay fault in the Nankai accretionary complex. *Geochemistry, Geophysics, Geosystems* 12 (5) doi:10.1029/2011GC003556
- Stipp, M., Rolfs, M., Kitamura, Y., Behrmann, J.H., Schumann, K., Schulte-Kornack, D., Feeser, V., in press. Strong sediments at the deformation front, and weak sediments at the rear of the Nankai accretionary prism, revealed by triaxial deformation experiments.
- Tobin, H., Kinoshita, M., Ashi, J., Lallement, S., Kimura, G., Sreaton, E., Moe, K.T., Masago, H., Curewitz, D., Expeditions 314/315/316 Scientists, 2009. NanTroSEIZE Stage 1 expeditions: introduction and synthesis of key results. In: Kinoshita, M., Tobin, H., Ashi, J., Kimura, G., Lallement, S., Sreaton, E.J., Curewitz, D., Masago, H., Moe, K.T., Expeditions 314/315/316 Scientists (ed.), 2009. Nantroseize Stage 1: Investigations of Seismogenesis, Nankai Trough, Japan : Expeditions 314, 315, and 316 of the Riser Drilling Platform from and to Shingu, Japan, Sites C0001-C0006, 21 September-15 November 2007, and Sites C0001 and C0002, 16 November-18 December 2007, and Sites C0004 and C0006-C0008, 19 December 2007-5 February 2008, IODP, Washington, DC, USA, Proceedings of the Integrated Ocean Drilling Program, 314/315/316, 1-20, doi:10.2204/iodp.proc.314315316.101.2009
- Tobin, H.J., Saffer, D.M., 2009. Elevated fluid pressure and extreme mechanical weakness of a plate boundary thrust, Nankai Trough subduction zone. *Geology* 37, 679–682, doi:10.1130/G25752A.1.
- Toby, B.H., 2006. R factors in Rietveld analysis: How good is good enough? *Powder Diffraction* 21, 67-70
- Tsuji, T., Dvorkin, J., Mavko, G., Nakata, N., Matsuoka, T., Nakanishi, A., Kodaira, S., Nishizawa, O., 2011. V_p/v_s ratio and shear-wave splitting in the Nankai Trough seismogenic zone: Insights into effective stress, pore pressure, and sediment consolidation. *Geophysics* 76 (3), 71-82, doi: 10.1190/1.3560018
- Ufer, K., Roth, G., Kleeberg, R., Stanjek, H., Dorhmann, R., Bergmann, J., 2004. Description of X-ray powder pattern of turbostratically disordered layer

structures with a Rietveld compatible approach. *Zeitschrift für Kristallographie* 219, 519-527

- Underwood, M.B., 2007. Sediment inputs to subduction zones: why lithostratigraphy and clay mineralogy matter. In: Dixon, T.H., Moore J.C., (ed.). *The seismogenic zone of subduction thrust faults*. Columbia University Press, New York, 42-85.
- van der Pluijm, B.A., Ho, N-C., Peacor, D.R., 1994. High-resolution X-ray texture goniometry. *Journal of Structural Geology* 16 (7), 1029-1032
- Vasin, R.N., Wenk, H.R., Kanitpanyacharoen, W., Matthies, S., Wirth, R. (2013) Elastic anisotropy modeling of Kimmeridge shale. *Journal of Geophysical Research*, 118, 1–26, doi:10.1002/jgrb.50259
- Vasseur, G., Djeran-Maigre, I., Grunberger, D., Rousset, G., Tessier, D., Velde, B., 1995. Evolution of structural and physical parameters of clays during experimental compaction. *Marine and Petroleum Geology* 12 (8), 941-954
- Voltolini, M., Wenk, H.-R., Mondol, N.H., Bjørlykke, K., Jahren, J., 2009. Anisotropy of experimentally compressed kaolinite-illite-quartz mixtures. *Geophysics* 74 (1), 13-23
- Wenk, H.R., Kanitpanyacharoen, W., Voltolini, M., 2010. Preferred orientation of phyllosilicates: Comparison of fault gouge, shale and schist. *Journal of Structural Geology* 32, 478-489, doi: 10.1016/j.jsg.2010.02.003
- Wenk, H.R., Lutterotti, L., Vogel, S., 2003. Texture analysis with the new HIPPO TOF diffractometer. *Nuclear Instruments and Methods in Physics Research* 515, 575-588, doi: 10.1016/j.nima.2003.05.001
- Wenk, H.R., Lutterotti, L., Vogel, S.C., 2010. Rietveld texture analysis from TOF neutron diffraction data. *Powder Diffraction* 25, 283-296, doi: 10.1154/1.3479004
- Wenk, H.R., Voltolini, M., Mazurek, M., van Loon, L.R., Vinsot, A., 2008. Preferred orientation and anisotropy in shale: Callovo-Oxfordian shale (France) and Opalinus Clay (Switzerland). *Clays and Clay Minerals* 56 (3), 285-306, doi: 10.1346/CCMN.2008.0560301
- Worden, R.H., Chappentier, D., Fisher, Q.J., Aplin, A.C., 2005. Fabric development and the smectite to illite transition in Upper Cretaceous mudstones from the North Sea: an image Analysis Approach. In: Shaw, R.P., (ed.). *Understanding the Micro to Macro Behaviour of Rock-Fluid Systems*. Geological Society, London, Special Publication, 249, 103-114
- Zanazzi, P.F., Comodi, P., Nazzareni, S., Andreozzi, G.B., 2009. Thermal behaviour of chlorite: an in situ single-crystal and powder diffraction study. *European Journal of Mineralogy* 21, 581-589, doi: 10.1127/0935-1221/2009/0021-1928

4 Manuscript #3

Geotechnical behavior of mudstones from the
Shimanto and Boso accretionary complexes, and
implications for the recently active Nankai
Accretionary Prism

Kai Schumann¹, Jan H. Behrmann¹, Michael Stipp¹, Yuzuru Yamamoto²,
Yujin Kitamura³ and Christof Lempp⁴

¹ *Marine Geodynamics, GEOMAR Helmholtz Centre for Ocean Research Kiel,
Wischhofstr. 1-3, Kiel, Germany*

² *JAMSTEC, 2-15 Natsushima-Cho, Yokosuka-City, Kanagawa 237-0061,
Japan*

³ *Dept. of Earth and Planetary Science, The University of Tokyo, Tokyo 113-
0033, Japan*

⁴ *Institut für Geowissenschaften und Geographie, Martin-Luther-Universität
Halle-Wittenberg, Von-Seckendorff-Platz 3, 06120 Halle/Saale, Germany*

submitted to
Earth Planets and Space

Geotechnical behavior of mudstones from the
Shimanto and Boso accretionary complexes, and
implications for the recently active Nankai
Accretionary Prism

Kai Schumann¹, Jan H. Behrmann¹, Michael Stipp¹, Yuzuru Yamamoto², Yujin
Kitamura³, and Christof Lempp⁴

¹ *Marine Geodynamics, GEOMAR Helmholtz Centre for Ocean Research Kiel,
Wischhofstr. 1-3, Kiel, Germany*

² *IFREE, JAMSTEC, 3173-25 Showa-machi, Kanazawa-ku, Yokohama 236-
0001, Japan*

³ *Dept. of Earth and Planetary Science, The University of Tokyo, Tokyo 113-
0033, Japan*

⁴ *Institut für Geowissenschaften und Geographie, Martin-Luther-Universität
Halle-Wittenberg, Von-Seckendorff-Platz 3, 06120 Halle/Saale, Germany*

*Corresponding author: K. Schumann, Marine Geodynamics, GEOMAR
Helmholtz Centre for Ocean Research Kiel, Wischhofstr. 1-3, 24148 Kiel,
Germany (kaschumann@geomar.de)*

Abstract

Triaxial shear tests on mudstone samples from the Shimanto Belt and the Boso accretionary prism (SW Japan) were carried out. Pre-exhumation burial depths in the two paleo-accretionary prisms were up to 9000 m and about 1000 m for the Shimanto and the Boso samples, respectively. Three methods were applied. (1) Pressure stepping tests at increasing confining pressures between 25 MPa and 65 MPa, and pore pressures between 20 MPa and 52 MPa. (2) Constant confining pressure tests at 55 MPa and 65 MPa, with stepwise pore pressure decrease from 80% to 50% and 25%, and from 90% to 60% and 30% of the confining pressure. (3) A cyclic loading test on one sample from Boso (19 cycles to 70 MPa differential stress). After some contraction due to pressurization in the first cycles the sample showed tendencies to creep rather than to fracture.

Effective shear parameters show that angles of internal friction between 30 and 50° are in part quite high in both sample subsets, and ranges of cohesion are between about 2 and 6 MPa (Boso), and 13 and > 30 MPa (Shimanto). The mechanical results from these paleo-accretionary prisms are taken to constrain the strength and frictional behavior of the deeper parts of the present Nankai accretionary wedge and forearc, as sample compositions are quite similar to Nankai sediments. Static friction resembles results from experiments on a wide range of phyllosilicate-quartz-feldspar gouges, and shows that the forearc is composed of relatively strong rock. Cohesion increase due to diagenesis and/or very low-grade metamorphism is of overriding importance, and probably permits stresses of up to 18 MPa to be transmitted to the updip end of the seismogenic zone at depth, and 5-13 MPa to the backstop of the actively deforming frontal prism.

Keywords: Shimanto Belt, Boso accretionary prism, Nankai, IODP, triaxial shear test, mudstone, subduction zone

1 Introduction

Subduction zones are the tectonically most active regions on Earth, and are known to generate large earthquakes by thrust faulting. These are caused by movements on the so-called plate boundary thrust in the seismogenic zone (e.g., Byrne et al. 1988; Scholz 1998; Moore and Saffer 2001) and/or by operation of splay faults (e.g., Moore et al. 2007; Park et al. 2002) further up in the thrust sequence. Splay faulting plays a critical role in the building of accretionary wedges, and it are clay-rich sediment that usually act as décollement horizon in the tectonic stacking process. Different hypotheses on the updip limit of the seismogenic zone exist. Hyndman and Wang (1993) assume a temperature-controlled dehydration of clays at 100 °C to 150 °C is followed by a difference in frictional strength (e.g., Saffer and Marone 2003). Multiple processes such as smectite to illite transition, pressure solution and quartz cementation resulting in increased effective stress (e.g., Moore and Saffer 2001) and lithification (e.g., Kimura and Ludden 1995; Matsumura et al. 2003) are thought to control the updip limit of the seismogenic zone.

This means that very-low-grade metamorphic phenomena and progressive lithification change the physical properties of clay-rich rocks, such as porosity, state of consolidation, mineral fabrics, and cementation. These changes are thought to be instrumental in controlling seismicity (e.g., Scholz 1998; Moore and Saffer 2001), and determining the transition from stable frictional sliding behavior to unstable stick slip (e.g., Byrne et al. 1988; Vrolijk 1990; Hyndman et al. 1995; Oleskevich et al. 1999; Moore and Saffer 2001).

Generally, earthquakes are thought to be the result of a sudden stress release along a slip surface (e.g., Reid 1911; Brace and Byerlee 1966; Scholz 1998). Scholz (1998) suggested that earthquakes occur on pre-existing faults and interfaces instead of newly generated faults. Thus, stress release along a slip surface is a frictional phenomenon (Scholz 1998). However, faulted rocks at depth change their physical properties during interseismic diagenesis, and the role of these processes needs to be investigated for a better understanding of earthquake generation in accretionary prisms. This lends justification to the approach to study samples of rocks that are candidates to host major seismic faults, which have

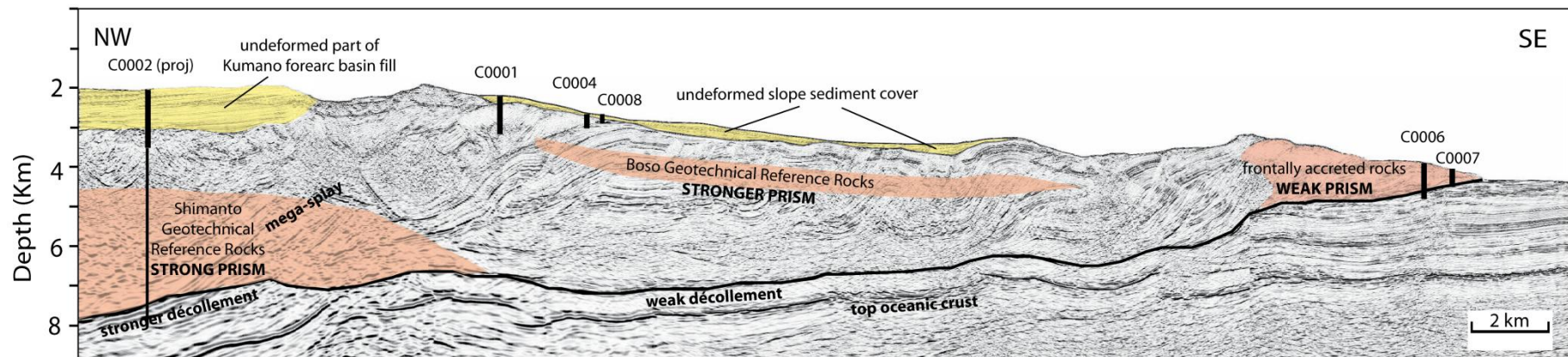


Figure 4. 1: Seismic section through the Nankai accretionary prism (Kumano transect; modified after Moore et al. 2009) showing the positions of rock units comparable to the tested Shimanto and Boso mudstones.

experienced a burial and diagenetic or metamorphic history comparable to those hosting the seismogenic zone at depth.

Here we present the results of a series of tests on rock samples believed to be present in plate boundary thrusts and splay faults under triaxial stress conditions. The key objective of the ongoing NanTroSeize drilling project (e.g., Tobin and Kinoshita 2006a; 2006b; Kuramoto et al. 2008) of the Integrated Ocean Discovery Program (IODP) is to penetrate, sample and instrument an active splay fault and the plate boundary thrust at the Nankai accretionary prism off SW Japan at depths up to 6000 m below sea floor (Figure 4. 1). The direct recovery of cores from both fault zones has not been achieved to date, and especially recovering samples suited for triaxial testing is likely to be an arduous task once the plate boundary and or megasplay faults have been reached by the drilling.

To make predictions regarding the geomechanical behavior of Nankai fault rocks at depth, we have taken the approach to sample rocks from analogous stratigraphic and/or structural contexts in two nearby fossil accretionary prisms: the Shimanto Belt along the coast of Shikoku Island, and the Boso accretionary prism on Boso Peninsula of Honshu Island. The rocks sampled from the Shimanto Belt could serve as good analogues for rocks now found at the updip limit of the seismogenic zone at Nankai (see Figure 4. 1). Samples were obtained from outcrops located at the coastline of eastern Shikoku Island (Figure 4. 2). The rocks sampled in the Boso accretionary prism are suitable analogues for the deeper parts of the frontal accretionary prism at Nankai (Figure 4. 1).

Complementary to the data of the Shimanto Belt and Boso accretionary prism, a data set of samples derived from the shallowest parts of the Nankai accretionary prism is provided by Stipp et al. (in press). Samples were recovered from the upper ~130 m of the Nankai accretionary prism by drilling during IODP Expeditions 315 and 316 southeast of Kii Peninsula (Figure 4. 2). The combination of geomechanical data from all three sample sets span the complete depth range down to the seismogenic zone, and provides the opportunity to correlate the mechanical properties from several meter below seafloor (Nankai accretionary complex) down to approximately nine km depth (Shimanto Belt analogues). We will attempt to use the data to make some predictions on the state of stress and conditions for failure of the Nankai accretionary prism as a whole.

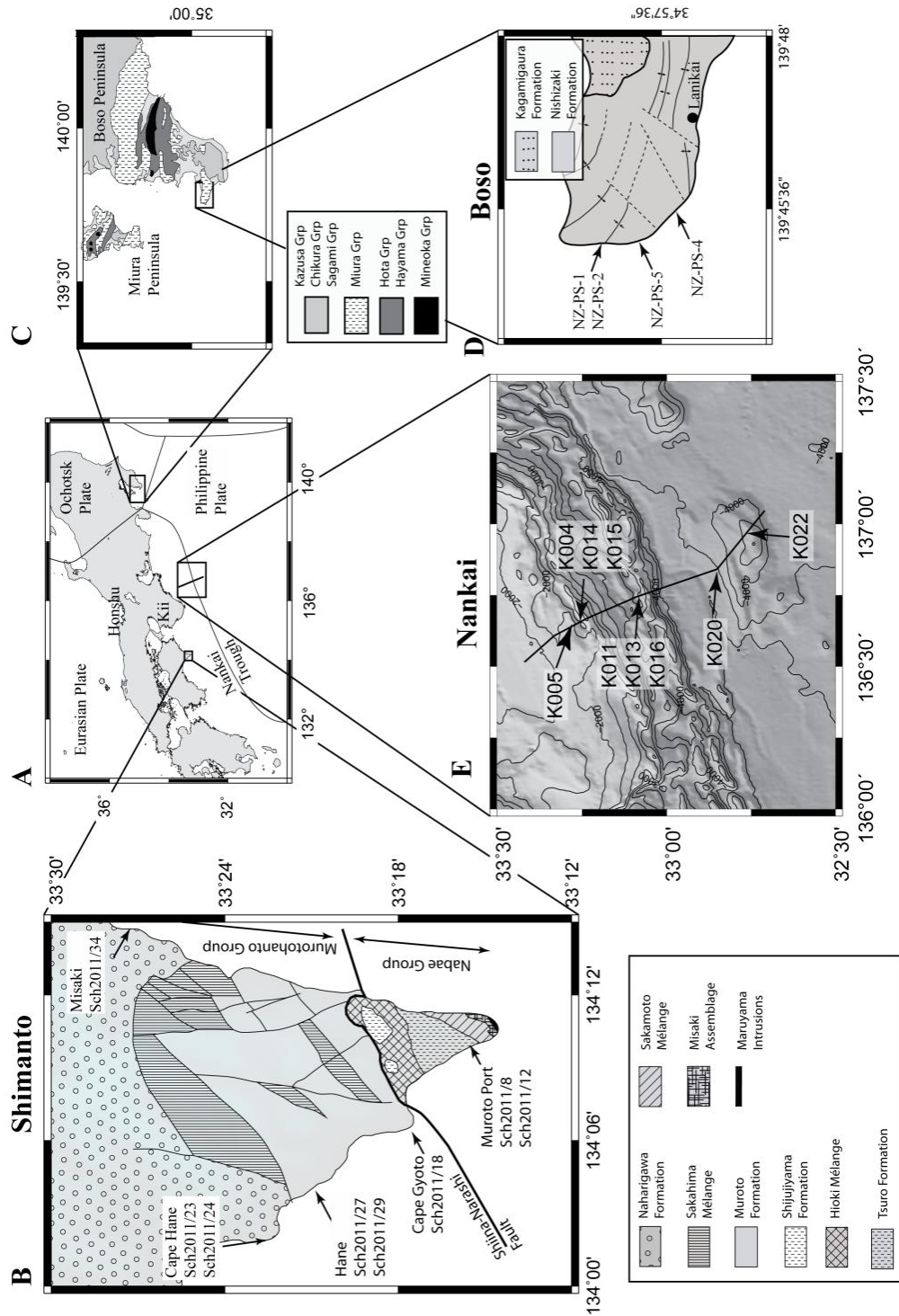


Figure 4. 2: (A) Map of central Japan. The position of the study areas are indicated by rectangular frames and shown in detail in B, C and E. (B) Geological map of Muroto Peninsula, southern Shikoku Island, after Katto et al. (1991). (C) Map of the Tokyo Bay area showing the location of the Miura and Boso Peninsulas, modified after Saito 1992 and Fujiwara et al., 1999. (D) Zoom-in of the western Boso Peninsula headlands, showing the sample positions in the Nishizaki Formation, geological units according to Yamamoto et al. (2005). (E) Bathymetric map of the Nankai Trough area with indicated sample locations at IODP drillsites. Black line marks the Kumano transect taken for the IODP drilling campaign in the Nankai Trough (see Figure 4. 1).

2 Regional geology and sample description

The Shimanto Belt is approximately parallel to the Nankai Trough (e.g., Taira et al., 1992; Moore et al. 2001; Kawabata et al. 2007) and was sampled along the coastline of eastern Shikoku Island (Figure 4. 2). The depositional ages of the sediments decreases from north to south (Taira et al. 1988). At Muroto Peninsula the Shimanto Belt is divided by the Aki Tectonic Line into a Cretaceous part to the north, and a Tertiary part to the south (e.g., Kumon 1983; Underwood et al. 1993c; DiTullio and Hada 1993). The Cretaceous part consists of the Taisho and the Shinjogawa Groups (Aitchison 1986). The present study only treats the Tertiary part. In the south of Muroto Peninsula it is subdivided into the Murotohanto Group of Eocene to Oligocene age in the north, and the Nabae Group of Oligocene to Miocene age in the south (Aitchison 1986; Underwood et al. 1992). Both groups are separated by the Shiina-Narashi out-of-sequence thrust fault (Figure 4. 2 and Figure 4. 3; Underwood et al. 1992). Based on vitrinite reflectance data, the paleotemperature of the Tertiary Shimanto belt is estimated to be between 140 and 315 °C (Underwood et al. 1992; Underwood et al. 1993b; 1993c).

The paleotemperatures increase from north to south in the Murotohanto and the Nabae Groups (Underwood et al. 1992). In the Murotohanto Group, paleotemperatures are higher (215°C – 290°C) than in the Nabae Group (135°C – 285°C, Underwood et al. 1992). This is consistent to a post-metamorphic vertical offset of ~1200 m (Underwood et al. 1992) across the Shiina-Narashi fault. Maximum pressures attained were not higher than 2.5 kbar (Underwood et al. 1992) representing burial depths of up to 9000 m (Kitamura et al. 2005). In the following, we describe the sampled formations in further detail. An overview of the Shimanto stratigraphy is given in Figure 4. 3 and in the literature (e.g., Taira et al. 1982; Aitchison 1986; Hibbard et al. 1993; Underwood et al. 1993c).

Within the Murotohanto Group, two stratigraphic formations were sampled, the Naharigawa Formation and the Muroto Formation (Figure 4. 2 and Figure 4. 3). The Naharigawa Formation is formed by sandstones and shales, interpreted as sand dominated turbidites (Taira et al. 1982). Two mudstone outcrops of the Naharigawa Formation were sampled, one approximately 750 m north of Cape

Tertiary	top unknown	Shijujiyama Fm (3)	late Oligocene to early Miocene (3)	sandstone, mudstone and conglomerate (3)
		<div style="display: flex; flex-direction: column; align-items: center;"> <div style="border: 1px solid black; padding: 2px;">Tsuru Ass (3)*</div> <div style="margin: 5px 0;">Sakamoto and Hioki melanges (3)</div> <div style="margin: 5px 0;">Maruyama intrusions (~15 Ma) (1; 3)</div> <div style="border: 1px solid black; padding: 2px;">Misaki Ass (3)</div> </div>	Oligocene to early Miocene (3)	sandstone rich (3) shales, mudstones, sandstones and conglomerates (3) sandstone rich (3)
	base unknown	Shiina-Narashi fault (1)		
	Murotohanto subbelt (Eocene to Oligocene) (1) Lower Shimanto Belt (2)	Muroto * FM (2)	Eocene to Oligocene (2)	mélange complex, basalt, chert, tuff, sandstones and shales (2)
Naharigawa * FM (2)		Eocene (2)	turbidite sandstones and shales (2)	
Ohyama-misaki FM (2)		Eocene (2)	conglomerates, sandstones and shale (2)	
Cretaceous	northern Muroto Peninsula not considered	Aki-Tectonic line (1)		<div style="border: 1px solid black; padding: 2px;"> (1) Underwood et al. (1993c) (2) Taira et al. (1982) (3) Hibbard et al. (1992) </div>

Figure 4. 3: Shimanto Belt stratigraphy on Muroto Peninsula (after Taira et al. 1982; Hibbard et al. 1992; Underwood et al. 1993c). Sampled formations are marked with an asterisk. FM = Formation, Ass = Assemblage

Hane (west coast, samples Sch2011/23 and Sch2011/24, Figure 4. 2) and one in Misaki (east coast, sample Sch2011/34, Figure 4. 2). At Cape Hane black mudstones outcropping between massive sandstone of several meters thickness were sampled (Sch2011/23 and Sch2011/24). The bedding of the mudstone dips 55° to the south (165/55). After sample preparation, some bedding parallel fissures were observed in both samples. At Misaki (Sch2011/34), no outcropping material could be sampled and loose mudstones had to be collected on the beach.

After sample preparation, some bedding normal and bedding parallel fissures were found in the black mudstone samples.

Shale dominated turbidites with small amounts of tuff (Aitchison 1986), interpreted as melange complex (Taira et al. 1982) forming the Muroto Formation. Olistostromal beds and extensive slumping structures were observed. Two mudstone outcrops (Hane and Cape Gyoto, Figure 4. 2) are located at the west coast of Muroto Peninsula. At Hane, an outcrop approximately 1000 m south of the mouth of Hane River was sampled (Sch2011/27 and Sch2011/29). A thick unit of black mudstone crops out at the coast. The weakly expressed and heavily faulted bedding dips steeply to the southeast (150/60) and was hardly recognizable because of an intensive cleavage formation. Two major cleavage planes directions were observed, dipping 55° to the southeast and 45° to the northwest (142/55 and 300/45). Two major fault directions were found, dipping 60° to the south and 65° to the northwest (180/60 and 315/65). Some bedding parallel fissures were observed after sample preparation. Mudstones at Cape Gyoto, outcropping directly southeast of the local fishing port, were also sampled (Sch2011/18). The bedding dips 60° to the southeast (155/60) and is slightly oblique to the cleavage (135/70). Furthermore, several joints (67/62; 238/44; 327/74) and fault sets (82/51; 330/68) crosscut the strata.

The Nabae Group further south is made up by six units (Figure 4. 3), from which we sampled the Tsuru assemblage at the southern tip of Muroto Peninsula. The Tsuru assemblage is formed by alternating sandstone-shale units (Hibbard et al. 1992; Underwood et al. 1993a) and olistostromal deposits (Aitchison 1986), and may be interpreted as a tectonic *mélange*. At Muroto Port (Sch2011/8 and Sch2011/12, Figure 4. 2) bedding in the mudstones is steep to east-southeast (110/75), and is crosscut by joints (345/57 and 232/50), faults (284/73 and 154/32) and steeply dipping cleavage (100/70 and 267/70). After sample preparation, we observed small-scale faults and veins in both samples.

The Boso accretionary prism, of Miocene age, is located in central Japan and crops out on the Boso and Miura Peninsulas (Figure 4. 2). Depositional ages range between 9.9 and 6.8 Ma (radiolarian biostratigraphy, Yamamoto and Kawakami 2005). The accretionary prism is formed by the Misaki Formation (Miura peninsula) and the Nishizaki Formation (Boso peninsula, Yamamoto 2006, Figure

4. 2). We focus in the following on the Nishizaki Formation, since all the samples were taken on Boso peninsula. The basal accretionary prism is formed by the Nishizaki Formation is unconformably overlain by trench slope cover sediments of the Kagamigaura Formation (Yamamoto et al., 2012) and by younger trench-fill sediments of the Chikura Group in the south of the Boso Peninsula (Kawakami and Shishikure 2006). The east-west trending structures on the Boso Peninsula consist of volcanoclastic rocks, scoriaceous and andesitic pebbles and beds of siltstone in the Kagamigaura Formation and siltstones, some scoriaceous sandstone and glassy tuff in the Nishizaki Formation (Yamamoto and Kawakami 2005). These shallow level accretionary prism samples (less than 1000 m burial; Yamamoto et al. 2005) show deformation structures caused by the process of sediment accretion (Yamamoto et al. 2005). Vitrinite reflectance analyses indicate paleotemperatures below 50°C (Yamamoto et al. 2005), indicating the upper structural level in the accretionary prism. High porosities between 30% and 50% are indicative for less than 1000 m burial depth (Yamamoto et al. 2005).

Four siltstone samples were taken from Boso Peninsula. Samples NZ-PS-1, NZ-PS-2 and NZ-PS-5 come from the upper part, and sample NZ-PS-4 comes from the lower part of the Nishizaki Formation (Figure 4. 2). All samples were drilled normal to the sedimentary bedding. In samples NZ-PS-1 and NZ-PS-2 bedding dips approximately 25° to the southwest. Sample NZ-PS-1 contains several healed fractures oriented approximately 45° with respect to the core axis. Some rust-colored spots were observed at the outside of the sample cylinders and relate to oxidized iron-bearing minerals, such as pyrite. A small-scale healed fault which offsets an older fault was found in sample NZ-PS-2. Rust-colored spots were also observed in this core. Sample NZ-PS-5 shows no fractures crosscutting the sample cylinder, but some angular clasts and some brighter patches, possibly indicative for slumping of the unlithified sediment were observed. Bedding dip in sample NZ-PS-5 is 45° to the northeast. In sample NZ-PS-4 from the lower part of the Nishizaki Formation, the bedding dip is approximately 45° to the northeast. A healed fracture at an angle of 25-30° to the core axis was found. Some darker gray oval-shaped patches of approximately 0.5 cm by 1 cm, possibly of reworked sediments were observed at the sidewalls of the core sample. A white spot at the sidewall of the sample cylinder is possibly formed by calcite.

3 Methods

3.1 Analysis of sample compositions

The mineralogical compositions of the Shimanto Belt samples were determined by synchrotron x-ray analysis using small drill cores of 2 cm diameter. Synchrotron x-ray measurements were conducted at the beam line W2 of HASYLAB at the German Electron Synchrotron source (DESY), Hamburg. High-energy short wavelength synchrotron radiation allows penetration of samples of several centimeters thickness. In this way intact samples can be measured without preparation. For further details on the measurement configuration, see Schumann et al. (subm). Additionally, an X'Pert Pro x-ray diffractometer at the department of mineralogy at the Martin-Luther-University Halle-Wittenberg, Germany, was used to analyze the composition of a sample from the Boso accretionary prism (NZ-PS-2). For this analysis, a powdered sample was measured from 5° to 70° 2-theta in steps of 0.016° 2-theta using Cu-K α radiation.

3.2 Sample preparation

At Muroto Peninsula, samples were collected from the outcrops (Figure 4. 2 and Table 4. 1). Because the claystones show a strong foliation, the samples required stabilization prior to coring. To achieve this, samples were embedded in high-viscosity epoxy resin (Epox4305 and resin hardener "Härter1203-F"). After hardening of the epoxy resin, cores of 70 mm diameter were. Cores were drilled perpendicular to bedding planes. To achieve parallel end faces, drill cores were cut and ground. Cutting the end faces also removed the epoxy resin. Thin caps of special gypsum (dental gypsum named "Japan Stone") were added to the end faces of some samples to achieve ideal core lengths. The limited availability of sample material precluded multiple tests. Prior to testing, cores were placed into water for several hours to achieve ground moisture.

3.3 Experimental setup

Specimens were tested using a triaxial apparatus at the geotechnical laboratory of the Institute of Geosciences at the Martin-Luther-University Halle-Wittenberg (Germany). A 70 MPa pressure vessel capable to control the pore pressure and a hydraulic 5 MN pressure device was used for triaxial testing. Samples were jacketed in a 3 mm fibre-enhanced rubber tube to prevent contact with the confining medium (oil). Deformation experiments were carried out at confining pressures (σ_3) ranging between 25 and 65 MPa and pore pressure conditions ranging between 25% and 90% of σ_3 at room temperature. Samples were axially loaded with displacement rates of 5.7×10^{-6} /s (length normalized strain rate) until maximum differential stress of the pre-failure phase was reached. Deformation was automatically stopped when the E-modulus was constant or decreased (the E-Modulus was continuously calculated by the steering computer). At this point, axial displacement was stopped and the pressure conditions were held constant for ~15 minutes. After the holding phase, axial load slowly was released and the confining pressure was adjusted for the next deformation phase. This procedure was repeated up to five times for each sample. A detailed overview of the experimental conditions during the different experiments is given in Table 4. 2.

Three different types of triaxial tests were performed: (1) pore pressure stepping tests at variable pore pressure conditions, (2) confining pressure stepping tests at up to five different confining pressures and (3) a cyclic test (19 cycles) at constant confining pressure and constant pore pressure. In the pore pressure stepping tests the confining pressure (σ_3) was held constant at 55 MPa and 65 MPa, respectively. The pore pressure was decreased in three steps from 80% to 50% and 25% of the confining pressure or from 90% to 60% and 30% of the confining pressure, respectively. In the confining pressure stepping tests, the confining pressure was increased in 10 MPa steps up to five times from 25 MPa to 65 MPa, while the pore pressure was generally 80% of the confining pressure. In the cyclic test, confining pressure and pore pressure were kept constant ($\sigma_3 = 55$ MPa, pore pressure = 80% of σ_3). In this test, the sample was cyclically loaded to a differential stress of 70 MPa. After the holding time, the axial load was decreased.

In the next cycle, the sample was again loaded to a differential stress of 70 MPa. This procedure was repeated 19 times.

Table 4. 1: Overview of the experimental samples

Location	sample	Latitude	Longitude	Pressure [kbar]	Burial depth [m]	Temperature [°C]
Cape Hane	Sch2011/23	33°22'38.1792'' N	134°2'2.3136''E	2.5 (a)	9000 (b)	215-230 (a)
	Sch2011/24					
Hane	Sch2011/27	33°21'38.8296'' N	134°3'47.5236'' E	2.5 (a)	9000 (b)	270-290 (a)
	Sch2011/29					
Cape Gyoto	Sch2011/18	33°17'42.2124'' N	134°7'1.5708''E	2.5 (a)	9000 (b)	275-285 (a)
Muroto Port	Sch2011/8	33°16'31.3104'' N	134°9'22.3164'' E	2.5 (a)	7800 (b)	190-225 (a)
	Sch2011/12					
Misaki	Sch2011/34	33°26'58.5528'' N	134°14'26.6712'' E		<1000	<50 (c)
Sunosaki	NZ-PS-1	34°58'20.1864'' N	139°45'12.9744'' E		<1000	<50 (c)
	NZ-PS-2					
	NZ-PS-5	34°57'57.2724'' N	139°45'13.284'' E		<1000	<50 (c)
Nishikawana	NZ-PS-4	34°57'30.3012'' N	139°45'50.67''E		<1000	<50 (c)

Sample locations and pressure and temperature conditions during burial according to (a) Underwood et al. (1993c), (b) Lewis et al. (2000) and (c) Yamamoto et al. (2005).

Table 4. 2: Experimental conditions

sample	experimental type	confining pressure [MPa]	pore pressure [% confining pressure]	pore pressure [MPa]	strain [%]	peak stress [MPa]
Sch2011/23	CPST	25 - 35 - 45 - 55 - 65	80	20 - 28 - 36 - 44 - 52	1 - 1.25 - 1.49 - 1.8 - 2.1	94.6 - 110 - 120 - 132 - 136.5
Sch2011/24	PPST	55	80 - 50 - 25	44.0 - 27.5 - 14.0	1.8 - 2.4 - 3.4	126.4 - 157.7 - 184.3
Sch2011/34	PPST	65	90 - 60 - 30	58.0 - 39.0 - 19.5	0.48 - 1.4 - 3.8	105 - 139.5 - 186.4
Sch2011/27-2	PPST	55	80 - 50 - 25	44.0 - 27.5 - 14.0	1.4 - 2 - 2.7	173 - 156 - 173.7
Sch2011/27-1	CPST	25 - 35 - 45 - 55 - 65	80	20 - 28 - 36 - 44 - 52	0.2 - 0.4 - 0.78 - 1.2 - 1.6	102 - 115 - 131 - 142 - 155.8
Sch2011/29 -2	CPST	25 - 35 - 45 - 55	80	20 - 28 - 36 - 44	0.8 - 1 - 1.1 - 1.2	120 - 104.3 - 123.6 - 141
Sch2011/18 -2	PPST	55	90 - 60 - 30	49.5 - 33.0 - 16.5	0.4 - 3.4 - 4.7	240 - 248.8 - 246.7
Sch2011/8	CPST	25 - 35 - 45 - 55 - 65	80	20 - 28 - 36 - 44 - 52	0.4 - 0.6 - 1.2 - 1.7 - 2	172.7 - 157.8 - 141 - 150.6 - 155.6
Sch2011/12	PPST	55	90 - 60 - 30	49.5 - 33.0 - 16.5	0.4 - 2.3 - 4.7	96 - 157 - 223.7
NZ PS-1/1	CPST	25 - 35 - 45 - 55 - 65	80	20 - 28 - 36 - 44 - 52	0.78 - 1 - 1.3 - 1.5 - 1.7	40.6 - 53.3 - 64.3 - 74.8 - 86
NZ PS-1/2	PPST	55	90 - 60 - 30	49.5 - 33.0 - 16.5	0.8 - 1.9 - 2.7	76.1 - 74.3 - 73.3
NZ PS-2	CPST	25 - 35 - 45 - 55 - 65	80	20 - 28 - 36 - 44 - 52	0.9 - 1.2 - 1.4 - 1.8 - 2	37.9 - 48.1 - 58.3 - 70.7 - 81.1
NZ PS-4/1	CPST	25 - 35	80	20 - 28	1 - 1.2	55.8 - 66.1
NZ PS-4/2	CPST	25 - 35	80	20 - 28	1.3 - 1.7	50.3 - 64.8
NZ PS-5	CPST	25 - 35 - 45 - 55 - 65	80	20 - 28 - 36 - 44 - 52	0.6 - 0.8 - 1.0 - 1.2 - 1.4	41 - 53.4 - 62.6 - 75 - 87.2
NZ PS-5-C	cyclic test	55	80	44	0.9 to 1.17	69 to 70.2

Experimental conditions of the triaxial tests presented in this study. In the confining pressure stepping tests (CPST), the confining pressure was increased in up to five steps, while in the pore pressure stepping tests (PPST), the pore pressure conditions were decreased in three steps. Confining and pore pressure conditions, achieved strains and peak stresses are given for each step.

Confining pressure stepping tests allow determination of the peak strength at different confining pressure conditions of a sample. To enable multiple tests, deformation had to be stopped at the yield point (peak stress) in the pre-failure phase. This method was conceived by Kovári and Tisa (1975), to avoid damage of the specimen and permit multiple tests. This approach allows construction of Mohr Circles from the data to determine cohesion and angles of internal friction. Also the influence of the variable pore pressure conditions can be studied in these tests. The cyclic test allows simulation of the effect of cyclic loading during earthquake cycles.

The study of samples from the Nankai accretionary wedge used for comparison in this paper (Stipp et al. in press) used up to 100 mm long whole round core samples obtained from IODP Expeditions 315, 316 and 333 for triaxial testing. Deformation experiments were conducted using a Moser Systemtechnik deformation apparatus with maximal axial load of 10 kN and 1000 kPa confining pressure. Deformation experiments were carried out under consolidated and undrained conditions at room temperature. Also in this study, three different types of geotechnical tests were conducted: (1) single step compression experiments, (2) pressure stepping experiments and (3) displacement rate stepping experiments. Especially the confining pressure stepping tests are similar to the tests presented in this study. For further details on the experimental setup and sample characterization, see Stipp et al. (in press). Here we focus on the results of the pressure stepping tests, enabling direct comparison.

4. Results

4.1 Sample composition

Compositions of the samples from the Shimanto Belt were determined by synchrotron x-ray based Rietveld refinement (Rietveld 1969). Although samples of visually similar lithology were collected at the outcrops, some variability in sample compositions was found after evaluating the x-ray data. The samples contain 30.5% to 51.5% quartz, and 14.8% to 23.9% feldspar. Only sample

Sch2011/18 shows a higher feldspar content of 32.3%. Lowest muscovite contents were found in the samples Sch2011/27 and Sch2011/29 with 8.5% and 6.5%, respectively. The other samples show muscovite contents of 10.7% to 16.4%. The total clay content ranges between 14.9% and 41.1%. A detailed overview of the compositions is given in Table 4.3.

The composition of the siltstones in the Boso samples was determined by Kameda et al. (2010). Samples NZ-PS-1 and NZ-PS-2 are taken from a place close to Sample SU23. Sample NZ-PS-4 is identical to NK26, and sample NZ-PS-5 is identical to NK24 of Kameda et al. (2010). According to Kameda et al. (2010), the sediments consist of quartz (30%), illite (10-20%), plagioclase (10%), kaolinite + chlorite (5%) and calcite (0-10%). The composition of sample NZ-PS-2 was determined in this study by quantitative x-ray powder diffraction (XRD) analysis. It contains 20.1% quartz, 32.9% plagioclase, 3.9% calcite and 22.9% clay, 4.7% muscovite and 10.5% chlorite. An overview of the Boso sample compositions is given in Table 4. 4. Beside of the additional phases found in our analysis, the composition is largely in accordance to the compositions observed by Kameda et al. (2010).

Table 4. 3: Mineralogical composition of samples from the Shimanto Belt

	Sch2011/23	Sch2011/24	Sch2011/27	Sch2011/29	Sch2011/18	Sch2011/34	Sch2011/8	Sch2011/12
quartz	41.80	30.50	51.60	42.10	35.00	38.80	46.00	36.50
feldspar	19.90	17.50	17.80	19.80	32.30	21.90	23.90	14.80
muscovite	14.70	10.70	8.58	6.20	13.20	16.40	14.70	12.70
smectite	1.20	14.70	3.00	0.00	2.30	1.20	0.30	9.70
illite	3.20	11.00	6.70	15.10	3.70	9.70	7.70	11.90
kaolinite	18.80	15.40	12.00	16.40	13.20	11.80	6.90	14.10
total clay	23.20	41.10	21.80	31.50	19.20	22.70	14.90	35.70
qz + fsp	61.7	48	69.4	61.99	67.3	60.7	70.8	51.3
clay + mica	37.9	51.8	30.3	37.7	32.4	39.1	29.6	48.4

Mineralogical composition were determined by synchrotron x-ray diffraction-based Rietveld refinement (Rietveld 1969). Contents are given in percent; qz = quartz, fsp = feldspar, clay = total clay, mica = muscovite.

Table 4. 4: Mineralogical composition of the samples from the Boso accretionary prism

this study	NZ-PS-1	NZ-PS-2	NZ-PS-4	NZ-PS-5		NZ-PS-2
Kameda et al. (2010)	SU-23	SU-23	NK-26	NK-24		
quartz	27	27	28	31	quartz	20.10
plagioclase	15	15	10	9	feldspar	32.90
calcite	3	3	6	0	muscovite	4.70
illite-smectite	38	38	43	40	calcite	3.90
illite	11	11	9	14	smectite	3.36
kaolinite	5	5	4	6	illite	1.94
					kaolinite	22.30
					chlorite	10.54
					total clay	38.14
qz+fsp	42	42	38	40	qz+fsp	53.00
total clay	54	54	56	60	clay+mica	42.84

Mineralogical composition of the samples from the Boso accretionary prism. Contents are given in percent. Sample compositions given in bold were taken from Kameda et al. (2010), while the composition of NZ-PS-2 was determined by x-ray powder diffraction (XRD) in this study; qz = quartz, fsp = feldspar, clay = total clay, mica = muscovite.

4.2 Stress-strain observations

As described in the methods section, three different geotechnical test procedures were applied. A detailed overview of the experimental conditions is given in Table 4. 2. In the following we focus on the deformation phases of the experiments. During the triaxial experiments maximal bulk axial strain of 4.7% was achieved (sample Sch2011/12). The peak stresses reached in the tests range between 94.6 MPa and 246.7 MPa for the Shimanto Belt samples and between 37.9 MPa and 87.2 MPa for the samples from the Boso accretionary prism (Table 4. 2). Additional plots of the samples are given in Appendix A 3.

4.2.1 Shimanto samples

During the confining pressure stepping tests of the samples Sch2011/8, Sch2011/23, Sch2011/27-1 and Sch2011/29, the confining pressure (σ_3) was

increased from 25 MPa in steps of 10 MPa to a maximum confining pressure of 65 MPa or 55 MPa for experiment Sch2011/29 (Table 4. 2). Pore pressure was set to be 80% of σ_3 . Sample Sch2011/23 is characterized by increasing stress levels during the five deformation phases. The maximal differential stress in this sample was 136.5 MPa at approximately 2.1% axial strain when the peak differential stress was reached (Figure 4. 4). When deforming sample Sch2011/27-1, peak stress of 155.8 MPa was reached after five deformation steps at 1.6% axial strain, (Figure 4. 4) without signs of a reduced differential stress increase. Samples Sch2011/8 and Sch2011/29 are characterized by stress drops on the order of 20 MPa after the first deformation phase. This stress drop is characteristic of a failure of the core sample after less than 1% axial strain, e.g., in sample Sch2011/29.

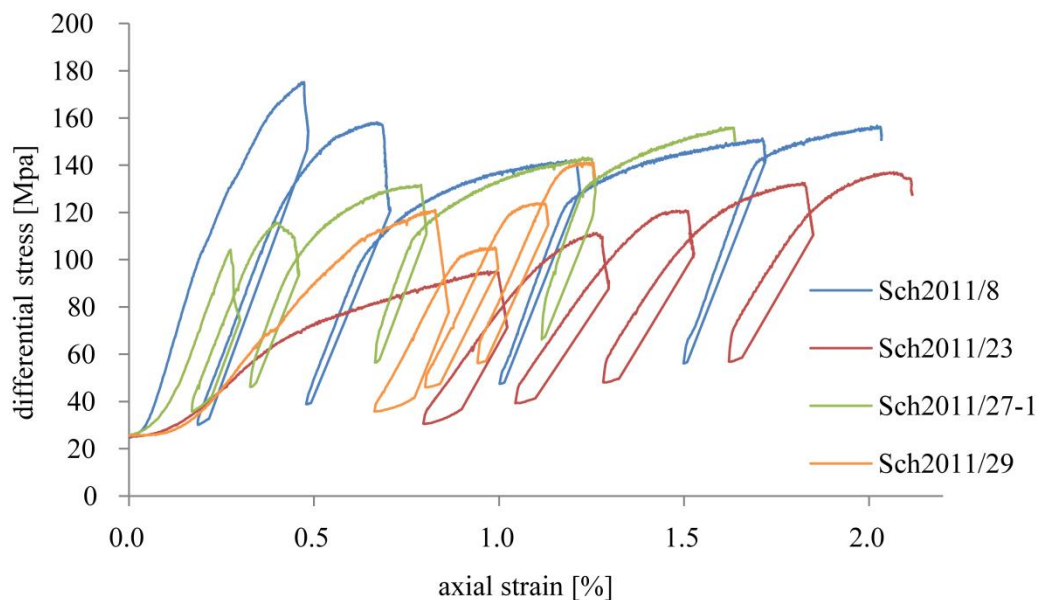


Figure 4. 4: Stress-strain plots of the confining pressure stepping tests of the Shimanto Belt samples. Samples Sch2011/8 and Sch2011/29 show a stress-strain record indicative of a failure in the first deformation stage (pressure step 1). Confining pressure was increased in steps of 10 MPa from 25 MPa to 65 MPa in maximum.

Sample Sch2011/8 did not reach the stress level of the first deformation phase in all later pressure steps (increasing confining pressure), while sample Sch2011/29 reached the previous stress level of the first deformation phase again in the third deformation phase, and exceeded this level in the last deformation step (Figure 4. 4). After the deformation experiments, conjugate sets of shear fractures (conjugate fractures) were observed in sample Sch2011/8, making angles of approximately 30° with the core axis (Figure 4. 5A). In Sample Sch2011/29 the

fracture pattern is much more complex. There are two fractures approximately at 70° to the core. Since the failure planes were rust-colored, these two fractures seem to have formed along preexisting structures, such as schistosity planes. It is likely that these fractures oriented at high angles to the core axis were formed as a stress rebound effect during unloading of the specimens or due to the pore pressure which was, due to low permeability, higher than the confining pressure during the reduction of the confining pressure. Conjugate shear fractures at approximately 40° to the core axis and extension fractures approximately parallel to the core axis were also observed (Figure 4. 5B).

In the pore pressure stepping tests at $\sigma_3 = 55$ MPa (Sch2011/12, Sch2011/18, Sch2011/24 and Sch2011/27-2) the pore pressure was decreased from 80% to 50% and finally 25% of σ_3 and at $\sigma_3 = 65$ MPa (Sch2011/34) the pore pressure was decreased from 90% to 60% and finally 30% of σ_3 (Sch2011/12, Sch2011/18 and Sch2011/34), respectively. Peak differential stresses were increasing during the deformation phases (Sch2011/12, Sch2011/24 and Sch2011/34). In samples Sch2011/18 and Sch2011/27-2, a rather constant maximum differential stress was observed at the end of each deformation phase (Figure 4. 6).

In experiment Sch2011/12, the maximum differential stress increased in the three deformation steps, and reached 223.7 MPa at 4.7% axial strain. Similar behavior was observed in experiment Sch2011/24, in which the peak differential stress also increased in each deformation step to a maximum of 184 MPa at 3.4% axial strain. In experiment Sch2011/34 the maximum differential stress in the third deformation step was 186 MPa at 3.8% axial strain (see Figure 4. 6).

In the first deformation step of sample Sch2011/18 the differential stress increased strongly and immediately dropped after the maximum value of 240.7 MPa at 0.4% axial strain. In the second and third deformation phases, differential stress quickly increased to ~ 180 MPa. After yielding at ~ 180 MPa, the stress increased linearly to 250 MPa. At this level, the deformation was stopped. Similar behavior was observed in experiment Sch2011/27-2, with differential stress increasing approximately linearly to 172 MPa in the first deformation step. In the second and third deformation steps, differential stress quickly increased to approximately 130 MPa. After yielding the sample hardened steadily to 156 MPa

and 173 MPa, respectively. In both samples (Sch2011/18 and Sch2011/27-2) there are prominent shear fractures at angles between 30° and 40° to the core axis (Figure 4. 5C and Figure 4. 5D). These through-going faults are accompanied by several schistosity-parallel failures (approximately 90° to the core axis), probably caused during unloading of the samples at the end of the deformation or by pore overpressure in the stages of decreasing confining pressure.

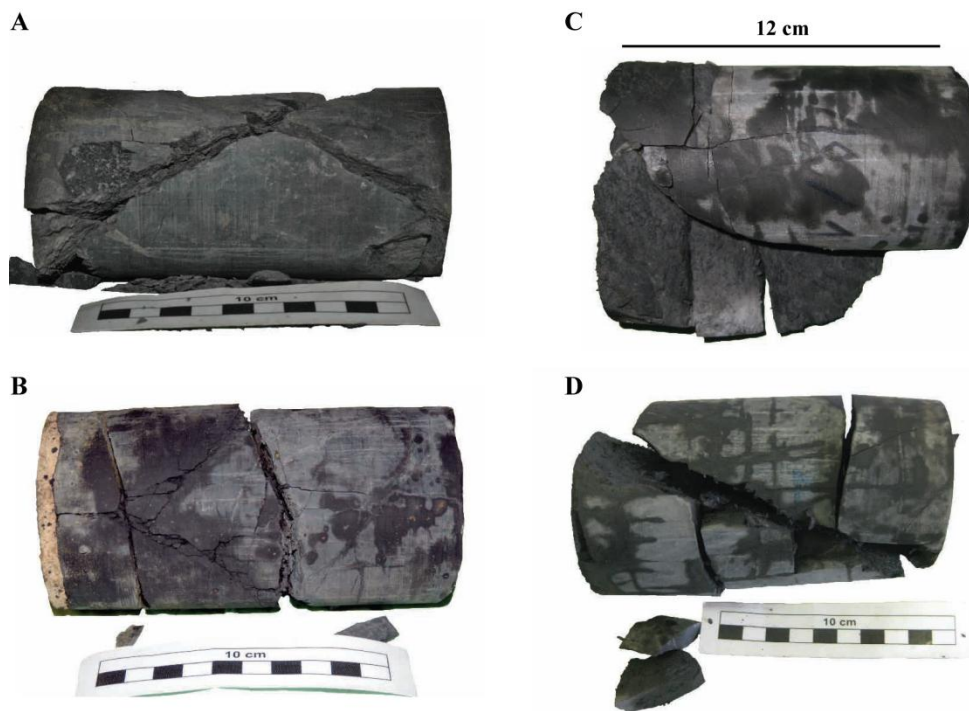


Figure 4. 5: Examples of drill cores after triaxial testing. (A) Sample Sch2011/8 shows a set of conjugate shear fractures. (B) Sample Sch2011/29 shows a set of conjugate shear fractures and extensional fractures parallel to the core axis. Fractures almost normal to the core axis probably formed during unloading of the sample. The gypsum cap to the left was added before the experiment to improve sample geometry. (C) Sample Sch2011/18 showing one extensional fracture parallel to the core axis, and the oblique view on one shear fracture. (D) Shear fracture crosscutting core sample Sch2011/27-2 and two fractures parallel to the bedding plane and normal to the core axis.

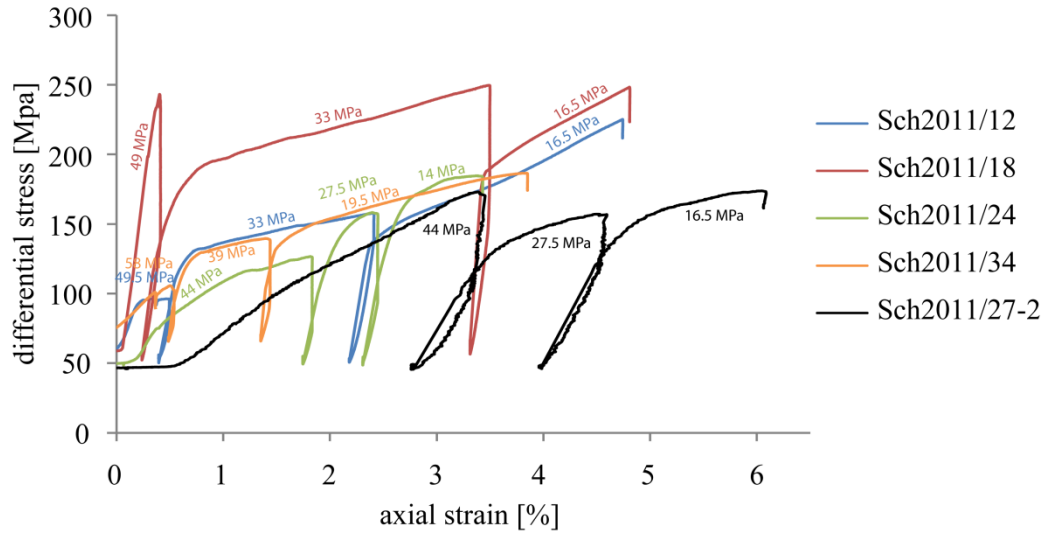


Figure 4. 6: Stress-strain plots of the pore pressure stepping tests conducted on the Shimanto Belt samples. The pore pressure was reduced between the deformation steps. Pore pressure conditions are indicated for each deformation step. Samples Sch2011/18 and Sch2011/27-2 show failure in the first deformation step and low peak stress in the subsequent steps.

4.2.2 Boso samples

Five confining pressure stepping tests were carried out on Boso samples. In the experiments NZ-PS-1/1, NZ-PS-2 and NZ-PS-5 σ_3 was increased from 25 MPa to 65 MPa in five steps of 10 MPa (Figure 4. 7). In experiments NZ-PS-4/1 and NZ-PS-4/2 only two steps (25 MPa and 35 MPa) were conducted (Figure 4. 7, Table 4. 2). One pore pressure stepping test was carried out on sample NZ-PS-1/2 at 55 MPa confining pressure and decreasing pore pressure conditions (90%, 60% and 30% of σ_3 ; Figure 4. 8). A cyclic test (NZ-PS-5-c) at constant confining pressure (55 MPa) and constant pore pressure (80% of σ_3) was also conducted. In this test, the specimen was axially loaded 19 times to 70 MPa (Figure 4. 9).

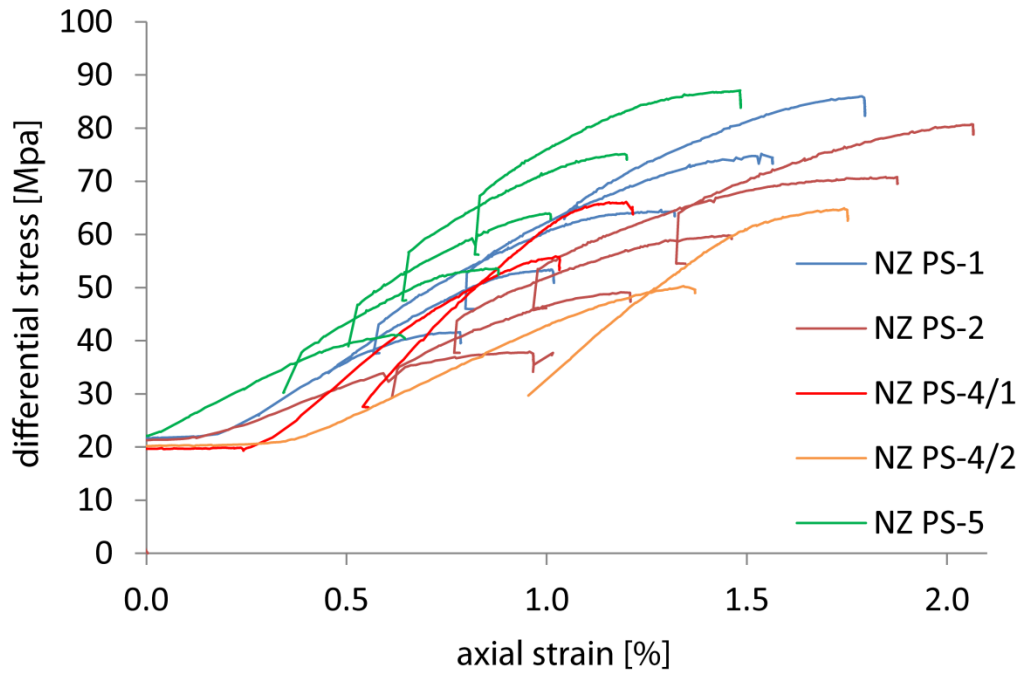


Figure 4. 7: Stress-strain plots of the confining pressure stepping tests of the Boso samples. The phases of pressure release during triaxial deformation are not shown for clarity. Confining pressure was increased in steps of 10 MPa from 25 MPa to 65 MPa in maximum.

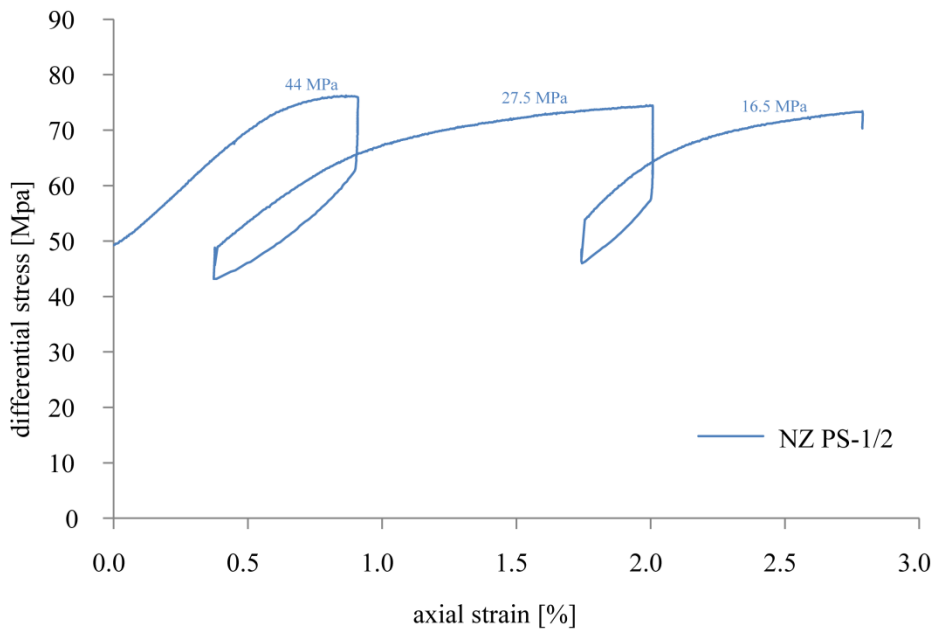


Figure 4. 8: Stress-strain plot of the pore pressure stepping test of sample NZ-PS-1/2 from Boso. The pore pressure was decreased between the deformation steps, yet there was no increase in strength. Pore pressure conditions are indicated for each deformation step.

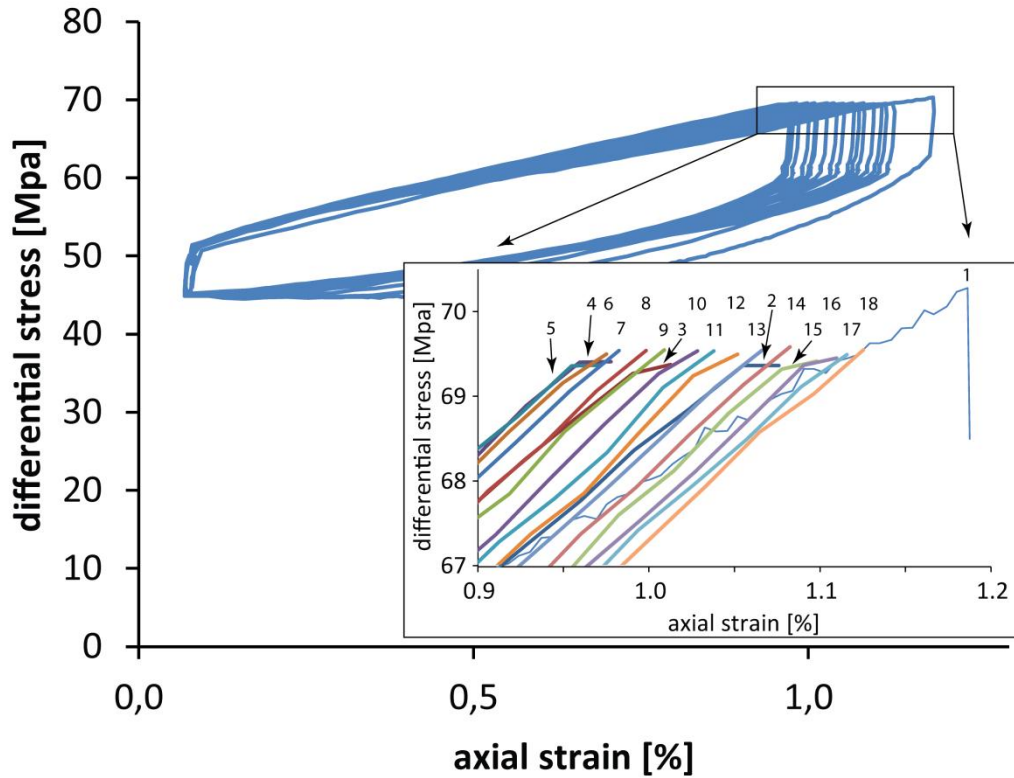


Figure 4. 9: Cyclic deformation experiment of sample NZ-PS-5-c. The sample was axially loaded 19 times to a differential stress of ~ 70 MPa at 55 MPa confining pressure and 44 MPa pore pressure. The inset shows the records of strain accumulation during the individual loading cycles labeled 1-19.

Five complete cycles of deformation were conducted in experiments NZ-PS-1, NZ-PS-2 and NZ-PS-5. These three samples behaved rather similar during deformation and reached similar maximum stress levels in the last deformation step of 85 MPa (NZ-PS-1), 80 MPa (NZ-PS-2) and 87 MPa (NZ-PS-5, Figure 4. 7). Since relatively large amounts of displacement were attained in experiments NZ-PS-4/1 and NZ-PS-4/2, the triaxial tests had to be stopped after the second deformation phase. At the end of the second deformation phase, the maximum stress was 65.9 MPa and 64.8 MPa, respectively (Figure 4. 7). In the constant confining pressure test of sample NZ-PS-1/2 the achieved peak stress decreased slightly from 76 MPa in the first deformation phase to 74 MPa in the second and 73 MPa in the last deformation phase with decreasing pore pressure condition (Figure 4. 8). The most likely explanation for this behavior is that due to the low permeability of the tested material, pore pressures in the sample could not equilibrate in deformation phases 2 and 3, and lead to a rise in effective stress within the sample. In the stress cycling test of experiment NZ-PS-5-c, peak stress

during the first of the 19 cycles was just over 70 MPa at almost 1.2% axial strain. In the subsequent cycles (2-5) peak stress decreased to about 69.4 MPa, and attained after somewhat smaller axial strain 65 MPa in the fifth cycle. From the sixth cycle onward axial strains increased again step by step to the end of the last cycle to 70 MPa (Figure 4. 9).

4.2.3 Nankai

In the present study, we make use of a data set from nine triaxial tests of core samples from the Nankai accretionary prism for comparison. The data are described in detail and interpreted by Stipp et al. (in press) and are discussed below.

4.3 Effective shear parameters

The effective shear parameters cohesion (C) and the angle of internal friction (ϕ) were first determined from Mohr-Coulomb plots. For the Shimanto Belt samples Sch2011/12, Sch2011/23, Sch2011/24, Sch2011/27-1 and Sch2011/34 and for the Boso samples NZ-PS-1, NZ-PS-2 and NZ-PS-5 maximum σ_1 and σ_3 could be determined for at least three deformation stages and the Mohr-Coulomb criteria could be plotted (Figure 4. 10 and Table 4. 5).

Table 4. 5: Effective shear parameters determined from the triaxial tests

method	Mohr Coulomb		stress path		fracture angle	
sample	ϕ [°]	C [MPa]	ϕ' [°]	C' [MPa]	ϕ_f [°]	C _f [MPa]
Sch2011/23	46.8	14	45.15	15.4	47.6	12.8
Sch2011/24	30.96	30	33.44	30.04	21.8	42.3
Sch2011/34	29.68	27	30.83	25.18		
Sch2011/27-1	49.47	14	49.45	13.2	43.6	19.06
Sch2011/27-2					23.2	52.3
Sch2011/29-2					9	58.48
Sch2011/8					31.68	45.68
Sch2011/12	41.5	17	41.42	16.55	40	18.6

NZ-PS-1	46.66	3	46.68	2.89
NZ-PS-2	47.07	2	46.28	2.31
NZ-PS-4/1			45.64	6.14
NZ-PS-4/2			50.9	2.65
NZ-PS-5	47.07	3	47.14	2.62
K004	27.1	0.0257		
K005	24.6	0.0249		
K011	35.8	0.0121		
K013	32	0.0293		
K014	28.7	0.0341		
K015	25.3	0.0497		
K016	40.4	0.0042		
K020	26.3	0.041		
K022	21.5	0.0354		

Effective shear parameters determined from the triaxial tests using Mohr-Coulomb criteria, stress path diagrams or fracture angle measurements. The Shimanto Belt samples (coded Sch 2011) and the Boso accretionary prism samples (coded NZ-PS) were tested in this study, while the data from the Nankai samples (coded K) are taken from Stipp et al. (in press).

Samples Sch2011/8, Sch2011/18-2, Sch2011/27-2, Sch2011/29-2 showed failure after the first deformation stage, and therefore no corresponding computation of fracture criteria was possible. Samples NZ-PS-4/1 and NZ-PS-4/2 were tested in only two pressure steps and Mohr circle constructions were not carried out. The values for cohesion of the Shimanto samples range between 14 MPa and 30 MPa, and for the samples from Boso the range is between 2 MPa and 3 MPa. Angles of internal friction range between 29° and 49°, and between 41° and 47° for Shimanto and Boso, respectively.

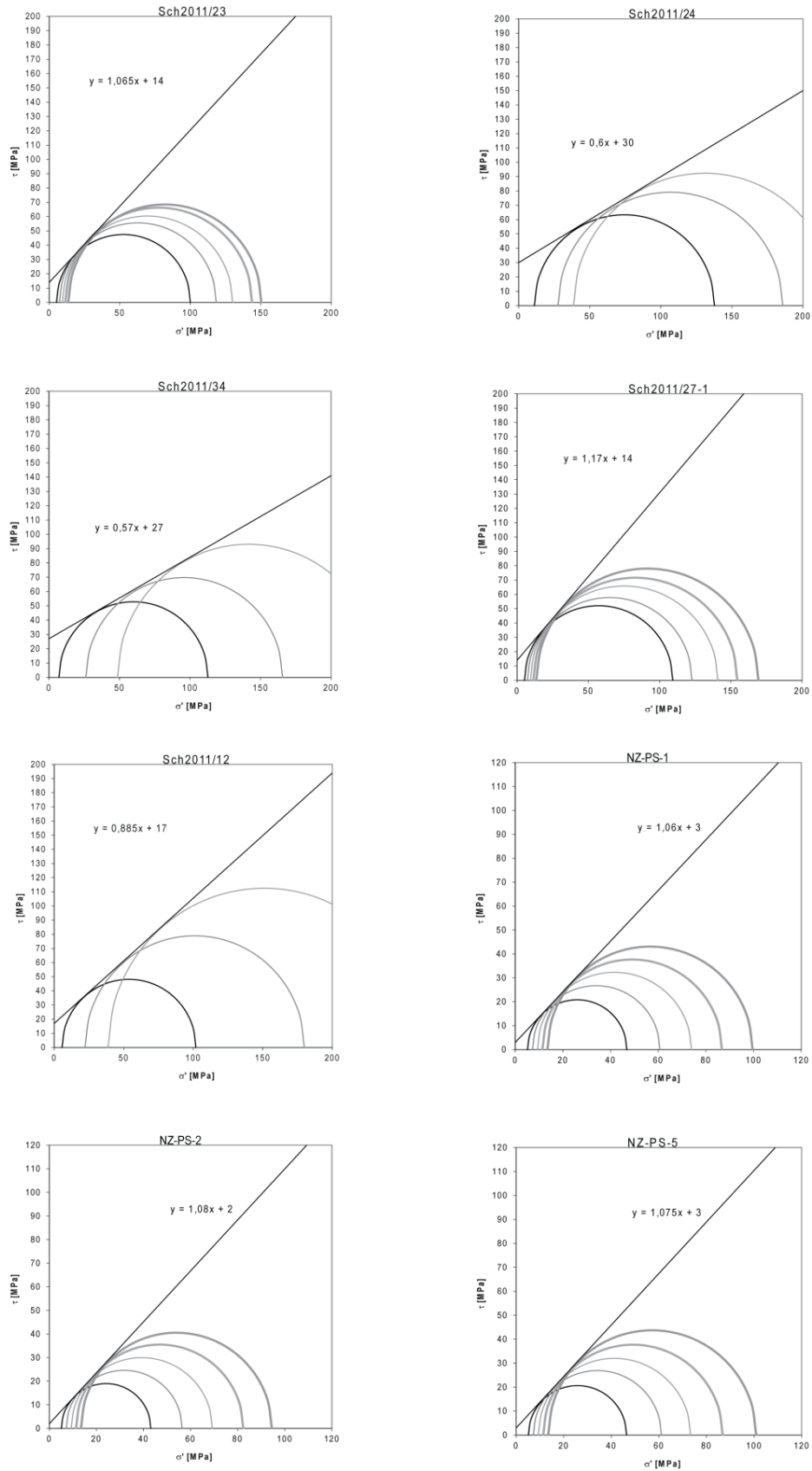


Figure 4. 10: Mohr Circle constructions to determine angles of internal friction and cohesion for eight of the tested samples.

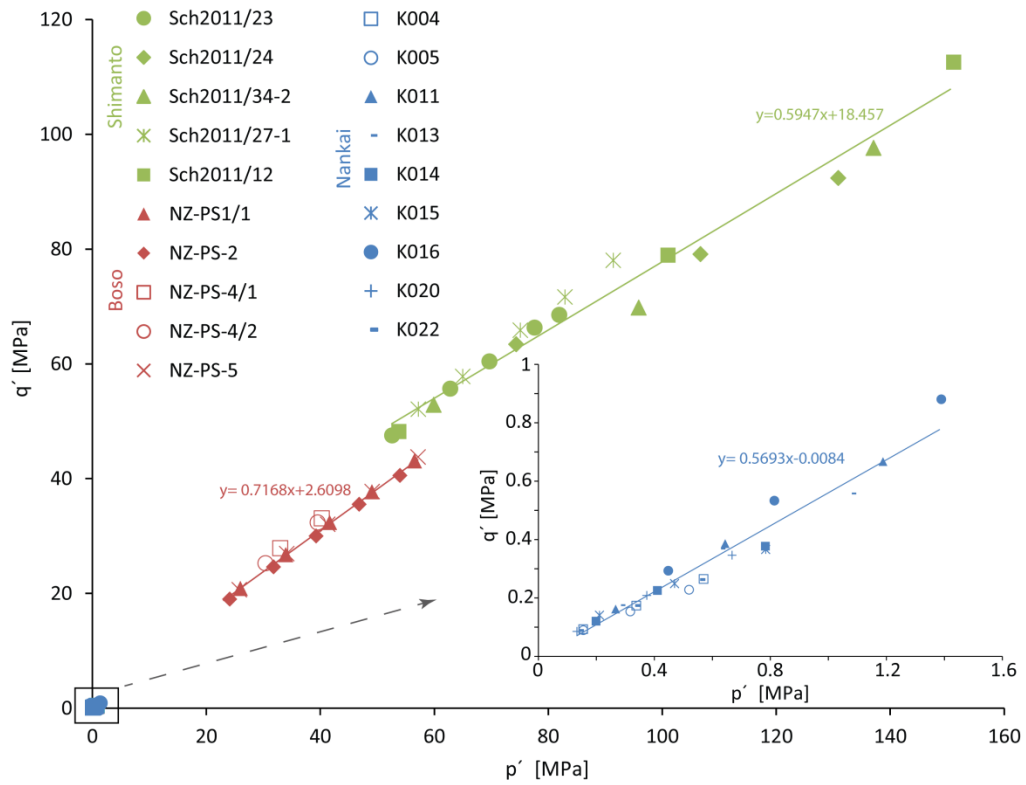


Figure 4. 11: p' - q' -plot determined from the maximum σ_1 and σ_3 conditions achieved during triaxial testing in each deformation stage. Note that the Mohr-Coulomb slopes of each sample group are very similar. However, there are important differences in the cohesion, mainly reflecting different degrees of diagenesis or very low-grade metamorphism in the different settings.

Second, the effective shear parameters were also determined from stress path constructions. Pore water pressure was constant during the deformation experiments, thus we only plotted the maximum σ_1 and σ_3 in a p' - q' -diagram (e.g., Burland 1990, Figure 4. 11), where p' and q' are

$$p' = (\sigma_1' + \sigma_3') / 2 \quad (1)$$

and

$$q' = (\sigma_1' - \sigma_3') / 2 \quad (2)$$

According to Lang et al. (2002) and the German Industry Standard (DIN 18137, part 2), the shear parameters C' and φ' can be calculated by plotting a regression line according to the following equations

$$\varphi' = \arcsin(\tan \beta') \quad (3)$$

and

$$C' = b' / \cos \varphi' \quad (4)$$

where β' is the angle of the regression line and b' is the intercept of the regression line with the y-axis (Table 4. 5). For the Shimanto Belt samples, cohesion values range between 13 MPa and 30 MPa, and between 2.3 MPa and 6.14 MPa for Boso. The angles of internal friction range between 33.4° and 49.5° and between 45° and 50° for Shimanto and Boso, respectively (Table 4. 5).

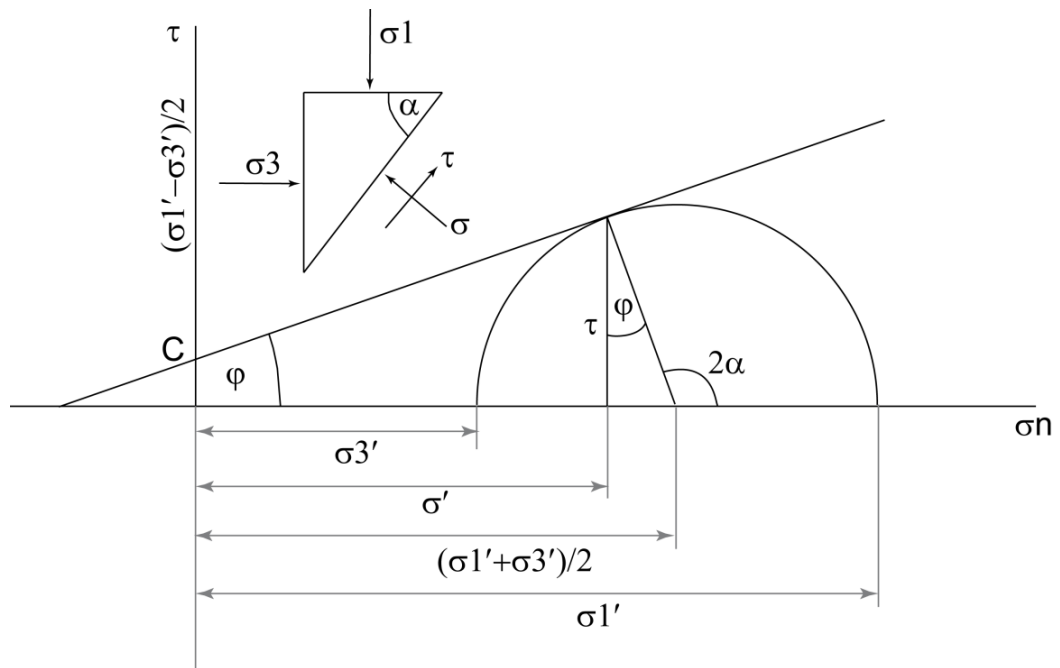


Figure 4. 12: Geometrical principle for the determination of effective shear parameters from fracture angles. Modified after Richter (1989). σ_1' = maximum effective stress, σ_3' = minimum effective stress, σ' = normal stress, φ = friction angle, C = cohesion, τ = shear stress, α = fracture angle

Additionally the fracture angle α , which is the angle between σ_1 and the fracture (Figure 4. 5 and Figure 4. 12) can be used to determine effective shear parameters (e.g., Richter 1989; Twiss and Moores 1992). The double fracture angle is used to define the critical state of stress as shown in the Mohr circle

construction in Figure 4. 12. The Coulomb criterion for fracture is defined by a tangent plotted from the intersection of the fracture angle plane and the Mohr circle. From this, cohesion (C_f) and the angle of internal friction (ϕ_f) can be calculated. Since the samples from the Boso accretionary prism have not been fractured in the experiments, the effective shear parameters could only be determined for those Shimanto Belt samples that showed clear evidence for shear failure. The cohesion values determined using this method are slightly higher (between 18.6 MPa and 42.3 MPa) than the values determined by Mohr Circle constructions or stress paths diagrams, except for sample Sch2011/23 which has a lower cohesion of 12.8 MPa. The angles of internal friction are lower (between 21.8° and 43.6°) except for sample Sch2011/23, which has a higher angle of internal friction compared to the other methods (Table 4. 5). Sample Sch2011/29-2 has a very low angle of internal friction of 9°. Especially for those samples that failed in the first deformation phase (Samples Sch2011/8; Sch2011/18-2; Sch2011/27-2 and Sch2011/29-2), the method is helpful in constraining the effective shear parameters as they could not be determined by the other two methods for these samples.

5 Discussion

5.1 Effective shear parameters

The effective shear parameters were determined using three different methods. The Mohr Circle construction and stress path construction (p' - q' -diagram) use the same experimental values (Figure 4. 10 and Figure 4. 11, Table 4. 5). The Mohr construction is based on a tangent fitted to the Mohr Circles, while the p' - q' -diagram is based on a regression line fitted to the maximum σ_1 and σ_3 of the experimental steps. Conversion between the two methods is possible using equations 3 and 4 (Lang et al. 2002; German Industry Standard 18137, part 2). Differences in the effective shear parameters are small (Table 4. 5) and may mainly result from the different fit of the tangent to the Mohr Circles and the fit of the regression line to the stress maxima. Shear parameters determined from the

fracture angles differ to a slightly larger extent. Since we conducted up to five experimental steps using single samples, maximum shear stresses at the moment of failure cannot be exactly determined. Thus we used the recorded maxima of σ_1 and σ_3 to plot Mohr Circles and p' - q' plots. The fracture angle method significantly depends on the measurement error of the fracture angle which was difficult to determine especially in those samples which were shattered or where multiple fracture planes occurred. Fracture angles, in turn, may be influenced by fabric anisotropies, such as the preferred alignment of sheet silicates, and reactivation of preexisting fractures and joints. Therefore, determination of effective shear parameters from fracture angles has some uncertainty.

5.2 Comparison with studies of related rocks

The high internal friction angles derived for the Shimanto and Boso siltstone samples studied here show that the response to pre-failure loading is similar to that of hard rocks (see e.g., discussion in Savage et al. 1997) and describes a mechanical state preceding the development of coalescing microcracks to produce failure. Studies of Hajdarwish and Shakoor (2006) and Lempp et al. (2010) determined the effective shear parameters for claystone, mudstone, siltstone, shale and slate. Hajdarwish and Shakoor (2006) report cohesion values between 0.24 MPa and 7.84 MPa and angles of internal friction range between 10.9° and 35.8° . Sediments from shallow marine settings of depths between 1000 and 2100 m investigated by Lempp et al. (2010) show cohesion between 1 MPa and 6 MPa for mudstones, between 2 MPa and 7 MPa for shales, and between 10 MPa and 20 MPa for more lithified slates (Lempp et al. 2010). The angle of internal friction ranges between 15° and 25° for mudstone and shale, and between 20° and 30° for the slates (Lempp et al. 2010). The higher level for cohesion and angle of friction found in the Shimanto Belt siltstones (see compositions in Table 4. 3) indicate that the deep burial (between 7800 m and 9000 m) went along with strong diagenesis and very low grade metamorphism at zeolite to prehnite-pumpellyite facies (DiTullio and Byrne 1990; Banno and Nakajima 1991) resulting in the formation of tough, strongly anisotropic, low-porosity rocks. More siliceous sedimentary

rocks similar to the Boso samples were investigated by Roller et al. (2003) from the Tohoku forearc further north along the Japan margin. Samples are from ODP (Ocean Drilling Program) Sites 1150 and 1151, two drillholes in the forearc slope cover. Cohesion values from depths similar to the Boso setting (between 864 mbsf and 1101 mbsf) range between 0.16 MPa and 2.3 MPa. The cohesion of the Boso samples is in a similar range except for sample NZ-PS-4/1, which has a higher cohesion (6.14 MPa; Table 4. 5).

5.3 Variation of strength with burial depth

To examine the evolution of the shear parameters with burial depth the dataset of the Shimanto Belt samples (representing depths between 7800 m and 9000 m) and the Boso samples (representing depths of about 1000 m) were supplemented by data of Stipp et al. (in press) from the Nankai subduction zone (representing depths between 28 mbsf and 128 mbsf, Stipp et al., in press). Experimental results of Stipp et al. (in press) are added to Table 4. 5. The dataset from Nankai spans the complete depth range from the incoming sediments, which are tectonically unaffected near-mudline sediments (sampled during IODP Expedition 333 Sites C0011 and C0012, experimental subsamples K020 and K022, 28 mbsf and 33 mbsf, Stipp et al. in press), to shallow sediments of the Nankai accretionary prism (sampled during IODP Expeditions 315 and 316, experimental subsample K004 to K016, 48 mbsf to 128 mbsf, Stipp et al. in press). The samples from the Boso accretionary prism are taken as structural and geomechanical analogues for sediments representing approximately 1000 m burial depth which is relatively close to the Nankai samples. The Shimanto Belt samples with burial depths up to 9000 m are taken to petrographically and geomechanically represent the updip end of the seismogenic zone. All available data were plotted in a summary p' - q' diagram (Figure 4. 11). It is immediately obvious that the fits within the individual sample subsets (Nankai, Boso, Shimanto) are quite good with only small data scattering. There is very little variation of slopes describing the relation of effective mean stress (p') and shear stress (q') between the three data sets. However, at the transition between the Shimanto and the Boso subsets, the Shimanto subset shows an about 8 MPa higher value for q' than the Boso subset,

where the effective mean stress overlaps around 50-60 MPa. We interpret this as being caused by diagenetic changes, cementation and compaction that has affected the deeply buried Shimanto sample subset. The temperature and pressure conditions of the Shimanto samples indicate zeolite to prehnite-pumpellyite facies (e.g., Hashimoto et al. 1970; Toriumi and Teruya 1988; DiTullio and Byrne 1990; Banno and Nakajima 1991). When linearly extrapolating the Nankai data set towards higher pressure conditions a smaller jump in values for q' between Boso and Nankai subsets could be, and this may reflect the higher degree of porosity reduction that the Boso samples have undergone during burial and tectonic deformation, without having been subjected to significant cementation (Yamamoto et al. 2005). The paleotemperatures have probably not exceeded 50°C for the Boso samples (Yamamoto et al. 2005), too low to induce any substantial mineralogical change. The samples of the Nankai subset come from the upper 120 m below the sea floor, and suffered only minor compaction in response to burial and tectonic overprint without any significant temperature increase.

5.4 Significance of the cyclic test

Decreasing axial strains at the beginning of the cyclic test on Sample NZ-PS-5-c are attributed to settlement of the sample material due to the applied load. The increasing axial strains after this phase of settlement (cycles 5 to 19, Figure 4. 9) are interpreted to reflect small amounts of irreversible creep in the sample material in each experimental cycle. The total amount of creep accumulated in cycles 5-19, however, is smaller than the amount of initial deformation due to pressurization. If this behavior is typical for the Boso rocks, it can be inferred that they seem to be prone to creep rather than to brittle deformation during earthquake shaking. This would be in accordance with the rather low cohesion of the samples, and is supported by the observation that the drill cores after triaxial deformation did not show through-going fractures. Low degrees of compaction, relatively high porosities and the absence of cementation (Yamamoto et al. 2005), as discussed above, supports this interpretation.

5.5 Tectonophysical implications for the Nankai forearc and accretionary wedge

Following the line of reasoning developed above, the observations on rock strength and effective shear parameters in the three sample subsets can in principle be used to make some predictions of the mechanical behavior of the Nankai accretionary prism and its décollement zone at depth. Figure 4. 13 shows the range of variation in cohesion to be expected to a depth of 9000 meters beneath the ocean floor, supposing that the prism and underlying units are dominantly composed of mudstones and siltstones with mechanical behavior

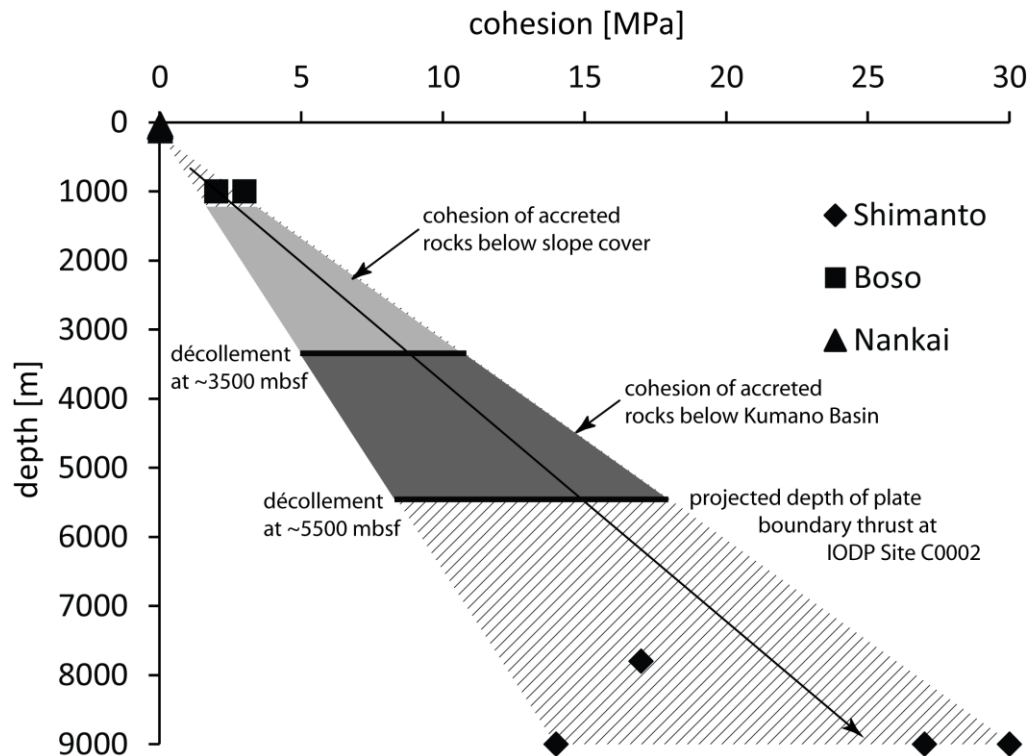


Figure 4. 13: Plot of cohesion versus depth of burial for the three sample sets from Shimanto Belt, Boso and Nankai accretionary prisms. The different data sets are used to extrapolate the cohesion of the sedimentary rocks beneath the slope cover and down to the updip end of the seismogenic zone in the active Nankai subduction zone. See text for discussion.

analogous to the Boso and Shimanto samples. The results from the testing of the Shimanto subset constrain a substantial amount of cohesion, between about 13 MPa and 30 MPa for 9000 m depth. If we consider the geometry of the Nankai accretionary wedge and forearc in the Kumano transect (Figure 4. 1) it is evident

that the rock suite overlying the basal décollement below the Kumano forearc basin is approximately 5500 m thick at IODP Site C0002, where the plate boundary fault is to be drilled, cored and instrumented. The strata of the forearc basin are undeformed, which means that the accreted rocks underneath must be cohesive enough to resist deformation, and constitute a “strong prism” akin to the conceptual model in Figure 4. 1, with cohesions of the rocks of about 8-18 MPa (Figure 4. 13). On the other hand the rocks in the décollement itself should be less cohesive at this depth, to assure concentration of the full rate of interplate movement there. The same line of reasoning can be developed for the part of the accretionary prism that is covered by undeformed slope cover (see Figure 4. 1). At about 1000 m depth beneath the cover the accreted rocks must be at least as cohesive as the rocks that were tested from Boso, i.e. 2-3 MPa. Above the level of the décollement, approximately 3000-4000 meters below sea floor, the rocks would be expected to have cohesions in the range of 5-12 MPa (Figure 4. 13), and be floored by a weaker plate boundary fault. At the toe of the prism strong rocks overlie a weak décollement, resulting in distributed strain in the wedge and frontal imbrication.

Figure 4. 11 shows that the frictional behavior of all three subsets of rocks approximates Coulomb-type laws (e.g., Marone et al. 1992) and is probably very similar, with estimated angles of static friction of about 30° (Nankai, Shimanto) and 35° (Boso). This translates to static friction coefficients of about 0.57 (Nankai), 0.59 (Shimanto) and 0.72 (Boso). These values are compatible with those measured from a wide range of fault gouges, especially those containing significant amounts of quartz and feldspar in addition to clay minerals such as kaolinite and illite (see e.g., Ikari et al. 2011 for a compilation). Smectite, which is present in significant amounts in the mudstones from Nankai (e.g., Underwood 2007; Guo and Underwood 2012; Stipp et al. in press) and Boso (see Table 4. 4), is thought to change frictional properties towards lower values (e.g., Logan and Rauenzahn 1987). However, the similar frictional properties of all three subsets would argue against the importance of such effects. The cohesions that can be derived from linear regression of the data from the three subsets of samples (Figure 4. 11) are about 8 kPa for Nankai, about 2.6 MPa for Boso, and about 18.5 MPa for the Shimanto Belt. Again this illustrates how important diagenesis,

cementation and very low-grade transformations are in defining the strength of forearc rocks.

In summary, it appears that the hydrological properties of the décollement and the accreted rocks (Morgan and Karig 1995; Skarbek and Saffer 2009) at Nankai, and geomechanical effects like structural strength or weakness (Stipp et al. in press) are very important controlling variables determining strain localization and fault propagation. Compositional variations are possibly too subtle to constrain differences in frictional behavior and they have also been found to be of only very little importance in the Nankai sample set (Stipp et al., in press). Burial-dependent increases in cohesion, resulting from diagenesis and, at greater depths, from very low-grade metamorphism, are probably of overriding importance in determining rock strength in the accretionary wedge and forearc. If the data presented in this study from the Boso and Shimanto belts are taken as analogues, then the prism is strong enough to transmit stresses as high as 5-13 MPa to the frontal 10 km (Figure 4. 1). The locked updip end of the seismogenic zone below IODP Site C0002 can probably support stresses up to 18 MPa without rupturing, if it is supposed that the fault zone is healed and recemented during the interseismic cycle.

6. Summary and conclusions

The results of triaxial shear tests on mudstone samples from the Shimanto Belt and the Boso accretionary prism (Japan) allowed an assessment of the strength evolution of terrigenous to hemipelagic active margin sediments with progressive burial and diagenesis. Effective shear parameters were derived from suites of triaxial pressure stepping tests at increasing confining pressures. A cyclic loading test on one sample from Boso (19 cycles to 70 MPa differential stress) showed that after some contraction due to pressurization in the first five cycles, the sample had tendencies to creep at constant stress rather than to fracture at maximum applied load. This may be typical for the Boso mudstones tested, as the other cores were also not fractured during the experiments. The samples from the Shimanto Belt, in turn, showed evidence of dominantly brittle behavior during

testing. In both sample subsets effective shear parameters indicate that the phyllosilicate-quartz-feldspar mudstones are relatively strong sediments. Internal angles of friction are partly quite high. Cohesion is in the range of 2 to 6 MPa for the Boso samples, and between 13 and > 30 MPa for those from the Shimanto Belt. Because the compositions of both sample subsets are similar to those of mudstones from the recently active Nankai accretionary prism and forearc, the results can be used to make some predictions about the strength and frictional behavior of the deeper parts of the Nankai active margin, and the décollement at its base. Static friction is similar to results in the literature, obtained from tests on a wide range of phyllosilicate-quartz-feldspar gouges. Cohesion increase due to diagenesis and/or very low-grade metamorphism is of overriding importance in determining the strength of the deeper parts of the forearc. Judging from the increase of cohesion with depth, pre-fracture stresses of up to 18 MPa may be transmitted through the updip end of the seismogenic zone at depth at Nankai, and about 5-13 MPa through the backstop of the actively deforming frontal prism. As the rocks above the updip end of the seismogenic zone and above the mid-slope part of the accretionary wedge are not deforming at present, it is inferred that cohesion of fault rocks in the décollement is lower than the values given above.

Acknowledgements

The authors sincerely thank Y. Hashimoto and W. Lin for logistical help and guidance during the fieldwork. We are grateful to the laboratory staff at Martin-Luther-University Halle-Wittenberg, and to R. Kaden for XRD measurements. This work was funded by Deutsche Forschungsgemeinschaft (DFG) through Grant BE1041/28 to JHB and MS.

References

- Aitchison J (1986) Stratigraphy, sedimentology and tectonic evolution of the Shimanto Terrane, Southwest Japan. *Earth Science; Journal of the association for the geological collaboration in Japan* 40:337-363
- Banno S, Nakajima T (1991) Metamorphic belts of Japan. *Episodes* 14:280-285
- Brace WF, Byerlee JD (1966) Stick-slip as a mechanism for earthquakes. *Science* 153:990-992
- Burland JB (1990) On the compressibility and shear strength of natural clays. *Géotechnique* 40:329-378
- Byrne DE, Davis DM, Sykes LR (1988) Loci and maximum size of thrust earthquakes and the mechanics of the shallow region of subduction zones. *Tectonics* 7:833-857
- DIN 18137 (1990) Testing procedures and apparatus: Triaxial test, part 2 (German industry standard). Deutsches Institut für Normung, Berlin
- DiTullio L, Byrne T (1990) Deformation paths in the shallow levels of an accretionary prism: The Eocene Shimanto belt of southwest Japan. *Geological Society of America Bulletin* 102:1420-1438. doi:10.1130/0016-7606(1990)102<1420:DPITSL>2.3.CO;2
- DiTullio L, Hada S (1993) Regional and local variations in the thermal history of the Shimanto Belt, southwest Japan. In: Underwood MB (ed) *Thermal Evolution of the tertiary Shimanto Belt, Southwest Japan: An example of Ridge-Trench Interaction*. Geological Society of America, Special Paper 273
- Fujiwara T, Kinoshita H, Morijiri R (1999) Magnetic structure of the southern Boso Peninsula, Honshu, Japan, and its implications for the formation of the Mineoka Ophiolite Belt. *Jamstec*
- Guo J, Underwood MB (2012) Data Report: Clay Mineral Assemblages from the Nankai Trough and Kumano Basin, IODP Expedition 315 and 316, NanTroSEIZE Stage 1. In: Kinoshita M, Tobin H, Ashi J, Kimura G, Lallemand S, Sreaton EJ, Curewitz D, Masago H, Moe KT and the Expedition 314/315/316 Scientists, Proc. IODP, 314/315/316. doi:10.2204/iodp.proc.314315316.202.2012
- Hajdarwish A, Shakoor A (2006) Predicting the shear strength parameters of mudrocks. *The Geological Society of London, IAEG2006, Paper number 607*
- Hanamura Y, Ogawa Y (1993) Layer-parallel faults, duplexes, imbricate thrusts and vein structures of the Miura Group: Keys to understanding the Izu fore-arc sediment accretion to the Honshu fore arc. *The Island Arc* 3:126-141
- Hashimoto M, Igi S, Seki Y, Banno S, Kojima G (1970) Metamorphic facies map of Japan. Geological Survey of Japan, Kawasaki, Japan.

-
- Hibbard J, Karig D, Taira A (1992) Anomalous structural evolution of the Shimanto Accretionary Prism at Murotomisaki, Shikoku Island, Japan. *The Island Arc* 1:133-147
- Hyndman RD, Wang K (1993) Thermal constraints on the zone of major thrust earthquake failure – the Cascadia subduction zone. *Journal of geophysical Research* 98:2039-2060
- Hyndman RY, Wang K, Yamano M (1995) Thermal constraints on the seismogenic portion of the southwestern Japan subduction thrust. *Journal of geophysical Research* 100:15373-15392
- Ikari MJ, Marone C, Saffer DM (2011) On the relation between fault strength and frictional stability. *Geology* 39:83-86. doi:10.1130/G31416.1
- Kameda J, Yamamoto Y, Kimura G (2010) Smectite swelling in the Miura-Boso accretionary prism: Possible cause for incipient décollement zone formation. *Tectonophysics* 494:75-84. doi:10.1016/j.tecto.2010.08.008
- Katto J, Hada M, Tashiro M, Taira A, Terado T (1991) Geological and Mineral Spring Resources Map of Kochi Prefecture. Kochi Prefecture Government
- Kawabata K, Tanaka H, Kimura G (2007) Mass transfer and pressure solution in deformed shale of accretionary complex: Examples from the Shimanto Belt, southwestern Japan. *Journal of Structural Geology* 29:697-711
- Kawakami S, Shishikura M (2006) Geology of the Tateyama District, Quadrangle Series, 1:50,000. Geological Survey of Japan, AIST, p. 82, (in Japanese with English abstract)
- Kimura G, Ludden J (1995) Peeling oceanic crust in subduction zones. *Geology* 23:217-220
- Kitamura Y, Sato K, Ikesawa E, Ikehara-Ohmori K, Kimura G, Kondo H, Ujiie K, Onishi CT, Kawabata K, Hashimoto Y, Mukoyoshi H, Masaga H (2005) Mélange and its seismogenic roof décollement: A plate boundary fault rock in the subduction zone – An example from the Shimanto Belt, Japan. *Tectonics* 24:15. doi:10.1029/2004TC001635
- Kovári K, Tisa A (1975) Multiple Failure State and strain controlled triaxial tests. *Rock Mechanics* 7:17-33
- Kumon F (1983) Coarse clastic rocks of the Shimanto Supergroup in eastern Shikoku and Kii Peninsula, southwest Japan. *Memories of the faculty of science, Kyoto University, Series of Geology and Mineralogy* 49:63-109
- Kuramoto S, Curewitz D, Thu MK, Masago H, and the Expedition 314, 315 and 316 Science Parties 2008. The first D/V Chikyu IODP operations: Successful logging and coring during NanTroSEIZE Stage 1 Expeditions. *Scientific Drilling* 6:38-42. doi:10.2204/iodp.sd.6.05.2008
- Lang HJ, Huder J, Amann P (2003) *Bodenmechanik und Grundbau*. 7th edn. Springer

- Lempp C, Witthaus M, Roeckel T, Hecht K, Herold M (2010) Geomechanisches Verhalten diagenetisch unterschiedlich stark verfestigter pelitischer Gesteine in tiefen Geothermiebohrungen. *Zeitschrift der Deutschen Gesellschaft für Geowissenschaften* 161/4:379-400. doi:10.1127/1860-1804/2010/0161-0379
- Lewis JC, Byrne TB, Pasteris JD, London D, Morgan GB (2000) Early Tertiary fluid flow and pressure-temperature conditions in the Shimanto accretionary complex of south-west Japan: constraints from fluid inclusions. *Journal of metamorphic Geology* 18:319-333
- Logan JM, Rauenzahn KA (1987) Frictional dependence of gouge mixtures of quartz and montmorillonite on velocity, composition, and fabric. *Tectonophysics* 144:87–108. doi:10.1016/0040-1951(87)90010-2
- Marone C, Hobbs BE, Ord A (1992) Coulomb constitutive laws for friction: Contrasts in frictional behavior for distributed and localized shear. *Pure and Applied Geophysics* 139:195–214. doi:10.1007/BF00876327
- Matsumura M, Hashimoto Y, Kimura G, Ohmori-Ikehara K, Enjoji M, Ikesawa E (2003) Depth of oceanic crust underplating in subduction zone – inference from fluid inclusion analysis of crack-seal veins. *Geology* 31:1005-1008. doi:10.1130/G19885-1
- Moore GF, Bangs NL, Taira A, Kuramoto S, Pangborn E, Tobin HJ (2007) Three-dimensional splay fault geometry and implications for tsunami generation. *Science* 318 (5853):1128-1131. doi:10.1126/science.1147195
- Moore JC, Saffer D (2001) Updip limit of the seismogenic zone beneath the accretionary prism of southwest Japan: An effect of diagenetic to low-grade metamorphic processes and increasing effective stress. *Geology* 29:183-186
- Morgan JK, Karig DE (1995) Décollement processes at the Nankai accretionary margin, southeast Japan: Propagation, deformation and dewatering. *Journal of Geophysical Research* 100:15221-15231
- Oleskevich DA, Hyndman RD, Wang R (1999) The updip and downdip limits to great subduction earthquakes: Thermal and structural models of Cascadia, south Alaska, SW Japan, and Chile. *Journal of Geophysical research* 104:14965-14991
- Park JO, Tsuru T, Kodaira S, Cummins PR, Kaneda Y (2002) Splay fault branching along the Nankai Subduction Zone. *Science* 297:1157-1160
- Pohl CM (2002). Triaxiale Verformungsexperimente feinkörniger Sedimente aus dem Bereich des Japan-Tiefseegrabens. Diploma Thesis
- Reid HF (1911) The Elastic-rebound theory of earthquakes. *Bulletin of the Department of Geology, University of California Publications* 6:413-444
- Richter D (1989) *Ingenieur- und Hydrogeologie*. Walter de Gruyter, Berlin New York
- Rietveld HM (1969) A Profile Refinement Method for Nuclear and Magnetic Structures. *Journal of Applied Crystallography* 2:65-71

- Roller S, Pohl C, Behrmann JH (2003) 17. Data Report: Triaxial shear strength investigation of sediments and sedimentary rocks from the Japan trench, ODP Leg 186. In: Suyehiro K, Sacks IS, Acton GD, Oda M (ed) Proceedings of the Ocean Drilling Program, Scientific Results. Volume 186
- Saffer DM, Marone C (2003) Comparison of smectite- and illite-rich gouge frictional properties: application to the updip limit of the seismogenic zone along subduction megathrusts. *Earth and Planetary Science Letters* 215:219-235. doi:10.1016/S0012-821X(03)00424-2
- Saito S (1992) Stratigraphy of Cenozoic strata in the southern terminus area of Boso Peninsula, Central Japan, Contributions of Institute of Geology and Paleontology, Tohoku University 93:1-37
- Savage JC, Byerlee JD, Lockner DA (1997) Is internal friction friction? *Geophysical Research Letters* 23:1944-8007. doi:10.1029/96GL00241
- Scholz CH (1998) Earthquakes and friction laws. *Nature* 391:37-42
- Schumann K, Stipp M, Leiss B, Behrmann JH (subm) Texture development of naturally compacted and experimentally deformed silty clay sediments from the Nankai trench, Japan (NanTroSEIZE, IODP Expedition 315, 316, 333)
- Skarbek RM, Saffer DM (2009) Pore pressure development beneath the décollement at the Nankai subduction zone: Implications for plate boundary fault strength and sediment dewatering. *Journal of Geophysical Research* 114:B07401. doi:10.1029/2008JB006205
- Stipp M, Rolfs M, Behrmann JH, Schumann K, Schulte-Kortnack D, Feeser V (in press). Strong sediments at the deformation front, and weak sediments at the rear of the Nankai accretionary prism, revealed by triaxial deformation experiments. *G-cubed*, doi:10.1002/2013GC004987
- Taheri A, Tani K (2008) Use of down-hole triaxial apparatus to estimate the mechanical properties of heterogeneous mudstone. *International Journal of Rock Mechanics and Mining Sciences* 45:1390-1402. doi:10.1016/j.ijrmms.2008.01.017
- Taira A, Hill I, Firth J, Berner U, Brückmann W, Byrne T, Chabernaud T, Fisher A, Foucher J-P, Gamo T, Gieskes J, Hyndman R, Karig D, Kastner M, Kato Y, Lallemand S, Lu R, Maltman A, Moore G, Moran K, Olafsson G, Owens W, Pickering K, Siena F, Taylor E, Underwood M, Wilkinson C, Yamano M, Zhang J (1992) Sediment deformation and hydrogeology of the Nankai Trough accretionary prism: Synthesis of shipboard results of ODP Leg 131. *Earth and Planetary Science Letters* 109:431-450
- Taira A, Katto J, Tashiro M, Okamura M, Kodama K (1988) The Shimanto Belt in Shikoku, Japan: evolution of Cretaceous to Miocene accretionary prism. *Modern Geology* 12:5-46
- Taira A, Okada H, Whitaker JH, Smith AJ (1982) The Shimanto Belt of Japan: Cretaceous-lower Miocene active-margin sedimentation. Geological Society, London, Special Publications 10:5-26

- Tobin HJ, Kinoshita M (2006a) NanTroSEIZE: The IODP Nankai Trough seismogenic zone experiment. *Scientific Drilling* 2:23-27. doi:10.2204/iodp.sd.2.06.2006
- Tobin HJ, Kinoshita M (2006b) Investigation of seismogenesis at the Nankai Trough, Japan. IODP Scientific Prospectus, NanTroSEIZE Stage 1. doi:10.2204/iodp.sp.nantroseize1.2006
- Toriumi M, Teruya J (1988) Tectono-metamorphism of the Shimanto Belt. *Modern Geology* 12:303-324
- Twiss RJ, Moores EM (1992) *Structural Geology*. Freeman, New York
- Underwood MB (2007) Sediment inputs to subduction zones: Why lithostratigraphy and clay mineralogy matter. In: Dixon TH, Moore JC (ed) *The seismogenic zone of subduction thrust faults*. Columbia University Press, New York, pp 42–85
- Underwood MB, Byrne T, Hibbard JP, DiTullio L, Laughland MM (1993c) The effect of ridge subduction on thermal structure of accretionary prisms: A Tertiary example from the Shimanto Belt of Japan. In: Underwood MB (ed): *Thermal Evolution of the tertiary Shimanto Belt, Southwest Japan: An example of Ridge-Trench Interaction*. Geological Society of America, Special Paper 273
- Underwood MB, Hibbard JP, DiTullio L (1993a) Geologic summary and conceptual framework for the study of thermal maturity within the Eocene-Miocene Shimanto Belt, Shikoku, Japan. In: Underwood MB (ed): *Thermal Evolution of the tertiary Shimanto Belt, Southwest Japan: An example of Ridge-Trench Interaction*. Geological Society of America, Special Paper 273
- Underwood MB, Hibbard JP, DiTullio L (1993b) A comparison among organic and inorganic indicators of diagenesis and low-temperature metamorphism, Tertiary Shimanto Belt, Shikoku, Japan. In: Underwood MB (ed): *Thermal Evolution of the tertiary Shimanto Belt, Southwest Japan: An example of Ridge-Trench Interaction*. Geological Society of America, Special Paper 273
- Underwood MB, Laughland MM, Byrne T, Hibbard JP, DiTullio L (1992) Thermal evolution of the Tertiary Shimanto Belt, Muroto Peninsula, Shikoku, Japan. *The Island Arc* 1:116-132
- Vrolijk P (1990) On the mechanical role of smectite in the subduction zones. *Geology* 18:703-707
- Yamamoto Y (2006) Systematic variation of shear-induced physical properties and fabric in the Miura-Boso accretionary prism: The earliest processes during off-scraping. *Earth and Planetary Science Letters* 244:270-284. doi:10.1016/j.epsl.2006.01.049
- Yamamoto Y, Chiyonobu S, Kurihara T, Yamaguchi Y, Hina S, Hamahashi M, Raimbourg H, Augier R, Gadenne L (2012) Unconformity between a Late Miocene–Pliocene accretionary prism (Nishizaki Formation) and Pliocene trench-slope sediments (Kagamigaura Formation), central Japan. *Island Arc* 21:231-234.

Yamamoto Y, Mukoyoshi H, Ogawa Y (2005) Structural characteristics of shallowly buried accretionary prism: Rapidly uplifted Neogene accreted sediments on the Miura-Boso Peninsula, central Japan. *Tectonics* 24:17p. doi:10.1029/2005TC001823

5 Manuscript #4

Strong sediments at the deformation front, and weak
sediments at the rear of the Nankai accretionary prism,
revealed by triaxial deformation experiments

Michael Stipp¹, Malte Rolfs², Yujin Kitamura³, Jan H. Behrmann¹, Kai
Schumann¹, Detlef Schulte-Kortnack⁴ and Volker Feeser⁴

¹ *Marine Geodynamics, GEOMAR Kiel, Germany*

² *TU Hamburg-Harburg, Germany*

³ *Department of Earth and Planetary Science, University of Tokyo, Japan*

⁴ *Engineering Geology, Institute of Geosciences, University of Kiel, Germany*

Geochemistry, Geophysics, Geosystems

Vol. 14, No. 11, doi: 10.1002/ggge.20290

Strong sediments at the deformation front, and weak sediments at the rear of the Nankai accretionary prism, revealed by triaxial deformation experiments

Michael Stipp^{1*}, Malte Rolfs², Yujin Kitamura³, Jan H. Behramm¹, Kai Schumann¹, Detlef Schulte-Kortnack⁴ and Volker Feeser⁴

¹) *Marine Geodynamics, GEOMAR Kiel, Germany, mstipp@geomar.de, jbehrmann@geomar.de, kaschumann@geomar.de*

²) *TU Hamburg-Harburg, Germany, malte.rolfs@gmail.com*

³) *Department of Earth and Planetary Science, University of Tokyo, Japan, ykitamura@eps.s.u-tokyo.ac.jp*

⁴) *Engineering Geology, Institute of Geosciences, University of Kiel, Germany, dsk@min.uni-kiel.de, vfeeser@gpi.uni-kiel.de*

**) Corresponding author*

Abstract

19 whole-round core samples from the Nankai accretionary prism (IODP Expeditions 315, 316 and 333) from a depth range of 28-128 m below sea floor were experimentally deformed in a triaxial cell under consolidated and undrained conditions at confining pressures of 400-1000 kPa, room temperature, axial displacement rates of 0.01-9.0 mm/min, and up to axially compressive strains of ~64%. Despite great similarities in composition and grain size distribution of the silty clay samples, two distinct 'rheological groups' are distinguished: The first group shows deviatoric peak stress after only a few percent of compressional strain (< 10%) and a continuous stress decrease after peak conditions. Simultaneous to this decrease is a pore pressure increase, indicating contractant behavior characteristic of structurally weak material. The second sample group weakens only moderately at a much higher strength level after significantly higher strain (> 10%), or does not weaken at all. This is characteristic of structurally strong material. The strong samples tend to be overconsolidated and are all from the drillsites at the accretionary prism toe, while the weak and normally consolidated samples come from the immediate hanging wall of a megasplay fault further upslope. Sediments from the incoming plate are also structurally weak. The observed differences in mechanical behavior may hold a key for understanding strain localization and brittle faulting within the uniform silty and clayey sedimentary sequence of the Nankai accretionary prism.

1. Introduction

Faulting (or fault slip) as well as earthquake nucleation and propagation are commonly assumed to be controlled by friction and stick-slip instabilities (e.g., Brace and Byerlee, 1966; Scholz, 1998). Many theoretical conceptions of friction on fault surfaces, especially the rate- and state-variable friction law, have been developed (e.g., Dieterich, 1972, 1979; Rice and Ruina, 1983; Chester, 1994; Scholz, 2002). They have been constrained and recessed by a wealth of experimental data (Tullis and Weeks, 1986; Blanpied et al., 1991; Linker and Dieterich, 1992; Beeler et al., 1994; Goldsby and Tullis, 2002). All these findings

well explain the mechanics and deformation processes within the upper seismogenic zone and towards its downdip termination. Deformation at the updip end of the seismogenic zone and the lack of earthquakes in the uppermost section of the crust in subduction zones is less well understood. It is also a matter of debate why faults do or do not cut through this crustal section when a major earthquake occurs in the seismogenic zone and propagates in updip direction.

The updip end of the seismogenic zone usually occurs in a depth range of 5-10 km at temperatures between 100 and 150°C where pore space reduction, dewatering and consolidation are already advanced (e.g. Cloos, 1982; von Huene, 1984; Byrne et al., 1988; Vrolijk, 1990; Hyndman and Wang, 1993; Moore and Saffer, 2001); for the Nankai accretionary prism the depth is approximately 5 km (Moore et al., 2001; Park et al., 2002a,b; Kimura et al., 2007). The transition from aseismic to seismic deformation towards depth is ascribed to a number of different processes including changes in the frictional behavior of clay minerals, hardening of the aseismic subduction thrust, the diagenesis of the involved sedimentary rocks, pore pressure reduction, and step-down of the subduction thrust due to underplating (e.g., Marone and Scholz, 1988; Hyndman and Wang, 1993; Hyndman et al., 1997; Oleskevich et al., 1999; Moore and Saffer, 2001; Saffer and Marone, 2003; Kitamura et al., 2005; Kimura et al., 2007). The contributions of these processes have been estimated by theoretical considerations on the critical wedge taper, experimental data and modelling. Most of these processes are controlled by temperature, but also rock composition, fluid pressure and regional stress field could be important (Hyndman and Wang, 1993; Tichelaar and Ruff, 1993; Oleskevich et al., 1999; Wallace et al., 2009).

For surface breaks and thus for the faulting of the crustal section above the seismogenic zone the mechanical as well as compositional and microstructural properties of the rocks are most important and temperature is only of minor importance. While the depth range of lithification is assumed to correspond to beginning seismicity increasing from there downwards, the rheological contrast between hard and soft rocks (sediments) upwards is crucial for the upward propagation of faults. Careful compositional and microstructural analyses as well as geotechnical experiments are essential to characterize this transition and the

capacity of the overlying sediments to establish and maintain discrete faults and produce surface breaks.

Sediments in accretionary prisms usually undergo considerable bulk strain, they tend to be underconsolidated with a low degree of lithification due to fast burial and high internal fluid pressure (for recent reviews see Underwood, 2007; Morgan et al., 2007). The accretionary prism sediments predominantly consist of mixtures of quartz, feldspar, carbonates and sheet silicates with different grain size distributions. The sheet silicates play a key role for rock friction and mechanically weak behavior (e.g., Byerlee, 1978; Vrolijk, 1990; Beeler, 2007). Mixtures of quartz and smectite, for example, weaken considerably when smectite contents in the fault zone exceed about 30% (Lupini et al., 1981; Logan and Rauenzahn, 1987).

For the clay-dominated soft sediments prevailing in accretionary prisms above the seismogenic zone, the brittle to plastic behavior, brittle or plastic peak stress and residual stress, pore pressure characteristics and the processes governing strain localization are important for faulting. The most promising approach to study these processes may be by consolidated and undrained triaxial testing (e.g., Laberg et al., 2003; Sultan et al., 2004; Morgan et al., 2007; Kitajima et al., 2012). While reaching peak deviatoric stress in constant displacement rate tests, the compressibility of the sediment increases together with an increase in pore pressure (Terzaghi et al., 1996). A significant decrease in deviatoric stress after reaching peak stress (failure point) combined with an increase in pore pressure under undrained conditions is characteristic of structurally weak material (e.g., Sultan et al., 2004). Such material shows contractant behavior, develops shear bands, and may be inherently unstable under application of a critical load. In contrast, for structurally strong material the residual stress remains constant at peak stress level or there is even a continuous stress increase together with a decrease in pore pressure towards high strain (> 20%). This material behavior is dilatant and deformation without the development of shear bands is believed to be stable under the same loading conditions as applied to the structurally weak material (Laberg et al., 2003).

The NanTroSEIZE (Nankai Trough Seismogenic Zone Experiment) drilling project of the Integrated Ocean Drilling Program (IODP) in the SW Japan forearc

is the first-ever attempt to core and instrument the updip end of the seismogenic part of a subduction zone (review in Dixon and Moore, 2007; Tobin and Kinoshita, 2007; Moore et al., 2009). Hence, the project is dedicated to plate boundary deformation, accretionary prism formation and the upper seismogenic zone of the Nankai trench at which the Philippine sea plate is subducted below the Japanese islands Honshu and Shikoku (Eurasian plate). IODP Expeditions 315, 316 and 333 from which our experimental samples are recovered, investigated the shallow frontal thrusts, the hanging wall to a major active splay fault of the active frontal thrust system and the incoming plate material (e.g., Kinoshita et al., 2009; Tobin et al., 2009; Henry et al., 2012). The sample material is well-suited to test whether the involved sediments are dominated by localized brittle deformation and subsequent fault slip, or alternatively, by distributed ductile deformation causing a slow, creep-like behavior on the megascopic scale. Knowing the mechanical behavior of the sediments within the accretionary wedge is equally important to the study of the decollement, as most of the interplate displacement must be accommodated there, and the response to loading (ductile flow, fracturing, slow aseismic or fast unstable slip) is crucial to the questions whether earthquake faulting can break towards the surface or not. Slow strain dissipation over days, weeks or months tends to prevent surface breaks, and associated devastating tsunamis. The undrained triaxial experiments reported here will, therefore, provide a first order indication as to whether tectonic mass movement in the frontal and middle part of the Nankai forearc constitutes a major tsunami risk.

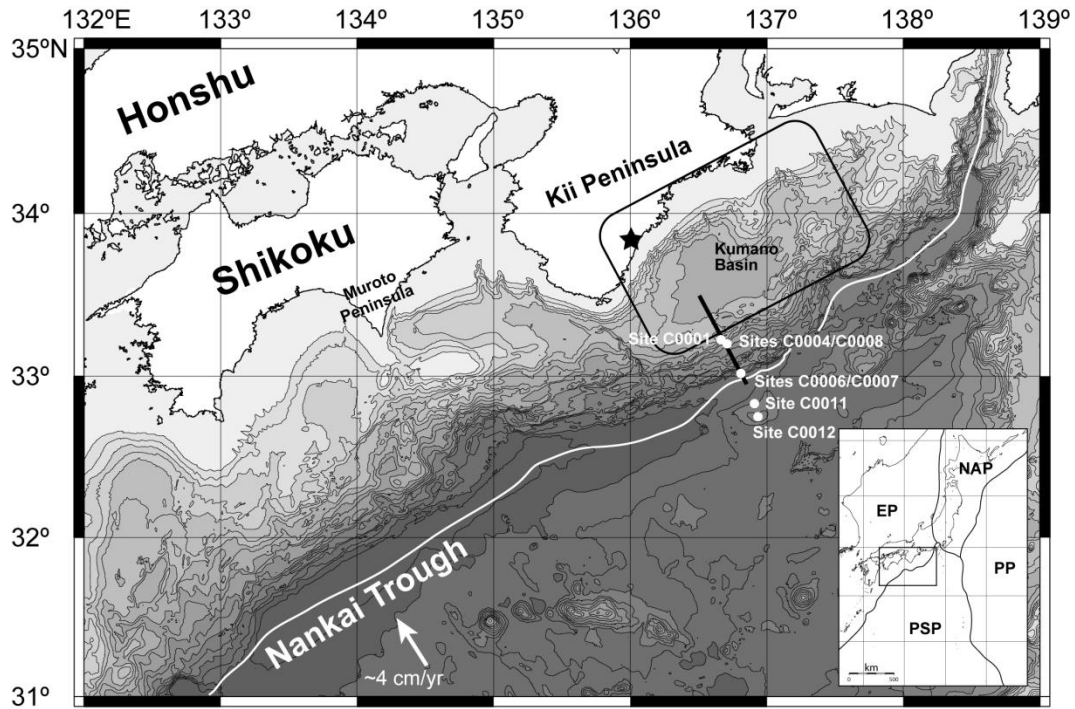


Figure 5. 1: Map of Nankai Trough area, showing the locations of NanTroSEIZE drilling sites C0001, C0004, C0006, C0007, C0008, C0011, C0012 with white dots (IODP legs 315, 316 and 333; modified after Kimura et al., 2007). Seismic reflection profile of Figure 5. 2a was obtained along the black line (seismic transect KR0108-5). Rectangular frame and star corresponds to the rupture zone and the epicenter of the 1944 Tonankai earthquake. EP = Eurasian plate, NAP = North American plate, PP = Pacific plate, PSP = Philippine Sea plate.

2. Geological Setting

The Nankai Trough is a convergent plate boundary where the Philippine Sea plate subducts beneath the Eurasian plate at rates of 4.0-6.0 cm/y (Figure 5. 1; Seno et al., 1993; Miyazaki and Heki, 2001). The subducting Shikoku Basin off southwestern Japan was formed by backarc spreading during a time period of approximately 15-25 Ma (e.g., Okino et al., 1994; Ike et al., 2008). The convergence direction is approximately normal to the trench, and sediments of the Shikoku Basin are actively accreting at the deformation front (e.g. Kimura et al., 2007).

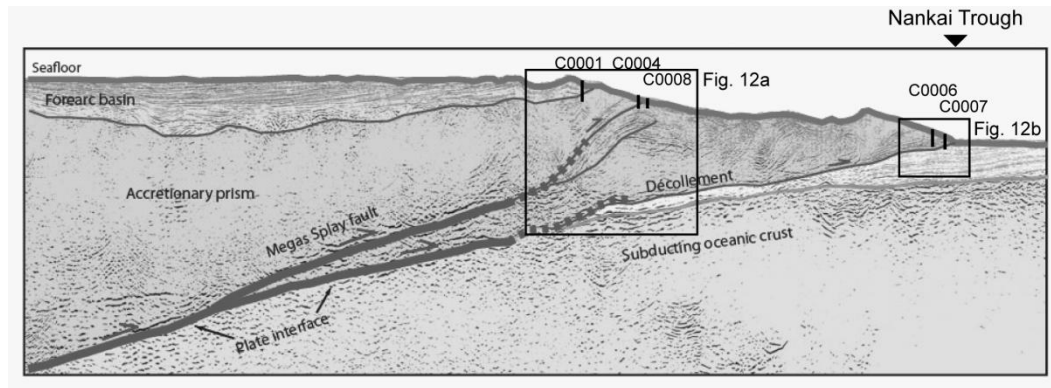


Figure 5. 2: Seismic cross section of the plate boundary from Park et al., (2002) with geological interpretation of Kimura et al. (2008) along the transect KR0108-5 (black line in Figure 5. 1). NanTroSEIZE drilling sites cored during IODP expeditions 315 and 316 are shown. The two rectangular frames indicate locations of detailed seismic sections of Figure 5. 12a and b.

NanTroSEIZE is a multi-expedition project in the framework of IODP, which consists of four research stages. By the end of the second stage, five expeditions conducted drilling at twelve sites (IODP Sites C0001 to C0012) along a transect almost perpendicular to the Nankai Trough offshore of Kii Peninsula, central Japan. Investigated samples in this paper are obtained from Site C0001 of Expedition 315 (Ashi et al., 2008), Sites C0004, C0006, C0007 and C0008 of Expedition 316 (Kimura et al., 2008) as well as Sites C0011 and C0012 of Expedition 333 (Henry et al., 2012; Table 5. 1). The 315 and 316 samples were recovered near one of two major fault systems of the megasplay fault and the frontal thrust (Figure 5. 2; Park et al., 2002; Tobin and Kinoshita, 2006). Sites C0001 and C0004 are located along the slope of the accretionary prism landward of the inferred intersection of the megasplay fault zone with the seafloor, and C0008 is in the slope basin seaward of the megasplay fault, while Sites C0006 and C0007 are from the frontal thrust region in the accretionary prism toe. Sites C0011 and C0012 represent sediments from the incoming plate (Henry et al., 2012).

Site C0001 was cored to 458 m core depth below seafloor (mbsf) covering a “slope basin” (Unit I: 0-207.17 mbsf; facies names with double quotations are from Kinoshita et al., 2009) within the slope apron facies and the underlying “accretionary prism” (Unit II: 207.17-456.50 mbsf). The slope basin is composed mainly of Quaternary to late Pliocene silty clay and clayey silt with intercalations

of volcanic ash. Unit II is composed of mud-dominated sediments of late Pliocene to late Miocene age. Our sample at this site is from Unit I.

Table 5. 1: List of drill core samples from Nankai Trough area with depth indication, porosity, pore water data and related experiment numbers. Porosity and pore water data are taken from IODP shipboard measurements carried out on core segments next to our core samples (Ashi et al., 2008; Kimura et al., 2008; Henry et al., 2012).

core number	depth [mbsf]	depth [mbsf]	porosity [vol.-%]	pore water [wt.-%]
315-C0001E-11H-1	90.62	K003/ K005	61.7	64.8
316-C0004C-8H-2	65.26	K004/ K010	63.8	62.1
316-C0006E-8H-1	48.23	K007/ K009	48.9	37.2
316-C0006E-20X-2	127.98	K013/ K019	47.7	34.8
316-C0007C-7X-1	62.89	K011/ K012/ K016	51.6	48.3
316-C0008A-9H-3	76.06	K002/ K006/ K014	52.2	40.0
316-C0008C-7H-8	60.96	K015/ K018	56.8	50.5
333-C0011D-2H-2	33.10	K020	64.0	41.0
333-C0011D-2H-2	28.90	K022	72.0	49.0

Site C0004 penetrates the megasplay fault zone, and four lithologic units were defined. The uppermost “slope-apron facies” (Unit I: 0-78.06 mbsf) is dominated by greenish gray silty clay with a substantial component of calcareous nannofossils and a lesser amount of siliceous biogenic debris, which have been deposited from early to late Pleistocene. Our sample at this site is from Unit I. Below an angular unconformity, separating Units I and II, the “upper accretionary prism” (Unit II: 78.06-258.01 mbsf) is characterized by silty clay of late to middle Pliocene. A mass transport complex was observed in the upper part of Unit II. Unit III (258.01-307.52 mbsf) is a middle Pliocene “structurally bounded package” with two age reversals at both the upper and lower boundary. Unit IV (307.52-398.79 mbsf) is an “underthrust slope facies” of the early Pleistocene and consists of silty clay with a moderate amount of calcareous nannofossils and a lesser amount of calcareous and siliceous microfossils.

Site C0008 is a slope basin located ~1 km seaward of Site C0004. Two lithologic units were recognized. The “slope sediments” of Unit I (0-272.46 mbsf at Hole C0008A, 0-176.20 mbsf at Hole C0008C) are divided into two Subunits IA and IB. Subunit IA from which our samples at this site come from is

characterized by greenish gray silty clay with a substantial component of calcareous nannofossils, siliceous biogenic debris, and volcanic ash. Volcanic ash layers are distributed throughout this subunit. Subunit IB consists of a series of interbedded mudclast gravels and silty clay beds, which are interpreted as a mass-transport complex. Underlying Unit II (272.46-329.36 mbsf at Hole C0008A) are “sand-rich turbidites” that consist of dark gray fine- to coarse-grained and locally pebbly sandstone with minor silty clay interbeds.

Sites C0006 and C0007 targeted the main frontal thrust at the seaward edge of the accretionary prism. Unit I (“trench to slope transition facies”) of Site C0006 consists of a fining-upward succession of silty clay, sand, silty sand, and rare volcanic ash layers of Pleistocene-Holocene age. Unit II are accreted “trench deposits” with coarsening upward trend which are divided into four Subunits IIA to IID based mainly on variations in silt and sand content. One of our samples was taken from the “sand-dominated trench wedge” of Subunit IIA, another one from the “mixed sand-mud trench wedge” of Subunit IIB, however, we chose the silty part. Underlying Unit III representing a “deep-marine basin” consists of greenish gray to grayish silty clay with some interbedded volcanic tuff layers, including dolomite-cemented and calcite-cemented ash. Site C0007 is located trenchward of Site C0006 and was drilled after the hole condition at Site C0006 precluded to reach the frontal thrust. The lithology of Site C0007 resembles that one of Site C0006 and has Unit IV of possible Pleistocene age sediments beneath the frontal thrust. Our sample at Site C0007 is from Unit IIA of the accreted trench deposits.

Sites C0011 and C0012 were drilled into the sedimentary sequence of the incoming Philippine Sea plate. The topmost Unit I ranges down to 347.82 mbsf at Site C0011 and 149.77 mbsf at Site C0012. The significant difference in layer thickness between the two adjacent drill sites is due to the fact that Site C0012 is located on top of a bathymetric and basement high whereas Site C0011 was cored on the lower northwest flank of this high. Both investigated samples from the two sites belong to Subunit IA consisting of greenish gray clay to silty clay with intercalations of clayey silt, grayish silty clay and < 50 cm thick volcanic ash layers. The clayey and silty sequence is composed of clay minerals, quartz, feldspar, calcareous nannofossils, and some diatoms (Henry et al., 2012) characteristic of deep-sea clay with some planktonic fossils. These “undisturbed”

sediments are used as experimental reference material in comparison to the Nankai accretionary prism samples which are partly deformed and variably consolidated.

3. Methods

Grain size and composition analysis, experimental sample preparation as well as set-up, re-saturation and pressurization of the geotechnical tests are given in the Appendix A 4, Figures A 4.1 and A 4.2. Here, we will describe the different types of triaxial deformation experiments on the 50 mm- diameter cylindrical samples (Figure 5. 3a) with a length to diameter ratio between 1:1 and 2:1 (cf. Vardoulakis, 1979) in axial compression (i.e., $\sigma_1 > \sigma_2 = \sigma_3$). The deformation experiments have been carried out in a triaxial cell according to the standards of Berre (1985) under consolidated and undrained conditions (CU-test) at confining pressures of 400-1000 kPa, room temperature, axial displacement rates of 0.01-9.0 mm/min and up to axial compressive strains of ~64% (Figure 5. 3b). Only core samples from low

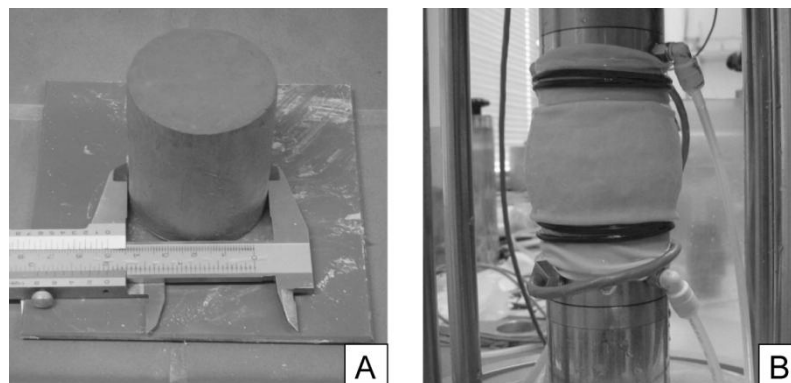


Figure 5. 3: a) Undeformed sample after resizing of the drill core to a 50 mm diameter cylinder. Whitish coloring on the sample sides indicate some drying effects at the end of the preparation procedure. b) Deformed sample after ~40% axial strain. The sample is still inside the rubber sleeve and between upper and lower forcing piston. Two O-rings (black) at each piston end prevent infiltration of confining water into the sample. The sample cell is demounted and the confining pressure cylinder is removed.

depth (< 128 m) have been selected (Table 5. 1) so that the maximum confining pressure of the triaxial cell comes close or above the in-situ overburden stress. Three different geotechnical deformation tests were performed: (1) single

step compression experiments at constant confining pressure and displacement rate, (2) pressure stepping compression experiments at constant displacement rate and three different confining pressures (cf. Head, 1998), and (3) displacement rate stepping compression experiments at constant confining pressure and increasing displacement rate (Appendix A 4, Table A 4.1). Single step compression experiments show the general stress/strain-record of a sample including elastic and plastic loading, peak or fracture strength, stress drop and residual strength in the brittle, and creep strength, weakening or hardening in the plastic deformation case. They were also carried out to record the pore pressure development, and to distinguish between structurally weak and strong behavior (e.g. Sultan et al., 2004). Pressure stepping experiments allow to determine peak strength at three different confining pressures in one and the same experiment. From that Mohr diagrams can be plotted and effective shear parameters (internal friction angle and cohesion) determined. The third group of experiments investigates displacement rate and pore fluid disequilibrium effects on sample strength. Both, pressure and displacement rate stepping experiments allow to investigate the same parameters as the single step compression experiments with the restriction of lower strain values in the individual steps.

Pressure and displacement rate steps were run until peak stress (stopped just before failure), i.e. when the slope of the stress-strain diagram is zero. In some experiments, however, there was a continuous strength increase without failure. These experiments were stopped after a certain amount of strain to allow additional steps at higher confining pressure or higher displacement rate. Only the ultimate pressure or displacement rate step in the experiments was run past peak stress in order to investigate weakening, high strain deformation behavior and residual strength. At the end of each pressure or displacement rate step the σ_1 -piston was retracted at rates of 0.01 to -0.1 mm/min until isotropic stress conditions were achieved. For the pressure stepping experiments the confining pressure was then increased under drained conditions. The pore pressure release lasted longer and was awaited until the pore pressure reached the back pressure level within a few kilopascal (usually overnight, 14-20 h) prior to starting the next deformation step (CU-test). We will focus on the deformation part(s) of each experiment under undrained conditions neglecting the experimental phases of

saturation, pressurization/(re-)consolidation, pore pressure equilibration, and piston retraction/force release carried out at drained conditions (see Appendix A 4).

4. Experimental starting material

4.1 Composition

The mineral composition of the core samples from the accretionary prism is indicated (Figure 5. 4) based on XRD analysis of the grain size fraction $< 2 \mu\text{m}$ (Guo and Underwood, 2012). Thus, a variation for the entire samples due to the existing larger grain size fractions, mainly the silt fraction, is possible, but full compositional data for that are not available. The content of illite amounts to 34-45% (wt.-% in the following), smectite to 16-33%, chlorite to 15-30%, quartz to 4-15% and kaolinite to 0-14% for all the investigated samples from the accretionary prism. Cores from the prism toe (C0006 and C0007) have the lowest contents in smectite (16- 23%), those from the slope apron facies in the hanging wall of the megasplay fault have the highest contents (29-33%; C0001 and C0004) and the slope sediments from the footwall of the megasplay fault are intermediate (23-29%; C0008). The other minerals are less clear in their distribution (Figure 5. 4). The prism toe deposits (C0006 and C0007) are relatively rich in illite (36-45%) and chlorite (20-30%) and poor in kaolinite (0-9%), but the variability is large. The slope apron facies (C0001 and C0004) is poor in kaolinite (4-6%) as well as in chlorite (15-21%) and mediocre in illite (36-37%). Slope sediments from below the megasplay fault have the highest kaolinite content and intermediate to low contents in chlorite (18-19%) and illite (34-40%). The quartz distribution seems to be arbitrary; prism toe and slope sediments vary from 4 to 15% and from 4 to 10%, respectively, while sediments of the slope apron facies are intermediate and constant at 9%. Overall the sample material is quite homogeneous, but slight, distinct differences especially in the smectite content are existing.

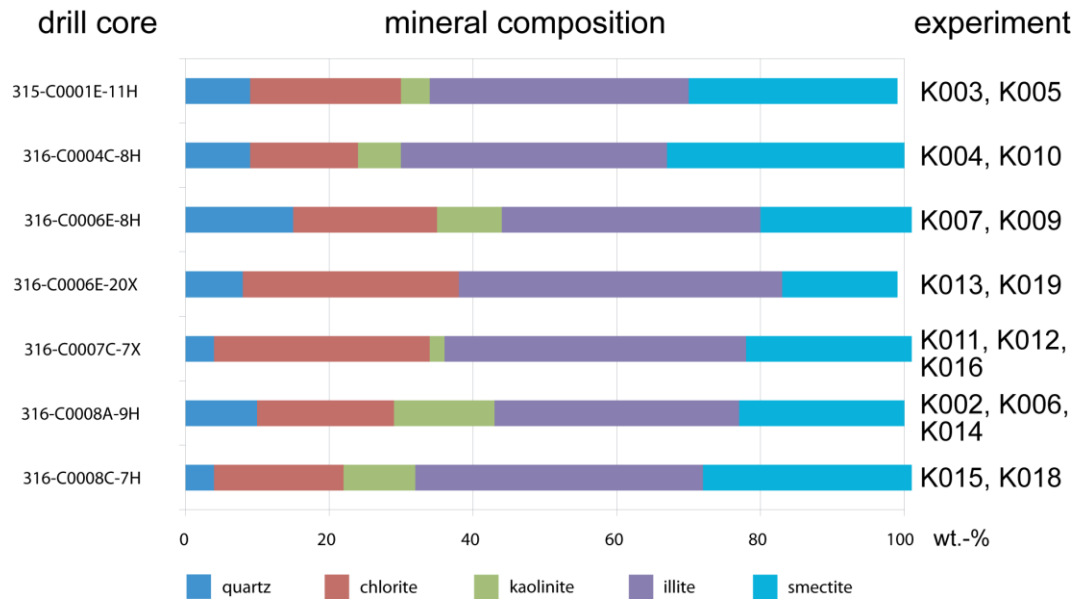


Figure 5. 4: Mineral composition of the grain size fraction <2 mm from XRD-analysis data of Guo and Underwood (2012) in weight-percentage. XRD measurements were carried out on the same core segment within 0.50 m from the experimental starting material. Correlated experimental sample numbers are indicated, but sample to sample variations are possible and not considered.

The point counting-analysis of the smear slides allows to semiquantitatively determine the content of biogenic and volcanoclastic material (mainly fossils and ash) versus the content of minerals and lithics and the content, which is too small for light-optical microscopy distinction (submicroscopic material; Figure 5. 5). Hence, by this method also the larger than clay-size fraction is analyzed. Fossils are mainly foraminifera, diatoms, silicoflagellates, sponge needles and radiolaria. Minerals consist of quartz, feldspar, pyroxene, hornblende, mica, olivine, augite, amphibole, calcite, and opaque minerals (pyrite, etc.). The submicroscopic content varies significantly from 33 to 78% (point counting-% in the following) across the entire sample set. The prism toe deposits (C0006 and C0007) have a relatively high content in submicroscopic particles (43-78%), while the slope apron facies (C0001 and C0004) and the slope sediments (C0008) have a lower content (37-51% and 33-56%, respectively; Figure 5. 5). Sites C0001 and C0004 are poor in minerals (7-10%) and lithics (4-11%), site C0008 is rich in minerals (13-16%) and lithics (11-29%), and sites C0006 and C0007 are rich in minerals (12-17%) and show an intermediate but variable lithics-content (2-26%). Sediments of the slope apron facies (C0001 and C0004) have only a small amount of ash (1-6%), slope sediments (C0008) have a large amount (6-8%) and the prism toe deposits (C0006

and C0007) have a variable amount (2-9%). The fossil content is very high for the slope apron facies (34-46%), intermediate for the slope sediments (11-24%) and low for the prism toe deposits (2-22%).

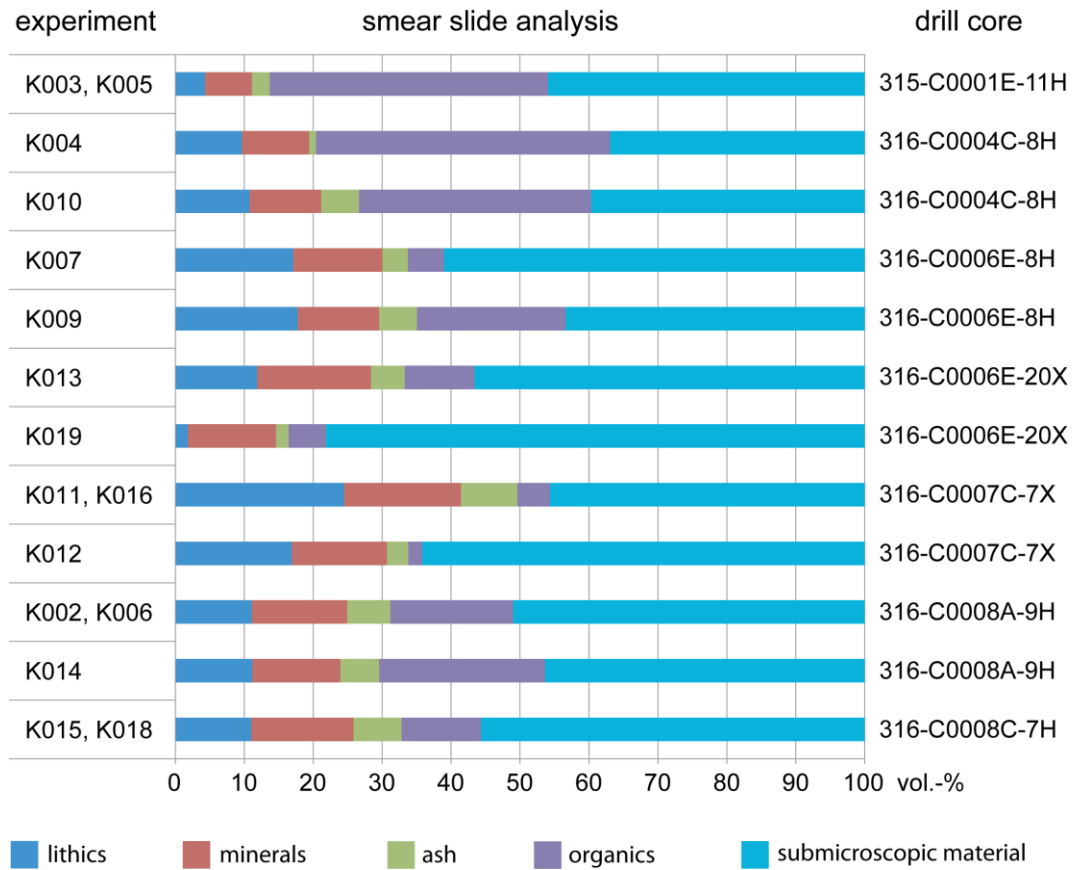


Figure 5. 5: Results of the smear slide analysis from the experimental samples in volume-percentage. The drill core number is also indicated. From some of the drill cores (e.g., 316-C0004C-8H) independent analyses of the different experimental samples (K004 and K010 for that core) have been carried out allowing to estimate internal drill core variations and measurement error. From other cores (e.g., 315-C0001E-11H; K003 and K005) only a sample average has been determined and variations are therefore unknown.

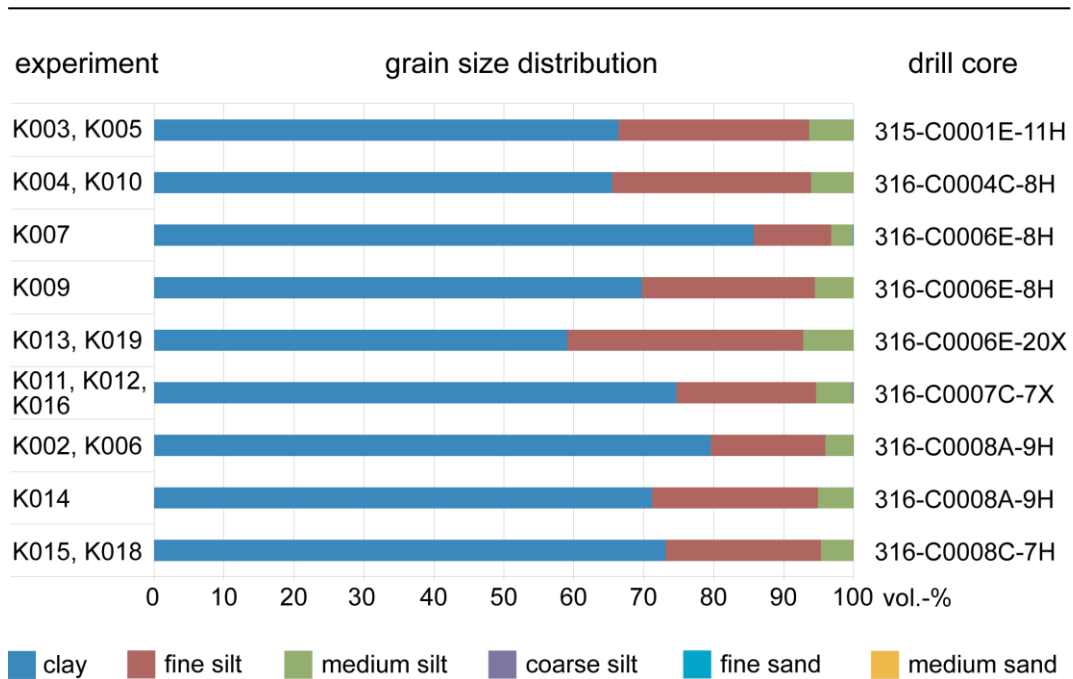


Figure 5. 6: Grain size distribution of drill cores / experimental samples as determined by laser particle size analysis in volume-percentage. Variations in grain size distribution are generally small. From two of the drill cores (e.g., 316-C0006E-8H) independent analyses of the different experimental samples (K007 and K010 for that core) have been carried out allowing to estimate internal drill core variations and measurement error. From other cores (e.g., 315-C0001E-11H; K003 and K005) only a sample average has been determined and variations are therefore unknown. See text for further explanation.

4.2 Particle size data

The grain size distributions of the investigated core samples determined by a laser particle size are shown in Figure 5. 6. The grain sizes of all the samples range from clay to fine sand, but the volume proportion of fine sand is always smaller than 0.03% (C0006E-8H; vol.-% in the following) and that one of coarse silt is below 0.4% (C0007C-7X). Hence, in the grain size distribution diagram only the three classes from clay to medium silt are recognizable (Figure 5. 6). Overall, the grain size distribution of the recovered sample material is very homogeneous; similar results are presented by Kopf et al. (2011). The clay content ranges from 65 to 80% apart from two exceptions which contain 59 and 86% (C0006E-20X and C0006E-8H section 1), respectively. The content of fine silt amounts to 16-29% again apart from the two exceptions with 34 and 11% (C0006E-20X and C0006E-8H section 1), respectively. Variability of the medium silt content is smaller ranging from 3-7% with cores C0006E-20X and C0006E-8H section 1 representing again the highest and lowest values, respectively.

The cores from the slope apron facies (C0001E-11H and C0004C-8H) show an almost identical grain size distribution (Figure 5. 6). Variations at one core site (C0008) can be small, but they can also be relatively large (C0006) at the prism toe. Even within one core segment (C0006E-8H), the variability is almost as great as over the entire sample set, but yet still in agreement to the overall homogeneous grain size distribution.

5. Geotechnical experiments

Results of (1) single step compression experiments at constant confining pressure and displacement rate („compression tests“; Figure 5. 7), (2) pressure stepping compression experiments at constant displacement rate and increasing confining pressures (“pressure stepping tests”; Figure 5. 8), (3) displacement rate stepping compression experiments at constant confining pressure and increasing displacement rate („rate stepping tests“; Figure 5. 9) will be described in the following. Attained bulk axial compressive strains in the experiments range from ~12% to ~48%, whereas most experiments reached more than 35%. There is one exception, experiment K009, which was deformed until 64% axial strain in three steps (Figure 5. 8) in order to check the stability of the assembly. Because it was a structurally strong sample with continuously increasing deviatoric stress with increasing strain, it was also a test if a peak stress exists not far outside the axial strain range usually applied. This was not the case, but the sample got a strongly bulged shape accompanied by inhomogeneous deformation above 45% strain. That is why step 2 and 3 of the pressure stepping experiment which achieved 49% and 64% bulk strain, respectively, cannot be taken to retrieve the absolute values of the mechanical data.

Bulk strain is composed of the initial compaction strain from pressurization, and either the single deformation step of the compression tests or three or more deformation steps of the pressure or rate stepping tests. Negative strains during piston retraction and stress release between the different steps of the stepping experiments are not accounted for, but can be identified on the stress-strain records (Figure 5. 8 and Figure 5. 9). Deviatoric stresses at peak conditions in the

experiments covered a wide range, which is ~250 kPa-1000 kPa for 1000 kPa confining pressure and a displacement rate of 0.1 mm/min. Of course, at lower confining pressure and usually also at slower displacement rate the deviatoric stress was lower than that, and at faster displacement rate it could be even higher.

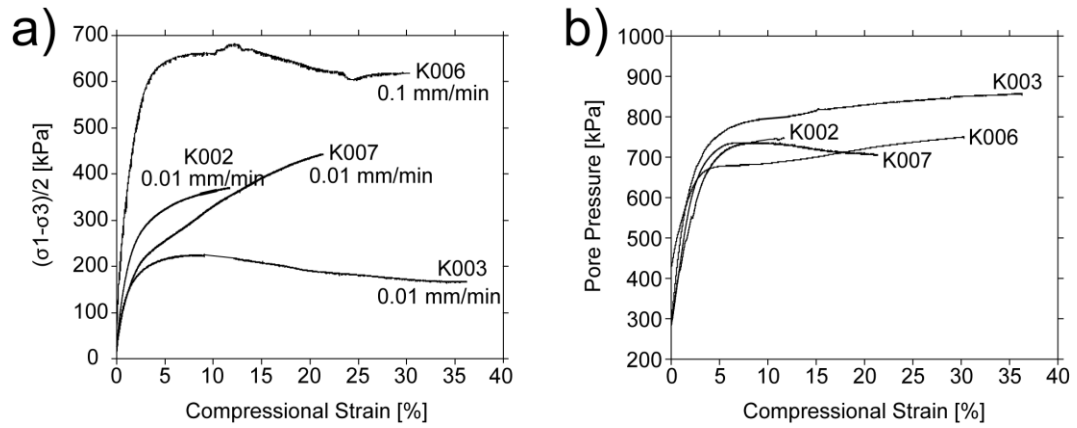


Figure 5. 7: Compression test results (single step axial compression experiments) at constant displacement rates (indicated in a) and constant confining pressure of 1000 kPa. a) Stress/strain-records; sample numbers and displacement rates are indicated. b) Related pore pressure/strain-records; sample numbers are indicated.

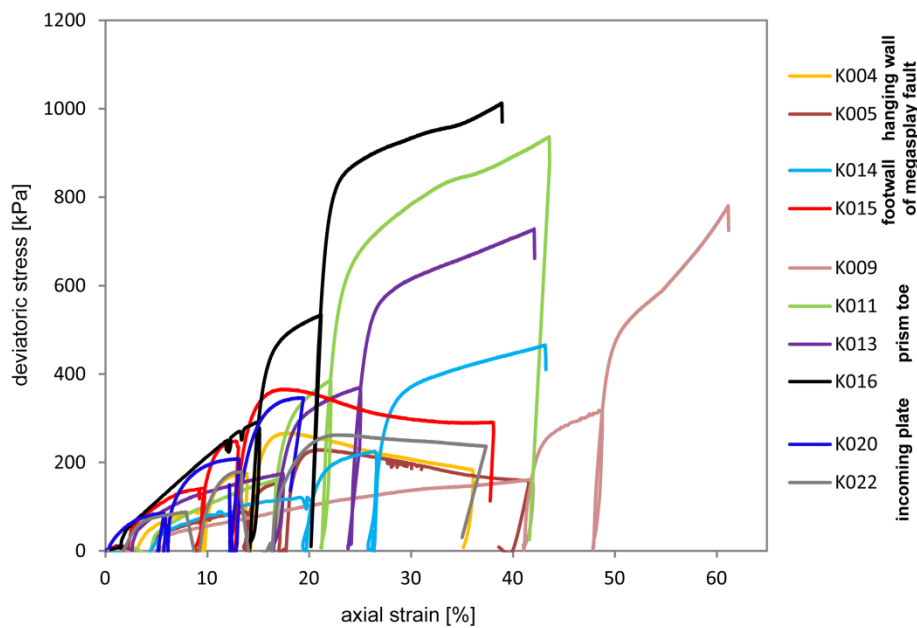


Figure 5. 8: Results of pressure stepping experiments at confining pressures of 400, ~640 and ~1000 kPa and constant displacement rate of 0.01 mm/min (for K020 and K022) or 0.1 mm/min (for all other experiments). Stress/strain-records, experimental sample numbers and original tectonic settings of the samples are indicated. Related pore pressure/strain-records are given in the Appendix A 4, Figure A 4.3. See text for further explanation.

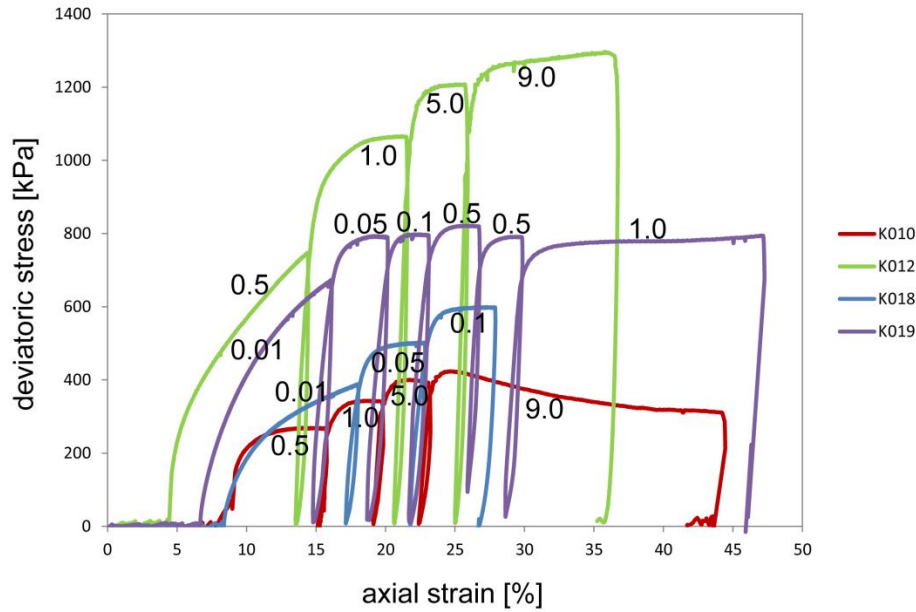


Figure 5. 9: Results of rate stepping experiments at constant confining pressure of 1000 kPa and variable displacement rate. Stress/strain-records, displacement rate steps (in mm/min) and experimental sample numbers are indicated. Related pore pressure/strain-records are given in the Appendix A 4, Figure A 4.4. See text for further explanation.

5.1 Compression tests

The cylindrical samples were deformed at a confining pressure of ~ 1000 kPa and constant displacement rates of 0.1 mm/min or 0.01 mm/min (Figure 5. 7; for all experiments see Table A 4.1). Elastic sample deformation is quite similar in the experiments, but after that stress-strain records develop quite differently. Sample K003 reaches a low deviatoric peak stress of 220 kPa after only 8% strain, while others have much higher stress values (e.g. 680 kPa, K006) or do not show a peak stress, but a continuous stress increase until finite strain (K007; Figure 5. 7a). Sample K003 weakens significantly after peak stress with a stress reduction of ~ 50 kPa until residual strength of 170 kPa (Figure 5. 7a). These characteristics can also be observed in single steps of the pressure and rate stepping tests presented below. Related pore pressure-strain rate records show all a strong increase parallel to the initial linear deviatoric stress increase. At pore pressures of around 600-700 kPa the curves start to bend. Sample K007 with a continuous and strong deviatoric stress increase until finite strain displays an almost constant or a slightly decreasing pore pressure (Figure 5. 7b). For sample K003, which is characterized by weakening after peak stress, the pore pressure further increases at

a more smooth slope. The two other samples (K002 and K006) show slightly increasing pore pressure records until the end of the experiments (Figure 5. 7b), but the finite strain of K002 is only about 12%.

5.2 Pressure and rate stepping tests

Pressure stepping tests were carried out at constant displacement rate of 0.1mm/min and three different confining pressure values of ~400 kPa, 640 kPa and 1000 kPa. Additional experiments with reference material from the incoming Philippine sea plate were conducted at a constant displacement rate of 0.01mm/min and the same pressure steps (K020, K022). From step to step with increasing confining pressure higher deviatoric stresses were achieved. Corresponding to the compression tests they show two groups of contrasting rheological behavior: (1) Samples which fail and weaken afterwards (K004, K005, K015, K022; Figure 5. 8), and (2) samples which do not fail, but show a continuous deviatoric stress increase until finite strain (K009, K011, K013, K014, K016; Figure 5. 8). In K016 a deviatoric stress of more than 1020 kPa could be attained at 1000 kPa confining pressure. The weakening samples (group 1) showed the tendency to approach a residual strength level which is ~290 kPa for K015 and ~160 kPa for K005. Also the pore pressure development corresponds with a few exceptions to what was observed for the two sample groups in the compression tests, i.e. high pore pressure values and a continuous increase in pore pressure for group 1 and lower pore pressure values and decreasing or almost constant pore pressure towards finite strain for group 2 (see Appendix A 4, Figures A 4.3 and A 4.4).

Rate stepping tests were carried out at constant confining pressure of 1000 kPa and from step to step increasing displacement rates from 0.01mm/min to 9 mm/min. With increasing displacement rate there is usually an increasing peak deviatoric stress (e.g., K012, K018; Figure 5. 9). However, there is one exception; K019 showed almost no strength increase or even a decrease from step to step, even though after each step the compressive piston was retracted and the differential stress was brought to a small value close to zero prior to advancing the

compressive piston at an increased rate. The two groups of contrasting rheological behavior occur also in the rate stepping tests. Group 1 with peak stress, weakening and residual strength is represented by K010 (Figure 5. 9). The maximum deviatoric stress of this sample at a displacement rate of 9 mm/min was quite low (~420 kPa). Experiments K012 and K018 with continuously, yet only slightly increasing deviatoric stress towards finite strain belong to group 2. K012 shows a maximum deviatoric stress of ~1300 kPa (Figure 5. 9). The pore pressure development in relation to deviatoric stress very much corresponds to the records of the compression and the pressure stepping tests (see Appendix A 4, Figure A 4.6). However, due to the fast rates of > 0.1 mm/min reaching even 9 mm/min an equilibrium pore pressure during each deformation step cannot be assumed and hence the records of the rate stepping tests partially indicate less well equilibrated pore pressure conditions.

5.3 Effective shear parameters

The effective shear parameters cohesion (C') and angle of internal friction (Φ' ; parameters with prime always indicate effective stress conditions) are determined using the results of the pressure stepping tests. For experiments K004, K005, K015, K020 and K022 σ_1 - σ_3 at max. σ_1'/σ_3' could be determined from the three pressure steps, and the Mohr-Coulomb condition could be plotted (Figure 5. 10, Table 5. 2; Appendix A 4, Figure A 4.5). For the other four pressure stepping experiments a peak strength could not be reached, but the stress-strain records display continuously increasing trends. The German standard DIN 18137 allots 20% axial strain if stress-strain records increase continuously until finite strain without indication of a stress maximum. However, our experiments have significantly smaller strain steps, because above 35-40% bulk strain the sample cylinders transform into bulged shapes making any further deformation more and more inhomogeneous. Hence, in order to get three reliable pressure steps, the first two were kept within ~10% axial strain each. Therefore, we define the criterion σ_1 - σ_3 at max. σ_1'/σ_3' up to 10% axial strain from which the Mohr-Coulomb condition was plotted for the experiments K009, K011, K013, K014 and K016. Because several of the individual pressure steps did not even reach 10% axial

strain (especially step 2 of the records), the stress-strain records were extrapolated for those. Strictly speaking, it is not correct to connect the three different pressure steps from those pressure stepping tests which pass the transition from over- to normally consolidated conditions according to their original overburden (cf. stress paths diagrams in the next paragraph). Nevertheless, the three individual Mohr circles of each pressure step fit very well to the tangential construction of these samples (Figure 5. 10; Appendix A 4, Figure A 4.5). Therefore, we are confident that this connection can be made for the samples and that the error introduced by different consolidation states of the different pressure steps is small.

Table 5. 2: Shear parameters from the pressure stepping experiments. For the experiments K004, K005, K015, K020 and K022 σ_1 - σ_3 at maximum σ_1'/σ_3' , for the other experiments σ_1 - σ_3 at maximum σ_1'/σ_3' within 10% axial strain were used. Related Mohr-Coulomb diagrams are shown in Figure 5. 10 the Appendix A 4, Figure A 4.5. See text for further discussion.

Experiment	K004	K005	K011	K013	K014	K015	K016	K020	K022
core number and section	C0004C-8H-2	C0001E-11H-1	C0007C-7X-1	C0006E-20X-2	C0008A-9H-3	C0008C-7H-8	C0007C-7X-1	C0011D-2H-2	C0012C-4H-5
depth [mbsf]	65.26	91.00	62.89	127.98	76.06	60.96	62.89	33.10	28.90
cohesion [kPa]	25.7	24.9	12.1	29.3	34.1	49.7	4.2	41.0	35.4
angle of friction [°]	27.1	24.6	35.8	32.0	28.7	25.3	40.4	26.3	21.5

The resulting C' - and Φ' -values from the Mohr-Coulomb plots are summarized in Table 5. 2. Experiments K004, K005, K014, K015, K020 and K022 show cohesion values of 25-50 kPa and angles of internal friction of 21.5 - 28.7° in accordance to clay or silty clay (e.g., Carter and Bentley, 1991). K013 agrees in the cohesion (29 kPa), but has a slightly too high internal friction angle of 32°. Internal friction angles of experiments K011 and K016 are much too high for the sample material (> 35°; cf. Carter and Bentley, 1991) and the cohesion of these two samples is low (12 and 4 kPa, respectively). Weak samples display astonishingly consistent Mohr diagrams whether they come from the megasplay area (K004, K015) or the incoming plate (K020), while strong samples, mostly from the prism toe area (e.g., K016), are considerably different (Figure 5. 10; Appendix A 4, Figure A 4.5).

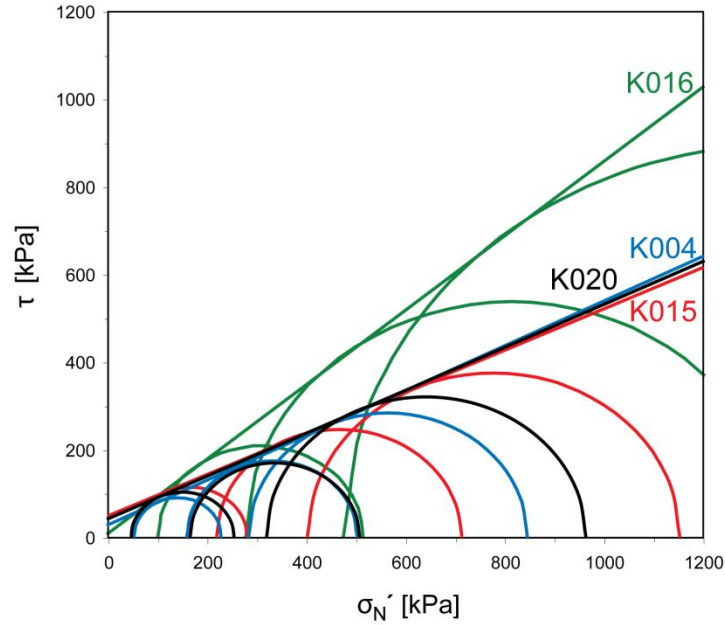


Figure 5. 10: Mohr-Coloumb diagrams from the experiments K004, K015, K016 and K020 with τ (shear stress) versus σ'_N (effective normal stress). Further plots are presented in the Appendix A 4, Figure A 4.5.

5.4 State of consolidation

The detected stress paths of the experiments is used to determine the state of sample consolidation, i.e. if the sample is normally consolidated or overconsolidated at the given deformation conditions (e.g. Lambe and Whitman, 1979; Head, 1998). The sample material suffered different compaction when solely taking the original depths of the cores into account (Table 5. 1) and neglecting any higher overburden previously removed by tectonic or erosive processes or any horizontal compression due to thrusting. Because of the high porosity and pore water content of the samples (Table 5. 1) we assume hydrostatic pressure as minimum pressure estimate. For most of the samples an effective preload of ~ 300 - 800 kPa can be derived in that case. Only the cores C0001E-11H (91 m) and C0006E-20X (128 m) came from significantly greater depth implying

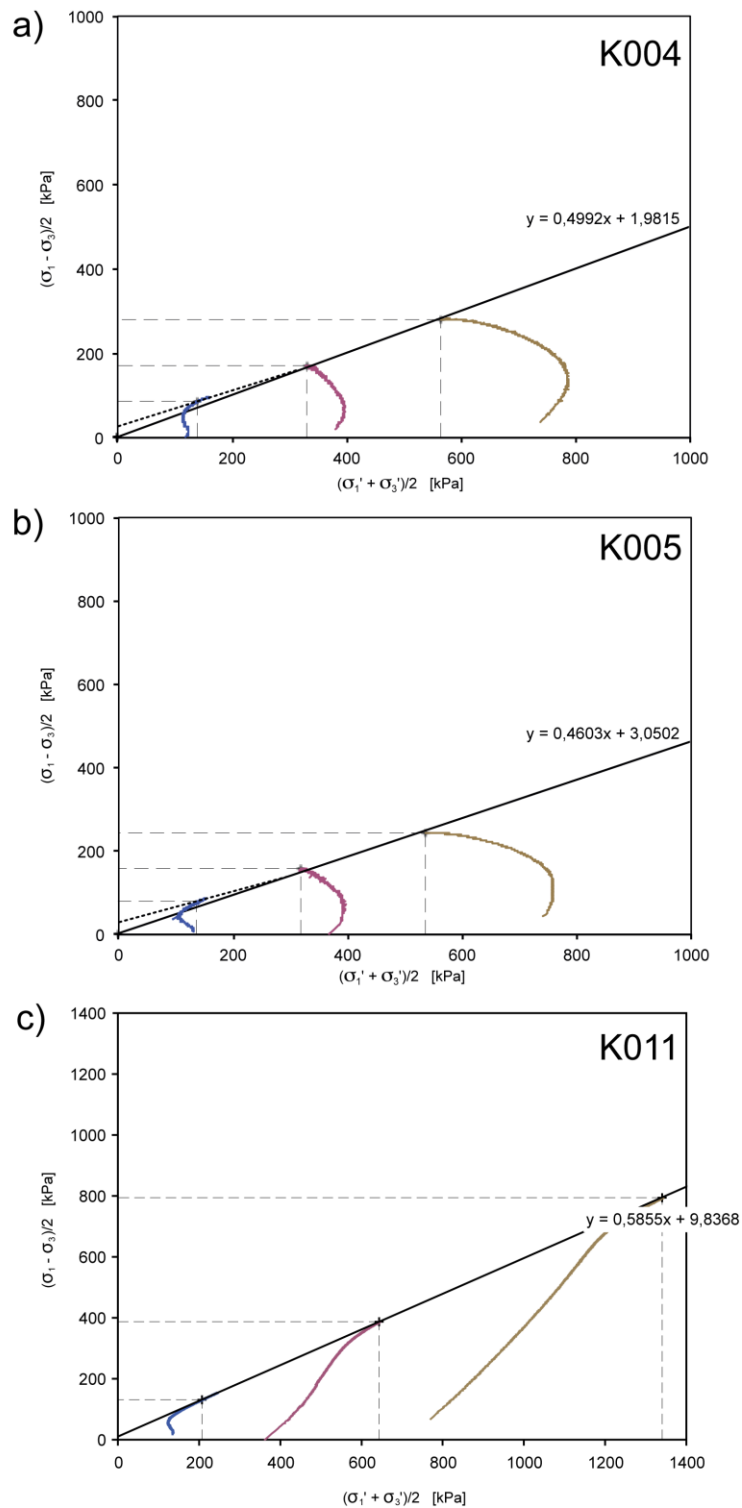


Figure 5. 11: Stress path diagrams with kf-line construction of pressure stepping tests (solid lines and possibly stippled lines) with examples of (a) normal consolidation (K004; 65 mbsf), (b) normal consolidation, but sample came from a depth and hence confining pressure greater than the one of the second and third pressure step with a stress path indicating new experimental consolidation (K005; 91 mbsf), and (c) overconsolidation (K011; 63 mbsf). Equations of kf-lines (solid lines) and the endpoints of different stress paths (depicted by dashed lines) are indicated.

preloads of > 900 kPa and > 1300 kPa, respectively. Experiments in which the transition from over- to normally consolidated conditions was passed, i.e. the consolidation level caused by the original effective confining pressure, were plotted with differing kf-lines (failure envelopes) according to their consolidation state.

The data (Figure 5. 11; Appendix A 4, Figures A 4.6 and A 4.7) show that five experiments indicate normal consolidation in agreement with their known overburden (K004, K013, K015, K020, K022). K005 is also characteristic of normal consolidation, but it displays conditions of new experimental consolidation already for the second pressure step at 640 kPa, while the core sample was recovered from 91 m depth and hence from greater overburden pressure (Figure 5. 11b). In contrast, K011 and K016 (~63 m depth, both from the same core) imply overconsolidation, because all of their stress paths are indicative of overconsolidated conditions. The stress path of sample K014 shows a reverse curvature and can therefore be termed 'quasi-overconsolidated' (Head, 1998). This record corresponds to what has been found for partially saturated compacted clay.

6. Discussion

6.1 Mechanical data

Despite the consistent low depth range and the lithological similarity of the sample cores, the samples studied can be separated into two distinct 'rheological groups', as pointed out before. The first group shows deviatoric peak stress after only a few percent of compressional strain ($< 10\%$) and a continuous stress decrease after peak conditions (Figure 5. 7a; Figure 5. 8; Figure 5. 9). Simultaneous to this decrease there is a pore pressure increase indicating contractant behavior characteristic of structurally weak material (Figure 5. 7b; Appendix A 4, Figures A 4.3 and A 4.4; e.g. Sultan et al., 2004). The second sample group does not weaken at all, but displays strengthening characteristics until finite strain (Figure 5. 7a; Figure 5. 8; Figure 5. 9). These samples are structurally strong (e.g. Sultan et al., 2004), and they are characterized by a

decreasing pore pressure with increasing compressional strain indicating dilatant behavior after a maximum pore pressure at $< 10\%$ strain (Figure 5. 7b; Appendix A 4, Figures A 4.3 and A 4.4). A few samples with somewhat intermediate behavior reach high deviatoric peak stresses after significantly higher strain ($> 10\%$) than the structurally weak samples. They weaken only moderately to a relatively high residual strength level or they show a steady-state like behavior at constant deviatoric stress (e.g., K006; Figure 5. 7a; K018, Figure 5. 9). Their pore pressure/strain-relationships more or less correspond to what is commonly expected for structurally weak material with some slight variations (Figure 5. 7b; Appendix A 4, Figures A 4.3 and A 4.4).

The pore pressure development during the individual CU-tests shows a largely consistent pattern for all the compression and pressure stepping experiments. Structurally weak samples display an increasing pore pressure (contractant behavior) which continues after peak deviatoric stress at or above the confining pressure level of the original sample depth; at low confining pressure (400 kPa) the pore pressure decreases in these samples. The latter suggests that the weakening of the samples at confining pressure lower than that one given by the original overburden is not related to a collapsing pore space. Structurally strong samples display a slightly decreasing pore pressure (dilatant behavior) at or below the confining pressure level of the original sample depth; at higher confining pressures the pore pressure increases in most of these samples. However, pore pressure values are significantly lower than for structurally weak samples.

The rate stepping experiments indicate structurally weak and strong behavior from 0.01 – 9.0 mm/min, i.e. over almost 3 orders of magnitude (Figure 5. 9). Due to the fast rates in the majority of these experiments pore pressure equilibration could not keep up with the changing stress conditions (Appendix A 4) as permeabilities are relatively low (e.g., Dugan and Daigle, 2011; Guo et al., 2011; Saffer et al., 2011). That is why the rate stepping tests with fast displacement rates are not appropriate to derive pore pressure state and development. Nevertheless, the pore pressure disequilibrium could also be relevant in nature, i.e. within the accretionary prism, when deformation is comparably fast. In two of the experiments the stepwise rate increase is always accompanied by an increase in the deviatoric stress level (Figure 5. 9). The structurally weak sample K010 shows

considerable weakening after failure of more than 100 kPa at the fastest displacement rate of 9.0 mm/min. The finite deviatoric stress is below the stress level of the previous steps at 5.0 and 1.0 mm/min, thus showing lower strength at higher displacement rate (Figure 5. 9). Sample K019 shows increasing deviatoric stress with displacement rate increase until 0.5 mm/min and decreasing stress with further increasing displacement rate up to 1.0 mm/min. The sample is relatively strong and does not show the characteristics of a structurally weak sample (Figure 5. 9). Nevertheless, there is almost no deviatoric stress increase above 0.05 mm/min or even a decrease above 0.5 mm/min. This could be interpreted as a kind of strain rate („velocity“) weakening behavior in the displacement rate stepping tests. It is different from what has been observed for the other rate stepping experiments and for single step compression experiments at different displacement rates, for which a faster rate comes along with a higher strength when comparing experiments of otherwise the same conditions and sample material, e.g., K002 and K006 of core sample C0008A-9H (Figure 5. 7). However, further tests are required to constrain this behavior and to check if it might be connected to the structural behavior of the samples.

6.2 Experimental errors

The distinct rheological behavior of the two groups of samples does not depend on the deformation homogeneity, as it is already effective after ~10% axial strain and remains similar until ~45% and even much further (64% strain of sample K009). This is despite significant buckling of the samples above 45% strain. Due to the scarce availability of sample material and short drill core segments we had to carry out experiments with cylindrical samples of a length to diameter ratio of ~1:1, i.e. deviating from the ideal ratio of 2:1. The smaller ratio results in a smaller sample domain of homogeneous deformation. It is also disadvantageous that the end face friction could not be reduced by a lubricant, because of otherwise insufficient coupling of the compression and shear wave transducers used in the experiments (cf. Schumann et al., *subm.*). Nevertheless, there was no effect on the mechanical behavior in comparison to a few experiments on samples with the ideal length to diameter ratio (Figure 5. 8; Appendix A 4, Table A 4.1). Both,

inhomogeneous deformation and small length to diameter ratio may cause a larger error in the mechanical data, especially in the absolute stress values, which are, however, not critical for our interpretations.

Stepping experiments inherently include errors related to peak stress and the failure criterion of the sample (e.g., Head, 1998). It is difficult to exactly terminate the experimental step at peak stress, and in order to avoid severe (micro)structural damage of the samples due to failure, pressure or displacement rate steps were tentatively stopped too early. This was confirmed by high-resolution plots of the stress-strain records around finite strain indicating that all of the experimental steps prior to the final step did not decrease in deviatoric stress and hence did not pass the peak stress (failure point). That means, however, that some of the steps of the stepping tests which turned out to be structurally weak were stopped at still increasing deviatoric stress conditions, causing an underestimation of the maximum stress or Mohr-Coulomb failure condition. This directly affects the shear parameters resulting in lower cohesion and internal friction angles (e.g., Smolczyk, 1980), as well as the stress path diagrams derived from the pressure stepping tests. Errors in stress are also related to the steps of the structurally strong samples in which a peak stress did not occur, and for which an extrapolation to the defined finite strain of 10% was made. As the Mohr-Coulomb plots (Figure 5. 10; Table 5. 2) and also most of the stress paths diagrams of the structurally strong samples (Figure 5. 11) were constructed from three data pairs, and fit quite consistently, we are confident that the stress errors of the data set are small and not critical for the interpretation of our experimental results.

6.3 Pore fluid pressure and its feedback on the mechanical behavior

Saturation and pore pressure (re-)equilibration are primarily time-dependent variables and thus critical for the sample conditions at the beginning and during an experiment. We have verified by a B-check (DIN 18137, part 2) that our re-saturation procedure of the samples at 300 kPa confining pressure and a back pressure of 280 kPa was successful (Appendix A 4). The subsequent increase in

confining pressure to reach the desired deformation conditions was accompanied by squeezing out pore water in the experiments as monitored by the water level in the pore water-burette. This pore water discharge during pressurization and prior to starting the CU-test further assured saturated and also equilibrated pore water conditions for the experiments.

Displacement rates of at least 0.05 mm/min are (according to DIN 18137) slow enough to allow homogeneous deformation at equilibrium pore pressure conditions for CU tests on our samples. Although experiments at 0.1 mm/min could be slightly too fast to fully equilibrate the pore fluid pressure in some of the pressure stepping experiments, the pore fluid pressure development is largely consistent and corresponds to either structurally weak or structurally strong behavior. Thus, all the structurally weak samples in Figure 5. 8 have lower deviatoric stresses than the structurally strong samples while the pore fluid pressure records (e.g., Appendix A 4, Figure A 4.3) show the opposite, all structurally weak samples show higher pore fluid pressures than the structurally strong samples. The records of experiments K002 and K006 are inconsistent (Figure 5. 7). While the faster experiment at 0.1 mm/min (K006) is stronger it shows lower pore fluid pressure. Whether this inconsistency is due to pore pressure disequilibrium in K006 deformed at a slightly too fast rate, due to the transitional structural behavior of K006 and maybe also K002, or due to inhomogeneities in composition or microfabrics cannot be explained based on the available data. Therefore, we have to concede that K006 is exceptional, also in comparison to the other compression tests (Figure 5. 7), and that its pore fluid pressure record might be biased.

The otherwise consistent stress and pore fluid pressure data of the experiments carried out at rates of 0.01 and 0.1 mm/min are in accordance with rather constant intrinsic permeabilities observed by other geotechnical studies on NanTroSEIZE samples at low confining pressures, i.e. down to a depth of ~130 mbsf (Dugan and Daigle, 2011; Guo et al., 2011; Saffer et al., 2011). Towards greater depth, however, the permeability can be pressure dependent (e.g., Guo et al., 2011; Reuschle, 2011; Saffer et al., 2011). This confining pressure or depth- dependence is superposed by a lithological effect; of course, clay-rich sediments are less permeable than clay-poor and sand-rich sediments (e.g., Reuschle, 2011; Rowe et

al., 2011). There might also be a reduction in permeability due to the triaxial stress state, especially at high deviatoric or differential stress (Saffer et al., 2011, Kitajima et al., 2012). We could not find such an effect at the low deviatoric stresses of our experiments.

6.4 Geological significance

The distinct rheological behavior of structurally weak and structurally strong samples has been observed over the range of applied displacement rates and confining pressures in our tests. Hence, it should be effective under comparable natural conditions, and probably also towards higher confining pressures, but this needs to be tested by experiments on samples from greater depth. The elucidation of the controlling parameters and the microphysical processes involved in weakening or strengthening requires microstructural investigations which are beyond the scope of this study. On the base of the presented data, we can spot three reasons which appear to be relevant for the contrasting rheological behavior.

First, the compositional differences: While the rheological differences in the sample set cannot be related to grain or particle size differences (Figure 5. 6), there is some evidence for a dependence on the composition. Structurally weak samples tend to have high contents of organic material and rather low contents of lithics, minerals and submicroscopic material (e.g., K003, K004, K010; Figure 5. 5). In contrast, structurally strong samples are characterized by high contents of lithics and minerals, and low contents of organic material. Surprisingly, ash contents do not show any clear correlation (Figure 5. 5). Structurally weak samples are high in smectite and structurally strong samples are low in smectite and high in quartz+chlorite (Figure 5. 4). Overall, a correlation of composition and rheological behavior is recognizable but not very strong. This is probably because the compositional differences between the samples are small.

Second, the state of consolidation: As has been pointed out before, samples show a range from overconsolidation to normal consolidation (Figure 5. 11; Appendix A 4, Figure A 4.7). The state of consolidation largely correlates with the origin of the samples and their original porosities (Table 5. 1). The young

sediments of the slope apron facies (hanging wall of the megasplay fault) and the slope sediments (footwall of the megasplay fault) are normally consolidated (K004, K015) with a tendency towards underconsolidation (K005). The low degree of consolidation probably results from the high sedimentation rates and the generally low permeabilities of the silty clay sediments (e.g., Screaton et al., 2002; Gamage and Screaton, 2003; Kinoshita et al., 2009). The off-scraped trench deposits at the accretionary prism toe (hanging wall of the main frontal thrust) are overconsolidated (K011, K016). Overconsolidation of these sediments is a consequence of erosion and slumping of the original overburden due to oversteepening of the prism toe (Kinoshita et al., 2009; Screaton et al., 2009), but may additionally be caused by lateral loading (e.g., Feeser et al., 1993). Lateral loading, however, is not fully consistent with the recorded strain in sediments of the prism toe, which generally shows vertical compression and only shifts to horizontal compression about 400 mbsf at Site C0006 (Kitamura et al., 2010). Vertical compression can also be derived from the horizontal alignment of clay minerals as indicated by shape and crystallographic preferred orientation analysis (Milliken and Reed, 2010; Guo et al., 2011; Saffer et al., 2011; Schumann et al., in prep.).

The sediments of the slope apron facies have the highest initial porosities and pore water contents, while the trench deposits have the lowest initial porosities (Table 5. 1). The initial compaction strain representing the consolidation after experimental confining pressure increase and pore pressure relaxation cannot be clearly correlated to the pre-consolidation of the samples, though (for porosity development during the drained sample pressurization see Schumann et al., *subm.*). There are normally consolidated samples from the slope apron facies that suffer the same amount of initial compaction during experimental pressurization as overconsolidated samples from the trench deposits at the same confining pressure: For example, 8% compaction at 1000 kPa confining pressure for samples K010 and K007, or 4% at 400 kPa for the normally consolidated sample K005 from greater depth, but even 5% and 6% for overconsolidated samples K009 and K011, respectively (Appendix A 4).

Overconsolidated samples (K011, K016) tend to be structurally strong, normally consolidated samples are weak (K004, K005). However, there are

several exceptions, especially for the normally consolidated slope sediments from the footwall of the megasplay fault which are weak (K015) and strong (K014). Hence, the state of consolidation is important, but it does not fully explain the distinct rheological behavior of the sample set.

The discrepancies cannot be explained by cementation as well, because cementation should be insignificant in samples from such shallow depth. Whereas most of the drill sites of the NanTroSEIZE section have been reported of being devoid of any cementation only for Site C0001 a weak cementation of relatively shallow samples has been described (Hashimoto et al., 2010; Raimbourg et al., 2011). From this site, however, our weakest samples (K003, K005) come from suggesting no effect on sample strength.

Third, the deformation conditions: The sediments in the accretionary prism toe above the main frontal thrust, i.e. above the plate boundary (Figure 5. 12), are characterized by intense internal deformation with folding and faulting (e.g., Karig and Lundberg, 1990; Moore et al., 1990; Maltman et al., 1993; Moore et al., 2009). This deformation is distributed and tends to make the sediments involved stronger by a process akin to strain hardening. In contrast, the sediments from the slope apron facies in the hanging wall of the megasplay fault (Figure 5. 12; Moore et al., 2009) are less deformed, and only affected by localized faulting (e.g., Milliken and Reed, 2010). As we avoided fault zone material for the experiments, the sampled sediments should show their original properties, i.e. those that are given prior to fault initiation. The sediments from the footwall of the megasplay fault (Figure 5. 12) represent slope sediments similar to those from the slope apron facies of the hanging wall, as they have a common sedimentary origin. Interestingly, these slope sediments are stronger than the samples from the hanging wall of the megasplay fault. If this greater strength is related to the various fault structures (Figure 5. 12; Moore et al., 2009) and hence intense faulting and deformation of the footwall block which could have a hardening effect already on the young slope sediments needs to be further tested on samples from greater depth. Alternatively, hardening could also be a consequence of internal working up due to slumping. Samples used for the experiments, however, have been described as slope sediments and not referred to the mass transport deposits which occur below at greater depth. Hence, the contrasting behavior of

hanging and footwall sediments is likely related to the differing deformation of the sediments in conjunction with the megasplay activity.

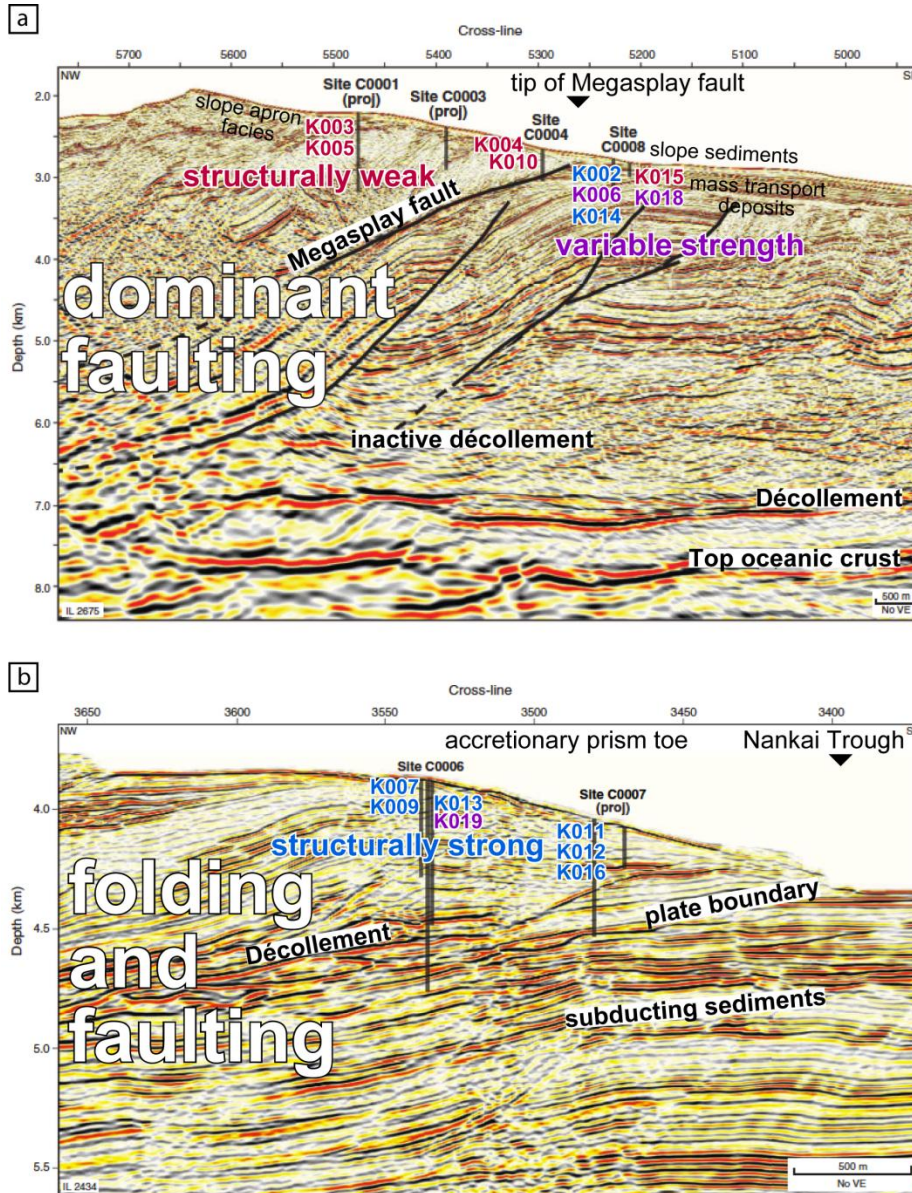


Figure 5. 12: Distribution of structurally weak and strong samples in two detailed seismic sections of (a) the tip of the Megasplay fault including drilling sites C0001, C0004 and C0008 (Moore et al., 2009) and (b) the toe of the accretionary prism including drilling sites C0006 and C0007 (Moore et al., 2009); the positions of these two detailed sections are indicated in Figure 5. 2b and Figure 5. 1 Figure 5. 2c. Strong samples are located in the prism toe, weak samples in the hanging wall of the Megasplay fault. In the footwall of the Megasplay fault, where the upper sedimentary cover consists of slope sediments, the samples show both, weak and strong behavior. The two experimental samples from Sites C0011 and C0012 which are both structurally weak are not shown as they are located 20 km away from the plate boundary on the incoming plate. See text for further discussion.

6.5 Fault activity

The megasplay fault is part of a large out-of-sequence thrust system (e.g., Park et al., 2002b; Gulick et al., 2010) and represents a potential coseismic rupture plane (Park et al., 2002a; Moore et al., 2007; Collot et al., 2008; Bangs et al., 2009). Indeed, recent vitrinite reflectance investigations have shown that both the megasplay fault and the frontal thrust were heated up significantly in the geological past and that this heat can only be attributed to friction by coseismic slip (Sakaguchi et al., 2011). The eastern portion of the megasplay fault, which crosscuts the NanTroSEIZE drilling section, has been continuously active since its inception approximately 1.95 Ma ago (Kimura et al., 2011). Hence, there is a distinct fault activity until present and this activity or at least the formation of this megasplay fault may be related to the rheological difference between the uppermost sediments from its hanging wall and footwall. Experimental constraints from the deeper sediments are needed to verify if these rheological properties extend further downward and if they are responsible for the megasplay development. Nevertheless, the investigated, originally undeformed sediments are crucial for the formation of surface breaks and tsunami generation in the Nankai accretionary prism.

The tests that we have conducted indicate that both, structurally strong and weak materials are present in different tectonic positions, indicating more distributed ductile deformation and folding at the prism toe and fracturing, faulting and so localized deformation in the megasplay zone. It should be emphasized here that our investigations do not say anything about the deformation along existing fault planes, but they are characteristic of the initial deformation of sediment volumes and the onset of fracturing and fault plane development. Based on our mechanical data, we postulate that the deformation of the structurally weak sediments of the megasplay zone in response to a large seismic event is capable of producing surface breaks and generating tsunamis. Hence, the weak sediments of the slope apron facies can be disrupted by runaway fracturing and faulting in the course of a major earthquake, which may propagate at deeper levels by high-velocity weakening along a pre-existing megasplay fault plane, as suggested by Ujiie and Tsutsumi (2010). In contrast, the structurally strong sediments from the accretionary prism toe are more amenable to slow and distributed deformation

(folding), involving large volumes of rock, and hampering the formation of surface breaks. The propagation of tsunami earthquakes is therefore difficult through this zone of structurally strong sediments. The observed difference in rheological behavior could thus be a key for understanding strain concentration and brittle faulting within the rather uniform silty and clayey sedimentary sequence of the Nankai accretionary prism.

7. Conclusions

Soft sediments from the Nankai accretionary prism have a variable strength in triaxial compression displayed by peak deviatoric stresses of approximately 200 kPa to 1000 kPa at 1000 kPa confining pressure and axial displacement rates of 0.01 and 0.1 mm/min. Strong samples occur at the prism toe, while weak samples predominate at and especially above the megasplay fault, located further upslope. Samples from the incoming plate are also weak, but not as weak as the samples from the hanging wall of the megasplay fault. The strongest sediments display the highest internal friction angles and tend to have lower values of cohesion. Accompanying this strength contrast samples show structurally weak and structurally strong behavior, characterized by strain weakening plus contraction and strain hardening plus dilatation, respectively. The actual reason for this contrasting mechanical behavior of the samples remains unclear. The small differences in composition and grain size seem to be unimportant. However, both the variable consolidation state and the deformation of the sediments explain the differences in behavior to a great extent. If these differences in mechanical behavior of the sediments persist also to greater depth, structurally weak sediments may facilitate strain concentration, cause the formation and stabilization of faults, and provoke mechanical runaway situations. Faulting below the upper and middle slope of the accretionary prism is capable of producing surface breaks, and induces associated tsunamis. Deformation of structurally strong sediments at the prism toe tend to involve large rock volumes and lead to strain dissipation. In this type of setting surface breaks are less likely.

Acknowledgements

The Integrated Ocean Drilling Program (IODP) provided the sample material for this study and we greatly acknowledge the Shipboard Parties of IODP Expeditions 315, 316 and 333 aboard D/V CHIKYU for their dedicated work. We appreciate the thorough reviews of Yoshitaka Hashimoto and two anonymous reviewers as well as the helpful comments of Thorsten Becker and an anonymous associate editor which significantly improved the Manuscript. Supported by Deutsche Forschungsgemeinschaft (DFG) through Grant BE1041/28 to J.H.B. and M.S.

References

- Ashi, J., Lallemand, S., Masago, H., and the Expedition 315 Scientists, 2008. NanTroSEIZE Stage 1A: NanTroSEIZE megasplay riser pilot. IODP Prel. Rept. 315. doi:10.2204/iodp.pr.315.2008
- Bangs, N.L.B., Moore, G.F., Gulick, S.P.S., Pangborn, E.M., Tobin, H.J., Kuramoto, S., and Taira, A., 2009. Broad, weak regions of the Nankai megathrust and implications for shallow coseismic slip. *Earth Planet. Sci. Lett.* 284, 44-49. doi:10.1016/j.epsl.2009.04.026
- Beeler, N.M., 2007. Laboratory-observed faulting in intrinsically and apparently weak materials. In: Dixon, T.H. & Moore J.C. (eds.) *The seismogenic zone of subduction thrust faults*. Columbia University Press, New York, pp. 370-449.
- Beeler, N.M., Tullis, T.E., and Weeks, J.D., 1994. The roles of time and displacement in the evolution effect in rock friction. *Geophys. Res. Lett.* 21, 1987-1990.
- Berre, T., 1985. Suggested international code of soil engineering practice for triaxial compression tests. NGI, Oslo.
- Blanpied, M.L., Lockner, D.A. and Byerlee, J.D., 1991. Fault stability inferred from granite sliding experiments at hydrothermal conditions. *Geophys. Res. Lett.* 18, 609-612.
- Brace, W.F. and Byerlee, J.D., 1966. Stick-slip as a mechanism for earthquakes. *Science* 153, 990-992.
- Byerlee, J., 1978. Friction of rocks. *Pure Appl. Geophys.* 116, 615-626.
- Byrne, D.E., Davis, D.M., and Sykes, L.R., 1988. Local and maximum size of thrust earthquakes and the mechanics of the shallow region of subduction zones. *Tectonics* 7, 833-857.
- Carter, M. and Bentley, S., 1991. *Correlations of soil properties*. Penetech Press Publishers, London, 130 pp.
- Chester, F.M., 1994. Effects of temperature on friction: Constitutive equations and experiments with quartz gouge. *J. Geophys. Res.* 99, 7247-7262.
- Cloos, M., 1982. Flow melanges: Numerical modeling and geologic constraints on their origin in the Franciscan subduction complex, California. *Geol. Soc. Amer. Bull.* 93, 330-345
- Collot, J.Y., Agudelo, W., Ribodetti, A. and Marcaillou, B., 2008. Origin of a crustal splay fault and its relation to the seismogenic zone and underplating at the erosional north Ecuador – south Colombia oceanic margin. *J. Geophys. Res.* 113, B12102.
- Dieterich, J., 1972. Time-dependence of rock friction. *J. Geophys. Res.* 77, 3690-3697.

- Dieterich, J.H., 1979. Modeling of rock friction. 1. Experimental results and constitutive equations. *J. Geophys. Res.* 84, 2161-2168.
- DIN 18137, 1990. Testing procedures and apparatus: Triaxial test, part 2 (German standard). Berlin, Deutsches Institut für Normung.
- Dixon, T.H. and Moore J.C., 2007. The seismogenic zone of subduction thrust faults. Columbia University Press, New York 665 pp.
- Dugan, B., and Daigle, H., 2011. Data report: permeability, compressibility, stress state, and grain size of shallow sediments from Sites C0004, C0006, C0007, and C0008 of the Nankai accretionary complex. In Kinoshita, M., Tobin, H., Ashi, J., Kimura, G., Lallement, S., Screaton, E.J., Curewitz, D., Masago, H., Moe, K.T., and the Expedition 314/315/316 Scientists, Proc. IODP, 314/315/316: Tokyo (IODP Management International, Inc.). doi:10.2204/iodp.proc.314315316.208.2011
- Feeser, V., Moran, K. and Brückmann, W., 1993. Stress-regime-controlled yield and strength behavior of sediment from the frontal part of the Nankai accretionary prism. In: Hill, I.A., Taira, A., Firth, J.V. et al. (eds.). Proceedings of the Ocean Drilling Program, Scientific Results 131, 261-273.
- Gamage, K. and Screaton, E., 2003. 18. Data report: Permeabilities of Nankai accretionary prism sediments. In: Mikada, H., Moore, G.F., Taira, A., Becker, K., Moore, J.C., and Klaus, A. (eds.) Proceedings of the Ocean Drilling Program, Scientific Results 190/196, 1-22 (online).
- Goldsby, D.L., and Tullis, T.E., 2002. Low frictional strength of quartz rocks at subseismic slip rates. *Geophys. Res. Lett.* 29, 1844; doi: 10.1029/2002GL015240.
- Gulick, S.P.S., Bangs, N.L.B., Moore, G.F., Ashi, J., Martin, K.M., Sawyer, D.S., Tobin, H.J., Kuramoto, S., and Taira, A., 2010. Rapid forearc basin uplift and megasplay fault development from 3D seismic images of Nankai margin off Kii Peninsula, Japan. *Earth Planet. Sci. Lett.* 300, 55-62. doi:10.1016/j.epsl.2010.09.034
- Guo, J. and Underwood, M., 2012. Data Report: Clay Mineral Assemblages from the Nankai Trough and Kumano Basin, IODP Expedition 315 and 316, NanTroSEIZE Stage 1. In: Kinoshita, M., Tobin, H., Ashi, J., Kimura, G., Lallement, S., Screaton, E.J., Curewitz, D., Masago, H., Moe, K.T., and the Expedition 314/315/316 Scientists, Proc. IODP, 314/315/316. doi:10.2204/iodp.proc.314315316.202.2012
- Guo, J., Likos, W.J., Underwood, M.B., Skarbak, R.M., Adamson, N., and Saffer, D., 2011. Data report: consolidation characteristics of sediments from Sites C0002, C0006, and C0007, IODP Expeditions 315 and 316, NanTroSEIZE Stage 1. In Kinoshita, M., Tobin, H., Ashi, J., Kimura, G., Lallement, S., Screaton, E.J., Curewitz, D., Masago, H., Moe, K.T., and the Expedition 314/315/316 Scientists, Proc. IODP, 314/315/316: Washington, DC (IODP Management International, Inc.). doi:10.2204/iodp.proc.314315316.213.2011

- Hashimoto, Y., Tobin, H., and Knuth, M., 2010. Velocity-porosity relationship for slope apron and accreted sediments in the Nankai Trough Seismogenic Zone Experiment, Integrated Ocean Drilling Program Expedition 315, Site C0001. *Geochem. Geophys., Geosys.* 11, Q0AD05, doi:10.1029/2010GC003217
- Head, K.H., 1998. *Manual of soil laboratory testing, volume 3: Effective stress tests.* Second edition, Wiley and Sons, Chichester, 428 pp.
- Henry, P., Kanamatsu, T., Moe, K., and the Expedition 333 Scientists, 2012. NanTroSEIZE Stage 2: Subduction Inputs 2 and Heat Flow. *Proceedings IODP, Volume 333.* IODP Management International, Inc., Tokyo. doi:10.2204/iodp.proc.333.104.2012
- Hyndman, R.D. and Wang, K., 1993. Thermal constraints on the zone of major thrust earthquake failure: The Cascadia subduction zone. *J. Geophys. Res.* 98, 2039-2060.
- Hyndman, R.D., Yamano, M. and Oleskevich, D.A., 1997. The seismogenic zone of subduction thrust faults. *Isl. Arc* 6(3), 244-260.
- Ike, T., Moore, G.F., Kuramoto, S., Park, J.-O., Kaneda, Y., and Taira, A., 2008. Variations in sediment thickness and type along the northern Philippine Sea plate at the Nankai Trough. *Isl. Arc*, 17(3), 342–357. doi:10.1111/j.1440-1738.2008.00624.x
- Karig, D.E., and Lundberg, N., 1990. Deformation bands from the toe of the Nankai accretionary prism. *J. Geophys. Res.* 95(B6), 9099-9109.
- Kimura, G., Kitamura, Y., Hashimoto, Y., Yamaguchi, A., Shibata, T., Ujiie, K., and Okamoto, S., 2007. Transition of accretionary wedge structures around the up-dip limit of the seismogenic subduction zone. *Earth Planet. Sci. Lett.* 225(3–4):471–484; doi:10.1016/j.epsl.2007.01.005.
- Kimura, G., Moore, G.F., Strasser, M., Sreaton, E., Curewitz, D., Streiff, C., and Tobin, H., 2011. Spatial and temporal evolution of the megasplay fault in the Nankai Trough. *Geochem. Geophys. Geosyst.* 12, Q0A008. doi:10.1029/2010GC003335
- Kimura, G., Sreaton, E.J., Curewitz, D., and the Expedition 316 Scientists, 2008. NanTroSEIZE Stage 1A: NanTroSEIZE shallow megasplay and frontal thrusts. *IODP Prel. Rept.*, 316. doi:10.2204/iodp.pr.316.2008.
- Kinoshita, M., Tobin, H., Ashi, J., Kimura, G., Lallemand, S., Sreaton, E.J., Curewitz, D., Masago, H., Moe, K.T., and the Expedition 314/315/316 Scientists, 2009. NanTroSEIZE Stage 1: Investigations of Seismogenesis, Nankai Trough, Japan. *Proc. IODP, 314/315/316: Washington, DC (IODP Management International, Inc.)*. doi:10.2204/iodp.proc.314315316.2009
- Kitajima, H., Chester, F.M., and Biscontin, G., 2012. Mechanical and hydraulic properties of Nankai accretionary prism sediments: effect of stress path. *Geochem. Geophys. Geosys.* 13, Q0AD27. doi:10.1029/2012GC004124

- Kitamura, Y., Kanamatsu, T., and Zhao, X., 2010. Structural evolution in accretionary prism toe revealed by magnetic fabric analysis from IODP NanTroSEIZE Expedition 316. *Earth Planet. Sci. Lett.* 292, 221-230, doi:210.1016/j.epsl.2010.1001.1040.
- Kitamura, Y., Sato, K., Ikesawa, E., Ikehara-Ohmori, K., Kimura, G., Kondo, H., Ujiie, K., Onishi, C.T., Kawabata, K., Hashimoto, Y., Mukoyoshi, H., and Masago, H., 2005, Melange and its seismogenic roof decollement: A plate boundary fault rock in the subduction zone - An example from the Shimanto Belt, Japan. *Tectonics* 24, TC5012, doi: 10.1029/2004TC001635.
- Kopf, A., Strasser, M., Monsees, N., Underwood, M.B., and Guo, J., 2011. Data report: particle size analysis of sediments recovered during IODP Expeditions 315 and 316, Sites C0001–C0008, Nankai Trough forearc, off Japan. In Kinoshita, M., Tobin, H., Ashi, J., Kimura, G., Lallemand, S., Screatton, E.J., Curewitz, D., Masago, H., Moe, K.T., and the Expedition 314/315/316 Scientists, Proc. IODP, 314/315/316: Washington, DC (IODP Management International, Inc.). doi:10.2204/iodp.proc.314315316.207.2011
- Laberg, J.S., Vorren, T.O., Mienert, J., Haflidason, H., Bryn, P., & Lien, R., 2003. Preconditions leading to the Holocene Trænadjupet Slide offshore Norway, in Locat, J., and Mienert, J. (eds.), *Advances in Natural and Technological Hazards Research*, Kluwer, Dordrecht, pp. 247-254.
- Lambe, T.W. and Whitman, R.V., 1979. *Soil mechanics (SI edition)*. Wiley and Sons, New York.
- Linker, M.F., and Dieterich, J.H., 1992. Effects of variable normal stress on rock friction: Observations and constitutive relations. *J. Geophys. Res.* 97, 4923-4940.
- Logan, J.M., & Rauenzahn, K.A., 1987. Frictional dependence of gouge mixtures of quartz and montmorillonite on velocity, composition and fabric. *Tectonophysics*, 144, 87-108.
- Lupini, J.F., Skinner, A.E., & Vaughan, P.R., 1981. The drained residual strength of cohesive soils. *Geotechnique*, 31, 181-213.
- Maltman, A.J., Byrne, T., Karig, D.E., Lallemand, S., Knipe, R., and Prior, D., 1993. Deformation structures at site 808, Nankai accretionary prism, Japan. In: Hill, I.A., Taira, A., Firth, J.V. et al. (eds.). *Proceedings of the Ocean Drilling Program, Scientific Results* 131, 123-133.
- Marone, C. and Scholz, C.H., 1988. The depth of seismic faulting and the upper transition from stable to unstable slip regimes. *Geophys. Res. Lett.* 15, 621–624.
- Milliken, K.L., and Reed, R.M., 2010. Multiple causes of diagenetic fabric anisotropy in weakly consolidated mud, Nankai accretionary prism, IODP Expedition 316. *J. Struct. Geol.* 32, 1887-1898.

- Miyazaki, S., and Heki, K., 2001. Crustal velocity field of southwest Japan: subduction and arc-arc collision. *J. Geophys. Res.* 106(B3), 4305–4326. doi:10.1029/2000JB900312
- Moore G.F., Park, J.-O., Bangs, N.L., Gulick, S.P., Tobin, H.J., Nakamura, Y., Sato, S., Tsuji, T., Yoro, T., Tanaka, H., Uraki, S., Kido, Y., Sanada, Y., Kuramoto, S., and Taira, A., 2009. Structural and seismic stratigraphic framework of the NanTroSEIZE Stage 1 transect. In Kinoshita, M., Tobin, H., Ashi, J., Kimura, G., Lallement, S., Screaton, E.J., Curewitz, D., Masago, H., Moe, K.T., and the Expedition 314/315/316 Scientists, *Proc. IODP, 314/315/316: Washington, DC (IODP Management International, Inc.)*. doi:10.2204/iodp.proc.314315316.102.2009
- Moore, G.F., Bangs, N.L., Taira, A., Kuramoto, S., Pangborn, E., and Tobin, H.J., 2007. Three-dimensional splay fault geometry and implications for tsunami generation. *Science*, 318, 1128-1131. doi:10.1126/science.1147195
- Moore, G.F., Shipley, T.H., Stoffa, P.L., Karig, D.E., Taira, S., Kuramoto, H., Tokuyama, K., and Suyehiro, K., 1990. Structure of the Nankai Trough accretionary zone from multichannel seismic-reflection data. *J. Geophys. Res.* 95, 8753-8765.
- Moore, G.F., Taira, A., Klaus, A., Becker, L., Boeckel, B., Cragg, B.A., Dean, A., Fergusson, C.L., Henry, P., Hirano, S., Hisamitsu, T., Hunze, S., Kastner, M., Maltman, A.J., Morgan, J.K., Murakami, Y., Saffer, D.M., Sanchez-Gomez, M., Screaton, E.J., Smith, D.C., Spivack, A.J., Steurer, J., Tobin, H.J., Ujiie, K., Underwood, M.B., Wilson, M., 2001. New insights into deformation and fluid flow processes in the Nankai Trough accretionary prism: Results of Ocean Drilling Program Leg 190. *Geochem. Geophys. Geosys.* 2, 2001GC000166.
- Moore, J.C. and Saffer, D.M., 2001. Updip limit of the seismogenic zone beneath the accretionary prism of southwest Japan: An effect of diagenetic to low-grade metamorphic processes and increasing effective stress. *Geology* 29, 183 - 186.
- Morgan, J.K., Ramsey, E.B., Ask, M.V.S., 2007. Deformation and mechanical strength of sediments at the Nankai subduction zone. In: Dixon, T.H. & Moore J.C. (eds.) *The seismogenic zone of subduction thrust faults*. Columbia University Press, New York, pp. 210-256.
- Okino, K., Shimakawa, Y., and Nagaoka, S., 1994. Evolution of the Shikoku Basin. *J. Geomagn. Geoelectr.*, 46(6):463–479
- Oleskevich, D.A., Hyndman, R.D. and Wang, K., 1999. The updip and downdip limits to great subduction earthquakes: Thermal and structural models of Cascadia, south Alaska, SW Japan, and Chile. *J. Geophys. Res.* 104(B7), 14965-14991.
- Park, J.-O., Tsuru, T., Kodaira, S., Cummins, P.R., and Kaneda, Y., 2002a. Splay Fault Branching Along the Nankai Subduction Zone. *Science* 297, 1157-1160.
- Park, J.-O., Tsuru, T., Takahashi, N., Hori, T., Kodaira, S., Nakanishi, A., Miura, S., and Kaneda, Y., 2002b. A deep strong reflector in the Nankai accretionary

- wedge from multichannel seismic data: implications for underplating and interseismic shear stress release. *J. Geophys. Res.* 107(B4), 2061, doi:10.1029/2001JB000262.
- Reuschle, T., 2011. Data report: permeability measurements under confining pressure, Expeditions 315 and 316, Nankai Trough. In Kinoshita, M., Tobin, H., Ashi, J., Kimura, G., Lallement, S., Screaton, E.J., Curewitz, D., Masago, H., Moe, K.T., and the Expedition 314/315/316 Scientists, Proc. IODP, 314/315/316: Washington, DC (IODP Management International, Inc.). doi:10.2204/iodp.proc.314315316.205.2011
- Rice, J.R., and Ruina, A.L., 1983. Stability of steady frictional slipping. *J. Appl. Mech.* 50, 343–349.
- Rowe, K., Screaton, E., Guo, J., and Underwood, M.B., 2011. Data report: permeabilities of sediments from the Kumano Basin transect off Kii Peninsula, Japan. In Kinoshita, M., Tobin, H., Ashi, J., Kimura, G., Lallement, S., Screaton, E.J., Curewitz, D., Masago, H., Moe, K.T., and the Expedition 314/315/316 Scientists, Proc. IODP, 314/315/316: Washington, DC (IODP Management International, Inc.). doi:10.2204/iodp.proc.314315316.211.2011
- Saffer, D., Guo, J., Underwood, M.B., Likos, W., Skarbek, R.M., Song, I., and Gildow, M., 2011. Data report: consolidation, permeability, and fabric of sediments from the Nankai continental slope, IODP Sites C0001, C0008, and C0004. In Kinoshita, M., Tobin, H., Ashi, J., Kimura, G., Lallement, S., Screaton, E.J., Curewitz, D., Masago, H., Moe, K.T., and the Expedition 314/315/316 Scientists, Proc. IODP, 314/315/316: Washington, DC (IODP Management International, Inc.). doi:10.2204/iodp.proc.314315316.218.2011
- Saffer, D.M. and Marone, C., 2003. Comparison of smectite- and illite-rich gouge frictional properties: application to the updip limit of the seismogenic zone along subduction megathrusts. *Earth Planet. Sci. Lett.* 215, 219-235.
- Sakaguchi, A., Chester, F., Curewitz, D., Fabbri, O., Goldsby, D., Kimura, G., Li, C.-F., Masaki, Y., Screaton, E.J., Tsutsumi, A., Ujiie, K., and Yamaguchi, A., 2011. Seismic slip propagation to the updip end of plate boundary subduction interface faults: vitrinite reflectance geothermometry on Integrated Ocean Drilling Program NanTroSEIZE cores. *Geology*, 39, 395-398. doi:10.1130/G31642.1
- Scholz, C.H., 1998. Earthquakes and friction laws. *Nature* 391, 37-42.
- Scholz, C.H., 2002. The mechanics of earthquakes and faulting. Cambridge University Press, 464p.
- Schumann, K., Stipp, M., Behrmann, J.H., Klaeschen, D. and Schulte-Kortnack, D., (subm.). P- and s- wave velocity measurements of water-rich sediments from Nankai Trough, Japan. *J. Geophys. Res.*
- Screaton E, Saffer D, Henry P, Hunze S, and the Leg 190 Shipboard Science Party, 2002. Porosity loss within the underthrust sediments of the Nankai accretionary complex: Implications for overpressures. *Geology* 30, 19-22.

- Screaton, E., Kimura, G., Curewitz, D., Moore, G., Chester, F., Fabbri, O., Fergusson, C., Girault, F., Goldsby, D., Harris, R., Inagaki, F., Jiang, T., Kitamura, Y., Knuth, M., Li, C.-F., Claesson Liljedahl, L., Louis, L., Milliken, K., Nicholson, U., Riedinger, N., Sakaguchi, A., Solomon, E., Strasser, M., Su, X., Tsutsumi, A., Yamaguchi, A., Ujiie, K., and Zhao, X., 2009. Interactions between deformation and fluids in the frontal thrust region of the NanTroSEIZE transect offshore the Kii Peninsula, Japan: Results from IODP Expedition 316 Sites C0006 and C0007. *Geochem. Geophys. Geosys.* 10, Q0AD01.
- Seno, T., Stein, S., and Gripp, A.E., 1993. A model for the motion of the Philippine Sea plate consistent with NUVEL-1 and geological data. *J. Geophys. Res.* 98(B10):17941–17948. doi:10.1029/93JB00782
- Smolczyk, U., 1980. *Grundbau Taschenbuch*. 3. edition, part 1. Verlag von Wilhelm Ernst & Sohn, Berlin, München, Düsseldorf.
- Sultan, N., Cochonat, P., Canals, M., Cattaneo, A., Dennielou, B., Haflidason, H., Laberg, J.S., Long, D., Mienert, J., Trincardi, F., Urgeles, R., Vorren, T.O. & Wilson, C., 2004. Triggering mechanisms of slope instability processes and sediment failures on continental margins; a geotechnical approach. In: COSTA, continental slope stability; a contribution to the Energy, Environment and Sustainable Development Programme FP5 of the European Commission, number EVK3-CT-1999-00006, Elsevier, Amsterdam, pp. 291-321.
- Terzaghi, K., Peck, R.B., and Mesri, G., 1996. *Soil mechanics in engineering practice*. John Wiley & Sons, 592 p.
- Tichelaar, B.W. and Ruff, L.J., 1993. Depth of seismic coupling along subduction zones. *J. Geophys. Res.* 98(B2), 2017-2037.
- Tobin, H., and Kinoshita, M., 2006. NanTroSEIZE: the IODP Nankai Trough Seismogenic Zone Experiment. *Sci. Drill.*, 2:23–27. doi:10.2204/iodp.sd.2.06.2006
- Tobin, H., and Kinoshita, M., 2007. The IODP Nankai Trough Seismogenic Zone Experiment. In *Reports on Deep Earth Sampling and Monitoring*. *Sci. Drill. Spec. Issue*, 1:39–41. doi:10.2204/iodp.sd.s01.30.2007
- Tobin, H., Kinoshita, M., Ashi, J., Lallemand, S., Kimura, G., Screaton, E.J., Moe, K.T., Masago, H., Curewitz, D., and the Expedition 314/315/316 Scientists, 2009. NanTroSEIZE Stage 1 expeditions: introduction and synthesis of key results. In Kinoshita, M., Tobin, H., Ashi, J., Kimura, G., Lallemand, S., Screaton, E.J., Curewitz, D., Masago, H., Moe, K.T., and the Expedition 314/315/316 Scientists, *Proc. IODP, 314/315/316: Washington, DC (IODP Management International, Inc.)*. doi:10.2204/iodp.proc.314315316.101.2009
- Tullis, T.E., and Weeks, J.D., 1986. Constitutive behavior and stability of frictional sliding of granite. *Pure Appl. Geophys.* 124, 383-414.
- Ujiie, K., and Tsutsumi, A., 2010. High-velocity frictional properties of clay-rich fault gouge in a megasplay fault zone, Nankai subduction zone. *Geophys. Res. Lett.* 37, L24310, doi:10.1029/2010GL046002.

- Underwood, M.B., 2007. Sediment inputs to subduction zones: why lithostratigraphy and clay mineralogy matter. In: Dixon, T.H. & Moore J.C. (eds.) *The seismogenic zone of subduction thrust faults*. Columbia University Press, New York, pp. 42-85.
- Vardoulakis, I., 1979. Bifurcation analysis of the triaxial test on sand samples. *Acta Mech.* 32, 35-54.
- von Huene, R., 1984. Tectonic processes along the front of modern convergent margins- research of the past decade. *Ann. Rev. Earth Planet. Sci.* 12, 359-382.
- Vrolijk, P., 1990. On the mechanical role of smectite in subduction zones. *Geology* 18, 703-707.
- Wallace, L.M. et al., 2009. Characterizing the seismogenic zone of a major plate boundary subduction thrust: Hikurangi Margin, New Zealand. *Geochem. Geophys. Geosys.* 10, Q10006.

6 Synopsis – conclusion – outlook

6.1 Synopsis

Large earthquakes are produced by thrust faulting in subduction zones (e.g. Mukyoshi et al., 2006; Beeler 2007). In some subductions zones, earthquakes are followed by tsunamis, while in other locations, large-scale aseismic slip is common (Beeler 2007). In the Nankai Trough, the seismic history can be traced back to A.D. 684 (e.g. Ando 1975; Tobin and Kinoshita 2006). During large earthquake events, the entire width of the seismogenic zone ruptured and thus the seismogenic zone is well defined and the rupture area of future earthquakes is predictable (Tobin and Kinoshita 2006). Earthquakes in the Nankai Trough area repeatedly produced devastating tsunamis (e.g. Park et al., 2002; Wang and Hu 2006; Kimura et al., 2011). The mechanical, compositional and microstructural properties of rocks are important to understand seismic faulting. Since the seismogenic zone lies in depths accessible by deep-sea drilling, the Nankai accretionary prism is an excellent natural laboratory to investigate subduction zone earthquakes and to improve the understanding of the conditions leading to seismic stick-slip behavior rather than aseismic stable slip behavior. To answer this seemingly simple question, knowledge on the physical, geotechnical and structural properties of the sediments and sedimentary rocks is essential (Carson et al., 1982; Moore and Vrolijk 1992; Erickson and Jarrard 1998; Bilek and Lay 1999; Morgan et al., 2007; Moore and Saffer 2001). Such information cannot be obtained from seismological observation alone. Fundamental parameters such as shear strength, internal angle of friction, cohesion, elastic moduli, can only be determined by deformation experiments (Beyerlee 1978). Especially triaxial testing yields important information on the micromechanics of deformation, brittle or plastic yield and residual stress (e.g. Laberg et al., 2003; Sultan et al., 2004; Morgan et al., 2007), which are important to understand faulting in the clay-dominated sediments (e.g. Stipp et al., 2013; manuscript #4). When reaching peak deviatoric stress during triaxial deformation, the sediments' compressibility and the pore pressure increases. Materials, showing significant drop in shear stress and increasing pore pressure are characterized as structurally weak (Laberg et al., 2003), while materials showing constant or increasing residual stress are

characterized as structurally strong (Sultan et al., 2004). Structurally weak materials develop shear bands and may be unstable, while the latter are stable under the same conditions (Laberg et al., 2003). Distinguishing the two rheological groups allows to evaluate the slip behavior of the Nankai forearc rocks. Drill core samples obtained during IODP Expeditions 315, 316 and 333 were used in this thesis to determine the geotechnical and microstructural characteristics of the sediments from the Nankai accretionary prism. During IODP expedition 315 and 316, the frontal thrust region and the vicinity of the major active splay fault were sampled, while sediments of the incoming Philippine Sea plate were sampled during IODP Expedition 333. Shipboard scientists measured the physical properties of the drilled sediments (Expedition 315 Scientists 2009; Expedition 316 Scientist 2009a-d, Expedition 333 Scientists 2012a, 2012b). Fundamental geotechnical parameters such as strength, stress paths and pore pressure evolution were measured during undrained triaxial deformation experiments (Stipp et al. 2013, manuscript #4). Sonic velocities measured during experimental deformation were related to the geotechnical parameters. For this, piezoelectric bender elements were added to the pistons of the triaxial apparatus allowing to monitor sonic velocity changes during triaxial deformation.

The main outcome of the sonic velocity measurements is that it is possible to measure p- and s-wave velocities during triaxial testing. The initial p-wave velocities (V_p) of the unconsolidated sediments lie in the range between ~ 1450 m/s and ~ 1650 m/s prior to the experimental deformation. During the experimental deformation, V_p is rather constant or increases slightly. P-wave velocities approximately similar to the V_p of water (1500 m/s) indicate that the sediments are water saturated and unconsolidated. Velocities for unconsolidated sediments were measured e.g. by Hamilton (1970) and are similar to measurements of Kinoshita et al. (2009), implemented during logging while drilling of Hole C0001D. V_p far below 1500 m/s in the experiments is attributed to incomplete pore water saturation. Rather constant to slightly increasing V_p during the undrained deformation is attributed to constant pore space and thus constant pore water content, which is thought to be the dominant control on V_p (Wyllie et al., 1956; Erickson and Jarrard 1998; Mavko et al., 1998). In contrast, shear wave velocity (V_s) strongly increases during deformation, attributed to

enhanced grain-grain contacts and microstructural rearrangement (Wyllie et al., 1956; Bourbié et al., 1987; Stoll 1989; Erickson and Jarrard 1998; Gettemy and Tobin 2003; Mondol et al., 2007; Hashimoto et al., 2011; Raimbourg et al., 2011). Different V_p levels observed for the accretionary prism toe and the megasplay fault setting are attributed to variable starting porosities and structural differences, while V_s is similar in the tectonic settings.

Since the experimental deformation directly influences V_p and V_s , Pickett (1963) and Tsuji et al. (2011) introduced the V_p/V_s ratio as indicator for the state of consolidation. In this study, however, it was not possible to distinguish the samples from the different tectonic settings by the V_p/V_s ratio, although V_p shows variation. The differences between the tectonic settings were revealed through calculating the shear, bulk, and elastic moduli.

The lowest moduli were determined for the incoming plate sediments, and the sediments from the hanging wall of the megasplay fault, while the samples from the accretionary prism toe have the highest values. In accordance to the erosional material removal reported for Sites C0006, C0007 and C0008 (Screaton et al., 2009; Kimura et al., 2011; Conin et al., 2011; and Strasser et al., 2011), my acoustic data indicate overconsolidation for the sediments of the accretionary prism toe (Site C0006 and C0007) and a lesser degree of consolidation for the footwall of the megasplay fault (C0008). Samples from the hanging wall of the megasplay fault and the incoming plate are normally consolidated. This observation is supported by triaxial test results of Stipp et al. (2013).

For calculation of the shear and bulk moduli, the sample material was assumed to be isotropic (e.g. Johnston and Christensen 1993). Fine-grained clay minerals are deposited as flocculated aggregates with isotropic orientation (e.g. Kranck 1980, 1986). Anisotropy cannot be excluded for the samples, since natural compacted sediments were used as starting materials and are deformed up to ~64% axial shortening strain (Stipp et al., 2013, manuscript #4). Microstructural analyses indicate preferred alignment of clay minerals in the topmost sediments (Manuscript #2), and data published by Miilliken and Reed (2010); Saffer et al. (2011); Raimbourg et al. (2011).

Not only the velocities are anisotropic, showing highest velocities parallel to the basal plane and lowest velocities parallel to the c-axis (Hamilton 1970; Franklin and Mattson 1972), also the shear strength is controlled by the sediment fabrics (e.g. Donath 1961; Rai and Hanson 1988; Shea and Kronenberg 1993; Johansen et al., 2004; Beeler 2007; Voltolini et al., 2009) and thus evolves anisotropies (e.g. Bennett et al., 1981; Fawad et al., 2010; Jones 1994; Rai and Hanson 1988; Voltolini et al., 2009). To quantify the sample microstructures, scanning electron microscopy and synchrotron x-ray based texture analyses were used. Texture analyses of the naturally compacted sediments indicate weak bedding-parallel crystallographic preferred orientation (CPO) of the phyllosilicate basal planes. The axisymmetric preferred orientations of clay minerals increases with drillhole depth. This observation is supported by increasing texture strength of clay-rich sediments from the Nankai accretionary prism (Morgan and Karig 1993, 1995). When bedding tilt due to tectonic deformation was observed, bedding-parallel orientation of phyllosilicate basal planes was preserved. These observations point to progressive burial and compaction as texture forming processes. Scanning electron micrographs of detrital illites and micropores also reflect vertical compaction as texture forming process in the naturally compacted sediments.

In the experimentally deformed samples, phyllosilicate and calcite CPOs develop normal to the experimental shortening and increases dependent on the strain, as predicted by the March theory (March 1932). These observations indicate that experimental deformation results in reorientation and/ or flattening of the micropores.

Natural and experimental textures were found to be similar. For this reason, the experimental results can be transferred to the natural case. Vertical shortening and consolidation due to normal compaction of the sediments continuously reduces porosity. Porosity reduction (and thus the loss of pore water) is accompanied by clay platelets rotation towards the bedding plane, as found by Behrmann and Kopf (1993) and Morgan and Karig (1993). Tectonically induced deformation and/or tectonic loading may cause further consolidation resulting in rotation of the clay minerals normal to the tectonic loading. Similar observations were made by Morgan et al. (2003).

The increase of V_s during deformation was attributed to enhanced grain-grain contacts and microstructural rearrangement, as described in the literature (e.g. Wyllie et al., 1956; Bourbié et al., 1987; Stoll 1989; Erickson and Jarrard 1998; Gettemy and Tobin 2003; Mondol et al., 2007; Hashimoto et al., 2011; Raimbourg et al., 2011). Reorientation and/ or rotation of the clay mineral basal planes normal to the axial shortening direction decreases the V_p , since V_p is lowest parallel to the c-axis (Hamilton 1970; Franklin and Mattson 1972). Reduction of V_p due to reorientation of mineral grains into the direction of the lowest velocity is counteracted by enhanced grain-grain contacts due to enhanced pressure conditions, as described by Mondol et al. (2007). Consequently, V_p is rather constant during the experimental deformation, while V_s increases due to the reduction of the amount of pore water and enhanced grain-grain contacts.

In order to extrapolate the results from the shallow levels in the sea floor to greater depth, natural samples from uplifted analogues to the Nankai accretionary prism were included in my investigation. The Cretaceous Shimanto belt and the upper Miocene Boso-Miura accretionary prism are equivalents to the Nankai accretionary prism, exposed on-land. Because of their compositional and structural similarities to Nankai, they are ideal natural cases to investigate geotechnical properties of those regions in the Nankai accretionary prism that are not accessible by drilling. Samples from Boso accretionary prism represent ~1000 m pre-exhumation depth (e.g. Yamamoto et al., 2005). During triaxial testing, Boso samples show tendencies to creep, and did not fracture. In contrast to Boso, the Shimanto samples reached peak stress conditions after small amounts of axial strain and showed brittle behavior. The effective shear parameters determined for both sample sets are indicative for relatively strong sediments.

Geotechnical data of the Shimanto Belt and the Boso accretionary prism in combination with the geomechanical data of the Nankai accretionary prism (Stipp et al., 2013) allowed to assess the strength evolution of terrigenous to hemipelagic active margin sediments with progressive burial and diagenesis. The dataset spans the complete depth range from the near seafloor (Nankai accretionary prism), over approximately 1000 m pre-exhumation burial depth (Boso accretionary prism, Yamamoto et al., 2005) to approximately 7800 m and down to the seismogenic depths of approximately 9000 m (Shimanto Belt; Kitamura et al., 2005). The data

point to a linear increase of the cohesion with increasing burial depth due to diagenesis and very low grade metamorphism in the Shimanto belt.

Geotechnical parameters of the décollement have been deduced in this work from presented triaxial test results and from seismic data of Moore et al. (2009). Slope-cover sediments in the Nankai accretionary prism are undeformed (e.g. Moore et al., 2009) indicating that cohesion of the décollement fault rocks is lower than the cohesion determined for the Shimanto and Boso samples.

6.2 Conclusion

- From the velocity measurements conducted during experimental deformation I learned that although p- and s-wave measurement is challenging in unconsolidated sediments, V_p and V_s data of unconsolidated sediments can be determined by applying seismic time series analysis to sonic velocity measurements. Especially V_s increases during deformation, attributed to reorientation of the microstructure and enhanced interparticle coupling. V_p and V_s can be used to determine shear, bulk and elastic modulus to characterize the sediments and to differentiate tectonic settings.
- V_p and V_s data indicate overconsolidated sediments at the accretionary prism toe, supported by the occurrence of overconsolidated structurally strong sediments at Sites C0006 and C0007 (Stipp et al., 2013, manuscript #4). Overconsolidation was also reported in literature for Sites C0006, C0007 and C0008 due to erosional material removal (Screaton et al., 2009; Kimura et al., 2011; Conin et al., 2011; and Strasser et al., 2011). Overconsolidated structurally strong sediments at the accretionary prism toe are amenable to stable slip and strain distribution (folding). This is further supported by the observation of active deformation of the frontal thrust sediments (e.g. Moore et al., 2009).
- Microstructural investigations indicate that ongoing deformation leads to rotation of the crystallographic preferred orientation of the

phyllosilicates, as predicted by the March theory (March 1932). Additionally, the texture strength increases due to deformation.

- Naturally and experimentally generated microstructures are similar. Therefore, the link between experimental parameters and the emerging textures provides realistic insights into the natural processes. Natural deformation results in reduction of the pore space, reorientation of the phyllosilicates and enhanced grain-grain contacts. Similar observations were made by Behrmann and Kopf (1993) and Morgan and Karig (1993). Enhanced grain-grain contacts are also reflected in decreasing V_p/V_s ratios during experimental deformation.
- IODP drilling in the Nankai Trough was focused on areas that show strong deformation, but did not address parts of the forearc that are currently not actively deforming. To compensate this shortcoming, reference samples from the Boso accretionary prism, representing the middle part of the Nankai accretionary prism, were taken on land and included in the investigation.
- The middle part of the accretionary prism, represented by Boso samples, is characterized by the tendency to creep rather than to fracture. This is supported by literature observation of undeformed slope cover sediments (Moore et al., 2009).
- To extend the experimental results to seismogenic depths, samples from the Shimanto Belt were investigated. These samples can be seen as equivalents to the updip limit of the seismogenic zone. The Shimanto samples are characterized by brittle behavior.
- Normally consolidated sediments at the megasplay fault setting are characterized as structurally weak (Stipp et al., 2013, manuscript #4), capable to unstable slip and brittle faulting. These observations indicate that coseismic slip can be transmitted along the splay fault upward to the seafloor, as proposed in the literature (e.g. Cummins and Kaneda 2000; Cummins et al., 2001; Park et al., 2002; Moore et al., 2007), similar as reported for the Shimanto Belt (Kitamura et al., 2005; Mukoyoshi et al., 2006). Dip-slip faults, such as the splay fault in the

Nankai accretionary prism are guided by zones of local weakness due to anisotropic friction (Scholz 2011). Reorientation and/ or rotation of the phyllosilicates due to tectonic deformation as found in this study and in the literature (e.g. Morgan and Karig 1993, 1995) contribute to the formation of zones of local weakness and propagation of co-seismic slip to the seafloor, responsible for the generation of surface breaks and related tsunamis (e.g. Ando 1975; Park et al., 2000, 2002).

- Based on the data presented in this thesis, the sediments at the frontal thrust are overconsolidated, able to distribute deformation within large volumes and thus aseismic behavior. Sediments in the middle part of the accretionary prism tend to creep and therefore will not cause surface breaks. Sediments at the updip limit of the seismogenic zone are amenable to brittle behavior. Coseismic slip during earthquakes might be transmitted by the splay fault to the seafloor and thus can cause surface breaks and resulting tsunamis.

6.3 Outlook

The results presented in this thesis yield an important scientific advance concerning the structural and geotechnical parameters of accretionary prism sediments, and how they may affect large-scale deformation processes, earthquake formation, and slip propagation. All those features may directly lead to large damage, and may subsequently generate tsunamis. As typical for complex questions, several aspects remain open, and some new questions arose from the findings, giving starting points for future study. The crucial ones of these are outlined below:

In the first Manuscript, I showed that V_p , and especially V_s , of unconsolidated sediments can be obtained by mounting piezoelectric bender elements to the pistons of a triaxial apparatus. The response of the sonic velocities to changing parameters during triaxial testing is broadly discussed in the literature (e.g. Santamarine and Fam 1997; Mondol 2007). Since several parameters, such as decreasing pore water contents, are counteracted by increasing pressure conditions and increasing grain-grain coupling, the response of the sonic velocity to single

parameters is not well understood. For a better understanding of the velocity response to geotechnical parameters, it would be necessary to conduct systematic studies in which only one single parameter is changed during the velocity measurement. In such a systematic study, higher frequencies should be used. Continuous and automatic velocity measurements will guarantee higher resolutions of the samples and velocity response to changing parameters.

The data of such a systematic study could be supplemented by samples from greater depth (burial depths greater than ~130 m, Manuscript #1) verify the extrapolation of the presented results. These data additionally allow to calibrate velocity models of accreted sediments which then lead to the refinement of seismic imaging of accretionary prisms. Additionally, this approach would facilitate the deduction of geotechnical properties from velocities and would contribute to a better understanding of the structure of accretionary prisms. Thereby also a better understand of the geomechanical background would be achieved. Comparison to other subduction zones could additionally contribute to the understanding of geotechnical background.

In the second Manuscript, I showed that texture information of unconsolidated and water-rich clays and clayey sediments can be obtained from synchrotron x-ray diffraction. In a possible future study, refined crystallographic information of the single phases could be applied. Disorder and solid solution is common in clay minerals (e.g. Ufer et al., 2004; Wenk et al., 2008). By applying enhanced models of disorder, the error of the refinement and may be decreased. In general, this would contribute to even better compositional and textural information.

The improved method for velocity and texture measurements could then be applied in further studies to additional materials: (1) materials derived from greater depth, i.e. more than 522 mbsf, Manuscript #2, (2) materials derived from the Nankai Trough analogs exposed on land (Manuscript #3) and, (3) after drilling into the plate boundary and the megasplay fault, to materials derived from recently active faults. In addition, Kitamura et al. (2005) and Mukoyoshi et al. (2006) identified pseudotachylite in the Shimanto belt. Samples from this plate boundary fault could be used to correlate results from shallow fault zones to greater depth.

Geotechnical data (Manuscripts #3 and #4) could be complemented by triaxial tests of fault zone materials. This would contribute to a better understanding of the geotechnical properties of faults in general and to a better understanding of the geotechnical properties of the Nankai Trough.

Finally, this type of investigation has not yet been carried out at in such detail. Integrating the results presented here with data from other subduction zones would be the next step for a more comprehensive understanding of the geodynamics of accretionary prisms in general, and towards the implications for possible global systematics.

6.4 References

- Ando, M. (1975): Source mechanisms and tectonic significance of historical earthquakes along the Nankai Trough, Japan. *Tectonophysics* 27, 119-140
- Beeler, N.M. (2007): Laboratory-observed faulting in intrinsically and apparently weak materials. In: Dixon, T.H.; Moore J.C. (eds.): *The seismogenic zone of subduction thrust faults*. Columbia University Press, New York, pp. 370-449
- Behrmann, J.H.; Kopf, A. (1993): Textures and microfabrics in fine-grained muds and mudstones from Site 808, Nankai accretionary prism. In: Hill, I.A.; Taira, A.; Firth, J.V.; et al.: *Proceedings of the Ocean Drilling Program, Scientific results* 131
- Bennett, R.; Bryant, W.; Keller, G. (1981): Clay fabric of selected submarine sediments: Fundamental properties and models. *Journal of Sedimentary Petrology* 51, 217-232
- Bilek, S.L.; Lay, T. (1999): Rigidity variations with depth along interplate megathrust faults in subduction zones. *Letters to Nature*, 400, 443-446.
- Bourbié, T.; Coussy, O.; Zinszner, B. (1987): *Acoustics of porous media*. Editions Technip, Paris
- Byerlee, J. (1978): Friction of rocks. *Pure and Applied Geophysics*, 116, 615-626
- Carson, B.; von Huene, R.; Arthur, M. (1982): Small-scale deformation structures and physical properties related to convergence in Japan Trench slope sediments, *Tectonics*, 1, 277-302.
- Conin, M.; Henry, P.; Bourlange, S.; Raimbourg, H.; Reuschlé, T. (2011): Interpretation of porosity and LWD resistivity from the Nankai accretionary wedge in light of clay physicochemical properties: Evidence for erosion and local overpressuring. *Geochemistry, Geophysics, Geosystems* 12, doi:10.1029/2010GC003381
- Cummins, P.R.; Hori, T.H.; Kaneda, Y. (2001): Splay fault and megathrust earthquake slip in the Nankai Trough. *Earth Planets and Space* 53, 243-248
- Cummins, P.R.; Kaneda, Y. (2000): Possible splay fault slip during the 1946 Nankai earthquake. *Geophysical Research Letters* Vol. 27, No. 17, 2725-2728
- Donath, F.A. (1961): Experimental study of shear failure in anisotropic rocks. *Bulletin of the Geological Society of America* 72, 155-163
- Erickson, S.; Jarrard, R. (1998): Velocity-porosity relationship for water-saturated siliciclastic sediments. *Journal of Geophysical Research* 103(B12), 30385-30406
- Erickson, S.; Jarrard, R. (1998): Velocity-porosity relationship for water-saturated siliciclastic sediments. *Journal of Geophysical Research*, 103(B12), 30385-30406.

- Expedition 315 Scientists (2009): Expedition 315 Site C0001. In: Kinoshita, M.; Tobin, H.; Ashi, J.; Kimura, G.; Lallemand, S.; Screaton, E.J.; Curewitz, D.; Masago, H.; Moe, K.T.; and Expedition 314/315/316 Scientists (2009), Proceedings of the International Ocean Drilling Program, Volume 314/315/316. Washington DC, doi: 10.2204/iodp.proc.314315316.123.2009
- Expedition 316 Scientists (2009a): Expedition 316 Site C0004. In: Kinoshita, M.; Tobin, H.; Ashi, J.; Kimura, G.; Lallemand, S.; Screaton, E.J.; Curewitz, D.; Masago, H.; Moe, K.T.; and Expedition 314/315/316 Scientists (2009), Proceedings of the International Ocean Drilling Program, Volume 314/315/316. Washington DC, doi: 10.2204/iodp.proc.314315316.133.2009
- Expedition 316 Scientists (2009c): Expedition 316 Site C0007. In: Kinoshita, M.; Tobin, H.; Ashi, J.; Kimura, G.; Lallemand, S.; Screaton, E.J.; Curewitz, D.; Masago, H.; Moe, K.T.; and Expedition 314/315/316 Scientists (2009), Proceedings of the International Ocean Drilling Program, Volume 314/315/316. Washington DC, doi: 10.2204/iodp.proc.314315316.135.2009
- Expedition 316 Scientists (2009d): Expedition 316 Site C0008. In: Kinoshita, M.; Tobin, H.; Ashi, J.; Kimura, G.; Lallemand, S.; Screaton, E.J.; Curewitz, D.; Masago, H.; Moe, K.T.; and Expedition 314/315/316 Scientists (2009), Proceedings of the International Ocean Drilling Program, Volume 314/315/316. Washington DC, doi: 10.2204/iodp.proc.314315316.136.2009
- Expedition 316 Scientists, (2009b): Expedition 316 Site C0006. In: Kinoshita, M.; Tobin, H.; Ashi, J.; Kimura, G.; Lallemand, S.; Screaton, E.J.; Curewitz, D.; Masago, H.; Moe, K.T.; and Expedition 314/315/316 Scientists (2009), Proceedings of the International Ocean Drilling Program, Volume 314/315/316. Washington DC, doi: 10.2204/iodp.proc.314315316.134.2009
- Expedition 333 Scientists (2012a): Expedition 333 Site C0011. In: Henry, P.; Kanamatsu, T.; Moe, K.T.; and Expedition 333 (2012), Proceedings of the International Ocean Drilling Program, 333, doi: 10.2204/iodp.proc.333.104.2012
- Expedition 333 Scientists (2012b): Expedition 333 Site C0012. In: Henry, P.; Kanamatsu, T.; Moe, K.T.; and Expedition 333 (2012), Proceedings of the International Ocean Drilling Program, 333, doi: 10.2204/iodp.proc.333.105.2012
- Fawad, M.; Mondol, N.H.; Jahren, J.; Bjørlykke, K. (2010): Microfabric and rock properties of experimentally compresses silty-clay mixtures. *Marine and Petroleum Geology* 27, 1698-1712
- Franklin, A.G.; Mattson, P.A. (1972): Directional variation of elastic wave velocities in oriented clay. *Clays and Clay Minerals* 20, 285-293
- Gettemy, G.L.; Tobin, H.J. (2003): Tectonic signatures in centimeter-scale velocity-porosity relationships of Costa Rica convergent margin sediments. *Journal of Geophysical Research* 108 (B10), 2494, doi: 10.1029/2001JB000738

-
- Hamilton, E.L. (1970): Sound velocity and related properties of marine sediments, North Pacific. *Journal of Geophysical Research* 75(23), 4423-4446
- Hashimoto, Y.; Tobin, H.J.; Knuth, M.; Harada, A. (2011): Data report: compressional and shear wave velocity measurements on sediment in the hanging wall and the footwall of megasplay fault, NanTroSEIZE Stage 1, in Kinoshita, M.; Tobin, H.J.; Ashi, J.; Kimura, G.; Lallemand, G.; Screaton, E.J.; Curewitz, D.; Masago, H.; Moe, K.T.; and the Expedition 314/315/316 Scientists. *Proceedings of the Integrated Ocean Drilling Program, Volume 314/315/316*, doi:10.2204/iodp.proc.314315316.217.2011
- Johansen, T.A.; Bent, O.R.; Jakobsen, M. (2004): Effect of grain scale alignment on seismic anisotropy and reflectivity of shales. *Geophysical Prospecting* 52, 133-149
- Johnston, J.E.; Christensen, N.I. (1993): Compressional to shear velocity ratios in sedimentary rocks. *International Journal of Rock Mechanics and Mining Sciences & Geomechanics Abstracts* 30(7), 751-754.
- Jones, M. (1994): Mechanical principles of sediment deformation. In: Maltman, A. (ed.): *The Geological Deformation of sediments*. Chapman and Hall, London, 37-71
- Kimura, G.; Moore, G.F.; Screaton, E.J.; Curewitz, D.; Streiff, C.; Tobin, H.J. (2011): Spatial and temporal evolution of the megasplay fault in the Nankai Trough. *Geochemistry, Geophysics, Geosystems* 12(3), 23, doi:10.1029/2010GC003335
- Kinoshita, M.; Tobin, H.J.; Ashi, J.; Kimura, G.; Lallemand, S.; Screaton, E.J.; Curewitz, D.; Masago, H.; Moe, K.T.; and the Expedition 314/315/316 Scientists (2009): *Proc. IODP, 314/315/316: Washington, DC (Integrated Ocean Drilling Program Management International, Inc.)*. doi:10.2204/iodp.proc.314315316.123.2009
- Kitamura, Y.; Sato, K.; Ikesawa, E.; Ikehara-Ohmori, K.; Kimura, G.; Kondo, H.; Ujiie, K.; Onishi, C.T.; Kawabata, K.; Hashimoto, Y.; Mukoyoshi, H.; Masaga, H. (2005): Mélange and its seismogenic roof décollement: A plate boundary fault rock in the subduction zone – An example from the Shimanto Belt, Japan. *Tectonics* 24, 15 doi:10.1029/2004TC001635
- Kranck, K. (1980): Experiments on the significance of flocculation in settling of fine grained sediments in still-water. *Canadian Journal of Earth Science*, 17, 1517-1526
- Kranck, K. (1986): Generation of grain size distribution of fine sediments. In: Wang, S.Y.; Ding, L.Z. (ed): *Proceedings of Third International Symposium on River Sedimentation*. The University of Mississippi.
- Laberg, J.S., Vorren, T.O., Mienert, J., Haflidason, H., Bryn, P., & Lien, R., 2003. Preconditions leading to the Holocene Trænadjupet Slide offshore Norway, in Locat, J., and Mienert, J. (eds.), *Advances in Natural and Technological Hazards Research*, Kluwer, Dordrecht, pp. 247-254.

- March, A. (1932): Mathematische Theorie der Regelung nach der Korngestalt bei affiner Deformation. *Zeitschrift für Kristallographie* 81, 285-297
- Mavko, G.; Mukerji, T.; Dvorkin, J. (1998): *The Rock Physical Handbook, Tool for Seismic Analysis in Porous Media*, 329 pp., Cambridge University Press, Cambridge, U. K.
- Milliken, K.L.; Reed, R.M. (2010): Multiple causes of diagenetic fabric anisotropy in weakly consolidated mud, Nankai accretionary prism, IODP Expedition 316. *Journal of Structural Geology*, 32, 1887-1898
- Mondol, N.H.; Bjørlykke, K.; Jahren, J.; Høeg, K. (2007): Experimental mechanical compaction of clay mineral aggregates – Changes in physical properties of mudstones during burial. *Marine and Petroleum Geology*, 24, 289-311
- Moore, G.F.; Bangs, N.L.; Taira, A.; Kuramoto, S.; Pangborn, E.; Tobin, H.J. (2007): Three-dimensional splay fault geometry and implications for tsunami generation. *Science* 318 (5853), 1128-1131 doi:10.1126/science.1147195
- Moore, G.F.; Park, J.-O.; Bangs, N.L.; Gulick, S.P.; Tobin, H.J.; Nakamura, Y.; Sato, S.; Tsuji, T.; Yoro, T.; Tanaka, H.; Uraki, S.; Kido, Y.; Sanada, Y.; Kuramoto, S.; Taira, A. (2009): Structural and seismic stratigraphic framework of the NanTroSEIZE Stage 1 transect. In: Kinoshita, M.; Tobin, H.; Ashi, J.; Kimura, G.; Lallemant, S.; Screaton, E.J.; Curewitz, D.; Masago, H.; Moe, K.T.; Expedition 314/315/316 Scientists, *Proceedings of the IODP, 314/315/316*, doi:10.2204/iodp.proc.314315316.102.2009
- Moore, J.C.; Saffer, D. (2001): Updip limit of the seismogenic zone beneath the accretionary prism of southwest Japan: An effect of diagenetic to low-grade metamorphic processes and increasing effective stress. *Geology* 29, 183-186, doi: 10.1130/0091-7613(2001)029<0183:ULOTSZ>2.0.CO;2.
- Moore, J.C.; Vrolijk, P. (1992): Fluids in Accretionary Prisms, *Reviews of Geophysics*, 30, 113-135.
- Morgan, J.K.; Karig, D.E. (1995): Décollement processes at the Nankai accretionary margin, southeast Japan: Propagation, deformation and dewatering. *Journal of Geophysical Research*, 100, 15221-15231
- Morgan, J.K.; Sunderland, E.B.; Ask, M.V.S. (2003): Deformation and mechanical strength of sediments at the Nankai subduction zone: implications for prism evolution and decollement initiation and propagation. In: Dixon, T.H.; Moore, J.C.: *The seismogenic zone of subduction thrust faults*. Columbia University Press, Now York
- Morgan, J.K.; Karig, D.E. (1993): Ductile strains in clay-rich sediments from Hole 808C: Preliminary results using X-ray pole figure goniometry. *Proceedings of the Ocean Drilling Program Scientific Results*, 131, 141-155
- Morgan, J.K.; Ramsey, E.B.; Ask, M.V.S. (2007): Deformation and mechanical strength of sediments at the Nankai subduction zone. In: Dixon, T.H.; Moore

-
- J.C. (eds.): The seismogenic zone of subduction thrust faults. Columbia University Press, New York, pp. 210-256.
- Mukoyoshi, H.; Skaguchi, A.; Otsuki, K.; Hirono, T.; Soh, W. (2006): Co-seismic frictional melting along an out-of-sequence thrust in the Shimanto accretionary complex. Implications on the tsunamigenic potential of splay faults in modern subduction zones. *Earth and Planetary Science Letters*, 245, 1-2, 330-343, doi:10.1016/j.epsl.2006.02.039
- Park, J.-O.; Tsuru, T.; Kodaira, S.; Cummins, P.R.; Kaneda, Y. (2002): Splay fault branching along the Nankai Subduction Zone. *Science* 297, 1157-1160
- Park, J.-O.; Tsuru, T.; Kodaira, S.; Nakanishi, A.; Miura, S.; Kaneda, Y.; Kono, Y. (2000): Out-of-sequence thrust faults developed in the coseismic slip zone of the 1946 Nankai earthquake (Mw=8.2) off Shikoku, southwest Japan. *Geophysical research letters* 27 (7), 1033-1036
- Pickett, G.R. (1963): Acoustic character logs and their application in formation evaluation. *Journal of the Canadian Petroleum Technology*, 15, 659-667.
- Rai, C.S.; Hanson, K.E. (1988): Shear-wave velocity anisotropy in sedimentary rocks: A laboratory study. *Geophysics* 53, 800-806
- Raimbourg, H.; Hamano, Y.; Saito, S.; Kinoshita, M.; Kopf, A. (2011): Acoustic and mechanical properties of Nankai accretionary prism core samples. *Geochemistry, Geophysics; Geosystems* 12, Q0AD10, doi:10.1029/2010GC003169
- Saffer, D.; Guo, J.; Underwood, M.B.; Likos, W.; Skarbek, R.M.; Song, I.; Gildow, M. (2011): Data report: consolidation, permeability, and fabric of sediments from the Nankai continental slope, IODP Sites C0001, C0008, and C0004. In: Kinoshita, M.; Tobin, H.J.; Ashi, J.; Kimura, G.; Lallemant, S.; Scretton, E.J.; Curewitz, D.; Masago, H.; Moe, K.T.; and the Expedition 314/315/316 Scientists, *Proceedings of the Integrated Ocean Drilling Program*, Washington, DC
- Santamarina, J. C., and M. A. Fam (1997), Interpretation of bender element tests – discussion, *Géotechnique*, 47(4), 873-877.
- Scholz, C.H. (2011): *The Mechanics of earthquakes and faulting*. Cambridge University Press, 2nd edition
- Scretton, E.; Kimura, G.; Curewitz, D.; Moore, G.; Chester, F.; Fabbri, O.; Fergusson, C.; Girault, F.; Goldsby, D.; Harris, R.; Inagaki, F.; Jiang, T.; Kitamura, Y.; Knuth, M.; Li, C.F.; Claesson Liljedahl, L.; Louis, L.; Milliken, K.; Nicholson, U.; Riedinger, N.; Sakaguchi, A.; Solomon, E.; Strasser, M.; Su, X.; Tsutsumi, A.; Yamaguchi, A.; Ujje, K.; Zhao, X. (2009): Interactions between deformation and fluids in the frontal thrust region of the NanTroSEIZE transect offshore the Kii Peninsula, Japan: Results from IODP Expedition 316 Sites C0006 and C0007. *Geochemistry, Geophysics, Geosystems* 10, doi:10.1029/2009GC002713.

- Shea, W.T.; Kronenberg, A.K. (1993): Strength and anisotropy of foliated rocks with varied mica content. *Journal of Structural Geology*, 15, 1097-1121
- Stipp, M.; Rolfs, M.; Behrmann, J.H.; Schumann, K.; Schulte-Kortnack, D.; Feeser, V. (2013): Strong sediments at the deformation front, and weak sediments at the rear of the Nankai accretionary prism, revealed by triaxial deformation experiments. *Geochemistry Geophysics Geosystems*, Vol. 14, 4791-4810, doi:10.1002/ggge.20290
- Stoll, R. D. (1989): *Sediment Acoustics*, Springer-Verlag, New York
- Strasser, M.; Moore, G.F.; Kimura, G.; Kopf, A.; Underwood, M.B.; Guo, J.; Screaton, E.J. (2011): Slumping and mass transport deposition in the Nankai fore arc: Evidence from IODP drilling and 3-D reflection seismic data. *Geochemistry, Geophysics, Geosystems* 12(5), doi:10.1029/2010GC003431.
- Sultan, N., Cochonat, P., Canals, M., Cattaneo, A., Dennielou, B., Haflidason, H., Laberg, J.S., Long, D., Mienert, J., Trincardi, F., Urgeles, R., Vorren, T.O. & Wilson, C., 2004. Triggering mechanisms of slope instability processes and sediment failures on continental margins; a geotechnical approach. In: COSTA, continental slope stability; a contribution to the Energy, Environment and Sustainable Development Programme FP5 of the European Commission, number EVK3-CT-1999-00006, Elsevier, Amsterdam, pp. 291-321.
- Tobin, H.J.; Kinoshita, M.; (2006): NanTroSEIZE: The IODP Nankai Trough seismogenic zone experiment. *Scientific Drilling* 2, 23-27, doi:10.2204/iodp.sd.2.06.2006
- Tsuji, T.; Dvorkin, J.; Mavko, G.; Nakata, N.; Matsuoka, K.; Nakanishi, A.; Kodaira, S.; Nishizawa, O. (2011): Vp/Vs ratio and shear-wave splitting in the Nankai Trough seismogenic zone: Insights into effective stress, pore pressure, and sediment consolidation. *Geophysics*, 76(3), 71-82, doi:10.1190/1.3560018
- Ufer, K., Roth, G., Kleeberg, R., Stanjek, H., Dorhmann, R., Bergmann, J., 2004. Description of X-ray powder pattern of turbostratically disordered layer structures with a Rietveld compatible approach. *Zeitschrift für Kristallographie* 219, 519-527
- Voltolini, M.; Wenk, H.-R.; Mondol, N.H.; Bjørlykke, K.; Jahren, J. (2009): Anisotropy of experimentally compressed kaolinite-illite-quartz mixtures. *Geophysics* 74 (1), 13-23
- Wang, K.; Hu, Y. (2006): Accretionary prisms in subduction earthquake cycles: the theory of dynamic Coulomb wedge. *Journal of Geophysical Research*, 111, B06410, doi:10.1029/2005JB004094
- Wenk, H.R., Voltolini, M, Mazurek, M., van Loon, L.R., Vinsot, A., 2008. Preferred orientation and anisotropy in shale: Callovo-Oxfordian shale (France) and Opalinus Clay (Switzerland). *Clays and Clay Minerals* 56 (3), 285-306, doi: 10.1346/CCMN.2008.0560301
- Wyllie, M.R.J.; Gregory, A.R.; Gardner, L.W. (1956): Elastic wave velocity in heterogeneous and porous media. *Geophysics*, 21(1), 41-70

Yamamoto, Y.; Mukoyoshi, H.; Ogawa, Y. (2005): Structural characteristics of shallowly buried accretionary prism: Rapidly uplifted Neogene accreted sediments on the Miura-Boso Peninsula, central Japan. *Tectonics* 24, 17p. doi:10.1029/2005TC001823

7 Appendix

7 Appendix

A 1 Appendix Manuscript #1	253
A 2 Appendix Manuscript #2	261
A 2.1 Scanning electron micrographs	261
A 2.2 Data processing	269
A 2.3 Synchrotron texture measurements, natural samples	287
A 2.4 Synchrotron texture measurements, sheared samples	297
A 3 Appendix Manuscript #3	309
A 4 Appendix Manuscript #4	323
Acknowledgements	339
Curriculum Vitae	341

List of Tables

Table A 1.1: Overview of the experimental conditions	259
Table A 2.1: Conversion of the detector dimensions from pixels to mm	272
Table A 2.2: Parameter settings.	274
Table A 2.3: Settings to rescale the plate detector image	275
Table A 2.4: Parameter settings for image integration	276
Table A 2.5: Parameters refined during the different refinement steps	280
Table A 4.1: Experimental conditions.	327

List of Figures

Figure A 1.1: Stress versus strain plots.....	256
Figure A 1.2: Pore pressure versus strain plots.....	257
Figure A 1.3: Vp, Vs and displacement versus time plots.....	258
Figure A 2.1: 315-C0001E-11H-1	261
Figure A 2.2: 315-C0001E-11H-1, K005	262
Figure A 2.3: 316-C0004C-8H-2, K010	263
Figure A 2.4: 316-C0006E-20X-3, K013	264
Figure A 2.5: 316-C0007C-7X-1, K011	265
Figure A 2.6: 316-C0007C-7X-1, K016	266
Figure A 2.7: 316-C0008A-9H-3, K014	267
Figure A 2.8: 316-C0008C-7H-8, K018	268
Figure A 2.9: Flowchart illustrating processing steps.....	269
Figure A 2.10: Origin of the coordinate system in Fit2D and Maud	272
Figure A 2.11: Setting up the instrument parameter file.....	274
Figure A 2.12: Adding data to Maud.	276
Figure A 2.13: Adding phase information to Maud.....	277
Figure A 2.14: Spectra computation	278
Figure A 2.15: Background refinement.	279
Figure A 2.16: Texture calculation	282
Figure A 2.17: Kaolinite pole figure - an example.	282
Figure A 2.18: Sample 333-C0012C-4H-5, 28.9 mbsf.....	287
Figure A 2.19: Sample 333-C0012C-9H-6, 75 mbsf.....	288
Figure A 2.20: Sample 333-C0012C-15H-5, 121.6 mbsf.....	289
Figure A 2.21: Sample 333-C0012E-3X-4, 522 mbsf	290
Figure A 2.22: Sample 333-C0011D-26X-1, 206.2 mbsf.....	291
Figure A 2.23: Sample 316-C0008A-9H-3, 76.1 mbsf.....	292
Figure A 2.24: Sample 315-C001E-11H-1, 90.6 mbsf	293
Figure A 2.25: Sample 316-C0006E-30X-1, 221 mbsf	294
Figure A 2.26: Sample 315-C0001F-14H-3, 210 mbsf.....	295
Figure A 2.27: Sample 315-C0001H-19R-2, 398.2 mbsf.....	296
Figure A 2.28: Sample 316-C0007C-7X-1, K012, 35% axial strain	297
Figure A 2.29: Sample 316-C0007C-7X-1, K016, 38% axial strain	298

Figure A 2.30: Sample 316-C0006E-8H-1, K007, 22% axial strain	299
Figure A 2.31: Sample 316-C0006E-8H-1, K009, 60% axial strain	300
Figure A 2.32: Sample 316-C0006E-20X-2, K019, 47% axial strain	301
Figure A 2.33: Sample 316-C0008C-7H-8, K018, 27% axial strain	302
Figure A 2.34: Sample 316-C0008C-7H-8, K015, 38% axial strain	303
Figure A 2.35: Sample 316-C0008A-9H-3, K006, 31% axial strain	304
Figure A 2.36: Sample 316-C0008A-9H-3, K014, 45% axial strain	305
Figure A 2.37: Sample 316-C0004C-8H-2, K004, 37% axial strain	306
Figure A 2.38: Sample 315-C0001E-11H-1, K003, 36% axial strain	307
Figure A 2.39: Sample 315-C0001E-11H-1, K006, 41% axial strain	308
Figure A 3.1: Sample Sch2011/8	309
Figure A 3.2: Sample Sch2011/12	310
Figure A 3.3: Sample Sch2011/18	311
Figure A 3.4: Sample Sch2011/23	312
Figure A 3.5: Sample Sch2011/24	313
Figure A 3.6: Sample Sch2011/27-1	314
Figure A 3.7: Sample Sch2011/27-2	315
Figure A 3.8: Sample Sch2011/29	316
Figure A 3.9: Sample Sch2011/34	317
Figure A 3.10: Sample NZ-PS-1	318
Figure A 3.11: Sample NZ-PS-2	319
Figure A 3.12: Sample NZ-PS-4/1 and NZ-PS-4/2	320
Figure A 3.13: Sample NZ-PS-5	321
Figure A 4.1: Deformation apparatus	330
Figure A 4.2: Experimental procedure	331
Figure A 4.3: Pore pressure/strain-records	332
Figure A 4.4: Pore pressure/strain-records	333
Figure A 4.5: Mohr-Coloumb diagrams	334
Figure A 4.6 Schematic stress path diagram	335
Figure A 4.7: Stress path diagrams	337

A 1 Appendix Manuscript #1

A 1.1 Methodical complement

IODP whole round drill cores of 66 mm diameter were reduced to 50 mm diameter to fit into the deformation apparatus. Sample cylinders lengths were in the range between 48 and 102 mm, depending on the available sample material. The accuracy of the initial length measurements on the samples is ± 1 mm, resulting in an error of 2%. After deformation samples were axially shortened up to 60%. Samples were jacketed into a 0.4 mm thick natural rubber sleeve to prevent fluid exchange between the sample and the surrounding cell water. Filter paper and sintered filter stone disks were placed at the sample ends to prevent particles being flushed out of the sample. A 1:1 mixture of boiled water and distilled water ($\sim 20^\circ\text{C}$) was used as confining pressure medium and pore fluid. The effect of smectite swelling due to the usage of distilled water can be neglected, since only small amounts of pore fluid needed to be added to the samples during the saturation phase. Hence, water loss during transport, storage and preparation of the samples was small, and it can be assumed that any salt largely remained in the samples (cf. Kitajima et al., 2012) and the addition of the used water mixture does not decrease the salinity of the pore water. Furthermore, the smectite content in our samples is small ranging between 1.5 and 6.2% except for one core sample (316-C0007C-7X-1) with a larger content of 15.4% smectite (Rietveld refinement of synchrotron radiation data; Schumann et al., in prep.). Sample saturation was checked by conducting B-Tests in some samples (DIN 18137 part 2). In this test, the ratio of pore pressure increase (Δu) versus confining pressure increase ($\Delta \sigma_3$) is indicative for the saturation (B) of the samples ($B = \Delta u / \Delta \sigma_3$). According to DIN 18137 part 2, saturation is achieved for $0.9 \leq B \leq 1.0$. Only sample K018 had a much lower B-value of 0.81. Sample saturation was additionally verified by controlling the pore pressure equilibration and the burette reading during pressure increase under drained conditions.

During the experiments, we continuously measured time, axial displacement, cell or confining pressure (σ_3), axial load (σ_1), pore fluid pressure and the amount of pore fluid expelled out of the sample during stages of drained pressurization. The recording interval during the pressure increase and the pressure stepping tests

was 5 seconds and during the displacement rate tests it was 5 seconds for displacement rates of 0.1 mm/min and faster and 1 second for rates slower than 0.1 mm/min. The triaxial deformation experiments are described in detail by Stipp et al. (in press.); stress/strain and pore pressure/strain-diagrams are shown in appendices A 1.1 and A 1. 2. Additional plots of V_p , V_s and displacement versus time of samples K020 and K022 are given in appendix A 1. 3.

Each triaxial experiment can be subdivided into three experimental stages:

Initial confining pressure increase and pore fluid saturation: The confining pressure was increased at 5 kPa/min. The axial load was always kept 5 to 10 kPa above confining pressure up to a value of 300 kPa. At 300 kPa confining pressure, pore fluid saturation of each sample was achieved by applying a back pressure with a ramp of 5 kPa/min. This experimental stage was carried out under drained conditions and was terminated when the pore pressure reached 280-282 kPa, i.e. the back pressure level which usually took several hours to one day. The initial pressure increase is not further considered in this study, since sample saturation during this stage is incomplete.

Pressure increase to experimental conditions: Prior to the deformation stage, the confining pressure conditions had to be adjusted to the experimental conditions (increase of $\sigma_1=\sigma_3$ to 400 kPa, 650 kPa and 1000 kPa). Pressurization was carried out under drained conditions and the back pressure was kept constant at 280 kPa. Hence these later stages of pressure increase were similar to the initial pressure increase apart from the saturated conditions.

Triaxial deformation: After completion of confining pressure increase and pore pressure equilibration to the back pressure level (overnight), the triaxial deformation test was carried out under consolidated and undrained conditions (CU-test). Three different types of triaxial deformation tests were performed.

In single step compression tests the samples were deformed beyond yield point to axial strains up to 36%. Tests were carried out at $\sigma_3 = 1000$ kPa and constant displacement rates of 0.01 and 0.1 mm/min. In pressure stepping tests, as the second type of test, confining pressure was increased stepwise (to 400 kPa, 640 kPa, and 1000 kPa), while at each step a constant displacement rate test (displacement rate of 0.01 or 0.1 mm/min) was carried out. Based on the three

different confining pressures Mohr Circle constructions can be made for each individual sample to determine cohesion and the internal friction angle of the samples. In the third type of tests, the rate stepping tests, σ_3 was kept constant at 1000 kPa, but the displacement rate was increased stepwise in the range between 0.01 and 9.0 mm/min. Experimental test conditions are summarized in Table 2.3 (main text). For further information on the triaxial deformation experiments see Stipp et al. (2013).

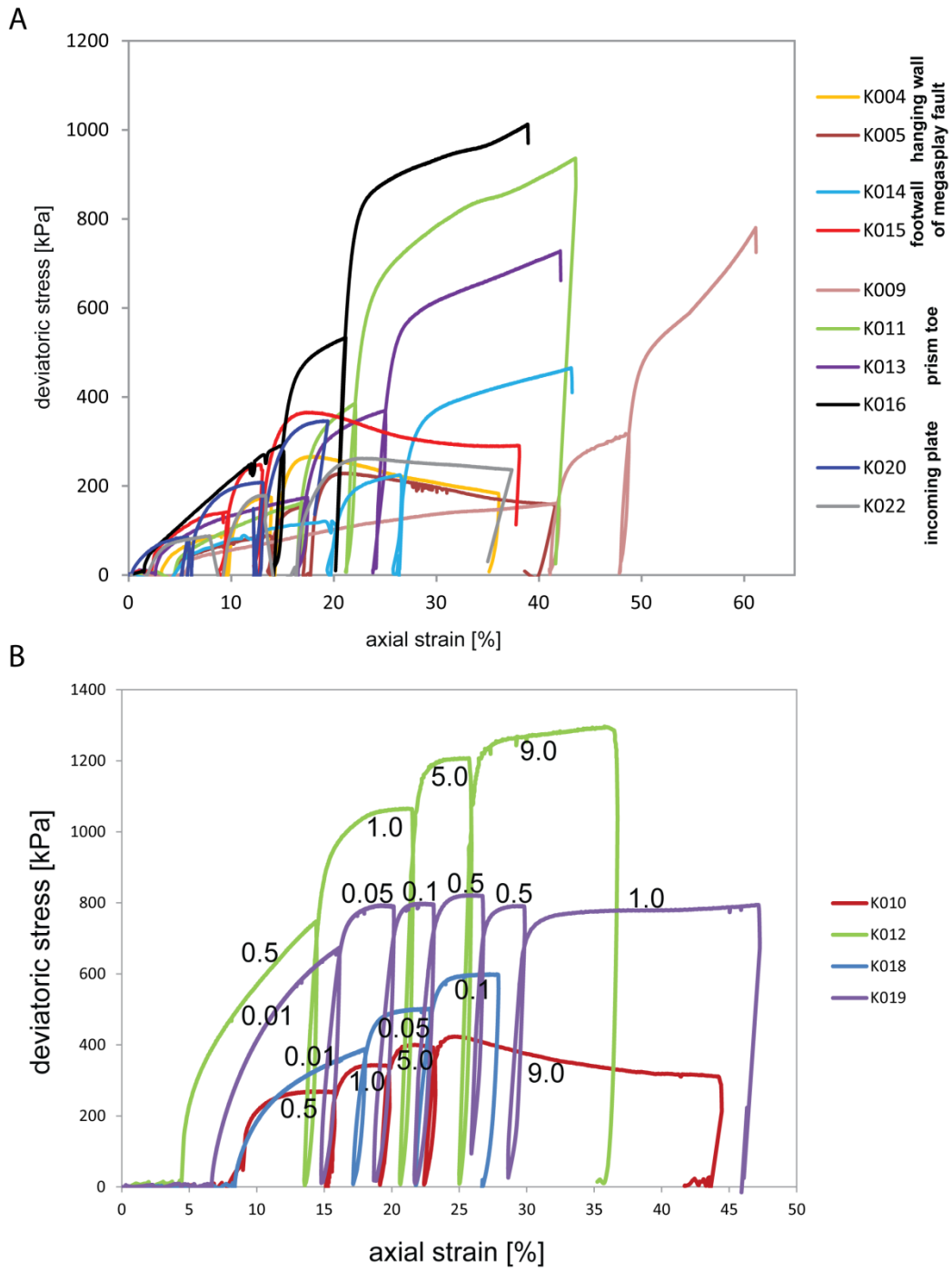


Figure A 1.1: Stress versus strain plots of the pressure stepping experiments (A) and the rate stepping experiments (B). Displacement rates of the rate stepping experiments are indicated. Data were taken from Stipp et al. (in press.).

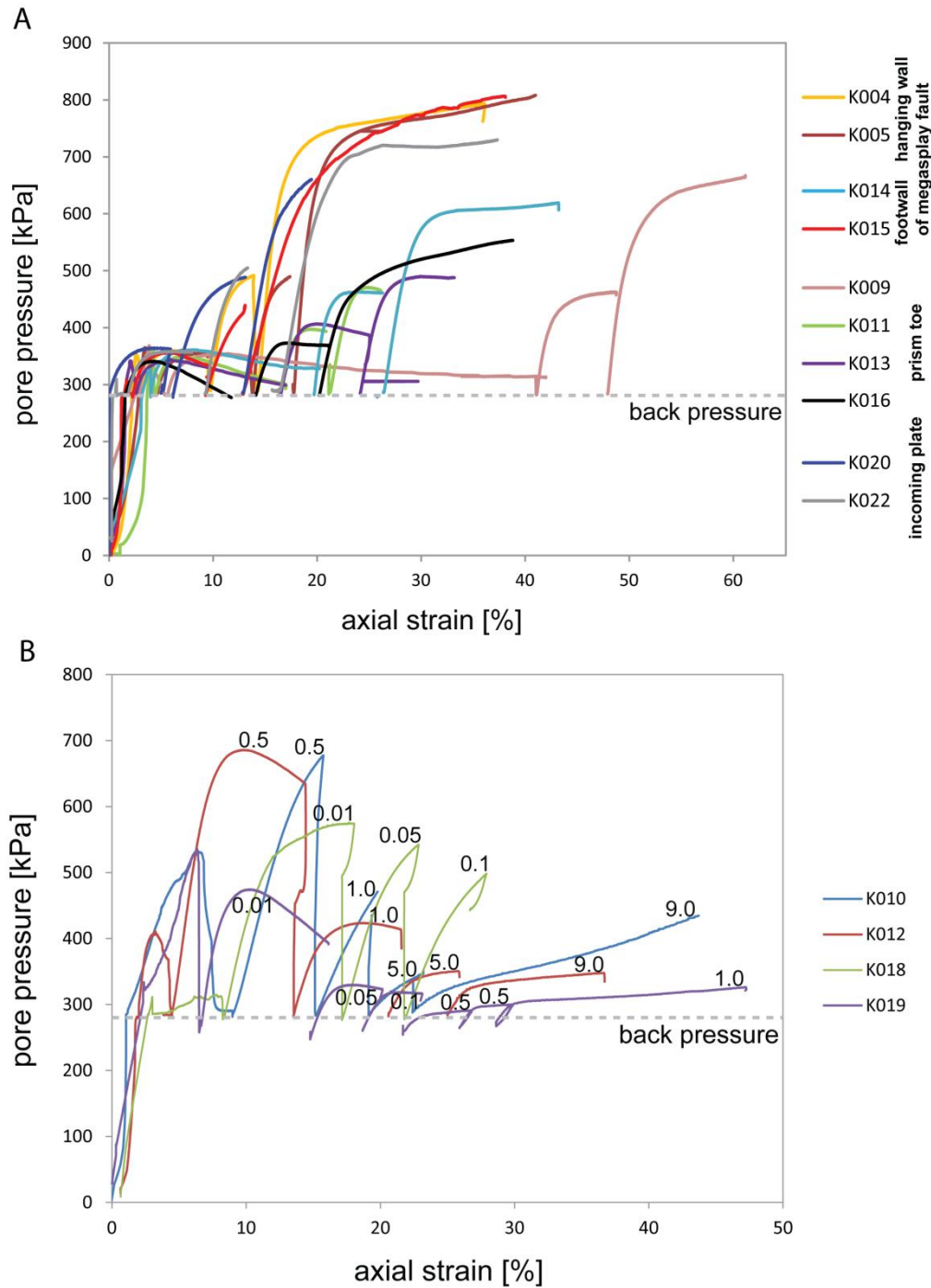


Figure A 1.2: Pore pressure versus strain plots of the pressure stepping experiments (A) and the rate stepping experiments (B). Displacement rates of the rate stepping tests are indicated. Data were taken from Stipp et al. (in press).

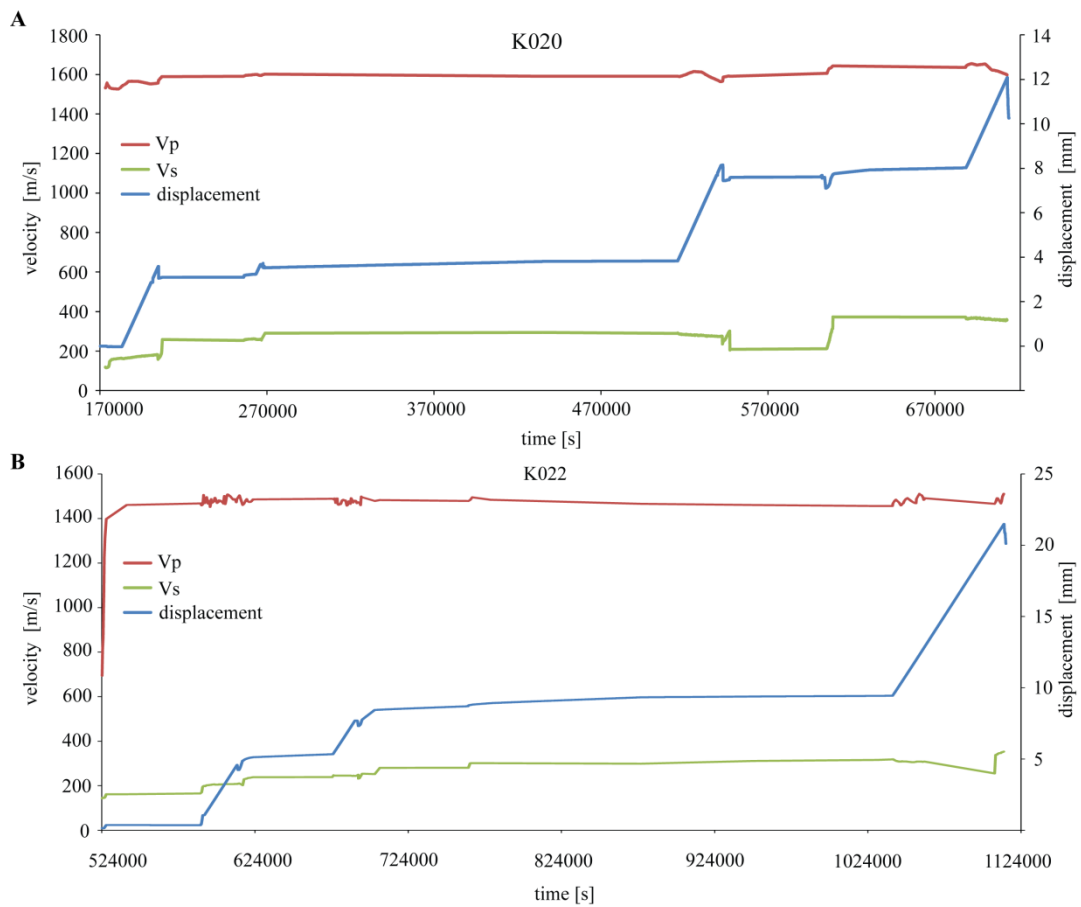


Figure A 1.3: V_p , V_s and displacement versus time plots of the samples K020 and K022. Phases of axial shortening are indicated by increasing displacement.

Table A 1.1: Overview of the experimental conditions

sample	core section	type	experimental conditions	axial strain
K002	316-C0008A-9H-3	constant strain rate	confining pressure: 1000 kPa displacement rate: 0.01 mm/min	12 %
K003	315-C0001E-11H-1	constant strain rate	confining pressure: 1000 kPa displacement rate: 0.01 mm/min	36 %
K004	316-C0004C-8H-2	pressure stepping	confining pressure: 400 kPa, 640 kPa, and 1000 kPa displacement rate: 0.01 mm/min	first step: 10 % second step: 14 % third step: 37 %
K005	315-C0001E-11H-1	pressure stepping	confining pressure: 400 kPa, 640 kPa, and 1000 kPa displacement rate: 0.01 mm/min	first step: 13 % second step: 17 % third step: 40 %
K006	316-C0008A-9H-3	constant strain rate	confining pressure: 1000 kPa displacement rate: 0.1 mm/min	31 %
K007	316-C0006E-8H-1	constant strain rate	confining pressure: 1000 kPa displacement rate: 0.01 mm/min	22 %
K009	316-C0006E-8H-1	pressure stepping	confining pressure: 400 kPa, 640 kPa, and 1000 kPa displacement rate: 0.01 mm/min	first step: 41 % second step: 46 % third step: 61 %
K010	316-C0004C-8H-2	velocity stepping	confining pressure: 1000 kPa displacement rate: 0.5 mm/min, 1.0 mm/min, 5.0 mm/min, and 9.0 mm/min	first step: 16 % second step: 19 % third step: 23 % fourth step: 44 %
K011	316-C0007C-7X-1	pressure stepping	confining pressure: 400 kPa, 640 kPa, and 1000 kPa displacement rate: 0.01 mm/min	first step: 19 % second step: 22 % third step: 42 %
K012	316-C0007C-7X-1	velocity stepping	confining pressure: 1000 kPa displacement rate: 0.5 mm/min, 1.0 mm/min, 5.0 mm/min, and 9.0 mm/min	first step: 14 % second step: 21 % third step: 25 % fourth step: 36 %
K013	316-C0006E-20X-2	pressure stepping	confining pressure: 400 kPa, 640 kPa, and 1000 kPa displacement rate: 0.01 mm/min	first step: 17 % second step: 24 % third step: 42 %

K014	316-C0008A9H-3	pressure stepping	confining pressure: 400 kPa, 640 kPa, and 1000 kPa displacement rate: 0.01 mm/min	first step: 20 % second step: 27 % third step: 43 %
K015	316-C0008C-7H-8	pressure stepping	confining pressure: 400 kPa, 640 kPa, and 1000 kPa displacement rate: 0.01 mm/min	first step: 9 % second step: 12 % third step: 19 %
K016	316-C0007C-7X-1	pressure stepping	confining pressure: 400 kPa, 640 kPa, and 1000 kPa displacement rate: 0.01 mm/min	first step: 15 % second step: 20 % third step: 38 %
K018	316-C0008C-7H-8	velocity stepping	confining pressure: 1000 kPa displacement rate: 0.01 mm/min, 0.05 mm/min, and 0.1 mm/min	first step: 19 % second step: 24 % third step: 28 %
K019	316-C0006E-20X-2	velocity stepping	confining pressure: 1000 kPa displacement rate: 0.01 mm/min, 0.05 mm/min, 0.1 mm/min, 0.5 mm/min, 0.5 mm/min, and 1.0 mm/min	first step: 16 % second step: 20 % third step: 23 % fourth step: 26 % fifth step: 29 % sixth step: 46 %
K020	333-C0011D-2H-2	pressure stepping	confining pressure: 400 kPa, 640 kPa, and 1000 kPa displacement rate: 0.01 mm/min	first step: 6 % second step: 13 % third step: 19 %
K022	333-C0012C-4H-5	pressure stepping	confining pressure: 400 kPa, 640 kPa, and 1000 kPa displacement rate: 0.01 mm/min	first step: 8 % second step: 13 % third step: 37 %

The type of triaxial shear test and the strain rates of the single deformation phases are given in the table.

A 2 Appendix Manuscript #2

A 2.1 Scanning electron micrographs

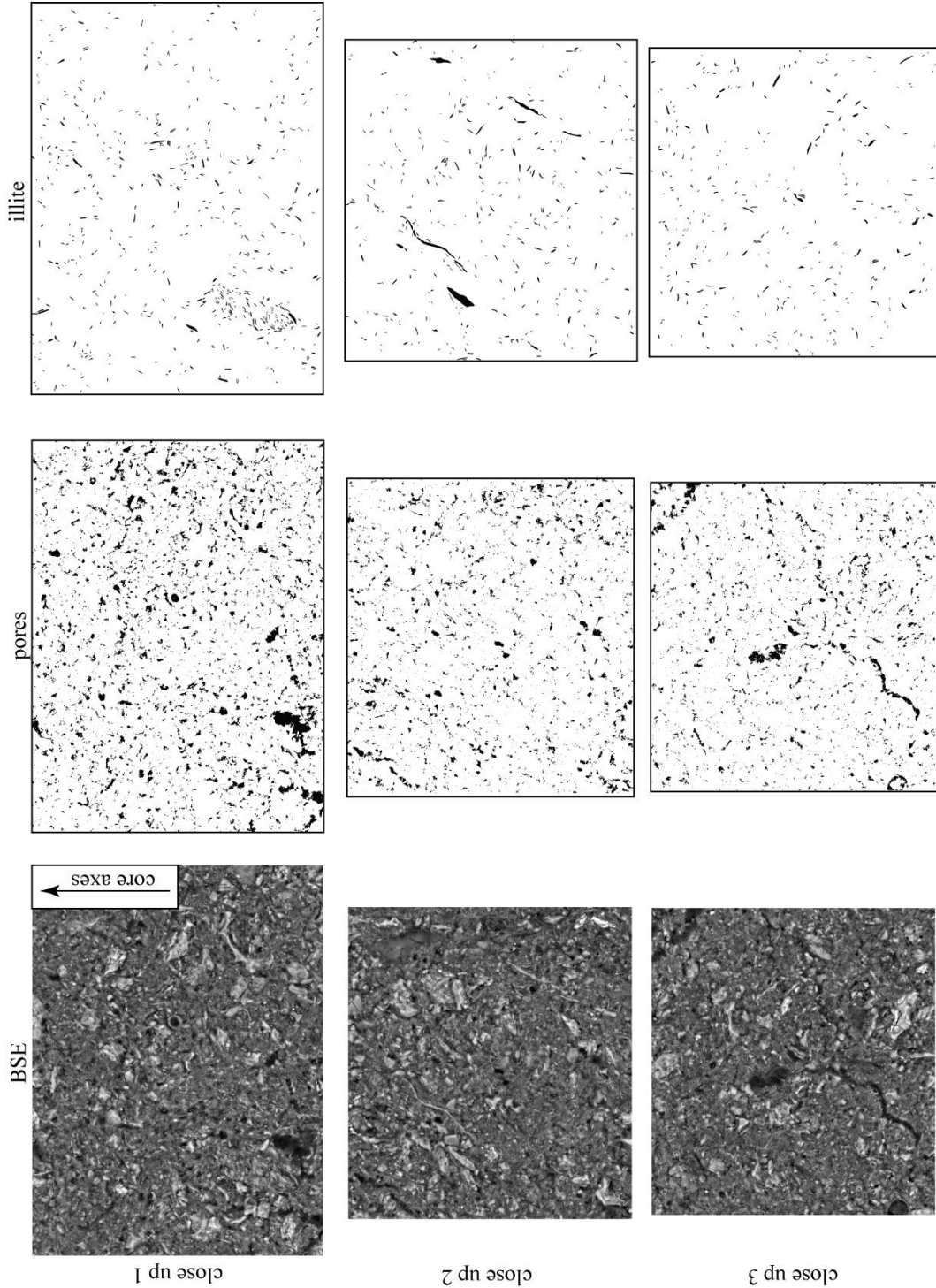


Figure A 2.1: 315-C0001E-11H-1

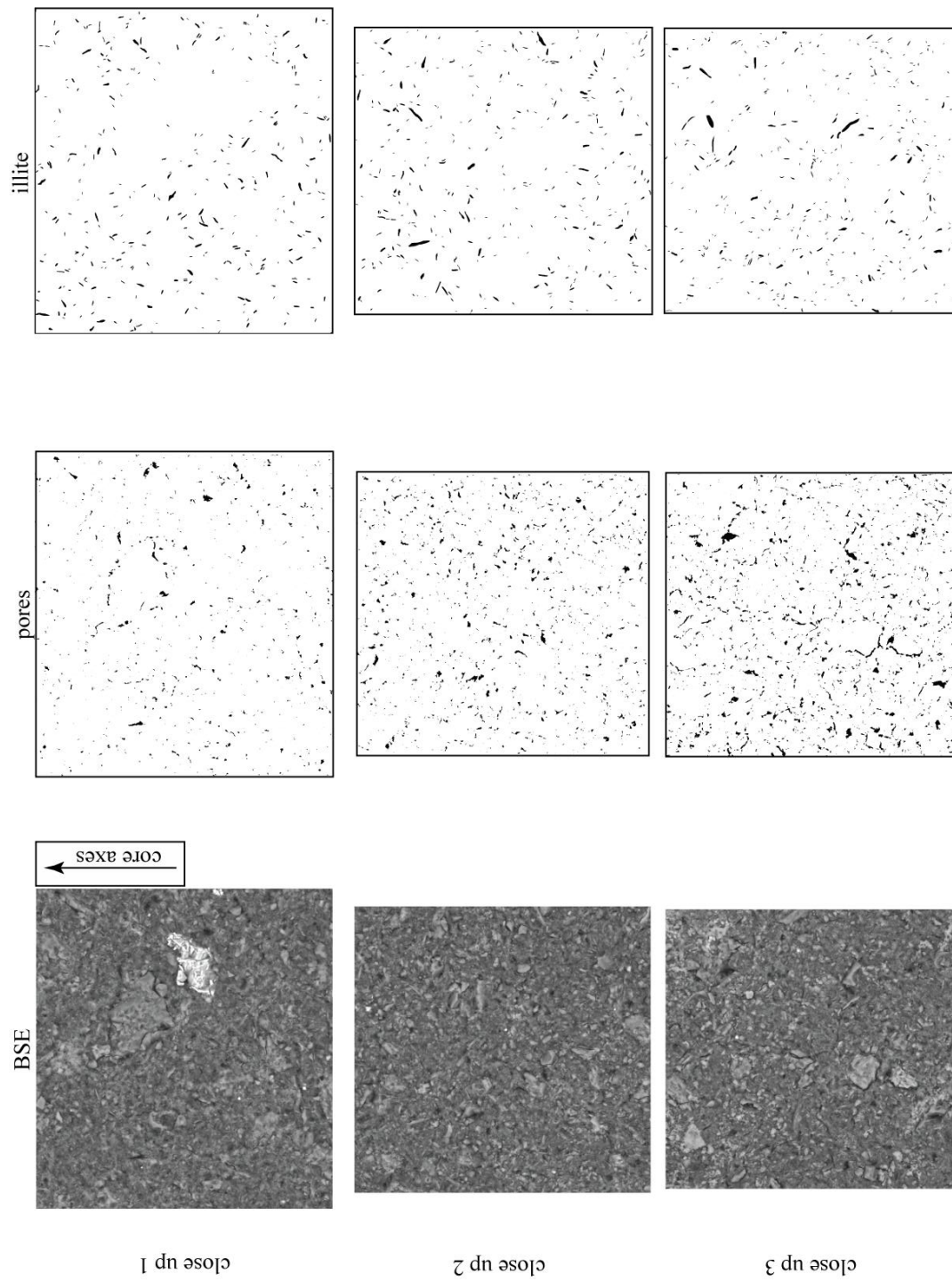


Figure A 2.2: 315-C0001E-11H-1, K005

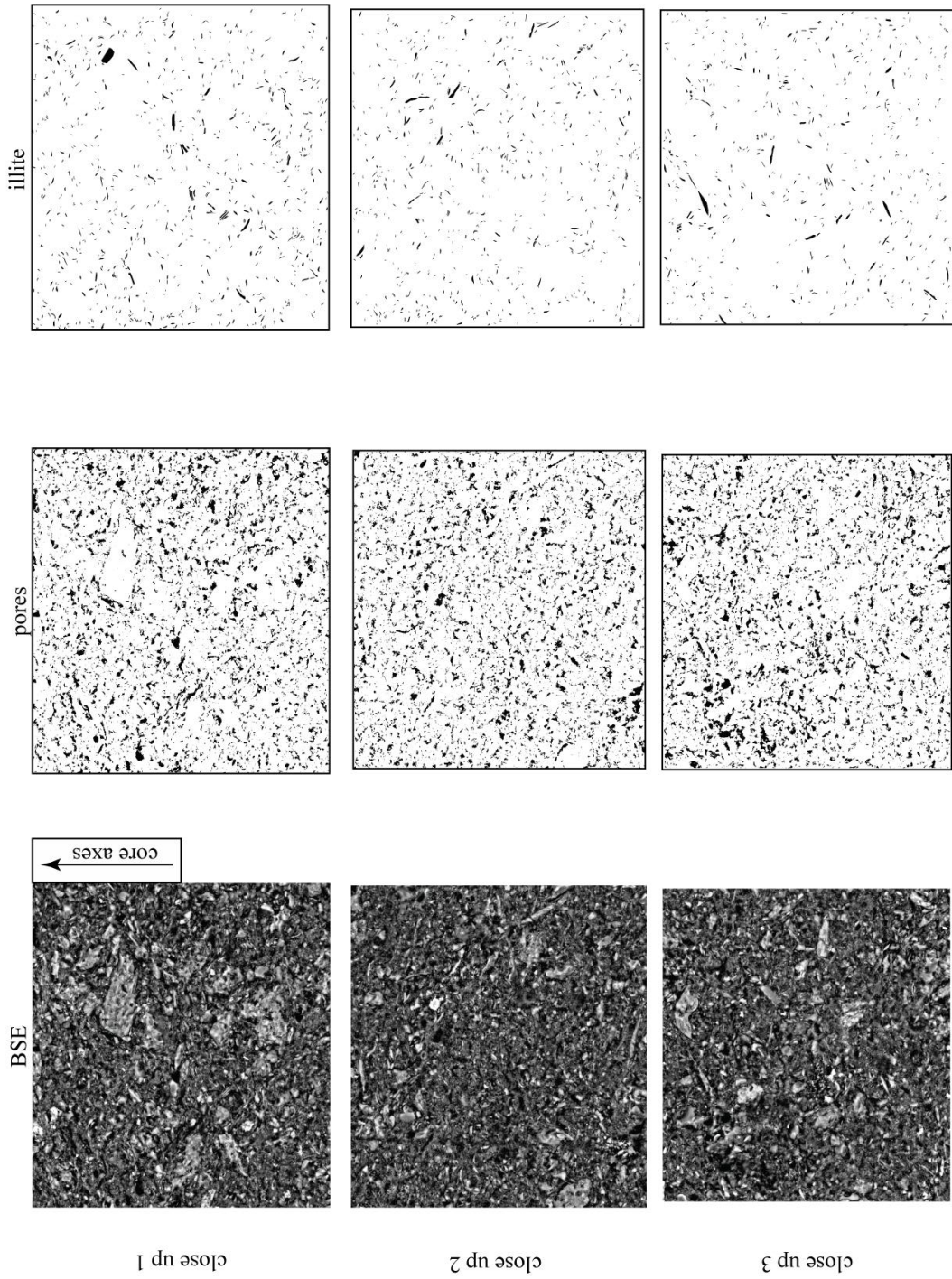


Figure A 2.3: 316-C0004C-8H-2, K010

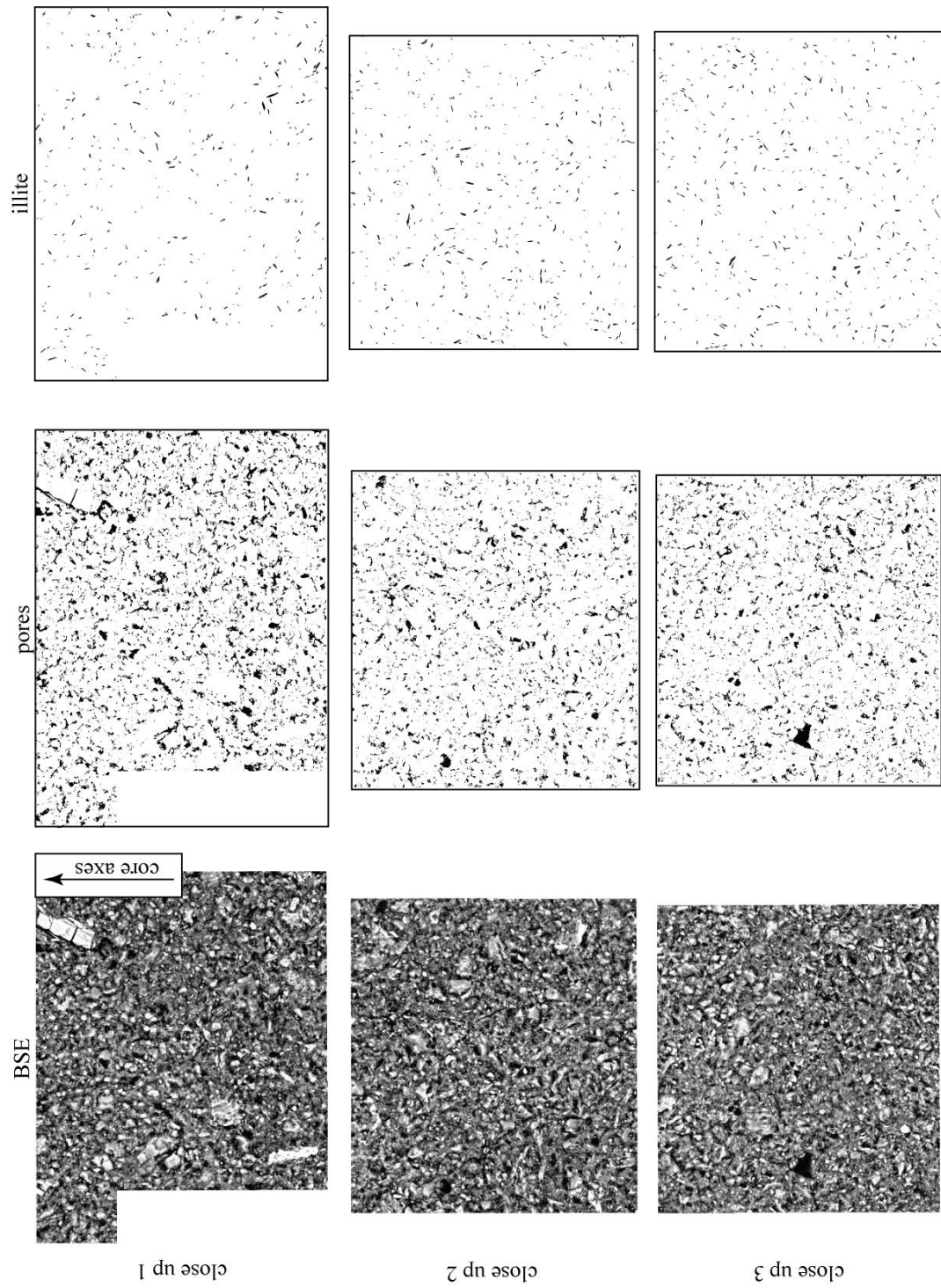


Figure A 2.4: 316-C0006E-20X-3, K013

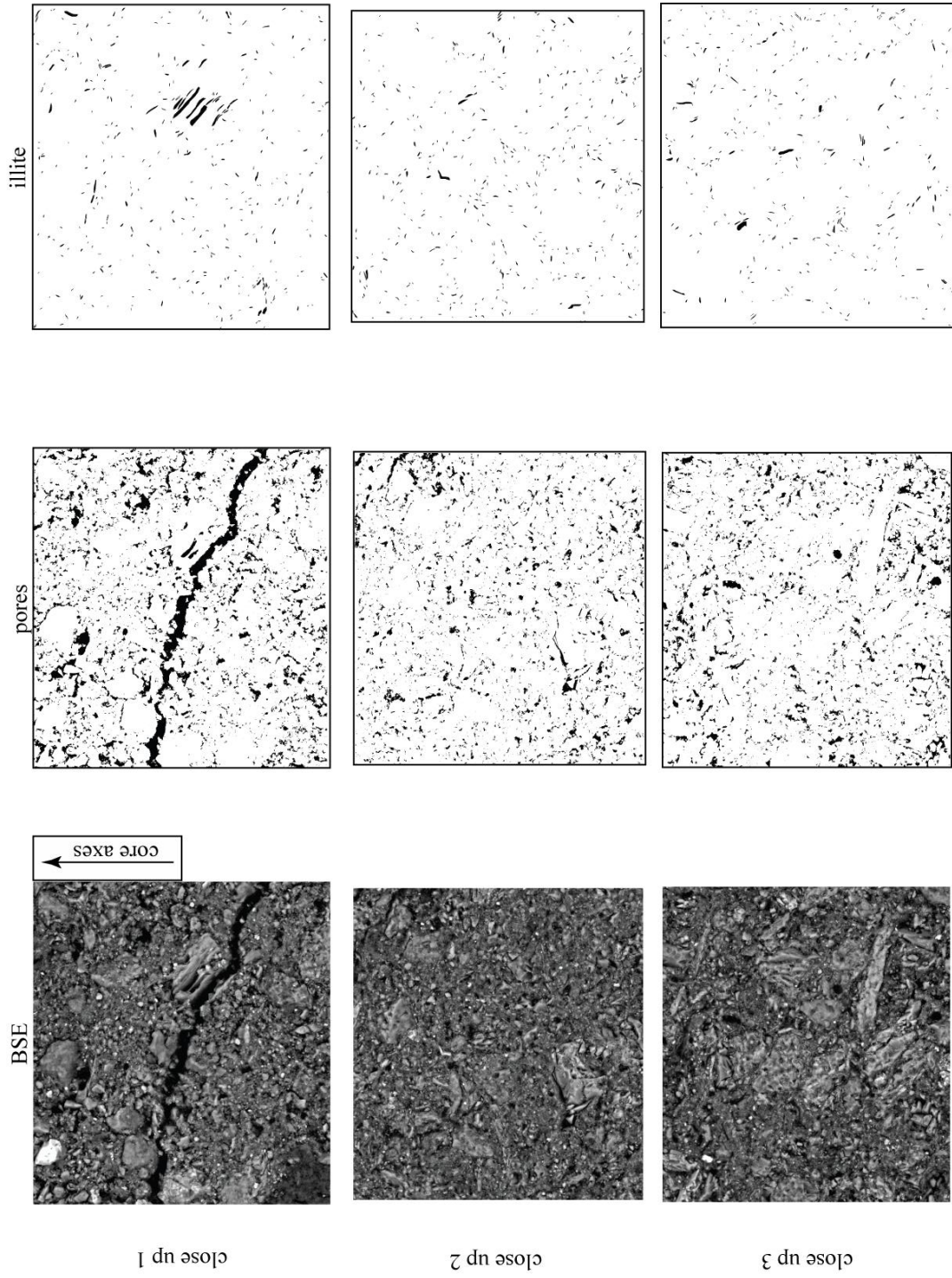


Figure A 2.5: 316-C0007C-7X-1, K011

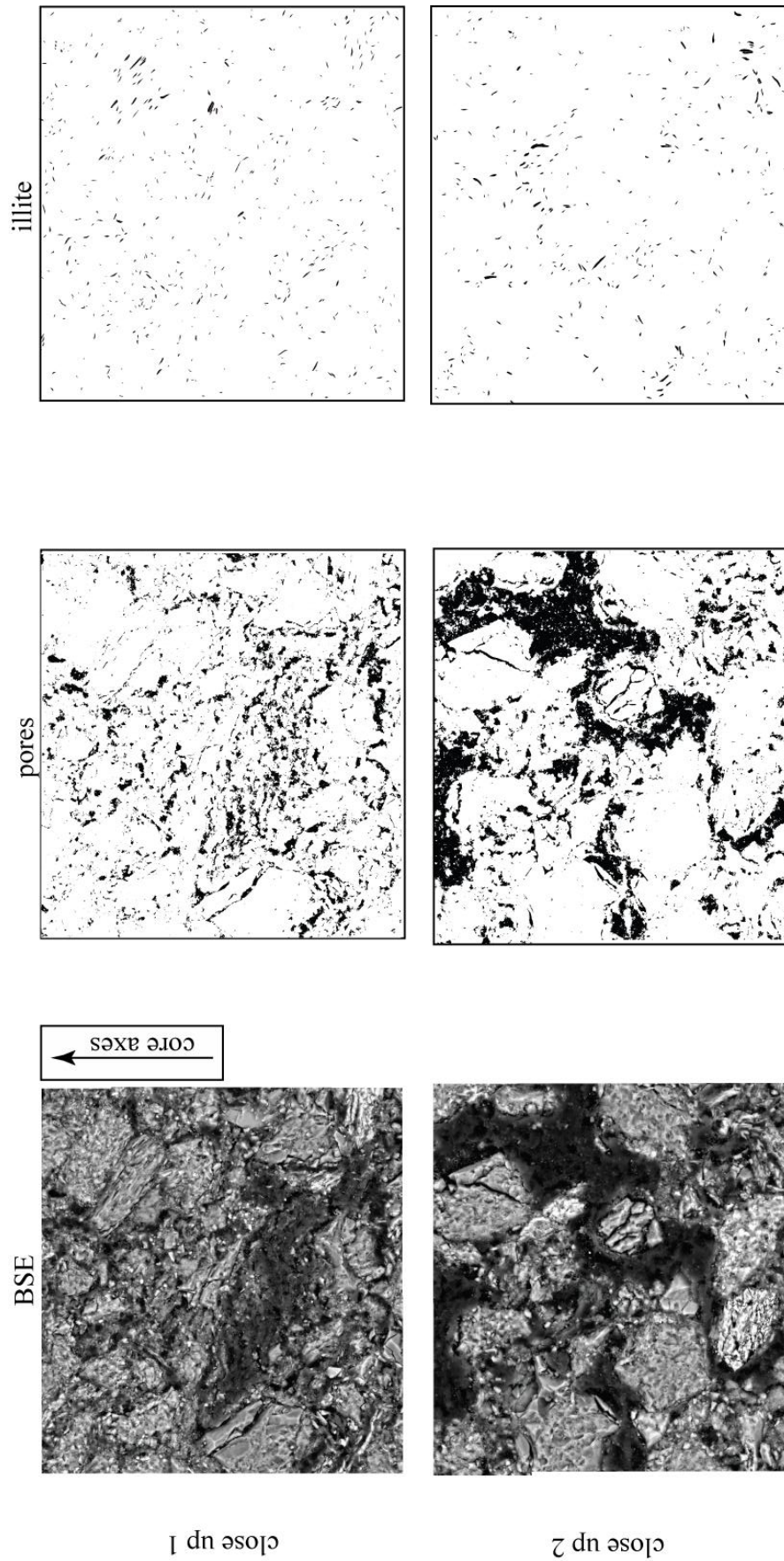


Figure A 2.6: 316-C0007C-7X-1, K016

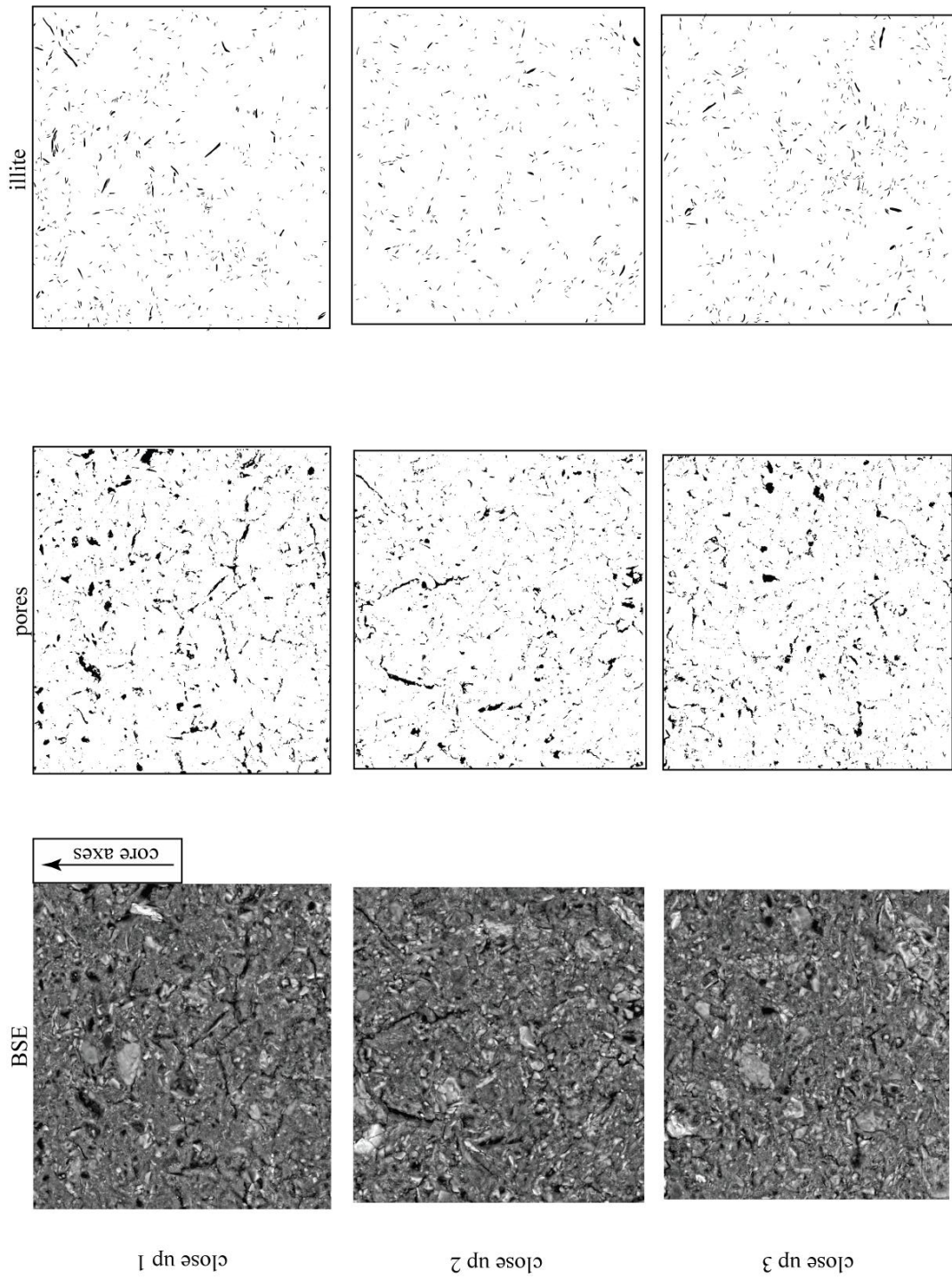


Figure A 2.7: 316-C0008A-9H-3, K014

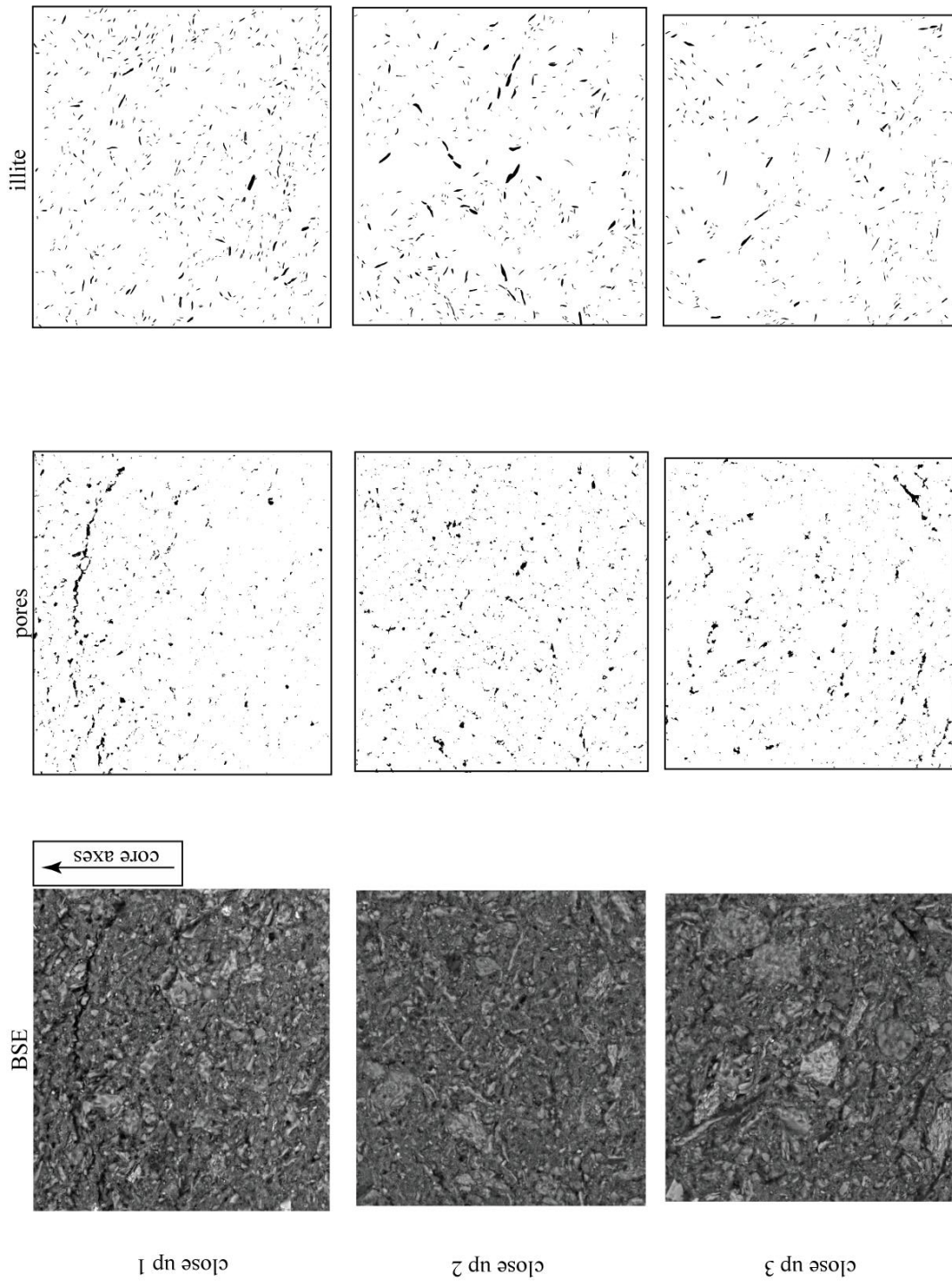


Figure A 2.8: 316-C0008C-7H-8, K018

A 2.2 Data processing

To obtain complete texture information from raw image plate detector files, several processing steps are required. In the following, I will shortly describe the principle steps of data processing used in this study. Data analysis and processing were done in four steps which are data conversion, data input into Maud, Rietveld refinement and texture calculation (Figure A 2.9).

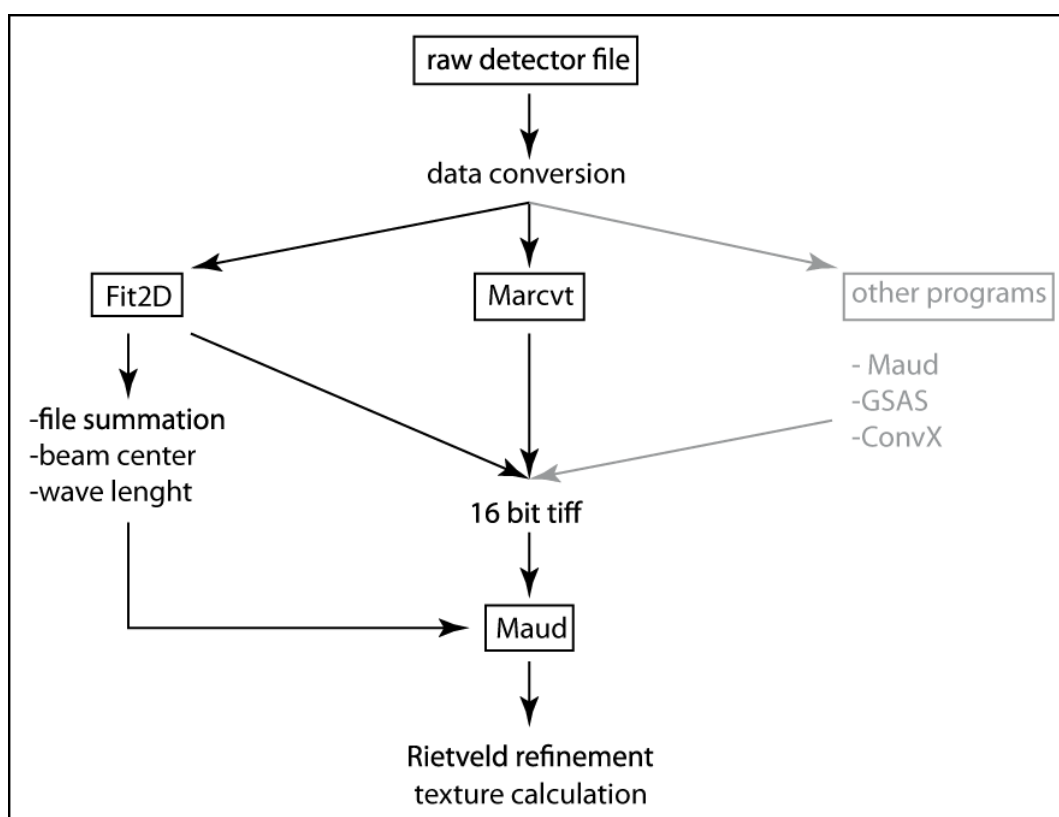


Figure A 2.9: Flowchart illustrating processing steps. Data conversion using Maud, GSAS and ConvX is not further considered here.

Raw data processing

As a first step of data processing, the image plate detector file format (.mar) was converted into 16-bit tiff, which is the input format of Maud. Data conversion using the Windows-based “Fit2D” program and the Linux-based “marcvt” will be described in the following. Programs such as “GSAS” and “ConvX” can also be used for data conversion, but are not further described. A detailed description of the data conversion using Maud is available on

<http://eps.berkeley.edu/~wenk/TexturePage/MAUD.htm#Introduction%20MAUD> and on <http://www.youtube.com/watch?v=3G6DGgYmO-g>.

Data conversion using Fit2D

The open source program Fit2D (Hammersley 1995, 1998) is available on the internet (<http://www.esrf.eu/computing/scientific/FIT2D/>). A detailed description and a manual of Fit2D are available on http://geoweb.princeton.edu/research/MineralPhy/private/fit2d_ref_10_3.pdf. After starting the program, the detector dimensions need to be specified in the “DIMENSION OF PROGRAM ARRAYS” window. The detector specifications are known from the laboratory. In this study the detector dimensions were added to the raw detector file as an extension. The ending .mar2000 indicate 2000x2000 pixels detector dimension. The default settings of Fit2D were used for the other parameters. After confirming the settings, the “IMAGE PROCESSING (GENERAL)” option enables the data file format to be converted. Using the “INPUT” button, the input file (raw detector format) was defined. The detector image was opened, visually controlled and stored as 16bit tiff using the “OUTPUT” option. This way of data conversion enabled the detector files to be checked. However, as only single files can be converted, processing of large datasets is complex and time consuming.

Data conversion using “marcvr”

The open source program “marcvr” uses simple Linux commands for data conversion. Marcvr was downloaded from the web page of the Marresearch GmbH (<http://www.marresearch.com>). The command line “`marcvr *.*.mar -tiff16 *.*`” was used to convert the raw detector files (.mar) into 16bit tiff files. With this method, processing of large datasets is possible within seconds, but visual checking of detector images is not possible.

Data visualization

Although the data files were converted into a .tiff format, the detector images cannot be visualized by standard image processing programs. For data visualization, the program “marView” from the Marresearch GmbH was downloaded (<http://www.marresearch.com>). Amongst other options, this program provides the ability to edit the color scale and to plot profiles across the detector image.

Further data processing steps

File summation

The summation of single files is advantageous using textured sample material because it provides a texture-free summed file to pre-refine parameters such as the sample detector distance, crystal size and to determine the beam center.

In the program menu of Fit2D, the option “FILE SERIES” and “AVERAGE” is chosen. After setting the storage path of the raw .mar-files and defining the first and the last file of the series, the data increment was defined by setting the option “1”. Then, all files of the dataset will be used for data summation. Choosing “2”, odd file numbers will be used (1, 3, 5...), while even file numbers will be used by choosing “3” (2, 4, 6...). Pressing the “OUTPUT” button, the file format of the summed average file is defined; ideally “TIFF 16 BIT”. After setting the output name, the summed file is stored. By pressing the “EXIT” button, the program returns to the main menu and the previously processed data will be stored in the temporary storage of Fit2D.

Beam centre

In the next step, the beam center is determined. The program menu of Fit2D is still open and the previously processed data are stored in the temporary storage. For this reason, determination of the beam center directly follows the step of file summation. The options “POWDER DIFFRACTION (2-D)” and “BEAM CENTRE” are selected in the program window. Several options for the beam center determination are available in the “BEAM CENTRE” menu. The option

“ELIPSE COORDINATES” was used in this study, since tilted sample cylinders would cause elliptic Debye-Scherrer rings on the detector image. The option “TWO CLICK” is used to define at least five points on a diffraction ring (note: this option is activated after clicking the “TWO CLICK” button and the selection of the two click option is indicated by the appearance of “ONE CLICK”). Clicking into the detector image presets the point which was refined in the loupe window. After defining at least five points on a single diffraction ring the points were confirmed by pressing the “CLICK TO FINISH” option and the coordinates of the beam center will appear immediately in the DOS-Window running in the background. The beam center coordinates are given in mm and pixels. These values cannot directly be used as beam center coordinates, since the coordinate origin of Fit2D and Maud are not identical (Figure A 2.10). The y-value has to be recalculated depending on the detector format.

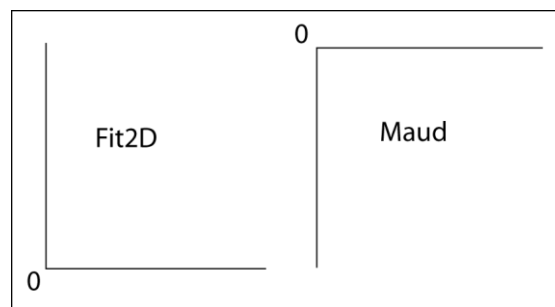


Figure A 2.10: Origin of the coordinate system in Fit2D and Maud

Table A 2.1: Conversion of the detector dimensions from pixels to mm

detector dimension [pixels]	detector dimension [mm]
1600 x 1600 (.mar1600)	240 x 240
2000 x 2000 (.mar2000)	300 x 300
2300 x 2300 (.mar2300)	345 x 345

The size of the detector image is known from the ending of the raw detector file (.mar2000). In case of a .mar2000 file (Table A 2.1), the equation $Y_{\text{Maud}} = 300 - Y_{\text{Fit2D}}$ follows. The x- and the y-coordinate were then used to define the beam center in Maud.

Wavelength

To determine the wavelength of the synchrotron beam, a corundum (Al_2O_3) standard from the National Institute of Standards and Technology (NIST) was measured prior to the texture measurements. The measured standard data were added as described above) using the “POWDER DIFFRACTION (2-D)” and “INPUT” options. When the detector image shows up, the standard material “ALUMINA (Al_2O_3)” needs to be defined in the “CALIBRANT” option. Starting values of the sample to detector distance and the wavelength are added to the “CALIBRANT PATTERN REFINEMENT” window. The sample detector distance is known from the laboratory and a wavelength of $\sim 0.12 \text{ \AA}$ was used as a starting value. These parameters will be refined in further steps of data processing. The default settings of Fit2D can be kept for the other parameters.

The option “REFINE X/Y BEAM CENTRE” is activated (“YES”) and the detector distance is kept constant (“NO”). When pressing the “O.K.” button, some points on the inner ring are defined (as described for the determination of the beam center). After using the “CLICK TO FINISH” button, the wave length will be given in the DOS-Window. The wavelength is later used as input for Maud.

Introduction to MAUD

A combined Rietveld Refinement and texture calculation is included in the Maud program (**m**aterial **a**nalysis **u**sing **d**iffraction; Lutterotti et al., 1999, 2007). The Maud program is distributed free of charge and can be downloaded from the Maud homepage (www.ing.unitn.it/~maud). Maud is written in Java and runs on Windows, MacOSX, Linux and Unix (32bit and 64bit versions are available). Maud is developed for Rietveld refinement and quantitative phase analysis and offers the possibility to analyze microstructure, texture and residual stress using part or full diffraction spectra (Lutterotti et al., 2007). Crystallographic information and structures are added as .cif to the Maud program. Maud manuals and helpful tutorial videos can be found on the internet. The first steps using Maud are described in detail in a tutorial video of Luca Lutterotti, available on http://www.youtube.com/watch?v=J5aP_j-3AXI.

Defining instrument parameters

From the previous processing steps, all parameters are known to start the data analysis in Maud. After starting Maud, the “DataFileSet_x” is activated by a single click (Figure A 2.11 A; a double click allows to rename the DataFileSet) and the “Eye-Icon” (Figure A 2.11 B) opens a new window. The tab “General” is selected and the “Edit-button” (Figure A 2.11 C) allows to add specific parameters in the “Diffraction Instrument” window. The “Incident intensity” is refined by a right mouse click into the red box. Further parameter settings are dependent on the diffraction instrument. The settings used in this study are given in Table A 2.2 (see also <http://www.youtube.com/watch?v=3G6DGgYmO-g>).

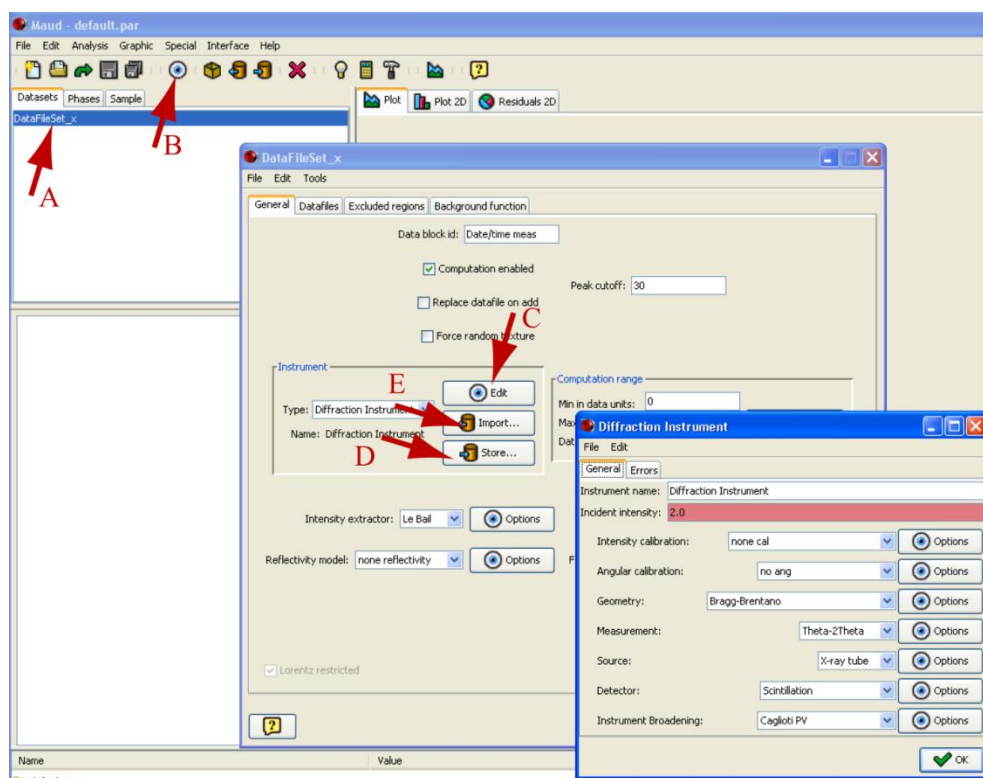


Figure A 2.11: Setting up the instrument parameter file in Maud. The instrument parameters are given in Table A 2.2.

Table A 2.2: Parameter settings.

option	parameter	specification (option button)
Intensity calibration	none cal	none
Angular calibration	Flat Image Transmission	detector distance (from Fit2D)

Geometry	Image 2D	none
Measurement	2Theta	none
Source	Synchrotron	wavelength (from Fit2D)
Detector	Standard	none
Instrument Broadening	Caglioti PV	_riet_par_asymmetry_value0 → 0, fixed _riet_par_asymmetry_value1 → 0, fixed

After confirming the parameter settings by pressing “OK”, the program automatically returns to the “DataFileSet_x” window. Storing of the instrument parameters (Figure A 2.11 D) allows to reload the settings for further analysis or repetition runs (Figure A 2.11 E).

Adding data files to Maud

To add data files to Maud, the option “From images” (Figure A 2.12 A) in the “DataFileSet_x” window is used (the option “Browse” will be used if .esg files are available, Figure A 2.12 B). The “From images” option opens the “Area Image” plug-in of Maud and the .tiff files are added using the “File” – “Open” option (Figure A 2.12 C). After choosing a data file, the respective detector image appears. In a first step, the scaling of the detector image is controlled. The size of the detector image is given in the upper left corner and should equal the dimension previously defined for the detector. If the dimensions deviate, the size of the file should be adjusted using the “Set scale” option in the “Analyze” menu (Figure A 2.12 D). The intrinsic values used in this study are given in Table A 2.3.

After adjusting the size, the option “Multi-spectra from normal transmission/reflection image” in the “Plugins” menu (Figure A 2.12 E) is used to set further parameters (Table A 2.4 4).

Table A 2.3: Settings to rescale the plate detector image

Distance in pixel	6.66667
Known distance	1
Pixel aspect	1
Unit of length	mm
Global	uncheck

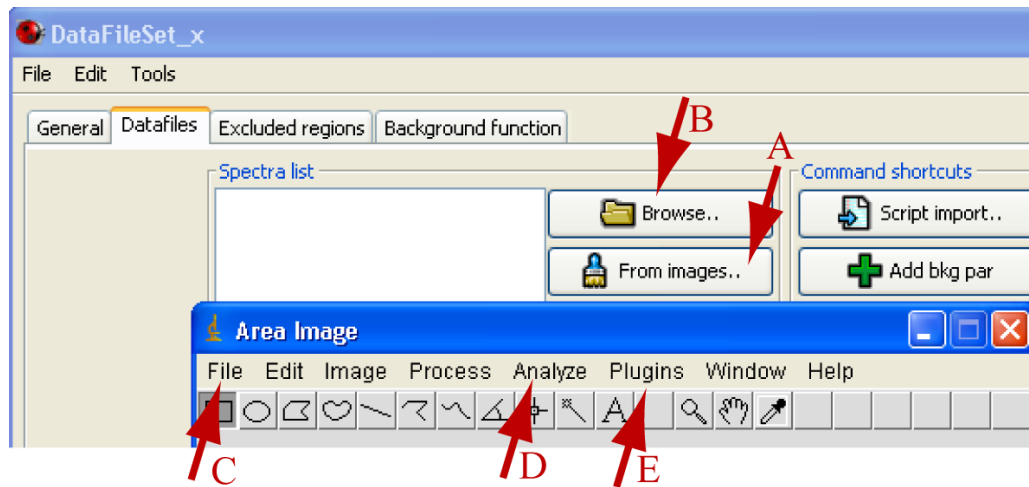


Figure A 2.12: Adding data to Maud.

Table A 2.4: Parameter settings for image integration

Parameter	Description	Value used in this study
Sample-Detector distance	known from the lab	dependent on the experimental settings
Center X	determined using Fit2D	
Center Y	determined using Fit2D	
Tracker circle radius	circle for optical beam center control	50
Starting angle	angle for image integration	0.0
Final angle	angle for image integration	360.0
Number of spectra	defines the size of the slices of data integration	72.0 (5° slices)
Omega angle	tilt of the sample	0
Chi angle	tilt of the sample	0
Phi angle	sample rotation around the cylinder axis	angle of rotation + 90
2-Theta angles calibrated		uncheck
Image tilting Sx		0.0
Image tilting Sy		0.0
Reflection image		uncheck

The parameter settings are checked using the “Update” button and are finally confirmed by pressing “OK”. After a view seconds a new window shows up and the storage location and the name of the newly generated .esg-files are defined. At this point, a diffractogram automatically appears in the main window of Maud (see

also <http://www.youtube.com/watch?v=XUkABul-yzY>). This step is repeated multiple times (37 times in case of this study) until all files from a sample are added to Maud.

Adding phase information

Prior to data refinement, appropriate phase information needs to be added to Maud. The tab “Phases” is activated in the main window of Maud (Figure A 2.13 A) and .cif-files (crystallographic information files) are added.

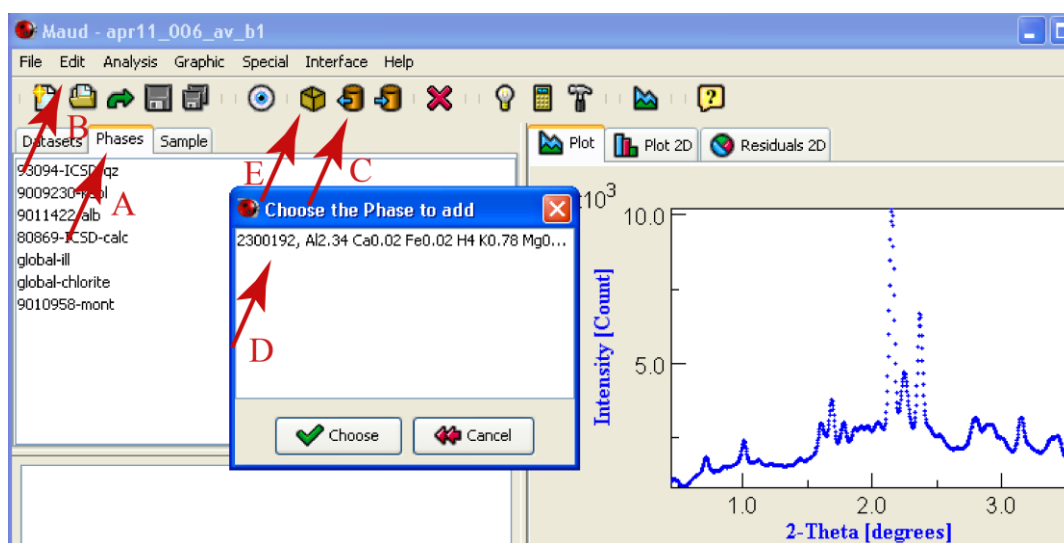


Figure A 2.13: Adding phase information to Maud.

Crystallographic information files are available on the internet from the Crystallography Open Data base (<http://www.crystallography.net/>) and are added to Maud using the “Load object from cif” option in the main menu (Figure A 2.13 B) or by using the shortcut button (Figure A 2.13 C). The crystallographic model is selected by a single click (Figure A 2.13 D) and is finally confirmed by pressing the “Choose” button.

Maud additionally provides the option to create new .cif-files by using the “Add new object” option in the “Edit” menu or the shortcut “box symbol” (Figure A 2.13 E). Creating new structures is described in detailed in the third video lesson of Luca Lutterotti (<http://www.youtube.com/watch?v=M4oFKr0oEqM>). This option was not used in this study, and thus is not further considered here.

The spectrum is computed by clicking the “Compute” button (Figure A 2.14 A). After some seconds, the simulated spectrum appears as a black line in the main window. A list of phases (Figure A 2.14 B) and a peak list indicating the peak positions (Figure A 2.14 C) is displayed below the spectrum. A differential plot (Figure A 2.14 D) indicates the error between the simulated and the measured spectra and the total error of the analysis is shown in the left box (Figure A 2.14E). A detailed description on adding phases to Maud is provided in the second video lesson by Luca Lutterotti (<http://www.youtube.com/watch?v=ZkMYKG40yVc>).

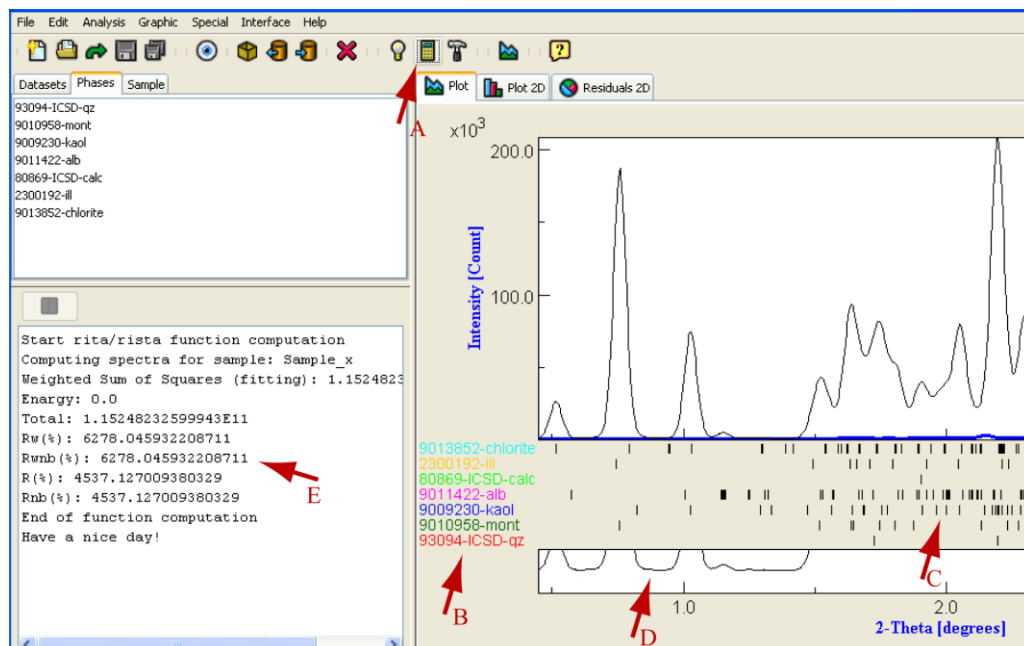


Figure A 2.14: Spectra computation

Background fit

After introducing phase information and first spectra computation, the background and scale parameters have to be defined. For the background, the “DataFileSet_x” is activated in the “Dataset” tab. The “Eye” opens the “DataFileSet_x” menu and the “Background function” tab was activated (Figure A 2.15 A). Several background options are available. A “Polynomial” background (Figure A 2.15 B), can be applied to the data and additional background coefficients allow to fit complex backgrounds to the dataset. More complex background functions can be configured using the “Interpolated” option (Figure A 2.15 C), allowing the presetting of a large number of interpolation points. Since

this option was not used in this study, it is not further described (for a detailed description see <http://www.youtube.com/watch?v=HpN2WwzloR0>).

The “Background and scale parameters” shortcut in the “Wizard tool” (Figure A 2.15 D, see also <http://www.youtube.com/watch?v=CuZ hXx6IZak>) was used in this study. After several iterations, the optical fit and the decreased error values indicate an improved fit between the simulated and the measured data.

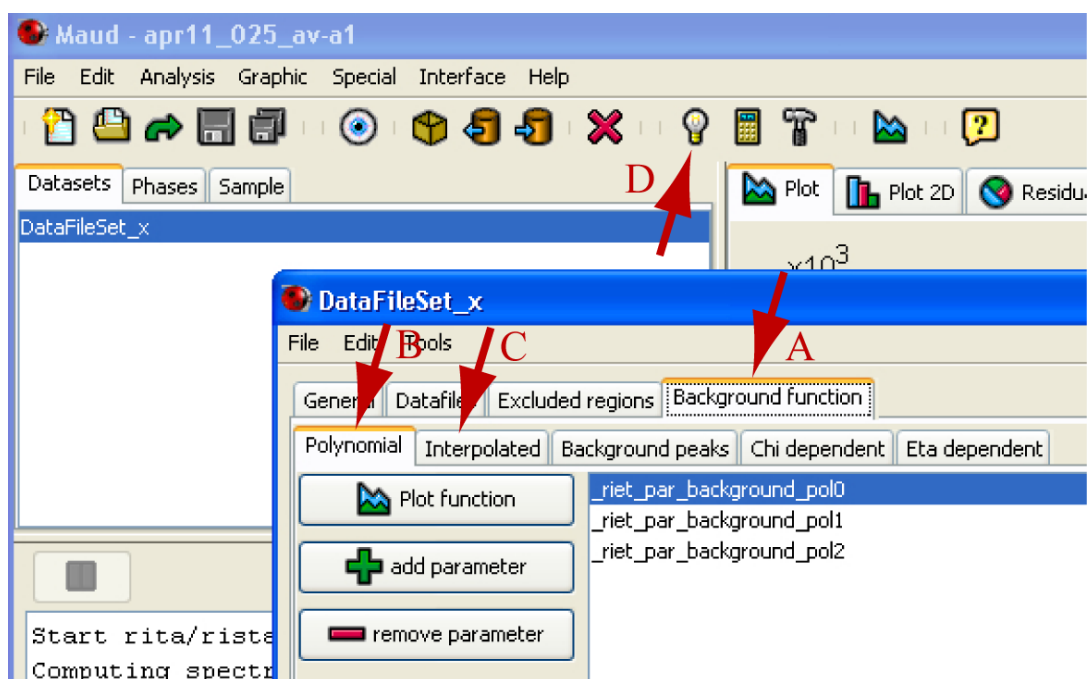


Figure A 2.15: Background refinement.

Data refinement

Before starting the data refinement, the initial parameters should be close to the best fit, otherwise the program is not able to find the best fit and will not converge during refinement. Several ways of parameter refinement are possible and are described in the following.

All parameters are listed in the bottom window of Maud. Clicking on “Status” of the parameters enables to fix, refine or bound them. When the status is adapted, the “Hammer” button (next to the “Compute” button) is used to start the data refinement. Parameters can be changed manually by clicking on “Value”. The activated parameter is highlighted and its value can be changed by clicking on the

“arrow keys” next to the parameter. The spectrum is immediately recalculated by the program and the change becomes visible (see also <http://www.youtube.com/watch?v=CuZhXx6IZak>) and an optical and adaption control of the refinement is possible.

Another option for data refinement is the “Parameter List” in the “Analysis” menu. All refinable parameters are listed in the same order as in the bottom window of Maud. Below the parameter list (“Tree Table”), some additional options and shortcuts for data refinement are available (<http://www.youtube.com/watch?v=NsXD5IYMzzk>). In the “Tree Table”, the values of the parameters can be changed as described and the recalculation starts after the “Tree Table” is closed. The refinement has to be started manually by clicking the “Hammer” button.

Table A 2.5: Parameters refined during the different refinement steps

refinement step	parameter	status
1	-wavelength	-refined
	-beam center	-refined
	-sample detector distance	-refined
2	-previous parameters	-fixed
	-crystal size	-refined
3	-previous parameters	-fixed
	-cell parameter	-refined
4	-previous parameters	-fixed
	-temperature coefficient	-refined
5	-previous parameters	-fixed
	-atom site occupancy	-refined
6	-previous parameters	-fixed
	-texture calculation	

A simple text editor provides the third way of parameter manipulation. All parameter settings are stored by the program in a .lst-file (in the same directory where the analysis is stored) and can be manipulated in this file. Individual parameters are not explained in detail here, but a list of the refined parameters is given in Table A 2.5.

Additional processing steps, such as stress model calculation and pressure correction were not used in this study and are therefore not further described (a detailed description is given in the second Maud video lesson of Luca Lutterotti). Further information on the data refinement are given in the third video lesson of Luca Lutterotti (see http://www.youtube.com/watch?v=_5ezLbjVwS0).

Texture calculation

When the fit of the simulated and the measured data is reasonable, the final step of texture calculation follows. The fit of the dataset was checked optically in the “Plot 2D” tab (Figure A 2.16 A) or by plotting the “Residuals 2D” (Figure A 2.16 B). Both plots are adequate to check the quality of the fit between the experimental and the simulated data. The peak position of the simulated and the experimental data should fit, while intensity variations along single rings directly represent the sample’s texture. To calculate the texture, the “Phase” tab is activated and the respective phase is selected. By clicking the “Eye” icon, a new window opens in which all parameters of the respective phase are finally checked. In the “Advanced models” menu (Figure A 2.16 C), parameters for the texture calculation are defined. The “E-WIMV” option (an enhanced WIMV model, Matthies and Vinel, 1982) is available in the texture drop-down menu (Figure A 2.16 D). The modification of the WIMV algorithm improves the integration of the Rietveld method and the texture calculation, and provides the possibility to enter data in arbitrary positions (Wenk et al., 2003). Clicking the “Options” button (Figure A 2.16 E), the “E-WIMV options panel” opens and further options can be set. By clicking the “Close”, “OK” and “Hammer” button, the parameter settings are confirmed and the refinement is started.

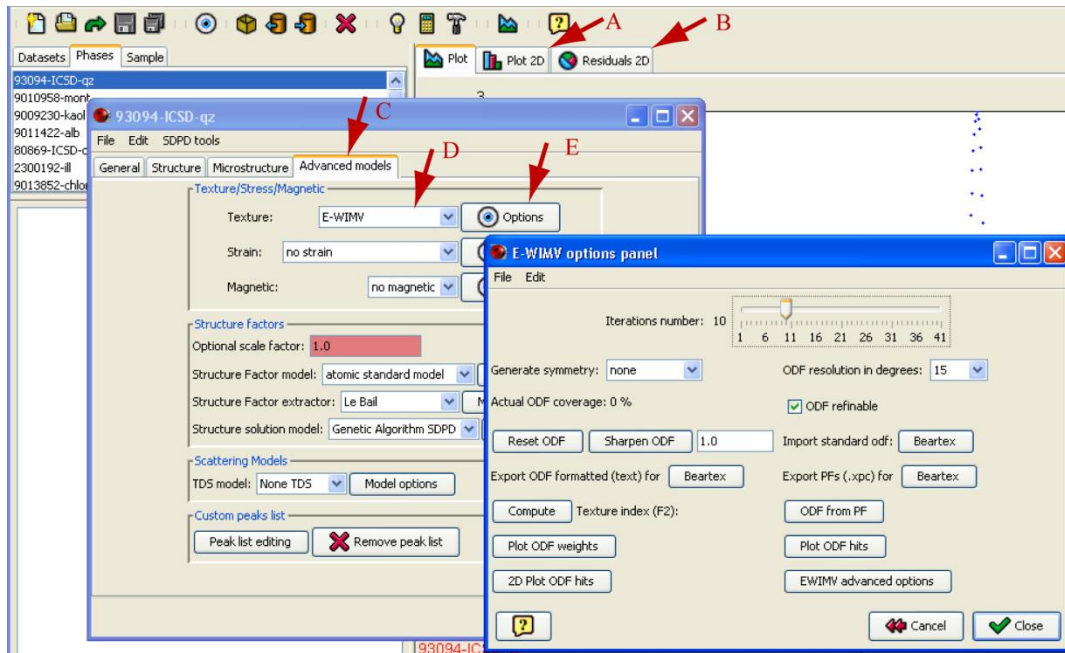


Figure A 2.16: Texture calculation

The results of a texture calculation are plotted using the “Graphic” menu in the main window of Maud. In the “Texture plotting” window, the phase and pole figure of interest is selected. Clicking the “Plot” button confirms the settings and the results will be plotted (Figure A 2.17). Because the texture plotting in this study is done using the program “Pfplot32” (by C. Umlauf and K. Ullemeyer), no further pole figure manipulations in Maud are applied.

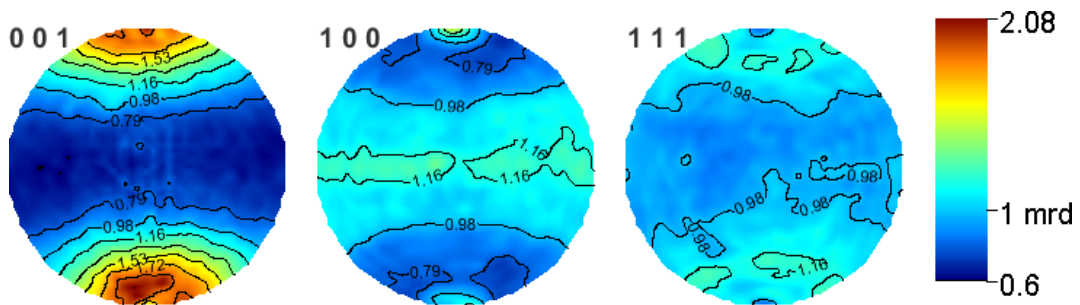


Figure A 2.17: Kaolinite pole figure plots as an example of a final output.

Helpful links

Numerous tutorials and manuals are available on the internet. The youtube tutorial video lessons of Luca Lutterotti are especially helpful.

http://www.youtube.com/watch?v=J5aP_j-3AXI

<http://www.youtube.com/watch?v=HpN2WwzloR0>

<http://www.youtube.com/watch?v=ZkMYKG40yVc>

<http://www.youtube.com/watch?v=CuZhXx6IZak>

<http://www.youtube.com/watch?v=UhgxqmbptxU>

<http://www.youtube.com/watch?v=NsXD5IYMzzk>

<http://www.youtube.com/watch?v=3G6DGgYmO-g>

<http://www.youtube.com/watch?v=XUkABul-yzY>

<http://www.youtube.com/watch?v=M4oFKr0oEqM>

http://www.youtube.com/watch?v=_5ezLbjVwS0

<http://www.youtube.com/watch?v=oXi-8fzFw2I>

<http://www.youtube.com/watch?v=EucQEunUsx8>

The new beta version of Maud is presented in three additional tutorial videos:

<http://www.youtube.com/watch?v=MX-Vzgv2PQ>

<http://www.youtube.com/watch?v=Zr30VnBIT4I>

http://www.youtube.com/watch?v=DSWse_vFzN4

Further links:

An introduction to Maud is available on:

<http://eps.berkeley.edu/~wenk/TexturePage/MAUD.htm#Introduction%20MAUD>

Further tutorials are available at the Maud homepage:

<http://www.ing.unitn.it/~maud/tutorial.html>

A Fit2D manual is available on:

http://geoweb.princeton.edu/research/MineralPhy/private/fit2d_ref_10_3.pdf

References

- Hammersley, A.P., 1998. FIT2D V10.3 Reference Manual V4.0 ESRF98HA01T.
- Hammersley, A.P., S.O. Svensson, M. Hanfland, A.N. Fitch and D. Häusermann (1995): Two-dimensional detector software from real detector to idealized image or two-theta scan. *High Pressure Research*, 14, 235-248
- Lutterotti, L., M. Bortolotti, G. Ischia, I. Lonardelli and H.-R. Wenk (2007): "Rietveld texture analysis from diffraction images", *Zeitschrift für Kristallographie, Suppl.* 26, 125-130
- Lutterotti, L., S. Matthies, and H.-R. Wenk (1999): "MAUD: a friendly Java program for material analysis using diffraction." *Proceeding of the Twelfth International Conference on Textures of Materials (ICOTOM-12)*, Vol. 1, 1599
- Matthies, S., Vinel. G.W., 1982. On the Reproduction of the Orientation Distribution Function of Texturized Samples from Reduced Pole Figures Using Conception of a Conditional Ghost Correction. *Physica Status Solidi (b)* 112, K111
- Wenk, H.R., Lutterotti, L., Vogel, S., 2003. Texture analysis with the new HIPPO TOF diffractometer. *Nuclear Instruments and Methods in Physics Research* 515, 575-588, doi: 10.1016/j.nima.2003.05.001
- Wenk, H.-R., M. Voltolini, H. Kern, T. Popp and M. Mazurek (2008): Anisotropy in shale from Mont Terri. *The Leading edge*, 742- 748
- Wenk, H.-R., S. Matthies and L. Lutterotti, (1994): "Texture analysis from diffraction spectra", *Mater. Sci. Forum*, 157-162, 473-480

A 2.3 Synchrotron texture measurements, natural samples

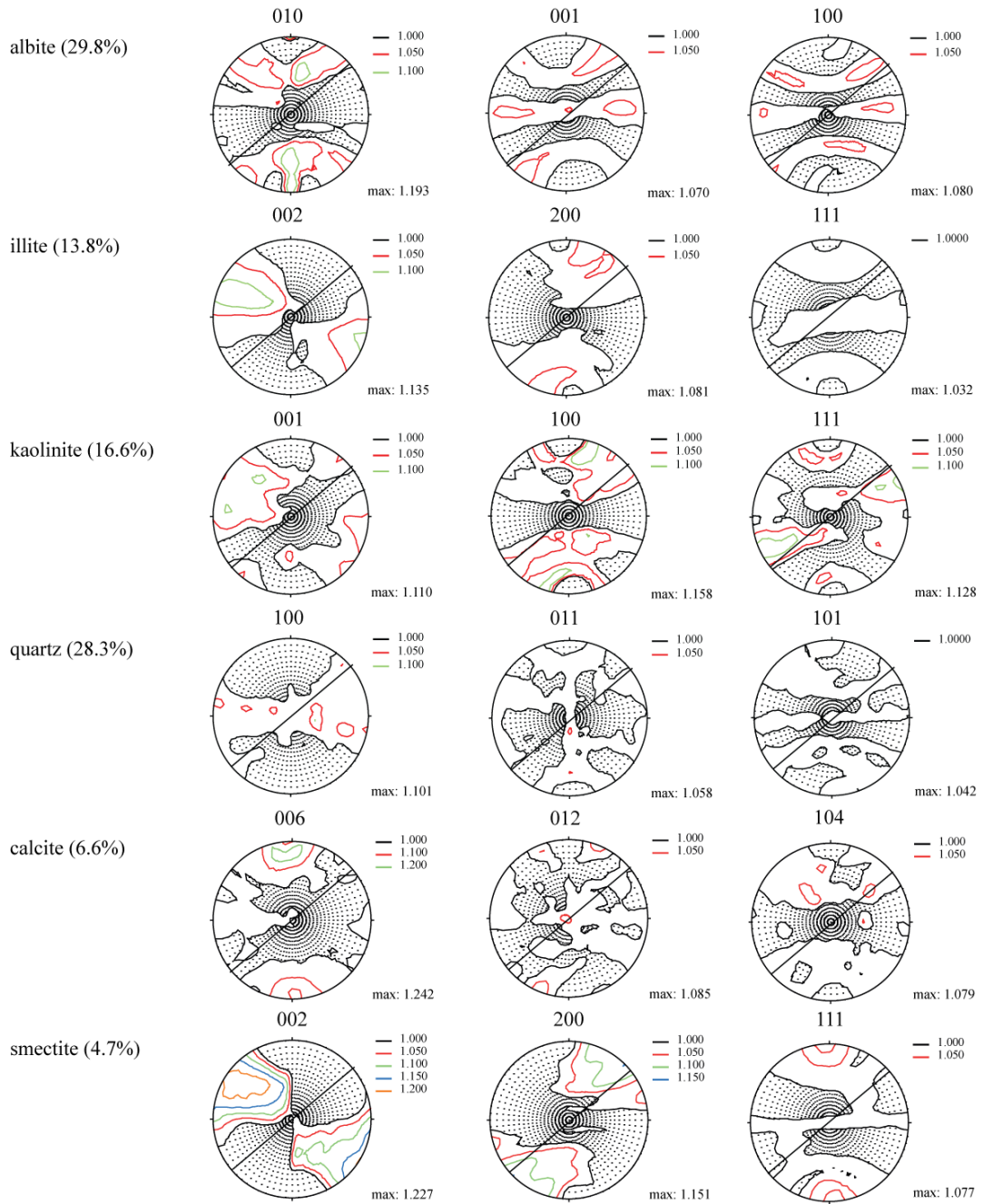


Figure A 2.18: Sample 333-C0012C-4H-5, 28.9 mbsf

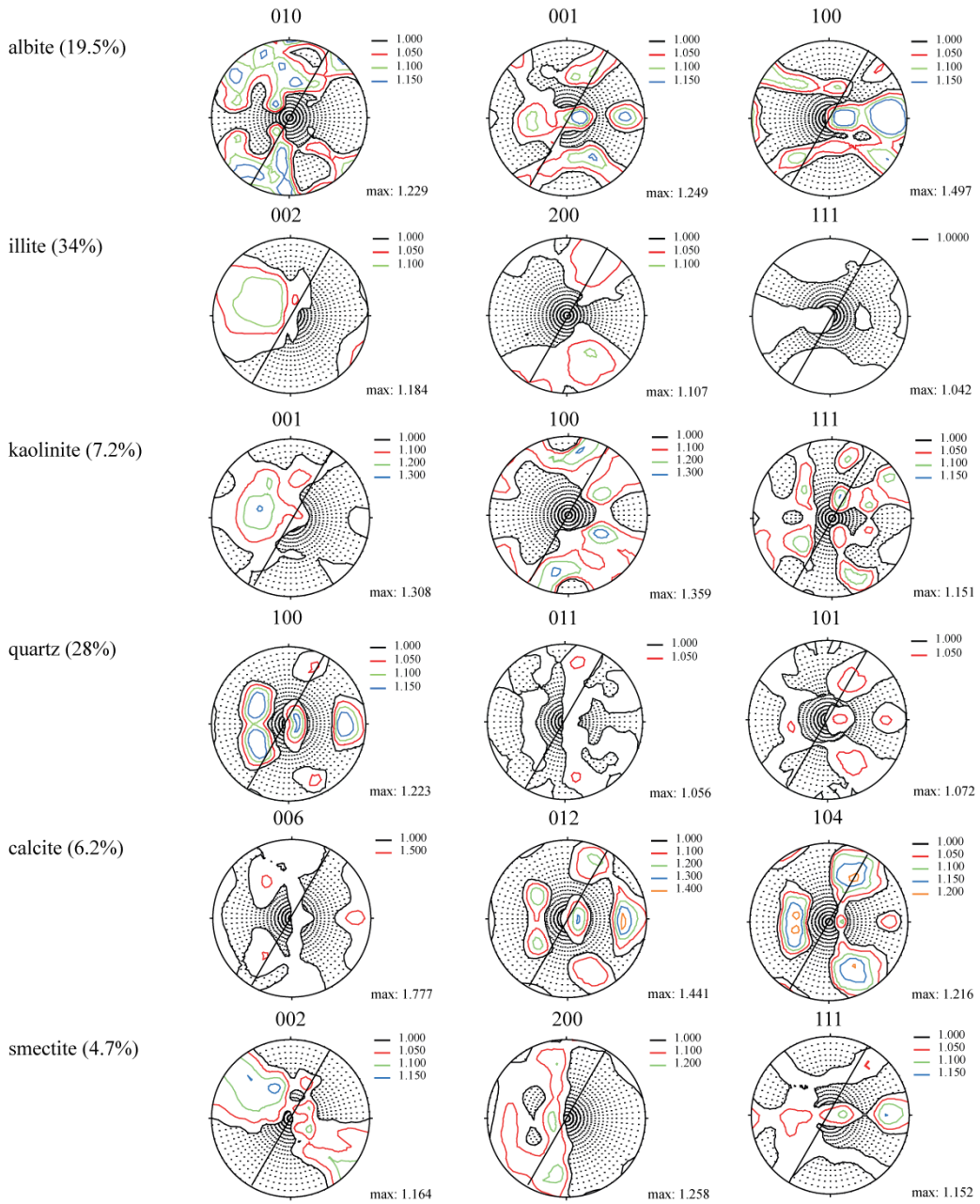


Figure A 2.19: Sample 333-C0012C-9H-6, 75 mbsf

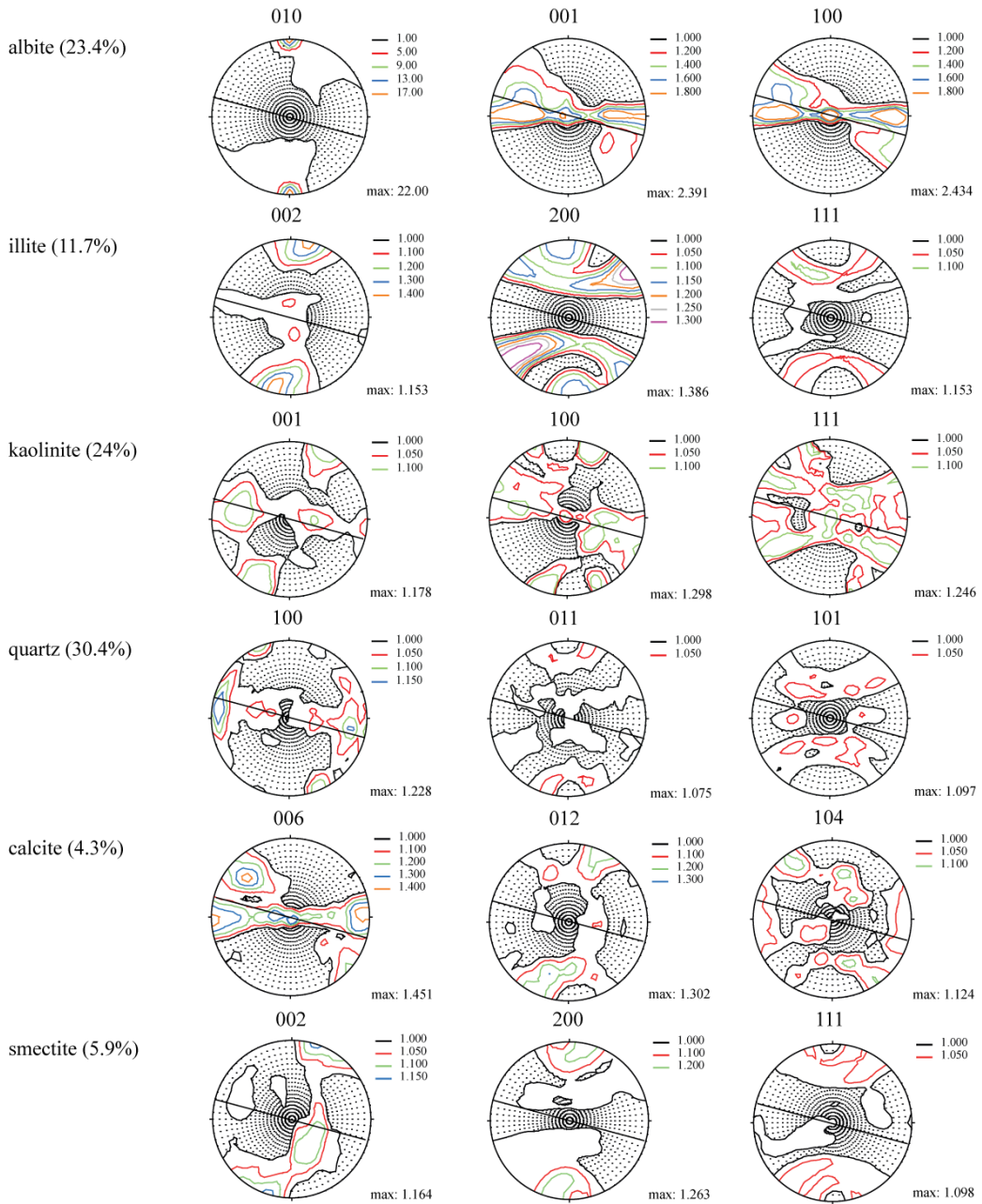


Figure A 2.20: Sample 333-C0012C-15H-5, 121.6 mbsf

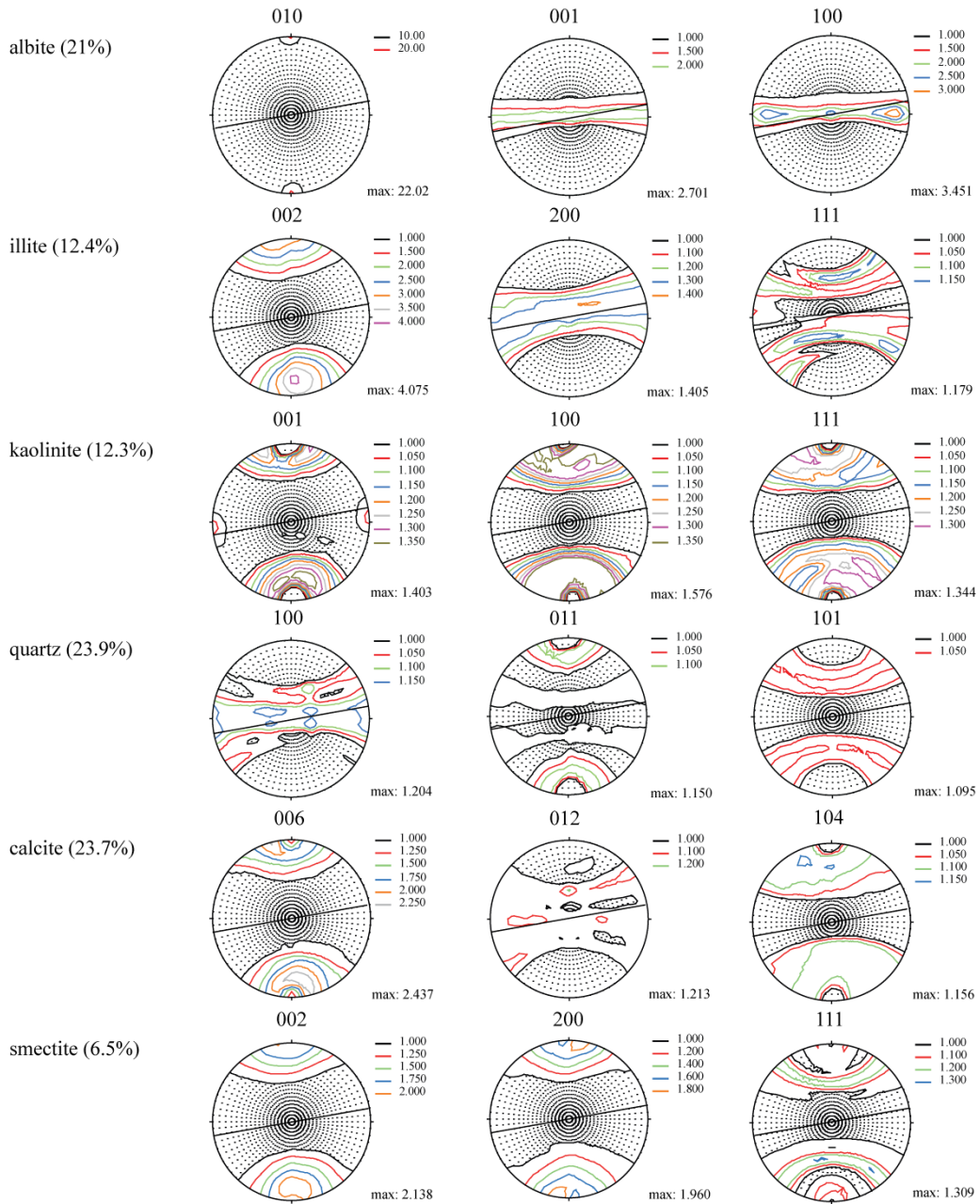


Figure A 2.21: Sample 333-C0012E-3X-4, 522 mbsf

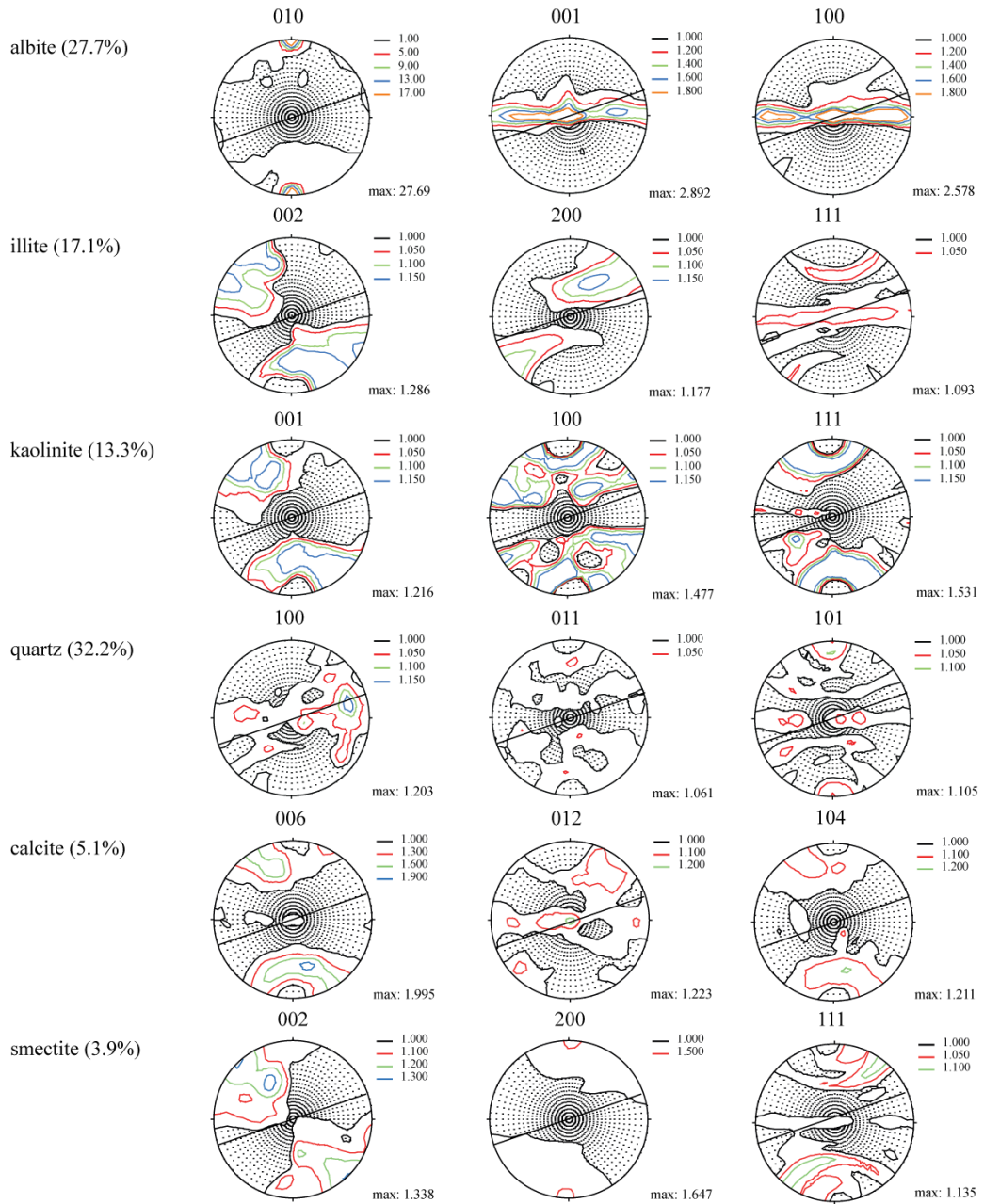


Figure A 2.22: Sample 333-C0011D-26X-1, 206.2 mbsf

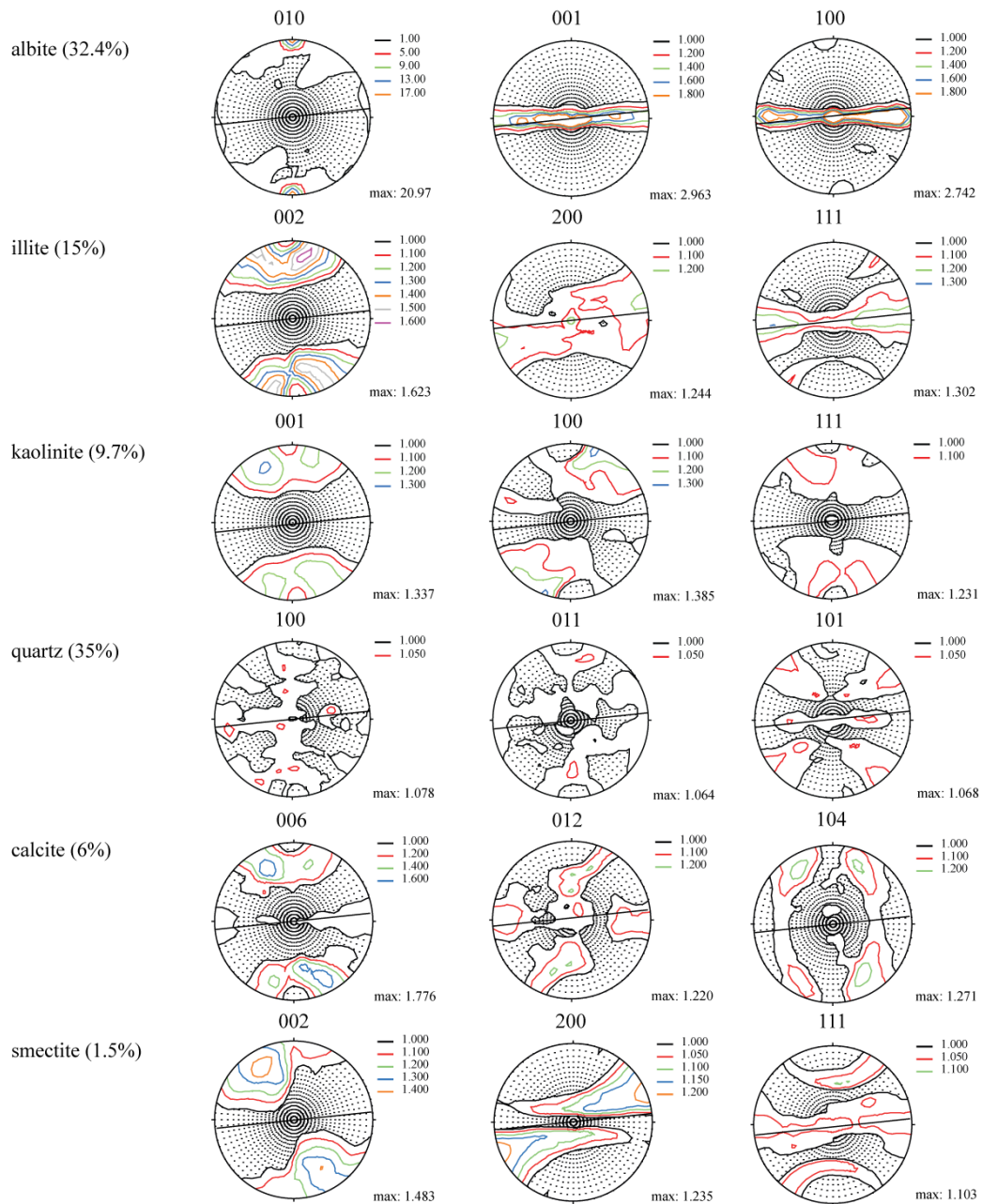


Figure A 2.23: Sample 316-C0008A-9H-3, 76.1 mbsf

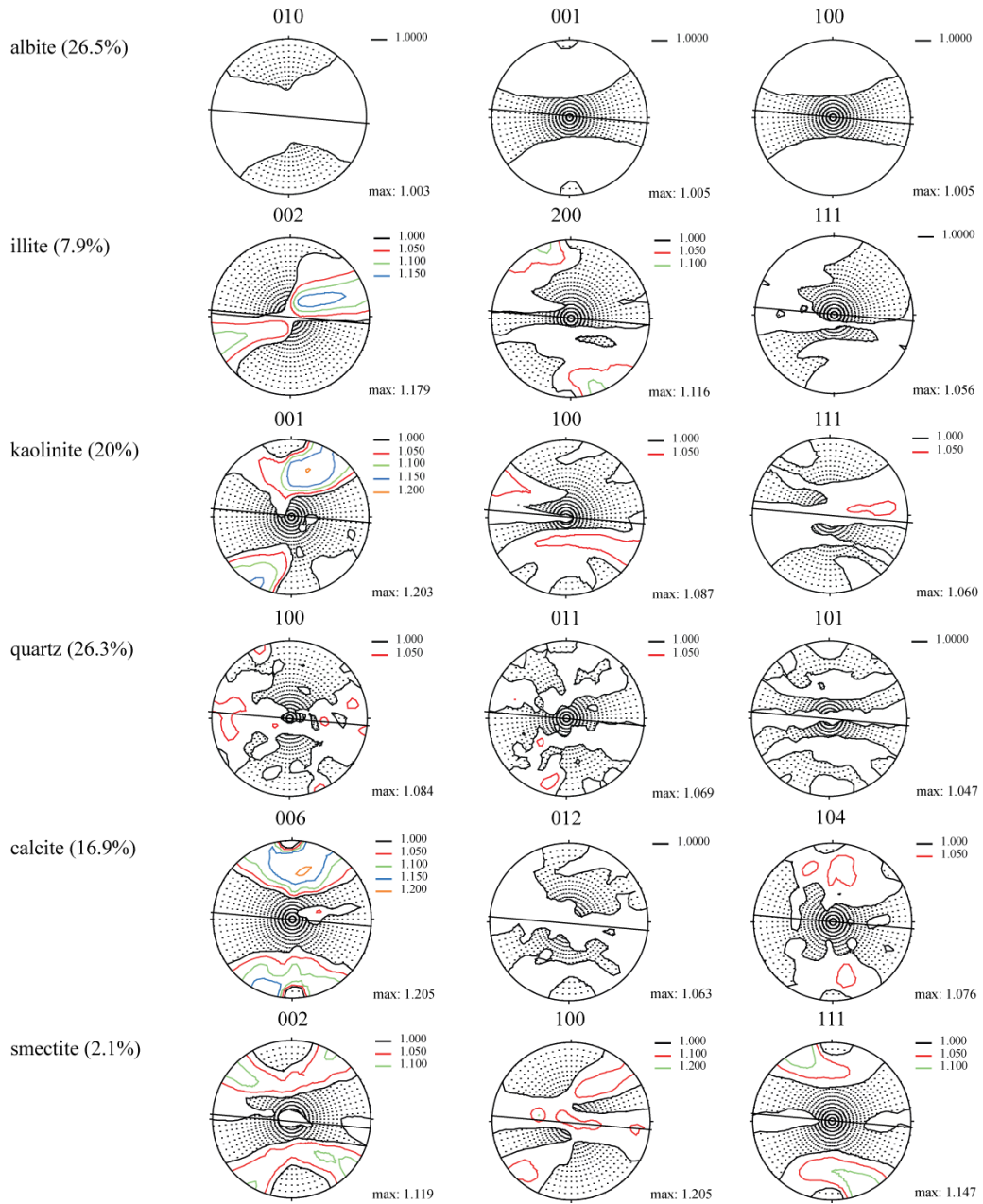


Figure A 2.24: Sample 315-C001E-11H-1, 90.6 mbsf

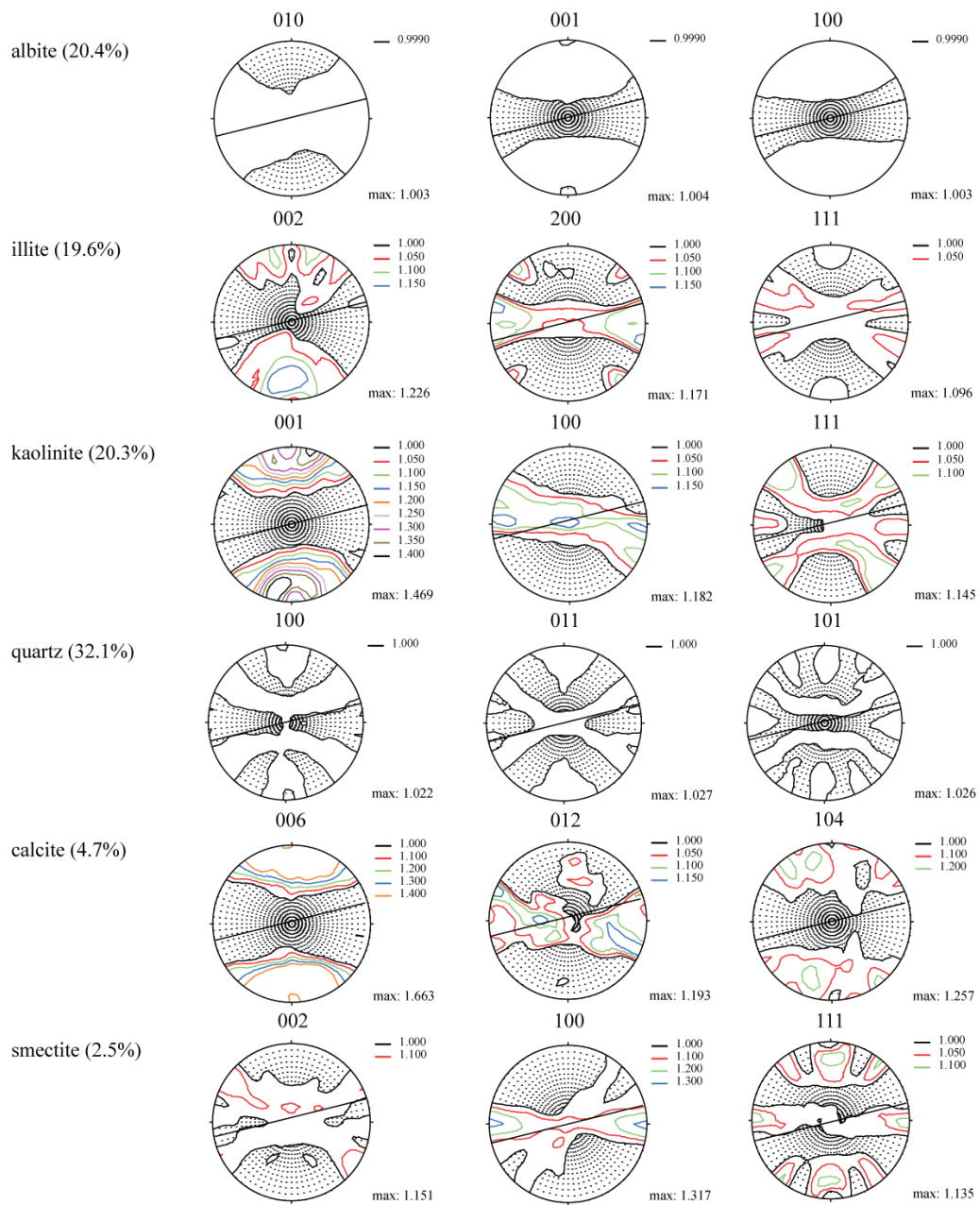


Figure A 2.25: Sample 316-C0006E-30X-1, 221 mbsf

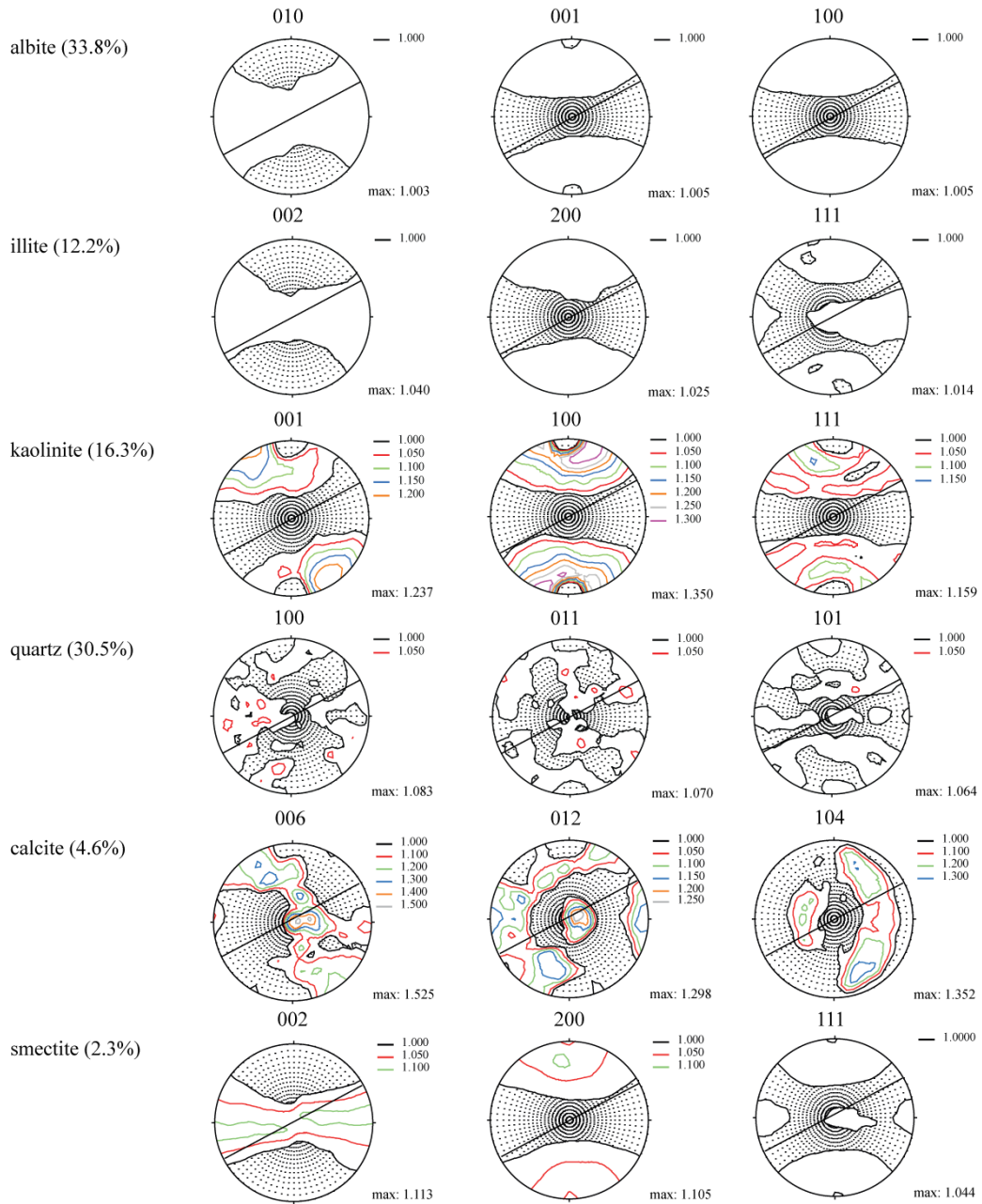


Figure A 2.26: Sample 315-C0001F-14H-3, 210 mbsf

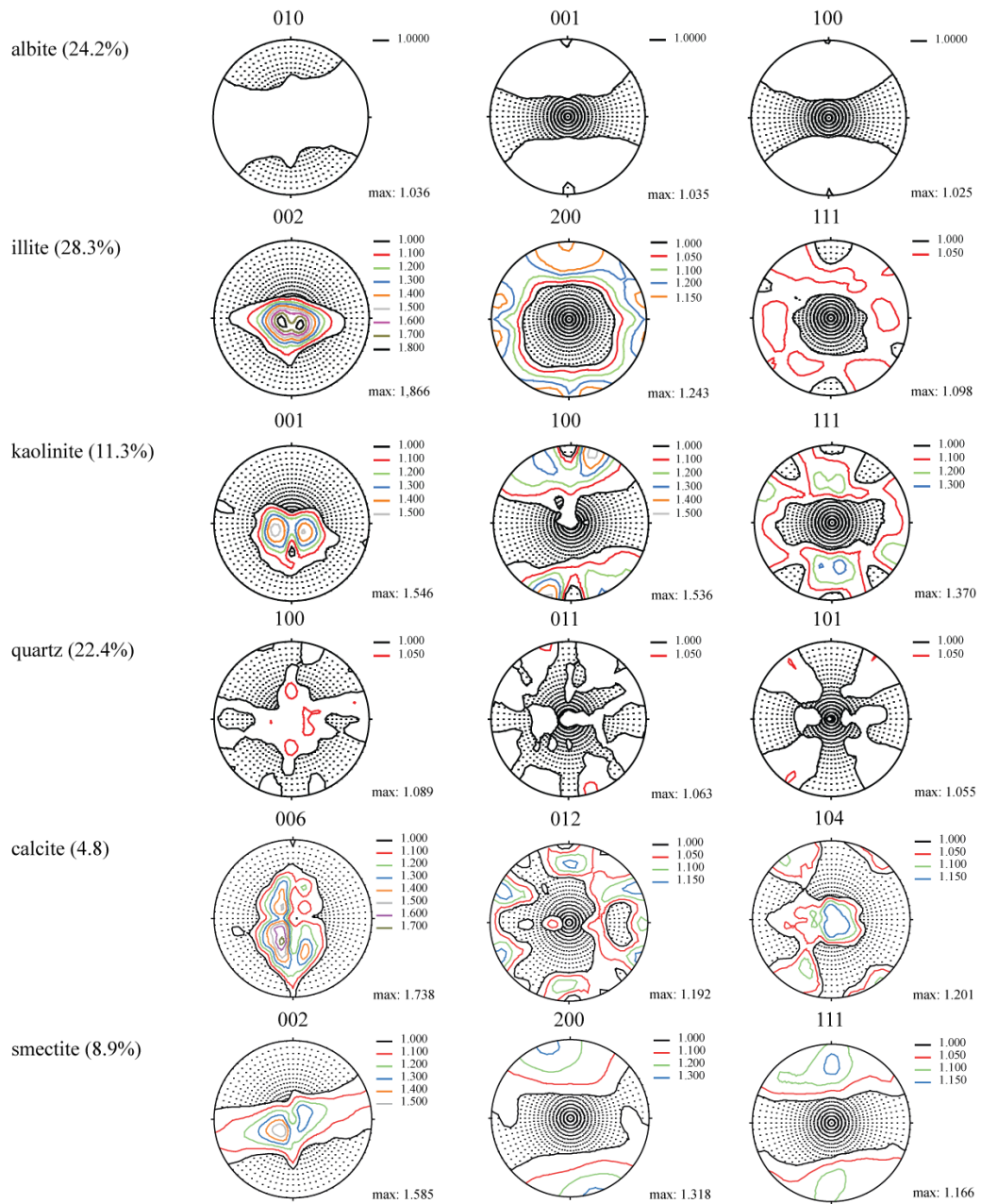


Figure A 2.27: Sample 315-C0001H-19R-2, 398.2 mbsf

A 2.4 Synchrotron texture measurements, sheared samples

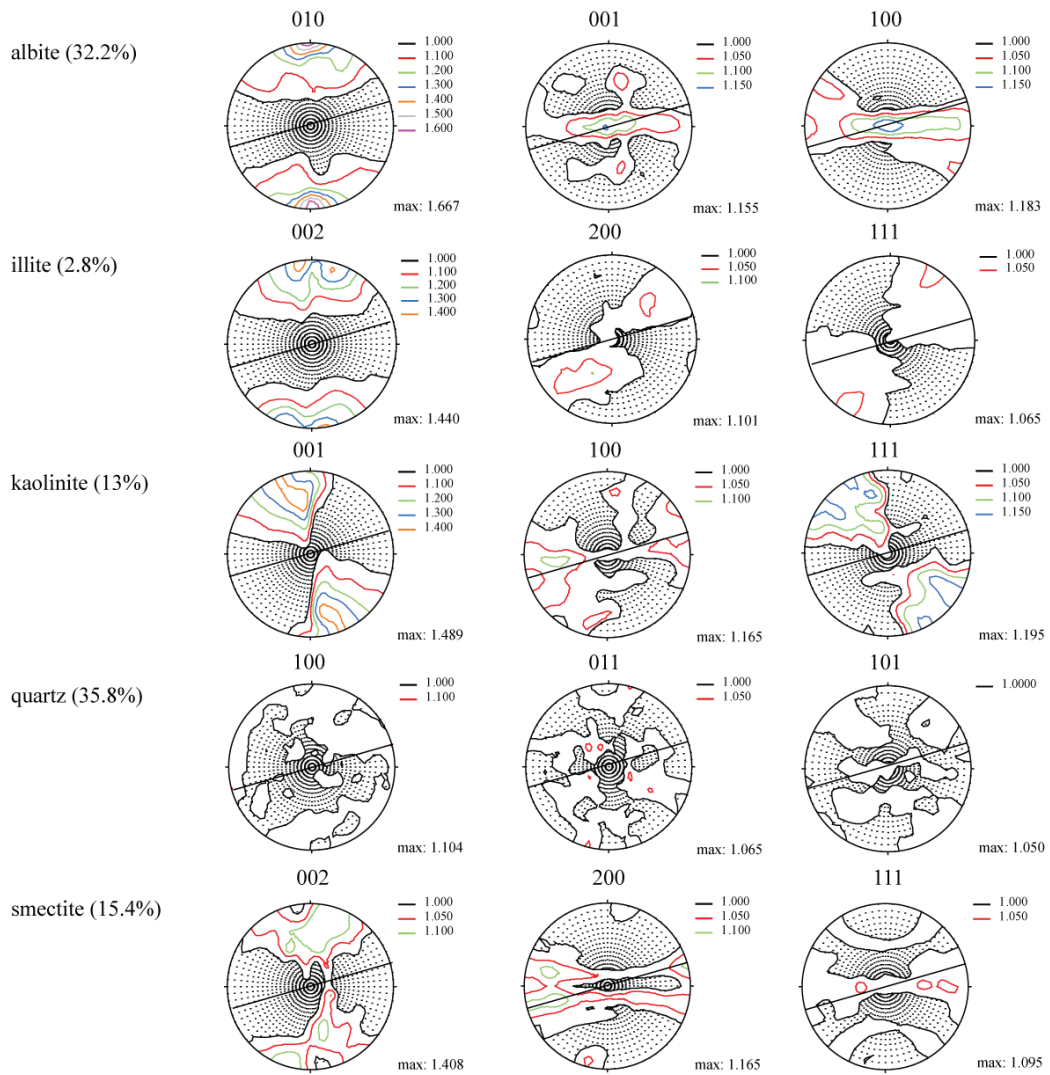


Figure A 2.28: Sample 316-C0007C-7X-1, K012, 35% axial strain, 62 mbsf

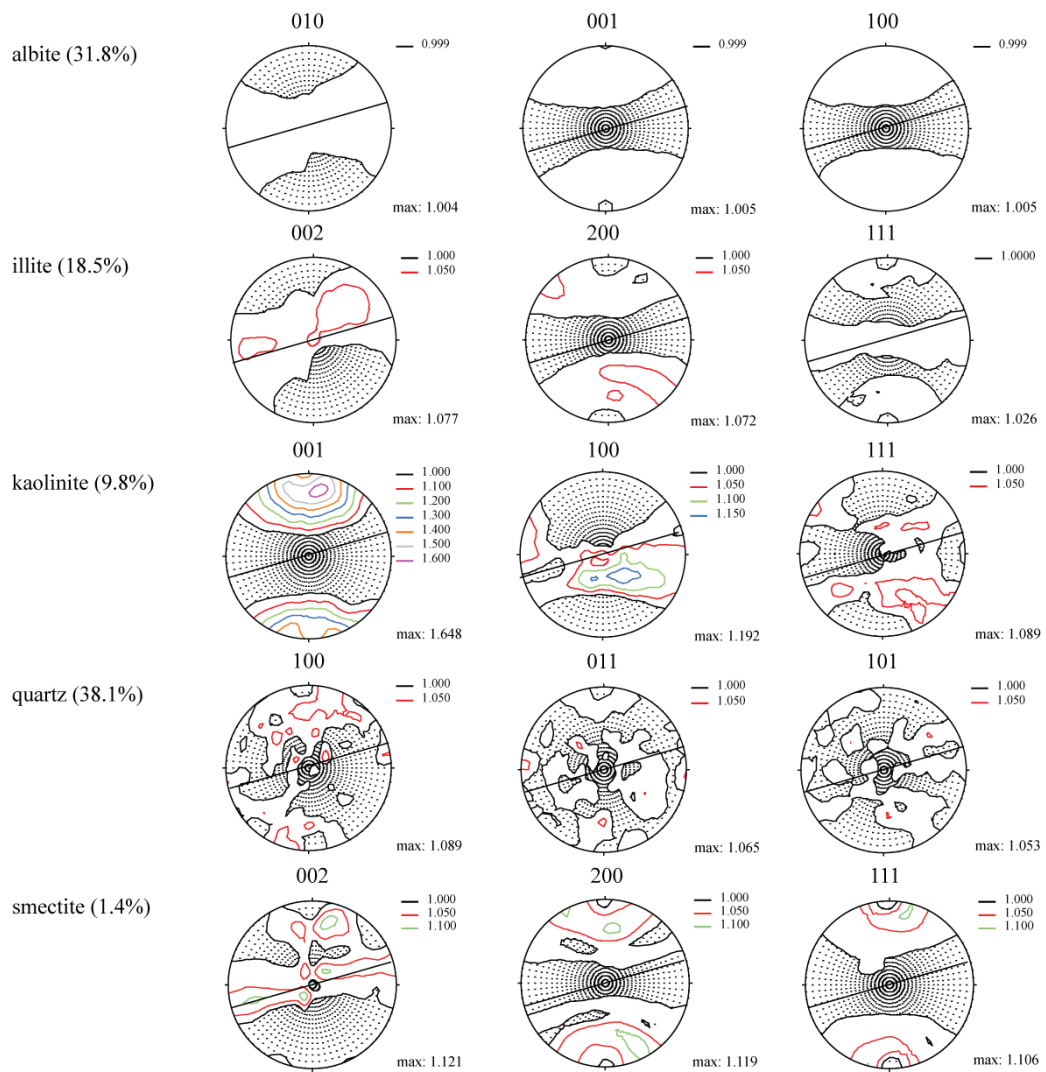


Figure A 2.29: Sample 316-C0007C-7X-1, K016, 38% axial strain, 62 mbsf

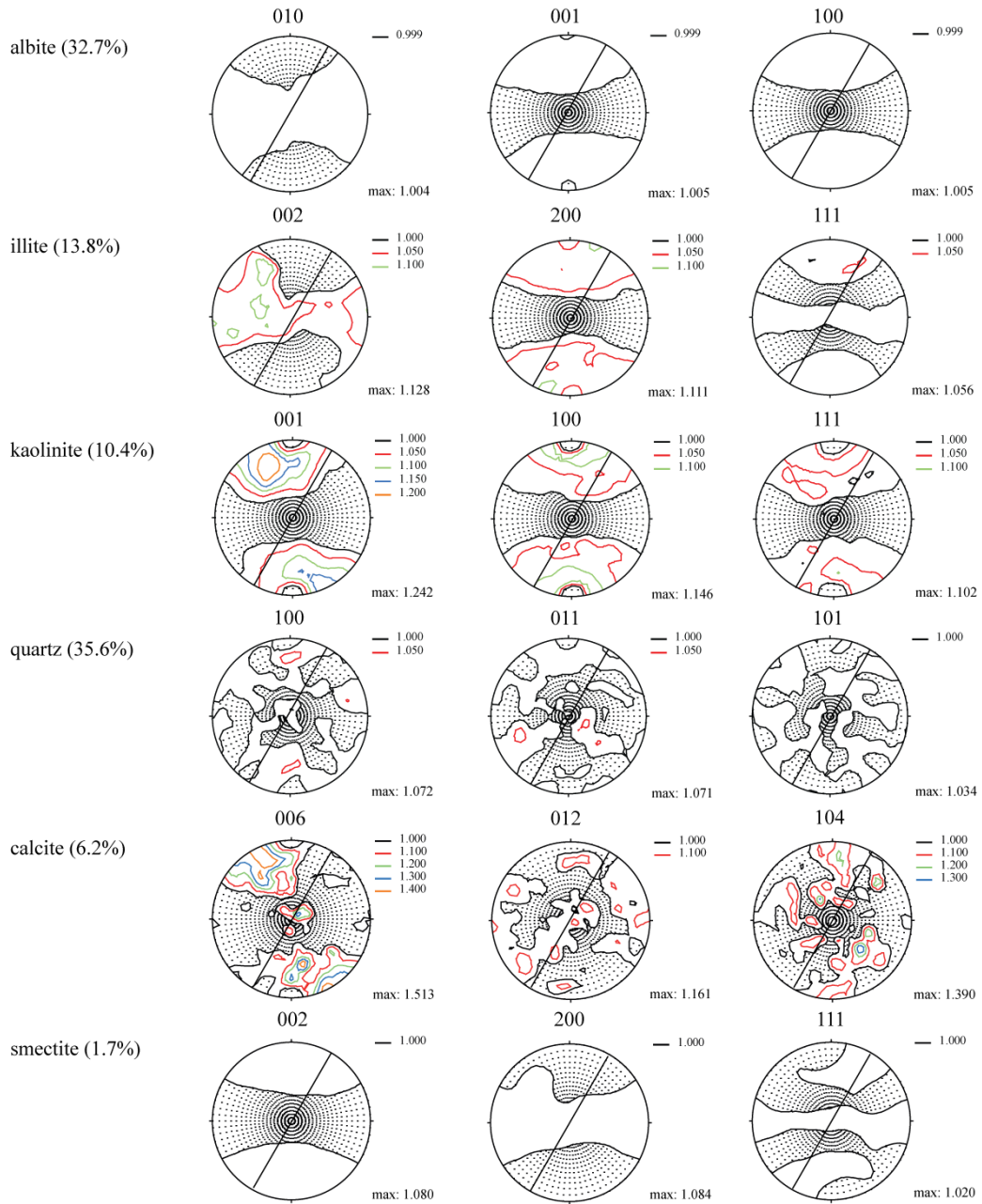


Figure A 2.30: Sample 316-C0006E-8H-1, K007, 22% axial strain, 48 mbsf

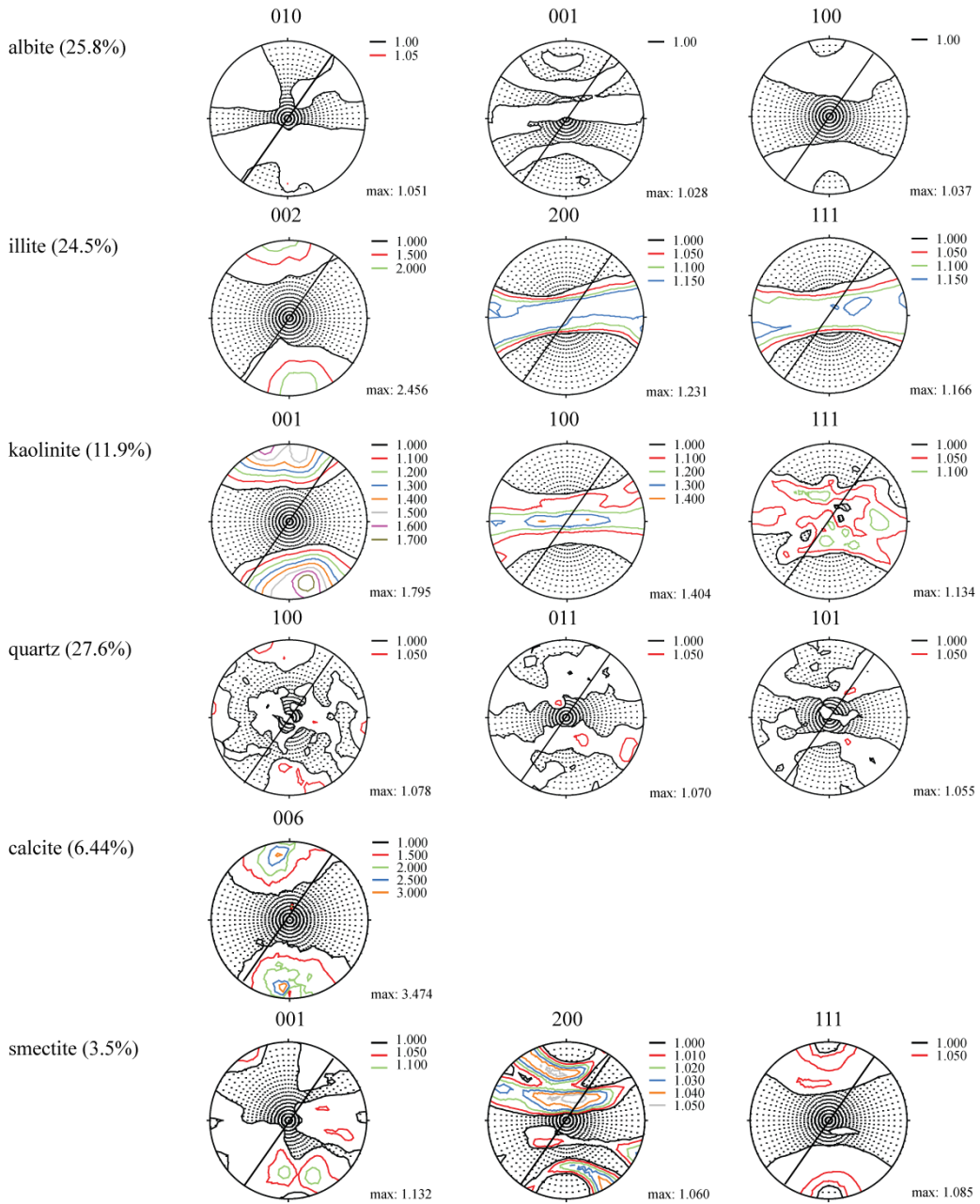


Figure A 2.31: Sample 316-C0006E-8H-1, K009, 60% axial strain, 48 mbsf

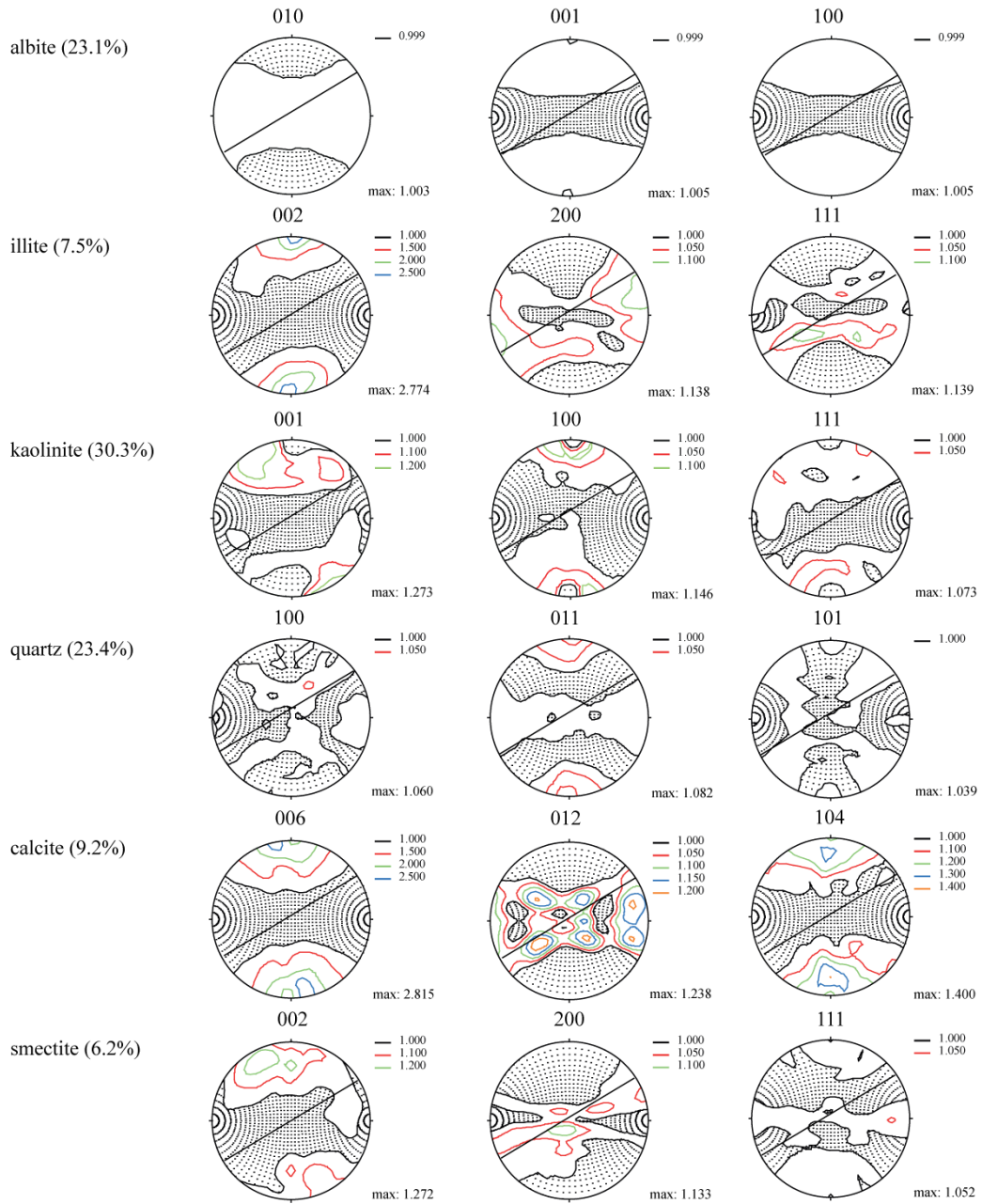


Figure A 2.32: Sample 316-C0006E-20X-2, K019, 47% axial strain, 127 mbsf

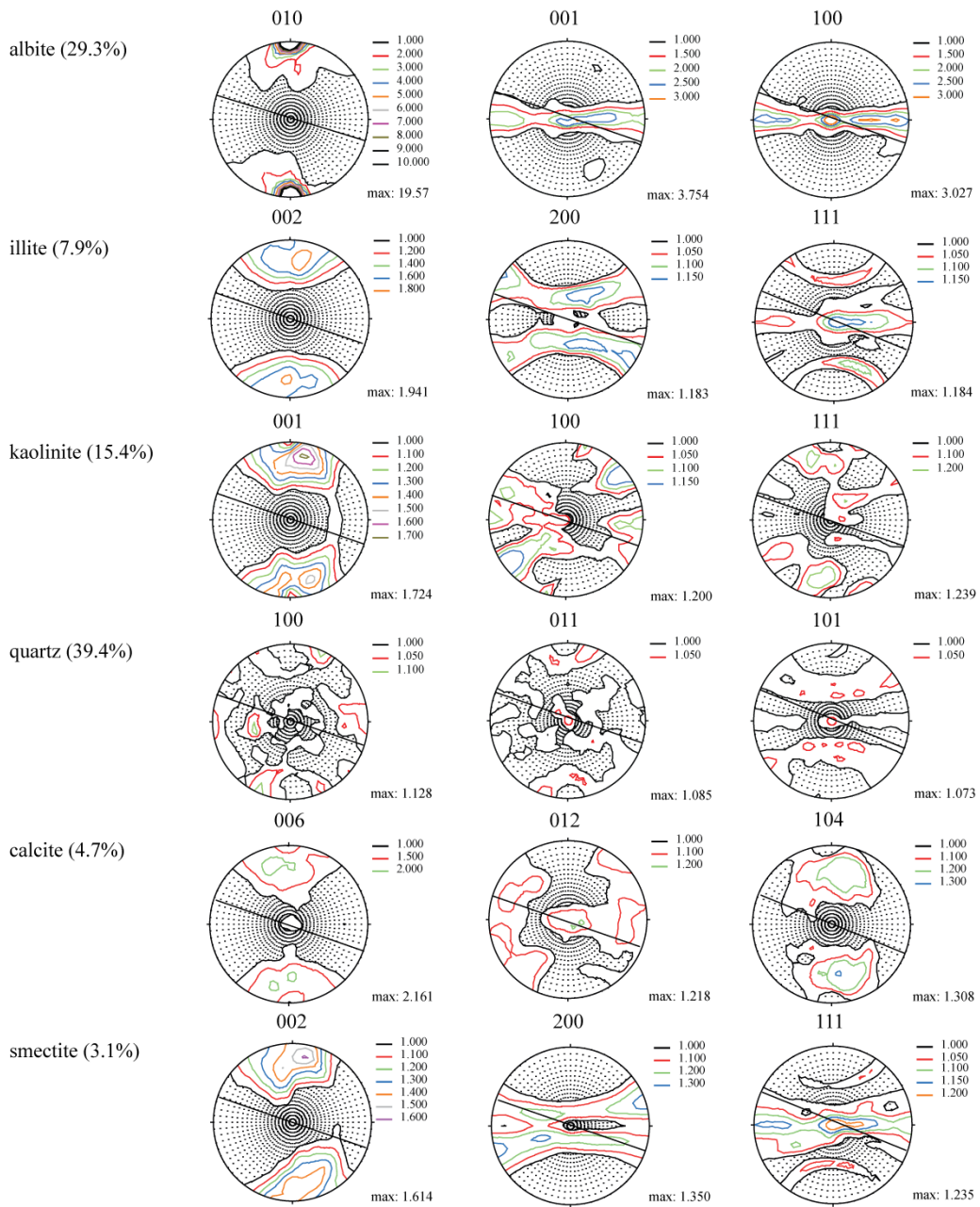


Figure A 2.33: Sample 316-C0008C-7H-8, K018, 27% axial strain, 60 mbsf

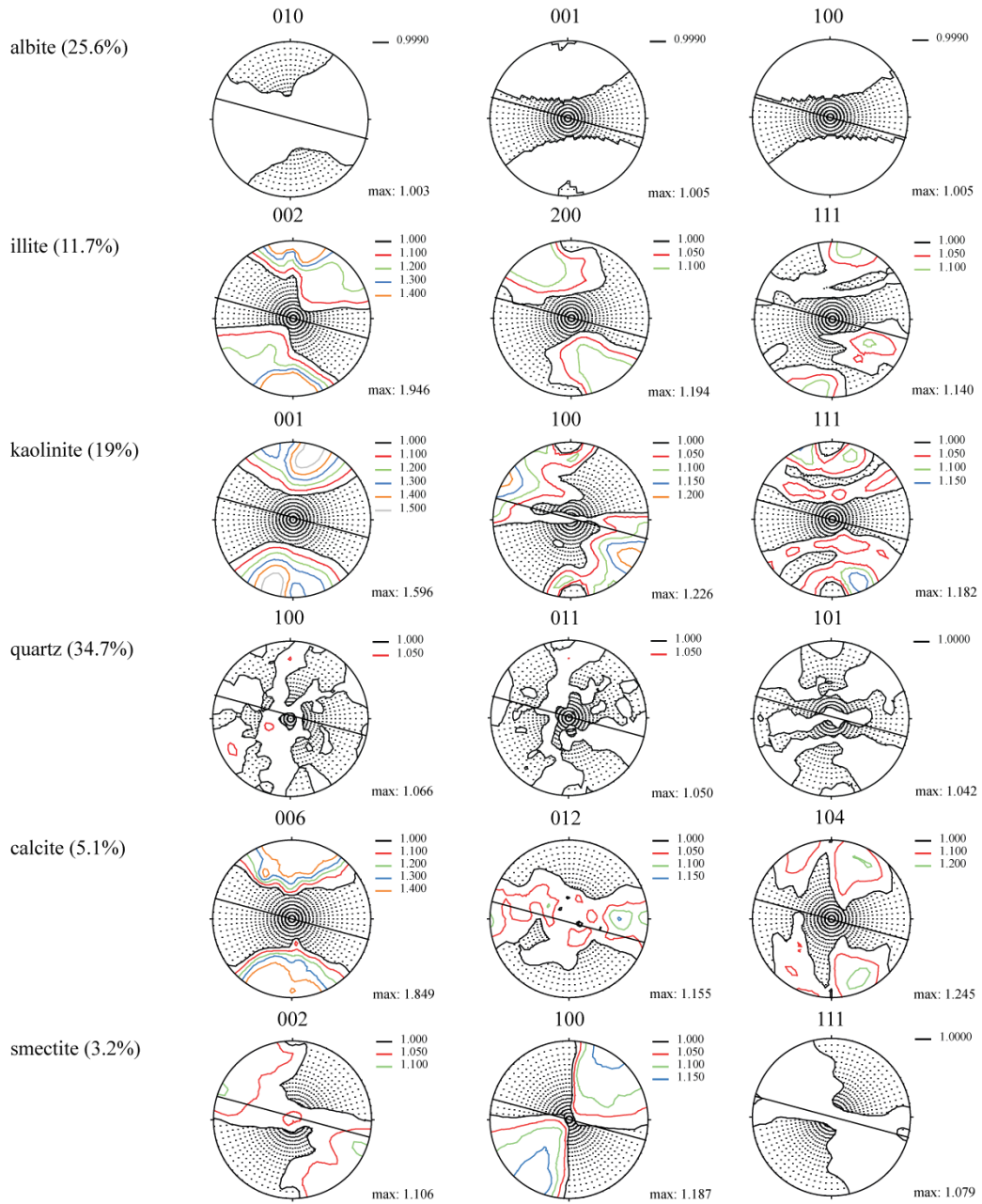


Figure A 2.34: Sample 316-C0008C-7H-8, K015, 38% axial strain, 60 mbsf

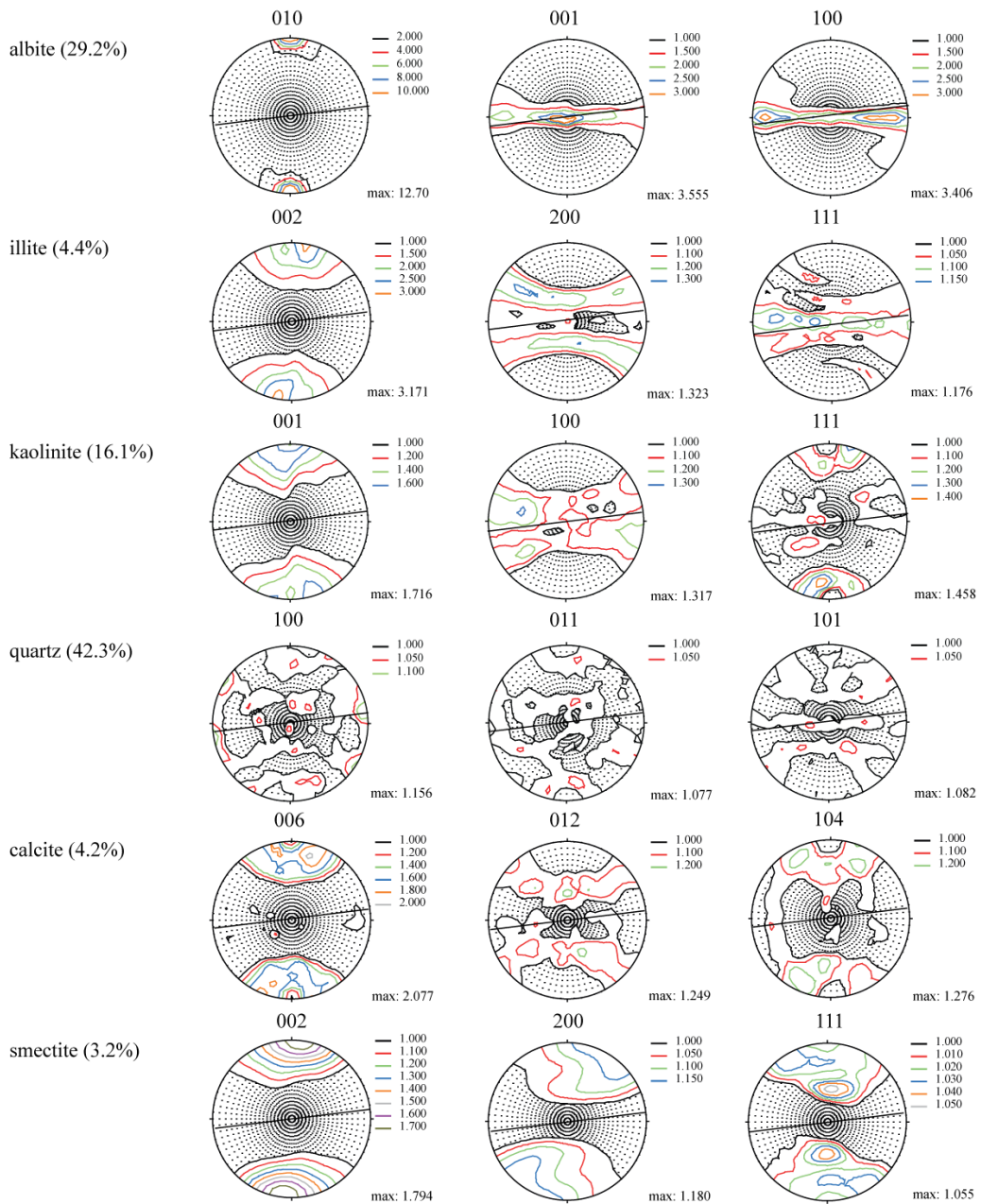


Figure A 2.35: Sample 316-C0008A-9H-3, K006, 31% axial strain, 76.1 mbsf

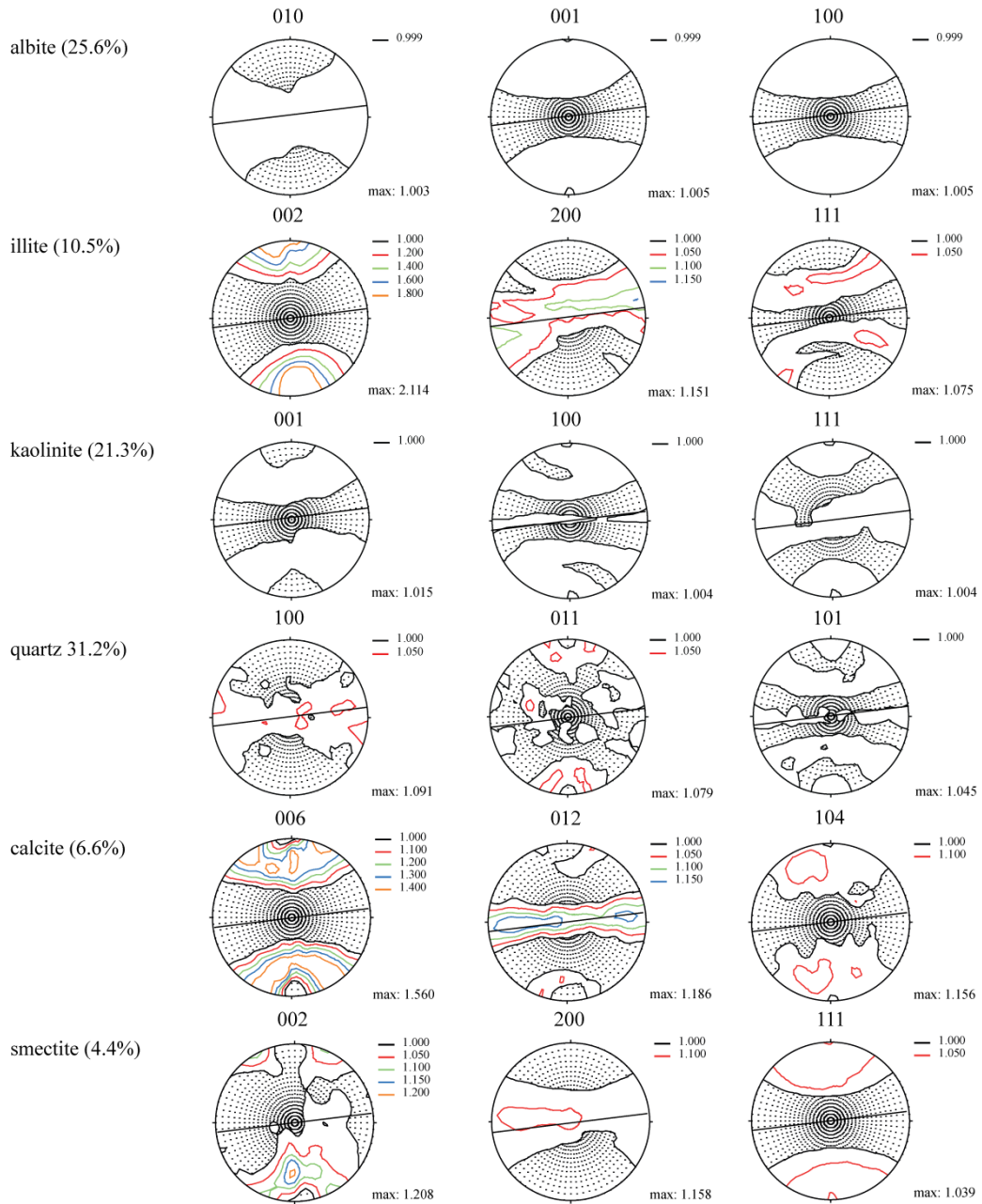


Figure A 2.36: Sample 316-C0008A-9H-3, K014, 45% axial strain, 76.1 mbsf

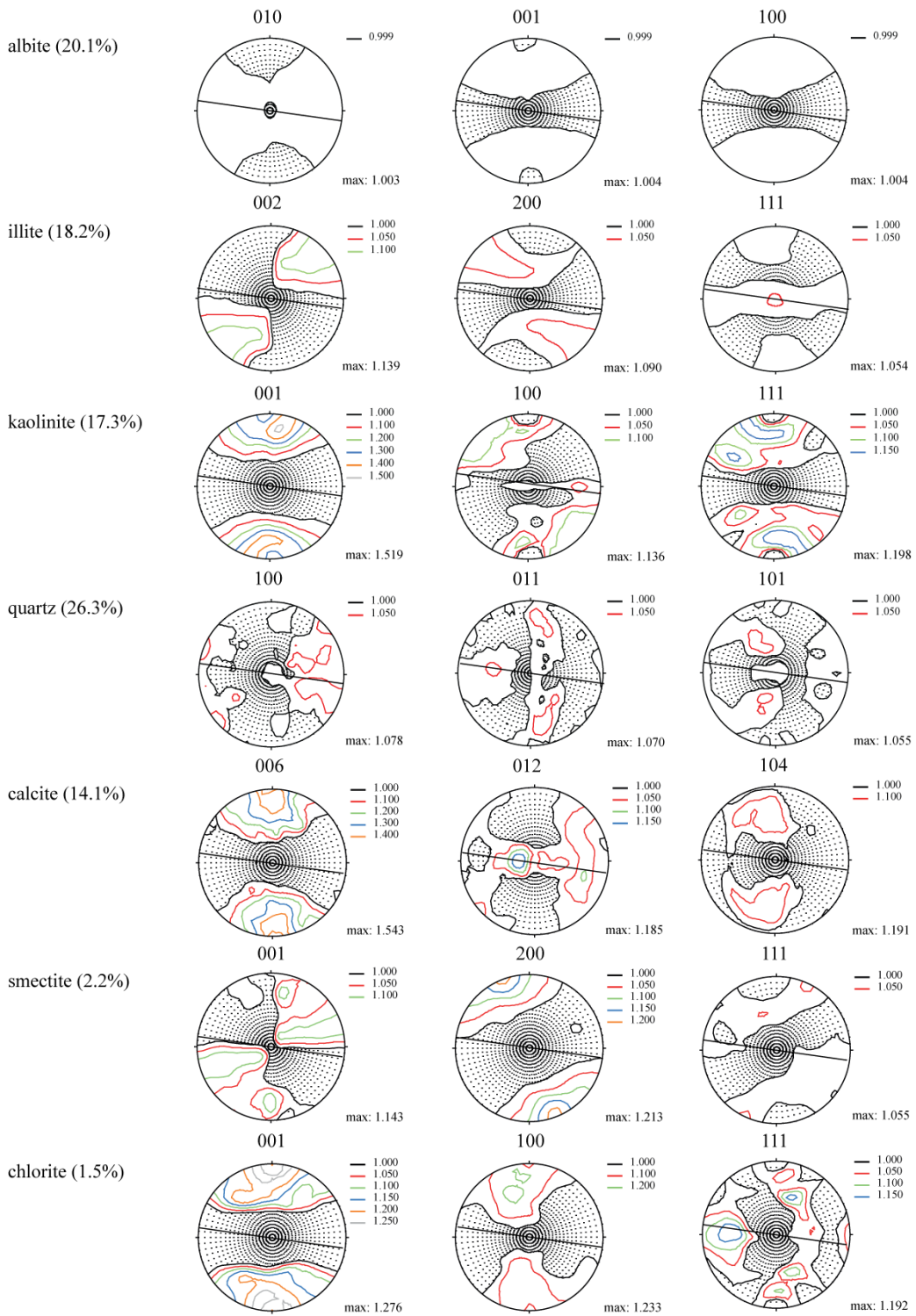


Figure A 2.37: Sample 316-C0004C-8H-2, K004, 37% axial strain, 65.3 mbsf

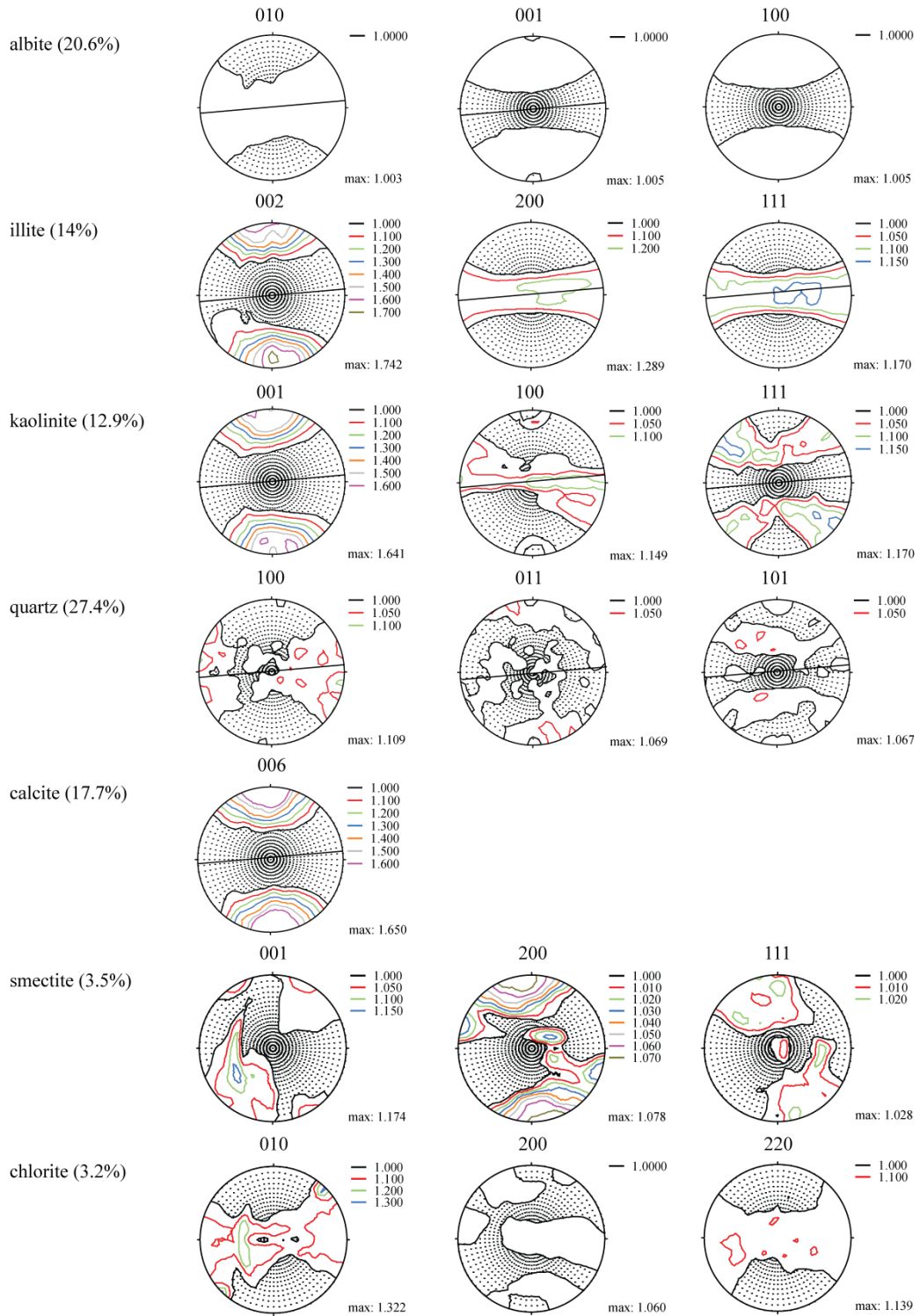


Figure A 2.38: Sample 315-C0001E-11H-1, K003, 36% axial strain, 90.6 mbsf

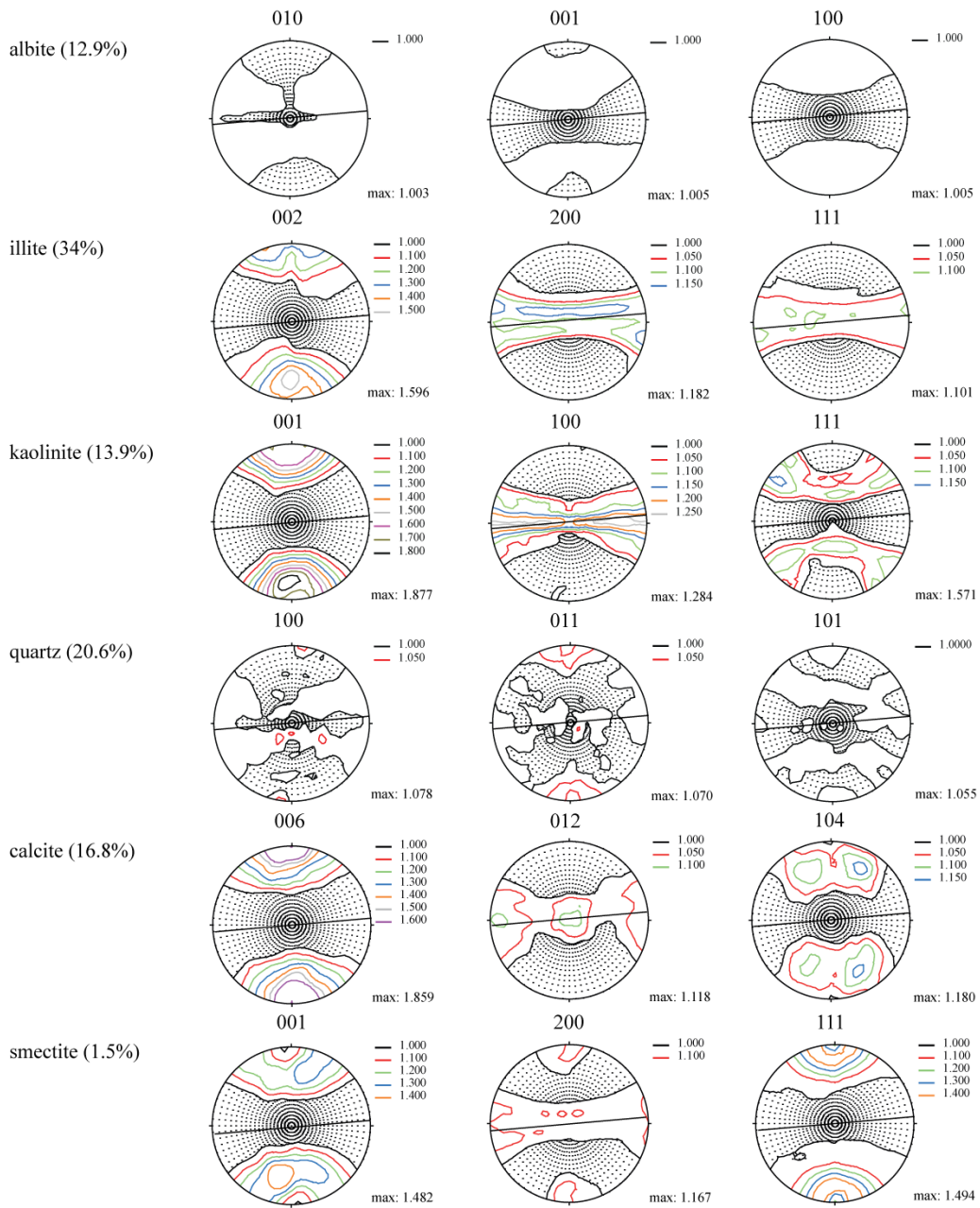


Figure A 2.39: Sample 315-C0001E-11H-1, K006, 41% axial strain, 90.6 mbsf

A 3 Appendix Manuscript #3

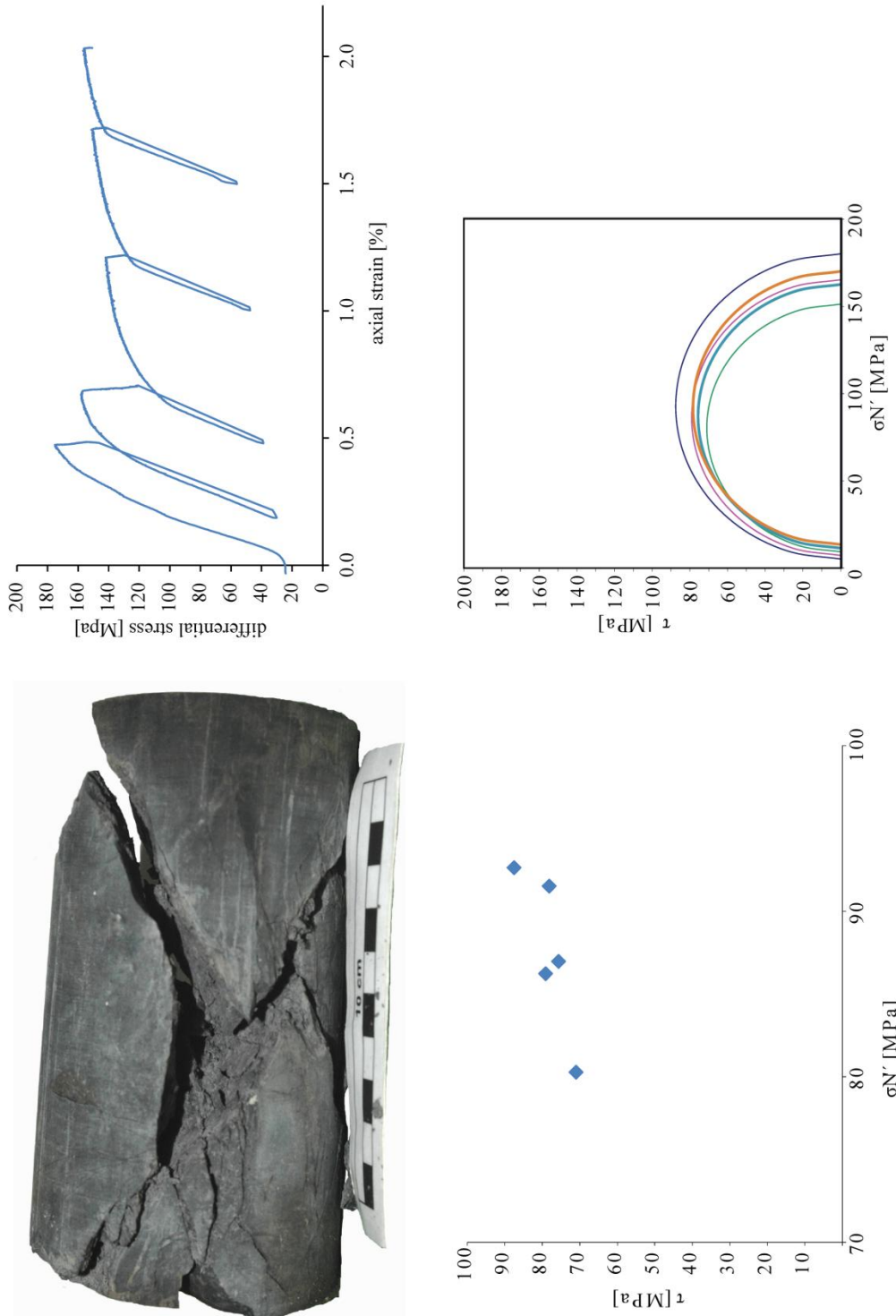


Figure A 3.1: Sample Sch2011/8

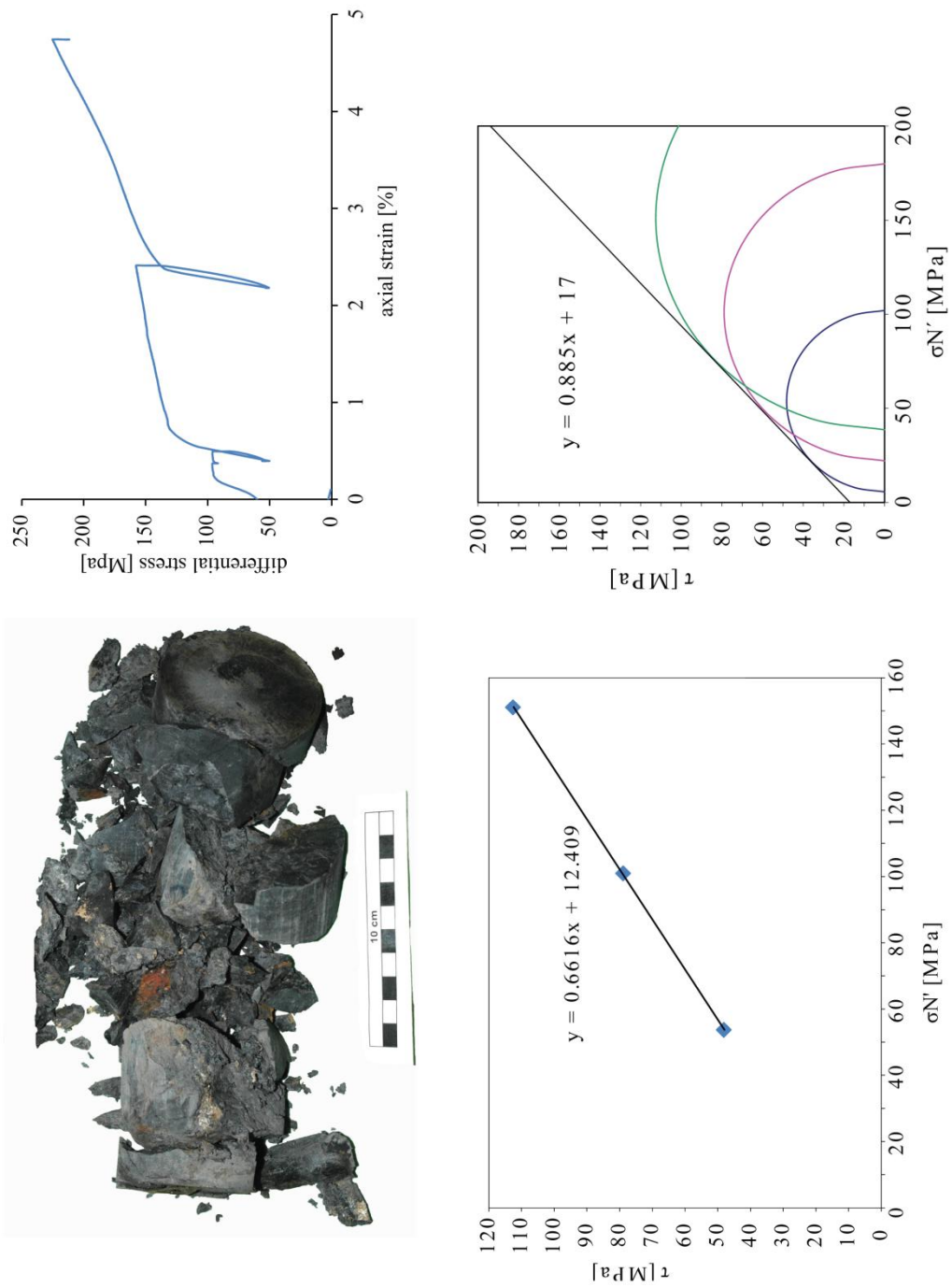


Figure A 3.2: Sample Sch2011/12

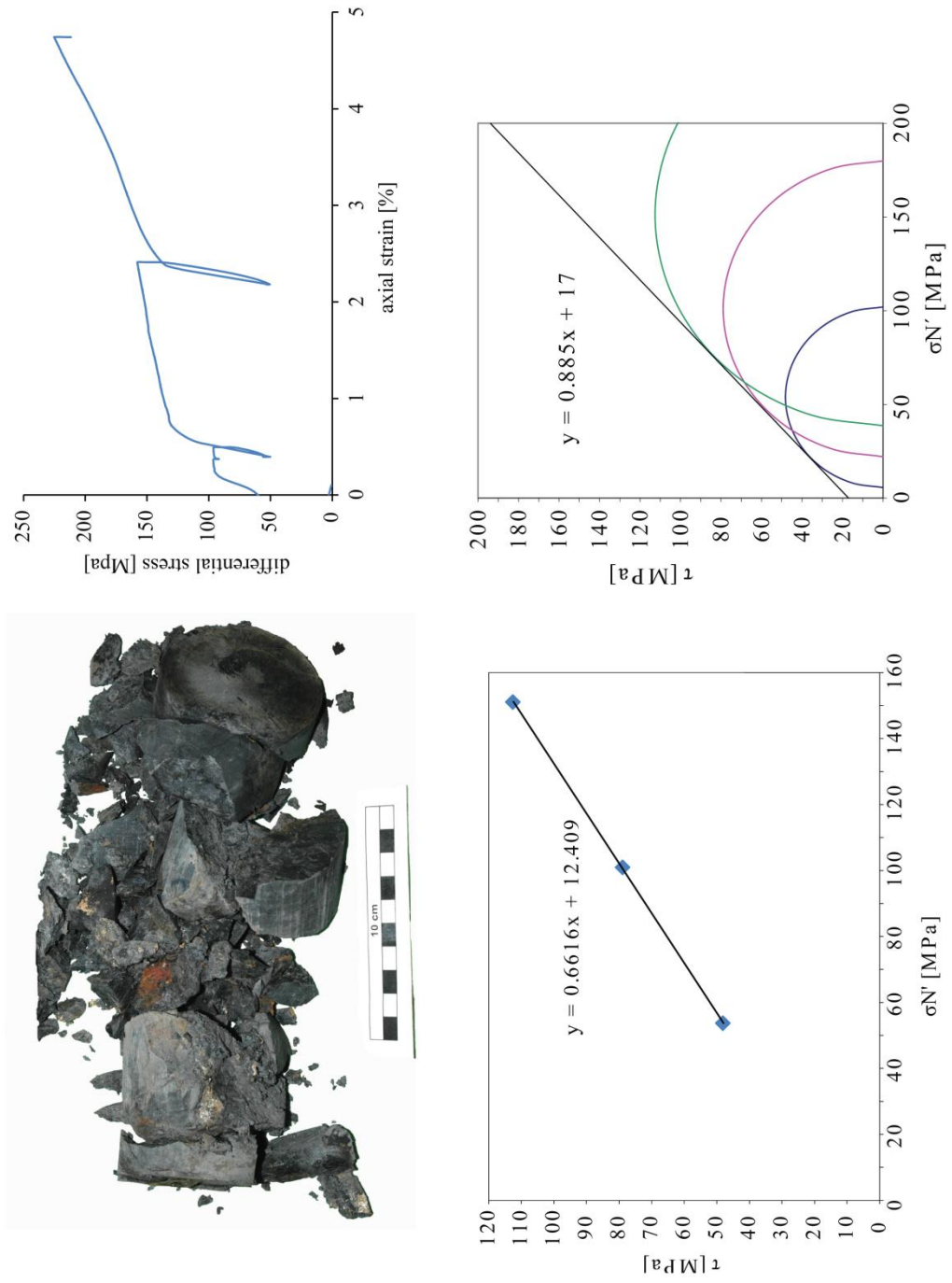


Figure A 3.3: Sample Sch2011/18

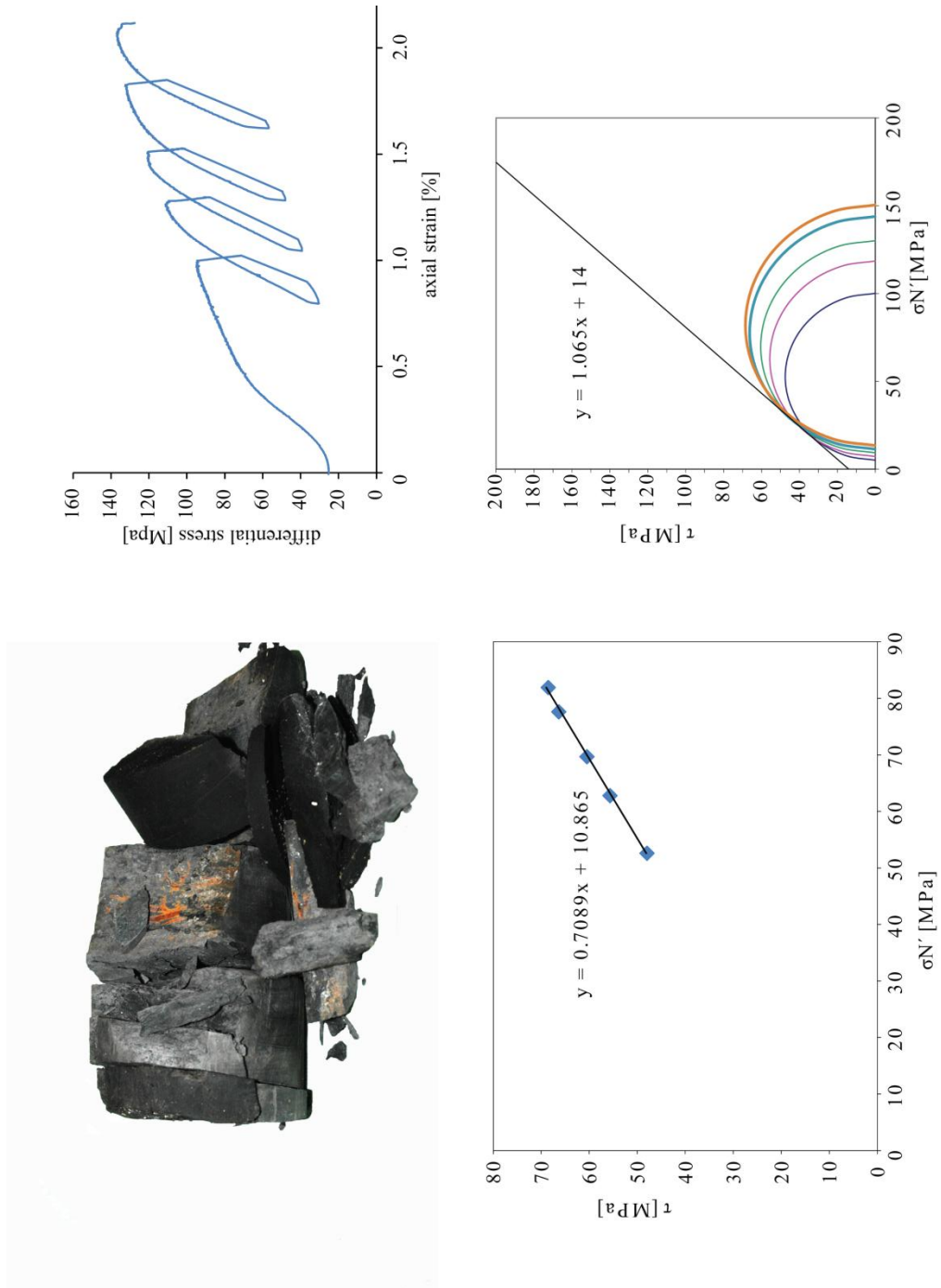


Figure A 3.4: Sample Sch2011/23

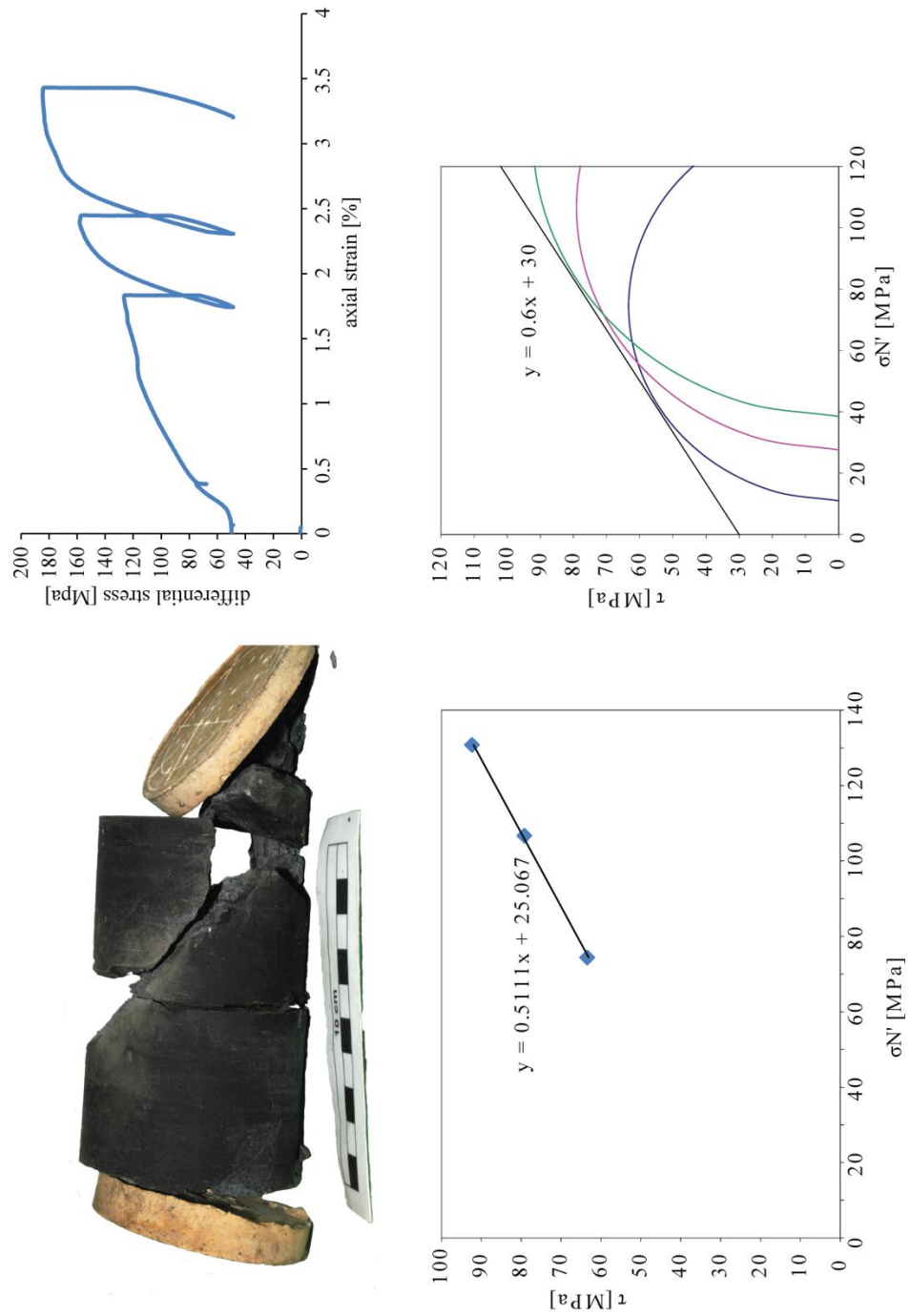


Figure A 3.5: Sample Sch2011/24

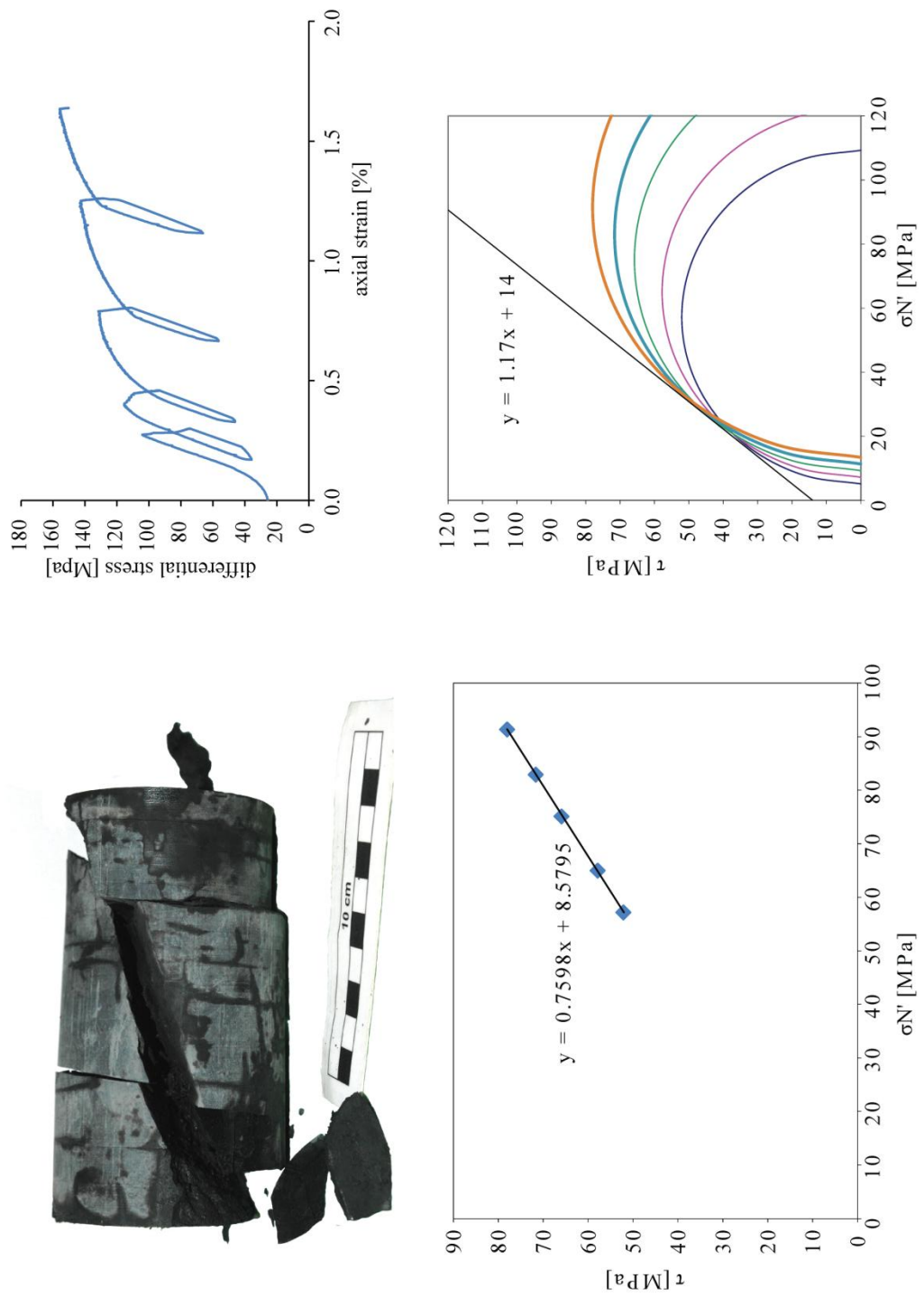


Figure A 3.6: Sample Sch2011/27-1

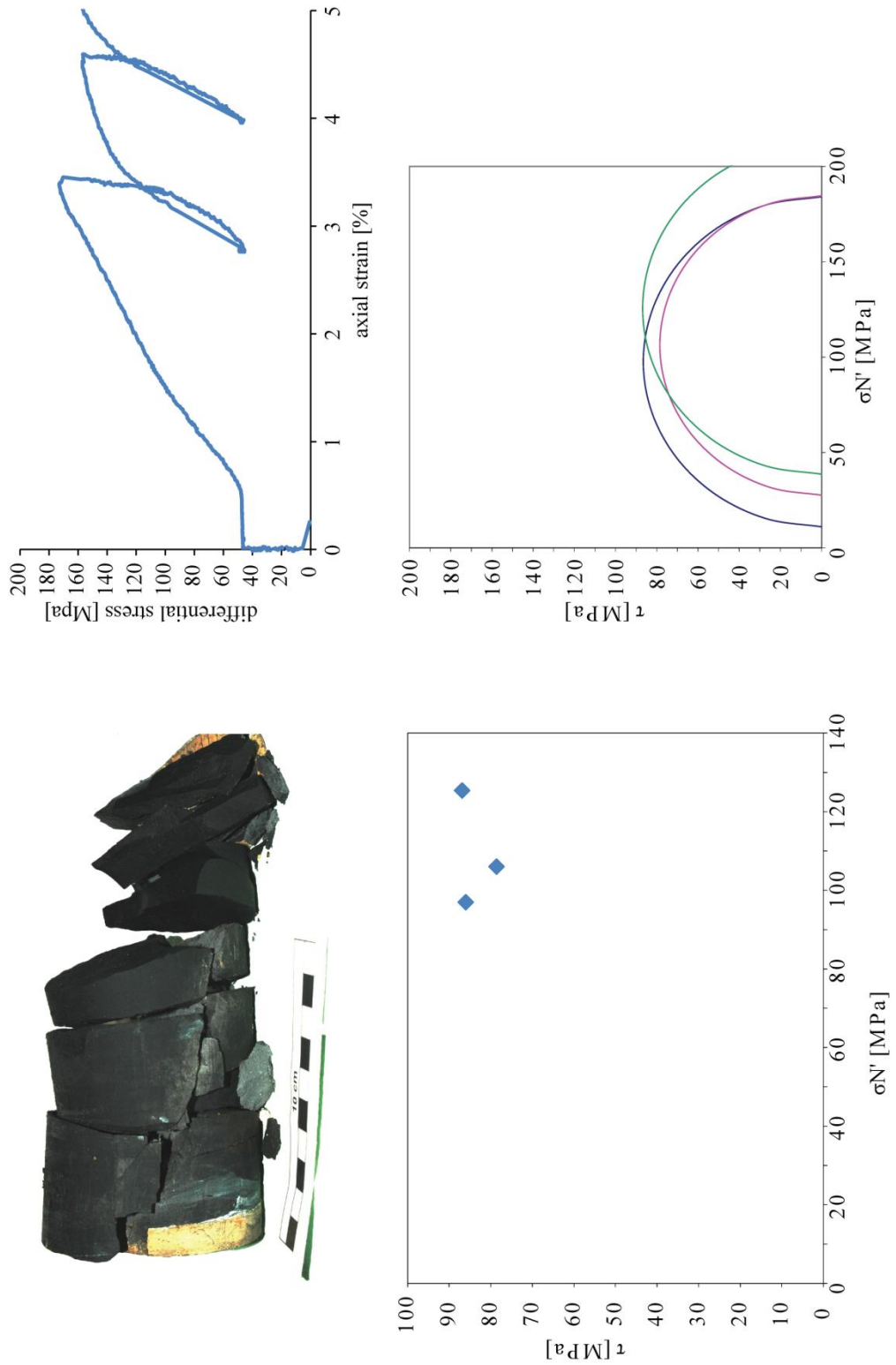


Figure A 3.7: Sample Sch2011/27-2

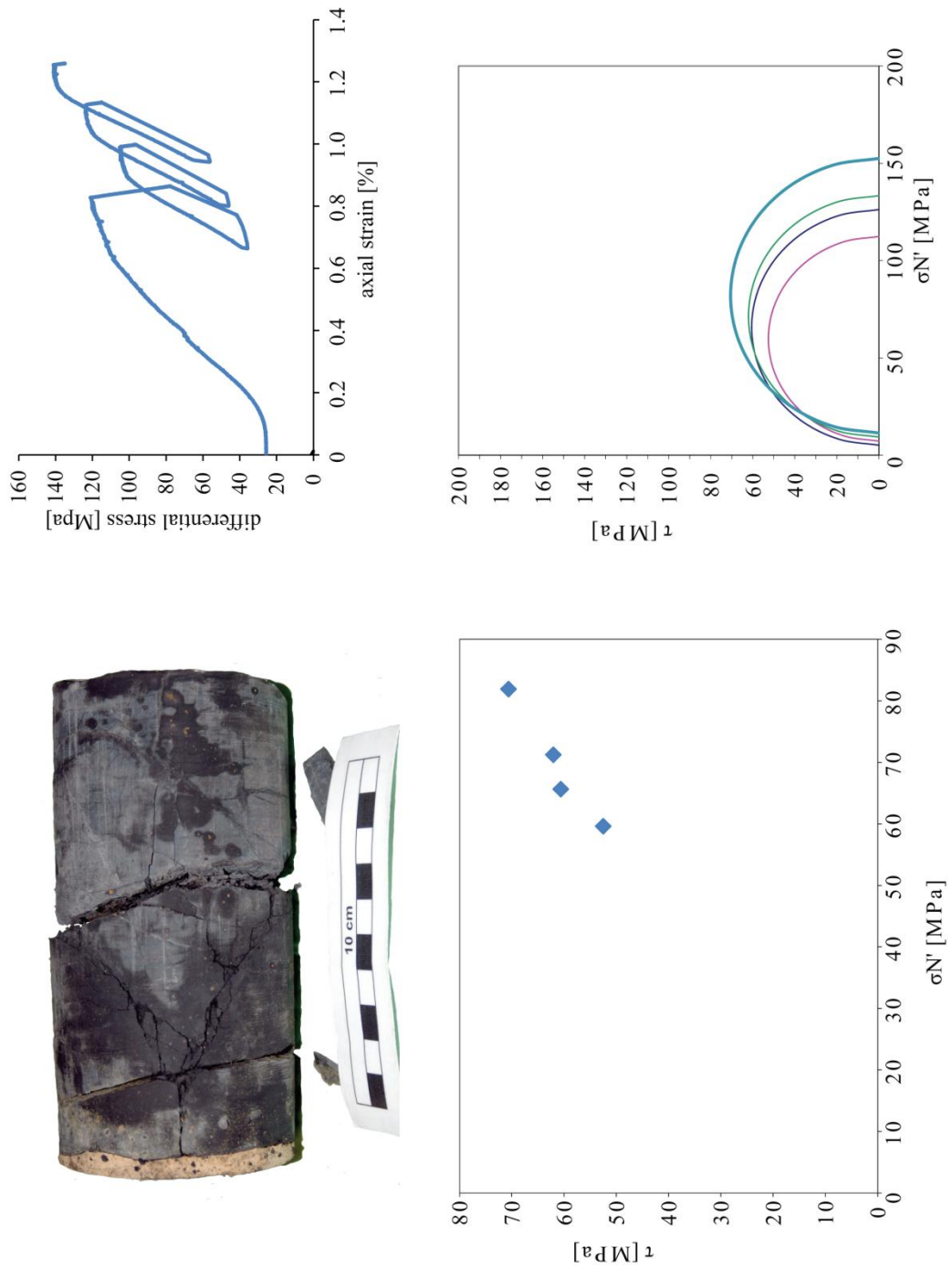


Figure A 3.8: Sample Sch2011/29

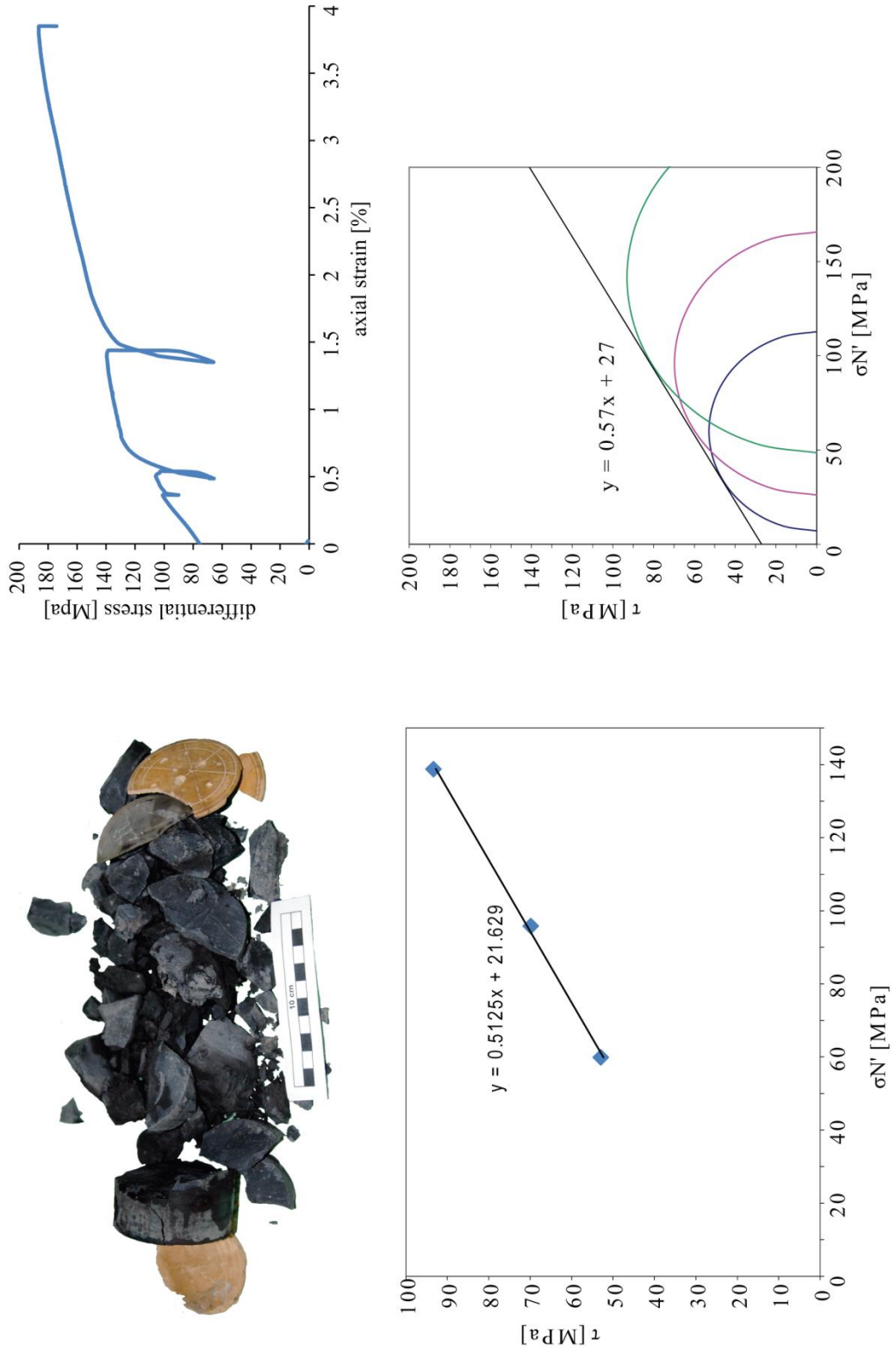


Figure A 3.9: Sample Sch2011/34

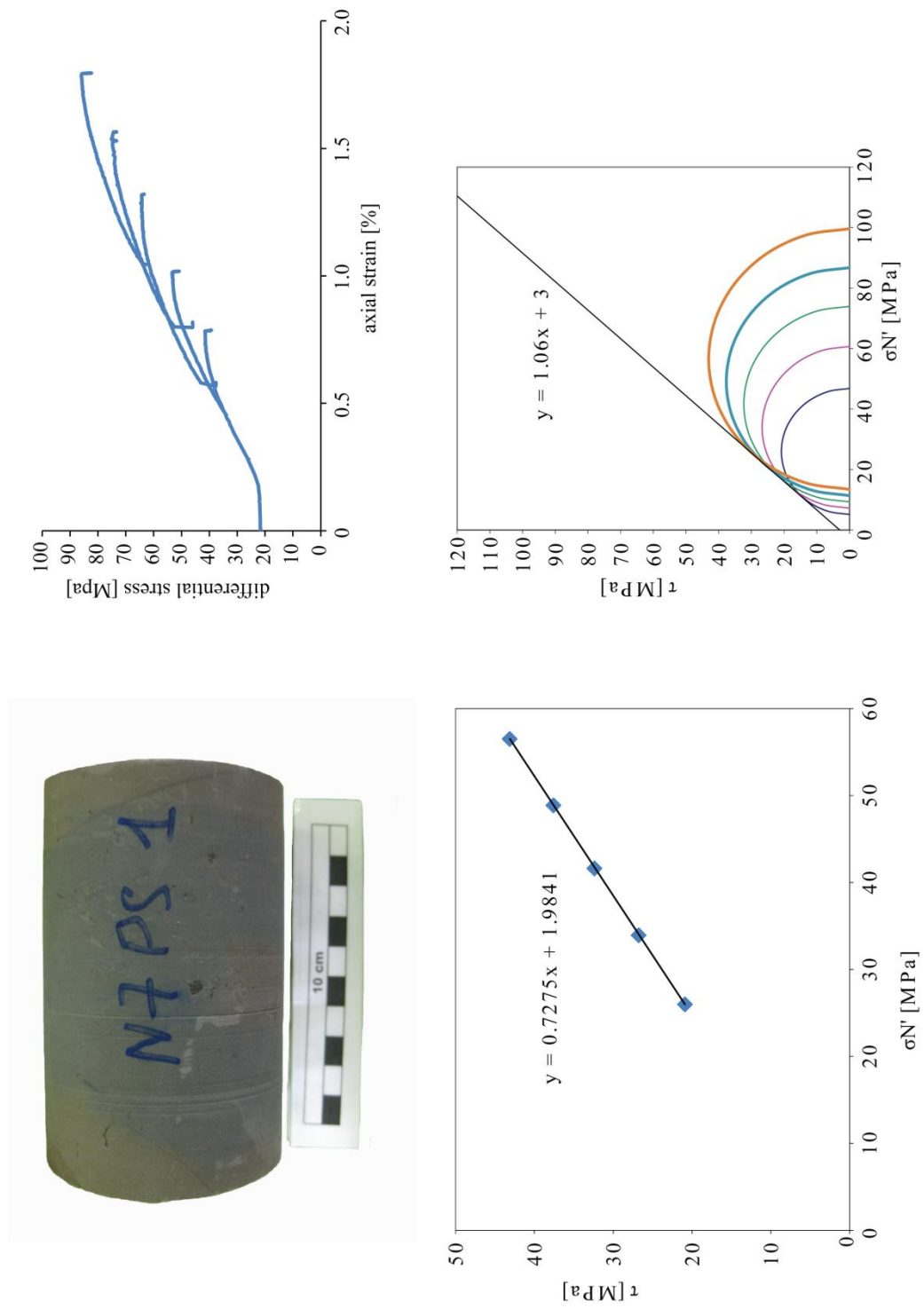


Figure A 3.10: Sample NZ-PS-1

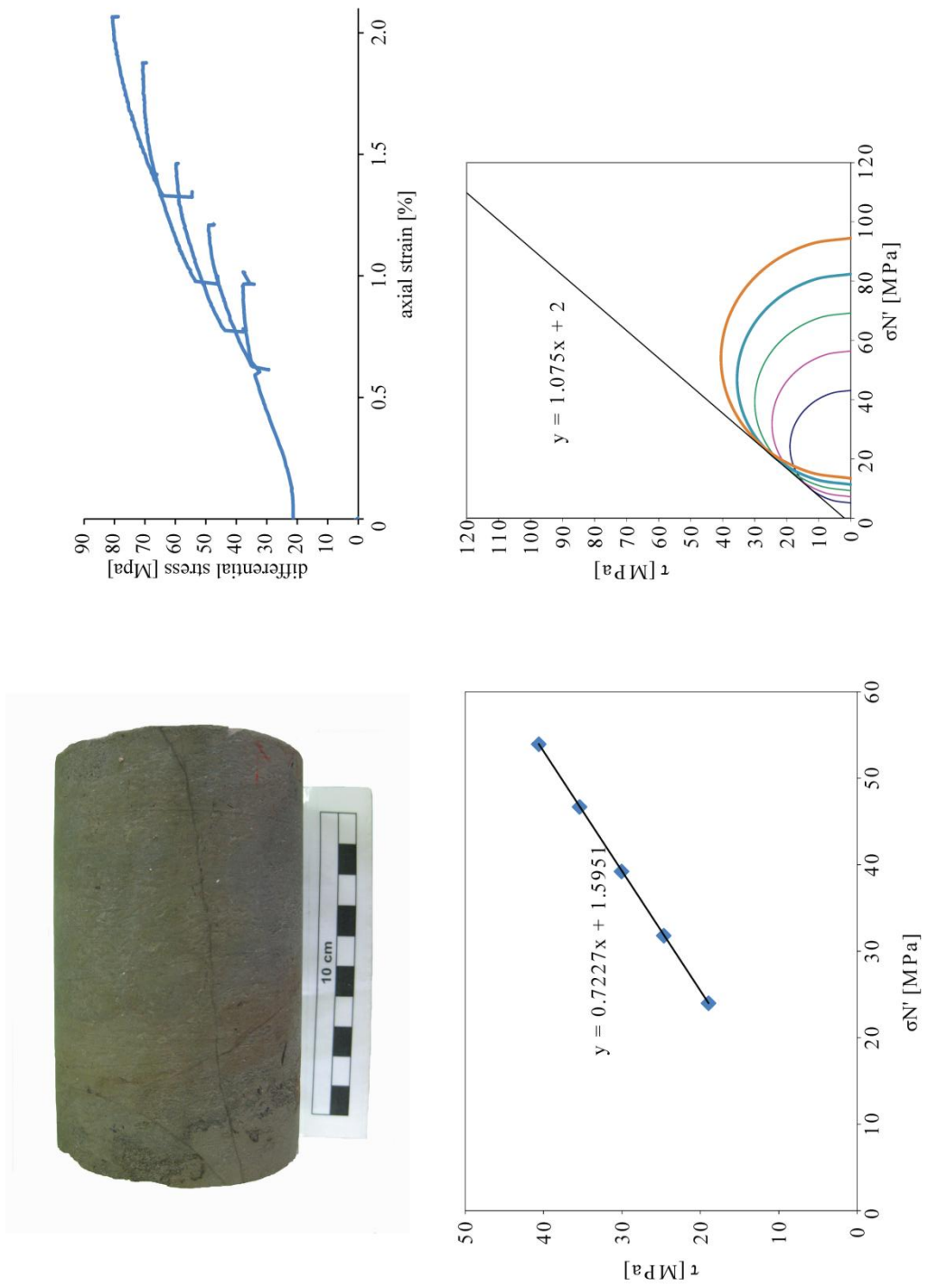


Figure A 3.11: Sample NZ-PS-2

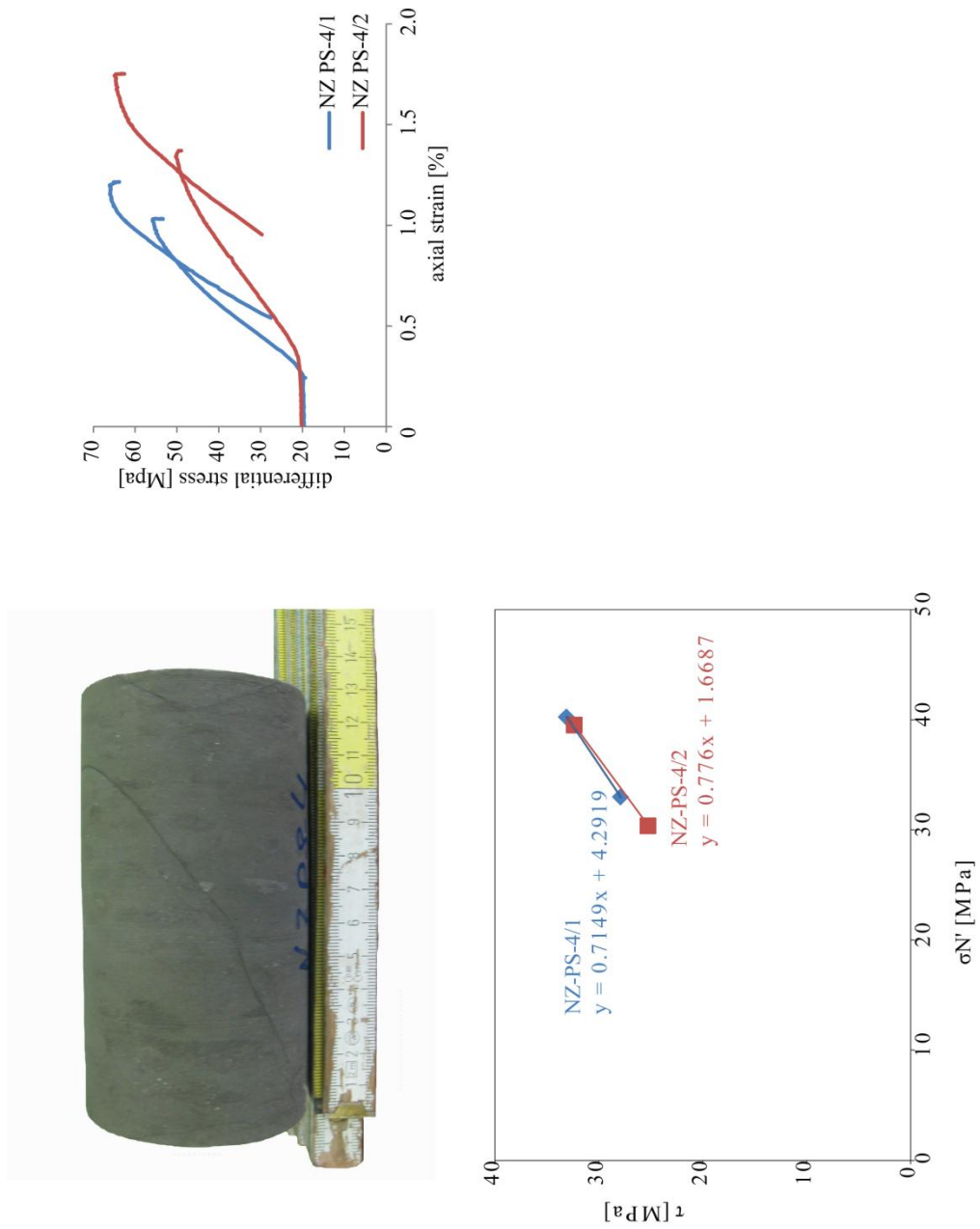


Figure A 3.12: Sample NZ-PS-4/1 and NZ-PS-4/2

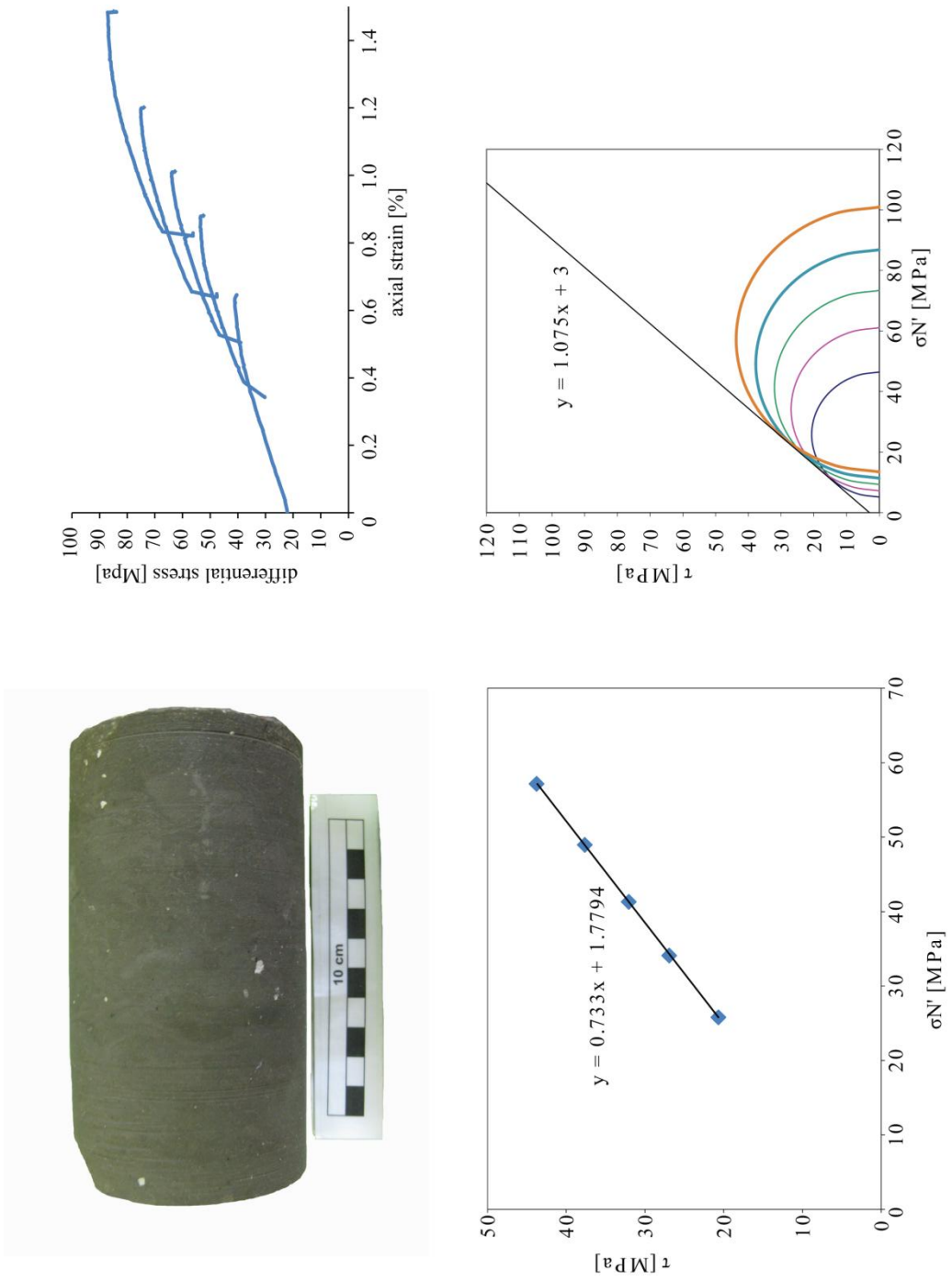


Figure A 3.13: Sample NZ-PS-5

A 4 Appendix Manuscript #4

Online data repository for “Strong sediments at the deformation front, and weak sediments at the rear of the Nankai accretionary prism, revealed by triaxial deformation experiments” by Michael Stipp, Malte Rolfs, Yujin Kitamura, Jan H. Behrmann, Kai Schumann, Detlef Schulte-Kortnack, and Volker Feeser

Grain size and composition analysis

Particle size distributions have been measured using the laser particle sizer Fritsch Analysette 22 NanoTec. The measurement range of the Analysette expands from 0.01 μm to 2 9 mm and covers the full grain size distribution of the investigated silty clay samples. Small pieces (a few 100 milligrams) from the soft sediments were brought into suspension with distilled water. Flocculation of the clay minerals was prevented by keeping the sample suspensions in ultrasonic bath. The suspensions were filled into the Analysette and transported through the laser beam in the measurement chamber for the analysis. Minimum 5 repetitions were analyzed from each sample displaying only slight variations. The given particle size distributions represent sample average values based on the repeated measurements.

Sample compositions represent the grain size fraction $< 2\mu\text{m}$ (Guo and Underwood, 2012). An additional smear slide analysis of the entire sample set has been carried out in order to quantify also the larger grain size fraction and the volcanoclastic and biogenic content of the samples. For the point counting a standard optical microscope equipped with the automated high precision Stepping Stage of PETROG was used; the related software PETROG defined the step size based on the input-measurement area. Minimum 386 particles were counted in each sample.

Geotechnical experiment set-up

NanTroSEIZE Leg 315, 316 and 333 whole round samples were transformed into cylinders of 50 mm in diameter and up to 100 mm in length (Figure 5.3a, main text) using a standard sample trimmer device. A height to diameter ratio $H_0/D_0 \approx 1$ was preferentially chosen instead of the commonly used ratio of 2, because NanTroSEIZE whole round samples are scarce. It has been observed that short cylindrical samples deform homogeneously when friction at the end faces of the sample cylinders is low (Vardoulakis, 1979; Feeser et al., 1993). Because of the set-up with bender elements and drainage system (see below) low friction is only conditionally valid, though. After preparation, samples were quickly inserted into the insulating rubber tubing and built into the deformation apparatus to prevent samples from further drying (Figure 5. 3b, main text). The rubber tubing separates the sample from the confining medium (water) in the sample chamber. The deformation apparatus is a modified triaxial cell from Moser Systemtechnik (Figure A 4.1) with maximum axial load of 20 kN and confining pressure of 1600 kPa. It is equipped with a spindle drive moving the bottom piston, a pneumatic system moving the top piston, axial load and cell pressure transducers, axial strain and displacement transducers, a pore pressure and back pressure control system, a computer for experimental operation and data acquisition, and GDS-bender elements for p- and s-wave velocity measurements (Figure A 4.1; compare also Schumann et al., *subm.*). Drainage and pore pressure measurements at the sample ends were assured by copper filter plates and filter paper.

Samples were positioned in the apparatus in their original drill core orientation. After set-up and water infill in the confining polycarbonate (Makrolon®) cylinder confining pressure and axial load were correspondingly and slowly increased to achieve an isotropic reconsolidation (Figure A 4.2). The water loss during coring, storage and preparation was compensated by a saturation stage at 300 kPa confining pressure with an applied back pressure of 280 kPa. Saturation was defined when the pore pressure reached the back pressure level within 1-2 kPa, i.e. at a difference of well below 1%. To additionally test the degree of saturation at the end of the saturation stage a so called B-check (German standard DIN 18137, part 2) was carried out resulting in B-values above 0.93 except for one sample with a low B-value of 0.81 (experiment K018). After saturation samples were brought

to experimental conditions and kept there overnight before starting axial compression (Figure A 4.2). Similar to the saturation stage also after each deformation step and the potentially following pressurization pore pressure equilibration under drained conditions was awaited for before starting the next deformation step under undrained conditions (see also methods section in main text).

Additional geotechnical results

Stress/strain-records of the pressure stepping and rate stepping experiments are presented in Figure 5. 8 and Figure 5. 9 of the main text and additional experimental data are summarized in Table A 4.1. Pore pressure/strain-records related to the experiments presented in Figure 5. 8 and Figure 5. 9 are given in Figure A 4.3 and Figure A 4.4, respectively. The pore pressure in each of the deformation steps behaves very similar to what has been observed for the single step compression tests in Figure 5. 7b of the main text. Samples which show peak stress after only a few percent axial strain followed by weakening show high and slightly further increasing pore pressure after peak stress and until finite strain. These make up the group of structurally weak samples. The other group of samples with contrasting mechanical behavior characterized by a usually strong and continuous deviatoric stress increase until finite strain shows constant or slightly decreasing pore pressure after a maximum pore pressure has been reached. Exceptions to these systematics are experiments K009, K014 and K016 (Figure A 4.3) which show increasing pore pressure in their finite deformation steps despite their structural strong behavior. These experiments, however, reached very high total strains and the imposed deformation is probably responsible for a reduced permeability in these samples. Furthermore, the rate stepping experiments at 0.5 mm/min or faster (especially K012 and K019; Figure A 4.4) did not allow for a full pore pressure equilibration during the individual deformation steps. Hence, their records cannot be interpreted in terms of a coupled stress- and pore pressure relationship. The pore pressure adaptation does not keep up with the stress change.

Remaining Mohr-diagrams from the pressure stepping experiments in addition to Figure 5. 10 of the main text are given in Figure A4.5. Also these data sets show

very consistent fits for the three Mohr circle constructions. Resulting internal friction angles and cohesion values from these plots are presented in Tab. 2 of the main text. The state of consolidation has been analyzed in deviatoric stress/effective mean stress-diagrams and the idealized paths for normal consolidation and overconsolidation are shown in Figure A 4.6 for comparison. In the normally consolidated case, the maximum σ_1 - σ_3 -values of the effective stress paths from the different confining pressure steps define the fracture line (the Mohr-Coulomb failure criterion; Figure A 4.6a). In the overconsolidated case, the effective stress path rotates into an orientation that defines the fracture line, i.e. the latter forming the tangent to the stress paths of the different confining pressure steps (Figure A 4.6b). Additional stress path diagrams which have already been described and discussed in the main text are presented in Figure A 4.7a-f. They show the range from normally consolidated to overconsolidated conditions over the different pressure levels for the accretionary prism samples (Figure A 4.7a-d) and different fracture lines have been constructed when conditions change during one pressure stepping experiment. The two samples from the incoming Philippine sea plate show the expected normal consolidation according to their low depth of recovery and the experimental confining pressures (Figure a 4.7e, f). The fit of sample K022 is not very good (dashed line in Figure A 4.7f). From the presented accretionary prism stress path diagrams in the online data repository only sample K015 from the footwall of the megasplay fault (Figure A 4.7c) shows a similar fit like the oceanic plate sediments implying undisturbed sedimentation. The other accretionary prism samples (Figure A 4.7a, d) are overconsolidated or 'quasi'-overconsolidated (Figure A 4.7b).

Table A 4.1: Experimental conditions.

experiment /steps	core number and section	type	length (mm)	displacement rate [mm/min]	confining press. [kPa]	time [s]	compaction strain [%]	strain per step [%]	bulk strain [%]	peak stress [kPa]	$(\sigma_1 - \sigma_3)/2 = $ [kPa]
K002	316-C0008A-9H-3	CT	52.8	0.01	1000	35380	6	11	17	370	
K003	315-C0001E-11H-2	CT	56.4	0.01	1000	53176	10	33	43	250	
K004 first step	316-C0004C-8H-2	PST	102.3	0.10	400	4058	3	7	10	92	88
second step				0.10	640	2979		4	14	174	172
third step				0.10	1000	13400		22	36	266	281
K005 first step	315-C0001E-11H-1	PST	95.0	0.10	400	5325	4	10	14	89	78
second step				0.10	640	2061		3	17	154	157
third step				0.10	1000	13673		25	42	228	245
K006	316-C0008A-9H-3	CT	47.0	0.10	1000	9217	4	30	34	680	
K007	316-C0006E-8H-1	CT	55.6	0.01	1000	143724	8	30	38	442	
K009 first step	316-C0006E-8H-1	CT	59.0	0.10	400	12900	6	36	42	161	
second step				0.10	655	2680		7	49	320	
third step				0.10	1000	5356		15	64	894	
K010 first step	316-C0004C-8H-2	RST	60.4	0.50	1000	40170	8	8	16	269	

A 4 Appendix Manuscript #4

second step			1,00	1000	224		2	18	342		
third step			5,0	1000	54		4	22	400		
fourth step			9,0	1000	37		22	44	423		
K011 first step	316-C0007C-7X-1	PST	55,4	0,10	400	4178	5	12	17	162	131
second step				0,10	640	1967		5	22	385	430
third step				0,10	1000	7633		22	44	936	794
K012 first step	316-C0007C-7X-1	RST	57,0	0,50	1000	742	4	10	14	746	
second step				1,00	1000	315		8	22	1064	
third step				5,0	1000	40		4	26	1207	
fourth step				9,0	1000	52		10	36	1295	
K013 first step	316-C0006E-20X-2	PST	50,5	0,10	400	4533	3	14	17	175	122
second step				0,10	640	2648		8	25	369	365
third step				0,10	1000	5608		17	42	727	605
K014 first step	316-C0008A-9H-3	PST	50,5	0,10	400	4898	4	16	20	120	95
second step				0,10	640	2117	7	27	225	246	
third step				0,10	1000	5171	16	43	465	406	
K015 first step	316-C0008C-7H-8	PST	50,4	0,10	400	2119	2	7	9	140	115
second step				0,10	640	1141		4	13	247	247
third step				0,10	1000	8308		25	38	365	376
K016 first step	316-C0007C-7X-1	PST	50,2	0,10	400	4135	2	13	15	293	206
second step				0,10	640	2206		6	21	533	535
third step				0,10	1000	5823		19	40	1013	895

K018 first step	316-C0008C-7H-8	RST	48,0	0,01	1000	28511	8	10	18	388	
second step				0,05	1000	3450		5	23	500	
third step				0,10	1000	1865		5	28	599	
K019 first step	316-C0006E-20X-2	RST	54,5	0,01	1000	31919	7	9	16	674	
second step				0,05	1000	3609		4	20	791	
third step				0,10	1000	1574		3	23	796	
fourth step				0,50	1000	365		4	27	821	
fifth step				0,50	1000	311		3	30	791	
sixth step				1,00	1000	625		18	48	794	
K020 first step	333-C0011D-2H-2	PST	62,1	0,01	400	21041	2	6	8	80	104
second step				0,01	640	25997		8	16	206	171
third step				0,01	1000	24704		7	23	346	322
K022 first step	333-C0012C-4H-5	PST	57,5	0,01	400	21001	2	6	8	88	86
second step				0,01	640	13846		4	12	179	149
third step				0,01	1000	69131		20	32	236	

Experimental deformation conditions of the compression, pressure stepping and rate stepping tests. For the stepping tests the conditions of different steps are indicated in separate rows. The undrained shear strength of the pressure stepping tests was determined as $\tau = (\sigma_1 - \sigma_3)/2$ at max. σ_1/σ_3' .

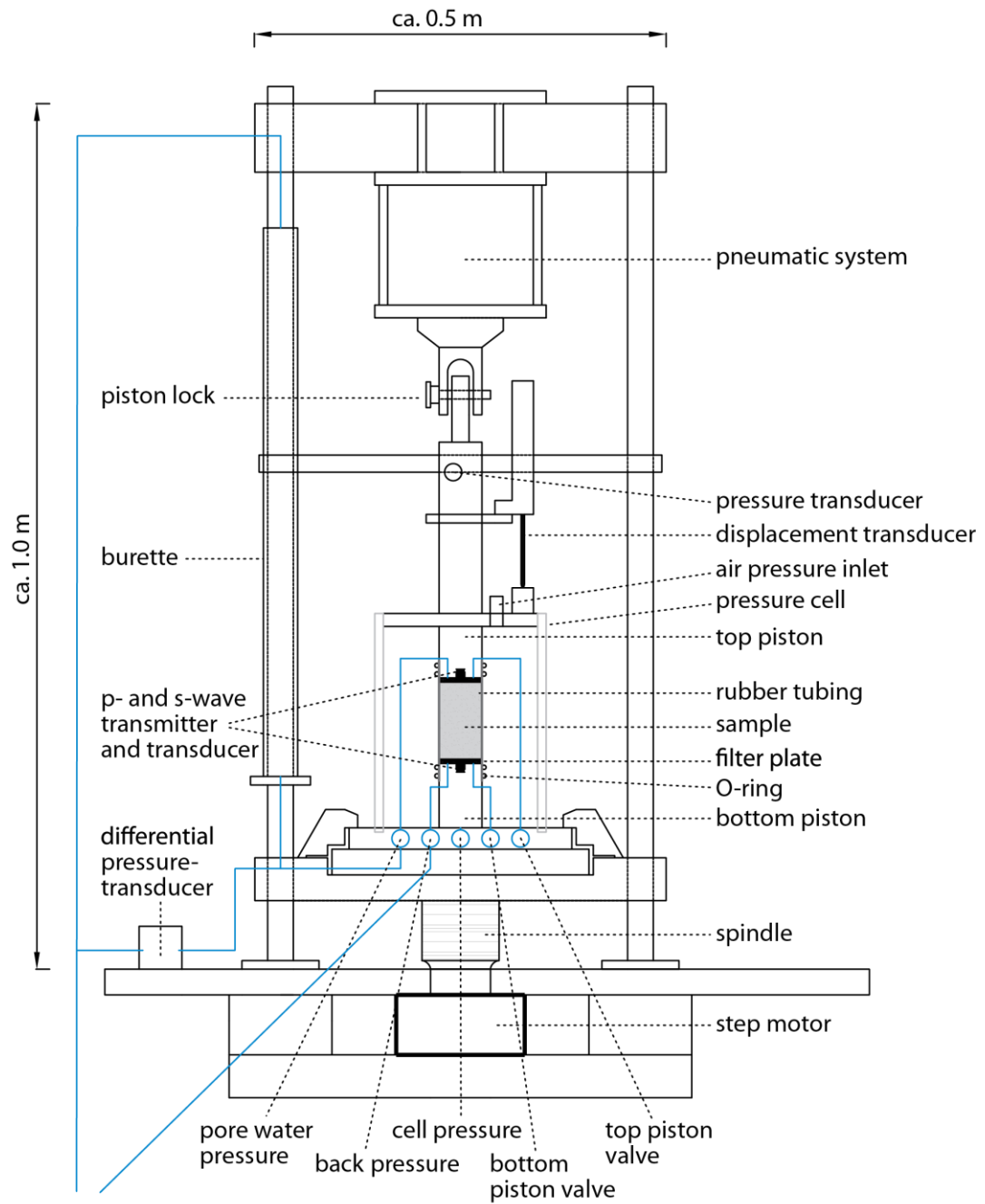


Figure A 4.1: Schematic drawing of the modified triaxial deformation apparatus from Moser Systemtechnik (only roughly to scale)

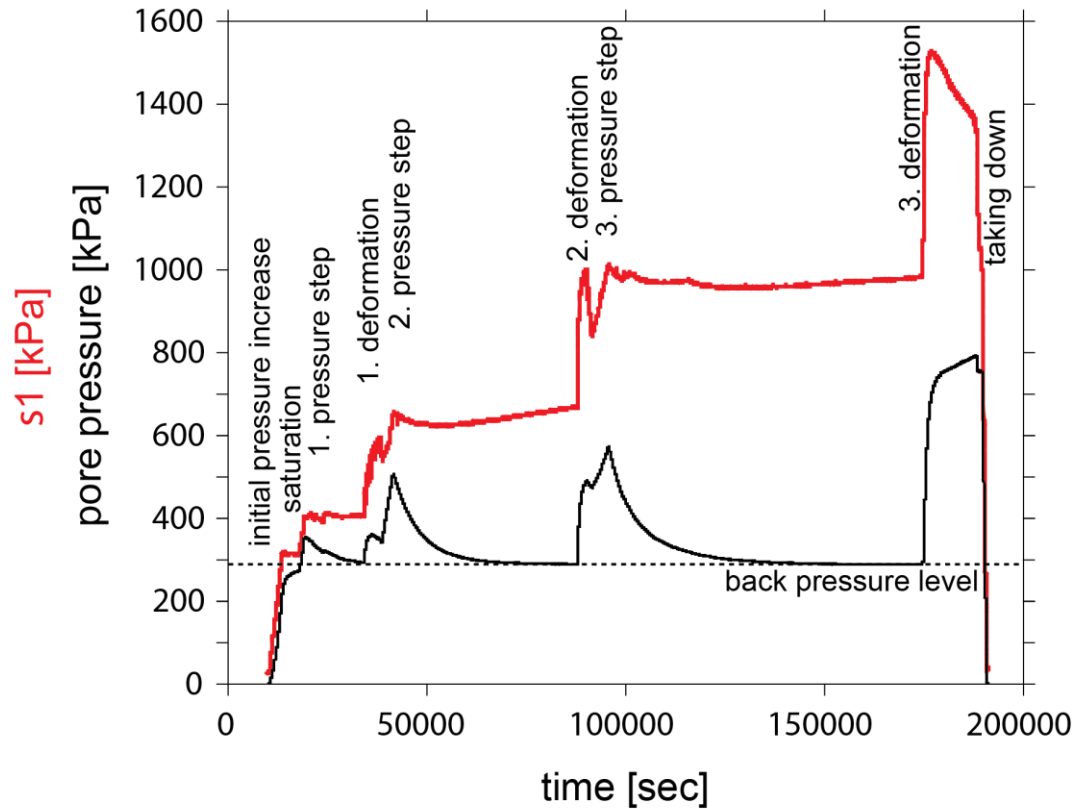


Figure A 4.2: Experimental procedure of a pressure stepping test (K005). σ_1 - (red) and pore pressure record (black) are displayed. Initial pressure increase, saturation stage, three pressurization stages, three related deformation steps (undrained conditions) and taking down of the experiment are indicated. Compression tests and rate stepping tests follow the same principal procedure; compression tests comprehend only one pressurization stage and one deformation step, in rate stepping tests the confining pressure is kept constant (one pressurization stage) and the rate is increased from step to step.

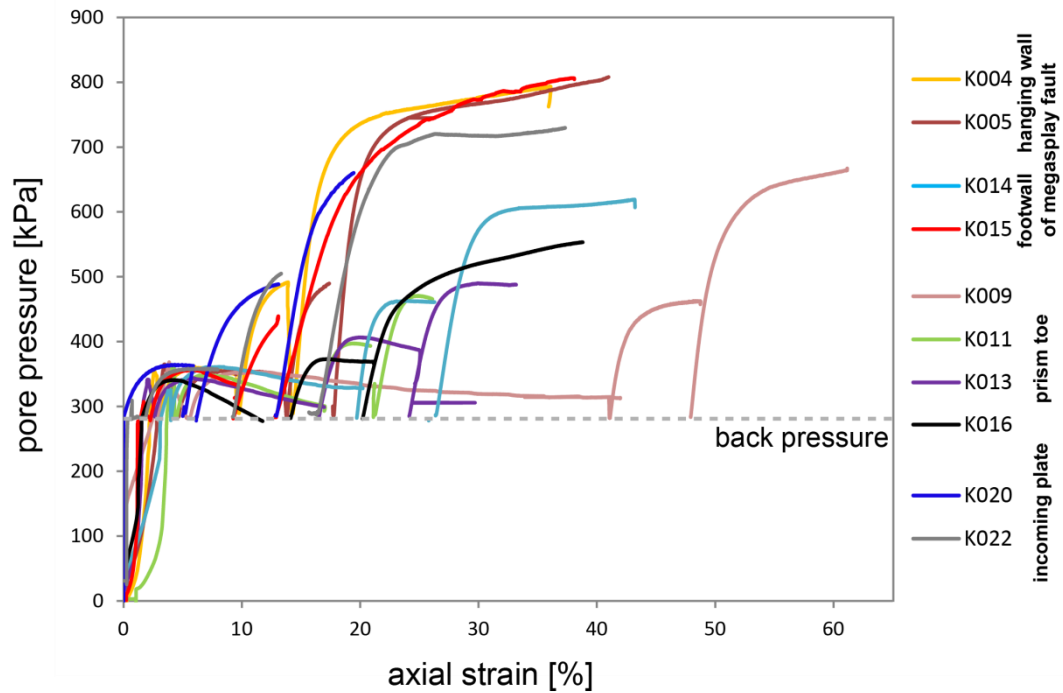


Figure A 4.3: Pore pressure/strain-records of the pressure stepping experiments at confining pressures of 400, ~640 and ~1000 kPa and constant displacement rate of 0.01 mm/min (for K020 and K022) or 0.1 mm/min (for all other experiments). Related stress/strain-records are given in Fig. 8 of the main text.

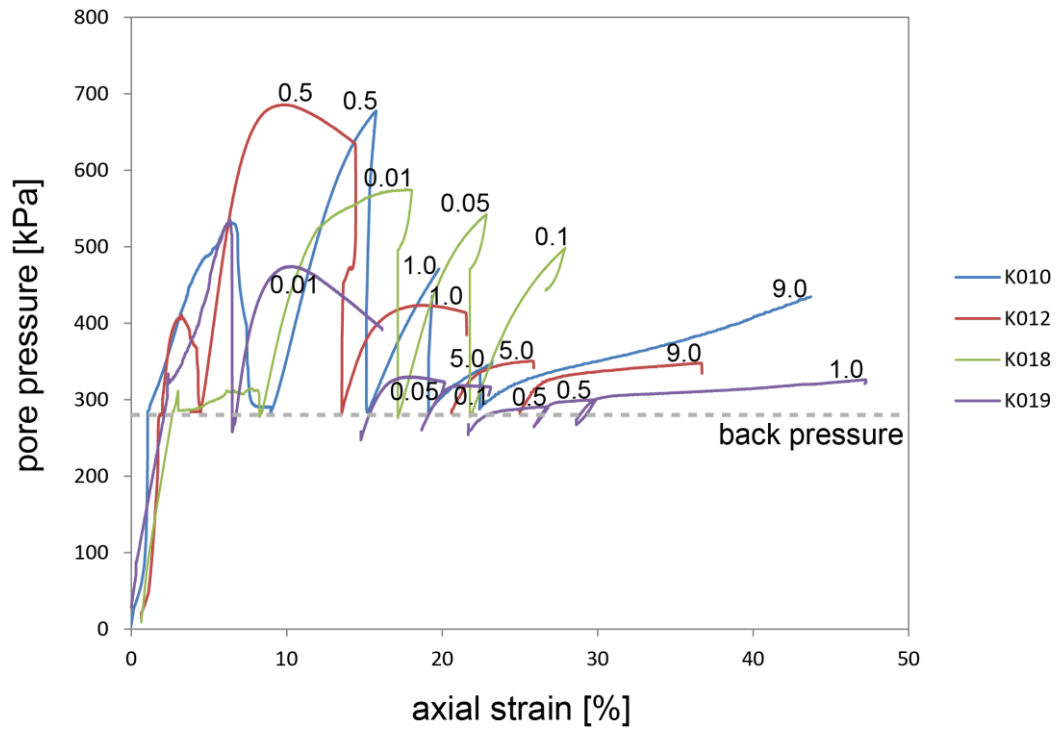


Figure A 4.4: Pore pressure/strain-records of the rate stepping experiments at constant confining pressure of ~ 1000 kPa and variable displacement rate (indicated in mm/min). Related stress/strain-records are given in Fig. 9 of the main text.

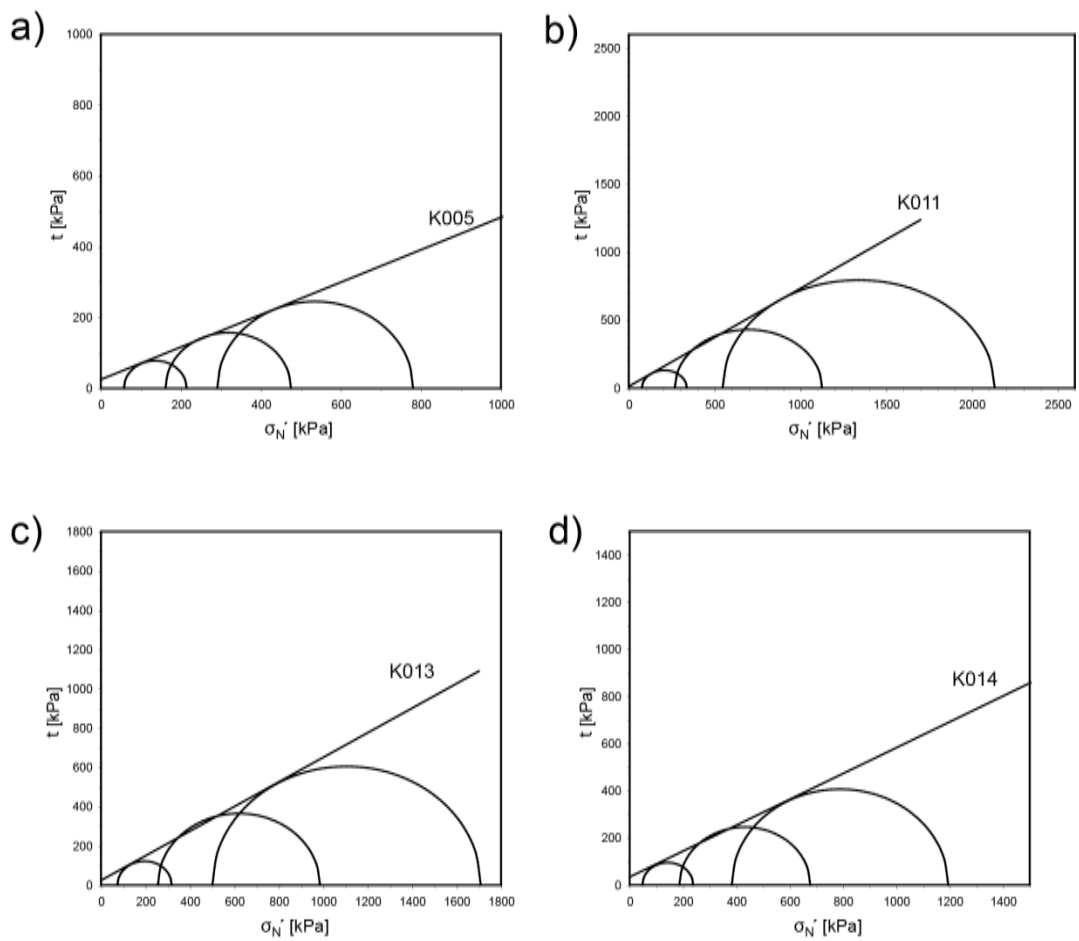


Figure A 4.5: Mohr-Coloumb diagrams from the experiments K005 (a), K011 (b), K013 (c), K014 (d) with τ (shear stress) versus σ'_N (effective normal stress) in addition to the plots presented in Fig 10 of the main text.

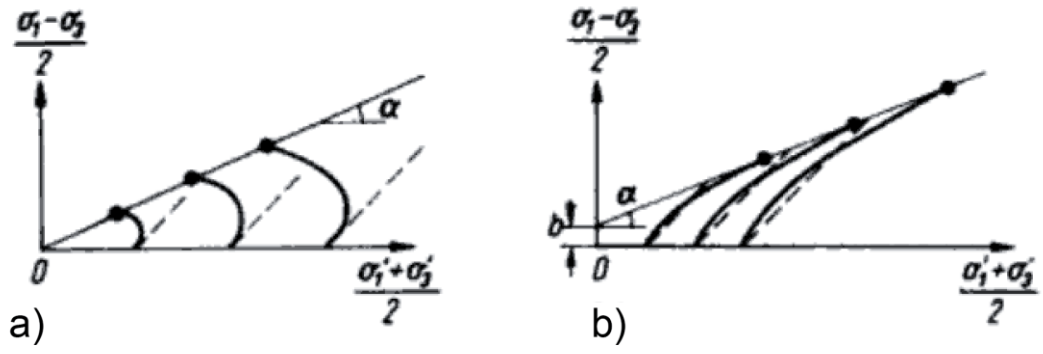
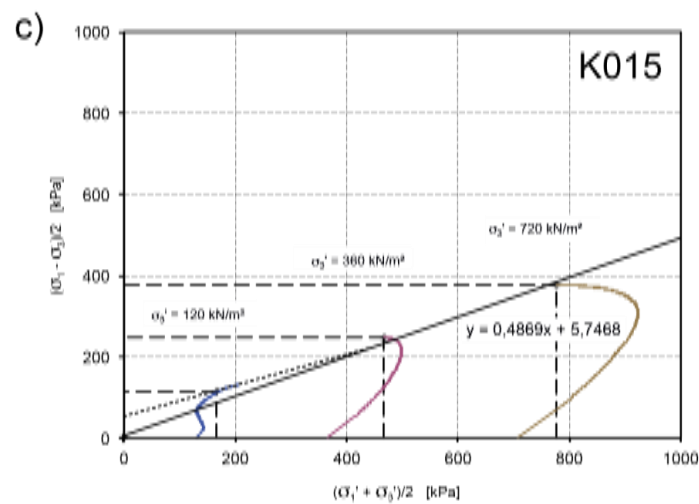
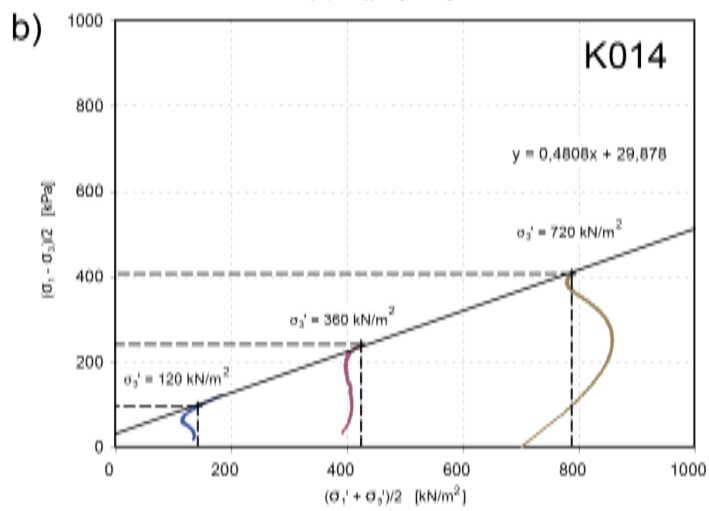
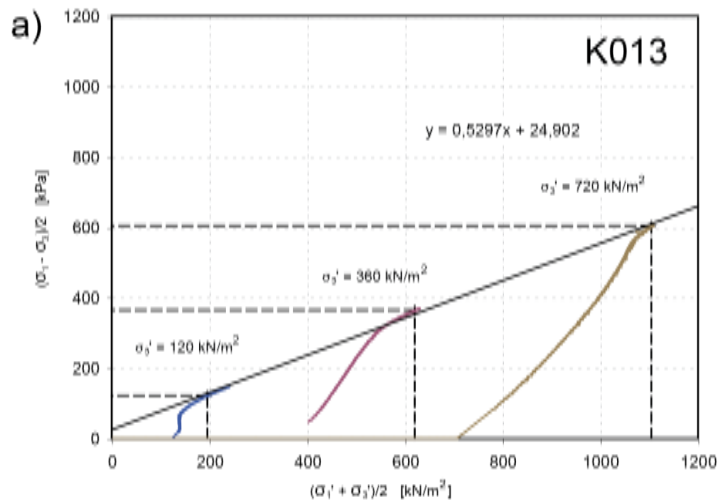


Figure A 4.6 Schematic stress path diagram indicating the state of consolidation of soft sediments in CU tests (taken from Smolczyk, 1980); a) normally consolidated and b) overconsolidated.



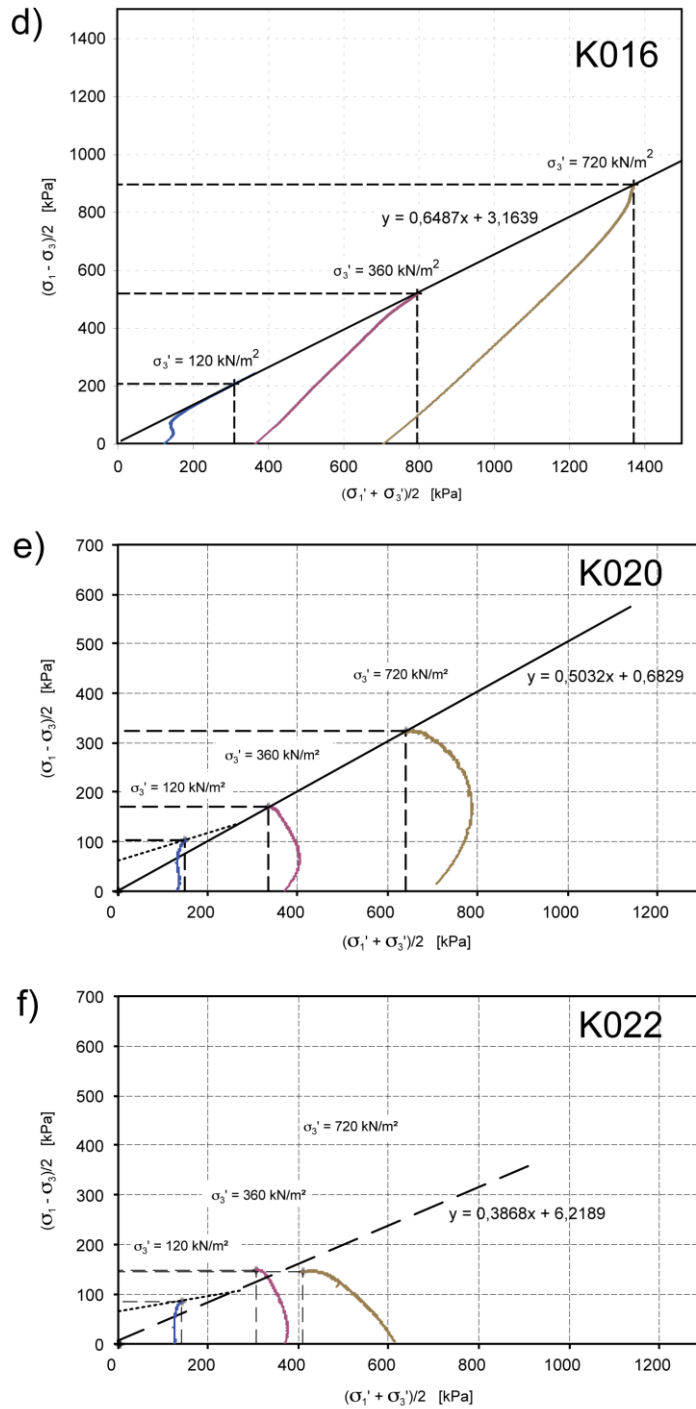


Figure A 4.7: Stress path diagrams with *kf*-line construction of the remaining pressure stepping tests (solid lines and possibly stippled lines) in addition to Fig. 11 of the main text: (a) over consolidation (K013; mbsf), (b) 'quasi'-overconsolidation (K014; 76mbsf), (c) normal consolidation (K015; 61mbsf), (d) overconsolidation (K016; 63 mbsf), (e) normal consolidation (K020; 33 mbsf), (f) normal consolidation (K022; 29 mbsf). Equations of solid *kf*-lines (solid lines; dashed line for K022, see text for explanation) and the endpoints of different stress paths (depicted by dashed lines) are indicated.

Acknowledgements

Many thanks to...

... Jan Behrmann for the scientific input, support and criticism throughout the last three years and the opportunity for free development on the scientific directions of this thesis.

... Michael Stipp for guidance, scientific input and the discussions throughout the past three years.

... Yujin Kitamura, Yoshitaka Hashimoto and Yuzuru Yamamoto for guidance during field work and sample supply.

... all colleagues who contributed to this work for the discussions and constructive criticism throughout the thesis. For the help with the data handling, providing laboratory equipment and guidance at the laboratory. Especially Dirk Klaeschen, Klaus Ullemeyer, Detlef Schulte-Kortnack, Robert Hinkens, Mario Thoener, Christof Lempp, Gerald Troeber, Bettina Domeyer and Anke Bleyer.

... Heidi Wehrmann and David Voelker for helpful advices, support and for having a sympathetic ear during the last years.

... all my friends at GEOMAR for the positive atmosphere

... Heidi Wehrmann, Jacek Raddatz, Edmund Hathorne and Jana Kunrede for proofreading.

... finally my special thanks to my wife Kerstin and my family for love, patience and support.

Curriculum Vitae

**KAI
SCHUMANN**

Permanent Address: Rusitz 5
D-07554 Gera
E-mail: kaschumann@geomar.de
Date of birth: 19.12.1983
Place of birth: Gera, Germany
Nationality: German

EDUCATION

Since 05/2010 Doctorate student at the GEOMAR
Helmholtz Centre for Ocean Research Kiel,
Germany

09/2004 – 04/2010 Diploma Study of Geology at the Martin-
Luther-Universität Halle-Wittenberg in
Halle/Saale

2000 – 2004 Secondary School in Gera